

# Fast modeling of electromagnetic fields for the design of phased array antennas in radar systems

**Citation for published version (APA):**

Morsink, B. J. (2005). *Fast modeling of electromagnetic fields for the design of phased array antennas in radar systems*. [Phd Thesis 2 (Research NOT TU/e / Graduation TU/e), Electrical Engineering]. Technische Universiteit Eindhoven. <https://doi.org/10.6100/IR596468>

**DOI:**

[10.6100/IR596468](https://doi.org/10.6100/IR596468)

**Document status and date:**

Published: 01/01/2005

**Document Version:**

Publisher's PDF, also known as Version of Record (includes final page, issue and volume numbers)

**Please check the document version of this publication:**

- A submitted manuscript is the version of the article upon submission and before peer-review. There can be important differences between the submitted version and the official published version of record. People interested in the research are advised to contact the author for the final version of the publication, or visit the DOI to the publisher's website.
- The final author version and the galley proof are versions of the publication after peer review.
- The final published version features the final layout of the paper including the volume, issue and page numbers.

[Link to publication](#)

**General rights**

Copyright and moral rights for the publications made accessible in the public portal are retained by the authors and/or other copyright owners and it is a condition of accessing publications that users recognise and abide by the legal requirements associated with these rights.

- Users may download and print one copy of any publication from the public portal for the purpose of private study or research.
- You may not further distribute the material or use it for any profit-making activity or commercial gain
- You may freely distribute the URL identifying the publication in the public portal.

If the publication is distributed under the terms of Article 25fa of the Dutch Copyright Act, indicated by the "Taverne" license above, please follow below link for the End User Agreement:

[www.tue.nl/taverne](http://www.tue.nl/taverne)

**Take down policy**

If you believe that this document breaches copyright please contact us at:

[openaccess@tue.nl](mailto:openaccess@tue.nl)

providing details and we will investigate your claim.

**Fast Modeling of Electromagnetic Fields  
for the Design of Phased Array  
Antennas in Radar Systems**



# **Fast Modeling of Electromagnetic Fields for the Design of Phased Array Antennas in Radar Systems**

PROEFSCHRIFT

ter verkrijging van de graad van doctor aan de  
Technische Universiteit Eindhoven, op gezag van de  
Rector Magnificus, prof.dr.ir. C.J. van Duijn, voor een  
commissie aangewezen door het College voor  
Promoties in het openbaar te verdedigen  
op maandag 17 oktober 2005 om 16.00 uur

door

**Bart Johan Morsink**

geboren te Alphen aan den Rijn

Dit proefschrift is goedgekeurd door de promotoren:

prof.dr. A.G. Tijhuis  
en  
prof.dr.ir. H. Blok

Copromotor:  
dr.ir. G.H.C. van Werkhoven

CIP-DATA LIBRARY TECHNISCHE UNIVERSITEIT EINDHOVEN

Morsink, Bart J.

Fast modeling of electromagnetic fields for the design of phased array antennas in radar systems / by Bart Johan Morsink. – Eindhoven : Technische Universiteit Eindhoven, 2005.

Proefschrift. – ISBN 90-386-1763-1

NUR 959

Trefw.: integraalvergelijkingen / elektromagnetische verstrooiing / elektromagnetisme ; numerieke methoden / fasegestuurde antennestelsels / frequentiefilters.

Subject headings: integral equations / electromagnetic wave scattering / computational electromagnetics / antenna phased arrays / frequency selective surfaces.

Copyright ©2005 by B.J. Morsink

Cover design: B.J. Morsink

Press: PrintPartners Ipskamp B.V., Enschede

The work presented in this thesis has been performed at and financed by Thales Nederland (formerly known as Hollandse Signaalapparaten B.V.).

# Contents

<b>Abstract</b>	<b>1</b>
<b>1 Introduction</b>	<b>3</b>
1.1 Modern Phased Array Antennas . . . . .	3
1.2 Aim of the Present Research . . . . .	6
1.3 Objectives of the Thesis . . . . .	8
1.4 Description of Array Structures . . . . .	8
1.5 Computational Method . . . . .	12
1.6 Acceleration Technique . . . . .	15
1.7 Organization of the Thesis . . . . .	16
<b>2 Basic Equations</b>	<b>19</b>
2.1 Mathematical Notation . . . . .	19
2.2 Maxwell's Equations . . . . .	22
2.2.1 Time-Domain Analysis . . . . .	23
2.2.2 Laplace-Domain Analysis . . . . .	26
2.2.3 Frequency-Domain Analysis . . . . .	28
2.3 Electromagnetic Fields in Planarly Stratified Media . . . . .	29
2.3.1 The Marcuvitz-Schwinger Equations . . . . .	30
2.3.2 The Helmholtz Equations . . . . .	30
2.4 Green's Function for a Planarly Stratified Medium . . . . .	31
2.4.1 Determination of the Mode Functions . . . . .	32
2.4.2 Mode Functions for a Cylindrical Waveguide . . . . .	37
2.4.3 Mode Functions for a Layered Space . . . . .	46
2.4.4 Modal Transmission Line Equations . . . . .	49
<b>3 Computational Method</b>	<b>55</b>
3.1 Description of the Configuration . . . . .	57
3.2 Formulation of the Boundary Conditions . . . . .	59
3.3 Application of the Equivalence Theorem . . . . .	60
3.4 Formulation of the Integral Equation . . . . .	64
3.5 Formulation of the Matrix Equation: Method of Moments . . . . .	69
3.6 Calculation of the Matrix/Vector Elements . . . . .	74
3.6.1 Calculation of the Matrix Elements . . . . .	74

3.6.2	Calculation of the Vector Elements . . . . .	77
3.7	Expansion and Weighting Functions . . . . .	79
3.7.1	Waveguide Mode Functions . . . . .	80
3.7.2	Thin Strip Functions . . . . .	81
3.7.3	Patch Functions . . . . .	82
3.7.4	Rooftop Functions . . . . .	83
3.7.5	RWG Functions . . . . .	85
3.8	Calculation of the Total Field . . . . .	86
3.8.1	Calculation of the Incident Field . . . . .	87
3.8.2	Calculation of the Scattered Field . . . . .	88
3.8.3	Formulation of the Scattering Matrix . . . . .	89
3.8.4	Formulation of the Cascading Procedure . . . . .	90
3.9	Energy Considerations . . . . .	92
3.9.1	Poynting's Theorem in its General Form . . . . .	92
3.9.2	Power Flow through the Probing Surfaces . . . . .	94
3.9.3	Reciprocal Basic Structure . . . . .	97
3.9.4	Lossless Basic Structure . . . . .	99
3.9.5	Direct Measure for Energy . . . . .	100
3.10	Calculation of the Far Field . . . . .	101
3.10.1	Far Away from a Transverse Plane . . . . .	102
3.10.2	Far Away from a Finite Volume . . . . .	103
3.11	Numerical Implementation . . . . .	106
3.11.1	Implementation of the Matrix Calculation . . . . .	106
3.11.2	Implementation of the Vector Calculation . . . . .	108
3.11.3	Reversed Transmission Line . . . . .	110
<b>4</b>	<b>Acceleration Technique</b>	<b>113</b>
4.1	General Series . . . . .	115
4.2	Subtraction of Asymptotic Series . . . . .	118
4.3	Evaluation of Asymptotic Series . . . . .	124
4.3.1	Integration for Large Argument . . . . .	125
4.3.2	Integration for Small Argument . . . . .	127
4.3.3	Determination of the Transition Point . . . . .	128
4.4	Exponential Regularization . . . . .	129
4.4.1	Rooftop Function Placed in an Orthogonal Grid . . . . .	131
4.4.2	Rooftop Function . . . . .	140
4.4.3	RWG Function . . . . .	147
4.5	Speed Improvement . . . . .	162
<b>5</b>	<b>Validation</b>	<b>169</b>
5.1	Overview of Validation Techniques . . . . .	170
5.1.1	Internal Consistency . . . . .	170
5.1.2	Commercial Software Packages . . . . .	170
5.1.3	Measurement Techniques . . . . .	170
5.2	Validation of the Computational Method . . . . .	174
5.2.1	Horizontal Dipole Frequency Selective Surface . . . . .	174

5.2.2	Crossed Dipole Frequency Selective Surface . . . . .	177
5.2.3	Gridded Square Frequency Selective Surface . . . . .	181
5.2.4	Circular Loop Frequency Selective Surface . . . . .	184
5.2.5	Square Patch Frequency Selective Surface . . . . .	187
5.2.6	Cavity Backed Patch Radiator . . . . .	192
5.2.7	Open-Ended Waveguide Radiator . . . . .	195
5.2.8	Open-Ended Waveguide with Patch Radiator . . . . .	197
<b>6</b>	<b>Conclusions and Recommendations</b>	<b>205</b>
6.1	Conclusions . . . . .	205
6.1.1	Computational Method . . . . .	205
6.1.2	Acceleration Technique . . . . .	207
6.1.3	Validation . . . . .	209
6.1.4	Applications . . . . .	209
6.2	Recommendations . . . . .	211
6.2.1	Computational Method . . . . .	211
6.2.2	Acceleration Technique . . . . .	211
6.2.3	Validation . . . . .	212
6.2.4	Applications . . . . .	212
<b>A</b>	<b>Evaluation of the Regularization Integral</b>	<b>213</b>
A.1	Reduction to Standard Integrals . . . . .	213
A.2	Integral over $-\infty < \ell < \infty$ . . . . .	214
A.3	Integral over $l_1 < \ell < \infty$ . . . . .	214
A.4	Convergence of Series . . . . .	216
<b>B</b>	<b>Transmission Line Examples</b>	<b>217</b>
B.1	Dielectric Junction with Source . . . . .	217
B.2	Dielectric Junction with Incident Wave . . . . .	219
B.3	Dielectric Junction with Offset Source . . . . .	221
B.4	Half Space with Dielectric Junction and Source . . . . .	223
B.5	Half Space with Offset Source . . . . .	224
B.6	Cavity with Source . . . . .	225
<b>C</b>	<b>Interaction between Two Waveguides</b>	<b>227</b>
C.1	TM Mode in Waveguide 1, TM Mode in Waveguide 2 . . . . .	229
C.2	TM Mode in Waveguide 1, TE Mode in Waveguide 2 . . . . .	231
C.3	TE Mode in Waveguide 1, TM Mode in Waveguide 2 . . . . .	232
C.4	TE Mode in Waveguide 1, TE Mode in Waveguide 2 . . . . .	233
C.5	Summary . . . . .	234
<b>D</b>	<b>Interaction between a Waveguide and a Layered Space</b>	<b>237</b>
D.1	TM Mode in Waveguide, TM Mode in Layered Space . . . . .	238
D.2	TM Mode in Waveguide, TE Mode in Layered Space . . . . .	239
D.3	TE Mode in Waveguide, TM Mode in Layered Space . . . . .	240
D.4	TE Mode in Waveguide, TE Mode in Layered Space . . . . .	241



---

D.5 Summary . . . . .	241
<b>E Interaction between a Rooftop and a Waveguide</b>	<b>243</b>
E.1 Magnetic TM Mode in Waveguide . . . . .	245
E.2 Magnetic TE Mode in Waveguide . . . . .	246
E.3 Electric TM Mode in Waveguide . . . . .	247
E.4 Electric TE Mode in Waveguide . . . . .	248
E.5 Summary . . . . .	249
<b>F Interaction between a Rooftop and a Layered Space</b>	<b>251</b>
<b>G Interaction between an RWG and a Waveguide</b>	<b>253</b>
G.1 Magnetic TM Mode in Waveguide . . . . .	256
G.2 Magnetic TE Mode in Waveguide . . . . .	259
G.3 Electric TM Mode in Waveguide . . . . .	263
G.4 Electric TE Mode in Waveguide . . . . .	267
G.5 Summary . . . . .	270
<b>H Interaction between an RWG and a Layered Space</b>	<b>273</b>
<b>I Interaction between a Thin Strip and a Layered Space</b>	<b>279</b>
<b>J Interaction between a Patch and a Layered Space</b>	<b>281</b>
<b>K Floquet Analysis of Periodic Structures</b>	<b>283</b>
<b>Bibliography</b>	<b>288</b>
<b>Summary</b>	<b>299</b>
<b>Samenvatting</b>	<b>303</b>
<b>Curriculum Vitae</b>	<b>307</b>
<b>Acknowledgements</b>	<b>309</b>

# Abstract

Phased array antennas (PAAs) used in military naval radar systems contain a large number of simple and identical radiating elements regularly arranged in a planar grid. To have a successful operating radar system in a stressful environment, these PAAs have to satisfy a large number of stringent requirements, such as a wide beam scanning range and a large frequency bandwidth with low losses. To achieve this, and further to reduce the costs of PAA prototype building, dedicated computational methods are used to simulate the electromagnetic (EM) behavior of PAAs. These methods support an efficient iterative PAA design process, where a number of specific design parameters is adjusted iteratively until the calculated EM response of the structure satisfies the requirements. Subsequently, a prototype is constructed and measurements are carried out. The comparison between the outcome of these measurements and the predictions determines whether the design can be finalized, or whether the design process should be continued.

On future PAAs the current requirements on beam scanning ranges and frequency bandwidths will be more stringent. Furthermore, new requirements such as a low radar cross-section signature and a low EM interference (EMI) and a high EM compatibility (EMC) will be introduced. These requirements can only be met by selecting more complex radiating elements and by increasing the number of computational design iterations. Furthermore, the design phase must include a sensitivity analysis, where the sensitivity of the EM behavior with respect to production variations is analyzed and minimized. The goal is to obtain a so-called production tolerant design. Most current design methods adjust the design parameters in a trial-and-error process. Future design methods will be more automated in this sense with the aid of synthesis techniques and search algorithms, so that a more structured design approach becomes available. All this leads to a strongly increased number of computational design iterations. With the currently available numerical methods, this would lead to unacceptably long simulation times. The objective of this thesis was to develop a computational method that can be used in this process.

Since the number of radiating elements is large, we use the infinite array approach, which assumes an infinite number of identical radiating elements with a constant progressive phase shift between the elements. This approach reduces the computation of the EM behavior for the infinite structure essentially to that of a single radiating element and rigorously takes into account the mutual

coupling between the elements. Typical radiating element structures, that can be analyzed with the computational method described in this thesis, consist of waveguide feeding elements, cavity backed patches, open-ended waveguides, and multi-layer frequency selective surfaces. To formalize the construction of such a typical unit-cell structure we use two types of building blocks: segments and junctions. Segments can be either pieces of waveguide or layered space (dielectric slabs that are infinitely long in one or two transverse directions). Each junction separates two segments and can/must contain infinitely thin arbitrarily shaped metal. Within a single radiating element there are parts (defined as basic structures) in which the junctions experience a significant EM coupling. Between the basic structures there is low EM coupling. To determine the total EM behavior efficiently we exploit this property, and separate the total calculation into one for each basic structure, and one for combining them. The calculation for a single basic structure is based on solving a coupled field integral equation with the Galerkin method of moments (MoM), and approximates this integral equation by an impedance matrix equation. The result can be used to determine a scattering matrix that characterizes the EM behavior of a single basic structure by treating the outgoing waves as being caused by the incident waves. To obtain the EM behavior of the complete configuration, we combine the scattering matrices of the corresponding separate basic structures with the aid of a cascading procedure based on the Redheffer star product.

Most of the computational effort in the procedure described above is spent in assembling the impedance matrices. We present a novel acceleration technique that translates the evaluation of an asymptotically slowly converging series, which needs to be evaluated in assembling the impedance matrices, into a numerical integration over an exponentially fast converging series by subsequently using a Kummer, an Ewald, and a Poisson transformation. This technique is applied to both rooftop and Rao-Wilton-Glisson expansion functions used in the MoM. We validate our computational method against available commercial tools such as the finite-element code HFSS, and against measurements for a variety of radiating structures. This leads to the conclusion that the computational method is indeed both accurate and fast.

# Chapter 1

## Introduction

### 1.1 Modern Phased Array Antennas

Phased array antennas are finding their way more frequently into radar systems [95, section 9.9]. These types of antennas are constructed by assembling radiating elements in a geometrical configuration, and are shortly referred to as an array. In most cases, the elements of the array are identical and they are placed in a regularly arranged planar grid. The total field of the array is determined as the superposition of the fields radiated by the individual elements. To provide for directive patterns, it is necessary to have the fields from the elements of the array interfere constructively (add) in the desired directions, and interfere destructively (cancel each other) in the remaining space. Further, by controlling the progressive phase difference between the elements, the maximum radiation can be steered into any desired direction to form a scanning beam [95, section 9.5].

The main advantage of phased array antennas over other types of antennas is this inertialess, rapid beam steering. The beam from an array can be scanned, or switched from one position to another, in a time limited by the switching speed of the phase shifters and the electronic control logic behind the phase shifter. This includes the calculation of the beam parameters for each individual array element. Therefore, electronic beam scanning in arrays facilitates multiple functions, for example, scanning, tracking and missile guiding. The ability to steer the beam electronically can also be used to stabilize the beam direction when the phased array antenna is on a platform, such as a ship or aircraft, that is subject to roll, pitch, or yaw.

Another advantage is the control of the radiation pattern [95, sections 9.11, 9.13, 9.15]. A particular radiation pattern may be more readily obtained with the array than with other microwave antennas since the amplitude (receive mode) and phase of each array element may be individually controlled. Thus, radiation patterns with extremely low sidelobes or with a specifically shaped main beam may be achieved. For example, a typical radar search pattern starts

with a wide beam to prescan a given large area in a short amount of time. Then directive narrow patterns zoom in on specific smaller areas of interest and perform a high-resolution scan. The natural lower limit for the narrowest beam is given by the size of the array. Typical radar track patterns use separate monopulse sum and difference beams, each with its own optimal shape. These beams allow for an accurate estimation of the target direction within the beam.

Phased array antennas can be used within digital beamforming [95, section 9.9]. In this situation, each element or line of elements is connected to an individual receiver with a digitized output. These outputs are then combined by using a digital beam-forming processor to form multiple, simultaneous and directive beams. This process can also be implemented with the use of analog components. The accompanying transmitting antenna must have a broad beamwidth that covers the same total angular region as the multiple receiving beams. The advantage of digital beamforming compared to classical beamforming is that with a single reception a multiple-beam response is obtained at once. The outputs from the multiple beams can further be processed in parallel by the radar.

The disadvantage that has limited the widespread use of phased array antennas in radar systems is their high cost [95, section 9.14]. This is mainly due to the mechanical and beamsteering complexity and the high costs of the various (mainly active) components. Also the development, full testing and calibration is more complicated for a phased array antenna than for conventional antennas. Usually the development is done step-by-step, where different prototypes with increased complexity are constructed and tested, which also increases the costs.

Another disadvantage of phased array antennas over other types of antennas is the complexity of the RF aspects of the design. The use of arrays implies the appearance of grating lobes, the presence of blind scan angles, beam broadening and gain loss for scanned beams, and a high variation in return loss. If these effects are not considered well enough during the design phase, they can have a negative influence on the array performance.

A recent and innovative example of an application of a phased array antenna in a naval radar system is the active phased array multi-function radar (APAR) from Thales Nederland B.V. (formerly known as Hollandse Signaalapparaten B.V.) [44, 96]. APAR meets the modern ship's stringent requirements for low-elevation detection, short reaction time and large defensive fire power by effectively integrating many different radar functions such as search, track and missile guidance capabilities (shown in figure 1.1). Its non-rotating antenna (shown on top of the latest LCF frigate of the Royal Dutch Navy in figure 1.2) houses four phased array antenna faces that together cover the full 360 degrees. Each phased array antenna face (shown in figure 1.3) is an X-band waveguide array and consists of more than 3000 radiating elements, each connected to an individual transmitter/receiver element.

To construct a successful operating radar system in a stressful environment, these phased array antennas have to satisfy a large number of stringent requirements. The main requirement on the electromagnetic behavior of the antenna is low return losses (better than -10[dB]) for a wide beam scanning range (at

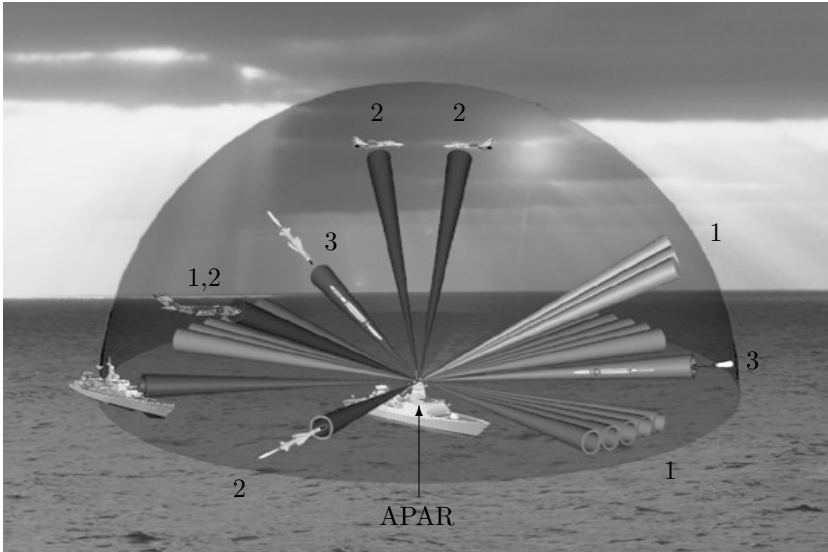


Figure 1.1: APAR search (1), track (2) and missile guidance (3) capabilities.



Figure 1.2: Complete operational APAR antenna on top of the latest LCF frigate of the Royal Dutch Navy.

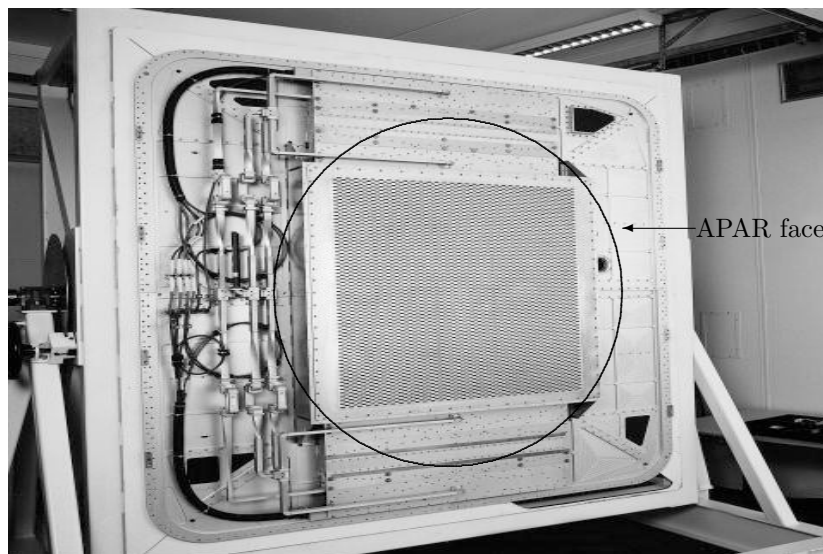


Figure 1.3: Single open APAR face from the front side in the preparation (“Setting to Work”) phase at Thales Nederland.

least 50[deg] off-broadside) and for a large relative frequency bandwidth.

## 1.2 Aim of the Present Research

To satisfy the stringent requirements, and further to reduce the costs of phased array antenna prototype design, dedicated computational methods are used to simulate the electromagnetic behavior of phased array antennas. These methods support an efficient iterative phased array antenna design process [9].

Each design process of an antenna, in particular an antenna array, is unique. The process is multi-disciplinary, flexible, influenced by circumstances and pragmatic decisions. Formulating the requirements of the antenna performance parameters is the start of the design process. The requirements are a quantification of two main goals of antenna design: the input energy should be radiated in a well defined direction and the energy loss should be minimized. The requirements are specified for a certain frequency bandwidth and a beam scanning range.

The selection of the antenna type and a first estimate of suitable geometry parameters is usually done by antenna engineers with extensive practical experience [95, section 9.8]. This decision is based on what is possible, how much it costs, and what is the desired performance. Subsequently, dedicated computational methods are used to predict the array or antenna performance. As long as the requirements are not met, the selection of antenna geometry parameters is adjusted. Generally, this process of adjusting parameters is a process of ed-

uated guess, where the practical experience of the antenna designers plays an important role. Subsequently, a prototype is constructed and measurements are carried out. The comparison between the outcome of these measurements and the predictions determines whether the design can be finalized, or whether the design should be continued.

On future phased array antennas the requirements on beam scanning ranges and frequency bandwidths will become more stringent. Wider frequency bandwidths can improve electronic counter-counter measures [94, section 14.5], and can reduce low-elevation multi-path effects [95, section 4.5]. Multiple frequency bands allow for integrated topside design concepts and can reduce the total number of antennas by integrating more functions into a single antenna [94, section 8.10]. Furthermore, higher frequency (up to Ku-band) bands are used to support new littoral warfare functions. Wider beam scanning ranges are used to increase scanning coverage and to reduce the number of phased array antennas per system (possibly from four to three) while maintaining a 360 degrees azimuthal view; thus a cost reduction is achieved. From a commercial (reducing cost to stay competitive) and project management point of view, we see a tendency towards an overall reduction of planned design time. This means that the construction of intermediate prototypes is reduced. Sometimes there is not even time for a single prototype. This requires reliable simulation tooling and design skills.

Furthermore, new requirements such as a low radar cross-section signature and a low electromagnetic interference (EMI) and a high electromagnetic compatibility (EMC) will be imposed [63]. Electromagnetic interference is defined as the degradation of the performance (vulnerability) of the equipment, transmission channel system caused by an electromagnetic disturbance. Electromagnetic compatibility is defined as the ability of a device or system to function satisfactorily in its electromagnetic environment without introducing intolerable electromagnetic disturbances (susceptibility) to anything in that environment. Both these requirements are imposed on modern phased array antenna systems, which are becoming increasingly more sensitive. This means that each system on its own cannot be disturbed by or disturb any other neighboring system.

Both the new requirements and the more stringent old requirements can only be met by selecting more complex radiating elements and by increasing the number of computational design iterations.

Furthermore, the design phase must include a sensitivity analysis, where the sensitivity of the electromagnetic behavior with respect to production variations is analyzed and minimized. This type of analysis gives us the optimal direction in which the system can be changed and the sensitivity to the various design parameters. The goal is to obtain a so-called production tolerant design. Each design parameter or combination of design parameters is varied along a nominal value within the production tolerance for a number of values. The electromagnetic behavior is calculated for each variation. A sensitivity analysis therefore also increases the number of computational design iterations. Furthermore, the real antenna performance can only be seen at the stage of the full scale prototype where the effects of all the production tolerances of the various parts are



combined. Major changes due to unforeseen errors cannot be made any more at that stage.

Most current design methods adjust the design parameters in a trial-and-error (engineering) process. Future design methods will be more automated in this sense with the aid of synthesis techniques and search algorithms, allowing for a more structured design approach. Search algorithms are based on minimizing a cost function that represents in some way how well the requirements are satisfied as a function of the design parameters. Each evaluation of this cost function involves a computational design iteration. Typical search algorithms make use of deterministic gradient methods or stochastic genetic algorithms. Synthesis techniques [102] use a conceptualization of the electromagnetic behavior in terms of filter and network circuit theory. These techniques also require a number of full-wave analysis iterations.

The developments described above lead to a strongly increased number of computational design iterations. With the currently available numerical methods, where a typical iteration for a typical structure can last from one to four hours (based on a computer with a Pentium 4 running at 2.6[GHz] with 2[Gb] of physical memory), this would lead to unacceptably long simulation times.

### 1.3 Objectives of the Thesis

The first objective of this thesis is to develop a computational method that can predict the electromagnetic behavior for an arbitrary radiating array structure consisting of waveguide feeding elements, cavities, patches, open-ended waveguides, and multilayer frequency selective surfaces.

The second objective of this thesis is to accelerate the computational method to speed up the current and future design process of phased array antennas.

### 1.4 Description of Array Structures

In this section we describe the typical array structures that we can analyze with the computational method developed in this thesis. Figure 1.4 shows such a configuration of a single radiating element (unit-cell structure) for an arbitrary but typical array structure. The element consists from the bottom to the top of a feeding slot with an opening in a cavity-backed patch structure. Above the patch we have a double-layer frequency selective surface (FSS) which consists of two thin metallic screens packed in between dielectric layers.

To formalize the construction of such a single unit-cell structure we identify two types of building blocks: segments and junctions. Segments can be either pieces of waveguide or layered space (dielectric slabs that are infinitely long in one or two transverse directions). Each junction separates two segments and contains infinitely thin arbitrarily shaped metal. To show this formalization, figure 1.5 shows in detail the construction of this typical unit-cell structure.

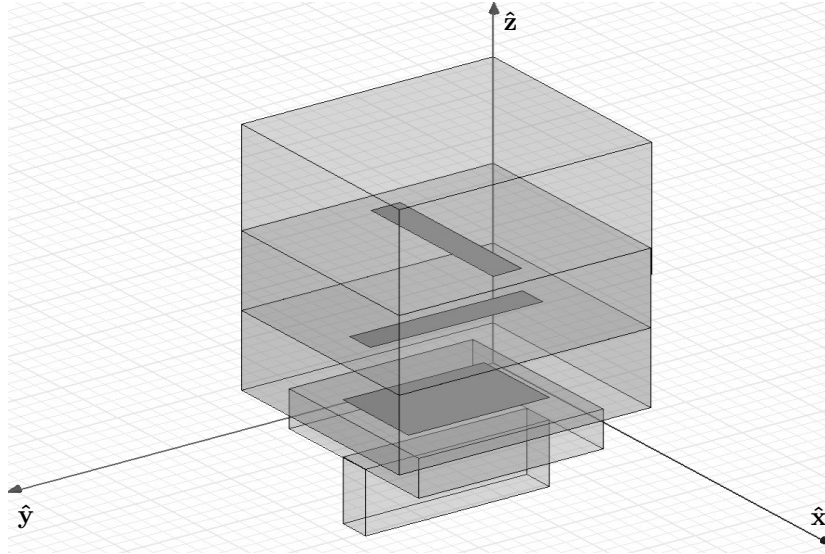


Figure 1.4: Typical unit-cell structure: feeding slot with an opening in a cavity-backed patch structure covered with a multilayer frequency selective surface.

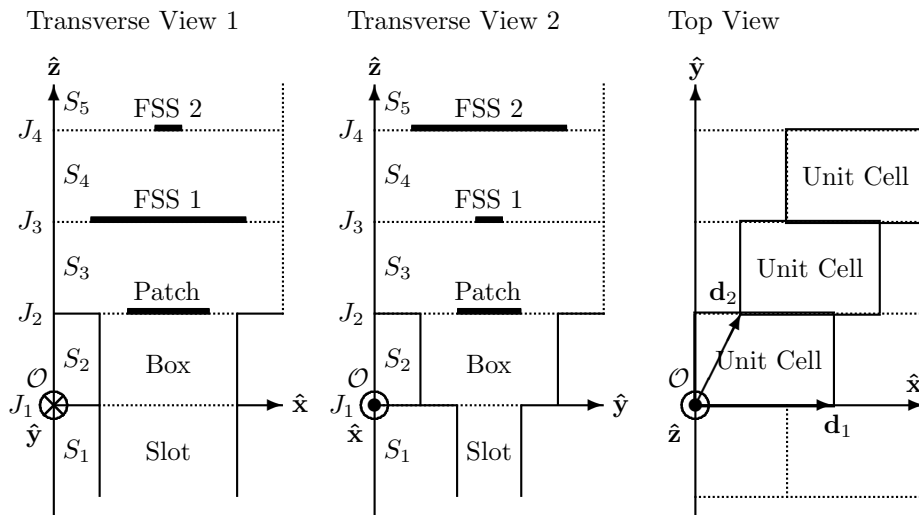


Figure 1.5: Typical unit-cell structure: feeding slot with an opening in a cavity backed patch structure covered with a multilayer frequency selective surface.

From this example configuration we recognize the following segments and junctions:

- segment  $S_5$ : free space (layered space),
- junction  $J_4$ : FSS 2,
- segment  $S_4$ : second dielectric layer (layered space),
- junction  $J_3$ : FSS 1,
- segment  $S_3$ : first dielectric layer (layered space),
- junction  $J_2$ : patch,
- segment  $S_2$ : box (waveguide),
- junction  $J_1$ : aperture between slot and box,
- segment  $S_1$ : slot or feeding waveguide (waveguide).

The unit-cell structures are placed in a regularly arranged planar grid which is spanned by two basis vectors  $\mathbf{d}_1$  and  $\mathbf{d}_2$  situated in the  $x, y$ -plane. Without loss of generality the  $x$ -axis has been chosen parallel to  $\mathbf{d}_1$ .

Note that we do not handle vertical metallic structures except for the vertical metallic walls in waveguide segments. This also means that we do not consider coaxial feeding structures with vertical feeding metallic lines. The method developed in this thesis can however be extended to include these type of structures. From a cost and complexity point of view, vertical metallic structures are difficult to fabricate and therefore significantly increase the costs of the antenna. The electromagnetic properties of a segment are further considered homogeneous and isotropic, and are characterized by the relative permittivity, relative permeability, and the electric loss tangent (conductivity). The metal in the junction is considered infinitely thin and perfectly electric conducting. The arbitrary shape must be constructed from rectangular or triangular primitive elements. Examples of a construction in terms of primitive elements are given in figures 1.6 and 1.7.

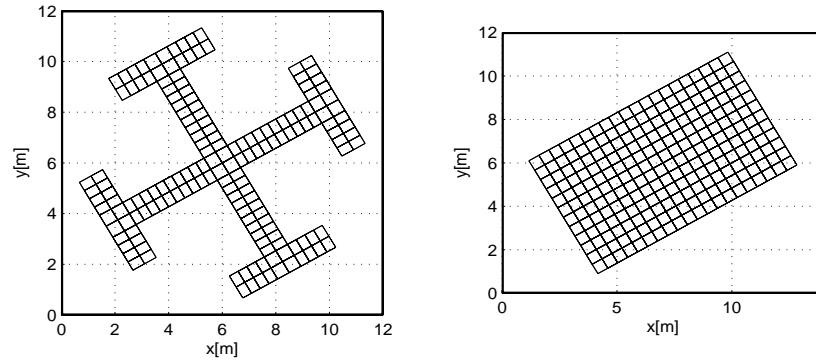


Figure 1.6: Examples of metal shapes in a junction, and their construction from the rectangular primitive element.

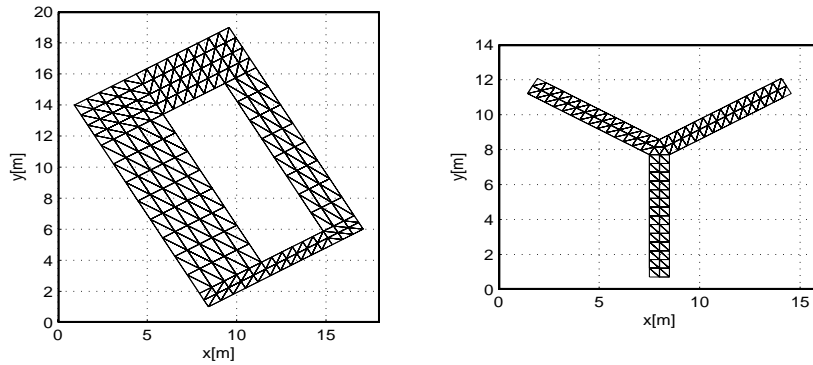


Figure 1.7: Examples of metal shapes in a junction, and their construction from the triangular primitive element.

The placement of building blocks is subject to a number of rules. First, the unit-cell structure must contain at least one segment. Second, a junction must always be placed between two adjacent segments. Third, for a given waveguide segment, the adjacent junctions must hide the outer side of the waveguide from the adjacent segments. This hiding process amounts to appropriately placing metal in the junction and reflects the construction of a practical unit-cell structure (an example of which is shown in figure 1.8).

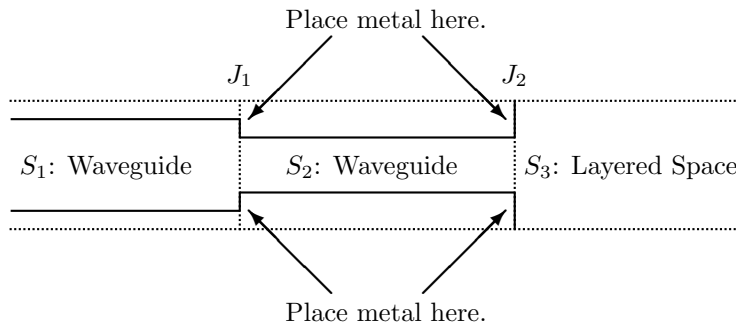


Figure 1.8: Hiding process: adjacent junctions  $J_1$  and  $J_2$  of a waveguide segment  $S_2$  must hide the outer side of the waveguide  $S_2$  from the adjacent segments  $S_1$  and  $S_3$  by placing metal in the junctions  $J_1$  and  $J_2$ .

With these two building blocks and placement rules we can construct a unit-cell structure by placing an arbitrary number of segments  $S_m$  separated by junctions  $J_m$  (shown in figure 1.9).

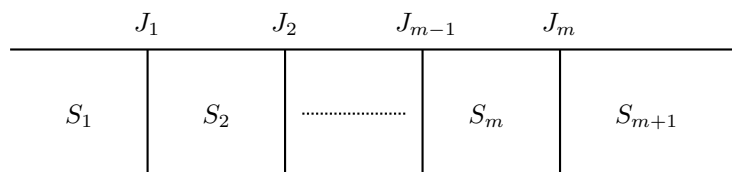


Figure 1.9: Arbitrary unit-cell structure: segments  $S_m$  separated by junctions  $J_m$ .

## 1.5 Computational Method

In this section we describe the computational method. Since the number of radiating elements is large, we use the infinite array approach, which assumes an infinite number of identical radiating elements with a constant progressive phase shift between the elements and a corresponding incident plane wave for the excitation. This approach reduces the computation of the electromagnetic behavior for the infinite structure essentially to that of a single radiating element [112, chapter 7] and rigorously takes into account the mutual coupling between radiating elements.

However, the infinite-array approach cannot account for edge effects caused by the finiteness of the array, and cannot account for the difference between the behavior of edge elements and their infinite-array behavior when mutual coupling between the elements is strong. If no surface waves are excited, these edge effects will only change the behavior of nearby located radiating elements, which represent only a small portion of the large array. This is further supported by the low mutual coupling design goal. The finite array thus behaves like a truncated infinitely large array. On the other hand, if the array is excited such that surface waves appear and resonate (due to reflection) between the edges of the finite array, these edge effects will have an impact on elements far away from these edges, and this will significantly change the array performance [9]. However, the appearance of surface waves can also be predicted with the infinite-array approach. So we can predict where this will happen, but not what will happen in that case. This creates a situation in which we can avoid the appearance of resonant surface waves already in the first phases of the phased array antenna design by using the infinite-array approach. Furthermore, finite-array simulation models are time consuming compared to infinite-array simulation models and consider relatively simple radiating element structures.

Within a single radiating element there are parts (basic structures) in which the junctions experience a significant electromagnetic coupling (the concept of electromagnetic coupling is based on the number of accessible modes in the neighboring segment, which will be defined and explained later in chapter 3). Between the basic structures there is low electromagnetic coupling. To determine the total electromagnetic behavior efficiently we exploit this property, and separate the total calculation into one for each basic structure, and one for

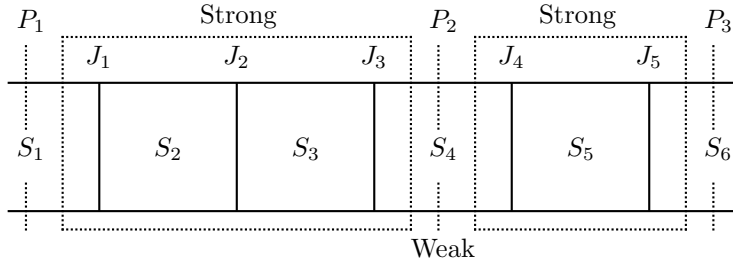


Figure 1.10: Discrimination of strong and weak electromagnetic coupling within the unit cell structure. Placing probing interfaces in between weakly electromagnetically coupled junctions. At the plane  $P_2$  the coupling is low if the number of accessible modes is small. At a plane within  $S_2$  and  $S_3$ , for instance, the number of accessible modes is in this case high. This is the reason why the junctions  $J_1$ ,  $J_2$  and  $J_3$  are analyzed by the coupled integral equations technique. Cascading the relevant generalized scattering matrices is not convenient because the cascading operation requires the inversion of a matrix whose size is equal to the number of accessible modes.

combining them. The separation of the total unit-cell structure into separate basic structures is done by placing probing interfaces  $P_m$  (shown in figure 1.10) in between the segments where the two adjacent junctions experience a low electromagnetic coupling.

For the calculation of the electromagnetic behavior within a single basic structure we formulate the scattering field problem and ensure the existence and uniqueness of a field solution within the basic structure by supplementing proper boundary conditions<sup>1</sup>.

The final objective of the simulation is to compute the field radiated by a given source in a complicated structure. If the Green's function of this structure were known, the computation could be carried out without difficulty and there would be no need to apply the equivalence theorem. However, by closing some gaps or removing some metal parts, we obtain simpler regions where the Green's function is known, as a modal expansion (also known as the Green's function in spectral form). The equivalence theorem says that in order to have the same field in the original and the modified structure, it is necessary to introduce suitable current distributions. The actual value of these currents cannot be given explicitly, but can be determined by the solution of an integral equation. Integral, because the relationship between currents and fields is always of integral type, with a kernel which is the Green's function, which is known in each sub-domain.

The equivalent scattering field problem is solved by using a so-called com-

<sup>1</sup>In electromagnetic engineering applications, the existence of the solution is taken for granted. Moreover, boundary conditions are not introduced to ensure uniqueness, even if one often reads this strange sentence, but to link the subdomains where Maxwell's equations in differential form are to be solved.

bined field integral equation technique. The unknown surface currents are discretized in terms of expansion functions, such as the rooftop [104] and Rao-Wilton-Glisson functions [88], and subsequently determined by the method of moments. The choice of the expansion functions depends on the shape of the support of the unknown surface currents. Complex shapes can be approximated with more freedom by using Rao-Wilton-Glisson functions, whereas simpler shapes such as rectangular regions require only rooftop functions. This method of moments approximates the integral equation by a matrix equation of the type  $L\mathbf{u} = \mathbf{f}$  with linear operator  $L$ , unknown vector  $\mathbf{u}$ , and forcing vector  $\mathbf{f}$ . Due to the infinite-array approach, the calculation of the matrix and vector elements is reduced from integrals to infinite summations over Floquet modes. The matrix equation can be solved by means of simple inversion of  $L$ , or by making use of more sophisticated iterative schemes [91, 109].

Once we have solved the unknown surface currents with the method of moments, we calculate the total electromagnetic field at any given location within the basic structure. To calculate the electromagnetic behavior of the total unit-cell structure, we must combine the individual electromagnetic behavior of all basic structures. For this purpose we formulate a so-called generalized scattering matrix [31], which characterizes this behavior for all basic structures individually, by expressing the outgoing waves in terms of the incident waves. Then we formulate a procedure that cascades two generalized scattering matrices [112, section 6.3] (the principle is illustrated in figure 1.11). The result is a new generalized scattering matrix that characterizes the electromagnetic behavior of the combination of the two basic structures. The scattering matrix approach gives us the opportunity to split the total structure into separate parts. Some parts such as complex balun-type feeding structures, that cannot be simulated with the computational method described in this thesis, can be simulated with other more dedicated (slower) software packages. As long as we are able to formulate a scattering matrix of such a part, it can be cascaded with the scattering matrices representing the other parts to arrive at the total electromagnetic behavior.

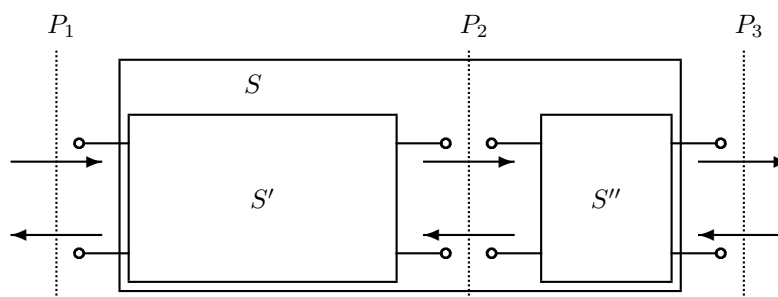


Figure 1.11: Characterization of total electromagnetic behavior in terms of separate scattering matrices per basic structure and by cascading scattering matrices of all separate basic structures.

## 1.6 Acceleration Technique

In this section we describe the acceleration technique that drastically reduces the computation time needed for calculating the unknown field within the basic structure. Most of the computational effort in the computational method is spent in assembling  $L$ , i.e., in the evaluation of an asymptotically slowly converging series, that needs to be evaluated for each element of  $L$ . This problem has been addressed in the literature [17, 80, 93]. We present a novel acceleration technique [89] that translates the evaluation of the asymptotically slowly converging series into a numerical integration over an exponentially fast converging series. This technique reduces the time needed to evaluate these series and consists of three steps.

The first step is a Kummer transformation [2, section 3.6.26], where the asymptotically slowly converging part of the series is subtracted (resulting in a rapidly converging reduced series) and added (resulting in a slowly converging correction series). The second step is an Ewald transformation [85, 40], where the asymptotically slowly converging correction series is converted into an integration over  $\tau$  of exponentially fast decaying functions. These functions contain an exponentially fast converging series for which the leading-order term is given by  $\exp(-k_t^2 \tau^{2\lambda})$ .  $k_t^2$  denotes the squared norm of the transverse wavevector.  $\lambda$  denotes an arbitrary parameter which must not be confused with the wavelength. The third step is to split the integration over  $\tau$  into one for small  $\tau$ , i.e., over the interval  $(0, \tau_1)$ , and one for large  $\tau$ , i.e., over the interval  $(\tau_1, \infty)$ . Then we apply a so-called Poisson transformation [79] for the integration over small  $\tau$ , where the relatively slow convergence of the series within the exponentially fast decaying function, caused by the behavior of  $\exp(-k_t^2 \tau^{2\lambda})$  for small  $\tau$ , is converted into an exponentially fast converging series. The leading-order term for the integration over small  $\tau$  is given by  $\exp(-\rho^2/(4\tau^{2\lambda}))$ .  $\rho^2$  denotes the squared norm of the position vector.

The so-called transition point  $\tau_1$  is a compromise between the convergence behavior of the leading-order terms  $\exp(-k_t^2 \tau^{2\lambda})$  and  $\exp(-\rho^2/(4\tau^{2\lambda}))$ . The Poisson transformation step results in the evaluation of a so-called exponential regularization of (a combination of) the expansion and weighting functions. The overall success of this acceleration technique critically depends on the possibility of being able to quickly evaluate the relevant integrals of the regularization. Since the regularization is independent of angle of incidence, frequency and medium parameters we calculate it at the beginning of the computation and store it in a lookup table. The generation of this table creates a trade-off situation where we can decide whether or not we use the acceleration technique. Since it takes time to generate the lookup table, a critical amount of simulations steps (break-even point) exists where the computational method with the acceleration technique becomes faster than the unaccelerated computational method.

Furthermore, we consider three specific choices for the expansion and weighting functions that lead to workable analytical solutions and numerical approximations for the exponential regularization. The first case is the rooftop function defined in an orthogonal grid, which creates a restriction in the modeling of the



unknown surface currents. However most structures do not consist of arbitrarily shaped metal patches and apertures, and can therefore be captured in this orthogonal grid. An advantage of this grid is that we can express the exponential regularization in terms of complementary error functions. In some cases where the unit-cell structure cannot be represented in an orthogonal grid we use the second case where the rooftop function is defined in an arbitrary grid. In this case, we express the exponential regularization as a convolution of two analytically known functions both with "almost" compact support. The third case is the more general Rao-Wilton-Glisson function. With this triangular expansion function we can model the unknown currents in the most arbitrary way. In this case, we can express the exponential regularization as a convolution of two numerically approximated functions both with "almost" compact support. These functions can also be evaluated by using an analytical approximation.

## 1.7 Organization of the Thesis

In chapter 2 we formulate the basic equations, i.e., Maxwell's equations, that describe the behavior of electromagnetic fields in general and within planarly stratified media. We derive a Green's function formulation for a planarly stratified medium. We distinguish here between two types of such media: the waveguide and the layered space.

In chapter 3 we then use these equations to develop a computational method (with a software implementation called Luxaflex) that calculates the unknown electromagnetic field within the array antenna structure. Since the number of radiating elements is large, we use the infinite array approach, which assumes an infinite number of identical radiating elements with a constant progressive phase shift between the elements. This approach reduces the computation of the electromagnetic behavior for the infinite structure essentially to that of a single radiating element. Within a single radiating element there are parts (basic structures) in which the junctions experience a significant electromagnetic coupling. Between the basic structures there is low electromagnetic coupling. To determine the total electromagnetic behavior efficiently we exploit this property, and separate the total calculation into one for each basic structure, and one for combining them. The calculation for a single basic structure is based on solving a coupled field integral equation with the Galerkin method of moments (MoM), and approximates this integral equation by an impedance matrix equation. The result can be used to determine a scattering matrix that characterizes the electromagnetic behavior of a single basic structure by treating the outgoing waves as being caused by the incident waves. To obtain the electromagnetic behavior of the complete configuration, we combine the scattering matrices of the corresponding separate basic structures with the aid of a cascading procedure based on the Redheffer star product.

Most of the computational effort in the procedure is spent in assembling the

impedance matrices. In chapter 4 we present a novel acceleration technique that translates the evaluation of an asymptotically slowly converging series, that needs to be evaluated in assembling the impedance matrices, into a numerical integration over an exponentially fast converging series by using a Kummer, an Ewald, and a Poisson transformation. This technique is applied to both rooftop and Rao-Wilton-Glisson expansion functions used in the method of moments.

Since *the proof of the pudding is in the eating*<sup>2</sup>, we validate in chapter 5 the outcome of Luxaflex against available commercial software tools (such as the finite-element code ©HFSS), and (some of them) against waveguide simulator measurements. We do this for eight different radiating structures, of which the first five structures represent different types of frequency selective surfaces, and where the last three structures are concerned with different types of realistic radiators.

Finally, in chapter 6 we formulate our conclusions, give a number of recommendations, and discuss the current and future industrial applicability of Luxaflex and the acceleration technique in phased array antenna design methods. The main purpose of appendices C-J has been to additionally make this thesis a complete manual for Thales Nederland B.V. regarding the theory behind the Luxaflex software implementation. These appendices can therefore be skipped during initial reading.

---

<sup>2</sup>Miguel de Cervantes (1547-1616), author of Don Quixote



## Chapter 2

# Basic Equations

*"Science is the century-old endeavour to bring together by means of systematic thought the perceptible phenomena of this world into as thorough-going an association as possible. To put it boldly, it is the attempt at a posterior reconstruction of existence by the process of conceptualization. Science can only ascertain what is, but not what should be, and outside of its domain value judgements of all kinds remain necessary."* Albert Einstein (1879-1955)

In this chapter we formulate the basic equations that describe the behavior of electromagnetic fields in general. Subsequently, we derive the special form that is used in planarly stratified media.

In section 2.1 we first give a summary of the mathematical notations used throughout this thesis. Then in section 2.2 we introduce Maxwell's equations that constitute the basis for calculating the electromagnetic field within any medium. Since we are dealing with a planarly stratified configuration, it is useful to eliminate some of the electromagnetic field components to be able to calculate the mode eigenfunctions of the stratified configuration. We do this by decomposing the vectors into transverse and longitudinal components. In section 2.3 we derive two dedicated systems of equations where the transverse and longitudinal components are taken to be the independent components, respectively. Finally in section 2.4 these two sets of equations are used to derive a Green's function formulation for a planarly stratified medium. We distinguish here between two types of such media: the waveguide and the layered space<sup>1</sup>.

### 2.1 Mathematical Notation

The physical laws that describe the behavior of electromagnetic waves were inferred from a series of experiments [62, 51]. To carry out these experiments, an

---

<sup>1</sup>In this thesis, the layered space is considered as a waveguide with phase shift walls, and whose modes are Floquet modes.

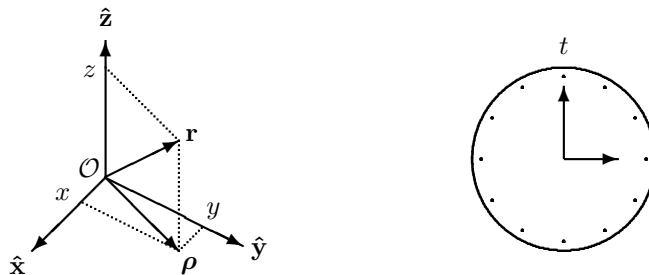


Figure 2.1: A reference frame and standard clock.

observer must be able to register the position and the instant at which an observation is made [38, 54]. To register position, the existence of an isotropic, three-dimensional (Euclidean) background space  $\mathbb{R}^3$  is preassumed. In this space, distance can be measured along three mutually perpendicular directions with one and the same position- and orientation-independent standard measuring rod. To register instants, the existence of a position- and orientation-independent standard clock is preassumed. The standard measuring rod is used to define, at a certain position denoted as the origin  $\mathcal{O}$ , an orthogonal Cartesian reference frame consisting of three mutually perpendicular unit basis vectors  $\{\hat{\mathbf{x}}, \hat{\mathbf{y}}, \hat{\mathbf{z}}\}$ , where the hat indicates a unit-length vector. In the indicated order the three vectors form a right-handed system. The bold-faced notation for vectors is used. Let  $\{x, y, z\}$  denote the ordered sequence of the three real numbers (Cartesian coordinates) that are needed to specify the position of an observer. Then this position is denoted by the vector  $\mathbf{r} = x\hat{\mathbf{x}} + y\hat{\mathbf{y}} + z\hat{\mathbf{z}}$ . The length of the vector  $\mathbf{r}$  is denoted by  $r = \|\mathbf{r}\| = \sqrt{x^2 + y^2 + z^2}$ . The unit-length vector in parallel with a given vector  $\mathbf{r}$  is denoted by  $\hat{\mathbf{r}} = \mathbf{r}/r$ . We write  $\mathbf{p} \parallel \mathbf{q}$  and  $\mathbf{p} \perp \mathbf{q}$  if two given vectors  $\mathbf{p}$  and  $\mathbf{q}$  are in parallel and perpendicular, respectively. The time coordinate is real and denoted by  $t$ . Due to a symmetry of the configuration in the  $x, y$ -plane we define (which is conventional) a so-called longitudinal direction along the  $z$ -axis. Accordingly, a so-called transverse plane is a plane for which  $z$  is arbitrary but fixed [34, section 2.1]. In a given transverse plane the position is fully specified by the transverse part  $\boldsymbol{\rho}$  of the position vector  $\mathbf{r}$ , given by  $\mathbf{r} = \boldsymbol{\rho} + z\hat{\mathbf{z}}$  where  $\boldsymbol{\rho} = x\hat{\mathbf{x}} + y\hat{\mathbf{y}}$ . A graphical representation of the reference frame and standard clock is given in figure 2.1.

Partial differentiation with respect to  $p$  is denoted by  $\partial_p$ . The nabla-operator  $\nabla$  is defined as  $\partial_x\hat{\mathbf{x}} + \partial_y\hat{\mathbf{y}} + \partial_z\hat{\mathbf{z}}$ . Assume we are given a scalar field  $\phi = \phi(\mathbf{r})$  and a vector field  $\mathbf{X} = \mathbf{X}(\mathbf{r})$ . The gradient of  $\phi$  is denoted by  $\nabla\phi$ . The divergence of  $\mathbf{X}$  is denoted by  $\nabla \cdot \mathbf{X}$ . The curl of  $\mathbf{X}$  is denoted by  $\nabla \times \mathbf{X}$ . The Laplace operator (or Laplacian) acting on  $\phi$  is denoted by  $\nabla^2\phi = \nabla \cdot (\nabla\phi)$ . The Hessian operator acting on  $\mathbf{X}$  is denoted by  $\nabla\nabla \cdot \mathbf{X} = \nabla(\nabla \cdot \mathbf{X})$ .

A complex number is denoted by  $z = z' + jz'' \in \mathbb{C}$ , where  $z', z'' \in \mathbb{R}$ ,  $j^2 = -1$ , and where  $\mathbb{C}$  denotes the set of complex numbers. The real part of  $z$  is denoted by  $\text{Re}(z) = z'$ . The imaginary part of  $z$  is denoted by  $\text{Im}(z) = z''$ . The complex conjugate of  $z$  is denoted by  $z^* = z' - jz''$ . The absolute value of  $z$  is denoted by  $|z| = \sqrt{z'^2 + z''^2}$ .

Let  $\mathcal{L}^2[a, b]$  be the space of square integrable functions on the interval  $[a, b]$  equipped with an inner product [4, section 2] denoted by  $\langle f | g \rangle$  (using the so-called bra-ket notation [83, chapter 4]) and defined as

$$\langle f | g \rangle = \int_{x=a}^b f(x)g^*(x)dx, \quad (2.1)$$

where  $f, g \in \mathcal{L}^2[a, b]$ . For every  $f, g, h \in \mathcal{L}^2[a, b]$  and  $\alpha \in \mathbb{C}$ , this inner product satisfies  $\langle f + h | g \rangle = \langle f | g \rangle + \langle h | g \rangle$ ,  $\langle \alpha f | g \rangle = \alpha \langle f | g \rangle$  and  $\langle f | g \rangle = \langle g | f \rangle^*$ . Further  $\langle f | f \rangle \geq 0$  and equals zero if and only if  $f = 0$ . The inner product induces a norm  $\|f\| = \sqrt{\langle f | f \rangle}$  and a distance (metric)  $d(f, g) = \|f - g\|$ . The (vector) space  $\mathcal{L}^2[a, b]$  has a denumerable infinity of dimensions and can be spanned by an orthonormal basis  $\phi_m$  with  $m \in \mathbb{N}$  where for every  $m, n \in \mathbb{N}$

$$\langle \phi_m | \phi_n \rangle = \delta_{m,n} = \begin{cases} 1 & \text{if } m = n, \\ 0 & \text{otherwise.} \end{cases} \quad (2.2)$$

$\delta_{m,n}$  denotes the Kronecker-delta symbol. A sequence  $\{f_m\}$  with  $f_m \in \mathcal{L}^2[a, b]$  and  $m \in \mathbb{N}$  is called a Cauchy sequence if  $\lim_{m,n \rightarrow \infty} d(f_m, f_n) = 0$ . For every Cauchy sequence  $\{f_m\}$ ,  $\lim_{m \rightarrow \infty} f_m \in \mathcal{L}^2[a, b]$ . Thus  $\mathcal{L}^2[a, b]$  is complete in the norm induced by the inner product and is hence a Hilbert space [34, appendix A.2]. Consider further  $\mathcal{L}^2(-\infty, \infty)$ , abbreviated as  $\mathcal{L}^2$ . The space  $\mathcal{L}^2$  however has a non-denumerable infinity of dimensions and can be spanned by for example a generalized orthonormal Fourier basis  $\phi_\omega(x) = \frac{1}{\sqrt{2\pi}} \exp(j\omega x)$  with  $\omega \in \mathbb{R}$  where for every  $\omega, \nu \in \mathbb{R}$

$$\langle \phi_\omega | \phi_\nu \rangle = \delta(\omega - \nu) = \frac{1}{2\pi} \int_{x=-\infty}^{\infty} \exp(j[\omega - \nu]x)dx. \quad (2.3)$$

$\delta(\omega)$  denotes the Dirac-delta function [55].

Let  $U \subset \mathbb{R}^3$  be an open set and let  $\mathbf{A} : U \rightarrow \mathbb{R}^3$  be a continuously differentiable vector field. Further let  $V \subset U$  be a closed bounded volume with a piecewise smooth boundary surface  $\partial V$ . Then the original form of Gauss' theorem [98, theorem 5.8] is given by

$$\int_V (\nabla \cdot \mathbf{A})dV = \oint_{\partial V} \mathbf{A} \cdot \hat{\nu}dA, \quad (2.4)$$

where  $\hat{\nu}$  is the outward directed unit vector normal to  $\partial V$ , where  $dV \equiv dx dy dz$  is the differential volume element, and where  $dA \equiv dx dy$  denotes the differential area element.

Let  $U \subset \mathbb{R}^2$  be an open set and let  $\mathbf{A}_t : U \rightarrow \mathbb{R}^2$  and  $\Psi : U \rightarrow \mathbb{R}$  be a continuously differentiable transverse vector field and scalar function, respectively. Further let  $S \subset U$  be a closed bounded surface with a piecewise smooth boundary curve  $\partial S$ . Then the reduced Gauss' theorem for  $\mathbf{A}_t$  is given by

$$\int_S (\nabla_t \cdot \mathbf{A}_t) dA = \oint_{\partial S} \mathbf{A}_t \cdot \hat{\nu} d\ell, \quad (2.5)$$

and for  $\Psi$  is given by

$$\int_S (\nabla_t \Psi) dA = \oint_{\partial S} \Psi \hat{\nu} d\ell, \quad (2.6)$$

where  $\hat{\nu}$  is the outward directed unit vector normal to  $\partial S$ , and where  $d\ell$  denotes the differential line element.

Let  $U \subset \mathbb{R}^3$  be an open set and let  $\mathbf{A} : U \rightarrow \mathbb{R}^3$  be a continuously differentiable vector field. Further let  $S \subset U$  be a piecewise smooth surface with orientation  $\hat{\nu}$ . Then Stokes' theorem [98, theorem 5.9] is given by

$$\int_S (\nabla \times \mathbf{A}) \cdot \hat{\nu} dA = \oint_{\partial S} \mathbf{A} \cdot \hat{\tau} d\ell, \quad (2.7)$$

where  $\hat{\tau}$  denotes the tangent vector to the boundary curve  $\partial S$  of  $S$ . Further,  $\hat{\nu}$  and  $\hat{\tau}$  follow the right-hand orientation rule. If some given proposition  $Q(x)$  of  $x$  is true for all  $x$ , or true for at least one  $x$ , we write

$$\forall x[Q(x)] \quad \text{and} \quad \exists x[Q(x)], \quad (2.8)$$

respectively [3, section 1.19]. Furthermore, we use the script and bold notation for time-domain and frequency-domain quantities, respectively. Finally, all quantities in this thesis are expressed in SI units.

## 2.2 Maxwell's Equations

The electromagnetic field present in a medium is governed by Maxwell's equations. These equations describe the coupled behavior of the electric and magnetic field and flux densities in space and time. The flux densities are related to the field densities through the constitutive relations. However this is not completely sufficient. First we must take into account the principle of causality. Then we have to consider the compatibility relations which are a consequence of Maxwell's equations. Finally, we deal with media with piecewise constant varying electromagnetic properties. To restrict the corresponding non-differentiabilities in the field and flux densities at the interfaces and boundaries where the electromagnetic properties vary discontinuously, we must impose the interface and compatibility boundary conditions, respectively.

### 2.2.1 Time-Domain Analysis

The coupled behaviour of the electric field/flux and the magnetic field/flux in space by vector  $\mathbf{r}[\text{m}]$  and time  $t[\text{s}]$  is described by the hyperbolic system of partial differential equations, also known as the time-domain Maxwell equations in matter [35, chapter 4], given by

$$-\nabla \times \mathcal{H} + \partial_t \mathcal{D} = -\mathcal{J}, \quad (2.9)$$

$$\nabla \times \mathcal{E} + \partial_t \mathcal{B} = -\mathcal{M}, \quad (2.10)$$

in which

$$\begin{aligned} \mathcal{E}(\mathbf{r}, t) &= \text{electric field strength} \quad [\text{Vm}^{-1}], \\ \mathcal{H}(\mathbf{r}, t) &= \text{magnetic field strength} \quad [\text{Am}^{-1}], \\ \mathcal{D}(\mathbf{r}, t) &= \text{electric flux density} \quad [\text{Cm}^{-2}], \\ \mathcal{B}(\mathbf{r}, t) &= \text{magnetic flux density} \quad [\text{T}], \\ \mathcal{J}(\mathbf{r}, t) &= \text{volume source density of electric current} \quad [\text{Am}^{-2}], \\ \mathcal{M}(\mathbf{r}, t) &= \text{volume source density of magnetic current} \quad [\text{Vm}^{-2}]. \end{aligned}$$

Furthermore, the volume source densities of electric and magnetic current must satisfy

$$\nabla \cdot \mathcal{J} = -\partial_t \rho_e, \quad (2.11)$$

$$\nabla \cdot \mathcal{M} = 0, \quad (2.12)$$

in which

$$\rho_e(\mathbf{r}, t) = \text{electric charge density} \quad [\text{Cm}^{-3}].$$

Equation 2.11 represents the conservation of electric charge (and is also known as the continuity equation), while equation 2.12 states that free magnetic charges do not exist.

All field quantities must be square integrable functions ( $\in \mathcal{L}^2$ ) over the space variable  $\mathbf{r}$ . This ensures that the electromagnetic energy is finite in any finite volume, the field solutions are mathematically unique and physically meaningful.

It is clear that the number of unknowns (four vectorial quantities if the source terms are assumed to be known) is larger than the number of equations (two vectorial equations). Consequently, the system of equations 2.9 and 2.10 is an underdetermined one. From a physical point of view, the electromagnetic field must be uniquely determined once the sources that generate the field and the distribution of matter are given. Hence, in order to make the number of equations equal to the number of unknown quantities, Maxwell's equations in matter have to be supplemented by another set of relations that is equivalent to two vectorial relations between the four field quantities occurring in 2.9 and 2.10. These supplementary relations are known as the constitutive relations; they are representative for the macroscopic electromagnetic response of a passive piece of matter to the presence of an electromagnetic field.



Our medium is assumed to be linear, time-invariant, causal, isotropic and locally reacting. We can write the constitutive relations in the following form

$$\mathcal{D} = \mathcal{K}^e * \mathcal{E}, \quad (2.13)$$

$$\mathcal{B} = \mathcal{K}^m * \mathcal{H}, \quad (2.14)$$

where  $*$  denotes convolution in time and in which

$$\begin{aligned} \mathcal{K}^e(\mathbf{r}, t) &= \text{dielectric relaxation function} \quad [\text{Fm}^{-1}\text{s}^{-1}], \\ \mathcal{K}^m(\mathbf{r}, t) &= \text{magnetic relaxation function} \quad [\text{Hm}^{-1}\text{s}^{-1}]. \end{aligned}$$

The dielectric and magnetic relaxation functions include electric and magnetic conducting behavior, respectively. They must also lead to positive definite stored electric and magnetic field energy densities and to non-negative definite loss phenomena.

This formulation, where the dielectric relaxation function includes the induced electric conducting behavior, deviates from the standard formulation where the induced electric current is incorporated in Maxwell's equations at the start.

Furthermore, we must take into account the property of causality, by which we mean that sources that act from instant  $t = t_0$  onwards, only cause fields for  $t \geq t_0$ . The causality conditions are satisfied if both relaxation functions vanish prior to  $t = 0$ .

We assume that the medium is instantaneously reacting, and that the medium parameters depend only on the  $z$ -coordinate. We can now write the constitutive relations in the following more specific form [37, chapter 2]

$$\partial_t \mathcal{D} = (\sigma + \varepsilon \partial_t) \mathcal{E}, \quad (2.15)$$

$$\partial_t \mathcal{B} = (\alpha + \mu \partial_t) \mathcal{H}, \quad (2.16)$$

in which

$$\begin{aligned} \sigma(z) &= \text{scalar electric conductivity} \quad [\text{Sm}^{-1}], \\ \varepsilon(z) &= \text{scalar permittivity} \quad [\text{Fm}^{-1}], \\ \alpha(z) &= \text{scalar magnetic conductivity} \quad [\text{Hs}^{-1}\text{m}^{-1}], \\ \mu(z) &= \text{scalar permeability} \quad [\text{Hm}^{-1}]. \end{aligned}$$

The so-called compatibility relations are a consequence of Maxwell's equations in time domain in matter. They are obtained by taking the divergence of both equations and by using equations 2.14 and 2.15. This results in

$$\nabla \cdot \mathcal{D} = \rho_e, \quad (2.17)$$

$$\nabla \cdot \mathcal{B} = 0, \quad (2.18)$$

where we have assumed that "the light has been switched on" at an instant  $t = t_0$ . This means that the flux densities must have been zero at  $t = t_0$  [103, section 4.1].

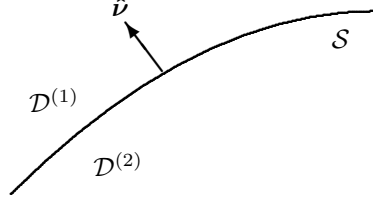


Figure 2.2: The interface and domains.

Now we consider an interface  $\mathcal{S}$  between two adjacent domains  $\mathcal{D}^{(1)}$  and  $\mathcal{D}^{(2)}$  with different electromagnetic properties. Furthermore we assume that the interface  $\mathcal{S}$  has a unique tangent plane in every point. We denote  $\hat{\nu}$  as the normal unit vector on the interface  $\mathcal{S}$ . A graphical representation of the interface and domains is given in figure 2.2.

Upon crossing this interface, the field quantities may vary discontinuously. Since all physical quantities must have bounded magnitudes, the relevant discontinuities are restricted to jump discontinuities. This means that the field quantities are not continuously differentiable in a domain that contains (part of) the interface  $\mathcal{S}$  and the partial differential equations 2.9 and 2.10 only hold in a distributional sense. When the properties of the media under consideration and the position of the interface are time invariant, the non-differentiability is restricted to the dependence on the spatial variables. The electromagnetic field equations must therefore be supplemented by so-called interface boundary conditions, that interrelate the field values at both sides of the interface, given by

$$\hat{\nu} \times \mathcal{E}_1 - \hat{\nu} \times \mathcal{E}_2 = \mathcal{M}^s, \quad (2.19)$$

$$\hat{\nu} \times \mathcal{H}_1 - \hat{\nu} \times \mathcal{H}_2 = \mathcal{J}^s. \quad (2.20)$$

$\mathcal{J}^s$  and  $\mathcal{M}^s$  are the electric and magnetic surface currents at the interface  $\mathcal{S}$ , respectively. These surface currents have a Dirac dependence along the  $\hat{\nu}$ -direction. Further,  $\mathcal{E}_1$  and  $\mathcal{H}_1$  are the field values in the domain  $\mathcal{D}^{(1)}$ .  $\mathcal{E}_2$  and  $\mathcal{H}_2$  are the field values in the domain  $\mathcal{D}^{(2)}$ .

The same line of argument shows that the flux quantities are not continuously differentiable in a domain that contains (part of) the interface  $\mathcal{S}$  and the partial differential equations 2.9 and 2.10 cease to hold. They must therefore be supplemented by so-called compatibility boundary conditions, that interrelate the flux values at either side of the interface, given by

$$\hat{\nu} \cdot (\partial_t \mathcal{D} + \mathcal{J}) = \text{continuous}, \quad (2.21)$$

$$\hat{\nu} \cdot (\partial_t \mathcal{B} + \mathcal{M}) = \text{continuous}. \quad (2.22)$$

### 2.2.2 Laplace-Domain Analysis

Since we are dealing with electromagnetic fields in a linear and time-invariant configuration, we can mathematically take advantage of this situation by carrying out a Laplace transformation with respect to time. As far as the time coordinate is concerned, we must, in addition, take into account the property of causality. This condition can mathematically most easily be accounted for by using the one-sided Laplace transformation.

We call the domain after carrying out the one-sided Laplace transformation the Laplace-domain or  $s$ -domain. In the  $s$ -domain relations, the time coordinate has been eliminated and a field problem in space remains, in which the transform parameter  $s$  occurs as a parameter.

Assume that the sources that generate the wave field are switched on at the instant  $t_0$ . Here,  $t_0(\mathbf{r})$  can also be a function of the space vector  $\mathbf{r}$ , which creates the possibility to include an incident plane wave. In view of the causality condition, the interest in the behavior of the field is then in the interval  $t > t_0$ . The one-sided Laplace transformation of some physical quantity  $\mathcal{F} = \mathcal{F}(\mathbf{r}, t)$ , defined for  $t > t_0$  and in some as yet unspecified domain in space, is then given by

$$F(\mathbf{r}, s) = \int_{t=t_0}^{\infty} \exp(-st)\mathcal{F}(\mathbf{r}, t)dt. \quad (2.23)$$

Now, causality is enforced by extending the range of  $\mathcal{F}$  to  $t < t_0$  and setting  $\mathcal{F}$  to zero in that domain. Now, we require that equation 2.23, considered as an integral equation to be solved for  $\mathcal{F}(\mathbf{r}, t)$ , at given  $F(\mathbf{r}, s)$ , has a unique solution, viz. zero if  $t < t_0$  and the reproduction of the function that we started with if  $t > t_0$ . Note that equation 2.23 can only be solved if  $\mathcal{F}(\mathbf{r}, t)$  is allowed to deviate from the original one on a set of zero measure.

It can be shown that this requirement can be met by a proper choice of the transformation parameter  $s$ . For the practical reason that in physics all quantities have bounded values, we restrict ourselves to functions  $\mathcal{F}$  that are bounded. Furthermore we assume that the functions  $\mathcal{F}$  are also square integrable. Then, the right-hand side of equation 2.23 is convergent if  $s$  is either real and positive, or complex with  $\text{Re}(s) \geq 0$ . Note that  $\text{Re}(s) = 0$  allows for a Fourier representation. Due to the analyticity of the Laplace transformation kernel  $\exp(-st)$ ,  $F(\mathbf{r}, s)$  is an analytic function of  $s$  in  $\{s \in \mathbb{C} | \text{Re}(s) \geq 0\}$ . The uniqueness of equation 2.23 considered as an integral equation is guaranteed if  $F$  is given at a sequence of points  $\{s_n \in \mathbb{R} | s_n = s_0 + nh\}$  with  $s_0$  real, positive and sufficiently large,  $h$  real and positive, and  $n = 0, 1, 2, \dots$  (Lerch's theorem, [113]). The inverse Laplace transformation can be carried out explicitly by evaluating the following inversion (Bromwich) integral in the complex  $s$ -plane

$$\lim_{\Omega \rightarrow \infty} \frac{1}{2\pi j} \int_{s=s_0-j\Omega}^{s_0+j\Omega} \exp(st)F(\mathbf{r}, s)ds = \chi_T(t)\mathcal{F}(\mathbf{r}, t), \quad (2.24)$$

where the path of integration (which is parallel to the imaginary  $s$ -axis) is

situated in the right half of the complex  $s$ -plane where  $F$  is analytic and where

$$\chi_T(t) = \begin{cases} 1 & \text{if } t < t_0, \\ 1/2 & \text{if } t = t_0, \\ 0 & \text{if } t > t_0. \end{cases} \quad (2.25)$$

The result when  $t = t_0$  holds on the assumption that the integration in the left-hand side is carried out as a Cauchy principal value integral around "infinity". A way to circumvent this is to assume a priori that  $\mathcal{F}(\mathbf{r}, t)$  is a continuous function of  $t$ , which means that a sudden switching on of the sources is simply not allowed. The one-sided Laplace transformation of the derivative  $\partial_t \mathcal{F}$  of  $\mathcal{F}$  is found by evaluating

$$\int_{t=t_0}^{\infty} \exp(-st) \partial_t \mathcal{F}(\mathbf{r}, t) dt = -\exp(-st_0) \lim_{t \downarrow t_0} \mathcal{F}(\mathbf{r}, t) + sF(\mathbf{r}, s), \quad (2.26)$$

where the first term on the right-hand side accounts for the presence of an impulse function at  $t = t_0$ , whose strength equals the jump in  $\mathcal{F}$  at the instant  $t = t_0$  in the direction of increasing  $t$ . If we incorporate this term into the definition of the time differentiation of  $\mathcal{F}$ , the  $s$ -domain equivalent corresponds to a multiplication of  $F$  by a factor of  $s$ . On the other hand, equation 2.26 gives us the tool to properly take into account the influence of a non-vanishing initial field.

When we subject the basic time-domain Maxwell equations in matter 2.9 and 2.10 to the one-sided Laplace transformation, we obtain Maxwell's equations in matter in the time-Laplace (or complex-frequency) domain

$$-\nabla \times \mathbf{H} + s\mathbf{D} = -\mathbf{J}, \quad (2.27)$$

$$\nabla \times \mathbf{E} + s\mathbf{B} = -\mathbf{M}. \quad (2.28)$$

The general  $s$ -domain constitutive relations are obtained from 2.13 and 2.14 as

$$\mathbf{D} = K^e \mathbf{E}, \quad (2.29)$$

$$\mathbf{B} = K^m \mathbf{H}, \quad (2.30)$$

while the more specific  $s$ -domain constitutive relations are obtained from 2.15 and 2.16 as

$$\mathbf{D} = (\varepsilon + s^{-1}\sigma) \mathbf{E}, \quad (2.31)$$

$$\mathbf{B} = (\mu + s^{-1}\alpha) \mathbf{H}. \quad (2.32)$$

$(\varepsilon + s^{-1}\sigma)$  and  $(\mu + s^{-1}\alpha)$  are the so-called complex permittivity and permeability, respectively. The  $s$ -domain compatibility relations are obtained from equations 2.17 and 2.18 as

$$\nabla \cdot \mathbf{D} = \rho_e, \quad (2.33)$$

$$\nabla \cdot \mathbf{B} = 0. \quad (2.34)$$

The  $s$ -domain interface boundary conditions are obtained from equations 2.19 and 2.20 as

$$\hat{\nu} \times \mathbf{E}_1 - \hat{\nu} \times \mathbf{E}_2 = \mathbf{M}^s, \quad (2.35)$$

$$\hat{\nu} \times \mathbf{H}_1 - \hat{\nu} \times \mathbf{H}_2 = \mathbf{J}^s. \quad (2.36)$$

The  $s$ -domain compatibility boundary conditions are obtained from equations 2.21 and 2.22 as

$$\hat{\nu} \cdot (s\mathbf{D} + \mathbf{J}) = \text{continuous}, \quad (2.37)$$

$$\hat{\nu} \cdot (s\mathbf{B} + \mathbf{M}) = \text{continuous}. \quad (2.38)$$

We define

$$\eta = \sigma + s\varepsilon, \quad (2.39)$$

$$\xi = \alpha + s\mu. \quad (2.40)$$

If we combine the Laplace-domain constitutive relations 2.31 and 2.32 with the basic  $s$ -domain Maxwell equations in matter 2.27 and 2.28, and if we make use of the definitions 2.39 and 2.40 we finally arrive at

$$-\nabla \times \mathbf{H} + \eta\mathbf{E} = -\mathbf{J}, \quad (2.41)$$

$$\nabla \times \mathbf{E} + \xi\mathbf{H} = -\mathbf{M}. \quad (2.42)$$

### 2.2.3 Frequency-Domain Analysis

In the frequency-domain analysis (or steady-state analysis), all field quantities are taken to depend sinusoidally on time with a common real and positive angular frequency,  $\omega$ . Each real quantity  $\mathcal{F}(\mathbf{r}, t)$  can then be associated with a complex amplitude  $F(\mathbf{r}, j\omega)$  and a common time factor  $\exp(j\omega t)$ , in which  $j$  denotes the imaginary unit. In doing so, the original quantity is found from its complex counterpart as

$$\mathcal{F}(\mathbf{r}, t) = \text{Re}[F(\mathbf{r}, j\omega) \exp(j\omega t)]. \quad (2.43)$$

The combination of the complex quantities of the type  $F(\mathbf{r}, j\omega) \exp(j\omega t)$ , and the basic time-domain Maxwell equations in matter, equations 2.9 and 2.10, yields, apart from the complex time factor  $\exp(j\omega t)$ , a set of basic equations identical to the one in the Laplace domain, equations 2.27 and 2.28. In these equations,  $F$  stands for the complex representation of the quantity  $\mathcal{F}$ , the common time factor  $\exp(j\omega t)$  is omitted, and  $s$  equals  $j\omega$ . We interpret the frequency-domain analysis with complex time factor  $\exp(j\omega t)$  as a limiting case of the  $s$ -domain analysis [15, section 2.2.2] by taking

$$s = \lim_{s_0 \downarrow 0} (s_0 + j\omega), \quad (2.44)$$

Now by enforcing  $F(\mathbf{r}, s)$  also to be analytic for  $\text{Re}(s) = 0$ , we have assured that the limit exists, and that the causality conditions remain satisfied.

## 2.3 Electromagnetic Fields in Planarly Stratified Media

Maxwell's equations describe the coupled behavior of the electric field/flux and the magnetic field/flux in space and time. However, in so-called planarly stratified media, the structure is invariant with respect to the transverse direction. In this case to be able to calculate the mode eigenfunctions of the stratified medium, it is useful to eliminate some of the electromagnetic field components. We do this by decomposing the vectors into transverse and longitudinal components. We either eliminate the longitudinal or the transverse field components and write them in terms of the transverse and longitudinal field components, respectively.

When the longitudinal field components are eliminated, the remaining transverse field components satisfy a system of coupled partial differential equations referred to as the Marcuvitz-Schwinger equations. The longitudinal field components can directly be expressed in terms of the transverse field components.

When the transverse field components are eliminated, the longitudinal field components satisfy two uncoupled scalar partial differential equations referred to as the Helmholtz equations. The transverse field components satisfy two uncoupled inhomogeneous ordinary differential equations.

In this section we derive both formulations. To do so we use the Laplace-domain Maxwell equations in matter 2.41 and 2.42 where  $\eta = \eta(z)$  and  $\xi = \xi(z)$  is assumed. Let us now decompose the vector quantities into their transverse and longitudinal components as

$$\mathbf{H} = \mathbf{H}_t + H_z \hat{\mathbf{z}}, \quad (2.45)$$

$$\mathbf{E} = \mathbf{E}_t + E_z \hat{\mathbf{z}}, \quad (2.46)$$

$$\mathbf{J} = \mathbf{J}_t + J_z \hat{\mathbf{z}}, \quad (2.47)$$

$$\mathbf{M} = \mathbf{M}_t + M_z \hat{\mathbf{z}}, \quad (2.48)$$

and the  $\nabla$ -operator into its transverse and longitudinal operator components as  $\nabla = \nabla_t + \partial_z \hat{\mathbf{z}}$  where  $\nabla_t = \partial_x \hat{\mathbf{x}} + \partial_y \hat{\mathbf{y}}$ . Expanding the quantities in equations 2.41 and 2.42 by using equations 2.45-2.48 we obtain

$$-\nabla_t \times \mathbf{H}_t - (\nabla_t H_z) \times \hat{\mathbf{z}} - \hat{\mathbf{z}} \times \partial_z \mathbf{H}_t + \eta \mathbf{E}_t + \eta E_z \hat{\mathbf{z}} = -\mathbf{J}_t - J_z \hat{\mathbf{z}}, \quad (2.49)$$

$$\nabla_t \times \mathbf{E}_t + (\nabla_t E_z) \times \hat{\mathbf{z}} + \hat{\mathbf{z}} \times \partial_z \mathbf{E}_t + \xi \mathbf{H}_t + \xi H_z \hat{\mathbf{z}} = -\mathbf{M}_t - M_z \hat{\mathbf{z}}. \quad (2.50)$$

To isolate the transverse components, we take the cross product between  $\hat{\mathbf{z}}$  and equations 2.49 and 2.50. This leads to

$$-\partial_z \mathbf{H}_t = \eta \hat{\mathbf{z}} \times \mathbf{E}_t - \nabla_t H_z + \hat{\mathbf{z}} \times \mathbf{J}_t, \quad (2.51)$$

$$-\partial_z \mathbf{E}_t = \xi \mathbf{H}_t \times \hat{\mathbf{z}} - \nabla_t E_z + \mathbf{M}_t \times \hat{\mathbf{z}}. \quad (2.52)$$

To isolate the longitudinal components, we take the inner product between  $\hat{\mathbf{z}}$

and equations 2.49 and 2.50. This leads to

$$\eta E_z = \nabla_t \cdot (\mathbf{H}_t \times \hat{\mathbf{z}}) - J_z, \quad (2.53)$$

$$\xi H_z = \nabla_t \cdot (\hat{\mathbf{z}} \times \mathbf{E}_t) - M_z. \quad (2.54)$$

We stress that equations 2.51, 2.52, 2.53 and 2.54 are completely equivalent to Maxwell's equations 2.41 and 2.42. We still have a coupled system of six first-order partial differential equations. We have merely rearranged the equations in transverse and longitudinal parts. Further note that equations 2.51 and 2.52 represent the transverse part even though they contain both transverse and longitudinal field components. A similar remark applies to equations 2.53 and 2.54.

### 2.3.1 The Marcuvitz-Schwinger Equations

To eliminate the longitudinal field components, we first need the transverse gradients of the longitudinal field components, given by

$$\eta \nabla_t E_z = \nabla_t \nabla_t \cdot (\mathbf{H}_t \times \hat{\mathbf{z}}) - \nabla_t J_z, \quad (2.55)$$

$$\xi \nabla_t H_z = \nabla_t \nabla_t \cdot (\hat{\mathbf{z}} \times \mathbf{E}_t) - \nabla_t M_z. \quad (2.56)$$

Combining equations 2.51 and 2.52 with equations 2.55 and 2.56 leads to

$$-\partial_z \mathbf{H}_t = \eta [I_t + k^{-2} \nabla_t \nabla_t] \cdot (\hat{\mathbf{z}} \times \mathbf{E}_t) + \hat{\mathbf{z}} \times \mathbf{J}_t^{\text{eff}}, \quad (2.57)$$

$$-\partial_z \mathbf{E}_t = \xi [I_t + k^{-2} \nabla_t \nabla_t] \cdot (\mathbf{H}_t \times \hat{\mathbf{z}}) + \mathbf{M}_t^{\text{eff}} \times \hat{\mathbf{z}}, \quad (2.58)$$

with  $k^2 = -\eta\xi$ , where  $I_t = \hat{\mathbf{x}}\hat{\mathbf{x}} + \hat{\mathbf{y}}\hat{\mathbf{y}}$  denotes the transverse identity operator, and where

$$\mathbf{J}_t^{\text{eff}} = \mathbf{J}_t + \xi^{-1} (\nabla_t M_z) \times \hat{\mathbf{z}}, \quad (2.59)$$

$$\mathbf{M}_t^{\text{eff}} = \mathbf{M}_t + \eta^{-1} \hat{\mathbf{z}} \times (\nabla_t J_z), \quad (2.60)$$

denote the effective volume source densities. The transverse field components now satisfy a system of coupled partial differential equations 2.57 and 2.58 referred to as the Marcuvitz-Schwinger equations [34, section 2.2]. The longitudinal field components can directly be expressed in terms of the transverse field components by dividing equations 2.53 and 2.54 by  $\eta$  and  $\xi$ , respectively. This results in

$$E_z = \eta^{-1} (\nabla_t \cdot (\mathbf{H}_t \times \hat{\mathbf{z}}) - J_z), \quad (2.61)$$

$$H_z = \xi^{-1} (\nabla_t \cdot (\hat{\mathbf{z}} \times \mathbf{E}_t) - M_z). \quad (2.62)$$

### 2.3.2 The Helmholtz Equations

To eliminate the transverse field components, we first need the transverse divergence of the transverse field components given by

$$-\nabla_t \cdot \partial_z \mathbf{H}_t = \eta \nabla_t \cdot (\hat{\mathbf{z}} \times \mathbf{E}_t) - \nabla_t^2 H_z + \nabla_t \cdot (\hat{\mathbf{z}} \times \mathbf{J}_t), \quad (2.63)$$

$$-\nabla_t \cdot \partial_z \mathbf{E}_t = \xi \nabla_t \cdot (\mathbf{H}_t \times \hat{\mathbf{z}}) - \nabla_t^2 E_z + \nabla_t \cdot (\mathbf{M}_t \times \hat{\mathbf{z}}). \quad (2.64)$$

Combining equations 2.53 and 2.54 with equations 2.63 and 2.64 leads to

$$\nabla_t^2 H_z + k^2 H_z - \partial_z(\nabla_t \cdot \mathbf{H}_t) = \eta M_z + \nabla_t \cdot (\hat{\mathbf{z}} \times \mathbf{J}_t), \quad (2.65)$$

$$\nabla_t^2 E_z + k^2 E_z - \partial_z(\nabla_t \cdot \mathbf{E}_t) = \xi J_z + \nabla_t \cdot (\mathbf{M}_t \times \hat{\mathbf{z}}). \quad (2.66)$$

Note that we have used  $\nabla_t \cdot \partial_z \mathbf{X}_t = \partial_z(\nabla_t \cdot \mathbf{X}_t)$ . At this point still two terms with transverse components are present. These can be further eliminated by using the compatibility relations written as

$$-\eta \nabla_t \cdot \mathbf{E}_t = \partial_z(\eta E_z) + \nabla \cdot \mathbf{J}, \quad (2.67)$$

$$-\xi \nabla_t \cdot \mathbf{H}_t = \partial_z(\xi H_z) + \nabla \cdot \mathbf{M}. \quad (2.68)$$

Combining these relations with equations 2.65 and 2.66 finally results in

$$\begin{aligned} \nabla_t^2 H_z + k^2 H_z + \partial_z(\xi^{-1} \partial_z(\xi H_z)) = & \eta M_z + \\ & \nabla_t \cdot (\hat{\mathbf{z}} \times \mathbf{J}_t) - \partial_z(\xi^{-1} \nabla \cdot \mathbf{M}), \end{aligned} \quad (2.69)$$

$$\begin{aligned} \nabla_t^2 E_z + k^2 E_z + \partial_z(\eta^{-1} \partial_z(\eta E_z)) = & \xi J_z + \\ & \nabla_t \cdot (\mathbf{M}_t \times \hat{\mathbf{z}}) - \partial_z(\eta^{-1} \nabla \cdot \mathbf{J}). \end{aligned} \quad (2.70)$$

The longitudinal field components now satisfy two uncoupled scalar partial differential equations 2.69 and 2.70 referred to as the Helmholtz equations [15, section 5.1]. The remaining transverse field components satisfy two uncoupled inhomogeneous ordinary differential equations. They can be obtained by solving equations 2.51 and 2.52 for  $\mathbf{E}_t$  and  $\mathbf{H}_t$ . This results in

$$\begin{aligned} \xi \partial_z(\xi^{-1} \partial_z \mathbf{E}_t) + k^2 \mathbf{E}_t = & \xi \partial_z(\xi^{-1} \nabla_t E_z) - \\ & \xi(\nabla_t H_z) \times \hat{\mathbf{z}} + \xi \mathbf{J}_t - \xi \partial_z(\xi^{-1} \mathbf{M}_t \times \hat{\mathbf{z}}), \end{aligned} \quad (2.71)$$

$$\begin{aligned} \eta \partial_z(\eta^{-1} \partial_z \mathbf{H}_t) + k^2 \mathbf{H}_t = & \eta \partial_z(\eta^{-1} \nabla_t H_z) - \\ & \eta \hat{\mathbf{z}} \times (\nabla_t E_z) + \eta \mathbf{M}_t - \eta \partial_z(\eta^{-1} \hat{\mathbf{z}} \times \mathbf{J}_t). \end{aligned} \quad (2.72)$$

If we are dealing with inhomogeneous media, we would not use this approach since we would have to additionally solve equations 2.71 and 2.72 for  $\mathbf{E}_t$  and  $\mathbf{H}_t$ .

## 2.4 Green's Function for a Planarly Stratified Medium

In this section we first show that the total electromagnetic field in a piecewise homogeneous planarly stratified medium can be decomposed into three independent field solutions where either the electric, the magnetic or both longitudinal field components vanish. We then argue that due to the invariance of the structure in the  $x, y$ -direction, we can use the technique of separation of variables, and separate the  $\mathbf{r}$ -dependence of the field solutions into a  $\rho$ -dependence and a  $z$ -dependence. For piecewise homogeneous media, the behavior in the



$z$ -direction is described in closed form by an exponential factor in the source-free case.

In this case, the  $\rho$ -dependent components are referred to as the mode functions. We use the Helmholtz equations to derive a set of equations that determine these mode functions in a general planarly stratified medium. Then, to be more specific, we determine the mode functions for two different types of such media: for the cylindrical waveguide and for the layered space. In both cases the modes form a basis in the space of the transverse electromagnetic field and therefore allow a very convenient field representation for the modeling of wave propagation problems in piecewise homogeneous planarly stratified media.

The  $z$ -dependent components are referred to as the modal voltages and currents for the electric and magnetic field components, respectively. They show an exponential  $z$ -dependence in the source-free case. We use the Marcuvitz-Schwinger equations combined with the mode functions to derive the modal transmission line equations that describe the evolution of the modal voltages and currents. This is independent of the type of planarly stratified medium and is allowed since the set of mode functions is complete. The advantages of this approach are that the three-dimensional field problem is reduced to a one-dimensional problem, and is rigorously reformulated in the language of circuit theory. It provides a framework in terms of quantities (voltages, currents, impedances and admittances) and equations (transmission line equations) that sounds familiar to electrical engineers. This enables us to cast any wave propagation problem within a planarly stratified medium in a form that is amenable to solution by circuit techniques.

### 2.4.1 Determination of the Mode Functions

The Helmholtz equations 2.69 and 2.70 suggest that the total electromagnetic field radiated by the volume source distributions in a piecewise homogeneous stratified medium can be decomposed into the following three independent field solutions:

1. Transverse magnetic (TM) fields, for which  $H_z$  vanishes over the entire transverse plane. These modes are also referred to as  $E$ -modes, since all of the field components derive from a non-vanishing  $E_z$  component. From equation 2.70 we infer that a volume distribution of only electric currents for which  $\mathbf{J}_t = \mathbf{0}$  and  $J_z \neq 0$  generates a pure TM wave. The non-vanishing  $E_z$  component then satisfies

$$[\nabla_t^2 + k^2 + \partial_z^2] E_z = (\xi - \eta^{-1} \partial_z^2) J_z. \quad (2.73)$$

2. Transverse electric (TE) fields, for which  $E_z$  vanishes over the entire transverse plane. These modes are also referred to as  $H$ -modes, since all of the field components derive from a non-vanishing  $H_z$  component. From equation 2.69 we infer that a volume distribution of only magnetic currents for which  $\mathbf{M}_t = \mathbf{0}$  and  $M_z \neq 0$  generates a pure TE wave. The non-vanishing

$H_z$  component then satisfies

$$[\nabla_t^2 + k^2 + \partial_z^2] H_z = (\eta - \xi^{-1} \partial_z^2) M_z. \quad (2.74)$$

3. Transverse electric-magnetic (TEM) fields, for which both  $E_z$  and  $H_z$  vanish over the entire transverse plane. In [15, section 5.3] TEM fields are considered as a special case of a TM field. This type of wave can only be generated if the right-hand sides of equations 2.69 and 2.70 both vanish identically. The resulting electromagnetic field then follows from equations 2.71 and 2.72 and satisfies

$$[\partial_z^2 + k^2] \mathbf{E}_t = \xi \mathbf{J}_t - \partial_z (\mathbf{M}_t \times \hat{\mathbf{z}}), \quad (2.75)$$

$$[\partial_z^2 + k^2] \mathbf{H}_t = \eta \mathbf{M}_t - \partial_z (\hat{\mathbf{z}} \times \mathbf{J}_t). \quad (2.76)$$

In metal waveguides, the TEM mode exists only if the transverse section is multiply connected, such as a coax or a parallel plate waveguide. These types of waveguides are not considered in this thesis. In the case of a layered space medium, the modes for which  $k_t = 0$  are TEM modes and are considered in this thesis. There are two linearly independent ones<sup>2</sup>, one with the electric field parallel to the  $x$ -axis and the other one with the electric field parallel to the  $y$ -axis (for example).

Due to the invariance of the structure in the  $z$ -direction, we can use the technique of separation of variables, and split the  $\mathbf{r}$ -dependence of the field solutions into a separate  $\boldsymbol{\rho}$ -dependence and a  $z$ -dependence. Furthermore, for piecewise homogeneous media considered for the source-free case, the  $z$ -dependent factors show an exponential  $z$ -dependence. In this case, the field components can be written in the following modal field representation [34, section 5.1] as

$$\mathbf{E}_t(\boldsymbol{\rho}, z) = C_E \mathbf{e}_t(\boldsymbol{\rho}, k_z) \exp(-jk_z z), \quad (2.77)$$

$$E_z(\boldsymbol{\rho}, z) = C_E e_z(\boldsymbol{\rho}, k_z) \exp(-jk_z z), \quad (2.78)$$

$$\mathbf{H}_t(\boldsymbol{\rho}, z) = C_H \mathbf{h}_t(\boldsymbol{\rho}, k_z) \exp(-jk_z z), \quad (2.79)$$

$$H_z(\boldsymbol{\rho}, z) = C_H h_z(\boldsymbol{\rho}, k_z) \exp(-jk_z z), \quad (2.80)$$

where  $C_E$  and  $C_H$  denote the amplitude coefficients and where  $k_z$  denotes the longitudinal wavenumber. If we subsequently fix the sign of  $k_z$  such that

$$\text{Im}(k_z) \leq 0 \quad \text{and} \quad \text{Re}(k_z) \geq 0 \quad \text{if} \quad \text{Im}(k_z) = 0, \quad (2.81)$$

then the modal field representation corresponds to a progressive mode, i.e., a radiated field propagating or decaying exponentially in the positive  $z$ -direction. To confirm this, consider first  $k_z$  to be imaginary. In this case,  $\text{Im}(k_z) \leq 0$  ensures that  $\exp(-jk_z z)$  decays exponentially as  $z \rightarrow \infty$ . Modes with imaginary  $k_z$  are called evanescent modes. Then consider  $k_z$  to be real. In this

<sup>2</sup>The same holds for the fundamental Floquet mode (0,0) in a phase shift wall waveguide in the case of zero phase shift ("normal incidence").

case,  $\text{Re}(k_z) \geq 0$  for  $\text{Im}(k_z) = 0$  ensures that  $\exp(-jk_z z + j\omega t)$  represents a physically acceptable progressive mode in the positive  $z$ -direction. Note that we have chosen the complex time factor  $\exp(j\omega t)$ . Modes with real  $k_z$  are called propagating modes. The modal field representation for a regressive mode, i.e., a radiated field propagating or decaying exponentially in the negative  $z$ -direction, can be found by simply changing signs in the exponential  $z$ -dependence from  $\exp(-jk_z z)$  to  $\exp(jk_z z)$ . Note that the same choice of the sign for  $k_z$  holds.

The transverse vector fields  $\mathbf{e}_t(\boldsymbol{\rho}, k_z)$  and  $\mathbf{h}_t(\boldsymbol{\rho}, k_z)$  are referred to as the mode functions or simply as modes even though the corresponding longitudinal components  $e_z(\boldsymbol{\rho}, k_z)$  and  $h_z(\boldsymbol{\rho}, k_z)$  may not vanish. For readability we drop from now onwards the functional  $k_z$ - and  $\boldsymbol{\rho}$ -dependence.

Consider first a pure transverse magnetic (TM) field. The substitution of the modal field representation for the longitudinal electric field component in the source-free version of equation 2.73 shows that  $e_z$  must satisfy

$$[\nabla_t^2 + k_t^2] e_z = 0. \quad (2.82)$$

Consider second a pure transverse electric (TE) field. The substitution of the modal field representation for the longitudinal magnetic field component in the source-free version of equation 2.74 shows that  $h_z$  must satisfy

$$[\nabla_t^2 + k_t^2] h_z = 0. \quad (2.83)$$

These equations represent so-called eigenvalue problems. For instance, in the case of equation 2.82 one has to find functions  $e_z$  that are square integrable functions<sup>3</sup> ( $\in \mathcal{L}^2$ ), satisfy some specific supplementary boundary conditions<sup>4</sup> (to make the differential operator acting on a vector space become meaningful and to describe the structure under study), and are eigenfunctions of the transverse Laplacian operator  $\nabla_t^2$ , with eigenvalues  $-k_t^2$ .  $k_t$  still has to be determined, which is at this point unknown.

Finally we show that the transverse field components of a mode function can be expressed in terms of the longitudinal ones. To do so, we take the source-free parts of equations 2.71 and 2.72 for a piecewise homogeneous medium, given by

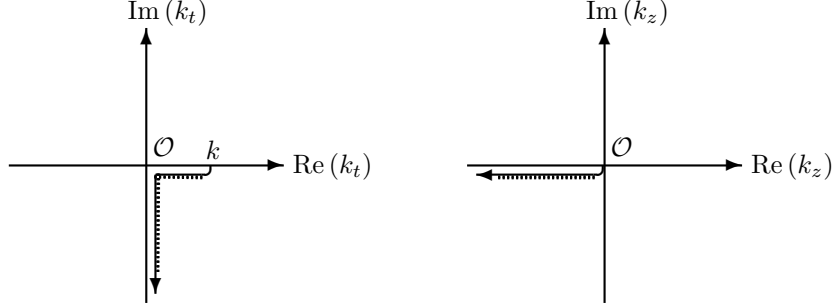
$$[\partial_z^2 + k^2] \mathbf{E}_t = \partial_z \nabla_t E_z - \xi (\nabla_t H_z) \times \hat{\mathbf{z}}, \quad (2.84)$$

$$[\partial_z^2 + k^2] \mathbf{H}_t = \partial_z \nabla_t H_z - \eta \hat{\mathbf{z}} \times (\nabla_t E_z). \quad (2.85)$$

By substituting the expressions for the modal field representations given in equations 2.77-2.80, we can express the transverse field components  $\mathbf{e}_t$  and  $\mathbf{h}_t$

<sup>3</sup>Note that for a layered space medium, the eigenfunctions are plane waves, and are not square integrable. Their orthonormality relation contains a Dirac delta function instead of the Kronecker delta symbol.

<sup>4</sup>The boundary condition for the layered space medium is that the solution is finite everywhere.

Figure 2.3: The branch cuts in the complex  $k_t$ -plane and  $k_z$ -plane.

in terms of the longitudinal components  $e_z$  and  $h_z$  as

$$\mathbf{e}_t = -\frac{\xi}{k_t^2} Y_\infty (\nabla_t h_z \times \hat{\mathbf{z}}) - j \frac{k_z}{k_t^2} \nabla_t e_z, \quad (2.86)$$

$$\mathbf{h}_t = -j \frac{k_z}{k_t^2} \nabla_t h_z - \frac{\eta}{k_t^2} Z_\infty (\hat{\mathbf{z}} \times \nabla_t e_z), \quad (2.87)$$

where we have introduced the modal admittance  $Y_\infty = C_H/C_E$  and the modal impedance  $Z_\infty = C_E/C_H = Y_\infty^{-1}$ . Further the transverse wavenumber  $k_t$  is defined as

$$k_t^2 = k^2 - k_z^2, \quad (2.88)$$

and is assumed to be non-zero. Finally note that the value of  $Y_\infty$  (and the corresponding  $Z_\infty$ ) is still arbitrary.  $k_z$  can be solved from equation 2.88 and is given by

$$k_z = \sqrt{k^2 - k_t^2}. \quad (2.89)$$

If we fix the branch of the logarithmic function  $\log(z)$  (used to calculate the square root) at  $\arg(z) = \pi$  ( $-\pi < \arg(z) \leq \pi$ ), then equation 2.81 is satisfied. In this case, a graphical representation of the branch cuts [61, section 6.1] in the complex  $k_t$ -plane and  $k_z$ -plane is given in figure 2.3.

### TM Mode Functions

The TM modes are traditionally indicated through a single prime [34, section 5.4.1]. They are characterized by a vanishing of  $h'_z$  over the entire transverse plane. All other field components are derived from a non-vanishing  $e'_z$ , which is considered as the fundamental unknown. The transverse field components now

follow from equation 2.86 and 2.87 by setting  $h'_z = 0$ . This results in

$$\mathbf{e}'_t = -j \frac{k'_z}{k_t'^2} \nabla_t e'_z, \quad (2.90)$$

$$\mathbf{h}'_t = -\frac{\eta}{k_t'^2} Z'_\infty (\hat{\mathbf{z}} \times \nabla_t e'_z). \quad (2.91)$$

Note that the mode functions  $\mathbf{e}'_t$  and  $\mathbf{h}'_t$  are related via the following algebraic relation

$$\mathbf{h}'_t = \frac{\eta}{jk'_z} Z'_\infty (\hat{\mathbf{z}} \times \mathbf{e}'_t). \quad (2.92)$$

At this point the value for the modal impedance  $Z'_\infty$  is still arbitrary. Therefore we now choose a value for it such that

$$\|\mathbf{e}'_t\|^2 = \|\mathbf{h}'_t\|^2. \quad (2.93)$$

By simple inspection of equation 2.92 we see that this latter condition is satisfied if we take

$$Z'_\infty = \frac{jk'_z}{\eta}. \quad (2.94)$$

This choice for the modal impedance with dimension  $[\text{S}^{-1}]$  leads to a physical interpretation in which the mode functions  $\mathbf{e}'_t$  and  $\mathbf{h}'_t$  can be regarded as geometrical quantities with dimension  $[\text{m}^{-1}]$ . Furthermore, the amplitude coefficients  $C_E$  and  $C_H$  take the meaning of a voltage and a current, respectively. Consequently they are denoted as  $V'$  and  $I'$  and have dimension  $[\text{V}]$  and  $[\text{A}]$ , respectively. Further, note that  $\mathbf{e}'_t$  is the gradient of a scalar function. As a consequence  $\mathbf{e}'_t$  is irrotational and  $\mathbf{h}'_t$  is solenoidal.

### TE Mode Functions

The TE modes are traditionally indicated through a double prime [34, section 5.4.2]. They are characterized by a vanishing of  $e''_z$  over the entire transverse plane. All other field components are derived from a non-vanishing  $h''_z$ , which is considered as the fundamental unknown. The transverse field components now follow from equation 2.86 and 2.87 by setting  $e''_z = 0$ . This results in

$$\mathbf{e}''_t = -\frac{\xi}{k_t''^2} Y''_\infty (\nabla_t h''_z \times \hat{\mathbf{z}}), \quad (2.95)$$

$$\mathbf{h}''_t = -j \frac{k''_z}{k_t''^2} \nabla_t h''_z. \quad (2.96)$$

Note that the mode functions  $\mathbf{e}''_t$  and  $\mathbf{h}''_t$  are related via the following algebraic relation

$$\mathbf{e}''_t = \frac{\xi}{jk''_z} Y''_\infty (\mathbf{h}''_t \times \hat{\mathbf{z}}). \quad (2.97)$$

At this point the value for the modal admittance  $Y_\infty''$  is still arbitrary. Therefore we now choose a value for it such that

$$\|\mathbf{e}_t''\|^2 = \|\mathbf{h}_t''\|^2. \quad (2.98)$$

By simple inspection of equation 2.97 we see that this latter condition is satisfied if we take

$$Y_\infty'' = \frac{j k_z''}{\xi}. \quad (2.99)$$

This choice for the modal admittance with dimension [S] leads to a physical interpretation in which the mode functions  $\mathbf{e}_t''$  and  $\mathbf{h}_t''$  can be regarded as geometrical quantities with dimension  $[\text{m}^{-1}]$ . Furthermore, the amplitude coefficients  $C_E$  and  $C_H$  take the meaning of a voltage and a current, respectively. Consequently they are denoted as  $V''$  and  $I''$  and have dimension [V] and [A], respectively. Further note that  $\mathbf{h}_t''$  is the gradient of a scalar function. As a consequence  $\mathbf{h}_t''$  is irrotational and  $\mathbf{e}_t''$  is solenoidal.

### 2.4.2 Mode Functions for a Cylindrical Waveguide

In this section we specify the mode functions for a cylindrical waveguide of arbitrary shape. Let us first consider the definition of a general cylindrical waveguide. The cross section occupies a finite area  $A$  in the transverse plane. We assume the waveguide to be bounded in the transverse direction by a perfectly electric conducting boundary  $\partial A$ . The in-plane unit-length vectors  $\hat{\nu}$  and  $\hat{\tau}$  denote the outward normal and the tangent with respect to  $\partial A$ , respectively.  $\hat{\nu}$ ,  $\hat{\tau}$ , and  $\hat{z}$  form a right-handed coordinate system. Furthermore, we assume that the waveguide is infinitely long and uniform, i.e., its shape and the electromagnetic properties of the filling are independent of  $z$ . This means that the cross section  $A$  with the line boundary  $\partial A$  can be extrapolated to a volume  $V$  with a surface boundary  $\partial V$ . A graphical representation of the definition of a cylindrical waveguide is given in figure 2.4.

The wall of the cylindrical waveguide is assumed to be a perfect electric conductor. This means that the following boundary condition must be satisfied

$$\forall \rho \in \partial V [\hat{\nu} \times \hat{\mathbf{E}} = \hat{\nu} \times (\mathbf{E}_t + E_z \hat{z}) = \hat{\nu} \times \mathbf{E}_t - \hat{\tau} E_z = \mathbf{0}]. \quad (2.100)$$

Note that equation 2.100 can be split into the following two parts

$$\forall \rho \in \partial V [\hat{\nu} \times \mathbf{E}_t = \mathbf{0} \quad \text{and} \quad E_z = 0]. \quad (2.101)$$

When substituting the modal field representation in equation 2.101, we obtain

$$\forall \rho \in \partial V [\hat{\nu} \times \mathbf{e}_t = \mathbf{0} \quad \text{and} \quad e_z = 0]. \quad (2.102)$$

The first part of equation 2.102 specifies the boundary conditions in terms of the transverse field components. However we aim at deriving equations involving

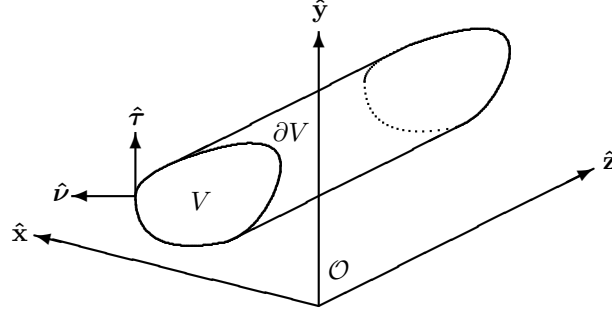


Figure 2.4: Definition of a cylindrical waveguide. Note that  $\hat{\nu}$  and  $\hat{\tau}$  are situated in the  $\hat{x}, \hat{y}$ -plane.

longitudinal components only. To solve this problem we take the cross product between  $\hat{\nu}$  and both sides of equation 2.86. We obtain

$$\hat{\nu} \times \mathbf{e}_t = -j \frac{k_z}{k_t^2} (\hat{\nu} \times \nabla_t e_z) - \frac{\xi}{k_t^2} Y_\infty \hat{\nu} \times (\nabla_t h_z \times \hat{z}), \quad (2.103)$$

which can be written in a more convenient form as

$$\hat{\nu} \times \mathbf{e}_t = -j \frac{k_z}{k_t^2} (\hat{z} \partial_\tau e_z) + \frac{\xi}{k_t^2} Y_\infty (\hat{z} \partial_\nu h_z). \quad (2.104)$$

The second boundary condition now follows from equation 2.104 by applying the boundary condition 2.102. We obtain

$$\forall \rho \in \partial V [\partial_\nu h_z = 0]. \quad (2.105)$$

For a pure TM waveguide mode, the longitudinal field components  $e'_z$  must be square integrable functions within  $V$  that satisfy

$$[\nabla_t^2 + k_t'^2] e'_z = 0, \quad (2.106)$$

and

$$\forall \rho \in \partial V [e'_z = 0]. \quad (2.107)$$

This constitutes a so-called Dirichlet boundary value problem. For a pure TE waveguide mode, the longitudinal field components  $h''_z$  must be square integrable functions within  $V$  that satisfy

$$[\nabla_t^2 + k_t''^2] h''_z = 0, \quad (2.108)$$

and

$$\forall \rho \in \partial V [\partial_\nu h''_z = 0]. \quad (2.109)$$

This constitutes a so-called Neumann boundary value problem. Both Dirichlet and Neumann boundary value problems have a doubly denumerable infinite number of solutions (modes). We label these solutions with an integer mode index  $m$  and a polarization index  $\alpha$  of which the latter can be either single (TM) or double (TE) prime. The single integer mode index  $m$  is to simplify notation. Since the problem is two-dimensional, we have two integer mode indices. The wavevectors<sup>5</sup> ( $\mathbf{k}_t^\alpha$  and  $k_z^\alpha$ ), field ( $\mathbf{u}_t^\alpha$  and  $u_z^\alpha$ ) and modal ( $U^\alpha$ ) components are written in the integer form as

$$\begin{cases} \mathbf{u}_t^\alpha(\boldsymbol{\rho}) \rightarrow \mathbf{u}_{t;m}^\alpha(\boldsymbol{\rho}), \\ u_z^\alpha(\boldsymbol{\rho}) \rightarrow u_{z;m}^\alpha(\boldsymbol{\rho}), \\ U^\alpha(z) \rightarrow U_m^\alpha(z), \\ \mathbf{k}_t^\alpha \rightarrow \mathbf{k}_{t;m}^\alpha, \\ k_z^\alpha \rightarrow k_{z;m}^\alpha. \end{cases} \quad (2.110)$$

Furthermore, the TM and TE sets of solutions combined form a basis in the space of the transverse fields [34, section 5.5] (a Hilbert space,  $\mathcal{L}^2[V]$ ). The transverse fields can therefore be written as

$$\mathbf{E}_t(\boldsymbol{\rho}, z) = \sum_{m,\alpha} V_m^\alpha(z) \mathbf{e}_{t;m}^\alpha(\boldsymbol{\rho}), \quad (2.111)$$

$$\mathbf{H}_t(\boldsymbol{\rho}, z) = \sum_{m,\alpha} I_m^\alpha(z) \mathbf{h}_{t;m}^\alpha(\boldsymbol{\rho}). \quad (2.112)$$

In the next two paragraphs, we examine some more interesting properties of the TM and TE waveguide mode functions.

### TM Mode Functions

In this paragraph we consider the properties for the TM mode functions for the cylindrical waveguide. First we prove that the Dirichlet Laplacian has (an infinite number of) real and negative eigenvalues, denoted as  $-k_{t;m}^{\prime 2}$ , with  $m = 1, 2, \dots$ . We start from the observation that a given TM mode  $e'_{z;m}$  satisfies Helmholtz' equation 2.106

$$[\nabla_t^2 + k_{t;m}^{\prime 2}] e'_{z;m} = 0. \quad (2.113)$$

Now, we take the inner product (using the bra-ket notation) of both sides of this equation with  $e'_{z;m}$ . We obtain

$$\langle [\nabla_t^2 + k_{t;m}^{\prime 2}] e'_{z;m} | e'_{z;m} \rangle = 0. \quad (2.114)$$

Solving equation 2.114 for  $k_{t;m}^{\prime 2}$  results in

$$k_{t;m}^{\prime 2} = -\frac{\langle \nabla_t^2 e'_{z;m} | e'_{z;m} \rangle}{\langle e'_{z;m} | e'_{z;m} \rangle}. \quad (2.115)$$

---

<sup>5</sup>Modes in a closed metal waveguide have in principle no wavevector, but are characterized by the eigenvalue  $-k_t^2$ .



We can simplify the numerator of this equation by using the following chain rule for differentiation by parts

$$e'_{z;m} \nabla_t^2 e'_{z;m} = \nabla_t \cdot (e'_{z;m} \nabla_t e'_{z;m}) - \nabla_t e'_{z;m} \cdot \nabla_t e'_{z;m}, \quad (2.116)$$

and by applying Gauss' divergence theorem 2.5 where  $\nabla_t \cdot \hat{\nu} dl = \partial_\nu dl$ . This leads to

$$\langle \nabla_t^2 e'_{z;m} | e'_{z;m} \rangle = \oint e'_{z;m} \partial_\nu e'_{z;m} dl - \langle \nabla_t e'_{z;m} | \nabla_t e'_{z;m} \rangle. \quad (2.117)$$

The contour integral in the right-hand side vanishes because of the boundary condition 2.107. With this result, equation 2.115 reduces to

$$k'_{t;m}{}^2 = \frac{\langle \nabla_t e'_{z;m} | \nabla_t e'_{z;m} \rangle}{\langle e'_{z;m} | e'_{z;m} \rangle} = \frac{\|\nabla_t e'_{z;m}\|^2}{\|e'_{z;m}\|^2}. \quad (2.118)$$

We conclude that the eigenvalue  $-k'_{t;m}{}^2$  is clearly real-valued and negative since it is equal to the quotient of two norms.

Next, we prove that the corresponding eigenfunctions  $e'_{z;m}$  are orthogonal. Any TM mode  $e'_{z;m}$  satisfies Helmholtz' equation 2.106

$$[\nabla_t^2 + k'_{t;m}{}^2] e'_{z;m} = 0, \quad (2.119)$$

where we have taken into account that  $k'_{t;n}{}^2$  is real-valued. Taking the inner product of equation 2.119 with  $e'_{z;n}$  and subtracting the counterpart with  $m$  and  $n$  interchanged, we obtain

$$\int (e'_{z;n} \nabla_t^2 e'_{z;m} - e'_{z;m} \nabla_t^2 e'_{z;n}) dA = -(k'_{t;m}{}^2 - k'_{t;n}{}^2) \langle e'_{z;m} | e'_{z;n} \rangle. \quad (2.120)$$

We can simplify the left-hand side of equation 2.120 by using the following chain rule for differentiation by parts

$$e'_{z;n} \nabla_t^2 e'_{z;m} - e'_{z;m} \nabla_t^2 e'_{z;n} = \nabla_t \cdot (e'_{z;n} \nabla_t e'_{z;m} - e'_{z;m} \nabla_t e'_{z;n}), \quad (2.121)$$

and by applying Gauss' divergence theorem. Doing this leads us to

$$\begin{aligned} \int (e'_{z;n} \nabla_t^2 e'_{z;m} - e'_{z;m} \nabla_t^2 e'_{z;n}) dA = \\ \oint (e'_{z;n} \partial_\nu e'_{z;m} - e'_{z;m} \partial_\nu e'_{z;n}) dl. \end{aligned} \quad (2.122)$$

Equation 2.122 is known as Green's second theorem. The contour integral in the right-hand side vanishes because of the boundary condition 2.107. With this result, equation 2.120 reduces to

$$\langle e'_{z;m} | e'_{z;n} \rangle = 0 \quad \text{if} \quad k'_{t;m}{}^2 \neq k'_{t;n}{}^2. \quad (2.123)$$

We conclude that the longitudinal field components are orthogonal for different eigenvalues. For equal eigenvalues  $k'_{t;m}{}^2 = k'_{t;n}{}^2$  the Gram-Schmidt process

always allows us to construct a set of orthogonal longitudinal field components  $\{e'_{z;m}, e'_{z;n}\}$  since every linear combination is also an eigenfunction [99, 3].

Subsequently, we prove that the corresponding mode functions  $\mathbf{e}'_{t;m}$  and  $\mathbf{h}'_{t;m}$  are orthogonal. To do so we rewrite the inner product between two given TM modes  $\mathbf{e}'_{t;m}$  and  $\mathbf{e}'_{t;n}$  with the aid of equation 2.90 as

$$\langle \mathbf{e}'_{t;m} | \mathbf{e}'_{t;n} \rangle = \frac{k'_{z;m} k'_{z;n}}{k'^2_{t;m} k'^2_{t;n}} \langle \nabla_t e'_{z;m} | \nabla_t e'_{z;n} \rangle. \quad (2.124)$$

Note that we have taken into account that  $k'^2_{t;n}$  is real-valued. The inner product in the right-hand side of equation 2.124 can be rewritten by using the following product rule for differentiation by parts

$$\begin{aligned} \nabla_t e'_{z;m} \cdot \nabla_t e'^*_{z;n} &= \nabla_t \cdot (e'_{z;m} \nabla_t e'^*_{z;n}) - e'_{z;m} \nabla_t^2 e'^*_{z;n} \\ &= \nabla_t \cdot (e'_{z;m} \nabla_t e'^*_{z;n}) + k'^2_{t;n} e'_{z;m} e'^*_{z;n}. \end{aligned} \quad (2.125)$$

In deriving equation 2.125 we have used Helmholtz' equation 2.106, the fact that  $k'^2_{t;n}$  is real-valued, and Gauss' divergence theorem. This leads to

$$\langle \mathbf{e}'_{t;m} | \mathbf{e}'_{t;n} \rangle = \frac{k'_{z;m} k'_{z;n}}{k'^2_{t;m} k'^2_{t;n}} \left( \oint e'_{z;m} \partial_\nu e'^*_{z;n} d\ell + k'^2_{t;n} \langle e'_{z;m} | e'_{z;n} \rangle \right). \quad (2.126)$$

First, the contour integral vanishes due to the boundary condition 2.107. Second, the inner product vanishes due to the orthogonality of the longitudinal field components, as given in equation 2.123. Thus, equation 2.126 reduces to

$$\langle \mathbf{e}'_{t;m} | \mathbf{e}'_{t;n} \rangle = 0 \quad \text{if } k'^2_{t;m} \neq k'^2_{t;n}. \quad (2.127)$$

As a consequence of equation 2.92 we also have

$$\langle \mathbf{h}'_{t;m} | \mathbf{h}'_{t;n} \rangle = 0 \quad \text{if } k'^2_{t;m} \neq k'^2_{t;n}. \quad (2.128)$$

We conclude that the transverse field components are orthogonal.

Finally, the complex power transported by a single TM mode can be obtained by invoking Poynting's theorem. This results in

$$S_m = P_m + jQ_m = V'_m I'^*_m \int (\mathbf{e}'_{t;m} \times \mathbf{h}'_{t;m}) \cdot \hat{\mathbf{z}} dA. \quad (2.129)$$

Relation 2.92 fixes the magnitude of  $\mathbf{h}'_{t;m}$  relative to  $\mathbf{e}'_{t;m}$ . Furthermore, due to the choice of  $Z'_{\infty;m}$ , the norm of  $\mathbf{h}'_{t;m}$  equals the norm of  $\mathbf{e}'_{t;m}$ . However, the value of the norm is still arbitrary. We take advantage of this situation by setting this norm equal to one. With this normalization, the value of the integral in equation 2.129 is known since

$$\|\mathbf{e}'_{t;m}\|^2 = \int \mathbf{e}'_{t;m} \cdot (\mathbf{h}'_{t;m} \times \hat{\mathbf{z}}) dA = \int (\mathbf{e}'_{t;m} \times \mathbf{h}'_{t;m}) \cdot \hat{\mathbf{z}} dA. \quad (2.130)$$

Consequently, the complex power transported by a single TM mode has the same form as the one used in circuit theory, i.e.

$$S_m = P_m + jQ_m = V'_m I'_m{}^* \quad (2.131)$$

By substituting  $m = n$  in equation 2.126, we obtain

$$\|\mathbf{e}'_{t;m}\|^2 = \frac{|k'_{z;m}|^2}{k'^2_{t;m}} \int |e'_{z;m}|^2 dA. \quad (2.132)$$

A careful inspection of equation 2.132 shows that we can obtain a normalized  $\mathbf{e}'_{t;m}$  by introducing a new set of scalar generating functions  $\Phi_m = \Phi_m(\boldsymbol{\rho})$  [34, section 5.4.1], such that

$$e'_{z;m} = -j \frac{k'_{t;m}}{k'_{z;m}} \Phi_m. \quad (2.133)$$

The scalar generating functions  $\Phi_m$  must be square integrable, satisfy

$$[\nabla_t^2 + k'^2_{t;m}] \Phi_m = 0, \quad (2.134)$$

and must be supplemented with the following boundary condition

$$\forall m, \forall \boldsymbol{\rho} \in \partial V [\Phi_m(\boldsymbol{\rho}) = 0]. \quad (2.135)$$

The functions  $\{\Phi_m\}$  are normalized by forcing

$$\langle \Phi_m | \Phi_n \rangle = \delta_{m,n}. \quad (2.136)$$

The TM mode functions can now be written as

$$\mathbf{e}'_{t;m} = -\frac{\nabla_t \Phi_m}{k'_{t;m}}, \quad (2.137)$$

$$\mathbf{h}'_{t;m} = \frac{\nabla_t \Phi_m}{k'_{t;m}} \times \hat{\mathbf{z}}. \quad (2.138)$$

From the definitions 2.134-2.138 it follows that the quantities  $\mathbf{k}'_{t;m}$ ,  $\Phi_m$  and  $\mathbf{e}'_{t;m}$  depend neither on the frequency nor on the value of the scalar constitutive parameters.  $e'_{z;m}$ , however, does depend on these latter two parameters via  $k'_{z;m}$ .

### TE Mode Functions

In this paragraph we consider the properties for the TE mode functions for the cylindrical waveguide. First we prove that the Neumann Laplacian has (an infinite number of) real and negative eigenvalues, denoted as  $-k''^2_{t;m}$ , with  $m = 1, 2, \dots$ . We start from the observation that a given TE mode  $h''_{z;m}$  satisfies Helmholtz' equation 2.108

$$[\nabla_t^2 + k''^2_{t;m}] h''_{z;m} = 0. \quad (2.139)$$

Next, we take the inner product (using the bra-ket notation) of both sides of this equation with  $h''_{z;m}$ . We obtain

$$\langle [\nabla_t^2 + k''_{t;m}] h''_{z;m} | h''_{z;m} \rangle = 0. \quad (2.140)$$

Solving equation 2.140 for  $k''_{t;m}$  results in

$$k''_{t;m} = -\frac{\langle \nabla_t^2 h''_{z;m} | h''_{z;m} \rangle}{\langle h''_{z;m} | h''_{z;m} \rangle}. \quad (2.141)$$

We can simplify the numerator of this equation by using the following chain rule for differentiation by parts

$$h''_{z;m} \nabla_t^2 h''_{z;m} = \nabla_t \cdot (h''_{z;m} \nabla_t h''_{z;m}) - \nabla_t h''_{z;m} \cdot \nabla_t h''_{z;m}, \quad (2.142)$$

and by applying Gauss' divergence theorem 2.5. This leads to

$$\langle \nabla_t^2 h''_{z;m} | h''_{z;m} \rangle = \oint h''_{z;m} \partial_\nu h''_{z;m} d\ell - \langle \nabla_t h''_{z;m} | \nabla_t h''_{z;m} \rangle. \quad (2.143)$$

The contour integral in the right-hand side vanishes because of the boundary condition 2.109. With this result, equation 2.141 reduces to

$$k''_{t;m} = \frac{\langle \nabla_t h''_{z;m} | \nabla_t h''_{z;m} \rangle}{\langle h''_{z;m} | h''_{z;m} \rangle} = \frac{\|\nabla_t h''_{z;m}\|^2}{\|h''_{z;m}\|^2}. \quad (2.144)$$

We conclude that the eigenvalue  $-k''_{t;m}$  is clearly real-valued and negative since it is equal to the quotient of two norms.

Next, we prove that the corresponding eigenfunctions  $h''_{z;m}$  are orthogonal. Any TE mode  $h''_{z;m}$  satisfies Helmholtz' equation 2.108

$$[\nabla_t^2 + k''_{t;m}] h''_{z;m} = 0, \quad (2.145)$$

where we have taken into account that  $k''_{t;n}$  is real-valued. Taking the inner product of equation 2.145 with  $h''_{z;n}$  and subtracting the counterpart with  $m$  and  $n$  interchanged, we obtain

$$\int (h''_{z;n} \nabla_t^2 h''_{z;m} - h''_{z;m} \nabla_t^2 h''_{z;n}) dA = -(k''_{t;m} - k''_{t;n}) \langle h''_{z;m} | h''_{z;n} \rangle. \quad (2.146)$$

By using the Green's second theorem as derived in equation 2.122 we can simplify the left-hand side of equation 2.146 to

$$\begin{aligned} \int (h''_{z;n} \nabla_t^2 h''_{z;m} - h''_{z;m} \nabla_t^2 h''_{z;n}) dA = \\ \oint (h''_{z;n} \partial_\nu h''_{z;m} - h''_{z;m} \partial_\nu h''_{z;n}) d\ell. \end{aligned} \quad (2.147)$$

The contour integral in equation 2.147 vanishes because of the boundary condition 2.109. With this result, equation 2.146 reduces to

$$\langle h''_{z;m} | h''_{z;n} \rangle = 0 \quad \text{if } k''_{t;m} \neq k''_{t;n}. \quad (2.148)$$

We conclude that the longitudinal field components are orthogonal for different eigenvalues. For equal eigenvalues  $k''_{t;m} = k''_{t;n}$  the Gram-Schmidt process always allows us to construct a set of orthogonal longitudinal field components  $\{e'_{z;m}, e'_{z;n}\}$  since every linear combination is also an eigenfunction [99, 3].

Subsequently, we prove that the corresponding mode functions  $\mathbf{e}''_{t;m}$  and  $\mathbf{h}''_{t;m}$  are orthogonal. To do so we rewrite the inner product between two given TE modes  $\mathbf{h}''_{t;m}$  and  $\mathbf{h}''_{t;n}$  with the aid of equation 2.96 as

$$\langle \mathbf{h}''_{t;m} | \mathbf{h}''_{t;n} \rangle = \frac{k''_{z;m} k''_{z;n}}{k''_{t;m} k''_{t;n}} \langle \nabla_t h''_{z;m} | \nabla_t h''_{z;n} \rangle, \quad (2.149)$$

where we have taken into account that  $k''_{t;n}$  is real-valued. The inner product in the right-hand side of equation 2.149 can be rewritten by using the following product rule for differentiation by parts

$$\begin{aligned} \nabla_t h''_{z;m} \cdot \nabla_t h''_{z;n} &= \nabla_t \cdot (h''_{z;m} \nabla_t h''_{z;n}) - h''_{z;m} \nabla_t^2 h''_{z;n} \\ &= \nabla_t \cdot (h''_{z;m} \nabla_t h''_{z;n}) + k''_{t;n} h''_{z;m} h''_{z;n}. \end{aligned} \quad (2.150)$$

In deriving equation 2.150 we have used Helmholtz' equation 2.108, the fact that  $k''_{t;n}$  is real-valued, and Gauss' divergence theorem. We end up with

$$\langle \mathbf{h}''_{t;m} | \mathbf{h}''_{t;n} \rangle = \frac{k''_{z;m} k''_{z;n}}{k''_{t;m} k''_{t;n}} \left( \oint h''_{z;m} \partial_\nu h''_{z;n} d\ell + k''_{t;n} \langle h''_{z;m} | h''_{z;n} \rangle \right). \quad (2.151)$$

First, the contour integral vanishes due to the boundary condition 2.109. Second, the inner product vanishes due to the orthogonality of the longitudinal field components, as given in equation 2.148. Thus, equation 2.151 reduces to

$$\langle \mathbf{h}''_{t;m} | \mathbf{h}''_{t;n} \rangle = 0 \quad \text{if } k''_{t;m} \neq k''_{t;n}. \quad (2.152)$$

As a consequence of equation 2.97 we also have

$$\langle \mathbf{e}''_{t;m} | \mathbf{e}''_{t;n} \rangle = 0 \quad \text{if } k''_{t;m} \neq k''_{t;n}. \quad (2.153)$$

We conclude that the transverse field components are orthogonal.

Finally, the complex power transported by a single TE mode can be obtained by invoking Poynting's theorem. This results in

$$S_m = P_m + jQ_m = V''_m I''_{m*} \int (\mathbf{e}''_{t;m} \times \mathbf{h}''_{t;m*}) \cdot \hat{\mathbf{z}} dA. \quad (2.154)$$

Relation 2.97 fixes the magnitude of  $\mathbf{e}''_{t;m}$  relative to  $\mathbf{h}''_{t;m}$ . Furthermore, due to the choice of  $Y''_{\infty;m}$ , the norm of  $\mathbf{e}''_{t;m}$  equals the norm of  $\mathbf{h}''_{t;m}$ . However,

the value of the norm is still arbitrary. We take advantage of this situation by setting this norm to be one. With this normalization, the integral in equation 2.154 has a fixed value since

$$\|\mathbf{h}''_{t;m}\|^2 = \int (\hat{\mathbf{z}} \times \mathbf{e}''_{t;m}) \cdot \mathbf{h}''_{t;m}{}^* dA = \int (\mathbf{e}''_{t;m} \times \mathbf{h}''_{t;m}{}^*) \cdot \hat{\mathbf{z}} dA. \quad (2.155)$$

Again, the complex power transported by a single TE mode has the same form as the one used in circuit theory, i.e.

$$S_m = P_m + jQ_m = V_m'' I_m''^*. \quad (2.156)$$

Choosing  $m = n$  in equation 2.151 results in

$$\|\mathbf{h}''_{t;m}\|^2 = \frac{|k''_{z;m}|^2}{k''_{t;m}} \int |h''_{z;m}|^2 dA. \quad (2.157)$$

A careful inspection of equation 2.157 shows that we can obtain a normalized  $\mathbf{h}''_{t;m}$  by introducing a new set of scalar generating functions  $\Psi_m = \Psi_m(\boldsymbol{\rho})$  [34, section 5.4.2], such that

$$h''_{z;m} = -j \frac{k''_{t;m}}{k''_{z;m}} \Psi_m. \quad (2.158)$$

The scalar generating functions  $\Psi_m$  must be square integrable, satisfy

$$[\nabla_t^2 + k''_{t;m}] \Psi_m = 0, \quad (2.159)$$

and must be supplemented with the following boundary condition

$$\forall m, \forall \boldsymbol{\rho} \in \partial V [\partial_\nu \Psi_m(\boldsymbol{\rho}) = 0]. \quad (2.160)$$

The functions  $\{\Psi_m\}$  are normalized by forcing

$$\langle \Psi_m | \Psi_n \rangle = \delta_{m,n}. \quad (2.161)$$

The TE mode functions can now be written as

$$\mathbf{h}''_{t;m} = -\frac{\nabla_t \Psi_m}{k''_{t;m}}, \quad (2.162)$$

$$\mathbf{e}''_{t;m} = \hat{\mathbf{z}} \times \frac{\nabla_t \Psi_m}{k''_{t;m}}. \quad (2.163)$$

From the definitions 2.159-2.163 it follows that the quantities  $k''_{t;m}$ ,  $\Psi_m$  and  $\mathbf{h}''_{t;m}$  depend neither on the frequency nor on the value of the scalar constitutive parameters.  $h''_{z;m}$ , however, does depend on these latter two parameters via  $k''_{z;m}$ .

### 2.4.3 Mode Functions for a Layered Space

In this section we determine the mode functions for the layered space. Let us first consider the definition of a layered space. The cross-section occupies an infinite area in the transverse plane. Furthermore we assume that the layered space is infinitely long and piecewise uniform in the  $z$ -direction, i.e., the electromagnetic properties of its filling are piecewise constant and independent of a finite interval in  $z$ .

For a pure TM mode, the longitudinal field components  $e'_z$  must be square integrable over any finite interval and satisfy

$$[\nabla_t^2 + k_t'^2] e'_z = 0. \quad (2.164)$$

In a similar way, for a pure TE mode, the longitudinal field components  $h''_z$  must be square integrable over any finite interval and satisfy

$$[\nabla_t^2 + k_t''^2] h''_z = 0. \quad (2.165)$$

Both equations 2.164 and 2.165 have a continuous set of solutions (modes or plane waves<sup>6</sup>). We label these solutions with a continuous mode index wavevector  $\mathbf{k}_t$  and a polarization index  $\alpha$  of which the latter can be either a single (TM) or a double prime (TE). The wavevectors ( $\mathbf{k}_t^\alpha$  and  $k_z^\alpha$ ), field ( $\mathbf{u}_t^\alpha$  and  $u_z^\alpha$ ) and modal ( $U^\alpha$ ) components are written in the continuous form as

$$\begin{cases} \mathbf{u}_t^\alpha(\boldsymbol{\rho}) \rightarrow \mathbf{u}_t^\alpha(\mathbf{k}_t, \boldsymbol{\rho}), \\ u_z^\alpha(\boldsymbol{\rho}) \rightarrow u_z^\alpha(\mathbf{k}_t, \boldsymbol{\rho}), \\ U^\alpha(z) \rightarrow U^\alpha(\mathbf{k}_t, z), \\ \mathbf{k}_t^\alpha \rightarrow \mathbf{k}_t^\alpha(\mathbf{k}_t) = \mathbf{k}_t, \\ k_z^\alpha \rightarrow k_z^\alpha(\mathbf{k}_t) = k_z. \end{cases} \quad (2.166)$$

Furthermore the TM and TE sets of solutions combined form a basis in the space of the transverse fields [104] (a Hilbert space,  $\mathcal{L}^2$ ). The transverse fields can therefore be written in the following general form as

$$\mathbf{E}_t(\boldsymbol{\rho}, z) = \sum_\alpha \int V^\alpha(\mathbf{k}_t, z) \mathbf{e}_t^\alpha(\mathbf{k}_t, \boldsymbol{\rho}) d\mathbf{k}_t, \quad (2.167)$$

$$\mathbf{H}_t(\boldsymbol{\rho}, z) = \sum_\alpha \int I^\alpha(\mathbf{k}_t, z) \mathbf{h}_t^\alpha(\mathbf{k}_t, \boldsymbol{\rho}) d\mathbf{k}_t. \quad (2.168)$$

In the next two paragraphs we examine the most interesting properties of the TM and TE layered space mode functions.

---

<sup>6</sup>The modes in this case can be either plane waves or cylindrical waves. Clearly, on account of the application to phased arrays, the modes are chosen in the form of plane waves.

### TM Mode Functions

Inspired by equation 2.133 we introduce a similar set of scalar generating functions  $\Phi(\mathbf{k}_t) = \Phi(\mathbf{k}_t, \boldsymbol{\rho})$ , such that

$$e'_z(\mathbf{k}_t) = -j \frac{k_t}{k_z} \Phi(\mathbf{k}_t). \quad (2.169)$$

The scalar generating functions  $\Phi(\mathbf{k}_t)$  must be square integrable and must satisfy the two-dimensional Helmholtz equation

$$[\nabla_t^2 + k_t^2] \Phi(\mathbf{k}_t) = 0. \quad (2.170)$$

The functions  $\{\Phi(\mathbf{k}_t)\}$  are normalized in distributional sense by forcing

$$\langle \Phi(\mathbf{k}'_t) | \Phi(\mathbf{k}''_t) \rangle = \delta(\mathbf{k}'_t - \mathbf{k}''_t). \quad (2.171)$$

This equation also ensures the orthogonality between two different TM layered space modes with index  $\mathbf{k}'_t$  and  $\mathbf{k}''_t$ . Solving equation 2.170 for  $\Phi(\mathbf{k}_t)$  and requiring 2.171 leads to

$$\Phi(\mathbf{k}_t) = \frac{1}{2\pi} \exp(-j\mathbf{k}_t \cdot \boldsymbol{\rho}). \quad (2.172)$$

By using equation 2.169, we find the corresponding longitudinal field component as

$$e'_z(\mathbf{k}_t) = -\frac{j}{2\pi} \frac{k_t}{k_z} \exp(-j\mathbf{k}_t \cdot \boldsymbol{\rho}). \quad (2.173)$$

The layered space TM mode functions are now obtained from equations 2.90 and 2.91. We find

$$\mathbf{e}'_t(\mathbf{k}_t) = \frac{j}{2\pi} \hat{\mathbf{k}} \exp(-j\mathbf{k}_t \cdot \boldsymbol{\rho}), \quad (2.174)$$

$$\mathbf{h}'_t(\mathbf{k}_t) = -\frac{j}{2\pi} \hat{\boldsymbol{\alpha}} \exp(-j\mathbf{k}_t \cdot \boldsymbol{\rho}), \quad (2.175)$$

in which  $\hat{\mathbf{k}} = \mathbf{k}_t/k_t$  and  $\hat{\boldsymbol{\alpha}} = \hat{\mathbf{k}} \times \hat{\mathbf{z}}$ .

### TE Mode Functions

To obtain the TE modes we introduce a similar set of scalar generating functions  $\Psi(\mathbf{k}_t) = \Psi(\mathbf{k}_t, \boldsymbol{\rho})$ , such that

$$h''_z(\mathbf{k}_t) = -j \frac{k_t}{k_z} \Psi(\mathbf{k}_t). \quad (2.176)$$

The scalar generating functions  $\Psi(\mathbf{k}_t)$  must be square integrable and must satisfy the two-dimensional Helmholtz equation

$$[\nabla_t^2 + k_t^2] \Psi(\mathbf{k}_t) = 0. \quad (2.177)$$



The functions  $\{\Psi(\mathbf{k}_t)\}$  are normalized in distributional sense by forcing

$$\langle \Psi(\mathbf{k}'_t) | \Psi(\mathbf{k}''_t) \rangle = \delta(\mathbf{k}'_t - \mathbf{k}''_t). \quad (2.178)$$

This equation inherently ensures the orthogonality between two different TE layered space modes with index  $\mathbf{k}'_t$  and  $\mathbf{k}''_t$ . Solving equation 2.177 for  $\Psi(\mathbf{k}_t)$  and requiring 2.178 leads to

$$\Psi(\mathbf{k}_t) = \frac{1}{2\pi} \exp(-j\mathbf{k}_t \cdot \boldsymbol{\rho}). \quad (2.179)$$

The corresponding longitudinal field component is now obtained from equation 2.176 as

$$h_z''(\mathbf{k}_t) = -\frac{j}{2\pi} \frac{k_t}{k_z} \exp(-j\mathbf{k}_t \cdot \boldsymbol{\rho}). \quad (2.180)$$

The layered space TE mode functions are now obtained from equations 2.95 and 2.96. We find

$$\mathbf{h}_t''(\mathbf{k}_t) = \frac{j}{2\pi} \hat{\mathbf{k}} \exp(-j\mathbf{k}_t \cdot \boldsymbol{\rho}), \quad (2.181)$$

$$\mathbf{e}_t''(\mathbf{k}_t) = \frac{j}{2\pi} \hat{\boldsymbol{\alpha}} \exp(-j\mathbf{k}_t \cdot \boldsymbol{\rho}). \quad (2.182)$$

Substituting the results for the TM and TE layered space mode functions in equations 2.167 and 2.168 finally results in

$$\mathbf{E}_t(\boldsymbol{\rho}, z) = \frac{1}{2\pi} \int \bar{\mathbf{E}}_t(\mathbf{k}_t, z) \exp(-j\mathbf{k}_t \cdot \boldsymbol{\rho}) d\mathbf{k}_t, \quad (2.183)$$

$$\mathbf{H}_t(\boldsymbol{\rho}, z) = \frac{1}{2\pi} \int \bar{\mathbf{H}}_t(\mathbf{k}_t, z) \exp(-j\mathbf{k}_t \cdot \boldsymbol{\rho}) d\mathbf{k}_t, \quad (2.184)$$

in which

$$\bar{\mathbf{E}}_t(\mathbf{k}_t, z) = j \frac{\mathbf{k}_t}{k_t} V'(\mathbf{k}_t, z) - j \left( \hat{\mathbf{z}} \times \frac{\mathbf{k}_t}{k_t} \right) V''(\mathbf{k}_t, z), \quad (2.185)$$

$$\bar{\mathbf{H}}_t(\mathbf{k}_t, z) = j \left( \hat{\mathbf{z}} \times \frac{\mathbf{k}_t}{k_t} \right) I'(\mathbf{k}_t, z) + j \frac{\mathbf{k}_t}{k_t} I''(\mathbf{k}_t, z). \quad (2.186)$$

In these equations we recognize the well-known spectral field representation expressed in terms of a two-dimensional Fourier transform [104].

The modes for which  $k_t = 0$  are TEM modes. There are two linearly independent ones, one with the electric field parallel to the  $x$ -axis and the other one with the electric field parallel to the  $y$ -axis (for example). Moreover, when phase shift walls are added, the modal spectrum becomes discrete and the modes are the Floquet modes.

### 2.4.4 Modal Transmission Line Equations

Without loss of generality, the transverse electromagnetic field in an arbitrary planarly stratified medium can be written as

$$\mathbf{E}_t(\boldsymbol{\rho}, z) = \mathcal{S}[V^\alpha(z)\mathbf{e}_t^\alpha(\boldsymbol{\rho})], \quad (2.187)$$

$$\mathbf{H}_t(\boldsymbol{\rho}, z) = \mathcal{S}[I^\alpha(z)\mathbf{h}_t^\alpha(\boldsymbol{\rho})], \quad (2.188)$$

where  $\mathcal{S}[\cdot]$  indicates a linear superposition of denumerable or non-denumerable modes. This field representation assumes the form of either equations 2.109 and 2.110 for the general cylindrical waveguide or equations 2.165 and 2.166 for the layered space. The  $z$ -dependent components  $V^\alpha(z)$  and  $I^\alpha(z)$  are referred to as the modal voltages and currents for the electric and magnetic field components, respectively [112, section 6.2]. They show an exponential  $z$ -dependence in the source-free case for piecewise homogeneous media.

In this section we use the Marcuvitz-Schwinger equations combined with the mode functions to derive the modal transmission line equations that describe the evolution of these modal voltages and currents. This only depends on the cross-section, and is allowed since the set of mode functions is complete. To start with the derivation of the modal transmission line equations, let us first substitute the field representation, equations 2.187 and 2.188, in the Marcuvitz-Schwinger equations 2.57 and 2.58. We obtain

$$-\mathcal{S}[\mathbf{e}_t^\alpha \partial_z V^\alpha(z)] = \xi \mathcal{S}[I^\alpha(z)\mathcal{W} \cdot (\mathbf{h}_t^\alpha \times \hat{\mathbf{z}})] + \mathbf{M}_t^{\text{eff}} \times \hat{\mathbf{z}}, \quad (2.189)$$

$$-\mathcal{S}[\mathbf{h}_t^\alpha \partial_z I^\alpha(z)] = \eta \mathcal{S}[V^\alpha(z)\mathcal{W} \cdot (\hat{\mathbf{z}} \times \mathbf{e}_t^\alpha)] + \hat{\mathbf{z}} \times \mathbf{J}_t^{\text{eff}}, \quad (2.190)$$

with  $\mathcal{W} = I_t + k^{-2}\nabla_t \nabla_t$ . Subsequently, we take the inner product of equations 2.189 and 2.190 with  $\mathbf{e}_t^\beta$  and  $\mathbf{h}_t^\beta$ , respectively. Note that  $\mathbf{e}_t^\beta$  and  $\mathbf{h}_t^\beta$  not only differ from  $\mathbf{e}_t^\alpha$  and  $\mathbf{h}_t^\alpha$  in polarization index  $\beta$  but can also differ in the indices  $m$  or  $\mathbf{k}_t$  for the waveguide or layered space, respectively. Doing this leads to

$$-\partial_z V^\beta(z) = \xi \mathcal{S}[I^\alpha(z) \langle \mathcal{W} \cdot \mathbf{e}_t^\alpha | \mathbf{e}_t^\beta \rangle] + \langle \mathbf{M}_t^{\text{eff}} \times \hat{\mathbf{z}} | \mathbf{e}_t^\beta \rangle, \quad (2.191)$$

$$-\partial_z I^\beta(z) = \eta \mathcal{S}[V^\alpha(z) \langle \mathcal{W} \cdot \mathbf{h}_t^\alpha | \mathbf{h}_t^\beta \rangle] + \langle \hat{\mathbf{z}} \times \mathbf{J}_t^{\text{eff}} | \mathbf{h}_t^\beta \rangle. \quad (2.192)$$

Furthermore, the inner products containing the  $\mathcal{W}$ -operator can be elaborated by using the orthogonality properties of the modes. For the waveguide modes this results in

$$\langle \mathcal{W} \cdot \mathbf{e}_{t;m}^\alpha | \mathbf{e}_{t;n}^\beta \rangle = \begin{cases} \frac{k_{z;n}^{\prime 2}}{k^2} \delta_{m,n} & \text{if } \alpha \text{ and } \beta \text{ are TM modes,} \\ \delta_{m,n} & \text{if } \alpha \text{ and } \beta \text{ are TE modes,} \\ 0 & \text{otherwise,} \end{cases} \quad (2.193)$$

and

$$\langle \mathcal{W} \cdot \mathbf{h}_{t;m}^\alpha | \mathbf{h}_{t;n}^\beta \rangle = \begin{cases} \delta_{m,n} & \text{if } \alpha \text{ and } \beta \text{ are TM modes,} \\ \frac{k_{z;n}^{\prime 2}}{k^2} \delta_{m,n} & \text{if } \alpha \text{ and } \beta \text{ are TE modes,} \\ 0 & \text{otherwise.} \end{cases} \quad (2.194)$$

For the layered space modes this results in

$$\langle \mathcal{W} \cdot \mathbf{e}_t^\alpha(\mathbf{k}'_t) | \mathbf{e}_t^\beta(\mathbf{k}''_t) \rangle = \begin{cases} \frac{k_z'^{1/2}}{k_z''} \delta(\mathbf{k}'_t - \mathbf{k}''_t) & \text{if } \alpha \text{ and } \beta \text{ are TM modes,} \\ \delta(\mathbf{k}'_t - \mathbf{k}''_t) & \text{if } \alpha \text{ and } \beta \text{ are TE modes,} \\ 0 & \text{otherwise,} \end{cases} \quad (2.195)$$

and

$$\langle \mathcal{W} \cdot \mathbf{h}_t^\alpha(\mathbf{k}'_t) | \mathbf{h}_t^\beta(\mathbf{k}''_t) \rangle = \begin{cases} \delta(\mathbf{k}'_t - \mathbf{k}''_t) & \text{if } \alpha \text{ and } \beta \text{ are TM modes,} \\ \frac{k_z'^{1/2}}{k_z''} \delta(\mathbf{k}'_t - \mathbf{k}''_t) & \text{if } \alpha \text{ and } \beta \text{ are TE modes,} \\ 0 & \text{otherwise.} \end{cases} \quad (2.196)$$

By substituting these simplifications for the inner products in equations 2.191 and 2.192, we arrive at the so-called modal transmission line equations, where  $V^\alpha(z)$  and  $I^\alpha(z)$  satisfy

$$-\partial_z V^\alpha(z) = jk_z^\alpha Z_\infty^\alpha I^\alpha(z) + v^\alpha(z), \quad (2.197)$$

$$-\partial_z I^\alpha(z) = jk_z^\alpha Y_\infty^\alpha V^\alpha(z) + i^\alpha(z), \quad (2.198)$$

and in which the voltages and currents are defined as

$$V^\alpha(z) = \langle \mathbf{E}_t(\boldsymbol{\rho}, z) | \mathbf{e}_t^\alpha(\boldsymbol{\rho}) \rangle, \quad (2.199)$$

$$I^\alpha(z) = \langle \mathbf{H}_t(\boldsymbol{\rho}, z) | \mathbf{h}_t^\alpha(\boldsymbol{\rho}) \rangle, \quad (2.200)$$

$$v^\alpha(z) = \langle \mathbf{M}_t^{\text{eff}}(\boldsymbol{\rho}, z) \times \hat{\mathbf{z}} | \mathbf{e}_t^\alpha(\boldsymbol{\rho}) \rangle, \quad (2.201)$$

$$i^\alpha(z) = \langle \hat{\mathbf{z}} \times \mathbf{J}_t^{\text{eff}}(\boldsymbol{\rho}, z) | \mathbf{h}_t^\alpha(\boldsymbol{\rho}) \rangle. \quad (2.202)$$

A circuit representation of the first and second modal transmission line equation is given in figures 2.5 and 2.6, respectively<sup>7</sup>. Combining these two circuits leads to a circuit representation of an infinitesimally small piece of transmission line, and is given in figure 2.7. Note that the order in which the two are combined is irrelevant. The circuit representation for a finite length transmission line between  $z = z_1$  and  $z = z_3$  with a voltage and current generator at  $z = z_2$  is given in figure 2.8, where for  $z_1 < z < z_2$  and  $z_2 < z < z_3$  the line is characterized by a characteristic admittance  $Y_\infty^{(1)}$  and  $Y_\infty^{(2)}$ , respectively.

A homogeneous solution for  $V^\alpha(z)$  and  $I^\alpha(z)$  can be found by solving the source-free modal transmission line equations with  $v^\alpha(z) = 0$  and  $i^\alpha(z) = 0$ . In a region where  $k_z^\alpha$  remains constant,  $V^\alpha(z)$  and  $I^\alpha(z)$  must then satisfy

$$\left[ \partial_z^2 + k_z^{\alpha 2} \right] V^\alpha(z) = 0, \quad (2.203)$$

$$\left[ \partial_z^2 + k_z^{\alpha 2} \right] I^\alpha(z) = 0, \quad (2.204)$$

<sup>7</sup>In principle these separate circuits do not exist and serve no purpose except for "visualizing" the Kirchhof laws. The equations 2.197 and 2.198 form a system, they are to be taken together, at the same time. The corresponding structure is that of figure 2.7.

which justifies the assumption for the exponential  $z$ -dependence of the field solutions. At discontinuous interfaces at  $z = z_0$ , appropriate boundary conditions for  $V^\alpha(z)$  and  $I^\alpha(z)$  can be found by integrating the modal transmission line equations across the interface. At  $z = z_0$ ,  $V^\alpha(z)$  and  $I^\alpha(z)$  must then satisfy

$$\lim_{z \uparrow z_0} V^\alpha(z) - \lim_{z \downarrow z_0} V^\alpha(z) = \lim_{\Delta z \rightarrow 0} \int_{z_0 - \Delta z}^{z_0 + \Delta z} v^\alpha(z) dz, \quad (2.205)$$

$$\lim_{z \uparrow z_0} I^\alpha(z) - \lim_{z \downarrow z_0} I^\alpha(z) = \lim_{\Delta z \rightarrow 0} \int_{z_0 - \Delta z}^{z_0 + \Delta z} i^\alpha(z) dz. \quad (2.206)$$

Finally, we consider the determination of the modal voltage  $v^\alpha(z)$  and current  $i^\alpha(z)$  generators which were defined as

$$v^\alpha(z) = \langle \mathbf{M}_t^{\text{eff}}(\boldsymbol{\rho}, z) \times \hat{\mathbf{z}} | \mathbf{e}_t^\alpha(\boldsymbol{\rho}) \rangle = \langle \mathbf{M}_t^{\text{eff}} | \mathbf{h}_t^\alpha \rangle, \quad (2.207)$$

$$i^\alpha(z) = \langle \hat{\mathbf{z}} \times \mathbf{J}_t^{\text{eff}}(\boldsymbol{\rho}, z) | \mathbf{h}_t^\alpha(\boldsymbol{\rho}) \rangle = \langle \mathbf{J}_t^{\text{eff}} | \mathbf{e}_t^\alpha \rangle, \quad (2.208)$$

in which

$$\mathbf{M}_t^{\text{eff}} = \mathbf{M}_t + \eta^{-1} \hat{\mathbf{z}} \times (\nabla_t J_z), \quad (2.209)$$

$$\mathbf{J}_t^{\text{eff}} = \mathbf{J}_t + \xi^{-1} (\nabla_t M_z) \times \hat{\mathbf{z}}. \quad (2.210)$$

Substituting equations 2.209 and 2.210 in equations 2.207 and 2.208 leads to

$$v^\alpha(z) = \langle \mathbf{M}_t | \mathbf{h}_t^\alpha \rangle + \eta^{-1} \int \mathbf{e}_t^{\alpha*} \cdot \nabla_t J_z dA, \quad (2.211)$$

$$i^\alpha(z) = \langle \mathbf{J}_t | \mathbf{e}_t^\alpha \rangle + \xi^{-1} \int \mathbf{h}_t^{\alpha*} \cdot \nabla_t M_z dA. \quad (2.212)$$

In some models of practical applications the impressed current distributions are not differentiable. To accommodate for this, it is convenient to employ integration by parts to remove the transverse gradient operating on  $J_z$  and  $M_z$ . To this end, we employ the identities

$$\mathbf{e}_t^{\alpha*} \cdot \nabla_t J_z = \nabla_t \cdot (J_z \mathbf{e}_t^{\alpha*}) - J_z \nabla_t \cdot \mathbf{e}_t^{\alpha*}, \quad (2.213)$$

$$\mathbf{h}_t^{\alpha*} \cdot \nabla_t M_z = \nabla_t \cdot (M_z \mathbf{h}_t^{\alpha*}) - M_z \nabla_t \cdot \mathbf{h}_t^{\alpha*}. \quad (2.214)$$

Using these identities and Gauss' divergence theorem results in

$$v^\alpha(z) = \langle \mathbf{M}_t | \mathbf{h}_t^\alpha \rangle + \eta^{-1} \oint J_z \hat{\nu} \cdot \mathbf{e}_t^{\alpha*} dl - \eta^{-1} \int J_z \nabla_t \cdot \mathbf{e}_t^{\alpha*} dA, \quad (2.215)$$

$$i^\alpha(z) = \langle \mathbf{J}_t | \mathbf{e}_t^\alpha \rangle + \xi^{-1} \oint M_z \hat{\nu} \cdot \mathbf{h}_t^{\alpha*} dl - \xi^{-1} \int M_z \nabla_t \cdot \mathbf{h}_t^{\alpha*} dA. \quad (2.216)$$

On account of:

1. the non-radiating behavior of an electric current source located at an infinitesimal distance from and oriented parallel to a perfectly electric conducting boundary,

$$2. \hat{\nu} \cdot \mathbf{h}_t^{\alpha*} = \hat{\nu} \cdot (\hat{\mathbf{z}} \times \mathbf{e}_t^{\alpha*}) = -\hat{\mathbf{z}} \cdot (\mathbf{e}_t^{\alpha*} \times \hat{\nu}) = 0,$$

the contour integrals vanish, and we finally obtain the following simple expressions for the generators

$$v^\alpha(z) = \langle \mathbf{M}_t | \mathbf{h}_t^\alpha \rangle + Z_\infty^{\alpha*} \langle J_z | e_z^\alpha \rangle, \quad (2.217)$$

$$i^\alpha(z) = \langle \mathbf{J}_t | \mathbf{e}_t^\alpha \rangle + Y_\infty^{\alpha*} \langle M_z | h_z^\alpha \rangle. \quad (2.218)$$

In appendix B, the transmission line equations are solved for a number of standard configurations used in the next chapters.

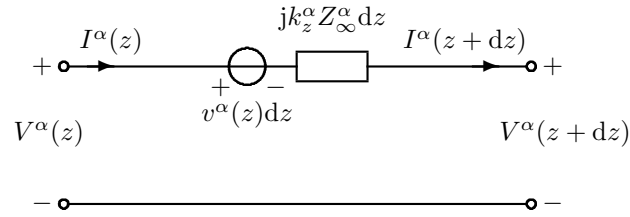


Figure 2.5: Circuit representation of the first modal transmission line equation: Kirchhoff's voltage law [70, section 1.2.1], which states that the sum of the voltages in a loop equals zero.

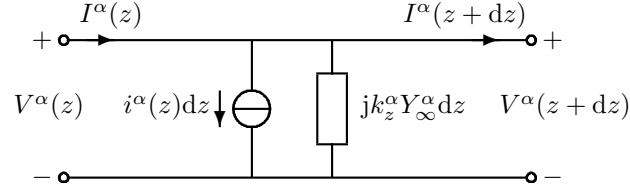


Figure 2.6: Circuit representation of the second modal transmission line equation: Kirchhoff's current law [70, section 1.2.1], which states that the sum of the currents in a node equals zero.

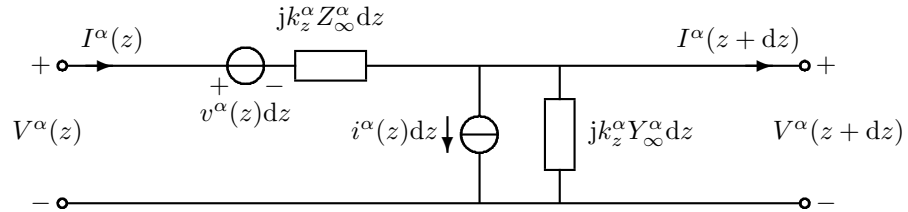


Figure 2.7: Circuit representation of an infinitesimally small piece of transmission line which is a combination of the circuit representations of the first and second modal transmission line equation. This circuit is representative for the modal transmission line equations.

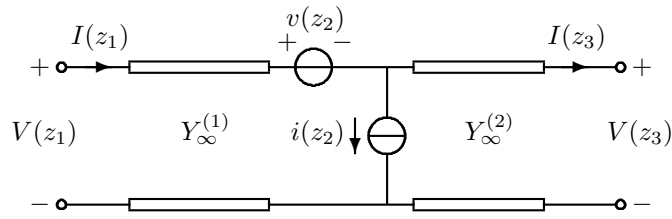


Figure 2.8: Circuit representation [112, section 6.2] for a finite-length transmission line between  $z = z_1$  and  $z = z_3$  with a lumped voltage and current generator at  $z = z_2$ . For  $z_1 < z < z_2$  and  $z_2 < z < z_3$  the line is characterized by a characteristic admittance  $Y_\infty^{(1)}$  and  $Y_\infty^{(2)}$ , respectively. Note that we have omitted the polarization index  $\alpha$ .



## Chapter 3

# Computational Method

*"Models should be made as simple as possible, but not any simpler."*  
Albert Einstein (1879-1955)

In this chapter we develop a computational method with which we can calculate the unknown electromagnetic field within the unit-cell structure.

To do so, first note that within the total unit-cell structure there are parts in which the junctions show a significant electromagnetic coupling (the concept of electromagnetic coupling is based on the number of accessible modes in the neighboring segment, which will be defined and explained later in this chapter) between modi (even for a junction between two different segments). We call these parts basic structures. Between the basic structures there is a low electromagnetic coupling. To calculate the total electromagnetic field efficiently, we exploit this property, and separate the total calculation into one for calculating it for each basic structure, and one for combining them.

We start with the calculation of the electromagnetic field for a single basic structure, and first give a detailed description of its configuration in section 3.1. Then to ensure the existence and uniqueness of a field solution within the basic structure, proper boundary conditions must be supplemented. From an electromagnetic engineer point of view these boundary conditions describe the domain where the Maxwell equations are to be solved. In section 3.2 we formulate the scattering field problem and describe these boundary conditions [35, chapter 6] for the basic structure.

The final objective of the simulation is to compute the field radiated by a given source in a complicated structure. If the Green's function of this structure were known, the computation could be carried out without difficulty and there would be no need to apply the equivalence theorem. On the contrary, by closing some gaps or removing some metal parts, we obtain simpler regions where the Green's function is known, as a modal expansion. The equivalence theorem [112, section 6.4] states that, in order to have the same field in the original and the modified structure, it is necessary to introduce suitable current distributions. The actual value of these currents cannot be given explicitly, but



can be determined by the solution of an integral equation. Integral, because the relationship between currents and fields is always of integral type, with a kernel which is the Green's function, which is known in each sub-domain. In section 3.3 we describe the equivalent scattering field problem. The equivalent scattering field problem is solved by using a so-called coupled field integral equation technique. This technique is described in section 3.4.

These unknown surface currents are discretized in terms of expansion functions in section 3.5 and subsequently determined by the method of moments. This method approximates the integral equation by a matrix equation of type  $L\mathbf{u} = \mathbf{f}$  with linear operator  $L$ , unknown vector  $\mathbf{u}$ , and forcing vector  $\mathbf{f}$ . The linear system can be solved by means of straightforward inversion of  $L$ , or by making use of more sophisticated iterative schemes [91, 109].

In section 3.6 we discuss in detail the calculation of the linear operator  $L$  and the forcing vector  $\mathbf{f}$ . To do this, we first incorporate the explicit form of the appropriate Green's function to express the electromagnetic fields in terms of the expansion surface currents. Doing this leads to an implementation of the equation for the waveguide. For the layered space, we have to incorporate the periodic arrangement of the unit cells, to allow for an interaction between unit cells. Two choices [112, section 7.3] are made for this purpose.

Depending on the geometrical shape of the support of the unknown surface current that is used to solve the field integral equation, a number of expansion and weighting functions have to be defined. In section 3.7, we discuss the choice of these functions [74, 76]. We distinguish between global and local functions. Global functions make use of the overall shape of the support of the unknown surface current by assigning to it a "transverse global expansion". These functions are more physical but less flexible. We discuss the waveguide mode [11, 14], the thin strip and the weighted Chebyshev [1] global functions. Local functions approximate the overall shape of the support of the unknown surface current by dividing it into small primitive elements. These functions are more flexible. We discuss the rectangular rooftop [104] and the triangular Rao-Wilton-Glisson functions [88]. We define these functions, and discuss the most relevant properties.

Once we have solved the unknown surface currents with the method of moments, we calculate in section 3.8 the total electromagnetic field at any given location within the configuration. To do so, we first define so-called probing interfaces at the left and right side of the basic structure at some finite distance away from the junctions. We calculate the total electromagnetic field at these probing interfaces. Due to the superposition principle [35, section 11.3], the total field at these probing interfaces can be written as a sum of the incident field and a scattered field. To calculate the electromagnetic behavior of the total unit-cell structure, we must combine the individual electromagnetic behaviors of all basic structures. For this purpose we formulate a so-called generalized scattering matrix, which characterizes this behavior for all basic structures individually, by expressing the outgoing waves in terms of the incident waves [31, 48]. Then we formulate a procedure that cascades two generalized scattering matrices [112, section 6.3] to obtain a new generalized scattering matrix which characterizes

the electromagnetic behavior of the combination of the two corresponding basic structures.

In section 3.9 we give an interpretation of the field solution based on energy principles. We first derive and then use Poynting's theorem [35, chapter 7], and find an expression for the energy conservation. We then give a physical interpretation of three different parts of this expression, i.e., power flow through the basic structure from outside, energy storage and loss within the basic structure, and power generation by sources inside the basic structure. Then we simplify the expression for the power flow by using the field expansions both for the waveguide and for the layered space. Finally, we show that the part responsible for power generated by sources inside the basic structure vanishes.

In section 3.10, we find leading order term expressions for the electromagnetic field far away from the radiating part of the basic structure. This is called the far-field approximation [35, section 10.7]. The expressions are used to calculate the active element pattern and the active reflection coefficient. The usefulness of calculating these parameters comes from the fact that the direct measurement of the active element pattern and the active reflection coefficient [86] involves only a reasonably large portion of the proposed array. It can thus be used to locate and correct array design problems before full-scale development, which reduces the risk of a costly design failure.

Finally in section 3.11 we discuss the numerical evaluation of the linear operator  $L$ , and of the forcing vector  $\mathbf{f}$ .

### 3.1 Description of the Configuration

An arbitrary basic structure is a part of the total unit-cell structure in which the junctions show a significant electromagnetic coupling. It consists without loss of generality of  $M + 1$  segments separated by  $M$  junctions, for a given positive integer  $M$ , and is schematized in figure 3.1.

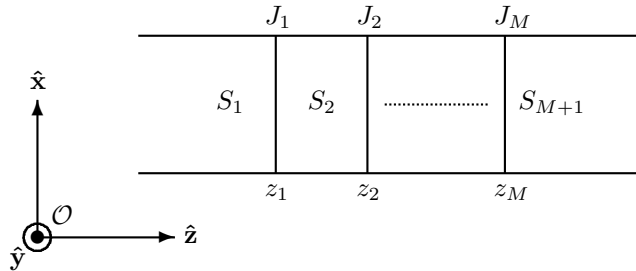


Figure 3.1: An arbitrary basic structure with  $M + 1$  segments  $S_m$  separated by  $M$  junctions  $J_m$  positioned at  $z = z_m$  for a given integer  $M$ .

In figure 3.2 we have schematized a single junction  $J_m$  positioned at  $z = z_m$  which separates two segments  $S_m$  and  $S_{m+1}$  where  $m \in \{1, 2, \dots, M\}$ .  $J_m$  is

representative for all junctions within the basic structure. The junction  $J_m$  can contain arbitrarily shaped infinitely thin perfectly electric conducting material (patches) represented by the surface  $\bar{C}_m$ . The complementary surface  $C_m$  of  $\bar{C}_m$  represents the gaps (apertures) in between the patches.  $C_m \cup \bar{C}_m$  equals the total surface of the junction. Further, we define a transversely unbounded (also bounded to be able to consider waveguide steps), longitudinally infinitesimal thin volume  $V_m$  centered around  $z = z_m$  as

$$V_m = \lim_{h \downarrow z_m} \{(x, y, z) \mid -h < z < h\}. \quad (3.1)$$

It has a boundary  $\partial V_m = \partial V_{m;1} \cup \partial V_{m;2}$  defined by

$$\partial V_{m;1} = \lim_{h \uparrow z_m} \{(x, y, h)\}, \quad \partial V_{m;2} = \lim_{h \downarrow z_m} \{(x, y, h)\}. \quad (3.2)$$

The complement  $\bar{V}_m$  of  $V_m$  shares the same boundary  $\partial V_m$ , and is referred to as the region of interest. It is defined by

$$\bar{V}_m = \lim_{h \downarrow z_m} \{(x, y, z) \mid z < -h \vee z > h\}, \quad (3.3)$$

The outward normal vectors  $\hat{\mathbf{n}}$  and  $\tilde{\mathbf{n}}$  with respect to the volume  $V_m$  are defined by

$$\hat{\mathbf{n}} = -\hat{\mathbf{z}}, \quad \tilde{\mathbf{n}} = \hat{\mathbf{z}}. \quad (3.4)$$

Any vector field quantity  $\mathbf{X}$  that is a function of the point of observation  $\mathbf{r}$  can be written as a function of the transverse position vector  $\boldsymbol{\rho}$  and the longitudinal coordinate  $z$  as

$$\mathbf{X}(\mathbf{r}) = \mathbf{X}(\boldsymbol{\rho} + z\hat{\mathbf{z}}) = \mathbf{X}(\boldsymbol{\rho}, z). \quad (3.5)$$

This vector field quantity  $\mathbf{X}$  can also be written in terms of transverse  $\mathbf{X}_t$  and longitudinal  $X_z$  components as

$$\mathbf{X}(\boldsymbol{\rho}, z) = \mathbf{X}_t(\boldsymbol{\rho}, z) + \hat{\mathbf{z}}X_z(\boldsymbol{\rho}, z). \quad (3.6)$$

The vector field quantity  $\mathbf{X}$  evaluated at an infinitesimal distance from the left and right side of the junction  $J_m$  is denoted by  $\hat{\mathbf{X}}_m$  and  $\tilde{\mathbf{X}}_m$ , respectively, and defined by

$$\hat{\mathbf{X}}_m(\boldsymbol{\rho}) = \lim_{z \uparrow z_m} \mathbf{X}(\boldsymbol{\rho}, z) = \mathbf{X}(\boldsymbol{\rho}, z_m^-), \quad \tilde{\mathbf{X}}_m(\boldsymbol{\rho}) = \lim_{z \downarrow z_m} \mathbf{X}(\boldsymbol{\rho}, z) = \mathbf{X}(\boldsymbol{\rho}, z_m^+). \quad (3.7)$$

The vector field quantity  $\mathbf{X}$  evaluated at  $z = z_m$  (which is continuous at  $z = z_m$ ) is denoted by  $\mathbf{X}_m$ , and defined by

$$\mathbf{X}_m(\boldsymbol{\rho}) = \mathbf{X}(\boldsymbol{\rho}, z_m). \quad (3.8)$$

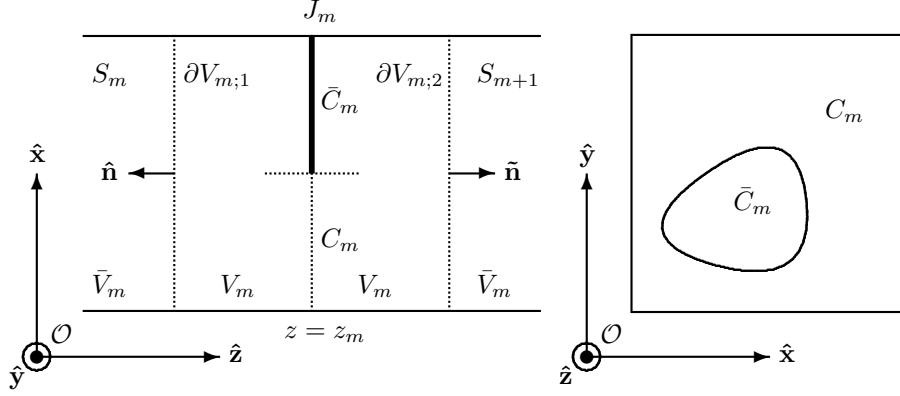


Figure 3.2: Description of the configuration for a single junction  $J_m$  positioned at  $z = z_m$  which separates two segments  $S_m$  and  $S_{m+1}$ .  $\bar{C}_m$  represents the patches, and  $C_m$  represents the apertures.

### 3.2 Formulation of the Boundary Conditions

Across certain boundary surfaces in the basic structure configuration, the electromagnetic properties, and hence the electromagnetic field quantities, may be discontinuous. Since at those positions the field quantities are no longer differentiable, Maxwell's equations in differential form cease to hold [35, chapter 6] in ordinary sense (but not in distributional sense). To overcome this problem, these equations must be supplemented with boundary conditions that interrelate the field values at both sides of the surfaces of discontinuity. From an electromagnetic engineering point of view these boundary conditions describe the domain where the Maxwell equations are to be solved.

The apertures  $C_m$  at the junction  $J_m$  represent the gaps in between the patches. Note that the constitutive parameters of each neighboring segment  $S_m$  and  $S_{m+1}$  at this junction may be chosen arbitrarily. The following boundary condition assures a continuous tangential electric and magnetic field when we approach the apertures  $C_m$  for  $z < z_m$  and  $z > z_m$

$$\forall \boldsymbol{\rho} \in C_m [\hat{\mathbf{E}}_{t;m}(\boldsymbol{\rho}) = \tilde{\mathbf{E}}_{t;m}(\boldsymbol{\rho}) \quad \text{and} \quad \hat{\mathbf{H}}_{t;m}(\boldsymbol{\rho}) = \tilde{\mathbf{H}}_{t;m}(\boldsymbol{\rho})], \quad (3.9)$$

respectively. The patches  $\bar{C}_m$  in the junction  $J_m$  are composed of infinitely thin perfectly electric conducting (PEC) material. This type of material is denoted as electrically impenetrable. The following boundary condition assures a vanishing tangential electric field when we approach the patches  $\bar{C}_m$  for  $z < z_m$  and  $z > z_m$

$$\forall \boldsymbol{\rho} \in \bar{C}_m [\hat{\mathbf{E}}_{t;m}(\boldsymbol{\rho}) = \mathbf{0} \quad \text{and} \quad \tilde{\mathbf{E}}_{t;m}(\boldsymbol{\rho}) = \mathbf{0}], \quad (3.10)$$

respectively.

### 3.3 Application of the Equivalence Theorem

The final objective of the simulation is to compute the field radiated by a given source in a complicated structure. If the Green's function of this structure were known, the computation could be carried out without difficulty and there would be no need to apply the equivalence theorem. On the contrary, by closing some gaps or removing some metal parts, we obtain simpler regions where the Green's function is known, as a modal expansion. The equivalence theorem says that in order to have the same field in the original and the modified structure, it is necessary to introduce suitable current distributions. The actual value of these currents cannot be given explicitly, but can be determined by the solution of an integral equation. Integral, because the relationship between currents and fields is always of integral type, with a kernel which is the Green's function, which is known in each sub-domain.

The mathematical basis for this procedure is the equivalence theorem [112, section 6.4]. Consider configuration A given in figure 3.3, where a general system of sources is radiating into a medium that is inhomogeneous because of the presence of bodies with arbitrary characteristics (e.g., metallic, dielectric, etc.). A regular closed surface  $\partial V$ , with outward normal  $\hat{\mathbf{n}}$ , is introduced to separate the inhomogeneous portion of space  $V$  from  $\bar{V}$ . Also, the sources are divided into internal ( $\mathbf{J}^{\text{int}}, \mathbf{M}^{\text{int}}$ ) and external ( $\mathbf{J}^{\text{ext}}, \mathbf{M}^{\text{ext}}$ ) ones. The theorem states that in the computation of the electromagnetic field in a point  $P$  outside the surface  $\partial V$  the internal sources can be ignored, provided that one introduces the equivalent surface currents

$$\mathbf{J}^{\text{s}} = \hat{\mathbf{n}} \times \mathbf{H}(\mathbf{r}_{\partial V}) \delta(\mathbf{r} - \mathbf{r}_{\partial V}), \quad (3.11)$$

$$\mathbf{M}^{\text{s}} = \mathbf{E}(\mathbf{r}_{\partial V}) \times \hat{\mathbf{n}} \delta(\mathbf{r} - \mathbf{r}_{\partial V}), \quad (3.12)$$

where  $\mathbf{r}_{\partial V}$  describes the surface  $\partial V$  and  $\delta(\mathbf{r} - \mathbf{r}_{\partial V})$  is the Dirac surface delta function with support on  $\partial V$ . Moreover, since the external sources and the equivalent ones radiate a null field in  $V$ , the constitutive relations of this region can be chosen arbitrarily. This means that the inhomogeneity can be removed. This is indicated in the equivalent configuration B in figure 3.3.

For our problem, we formulate an equivalent field problem by choosing the boundary surface  $\partial V_m$  that encloses  $V_m$  to be the imaginary closed surface. The region inside this surface is defined as  $V_m$ , whereas the region outside this surface is defined as the region of interest  $\bar{V}_m$ . The equivalent configuration is indicated in figure 3.4. By using the equivalence theorem, we have to place the following (still unknown) equivalent surface currents on  $\partial V_m$ :

$$\hat{\mathbf{J}}_m(\boldsymbol{\rho}, z) = [\hat{\mathbf{n}} \times \hat{\mathbf{H}}_m(\boldsymbol{\rho})] \delta(z - z_m), \quad (3.13)$$

$$\tilde{\mathbf{J}}_m(\boldsymbol{\rho}, z) = [\tilde{\mathbf{n}} \times \tilde{\mathbf{H}}_m(\boldsymbol{\rho})] \delta(z - z_m), \quad (3.14)$$

$$\hat{\mathbf{M}}_m(\boldsymbol{\rho}, z) = [\hat{\mathbf{E}}_m(\boldsymbol{\rho}) \times \hat{\mathbf{n}}] \delta(z - z_m), \quad (3.15)$$

$$\tilde{\mathbf{M}}_m(\boldsymbol{\rho}, z) = [\tilde{\mathbf{E}}_m(\boldsymbol{\rho}) \times \tilde{\mathbf{n}}] \delta(z - z_m). \quad (3.16)$$

Note that we have to distinguish between the two sides  $z_m^-$  (quantities with a caret) and  $z_m^+$  (quantities with a tilda) of  $z_m$ . Note that these surface currents

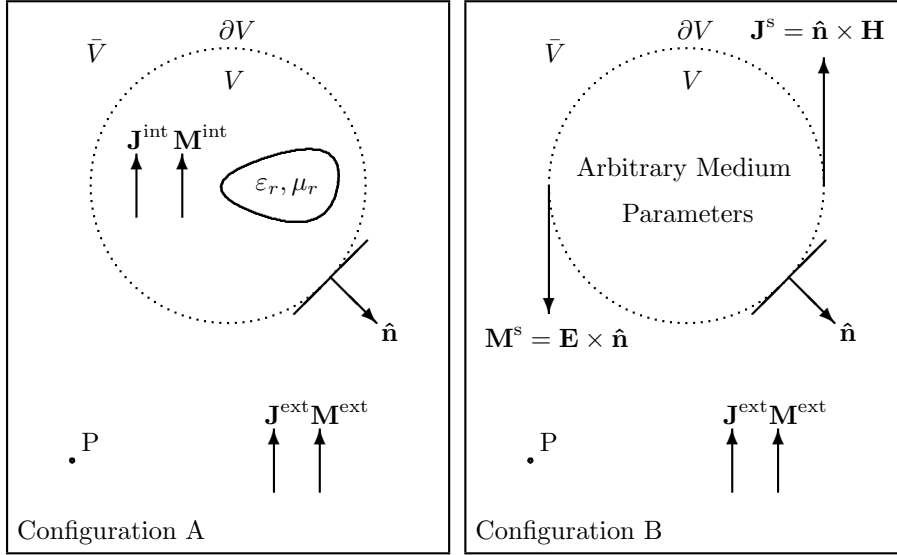


Figure 3.3: Illustration of the equivalence theorem: a general system of sources is radiating in an inhomogeneous medium where the electromagnetic field at a point of observation  $P$  in a region  $\bar{V}$  is identical for the two configurations where in  $V$  the internal sources  $\mathbf{J}^{\text{int}}$  and  $\mathbf{M}^{\text{int}}$  are switched off and surface currents  $\mathbf{J}^{\text{s}}$  and  $\mathbf{M}^{\text{s}}$  are placed on the boundary surface  $\partial V$ .

show a Dirac dependence  $\delta(z - z_m)$  with dimension  $[\text{m}^{-1}]$  in the longitudinal  $z$ -coordinate. This  $z$ -dependence is omitted from now on.

The boundary conditions 3.9 and 3.10 are defined on the apertures  $C_m$  and on the patches  $\bar{C}_m$ , respectively. Due to the infinitesimal distance between the sheets  $\partial V_{m;1}$  and  $\partial V_{m;2}$ , these surfaces coincide with the boundary  $\partial V_m$ . The boundary conditions can therefore be translated into conditions on the equivalent electric and magnetic surface currents.

To be more specific, the boundary condition 3.9, which is necessary to assure a continuous tangential electric and magnetic field when we approach the apertures  $C_m$  for  $z < z_m$  and  $z > z_m$ , is translated into

$$\forall \boldsymbol{\rho} \in C_m [\hat{\mathbf{M}}_m(\boldsymbol{\rho}) = -\tilde{\mathbf{M}}_m(\boldsymbol{\rho}) \quad \text{and} \quad \hat{\mathbf{J}}_m(\boldsymbol{\rho}) = -\tilde{\mathbf{J}}_m(\boldsymbol{\rho})], \quad (3.17)$$

while the boundary condition 3.10, which is necessary to assure a vanishing tangential electric field when we approach the patches  $\bar{C}_m$  for  $z < z_m$  and  $z > z_m$ , is translated into

$$\forall \boldsymbol{\rho} \in \bar{C}_m [\hat{\mathbf{M}}_m(\boldsymbol{\rho}) = \mathbf{0} \quad \text{and} \quad \tilde{\mathbf{M}}_m(\boldsymbol{\rho}) = \mathbf{0}]. \quad (3.18)$$

Moreover, the electromagnetic field inside  $V_m$  vanishes. This means that we can choose arbitrary the constitutive relations inside this region, and remove any inhomogeneity, such as the patches. There are in general two ways to do this.

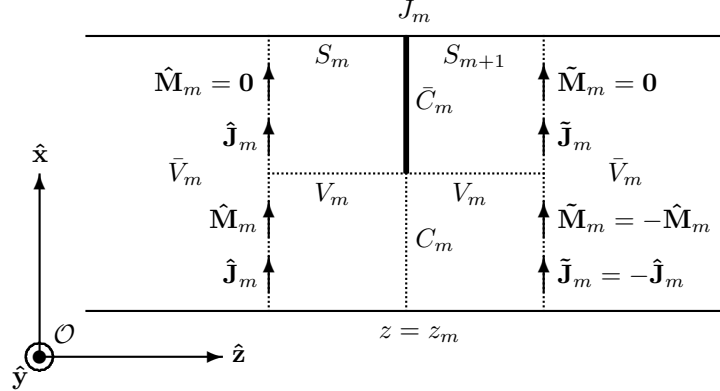


Figure 3.4: Equivalent configuration for the single junction  $J_m$  located at  $z = z_m$  which separates the two segments  $S_m$  and  $S_{m+1}$ .

1. The first way to remove the inhomogeneity is to remove all the patches within  $V_m$ , i.e.  $\bar{C}_m$ . We denote this as the type I equivalent formulation. Due to the infinitesimal distance between the sheets  $\partial V_{m,1}$  and  $\partial V_{m,1}$ , the surface currents tend to have coincident supports, and can be added. The total electric and magnetic surface currents at  $z = z_m$  are now given by

$$\mathbf{J}_m(\boldsymbol{\rho}) = \hat{\mathbf{J}}_m(\boldsymbol{\rho}) + \tilde{\mathbf{J}}_m(\boldsymbol{\rho}), \quad (3.19)$$

$$\mathbf{M}_m(\boldsymbol{\rho}) = \hat{\mathbf{M}}_m(\boldsymbol{\rho}) + \tilde{\mathbf{M}}_m(\boldsymbol{\rho}). \quad (3.20)$$

The result is a non-zero electric surface current on  $\bar{C}_m$  (representing a discontinuous tangential magnetic field on the patches), and a zero electric surface current on  $C_m$  (representing a continuous tangential magnetic field in the apertures). The magnetic surface current is zero on  $C_m$  (representing a continuous tangential electric field in the apertures) and on  $\bar{C}_m$ . Further, we consider  $\mathbf{J}_m(\boldsymbol{\rho})$  to be the unknown surface current. Although the magnetic surface current is zero on  $\bar{C}_m$ , it does not assure a vanishing tangential electric field on the patches. This condition must therefore be explicitly enforced and is given by equation 3.10

$$\forall \boldsymbol{\rho} \in \bar{C}_m [\mathbf{E}_{t;m}(\boldsymbol{\rho}) = \mathbf{0}]. \quad (3.21)$$

Both the configuration and the circuit representation [112, section 6.4] associated with the type I equivalent formulation is schematized in figure 3.5.

2. The second way to remove the inhomogeneity is to fill all the apertures within  $V_m$  with patches, i.e. within  $C_m$ . We denote this as the type II equivalent formulation. Due to the infinitesimal distance between the

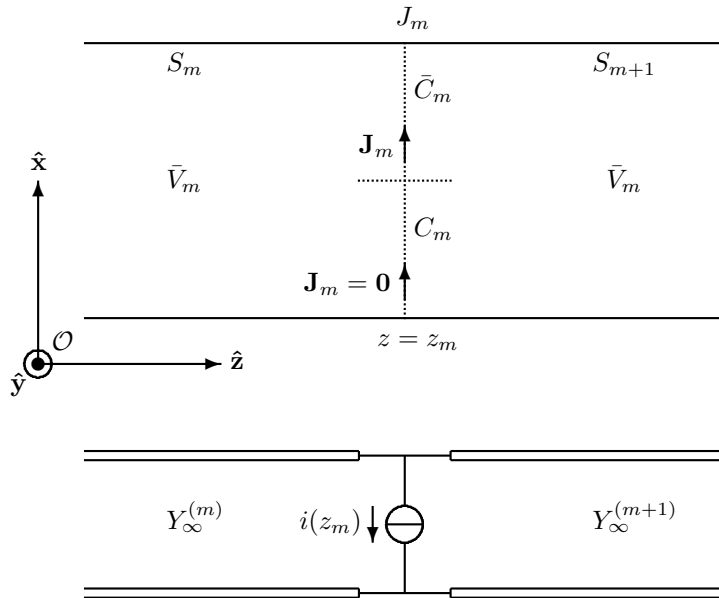


Figure 3.5: Type I equivalent configuration for the single junction  $J_m$  located at  $z = z_m$  which separates the two segments  $S_m$  and  $S_{m+1}$ , and circuit representation with single shunt current generator [112, section 6.4]. Note that this circuit applies for every mode.



sheets  $\partial V_{m;1}$  and  $\partial V_{m;2}$ , the surface currents on both sides are separated by an infinitely thin perfectly electric conducting (PEC) sheet. The result is a short-circuited electric surface current on both sides of  $\tilde{C}_m$  and  $C_m$  and must be disregarded since they radiate no field. The magnetic surface currents on both sides of  $\tilde{C}_m$  are zero (representing a vanishing tangential electric field on the patches), and are equal in strength but opposite in sign on both sides of  $C_m$  (representing a continuous tangential electric field in the apertures). Further, we consider  $\hat{\mathbf{M}}_m(\boldsymbol{\rho})$  which has support on  $C_m$  to be the unknown surface current. By explicitly enforcing 3.18, the tangential electric field on the patches vanishes. Subsequently, by explicitly enforcing the first part of equation 3.17 (since these currents face a PEC sheet), a continuous tangential electric field in the apertures is assured. However, due to the short-circuited electric surface currents, the second part of equation 3.9 is not satisfied. The continuity of the tangential magnetic field in the apertures must therefore be explicitly enforced and is given by

$$\forall \boldsymbol{\rho} \in C_m [\hat{\mathbf{H}}_{t;m}(\boldsymbol{\rho}) = \tilde{\mathbf{H}}_{t;m}(\boldsymbol{\rho})]. \quad (3.22)$$

Both the configuration and the circuit representation<sup>1</sup> [112, section 6.4.2] associated with the type II equivalent formulation is schematized in figure 3.6.

### 3.4 Formulation of the Integral Equation

In the previous section we have transformed the original scattering field problem into an equivalent one in which we have replaced each of the  $M$  junctions within the original basic structure by either a type I or type II equivalent configuration. In both cases,  $M$  unknown equivalent surface currents are introduced and  $M$  additional boundary conditions have been supplemented. Note that we do not consider scattering by dielectric objects.

To solve the equivalent scattering field problem, we must simultaneously solve the set of  $M$  unknown surface currents for each junction by simultaneously enforcing the set of  $M$  supplemented boundary conditions. These conditions form the starting point of the formulation for a coupled field integral equation.

Within the equivalent configuration, the surface currents radiate through the segments and influence the electromagnetic fields at other junctions. This influence explicitly stops at a junction for which a type II equivalent configuration has been selected, which is due to the presence of the metal sheet at this junction. Implicitly, the influence is tunneled through this junction by the unknown magnetic surface current which is equal in strength but opposite in sign on both sides of the metal sheet. Furthermore, an external incident elec-

<sup>1</sup>In the circuit it is evident that the voltage at the junction is continuous. Since this holds true for all the modes independently, the transverse electric field is continuous on the complete cross section of the junction.

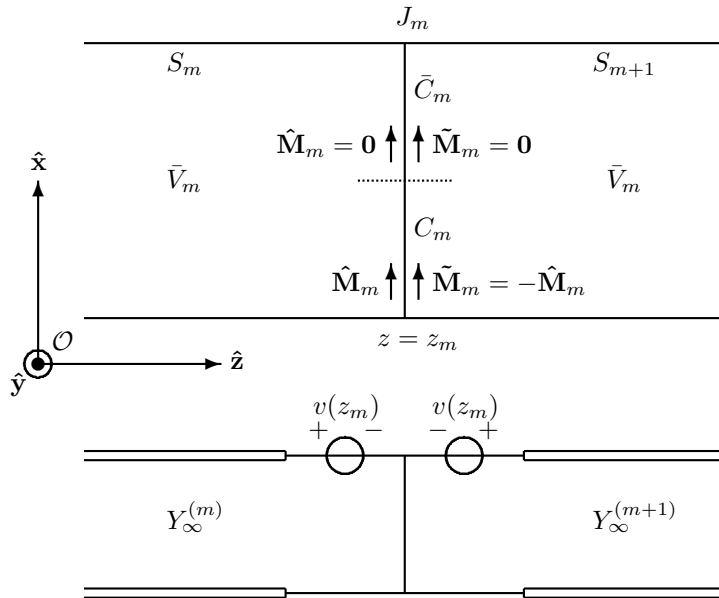


Figure 3.6: Type II equivalent configuration for the single junction  $J_m$  located at  $z = z_m$  which separates the two segments  $S_m$  and  $S_{m+1}$ , and circuit representation with two series voltage generators [112, section 6.4.2]. Note that this circuit applies for every mode.

tromagnetic field (represented by an incident surface current) may be present on both sides of the basic structure.

### Electric-Field Integral Equation

If a junction  $J_m$  is replaced with a type I equivalent formulation, a unknown equivalent electric surface current  $\mathbf{J}_m(\boldsymbol{\rho})$  is introduced, and the following additional boundary condition for a vanishing tangential electric field on the patches  $\bar{C}_m$  must be enforced:

$$\forall \boldsymbol{\rho} \in \bar{C}_m [\mathbf{E}_{t;m}(\text{CurrentDistributions}, \boldsymbol{\rho}) = \mathbf{0}]. \quad (3.23)$$

The substitution of the appropriate field representation in equation 3.23 leads to the so-called electric-field integral equation (EFIE). The tangential electric field  $\mathbf{E}_{t;m}$  is a function (of the integral type) of the surface currents present in the equivalent configuration on the left and right sides of junction  $J_m$ . At the junction, the unknown electric surface current  $\mathbf{J}_m(\boldsymbol{\rho})$  is added to the list of unknown current distributions. Four different kind of junction combinations exist with corresponding current distributions.

1. At the left side of junction  $J_m$  we have, in descending order,  $p$  junctions with a type I configuration (no patches), and a source of the incident field from the left of the entire domain. At the right side of junction  $J_m$  we have, in ascending order,  $q$  junctions with a type I configuration, and a source of the incident field from the right of the entire domain. The set of surface currents can be written as:

$$\left\{ \hat{\mathbf{J}}^{\text{inc}}, \hat{\mathbf{M}}^{\text{inc}}, \mathbf{J}_{m-p}, \dots, \mathbf{J}_{m-1}, \mathbf{J}_m, \mathbf{J}_{m+1}, \dots, \mathbf{J}_{m+q}, \tilde{\mathbf{J}}^{\text{inc}}, \tilde{\mathbf{M}}^{\text{inc}} \right\} (\boldsymbol{\rho}).$$

2. At the left side of junction  $J_m$  we have, in descending order  $p$  junctions with a type I configuration, and a source of the incident field from the left of the entire domain. At the right side of junction  $J_m$  we have, in ascending order  $q$  junctions with a type I configuration, and a final junction with a type II configuration (no apertures). The set of surface currents can be written as:

$$\left\{ \hat{\mathbf{J}}^{\text{inc}}, \hat{\mathbf{M}}^{\text{inc}}, \mathbf{J}_{m-p}, \dots, \mathbf{J}_{m-1}, \mathbf{J}_m, \mathbf{J}_{m+1}, \dots, \mathbf{J}_{m+q}, \hat{\mathbf{M}}_{m+q+1} \right\} (\boldsymbol{\rho}).$$

3. At the left side of junction  $J_m$  we have, in descending order  $p$  junctions with a type I configuration, and a final junction with a type II configuration. At the right side of junction  $J_m$  we have, in ascending order  $q$  junctions with a type I configuration, and a source of the incident field from the right of the entire domain. The set of surface currents can be written as:

$$\left\{ \tilde{\mathbf{M}}_{m-p-1}, \mathbf{J}_{m-p}, \dots, \mathbf{J}_{m-1}, \mathbf{J}_m, \mathbf{J}_{m+1}, \dots, \mathbf{J}_{m+q}, \tilde{\mathbf{J}}^{\text{inc}}, \tilde{\mathbf{M}}^{\text{inc}} \right\} (\boldsymbol{\rho}).$$

4. At the left side of junction  $J_m$  we have, in descending order  $p$  junctions with a type I configuration, and a final junction with a type II configuration. At the right side of junction  $J_m$  we have, in ascending order  $q$  junctions with a type I configuration, and a final junction with a type II configuration. The set of surface currents can be written as:

$$\left\{ \tilde{\mathbf{M}}_{m-p-1}, \mathbf{J}_{m-p}, \dots, \mathbf{J}_{m-1}, \mathbf{J}_m, \mathbf{J}_{m+1}, \dots, \mathbf{J}_{m+q}, \hat{\mathbf{M}}_{m+q+1} \right\} (\boldsymbol{\rho}).$$

### Magnetic-Field Integral Equation

If a junction  $J_m$  is replaced with a type II equivalent formulation, two coupled (thus in principle one) unknown equivalent magnetic surface currents  $\hat{\mathbf{M}}_m(\boldsymbol{\rho})$  and  $\tilde{\mathbf{M}}_m(\boldsymbol{\rho}) = -\hat{\mathbf{M}}_m(\boldsymbol{\rho})$  are introduced, and the following additional boundary condition for the continuity of the tangential magnetic field in the apertures  $C_m$  must be enforced:

$$\forall \boldsymbol{\rho} \in C_m \left[ \hat{\mathbf{H}}_{t;m}(\text{LeftCurrentDistribution}, \boldsymbol{\rho}) = \tilde{\mathbf{H}}_{t;m}(\text{RightCurrentDistribution}, \boldsymbol{\rho}) \right]. \quad (3.24)$$

The substitution of the appropriate field representation in equation 3.24 leads to the so-called magnetic-field integral equation (MFIE). The tangential magnetic field  $\hat{\mathbf{H}}_{t;m}$  is a function (of the integral type) of the current distributions present in the equivalent configuration at the left side of junction  $J_m$ . At the junction, the unknown magnetic surface current  $\hat{\mathbf{M}}_m$  is added to the list of unknown current distributions. Two different kind of junction combinations exist with corresponding current distributions.

1. At the left side of junction  $J_m$  we have, in descending order  $p$  junctions with a type I configuration, and a source of the incident field from the left of the entire domain. The set of surface currents can be written as:

$$\left\{ \hat{\mathbf{J}}^{\text{inc}}, \hat{\mathbf{M}}^{\text{inc}}, \mathbf{J}_{m-p}, \dots, \mathbf{J}_{m-1}, \hat{\mathbf{M}}_m \right\} (\boldsymbol{\rho}).$$

2. At the left side of junction  $J_m$  we have, in descending order  $p$  junctions with a type I configuration, and a final junction with a type II configuration. The set of surface currents can be written as:

$$\left\{ \tilde{\mathbf{M}}_{m-p-1}, \mathbf{J}_{m-p}, \dots, \mathbf{J}_{m-1}, \hat{\mathbf{M}}_m \right\} (\boldsymbol{\rho}).$$

The tangential magnetic field  $\tilde{\mathbf{H}}_{t;m}$  is a function of the currents present in the equivalent configuration at the right side of junction  $J_m$ . At the junction, the unknown magnetic surface current  $\tilde{\mathbf{M}}_m(\boldsymbol{\rho})$  is added to the list of unknown current distributions. For this side, two different kind of junction combinations exist with corresponding current distributions.

1. At the right side of junction  $J_m$  we have, in ascending order  $q$  junctions with a type I configuration, and a source of the incident field from the right of the entire domain. The set of surface currents can be written as:

$$\left\{ \tilde{\mathbf{M}}_m, \mathbf{J}_{m+1}, \dots, \mathbf{J}_{m+q}, \tilde{\mathbf{J}}^{\text{inc}}, \tilde{\mathbf{M}}^{\text{inc}} \right\} (\boldsymbol{\rho}).$$

2. At the right side of junction  $J_m$  we have, in ascending order  $q$  junctions with a type I configuration, and a final junction with a type II configuration. The set of surface currents can be written as:

$$\left\{ \tilde{\mathbf{M}}_m, \mathbf{J}_{m+1}, \dots, \mathbf{J}_{m+q}, \hat{\mathbf{M}}_{m+q+1} \right\} (\boldsymbol{\rho}).$$

### Coupled-Field Integral Equation

Subsequently, we apply a number of operations on the set of  $M$  given boundary conditions. First, consider all junctions with a type II equivalent configuration. We apply the boundary conditions for the continuity of the electric field in the apertures, i.e.,

$$\left\{ \dots, \tilde{\mathbf{M}}_n, \dots \right\} (\boldsymbol{\rho}) = \left\{ \dots, -\hat{\mathbf{M}}_n, \dots \right\} (\boldsymbol{\rho}). \quad (3.25)$$

Then, since Maxwell's equations are linear in terms of the sources, we can apply the superposition principle. This means that we can write the total field as a linear combination of the fields for each source contribution as

$$\begin{aligned} \hat{\mathbf{H}}_{t;m}(\{\dots, \alpha \hat{\mathbf{M}}_p, \dots, \beta \mathbf{J}_q, \dots\}, \boldsymbol{\rho}) = & \dots + \alpha \hat{\mathbf{H}}_{t;m}(\hat{\mathbf{M}}_p, \boldsymbol{\rho}) + \\ & \dots + \beta \hat{\mathbf{H}}_{t;m}(\mathbf{J}_q, \boldsymbol{\rho}) + \dots \end{aligned} \quad (3.26)$$

The terms that are a function of the unknowns are moved to and ordered at the left-hand side of the equality sign, whereas those that are a function of the incident currents are moved to and ordered at the right-hand side of the equality sign. The substitution of the appropriate field representations in the set of  $M$  given boundary conditions leads to the so-called coupled-field integral equations (CFIE). The form of the field representation depends on the type (waveguide or layered space), and is therefore postponed until section 3.6 where both cases are discussed in detail.

### Example

As an example, we consider the boundary conditions for two arbitrary coupled junctions  $J_1$  and  $J_2$  that both have been replaced by type II configurations. The configuration are given in figure 3.7. We then assume:

1. The "LeftCurrentDistribution" and "RightCurrentDistribution" of junction  $J_1$  is given by

$$\left\{ \hat{\mathbf{M}}^{\text{inc}}, \hat{\mathbf{M}}_1 \right\} (\boldsymbol{\rho}) \quad \text{and} \quad \left\{ \tilde{\mathbf{M}}_1, \hat{\mathbf{M}}_2 \right\} (\boldsymbol{\rho}),$$

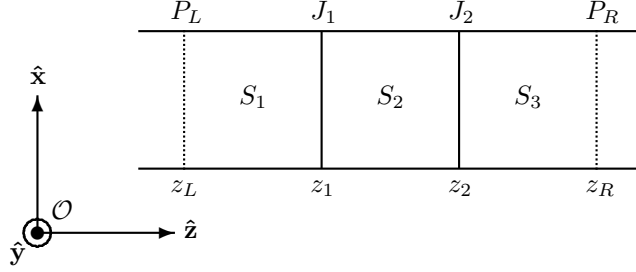


Figure 3.7: An example basic structure with three segments  $S_m$  separated by two junctions  $J_m$  positioned at  $z = z_m$ , and enclosed with two probes  $P_L$  and  $P_R$  positioned at  $z = z_L$  and  $z = z_R$ , respectively.

respectively. When applying the prescribed operations, i.e., equations 3.25 and 3.26, and moving and ordering to the appropriate place of the equality sign, we obtain the following magnetic-field integral equation (MFIE) for junction  $J_1$

$$\forall \rho \in C_1 [\hat{\mathbf{H}}_{t;1}(\hat{\mathbf{M}}_1, \rho) + \tilde{\mathbf{H}}_{t;1}(\hat{\mathbf{M}}_1, \rho) - \tilde{\mathbf{H}}_{t;1}(\hat{\mathbf{M}}_2, \rho) = -\hat{\mathbf{H}}_{t;1}(\hat{\mathbf{M}}^{\text{inc}}, \rho)]. \quad (3.27)$$

2. The "LeftCurrentDistribution" and "RightCurrentDistribution" of junction  $J_2$  are given by

$$\{\tilde{\mathbf{M}}_1, \hat{\mathbf{M}}_2\}(\rho) \quad \text{and} \quad \{\tilde{\mathbf{M}}_2, \hat{\mathbf{M}}^{\text{inc}}\}(\rho),$$

respectively. When applying the two prescribed operations, i.e., equations 3.25 and 3.26, and moving and ordering to the appropriate place of the equality sign, we obtain the following magnetic-field integral equation (MFIE) for junction  $J_2$

$$\forall \rho \in C_2 [\hat{\mathbf{H}}_{t;2}(\hat{\mathbf{M}}_2, \rho) + \tilde{\mathbf{H}}_{t;2}(\hat{\mathbf{M}}_2, \rho) - \hat{\mathbf{H}}_{t;2}(\hat{\mathbf{M}}_1, \rho) = \tilde{\mathbf{H}}_{t;2}(\tilde{\mathbf{M}}^{\text{inc}}, \rho)]. \quad (3.28)$$

### 3.5 Formulation of the Matrix Equation: Method of Moments

In general, the coupled field integral equation cannot be solved in closed form. This means that we need to invoke numerical solution techniques. To this end, we must first reduce the infinite number of unknowns to a finite number by discretizing the unknown surface currents. For this purpose we introduce general vectorial patch and aperture type expansion functions  $\mathbf{f}_p^{(m)}(\rho)$  and  $\mathbf{g}_q^{(m)}(\rho)$  with dimension  $[\text{m}^{-1}]$  to approximate the unknown electric  $\mathbf{J}_m$  and magnetic  $\hat{\mathbf{M}}_m$

surface currents, respectively. They are written as a linear combination of the expansion functions

$$\mathbf{J}_m(\boldsymbol{\rho}) = \sum_{p=1}^{P_m} I_p^{(m)} \mathbf{f}_p^{(m)}(\boldsymbol{\rho}), \quad (3.29)$$

$$\hat{\mathbf{M}}_m(\boldsymbol{\rho}) = \sum_{q=1}^{Q_m} V_q^{(m)} \mathbf{g}_q^{(m)}(\boldsymbol{\rho}), \quad (3.30)$$

where  $I_p^{(m)}$  and  $V_q^{(m)}$  represent the unknown scalar coefficients with dimension [A] and [V], respectively. Further  $P_m$  and  $Q_m$  denote the number of expansion functions. By choosing  $\mathbf{f}_p^{(m)}(\boldsymbol{\rho})$  to be a patch-type function (which is zero on the apertures), a continuous magnetic field in the aperture is guaranteed. By choosing  $\mathbf{g}_q^{(m)}(\boldsymbol{\rho})$  to be an aperture-type function (which is zero on the patches), a vanishing electric field on the patch is guaranteed.

Now let us consider again the example given at the end of the previous section. When we substitute the discretized surface currents into the relevant parts of the magnetic-field integral equation 3.27 for junction  $J_1$ , and when we apply the superposition principle, we obtain

$$\forall \boldsymbol{\rho} \in C_1 \left[ \sum_{r=1}^{Q_1} V_r^{(1)} [\hat{\mathbf{H}}_{t;1}(\mathbf{g}_r^{(1)}, \boldsymbol{\rho}) + \tilde{\mathbf{H}}_{t;1}(\mathbf{g}_r^{(1)}, \boldsymbol{\rho})] - \sum_{s=1}^{Q_2} V_s^{(2)} \tilde{\mathbf{H}}_{t;1}(\mathbf{g}_s^{(2)}, \boldsymbol{\rho}) = -\hat{\mathbf{H}}_{t;1}(\hat{\mathbf{M}}^{\text{inc}}, \boldsymbol{\rho}) \right]. \quad (3.31)$$

When we apply the same procedure to magnetic-field integral equation 3.28 for junction  $J_2$ , we obtain

$$\forall \boldsymbol{\rho} \in C_2 \left[ \sum_{s=1}^{Q_2} V_s^{(2)} [\hat{\mathbf{H}}_{t;2}(\mathbf{g}_s^{(2)}, \boldsymbol{\rho}) + \tilde{\mathbf{H}}_{t;2}(\mathbf{g}_s^{(2)}, \boldsymbol{\rho})] - \sum_{r=1}^{Q_1} V_r^{(1)} \hat{\mathbf{H}}_{t;2}(\mathbf{g}_r^{(1)}, \boldsymbol{\rho}) = \tilde{\mathbf{H}}_{t;2}(\tilde{\mathbf{M}}^{\text{inc}}, \boldsymbol{\rho}) \right]. \quad (3.32)$$

Note that the system of equations given by equations 3.31 and 3.32 constitutes an infinitely over-determined system, i.e., a finite  $(Q_1 + Q_2)$  number of unknowns and an infinite  $(\forall \boldsymbol{\rho} \in C_m)$  number of equations. We introduce general patch and aperture type weighting functions  $\mathbf{f}_v^{(m)}(\boldsymbol{\rho})$  and  $\mathbf{g}_w^{(m)}(\boldsymbol{\rho})$  to reduce the number of equations to a finite number  $(Q_1 + Q_2)$ . To obtain this so-called weak form of the coupled field integral equation, we take the following inner product of the discretized coupled field integral equations with the weighting functions

$$\forall 1 \leq v \leq Q_m \left[ \langle \dots | \mathbf{f}_v^{(m)} \rangle \right], \quad (3.33)$$

$$\forall 1 \leq w \leq Q_m \left[ \langle \dots | \mathbf{g}_w^{(m)} \rangle \right]. \quad (3.34)$$

Note that we must choose weighting procedure 3.33 and 3.34, if junction  $J_m$  has been replaced with a type I and type II equivalent formulation, respectively. A so-called Galerkin scheme is obtained when we choose the same set of weighting and expansion functions.

Subsequently, we have to select the expansion functions that represent the unknown surface currents. This choice depends on the geometrical shape of the support of these surface currents [74, 76]. We distinguish between global and local functions which are discussed in more detail in section 3.7.

Global functions make use of the overall shape of the support of the unknown surface current by assigning to it a "transverse global expansion". With these functions we can explicitly build in the expected physical behavior of the unknown surface currents. An example is the known behavior of surface currents near the edges on a patch or in an aperture (either of singular  $1/\sqrt{x}$  or non-singular  $\sqrt{x}$  type). A disadvantage of global functions is the lack of flexibility to describe arbitrarily shaped surface currents. An advantage is that in general using global functions leads to a smaller size of the matrix  $L$ .

Local functions approximate the overall shape of the support of the unknown surface current by dividing it into small primitive elements. These functions are more flexible when we want to describe arbitrarily shaped surface currents. With these functions we can implicitly build in the expected physical behavior of the unknown surface currents by for example choosing more local expansion functions near edges where we expect some special behavior (so-called mesh refinement). A disadvantage is that in general using local functions leads to a larger size of the matrix  $L$ .

The overall goal should be to have a good accuracy. Achieving this goal requires a lot of hands-on experience and a good understanding of the expected physical behavior. The result is a linear system which can be solved by means of either straightforward inversion of  $L$  (for a small sized  $L$ ), or by using more sophisticated iterative schemes (for a large sized  $L$ ).

Let us consider again the example given at the end of the previous section. The application of the weighting procedure to equation 3.31 for junction  $J_1$  results in

$$\forall 1 \leq v \leq Q_1 \left[ \sum_{r=1}^{Q_1} V_r^{(1)} [\langle \hat{\mathbf{H}}_{t;1}(\mathbf{g}_r^{(1)}, \boldsymbol{\rho}) | \mathbf{g}_v^{(1)} \rangle + \langle \tilde{\mathbf{H}}_{t;1}(\mathbf{g}_r^{(1)}, \boldsymbol{\rho}) | \mathbf{g}_v^{(1)} \rangle] - \sum_{s=1}^{Q_2} V_s^{(2)} \langle \tilde{\mathbf{H}}_{t;1}(\mathbf{g}_s^{(2)}, \boldsymbol{\rho}) | \mathbf{g}_v^{(1)} \rangle = - \langle \hat{\mathbf{H}}_{t;1}(\hat{\mathbf{M}}^{\text{inc}}, \boldsymbol{\rho}) | \mathbf{g}_v^{(1)} \rangle \right], \quad (3.35)$$



while the same principle applied to equation 3.32 for junction  $J_2$  results in

$$\forall 1 \leq w \leq Q_2 \left[ \sum_{s=1}^{Q_2} V_s^{(2)} [\langle \hat{\mathbf{H}}_{t;2}(\mathbf{g}_s^{(2)}, \boldsymbol{\rho}) | \mathbf{g}_w^{(2)} \rangle + \langle \tilde{\mathbf{H}}_{t;2}(\mathbf{g}_s^{(2)}, \boldsymbol{\rho}) | \mathbf{g}_w^{(2)} \rangle] - \sum_{r=1}^{Q_1} V_r^{(1)} \langle \hat{\mathbf{H}}_{t;2}(\mathbf{g}_r^{(1)}, \boldsymbol{\rho}) | \mathbf{g}_w^{(2)} \rangle = \langle \tilde{\mathbf{H}}_{t;2}(\tilde{\mathbf{M}}^{\text{inc}}, \boldsymbol{\rho}) | \mathbf{g}_w^{(2)} \rangle \right]. \quad (3.36)$$

These two equations can be rewritten in a more convenient form:

$$\forall 1 \leq v \leq Q_1 \left[ \sum_{r=1}^{Q_1} V_r^{(1)} (A_{v,r} + B_{v,r}) + \sum_{s=1}^{Q_2} V_s^{(2)} C_{v,s} = D_v \right], \quad (3.37)$$

$$\forall 1 \leq w \leq Q_2 \left[ \sum_{r=1}^{Q_1} V_r^{(1)} G_{w,r} + \sum_{s=1}^{Q_2} V_s^{(2)} (E_{w,s} + F_{w,s}) = H_w \right], \quad (3.38)$$

which can be written formally as the following matrix equation

$$L\mathbf{u} = \mathbf{f}. \quad (3.39)$$

The square matrix  $L$  represents the linear operator of the basic structure, and describes the interaction between the junctions. Its elements either have the dimension of impedance, admittance, or are dimensionless. We can write  $L$  as

$$L = \begin{pmatrix} A_{v,r} + B_{v,r} & C_{v,s} \\ G_{w,r} & E_{w,s} + F_{w,s} \end{pmatrix}, \quad (3.40)$$

where the matrix elements are given and physically interpreted by:

1.  $A_{v,r} = \langle \hat{\mathbf{H}}_{t;1}(\mathbf{g}_r^{(1)}, \boldsymbol{\rho}) | \mathbf{g}_v^{(1)} \rangle$  is the self interaction of the magnetic field strength at the left side of the first interface due to a magnetic surface current at the left side of the first interface,
2.  $B_{v,r} = \langle \tilde{\mathbf{H}}_{t;1}(\mathbf{g}_r^{(1)}, \boldsymbol{\rho}) | \mathbf{g}_v^{(1)} \rangle$  is the self interaction of the magnetic field strength at the right side of the first interface due to a magnetic surface current at the right side of the first interface,
3.  $C_{v,s} = - \langle \tilde{\mathbf{H}}_{t;1}(\mathbf{g}_s^{(2)}, \boldsymbol{\rho}) | \mathbf{g}_v^{(1)} \rangle$  is the coupling between the magnetic field strength at the right side of the first interface due to a magnetic surface current at the left side of the second interface,
4.  $G_{w,r} = - \langle \hat{\mathbf{H}}_{t;2}(\mathbf{g}_r^{(1)}, \boldsymbol{\rho}) | \mathbf{g}_w^{(2)} \rangle$  is the coupling between the magnetic field strength at the left side of the second interface due to a magnetic surface current at the right side of the first interface,
5.  $E_{w,s} = \langle \hat{\mathbf{H}}_{t;2}(\mathbf{g}_s^{(2)}, \boldsymbol{\rho}) | \mathbf{g}_w^{(2)} \rangle$  is the self interaction of the magnetic field strength at the left side of the second interface due to a magnetic surface current at the left side of the second interface,

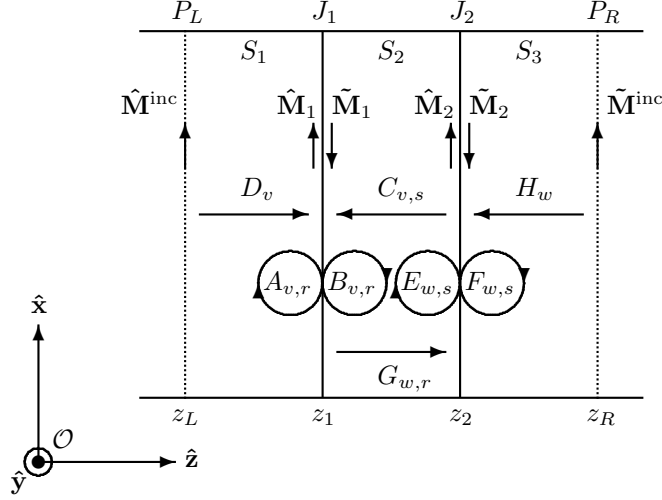


Figure 3.8: A graphical interpretation of the different terms ( $A_{v,r}$ ,  $B_{v,r}$ ,  $C_{v,s}$ ,  $E_{w,s}$ ,  $F_{w,s}$ ,  $G_{w,r}$ ) in the linear operator  $L$  and ( $D_v$ ,  $H_w$ ) in the forcing vector  $\mathbf{f}$  for the example basic structure with three segments  $S_m$  separated by two junctions  $J_m$ .

6.  $F_{w,s} = \langle \tilde{\mathbf{H}}_{t,2}(\mathbf{g}_s^{(2)}, \boldsymbol{\rho}) | \mathbf{g}_w^{(2)} \rangle$  is the self interaction of the magnetic field strength at the right side of the second interface due to a magnetic surface current at the right side of the second interface.

The column vector  $\mathbf{f}$  represents the forcing vector, and describes the external incident electromagnetic field. We can write  $\mathbf{f}$  as

$$\mathbf{f} = \begin{pmatrix} D_v \\ H_w \end{pmatrix}, \quad (3.41)$$

where each vector element is given and physically interpreted by:

1.  $D_v = - \langle \hat{\mathbf{H}}_{t,1}(\hat{\mathbf{M}}^{\text{inc}}, \boldsymbol{\rho}) | \mathbf{g}_v^{(1)} \rangle$  is the magnetic field strength at the left side of the first interface due to a incident magnetic surface current at the left probing side,
2.  $H_w = \langle \tilde{\mathbf{H}}_{t,2}(\tilde{\mathbf{M}}^{\text{inc}}, \boldsymbol{\rho}) | \mathbf{g}_w^{(2)} \rangle$  is the magnetic field strength at the right side of the second interface due to a incident magnetic surface current at the right probing side.

A graphical interpretation of the different terms in the linear operator  $L$  and the forcing vector  $\mathbf{f}$  for the example basic structure is given in figure 3.8. The vector  $\mathbf{u}$  represents the unknowns, and is given by

$$\mathbf{u} = \begin{pmatrix} V_r^{(1)} \\ V_s^{(2)} \end{pmatrix}. \quad (3.42)$$

Once the matrix equation 3.39 (linear system) is solved for the unknown vector  $\mathbf{u}$  by means of either straightforward inversion of  $L$ , or by using more sophisticated iterative schemes [91, 109], the unknown surface currents

$$\{\hat{\mathbf{M}}_1, \hat{\mathbf{M}}_2\}(\boldsymbol{\rho}),$$

can be found by substituting the vector  $\mathbf{u}$  into the surface current expansion, i.e. equations 3.29 and 3.30.

### 3.6 Calculation of the Matrix/Vector Elements

In the previous section we have formulated a matrix equation  $L\mathbf{u} = \mathbf{f}$  that solves the unknown surface currents with the method of moments. In this section, we discuss in detail the calculation of the individual linear operator  $L$ , and the forcing vector  $\mathbf{f}$ .

#### 3.6.1 Calculation of the Matrix Elements

As an example, we focus on the calculation of the matrix elements for the contribution  $A_{v,r}$  to  $L$ , which is given by

$$A_{v,r} = \langle \hat{\mathbf{H}}_{t;1}(\mathbf{g}_r^{(1)}, \boldsymbol{\rho}) | \mathbf{g}_v^{(1)} \rangle, \quad (3.43)$$

#### Waveguide

First, we consider the first section to be a waveguide. Then, the field representation for the transverse magnetic field is given by equation 2.115, and can be written as

$$\hat{\mathbf{H}}_{t;1}(\mathbf{g}_r^{(1)}, \boldsymbol{\rho}) = \sum_{j,\alpha} I_j^\alpha(z_1^-) \mathbf{h}_{t;j}^\alpha(\boldsymbol{\rho}). \quad (3.44)$$

When we substitute this field expansion in equation 3.43, we obtain

$$A_{v,r} = \sum_{j,\alpha} I_j^\alpha(z_1^-) \langle \mathbf{h}_{t;j}^\alpha | \mathbf{g}_v^{(1)} \rangle, \quad (3.45)$$

where  $I_j^\alpha(z_1^-)$  is a linear function of the inner product  $\langle \mathbf{g}_r^{(1)} | \mathbf{h}_{t;j}^\alpha \rangle$ . We can rewrite equation 3.45 as

$$A_{v,r} = \sum_{j,\alpha} I_j^\alpha(z_1^-) \langle \mathbf{g}_r^{(1)} | \mathbf{h}_{t;j}^\alpha \rangle \langle \mathbf{h}_{t;j}^\alpha | \mathbf{g}_v^{(1)} \rangle, \quad (3.46)$$

where we have explicitly isolated  $\langle \mathbf{g}_r^{(1)} | \mathbf{h}_{t;j}^\alpha \rangle$  from  $I_j^\alpha(z_1^-)$ . For  $A_{v,r}$ , we have  $I_j^\alpha(z_1^-) = -Y_{\infty;j}^\alpha$  which represents the transmission line solution for a left half space with source described in appendix B.1.

### Layered Space

Second, we consider the first section to be a layered space. Then, the field representation for the transverse magnetic field is given by equation 2.168, and can be written as

$$\hat{\mathbf{H}}_{t;1}(\mathbf{g}_r^{(1)}, \boldsymbol{\rho}) = \sum_{\alpha} \int I^{\alpha}(\mathbf{k}_t, z_1^-) \mathbf{h}_t^{\alpha}(\mathbf{k}_t, \boldsymbol{\rho}) d\mathbf{k}_t. \quad (3.47)$$

When we substitute this field expansion in equation 3.43, we obtain

$$A_{v,r} = \sum_{\alpha} \int I^{\alpha}(\mathbf{k}_t, z_1^-) \langle \mathbf{h}_t^{\alpha}(\mathbf{k}_t) | \mathbf{g}_v^{(1)} \rangle d\mathbf{k}_t, \quad (3.48)$$

where  $I^{\alpha}(\mathbf{k}_t, z_1^-)$  is a linear function of the inner product  $\langle \mathbf{g}_r^{(1)} | \mathbf{h}_t^{\alpha}(\mathbf{k}_t) \rangle$ . We can rewrite equation 3.48 as

$$A_{v,r} = \sum_{\alpha} \int I^{\alpha}(\mathbf{k}_t, z_1^-) \langle \mathbf{g}_r^{(1)} | \mathbf{h}_t^{\alpha}(\mathbf{k}_t) \rangle \langle \mathbf{h}_t^{\alpha}(\mathbf{k}_t) | \mathbf{g}_v^{(1)} \rangle d\mathbf{k}_t, \quad (3.49)$$

where we have explicitly extracted  $\langle \mathbf{g}_r^{(1)} | \mathbf{h}_t^{\alpha}(\mathbf{k}_t) \rangle$  from  $I^{\alpha}(\mathbf{k}_t, z_1^-)$ . For  $A_{v,r}$ , we have  $I^{\alpha}(\mathbf{k}_t, z_1^-) = -Y_{\infty}^{\alpha}(\mathbf{k}_t)$  which represents the transmission line solution for a left half space with source described in appendix B.1.

### Periodic Arrangement

Subsequently, we must take into account the periodic arrangement, to allow for an interaction (mutual coupling) between unit cells. The only place where the unit cells can interact is within the layered space via the equivalent magnetic surface current  $\hat{\mathbf{M}}_1$  within the first section. To incorporate this behavior, we extend the expansion surface current  $\mathbf{g}_r^{(1)}$ , which is defined only on a single unit cell, to a periodic version. Consequently, the Green's function, the transmission line solution, for the magnetic field evaluated at  $z = z_1^-$  due to a single magnetic surface current must be replaced by a periodic version as well. For this purpose, we first assume an incident plane wave with transverse wavevector  $\mathbf{k}_t^{\text{inc}}$ . Then we consider two types of periodical extensions [112, section 7.3]. These two types are explained in detail in appendix K.

### Staircase Phase Function

The first choice for a periodical extension of  $\mathbf{g}_r^{(1)}$  is the so-called staircase phase function  $\mathbf{g}_r^{(1),\mathcal{S}}$  (see equation K.19), and is expressed as

$$\mathbf{g}_r^{(1),\mathcal{S}}(\boldsymbol{\rho}) = \exp(-j\mathbf{k}_t^{\text{inc}} \cdot \boldsymbol{\rho}) \left[ \left( \mathbf{g}_r^{(1)}(\boldsymbol{\rho}) \exp(j\mathbf{k}_t^{\text{inc}} \cdot \boldsymbol{\rho}) \right) * \prod_{\mathbf{d}_1, \mathbf{d}_2} (\boldsymbol{\rho}) \right], \quad (3.50)$$

where the so-called Dirac brush function  $\prod_{\mathbf{d}_1, \mathbf{d}_2}(\boldsymbol{\rho})$ , which is a two-dimensional generalization of the Dirac comb function, is defined as

$$\prod_{\mathbf{d}_1, \mathbf{d}_2}(\boldsymbol{\rho}) = \sum_{p, q} \delta(\boldsymbol{\rho} - p\mathbf{d}_1 - q\mathbf{d}_2). \quad (3.51)$$

The corresponding spectrum<sup>2</sup> (see equation K.20) is given by

$$\langle \mathbf{g}_r^{(1), \mathcal{S}} | \mathbf{h}_t^\alpha(\mathbf{k}_t) \rangle = \frac{4\pi^2}{A} \langle \mathbf{g}_r^{(1)} | \mathbf{h}_t^\alpha(\mathbf{k}_t) \rangle \prod_{\mathbf{k}_1, \mathbf{k}_2} (\mathbf{k}_t - \mathbf{k}_t^{\text{inc}}). \quad (3.52)$$

The Galerkin procedure suggests that expansion and weighting functions must be identical. However this causes mathematical difficulties since integrals of products of delta functions with identical support are undefined. To solve this problem, we select non-periodical weighting functions. This makes sense since the periodicity of the structure is already built in through the periodical expansion functions. There is no need to enforce it again in the weighting functions. If we choose

$$\mathbf{g}_v^{(1), \mathcal{S}}(\boldsymbol{\rho}) = \mathbf{g}_v^{(1)}(\boldsymbol{\rho}), \quad (3.53)$$

we look into a single cell only, and we avoid the mathematical difficulties. The corresponding spectrum is given by

$$\langle \mathbf{h}_t^\alpha(\mathbf{k}_t) | \mathbf{g}_v^{(1), \mathcal{S}} \rangle = \langle \mathbf{h}_t^\alpha(\mathbf{k}_t) | \mathbf{g}_v^{(1)} \rangle. \quad (3.54)$$

By substituting 3.52 and 3.54 in 3.49, we arrive at

$$A_{v,r} = \frac{4\pi^2}{A} \sum_{j, \alpha} I^\alpha(\mathbf{k}_{t;j}, z_1^-) \langle \mathbf{g}_r^{(1)} | \mathbf{h}_t^\alpha(\mathbf{k}_{t;j}) \rangle \langle \mathbf{h}_t^\alpha(\mathbf{k}_{t;j}) | \mathbf{g}_v^{(1)} \rangle. \quad (3.55)$$

The transverse wavevector  $\mathbf{k}_t$  is defined in a reciprocal lattice and is a function of the index  $j$  and can be expressed as

$$\mathbf{k}_{t;j} = R\mathbf{m}_j + \mathbf{k}_t^{\text{inc}}, \quad D^T R = 2\pi I, \quad \mathbf{m}_j = \begin{pmatrix} m_{1,j} \\ m_{2,j} \end{pmatrix}. \quad (3.56)$$

The 2 by 2 matrix  $D$  represents the elementary dimensions of the periodical structure. The columns of  $D$  form the basis vectors  $\mathbf{d}_1$  and  $\mathbf{d}_2$  of a single unit cell. Given  $D$ , the matrix  $R$  is determined by equation 3.56, and represents the corresponding reciprocal transverse wavevector lattice, which is discussed in detail in appendix K. Both indices  $m_{1,j}$  and  $m_{2,j}$  are integers and range from  $-\infty$  to  $\infty$ .

In general,  $\mathbf{k}_t^{\text{inc}}$  changes when the frequency or the angle of incidence of the plane wave is varied. Consequently, the reciprocal lattice  $\mathbf{k}_{t;j}$  moves along in the spectral plane. This means that the inner products  $\langle \mathbf{g}_r^{(1)} | \mathbf{h}_t^\alpha(\mathbf{k}_{t;j}) \rangle$  and  $\langle \mathbf{h}_t^\alpha(\mathbf{k}_{t;j}) | \mathbf{g}_v^{(1)} \rangle$  are sampled at different points when  $\mathbf{k}_t^{\text{inc}}$  changes.

<sup>2</sup>We call this a spectrum because  $\mathbf{h}_t^\alpha(\mathbf{k}_t)$  are plane waves, i.e., exponentials.

### Linear Phase Function

The second choice for a periodical extension of  $\mathbf{g}_r^{(1)}$  is the so-called linear phase function  $\mathbf{g}_r^{(1),\mathcal{L}}$  (see equation K.21), and is expressed as

$$\mathbf{g}_r^{(1),\mathcal{L}}(\boldsymbol{\rho}) = \exp(-j\mathbf{k}_t^{\text{inc}} \cdot \boldsymbol{\rho}) \left[ \mathbf{g}_r^{(1)}(\boldsymbol{\rho}) * \prod_{\mathbf{d}_1, \mathbf{d}_2} (\boldsymbol{\rho}) \right]. \quad (3.57)$$

The corresponding spectrum (see equation K.22) is given by

$$\langle \mathbf{g}_r^{(1),\mathcal{L}} | \mathbf{h}_t^\alpha(\mathbf{k}_t) \rangle = \frac{4\pi^2}{A} \langle \mathbf{g}_r^{(1)} | \mathbf{h}_t^\alpha(\mathbf{k}_t - \mathbf{k}_t^{\text{inc}}) \rangle \prod_{\mathbf{k}_1, \mathbf{k}_2} (\mathbf{k}_t - \mathbf{k}_t^{\text{inc}}). \quad (3.58)$$

If we choose

$$\mathbf{g}_v^{(1),\mathcal{L}}(\boldsymbol{\rho}) = \mathbf{g}_v^{(1)}(\boldsymbol{\rho}) \exp(-j\mathbf{k}_t^{\text{inc}} \cdot \boldsymbol{\rho}). \quad (3.59)$$

we avoid similar mathematical difficulties (that integrals of products of delta functions with identical support are undefined) described for the staircase phase function. The corresponding spectrum is given by

$$\langle \mathbf{h}_t^\alpha(\mathbf{k}_t) | \mathbf{g}_v^{(1),\mathcal{L}} \rangle = \langle \mathbf{h}_t^\alpha(\mathbf{k}_t - \mathbf{k}_t^{\text{inc}}) | \mathbf{g}_v^{(1)} \rangle. \quad (3.60)$$

By substituting 3.58 and 3.60 in 3.49, we arrive at

$$A_{v,r} = \frac{4\pi^2}{A} \sum_{j,\alpha} I^\alpha(\mathbf{k}_{t;j}, z_1^-) \langle \mathbf{g}_r^{(1)} | \mathbf{h}_t^\alpha(R\mathbf{m}_j) \rangle \langle \mathbf{h}_t^\alpha(R\mathbf{m}_j) | \mathbf{g}_v^{(1)} \rangle. \quad (3.61)$$

Note that  $\langle \mathbf{g}_r^{(1)} | \mathbf{h}_t^\alpha(R\mathbf{m}_j) \rangle$  and  $\langle \mathbf{h}_t^\alpha(R\mathbf{m}_j) | \mathbf{g}_v^{(1)} \rangle$  are sampled at fixed points in the reciprocal lattice when  $\mathbf{k}_t^{\text{inc}}$  changes. Hence they may be computed once and then stored. This procedure leads to a saving of computer time if the basic structure is complicated and the computation of the spectra is time consuming.

### 3.6.2 Calculation of the Vector Elements

As an example, we focus on the calculation of the vector elements for the contribution  $D_v$  to  $\mathbf{f}$ , which is given by

$$D_v = - \langle \hat{\mathbf{H}}_{t;1}(\hat{\mathbf{M}}^{\text{inc}}, \boldsymbol{\rho}) | \mathbf{g}_v^{(1)} \rangle. \quad (3.62)$$

#### Waveguide

First, we consider the first section to be a waveguide. Then, the field representation for the transverse magnetic field is given by equation 2.115, and can be written as

$$\hat{\mathbf{H}}_{t;1}(\hat{\mathbf{M}}^{\text{inc}}, \boldsymbol{\rho}) = \sum_{j,\alpha} I_j^\alpha(z_1^-) \mathbf{h}_{t;j}^\alpha(\boldsymbol{\rho}). \quad (3.63)$$

When we substitute this field expansion in equation 3.62, we obtain

$$D_v = - \sum_{j,\alpha} I_j^\alpha(z_1^-) \langle \mathbf{h}_{t;j}^\alpha | \mathbf{g}_v^{(1)} \rangle, \quad (3.64)$$

where  $I_j^\alpha(z_1^-)$  is a linear function of the inner product  $\langle \hat{\mathbf{M}}^{\text{inc}} | \mathbf{h}_{t;j}^\alpha \rangle$ . We can rewrite equation 3.64 as

$$D_v = - \sum_{j,\alpha} I_j^\alpha(z_1^-) \langle \hat{\mathbf{M}}^{\text{inc}} | \mathbf{h}_{t;j}^\alpha \rangle \langle \mathbf{h}_{t;j}^\alpha | \mathbf{g}_v^{(1)} \rangle, \quad (3.65)$$

where we have explicitly isolated  $\langle \hat{\mathbf{M}}^{\text{inc}} | \mathbf{h}_{t;j}^\alpha \rangle$  from  $I_j^\alpha(z_1^-)$ . For  $D_v$ ,  $I_j^\alpha(z_1^-)$  is given by the transmission line solution for a half space with offset source described in appendix B.5.

### Layered Space

Second, we consider the first section to be a layered space. Then, the field representation for the transverse magnetic field is given by equation 2.168, and can be written as

$$\hat{\mathbf{H}}_{t;1}(\hat{\mathbf{M}}^{\text{inc}}, \boldsymbol{\rho}) = \sum_{\alpha} \int I^\alpha(\mathbf{k}_t, z_1^-) \mathbf{h}_t^\alpha(\mathbf{k}_t, \boldsymbol{\rho}) d\mathbf{k}_t. \quad (3.66)$$

When we substitute this field expansion in equation 3.62, we obtain

$$D_v = - \sum_{\alpha} \int I^\alpha(\mathbf{k}_t, z_1^-) \langle \mathbf{h}_t^\alpha(\mathbf{k}_t) | \mathbf{g}_v^{(1)} \rangle d\mathbf{k}_t, \quad (3.67)$$

where  $I^\alpha(\mathbf{k}_t, z_1^-)$  is a linear function of the inner product  $\langle \hat{\mathbf{M}}^{\text{inc}} | \mathbf{h}_t^\alpha(\mathbf{k}_t) \rangle$ . We can rewrite equation 3.67 as

$$D_v = - \sum_{\alpha} \int I^\alpha(\mathbf{k}_t, z_1^-) \langle \hat{\mathbf{M}}^{\text{inc}} | \mathbf{h}_t^\alpha(\mathbf{k}_t) \rangle \langle \mathbf{h}_t^\alpha(\mathbf{k}_t) | \mathbf{g}_v^{(1)} \rangle d\mathbf{k}_t, \quad (3.68)$$

where we have explicitly extracted  $\langle \hat{\mathbf{M}}^{\text{inc}} | \mathbf{h}_t^\alpha(\mathbf{k}_t) \rangle$  from  $I^\alpha(\mathbf{k}_t, z_1^-)$ . For  $D_v$ ,  $I^\alpha(\mathbf{k}_t, z_1^-)$  is given by the transmission line solution for a half space with offset source described in appendix B.5.

### Periodic Arrangement

Subsequently, we must take into account the periodic arrangement, to allow for an interaction (mutual coupling) between unit cells. For this purpose, we first assume an incident plane wave with transverse wavevector  $\mathbf{k}_t^{\text{inc}}$ . In general, when the plane wave changes its direction, the system matrix  $S$  has to be recomputed since  $\mathbf{k}_t$  depends on  $\mathbf{k}_t^{\text{inc}}$ . However, if this shift is a lattice vector, i.e.  $R\mathbf{m}_j$ , then the system matrix  $S$  does not change [112, section 7.3]. The points of the lattice are simply relabeled. This means that the system matrix is a periodic function

of  $\mathbf{k}_t$ . With just a single system matrix inversion it is possible to compute the response of the basic structure for a given incident field consisting of a discrete spectrum of plane waves directly linked to the same reciprocal lattice, i.e.

$$\langle \hat{\mathbf{M}}^{\text{inc}} | \mathbf{h}_t^\alpha(\mathbf{k}_t) \rangle = \hat{\mathbf{V}}^{\text{inc}}(\mathbf{k}_t) \prod_{\mathbf{k}_1, \mathbf{k}_2} (\mathbf{k}_t - \mathbf{k}_t^{\text{inc}}). \quad (3.69)$$

Then we consider two types of periodical extensions. These two types are explained in detail in appendix K and have also been used in the previous section.

### Staircase Phase Function

The first choice for a periodic extension of  $\mathbf{g}_r^{(1)}$  is the so-called staircase phase function  $\mathbf{g}_r^{(1),\mathcal{S}}$  (see equation 3.53). If we choose the weighting function

$$\mathbf{g}_v^{(1),\mathcal{S}}(\boldsymbol{\rho}) = \mathbf{g}_v^{(1)}(\boldsymbol{\rho}), \quad (3.70)$$

we avoid the mathematical difficulties (that integrals of products of delta functions with identical support are undefined) described in the previous section. By using equations 3.69 and 3.70, we can rewrite equation 3.68 as

$$D_v = -\frac{4\pi^2}{A} \sum_{j,\alpha} I^\alpha(\mathbf{k}_{t;j}, z_1^-) \hat{\mathbf{V}}^{\text{inc}}(\mathbf{k}_{t;j}) \langle \mathbf{h}_t^\alpha(\mathbf{k}_{t;j}) | \mathbf{g}_v^{(1)} \rangle. \quad (3.71)$$

### Linear Phase Function

The second choice for a periodic extension of  $\mathbf{g}_r^{(1)}$  is the so-called linear phase function  $\mathbf{g}_r^{(1),\mathcal{L}}$  (see equation 3.59). If we choose the weighting function

$$\mathbf{g}_v^{(1),\mathcal{L}}(\boldsymbol{\rho}) = \mathbf{g}_v^{(1)}(\boldsymbol{\rho}) \exp(-j\mathbf{k}_t^{\text{inc}} \cdot \boldsymbol{\rho}), \quad (3.72)$$

we avoid the mathematical difficulties (that integrals of products of delta functions with identical support are undefined) described in the previous section. By using equations 3.69 and 3.72, we can rewrite equation 3.68 as

$$D_v = -\frac{4\pi^2}{A} \sum_{j,\alpha} I^\alpha(\mathbf{k}_{t;j}, z_1^-) \hat{\mathbf{V}}^{\text{inc}}(\mathbf{k}_{t;j}) \langle \mathbf{h}_t^\alpha(R\mathbf{m}_j) | \mathbf{g}_v^{(1)} \rangle. \quad (3.73)$$

Note that  $\langle \mathbf{h}_t^\alpha(R\mathbf{m}_j) | \mathbf{g}_v^{(1)} \rangle$  is sampled at fixed points in the reciprocal lattice when  $\mathbf{k}_t^{\text{inc}}$  changes. Hence they may be computed once and then stored.

## 3.7 Expansion and Weighting Functions

If we use the method of moments to solve the coupled field integral equation described in this chapter, we have to define a number of expansion and weighting functions for the unknown surface current at the junctions. This choice depends



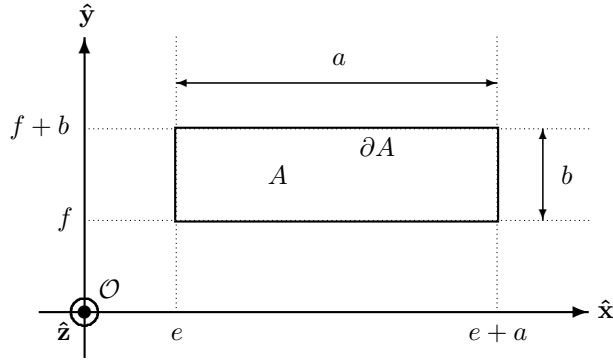


Figure 3.9: Cross section of a rectangular waveguide in the  $x, y$ -plane.

on the geometrical shape of the support of these surface currents. We discuss this in this section, and we distinguish between global and local functions.

Global functions make use of the overall shape of the support of the unknown surface current by assigning to it a "transverse global expansion". We discuss the rectangular waveguide mode functions, the thin strip functions, and the weighted Chebyshev functions. We define these functions in sections 3.7.1, 3.7.2 and 3.7.3 and discuss some valuable properties.

Local functions approximate the overall shape of the support of the unknown surface current by dividing it into small primitive elements for which the local edge conditions are taken into account. We discuss the rectangular rooftop and the triangular Rao-Wilton-Glisson (RWG) functions. We define these functions in sections 3.7.4 and 3.7.5 and discuss the most relevant properties.

### 3.7.1 Waveguide Mode Functions

The unknown surface current is approximated by using rectangular waveguide mode functions [11, 14]. First, a cross section of the waveguide is drawn in figure 3.9.

The waveguide has a cross section  $A$  with a boundary  $\partial A$ . The cross section is rectangular in shape with length  $a$  and height  $b$ . The lower left corner of this waveguide is shifted from the origin towards  $x = e$  and  $y = f$ . This is done to allow for a shifted waveguide within the unit cell.

The electric and magnetic modal fields within this waveguide can be written in terms of square integrable and normalized scalar generating functions  $\Phi_m$  and  $\Psi_m$  given by equations 2.137, 2.138, 2.162 and 2.163. Further,  $\Phi_m$  and  $\Psi_m$  satisfy equations 2.134 and 2.159, respectively. Given the rectangular shape of the waveguide, we can solve these equations. For  $\Phi_m$ , we obtain the following

analytical solution.

$$\Phi_m(\boldsymbol{\rho}) = \begin{cases} \frac{2}{\sqrt{ab}} \sin\left(\frac{m\pi}{a}(x-e)\right) \sin\left(\frac{n\pi}{b}(y-f)\right) & \text{if } \boldsymbol{\rho} \in A, \\ 0 & \text{otherwise,} \end{cases} \quad (3.74)$$

$$k'_{t;m} = \sqrt{\left(\frac{m\pi}{a}\right)^2 + \left(\frac{n\pi}{b}\right)^2}, \quad (3.75)$$

where  $m, n = 1, 2, 3, \dots$ . For  $\Psi_m$ , we obtain the following analytical solution.

$$\Psi_m(\boldsymbol{\rho}) = \begin{cases} \sqrt{\frac{\epsilon_m \epsilon_n}{ab}} \cos\left(\frac{m\pi}{a}(x-e)\right) \cos\left(\frac{n\pi}{b}(y-f)\right) & \text{if } \boldsymbol{\rho} \in A, \\ 0 & \text{otherwise,} \end{cases} \quad (3.76)$$

$$k''_{t;m} = \sqrt{\left(\frac{m\pi}{a}\right)^2 + \left(\frac{n\pi}{b}\right)^2}, \quad (3.77)$$

where  $m, n = 0, 1, 2, \dots$  but where  $m = n = 0$  is excluded because it corresponds to a vanishing field. Note that we have replaced the single index  $m$  with an index pair  $(m, n)$ . Further, we have used the Neumann symbol [34, definition 4.50] defined as

$$\epsilon_m = \begin{cases} 1 & \text{if } m = 0, \\ 2 & \text{otherwise.} \end{cases} \quad (3.78)$$

The inner product between the rectangular waveguide mode expansion/weighting functions and the waveguide mode functions is evaluated in appendix C. The inner product between the rectangular waveguide mode expansion/weighting functions and the layered space mode functions is evaluated in appendix D.

### 3.7.2 Thin Strip Functions

The so-called thin strip function is particularly suited when the geometrical shape of the support of the surface current consists of separate thin rectangular regions, whose width is small compared to the length of the strip. The behavior of the surface current in such a region can be written as the product of a modal  $\sin(x)$ -function in the length direction, and a  $1/\sqrt{x}$ -function in the width direction which satisfies the edge conditions analytically. The thin strip function with label  $n$  has a support  $S_n$ , and is defined as

$$\mathbf{f}_n(\boldsymbol{\rho}) = \begin{cases} \hat{\mathbf{p}}_n \frac{1}{\sqrt{1-\left(\frac{2y'}{w_n}\right)^2}} \sin\left(\frac{\pi m_n}{l_n} \left[x' + \frac{l_n}{2}\right]\right) & \text{if } \boldsymbol{\rho} \in S_n, \\ \mathbf{0} & \text{otherwise,} \end{cases} \quad (3.79)$$

in which

$$x' = \boldsymbol{\rho} \cdot \hat{\mathbf{d}}_n, \quad y' = \boldsymbol{\rho} \cdot (\hat{\mathbf{z}} \times \hat{\mathbf{d}}_n), \quad \hat{\mathbf{d}}_n = \hat{\mathbf{x}} \cos(\alpha) + \hat{\mathbf{y}} \sin(\alpha), \quad (3.80)$$

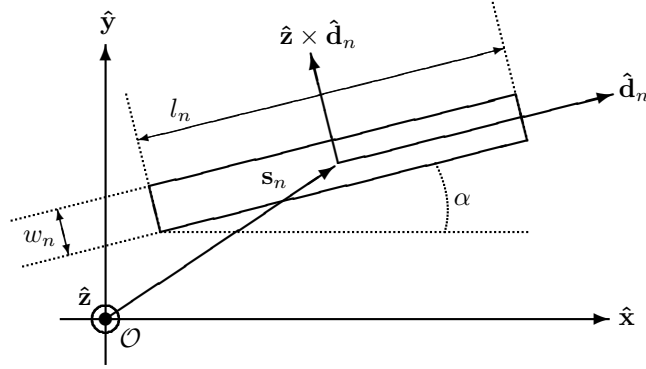


Figure 3.10: Domain, vectors and scalars used in the definition of the thin strip function.

and in which

$$\hat{\mathbf{p}}_n = \begin{cases} \hat{\mathbf{d}}_n & \text{for an electric current on the patch,} \\ \hat{\mathbf{z}} \times \hat{\mathbf{d}}_n & \text{for a magnetic current in the aperture.} \end{cases} \quad (3.81)$$

$\hat{\mathbf{d}}_n$  denotes the unit-length vector along the length of the thin strip which is rotated by an angle  $\alpha$  with respect to the  $x$ -axis.  $\hat{\mathbf{p}}_n$  denotes the direction of the surface current.  $\mathbf{s}_n$  denotes the transverse vector from the origin to the center of the thin strip.  $m_n$  denotes the mode number.  $l_n$  denotes the length of the thin strip.  $w_n \ll l_n$  denotes the width of the thin strip. See figure 3.10 for a graphical representation of the domain, vectors and scalars used in the definition of the thin strip function. The inner product between the thin strip functions and the layered space mode functions is evaluated in appendix I.

### 3.7.3 Patch Functions

The so-called patch function is particularly suited when the geometrical shape of the support of the surface current consists of separate rectangular regions. The behavior of the surface current in such a region can be written as the product of  $\sqrt{x}$  functions  $C_m(x, w)$  and  $1/\sqrt{x}$  functions  $D_m(x, w)$  that satisfy the edge conditions analytically [1]. The patch function with label  $n$  has a rectangular support  $S_n$ , and is defined as

$$\mathbf{f}_n(\boldsymbol{\rho}) = \begin{cases} \hat{\mathbf{u}}_n C_{p_n}(x', l_n) D_{q_n}(y', w_n) & \text{if } \boldsymbol{\rho} \in S_n \text{ and } \hat{\mathbf{u}}_n\text{-directed,} \\ \hat{\mathbf{v}}_n D_{q_n}(x', l_n) C_{p_n}(y', w_n) & \text{if } \boldsymbol{\rho} \in S_n \text{ and } \hat{\mathbf{v}}_n\text{-directed,} \\ \mathbf{0} & \text{otherwise,} \end{cases} \quad (3.82)$$

in which

$$x' = \boldsymbol{\rho} \cdot \hat{\mathbf{u}}_n, \quad y' = \boldsymbol{\rho} \cdot \hat{\mathbf{v}}_n, \quad \hat{\mathbf{u}}_n = \hat{\mathbf{x}} \cos(\alpha) + \hat{\mathbf{y}} \sin(\alpha), \quad \hat{\mathbf{v}}_n = \hat{\mathbf{z}} \times \hat{\mathbf{u}}_n, \quad (3.83)$$

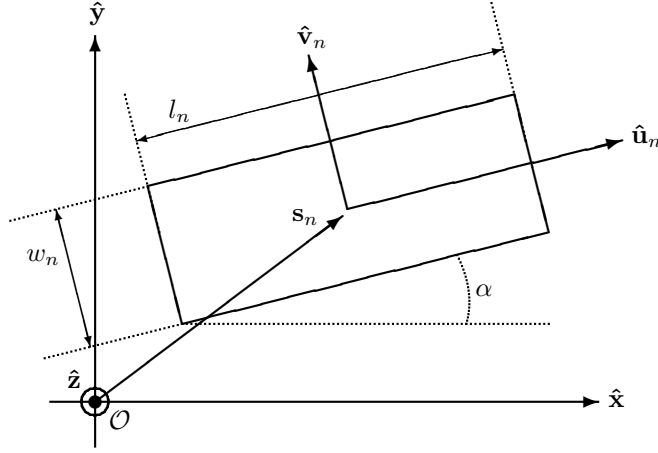


Figure 3.11: Domain, vectors and scalars used in the definition of the patch function.

and in which

$$C_m(x, w) = \mathcal{U}_m\left(\frac{2x}{w}\right) \sqrt{1 - \left(\frac{2x}{w}\right)^2}, \quad (3.84)$$

$$D_m(x, w) = \mathcal{T}_m\left(\frac{2x}{w}\right) \frac{1}{\sqrt{1 - \left(\frac{2x}{w}\right)^2}}, \quad (3.85)$$

where  $m = 0, 1, 2, \dots$ , and where  $\mathcal{T}_m(x) = \cos(m \arccos(x))$  and  $\mathcal{U}_m(x) = \sin((m+1) \arccos(x)) / \sin(\arccos(x))$  are the Chebyshev polynomials of the first and second kind, respectively [2, chapter 22].  $\hat{\mathbf{u}}_n$  and  $\hat{\mathbf{v}}_n$  denote the unit-length vectors parallel and perpendicular to the longitudinal axis of the rectangle, respectively, which is rotated by an angle  $\alpha$  with respect to the  $x$ -axis.  $\mathbf{s}_n$  denotes the transverse vector from the origin to the center of the rectangle.  $p_n$  and  $q_n$  denote the order of the Chebyshev polynomials.  $l_n$  denotes the length of the rectangle.  $w_n$  denotes the width of the rectangle. See figure 3.11 for a graphical representation of the domain, vectors and scalars used in the definition of the patch function.

The inner product between the patch functions and the layered space mode functions is described in detail in appendix J.

### 3.7.4 Rooftop Functions

The so-called rooftop function is particularly suited when the geometrical shape of the support of the surface current consists of rectangular regions. These regions are broken up in (almost) square subdomains and the rooftop functions are defined on every two adjacent subdomains [104].

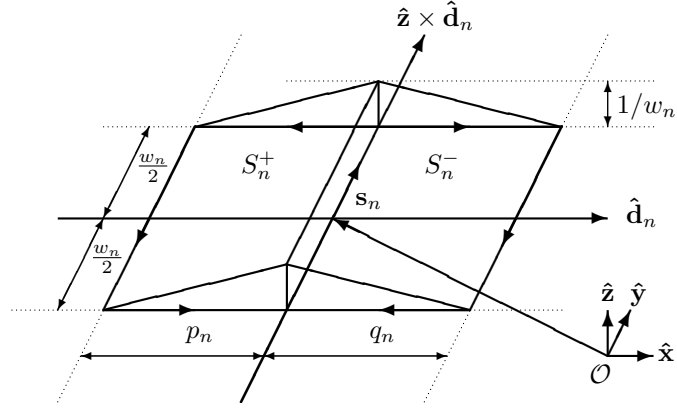


Figure 3.12: Domain, vectors and scalars used in the definition of the rooftop function.

Two given adjacent rectangular subdomains have an interior edge with label  $n$  in common. We assign to this edge a preferred direction which allows us to discriminate between a so-called positive  $S_n^+$  and negative  $S_n^-$  rectangular subdomain. The rooftop function associated with this interior edge is now defined as

$$\mathbf{f}_n(\boldsymbol{\rho}) = \hat{\mathbf{d}}_n \Lambda((\boldsymbol{\rho} - \mathbf{s}_n) \cdot \hat{\mathbf{d}}_n, p_n, q_n) \Pi((\boldsymbol{\rho} - \mathbf{s}_n) \cdot (\hat{\mathbf{z}} \times \hat{\mathbf{d}}_n), w_n), \quad (3.86)$$

in which the triangle function is defined as

$$\Lambda(x, p, q) = \begin{cases} 1 + \frac{x}{p} & \text{if } -p < x < 0, \\ 1 - \frac{x}{q} & \text{if } 0 < x < q, \\ 0 & \text{otherwise,} \end{cases} \quad (3.87)$$

and in which the block function is defined as

$$\Pi(y, w) = \begin{cases} \frac{1}{w} & \text{if } -\frac{w}{2} < y < \frac{w}{2}, \\ 0 & \text{otherwise.} \end{cases} \quad (3.88)$$

Further,  $\hat{\mathbf{d}}_n$  denotes the unit-length vector perpendicular to the interior edge.  $\mathbf{s}_n$  denotes the transverse vector from the origin to the center of the rooftop function.  $p_n$  and  $q_n$  denote the lengths of the rectangular subdomains  $S_n^+$  and  $S_n^-$ , respectively.  $w_n$  denotes the height of the rooftop function. See figure 3.12 for a graphical representation of the domain, vectors and scalars used in the definition of the rooftop function.

The rooftop function has some valuable properties. First, the surface current has no component normal to the exterior boundary of the surface formed its own rectangular subdomains. This is why two rooftop functions must overlap. This means that line charges will not exist along boundaries between the subdomains.

Second, the normal component of the surface current on the interior edge is constant and continuous across this edge. This ensures that also this edge is free of line charges. Third, the surface charge density is proportional to the surface divergence of the surface current given by

$$\nabla_t \cdot \mathbf{f}_n(\boldsymbol{\rho}) = \begin{cases} \frac{1}{w_n p_n} & \text{if } \boldsymbol{\rho} \in S_n^-, \\ -\frac{1}{w_n q_n} & \text{if } \boldsymbol{\rho} \in S_n^+, \\ 0 & \text{otherwise,} \end{cases} \quad (3.89)$$

and is a constant within each rectangular subdomain. Fourth, the total charge, i.e. surface charge density times area, over both rectangular subdomains equals zero. Finally, since the normal component of the surface current on the interior edge is of unit length, each coefficient in the unknown current expansion may be interpreted as the normal component of current density flowing through the interior edge.

The inner product between the rooftop functions and the waveguide mode functions is evaluated in appendix E. The inner product between the rooftop functions and the layered space mode functions is evaluated in appendix F.

### 3.7.5 RWG Functions

The so-called Rao-Wilton-Glisson (RWG) function is particularly suited when the geometrical shape of the support of the surface current consists of arbitrarily shaped regions. These regions are broken up in (almost) equilateral triangular subdomains and the RWG functions are defined on every pair of adjacent subdomains [88].

Two given adjacent triangular subdomains have an interior edge with label  $n$  in common. The vertices of this edge are given by  $\boldsymbol{\rho}_n^{(1)}$  and  $\boldsymbol{\rho}_n^{(2)}$ . We assign to this edge an arbitrary preferred direction  $\boldsymbol{\rho}_n^{(12)} = \boldsymbol{\rho}_n^{(2)} - \boldsymbol{\rho}_n^{(1)}$  which allows us to discriminate between a so-called positive  $T_n^+$  and negative  $T_n^-$  triangular subdomain by using the right-hand rule for the contour of these two triangles. The RWG function associated with this interior edge is now defined as

$$\mathbf{f}_n(\boldsymbol{\rho}) = \begin{cases} \frac{l_n}{2A_n^+}(\boldsymbol{\rho} - \boldsymbol{\rho}_n^+) & \text{if } \boldsymbol{\rho} \in T_n^+, \\ \frac{l_n}{2A_n^-}(\boldsymbol{\rho}_n^- - \boldsymbol{\rho}) & \text{if } \boldsymbol{\rho} \in T_n^-, \\ \mathbf{0} & \text{otherwise.} \end{cases} \quad (3.90)$$

$l_n$  denotes the length of the interior edge,  $\boldsymbol{\rho}_n^+$  and  $\boldsymbol{\rho}_n^-$  denote the outer vertices of the triangular subdomains  $T_n^+$  and  $T_n^-$ , respectively.  $A_n^+$  and  $A_n^-$  denote the areas of the triangular subdomains  $T_n^+$  and  $T_n^-$ , respectively. See figure 3.13 for a graphical representation of the domain, vectors and scalars used in the RWG function.

The RWG function has some valuable properties. First, the surface current has no component normal to the exterior boundary of the surface formed by the triangular subdomains. This means that no line charges will exist along this

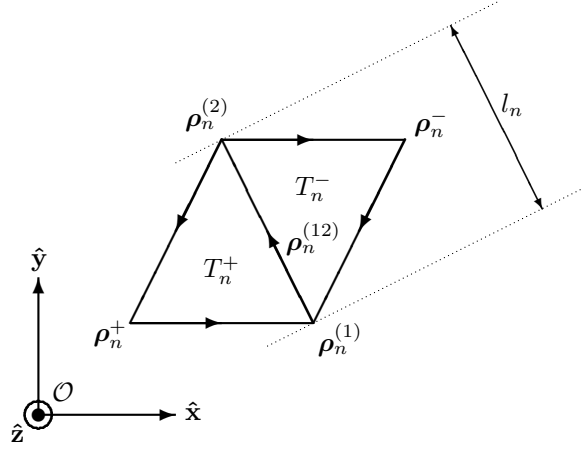


Figure 3.13: Domain, vectors and scalars used in the RWG function.

boundary. Second, the normal component of the current on the interior edge is constant and continuous across this edge. This ensures that also this edge is free of line charges. Third, the surface charge density is proportional to the surface divergence of the surface current given by

$$\nabla_t \cdot \mathbf{f}_n(\boldsymbol{\rho}) = \begin{cases} \frac{l_n}{A_n^+} & \text{if } \boldsymbol{\rho} \in T_n^+, \\ -\frac{l_n}{A_n^-} & \text{if } \boldsymbol{\rho} \in T_n^-, \\ 0 & \text{otherwise,} \end{cases} \quad (3.91)$$

and is a constant within each triangular subdomain. Fourth, the total charge, i.e. surface charge density times area, over both triangular subdomains equals zero. Fifth, by using an appropriate linear combination of three RWG functions corresponding to the three (interior) edges within a single triangular subdomain, we are able to construct a uniform current flowing in an arbitrary direction within this triangular subdomain. Finally, since the normal component of the surface current on the interior edge is of unit length, each coefficient in the unknown current expansion may be interpreted as the normal component of current density flowing through the interior edge.

The inner product between the RWG functions and the waveguide mode functions is evaluated in appendix G. The inner product between the RWG functions and the layered space mode functions is evaluated in appendix H.

### 3.8 Calculation of the Total Field

We calculate the total electromagnetic field at any given location within the configuration. To do so, we first define so-called probing interfaces at the left and right side of the basic structure at some finite distance away from the junctions.

We calculate the total electromagnetic field at these probing interfaces. Due to the superposition principle [35, section 11.3], the total field at these probing interfaces can be written as a sum of an incident and a scattered field, which is discussed in sections 3.8.1 and 3.8.2, respectively.

Then, in section 3.8.3 we formulate a so-called generalized scattering matrix, which characterizes the electromagnetic behavior for a single basic structure, by expressing the outgoing waves in terms of the incident waves [31, 48].

Finally, in section 3.8.4 we formulate a procedure that cascades two generalized scattering matrices [112, section 6.3] to obtain a new generalized scattering matrix which characterizes the electromagnetic behavior of the combination of the two corresponding basic structures.

First, we define so-called probing interfaces at which we calculate the total electromagnetic field. Without loss of generality, we define a left probing interface in the first segment at  $z = z_L < z_1$ , where  $z_1$  denotes the location of the first junction. At an infinitesimally small negative distance away from  $z_L$  at  $z = z_L^-$ , we place an incident magnetic surface current  $\hat{\mathbf{M}}^{\text{inc}}$ . We calculate the total transverse electromagnetic field at this interface, i.e.,  $\mathbf{E}_t(\boldsymbol{\rho}, z_L)$  and  $\mathbf{H}_t(\boldsymbol{\rho}, z_L)$ .

Further, we define a right probing interface in the last segment at  $z = z_R > z_M$ , where  $z_M$  denotes the location of the last junction for a given  $M$ . At an infinitesimally small positive distance away from  $z_R$  at  $z = z_R^+$ , we place an incident magnetic surface current  $\tilde{\mathbf{M}}^{\text{inc}}$ . We calculate the total transverse electromagnetic field at this interface, i.e.,  $\mathbf{E}_t(\boldsymbol{\rho}, z_R)$ , and  $\mathbf{H}_t(\boldsymbol{\rho}, z_R)$ .

Consider again the example at the end of section 3.4. The application of the field equivalence principle divides the original basic structure into three separate closed sections with the following equivalent magnetic surface currents:  $\{\hat{\mathbf{M}}^{\text{inc}}, \tilde{\mathbf{M}}_1\}$  if  $z < z_1$ ,  $\{\tilde{\mathbf{M}}_1 = -\tilde{\mathbf{M}}_1, \tilde{\mathbf{M}}_2\}$  if  $z_1 < z < z_2$ , and  $\{\tilde{\mathbf{M}}_2 = -\tilde{\mathbf{M}}_2, \mathbf{M}^{\text{inc}}\}$  if  $z > z_2$ .

Due to the superposition principle, the total electromagnetic field at the left probing interface can be written as a sum of the incident field and a scattered field as

$$\mathbf{E}_t(\boldsymbol{\rho}, z_L) = \mathbf{E}_t^{\text{inc}}(\boldsymbol{\rho}, z_L) + \mathbf{E}_t^{\text{scat}}(\boldsymbol{\rho}, z_L), \quad (3.92)$$

$$\mathbf{H}_t(\boldsymbol{\rho}, z_L) = \mathbf{H}_t^{\text{inc}}(\boldsymbol{\rho}, z_L) + \mathbf{H}_t^{\text{scat}}(\boldsymbol{\rho}, z_L). \quad (3.93)$$

$\mathbf{E}_t^{\text{inc}}(\boldsymbol{\rho}, z_L)$  and  $\mathbf{H}_t^{\text{inc}}(\boldsymbol{\rho}, z_L)$  denote the incident electric and magnetic field, respectively, and are a consequence of  $\hat{\mathbf{M}}^{\text{inc}}$ .  $\mathbf{E}_t^{\text{scat}}(\boldsymbol{\rho}, z_L)$  and  $\mathbf{H}_t^{\text{scat}}(\boldsymbol{\rho}, z_L)$  denote the scattered electric and magnetic field, respectively, and are a consequence of  $\tilde{\mathbf{M}}_1$ . The same argument can be applied to the total electromagnetic field at the right probing interface for  $\mathbf{E}_t(\boldsymbol{\rho}, z_R)$  and  $\mathbf{H}_t(\boldsymbol{\rho}, z_R)$ , which are a consequence of  $\tilde{\mathbf{M}}_2$  and  $\tilde{\mathbf{M}}^{\text{inc}}$ .

### 3.8.1 Calculation of the Incident Field

As an example, we calculate  $\mathbf{H}_t^{\text{inc}}(\boldsymbol{\rho}, z_L)$  for a waveguide section. The field representation for a transverse magnetic field is given by equation 2.115 and



can be written as

$$\mathbf{H}_t^{\text{inc}}(\boldsymbol{\rho}, z_L) = \sum_{j,\alpha} I_j^\alpha(z_L) \mathbf{h}_{t;j}^\alpha(\boldsymbol{\rho}), \quad (3.94)$$

where the Green's function  $I_j^\alpha(z_L)$  is a linear function of the inner product  $\langle \hat{\mathbf{M}}^{\text{inc}} | \mathbf{h}_{t;j}^\alpha \rangle$ . We can rewrite equation 3.94 as

$$\mathbf{H}_t^{\text{inc}}(\boldsymbol{\rho}, z_L) = \sum_{j,\alpha} I_j^\alpha(z_L) \langle \hat{\mathbf{M}}^{\text{inc}} | \mathbf{h}_{t;j}^\alpha \rangle \mathbf{h}_{t;j}^\alpha(\boldsymbol{\rho}), \quad (3.95)$$

where we have isolated  $\langle \hat{\mathbf{M}}^{\text{inc}} | \mathbf{h}_{t;j}^\alpha \rangle$  from the Green's function  $I_j^\alpha(z_L)$ . Furthermore,  $I_j^\alpha(z_L)$  is given by the Green's function for a half space with offset source derived in appendix B.5. Finally, if we choose for  $\hat{\mathbf{M}}^{\text{inc}}$  the waveguide mode  $\mathbf{h}_{t;k}^\beta$  for a given  $\beta$  and  $k$ , then  $\mathbf{H}_t^{\text{inc}}(\boldsymbol{\rho}, z_L)$  reduces to

$$\mathbf{H}_t^{\text{inc}}(\boldsymbol{\rho}, z_L) = I_k^\beta(z_L) \mathbf{h}_{t;k}^\beta(\boldsymbol{\rho}). \quad (3.96)$$

The same line of argument can be used to obtain an expression for  $\mathbf{E}_t^{\text{inc}}(\boldsymbol{\rho}, z_L)$ .

### 3.8.2 Calculation of the Scattered Field

As an example, we calculate  $\mathbf{H}_t^{\text{scat}}(\boldsymbol{\rho}, z_L)$  for a waveguide section.  $\mathbf{H}_t^{\text{scat}}(\boldsymbol{\rho}, z_L)$  is the result of  $\hat{\mathbf{M}}_1$  which is obtained by solving  $L\mathbf{u} = \mathbf{f}$  for a given incident field, i.e., for a given forcing vector  $\mathbf{f}$ .  $\hat{\mathbf{M}}_1$  can be written in the form of equation 3.30 as

$$\hat{\mathbf{M}}_1(\boldsymbol{\rho}) = \sum_{q=1}^{Q_1} V_q^{(1)} \mathbf{g}_q^{(1)}(\boldsymbol{\rho}). \quad (3.97)$$

The field representation for a transverse magnetic field is given by equation 2.115 and can be written as

$$\mathbf{H}_t^{\text{scat}}(\boldsymbol{\rho}, z_L) = \sum_{j,\alpha} I_j^\alpha(z_L) \mathbf{h}_{t;j}^\alpha(\boldsymbol{\rho}), \quad (3.98)$$

where the Green's function  $I_j^\alpha(z_L)$  is a linear function of the inner product  $\langle \hat{\mathbf{M}}_1 | \mathbf{h}_{t;j}^\alpha \rangle$ . We can rewrite equation 3.98 as

$$\mathbf{H}_t^{\text{scat}}(\boldsymbol{\rho}, z_L) = \sum_{j,\alpha} I_j^\alpha(z_L) \langle \hat{\mathbf{M}}_1 | \mathbf{h}_{t;j}^\alpha \rangle \mathbf{h}_{t;j}^\alpha(\boldsymbol{\rho}), \quad (3.99)$$

where we have extracted  $\langle \hat{\mathbf{M}}_1 | \mathbf{h}_{t;j}^\alpha \rangle$  from the Green's function  $I_j^\alpha(z_L)$ . Furthermore,  $I_j^\alpha(z_L)$  is given by the Green's function for a left half space with source described in appendix B.1. Finally, if we substitute equation 3.97 in 3.99, we arrive at

$$\mathbf{H}_t^{\text{scat}}(\boldsymbol{\rho}, z_L) = \sum_{j,\alpha} I_j^\alpha(z_L) \sum_{q=1}^{Q_1} V_q^{(1)} \langle \mathbf{g}_q^{(1)} | \mathbf{h}_{t;j}^\alpha \rangle \mathbf{h}_{t;j}^\alpha(\boldsymbol{\rho}). \quad (3.100)$$

The same argument can be used to obtain an expression for  $\mathbf{E}_t^{\text{scat}}(\boldsymbol{\rho}, z_L)$ .

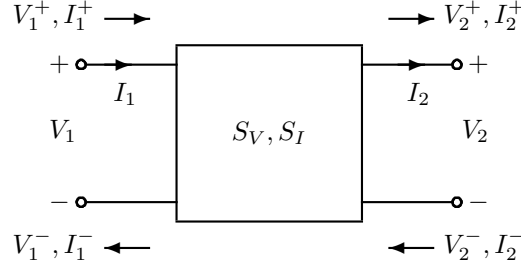


Figure 3.14: Definition of the wave amplitudes for a scattering matrix.

### 3.8.3 Formulation of the Scattering Matrix

We formulate a so-called generalized scattering matrix, which characterizes the electromagnetic behavior for a single basic structure, by expressing the outgoing waves in terms of the incident waves [31, 48].

We consider an arbitrary basic structure with left and right probing interfaces at  $z = z_1$  and  $z = z_2$ , respectively. Since the basic structure is linearly reacting, the relation between the corresponding incident and outgoing voltage/current amplitudes at the probes (also known as the ports) can be written as

$$\begin{pmatrix} V_1^- \\ V_2^+ \end{pmatrix} = S_V \begin{pmatrix} V_1^+ \\ V_2^- \end{pmatrix}, \quad \begin{pmatrix} I_1^- \\ I_2^+ \end{pmatrix} = S_I \begin{pmatrix} I_1^+ \\ I_2^- \end{pmatrix}, \quad (3.101)$$

where

$$S_V = \begin{pmatrix} S_{V,11} & S_{V,12} \\ S_{V,21} & S_{V,22} \end{pmatrix} = \begin{pmatrix} V_1^-/V_1^+ & V_1^-/V_2^- \\ V_2^+/V_1^+ & V_2^+/V_2^- \end{pmatrix}, \quad (3.102)$$

and where

$$S_I = \begin{pmatrix} S_{I,11} & S_{I,12} \\ S_{I,21} & S_{I,22} \end{pmatrix} = \begin{pmatrix} I_1^-/I_1^+ & I_1^-/I_2^- \\ I_2^+/I_1^+ & I_2^+/I_2^- \end{pmatrix}. \quad (3.103)$$

The signs  $\pm$  indicate the direction of propagation.  $\{V_1^+, I_1^+\}$  and  $\{V_1^-, I_1^-\}$  denote the incident and outgoing voltage/current amplitudes at the left probe for a given mode, respectively.  $\{V_2^+, I_2^+\}$  and  $\{V_2^-, I_2^-\}$  denote the outgoing and incident voltage/current amplitude at the right probe for a given mode, respectively. This is schematized in figure 3.14.

$S_V$  and  $S_I$  are known as the generalized scattering matrices referred to voltages and currents, respectively. The term generalized refers to the fact that the incident and outgoing waves at both probes are allowed to be propagating and/or evanescent. Further:

1.  $S_{X,11}$  is the reflection coefficient at the left probe,
2.  $S_{X,12}$  is the transmission coefficient from the right to the left probe,

3.  $S_{X,21}$  is the transmission coefficient from the left to the right probe,
4.  $S_{X,22}$  is the reflection coefficient at the right probe.

$X$  can be either  $V$  or  $I$ . Note that, for example,  $V_1^+ \equiv V_n^+(z_1)$  for the waveguide, whereas  $V_1^+ \equiv V^+(\mathbf{k}_t, z_1)$  for the layered space. With the mode index  $n$  and transverse wavevector  $\mathbf{k}_t$  we are able to select different modes at the probes. Furthermore, we can extend the single-mode probe to a multi-mode probe. In this case, the scalars  $X_n^\pm$  become vectors, and the scalars  $S_{X,mn}$  become matrices.  $X$  can be either  $V$  or  $I$ .

### 3.8.4 Formulation of the Cascading Procedure

We formulate a procedure that cascades two generalized scattering matrices [112, section 6.3] to obtain a new generalized scattering matrix which characterizes the electromagnetic behavior of the combination of the two corresponding basic structures.

The first basic structure has a left and right probing interface<sup>3</sup> at  $z = z_1$  and  $z = z_2$ , respectively. It is characterized by the generalized scattering matrix  $S_X^a$ . The relation between the incident and outgoing waves is given by

$$\begin{pmatrix} X_1^- \\ X_2^+ \end{pmatrix} = S_X^a \begin{pmatrix} X_1^+ \\ X_2^- \end{pmatrix}, \quad \text{where} \quad S_X^a = \begin{pmatrix} S_{X,11}^a & S_{X,12}^a \\ S_{X,21}^a & S_{X,22}^a \end{pmatrix}, \quad (3.104)$$

where  $X$  can be  $V$  or  $I$ . The second basic structure has a left and right probing interface at  $z = z_2$  and  $z = z_3$ , respectively. It is characterized by the generalized scattering matrix  $S_X^b$ . The relation between the incident and outgoing waves is given by

$$\begin{pmatrix} X_2^- \\ X_3^+ \end{pmatrix} = S_X^b \begin{pmatrix} X_2^+ \\ X_3^- \end{pmatrix}, \quad \text{where} \quad S_X^b = \begin{pmatrix} S_{X,11}^b & S_{X,12}^b \\ S_{X,21}^b & S_{X,22}^b \end{pmatrix}. \quad (3.105)$$

If we connect the right probe of the first basic structure with the left probe of the second basic structure, we obtain a new basic structure that has a left and right probing interface at  $z = z_1$  and  $z = z_3$ , respectively. It is characterized by the generalized scattering matrix  $S_X$ . The relation between the incident and outgoing waves is given by

$$\begin{pmatrix} X_1^- \\ X_3^+ \end{pmatrix} = S_X \begin{pmatrix} X_1^+ \\ X_3^- \end{pmatrix}, \quad \text{where} \quad S_X = \begin{pmatrix} S_{X,11} & S_{X,12} \\ S_{X,21} & S_{X,22} \end{pmatrix}. \quad (3.106)$$

The various incident and outgoing wave amplitudes are schematized in figure 3.15. If we want to determine  $S_X$  for a given  $S_X^a$  and  $S_X^b$ , we have to eliminate  $X_2^+$  and  $X_2^-$  from the set of equations given by 3.104 and 3.105, and express

<sup>3</sup>Also called reference planes.

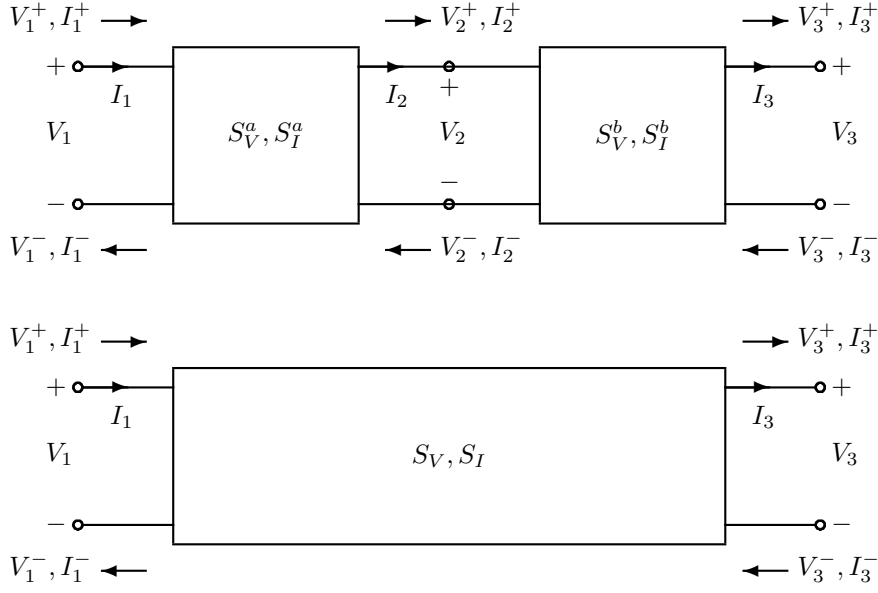


Figure 3.15: Definition of the wave amplitudes for the cascading procedure.

the remaining unknowns in the form of equation 3.106. Doing this leads to

$$S_{X,11} = S_{X,11}^a + S_{X,12}^a R_{X,2} S_{X,11}^b S_{X,21}^a, \quad (3.107)$$

$$S_{X,12} = S_{X,12}^a R_{X,2} S_{X,12}^b, \quad (3.108)$$

$$S_{X,21} = S_{X,21}^b R_{X,1} S_{X,21}^a, \quad (3.109)$$

$$S_{X,22} = S_{X,22}^b + S_{X,21}^b R_{X,1} S_{X,22}^a S_{X,12}^b, \quad (3.110)$$

in which

$$R_{X,1} = (I - S_{X,22}^a S_{X,11}^b)^{-1}, \quad (3.111)$$

$$R_{X,2} = (I - S_{X,11}^b S_{X,22}^a)^{-1}. \quad (3.112)$$

This procedure is known as the Redheffer star product. In short notation we write  $S_X = S_X^a \otimes S_X^b$ .

In the case of single-mode probes<sup>4</sup>, the transmission and reflection coefficients are complex scalars. This implies that  $R_{X,1} = R_{X,2}$ . However, for multi-mode probes (scattering matrices), this is in general not the case. This means that the order of the various products in the Redheffer star product cannot be disregarded.

Finally note that we will perform the Redheffer star product twice<sup>5</sup>: for

<sup>4</sup>In the case of single mode scattering matrices.

<sup>5</sup>Since the separate scattering matrices cannot be made unitary when both propagating and evanescent modes are taken into account at the probes. The unitary property is convenient for defining a consistent definition of energy. We propose a new definition in section 3.9.5.

the generalized scattering matrices referred to both voltages and currents. This means that  $S_V = S_V^a \otimes S_V^b$  and  $S_I = S_I^a \otimes S_I^b$ .

A key concept in selecting the number of modes of interest at each probe between two interacting basic structures is that of accessible and localized modes [90]. This choice determines the overall size of the generalized scattering matrix. A major role in this interaction is played by the fact whether a mode is above or below cutoff at that probe. It is convenient to classify modes as accessible or localized when their attenuation between adjacent basic structures is lower or higher than a specified threshold.

Accessible modes, either propagating or evanescent are responsible for the interaction between two adjacent basic structures. Localized modes however are so attenuated that they do not see the other basic structure and give rise only to energy storage if the structure is lossless. In cascading the various generalized scattering matrices, only the accessible modes at the probing interfaces are involved, whereas the localized modes are disregarded. This amounts to terminating these modes with the corresponding characteristic impedances.

### 3.9 Energy Considerations

In this section we give an interpretation of the field solution based on energy principles. We first derive and then use Poynting's theorem [35, chapter 7] in section 3.9.1, and find an expression for the energy conservation. We then give a physical interpretation of three different parts of this expression, i.e., power flow through the basic structure from the outside, energy storage and loss within the basic structure and power generation by sources inside the basic structure. Then in section 3.9.2 we simplify the expression for the power flow by using the field expansions both for the waveguide and for the layered space.

A reciprocal structure can usually be characterized by a symmetrical generalized scattering matrix. However,  $S_V$  and  $S_I$  are in general not symmetrical. In section 3.9.3 we introduce a normalization of the wave amplitudes, to obtain so-called symmetrical power wave generalized scattering matrices. In section 3.9.4 we rewrite the energy conservation, derived in section 3.9.1, in terms of the generalized scattering matrix for a lossless basic structure. In section 3.9.5 we define a specific energy related quantity that uses a combination of both generalized scattering matrices referred to voltages and currents. This quantity is a direct measure of the amount of complex energy reflected and transmitted by the basic structure, and can also be used when both propagating and evanescent modes are present at both probing interfaces.

#### 3.9.1 Poynting's Theorem in its General Form

Since electric and magnetic field strengths are defined through a force exerted on a point charge moving in vacuum, a logical starting point for energy considerations is the expression for the work done by this force. Thus, the Poynting

vector is found to be the quantity that characterizes the area density of the power flow in the electromagnetic field in vacuum.

In (stationary) matter the exchange of energy between a bounded piece of matter and the vacuum that surrounds it takes place across the boundary surface of the relevant piece of matter. Further on account of the boundary condition 3.9, the normal component of Poynting's vector is continuous across any source-free interface, in particular across the one between vacuum and matter.

Furthermore, a necessary prerequisite for some vectorial quantity to be a candidate for the area density of power flow is the continuity of its normal component across any interface that is free from surface sources. If this condition wasn't satisfied, there would be a net gain/loss of energy in a domain of zero thickness, which would contradict the physical condition that storage of energy requires volume.

The Poynting vector  $\mathcal{S}$ [VAm<sup>-2</sup>] is the area density of electromagnetic power flow and is defined as

$$\mathcal{S}(\mathbf{r}, t) = \mathcal{E}(\mathbf{r}, t) \times \mathcal{H}(\mathbf{r}, t). \quad (3.113)$$

In the frequency-domain (or steady-state) analysis, the time-averaged energy flow  $\langle \mathcal{S} \rangle_T$  is defined as the time average of the Poynting vector

$$\langle \mathcal{S} \rangle_T = \frac{1}{T} \int_{t=t'}^{t=t'+T} \mathcal{E}(\mathbf{r}, t) \times \mathcal{H}(\mathbf{r}, t) dt, \quad (3.114)$$

where  $T = 2\pi/\omega$  denotes the period in time of the fields. Now by using the frequency-domain field representations, i.e., the  $s$ -domain equivalents with  $s = j\omega$ , it follows that

$$\langle \mathcal{S} \rangle_T = \frac{1}{2} \text{Re} (\mathbf{E}(\mathbf{r}, j\omega) \times \mathbf{H}^*(\mathbf{r}, j\omega)). \quad (3.115)$$

To calculate the time-averaged power flow, we start with the  $s$ -domain Maxwell equations 2.41 and 2.42 given by

$$-\nabla \times \mathbf{H} + \eta \mathbf{E} = -\mathbf{J}, \quad (3.116)$$

$$\nabla \times \mathbf{E} + \xi \mathbf{H} = -\mathbf{M}, \quad (3.117)$$

with  $s = j\omega$ ,  $\eta = \sigma + j\omega\varepsilon$  and  $\xi = \alpha + j\omega\mu$ . Then we take the inner product between the complex conjugate of equation 3.116 and  $\mathbf{E}$ , the inner product between equation 3.117 and  $\mathbf{H}^*$ , and add the results. We find

$$\nabla \cdot (\mathbf{E} \times \mathbf{H}^*) + \eta^* \mathbf{E} \cdot \mathbf{E}^* + \xi \mathbf{H} \cdot \mathbf{H}^* = -\mathbf{J}^* \cdot \mathbf{E} - \mathbf{M} \cdot \mathbf{H}^*, \quad (3.118)$$

where we have used the vector identity

$$\nabla \cdot (\mathbf{E} \times \mathbf{H}^*) = -\mathbf{E} \cdot (\nabla \times \mathbf{H}^*) + \mathbf{H}^* \cdot (\nabla \times \mathbf{E}). \quad (3.119)$$

Equation 3.118 is known as the local complex Poynting's theorem. Subsequently, we integrate this equation over an elementary domain  $D$  that is bounded by a

surface  $\partial D$  with outward normal  $\hat{\nu}$ . We obtain

$$\oint_{\partial D} (\mathbf{E} \times \mathbf{H}^*) \cdot \hat{\nu} dA + \int_D (\eta^* \mathbf{E} \cdot \mathbf{E}^* + \xi \mathbf{H} \cdot \mathbf{H}^*) dV = - \int_D (\mathbf{J}^* \cdot \mathbf{E} + \mathbf{M} \cdot \mathbf{H}^*) dV, \quad (3.120)$$

where we have used Gauss' divergence theorem. Equation 3.120 is known as the complex Poynting's theorem in integral form. The conservation of energy flow finally follows from this equation by taking half of its real part in accordance with equation 3.115. This leads to

$$\frac{1}{2} \text{Re} \oint_{\partial D} (\mathbf{E} \times \mathbf{H}^*) \cdot \hat{\nu} dA + \frac{1}{2} \int_D (\sigma \mathbf{E} \cdot \mathbf{E}^* + \alpha \mathbf{H} \cdot \mathbf{H}^*) dV = - \frac{1}{2} \text{Re} \int_D (\mathbf{J}^* \cdot \mathbf{E} + \mathbf{M} \cdot \mathbf{H}^*) dV. \quad (3.121)$$

The different terms within equation 3.121 have the following physical interpretation.

1. The first term on the left-hand side is interpreted as the time-averaged power flow that is transferred from  $D$  across  $\partial D$  into its surroundings.
2. The second term on the left-hand side is interpreted as the time-averaged ohmic loss of power (both electric and magnetic) that is irreversibly dissipated into heat.
3. The first term on the right-hand side is interpreted as the time-averaged power that is generated by the electromagnetic sources within  $D$ .

This interpretation is symbolically schematized in figure 3.16.

### 3.9.2 Power Flow through the Probing Surfaces

Let the volume  $D$  represent an arbitrary basic structure given in figure 3.17. Further, let  $\partial D_L$  and  $\partial D_R$  represent the probing interfaces at the left and right sides of the basic structure at  $z = z_L$  and  $z = z_R$ , respectively. Note that  $\partial D = \partial D_L \cup \partial D_R$ . The time-averaged power flow that is transferred from  $D$  across  $\partial D$  into its surroundings is now given by the flow through these probing interfaces. This means that the first term on the left-hand side of equation 3.121 can be written as

$$\frac{1}{2} \text{Re} \oint_{\partial D} (\mathbf{E} \times \mathbf{H}^*) \cdot \hat{\nu} dA = \frac{1}{2} \text{Re} \int_{\partial D_R} (\mathbf{E}_t \times \mathbf{H}_t^*) \cdot \hat{\mathbf{z}} dA - \frac{1}{2} \text{Re} \int_{\partial D_L} (\mathbf{E}_t \times \mathbf{H}_t^*) \cdot \hat{\mathbf{z}} dA. \quad (3.122)$$

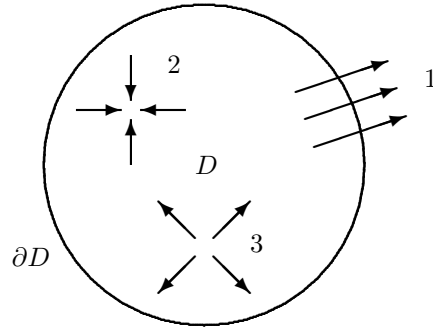


Figure 3.16: Physical interpretation of conservation of energy: 1=power flow that is transferred from  $D$  across  $\partial D$  to its surroundings, 2=ohmic loss of power that is irreversibly dissipated into heat, 3=power that is generated by the electromagnetic sources within  $D$ .

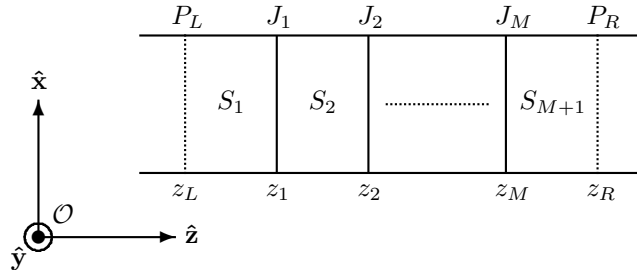


Figure 3.17: An arbitrary basic structure with  $M + 1$  segments  $S_m$  separated by  $M$  junctions  $J_m$  positioned at  $z = z_m$  for a given integer  $M$ , and enclosed between two probes  $P_L$  and  $P_R$  positioned at  $z = z_L$  and  $z = z_R$ , respectively.



First, we consider the first section to be a waveguide. Then, the transverse electromagnetic field can be written as

$$\mathbf{E}_t(\boldsymbol{\rho}, z) = \sum_{m,\alpha} V_m^\alpha(z) \mathbf{e}_{t;m}^\alpha(\boldsymbol{\rho}), \quad (3.123)$$

$$\mathbf{H}_t(\boldsymbol{\rho}, z) = \sum_{m,\alpha} I_m^\alpha(z) \mathbf{h}_{t;m}^\alpha(\boldsymbol{\rho}). \quad (3.124)$$

The time-averaged power flow that is transferred from  $D$  across  $\partial D_L$  can now be expressed as

$$\begin{aligned} -\frac{1}{2} \operatorname{Re} \int_{\partial D_L} (\mathbf{E}_t \times \mathbf{H}_t^*) \cdot \hat{\mathbf{z}} dA &= -\frac{1}{2} \operatorname{Re} \sum_{m,\alpha} \sum_{n,\beta} V_m^\alpha(z_L) I_n^{\beta*}(z_L) \\ &\int_{\partial D_L} (\mathbf{e}_{t;m}^\alpha(\boldsymbol{\rho}) \times \mathbf{h}_{t;n}^{\beta*}(\boldsymbol{\rho})) \cdot \hat{\mathbf{z}} dA. \end{aligned} \quad (3.125)$$

Using the orthonormality relation

$$\int_{\partial D_L} (\mathbf{e}_{t;m}^\alpha(\boldsymbol{\rho}) \times \mathbf{h}_{t;n}^{\beta*}(\boldsymbol{\rho})) \cdot \hat{\mathbf{z}} dA = \delta_{m,n} \delta_{\alpha,\beta}, \quad (3.126)$$

reduces (see section 2.4.2) equation 3.125 to

$$\begin{aligned} -\frac{1}{2} \operatorname{Re} \int_{\partial D_L} (\mathbf{E}_t \times \mathbf{H}_t^*) \cdot \hat{\mathbf{z}} dA &= \\ &-\frac{1}{2} \operatorname{Re} \sum_{m,\alpha} V_m^\alpha(z_L) I_m^{\alpha*}(z_L). \end{aligned} \quad (3.127)$$

Second, we consider the first section to be a layered space. Then, the transverse electromagnetic field can be written as

$$\mathbf{E}_t(\boldsymbol{\rho}, z) = \sum_{\alpha} \int V^\alpha(\mathbf{k}_t, z) \mathbf{e}_t^\alpha(\mathbf{k}_t, \boldsymbol{\rho}) d\mathbf{k}_t, \quad (3.128)$$

$$\mathbf{H}_t(\boldsymbol{\rho}, z) = \sum_{\alpha} \int I^\alpha(\mathbf{k}_t, z) \mathbf{h}_t^\alpha(\mathbf{k}_t, \boldsymbol{\rho}) d\mathbf{k}_t. \quad (3.129)$$

The time-averaged power flow that is transferred from  $D$  across  $\partial D_L$  can now be expressed as

$$\begin{aligned} -\frac{1}{2} \operatorname{Re} \int_{\partial D_L} (\mathbf{E}_t \times \mathbf{H}_t^*) \cdot \hat{\mathbf{z}} dA &= -\frac{1}{2} \operatorname{Re} \sum_{\alpha} \sum_{\beta} \int \int V^\alpha(\mathbf{k}'_t, z_L) I^{\beta*}(\mathbf{k}''_t, z_L) \\ &\int_{\partial D_L} (\mathbf{e}_t^\alpha(\mathbf{k}'_t, \boldsymbol{\rho}) \times \mathbf{h}_t^{\beta*}(\mathbf{k}''_t, \boldsymbol{\rho})) \cdot \hat{\mathbf{z}} dA d\mathbf{k}'_t d\mathbf{k}''_t. \end{aligned} \quad (3.130)$$

Using the following orthonormality relation

$$\int_{\partial D_L} (\mathbf{e}_t^\alpha(\mathbf{k}'_t, \boldsymbol{\rho}) \times \mathbf{h}_t^{\beta*}(\mathbf{k}''_t, \boldsymbol{\rho})) \cdot \hat{\mathbf{z}} dA = \delta(\mathbf{k}'_t - \mathbf{k}''_t) \delta_{\alpha, \beta}, \quad (3.131)$$

reduces (see section 2.4.3) equation 3.130 to

$$\begin{aligned} -\frac{1}{2} \text{Re} \int_{\partial D_L} (\mathbf{E}_t \times \mathbf{H}_t^*) \cdot \hat{\mathbf{z}} dA = \\ -\frac{1}{2} \text{Re} \sum_{\alpha} \int V^\alpha(\mathbf{k}_t, z_L) I^{\alpha*}(\mathbf{k}_t, z_L) d\mathbf{k}_t. \end{aligned} \quad (3.132)$$

We conclude from equations 3.127 and 3.132 that the time-averaged power flow through a probing interface is related to the modal voltages and currents at the probe and has the same form as the one used in circuit theory.

### 3.9.3 Reciprocal Basic Structure

If the basic structure does not contain any non-reciprocal media (such as a plasma or a ferrite with an applied DC magnetic biasing field), then the impedance matrix of this so-called reciprocal basic structure which is described in [31] must be symmetrical. The corresponding scattering matrix can in this case be symmetrical if it relates power waves instead of voltage or current waves.

The two single-mode probing ports in the basic structure have in general different characteristic impedances; thus  $S_V$  and  $S_I$  are in general not symmetrical. By introducing the following normalization of the wave voltage and current amplitudes

$$V_k \leftarrow V_k \sqrt{Y_\infty^{(k)}}, \quad \text{and} \quad I_k \leftarrow I_k \sqrt{Z_\infty^{(k)}},$$

where  $V_k$  and  $I_k$  now represent power waves<sup>6</sup>, we can rewrite the generalized scattering matrices as

$$S_V^N = \begin{pmatrix} \sqrt{Y_\infty^{(1)}} & 0 \\ 0 & \sqrt{Y_\infty^{(2)}} \end{pmatrix} S_V \begin{pmatrix} \sqrt{Z_\infty^{(1)}} & 0 \\ 0 & \sqrt{Z_\infty^{(2)}} \end{pmatrix}, \quad (3.133)$$

and

$$S_I^N = \begin{pmatrix} \sqrt{Z_\infty^{(1)}} & 0 \\ 0 & \sqrt{Z_\infty^{(2)}} \end{pmatrix} S_I \begin{pmatrix} \sqrt{Y_\infty^{(1)}} & 0 \\ 0 & \sqrt{Y_\infty^{(2)}} \end{pmatrix}. \quad (3.134)$$

With this normalization, we obtain symmetrical scattering matrices  $S_V^N$  and  $S_I^N$ . These matrices are known as the power wave generalized scattering matrices (PWGSM) referred to voltages and currents, respectively.

<sup>6</sup>It is customary to use  $a$  and  $b$  for incident and scattered waves, respectively.

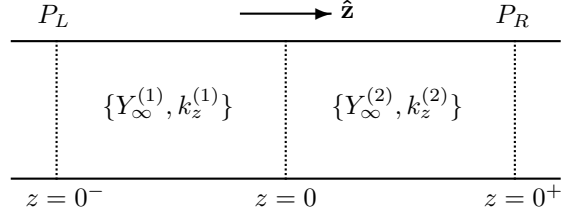


Figure 3.18: Dielectric junction.

To show the asymmetry of the generalized scattering matrices and the symmetry of the power wave generalized scattering matrices, we consider a simple basic structure with a single (empty) junction located at  $z = 0$ . The medium for  $z < 0$  and  $z > 0$  is characterized by  $\{Y_\infty^{(1)}, k_z^{(1)}\}$  and  $\{Y_\infty^{(2)}, k_z^{(2)}\}$ , respectively<sup>7</sup>. We place the left and right probing interfaces at an infinitesimal distance from the junction at  $z = z_1 = 0^-$  and  $z = z_2 = 0^+$ , respectively. This basic structure is known as the dielectric junction, is described in appendix B.1, and is schematized in figure 3.18. The generalized scattering matrix has the following closed-form expression [16, chapter 4]

$$S_V = \frac{1}{Y_\infty^{(1)} + Y_\infty^{(2)}} \begin{pmatrix} Y_\infty^{(1)} - Y_\infty^{(2)} & 2Y_\infty^{(2)} \\ 2Y_\infty^{(1)} & Y_\infty^{(2)} - Y_\infty^{(1)} \end{pmatrix}, \quad (3.135)$$

and

$$S_I = \frac{1}{Y_\infty^{(1)} + Y_\infty^{(2)}} \begin{pmatrix} Y_\infty^{(1)} - Y_\infty^{(2)} & 2Y_\infty^{(1)} \\ 2Y_\infty^{(2)} & Y_\infty^{(2)} - Y_\infty^{(1)} \end{pmatrix}. \quad (3.136)$$

Note the asymmetry in both  $S_V$  and  $S_I$ . If we apply the normalization to the simple basic structure, we find

$$S_V^N = \frac{1}{Y_\infty^{(1)} + Y_\infty^{(2)}} \begin{pmatrix} Y_\infty^{(1)} - Y_\infty^{(2)} & 2\sqrt{Y_\infty^{(1)}Y_\infty^{(2)}} \\ 2\sqrt{Y_\infty^{(1)}Y_\infty^{(2)}} & Y_\infty^{(2)} - Y_\infty^{(1)} \end{pmatrix}, \quad (3.137)$$

and

$$S_I^N = \frac{1}{Y_\infty^{(1)} + Y_\infty^{(2)}} \begin{pmatrix} Y_\infty^{(1)} - Y_\infty^{(2)} & 2\sqrt{Y_\infty^{(1)}Y_\infty^{(2)}} \\ 2\sqrt{Y_\infty^{(1)}Y_\infty^{(2)}} & Y_\infty^{(2)} - Y_\infty^{(1)} \end{pmatrix}. \quad (3.138)$$

Further, note that  $S_V^N = S_I^N$ . This is a very general statement and not only holds for the special case considered in this section. The normalization discussed in this section can be generalized to multi-mode probes.

<sup>7</sup>The structure is a junction between two transmission lines of different characteristic admittance.

### 3.9.4 Lossless Basic Structure

To determine an expression for the conservation of energy for a lossless basic structure, we consider a basic structure for which  $\sigma = \alpha = 0$ . The conservation of energy now follows from equations 3.121 and 3.122, and can be written as

$$-\frac{1}{2}\text{Re} \int_{\partial D_L} (\mathbf{E}_t \times \mathbf{H}_t^*) \cdot \hat{\mathbf{z}} dA + \frac{1}{2}\text{Re} \int_{\partial D_R} (\mathbf{E}_t \times \mathbf{H}_t^*) \cdot \hat{\mathbf{z}} dA = 0, \quad (3.139)$$

where the left and right probing interfaces  $\partial D_L$  and  $\partial D_R$  are located at  $z = z_1$  and  $z = z_2$ , respectively. By using equation 3.127 for a probe in a waveguide, or equation 3.132 for a probe in a layered space, we can rewrite equation 3.139 as

$$-\frac{1}{2}\text{Re}[V_1 I_1^*] + \frac{1}{2}\text{Re}[V_2 I_2^*] = 0. \quad (3.140)$$

The terms on the left-hand side of equation 3.140 can be elaborated by separating the incident waves from the outgoing waves. Doing this leads to

$$\text{Re}[V_1^- I_1^{-*} + V_2^+ I_2^{+*}] = \text{Re}[V_1^+ I_1^{+*} + V_2^- I_2^{-*}], \quad (3.141)$$

which can be rewritten in terms of a row and column vector product as

$$\text{Re} \left[ \begin{pmatrix} V_1^- \\ V_2^+ \end{pmatrix}^T \begin{pmatrix} I_1^- \\ I_2^+ \end{pmatrix}^* \right] = \text{Re} \left[ \begin{pmatrix} V_1^+ \\ V_2^- \end{pmatrix}^T \begin{pmatrix} I_1^+ \\ I_2^- \end{pmatrix}^* \right]. \quad (3.142)$$

The outgoing waves are related to the incident waves through the generalized scattering matrix defined in equation 3.101. Using this leads to

$$\text{Re} \left[ \left( S_V \begin{pmatrix} V_1^+ \\ V_2^- \end{pmatrix} \right)^T \left( S_I \begin{pmatrix} I_1^+ \\ I_2^- \end{pmatrix} \right)^* \right] = \text{Re} \left[ \begin{pmatrix} V_1^+ \\ V_2^- \end{pmatrix}^T \begin{pmatrix} I_1^+ \\ I_2^- \end{pmatrix}^* \right], \quad (3.143)$$

which can be rewritten as

$$\text{Re} \left[ \begin{pmatrix} V_1^+ \\ V_2^- \end{pmatrix}^T S_V^T S_I^* \begin{pmatrix} I_1^+ \\ I_2^- \end{pmatrix}^* \right] = \text{Re} \left[ \begin{pmatrix} V_1^+ \\ V_2^- \end{pmatrix}^T \begin{pmatrix} I_1^+ \\ I_2^- \end{pmatrix}^* \right]. \quad (3.144)$$

This relation must hold for arbitrary  $V_1^+$ ,  $V_2^-$ ,  $I_1^+ = Y_\infty^{(1)} V_1^+$  and  $I_2^- = Y_\infty^{(2)} V_2^-$ . It can be satisfied if

$$\text{Re} (S_V^T S_I^*) = I, \quad (3.145)$$

where the superscript  $T$  denotes the transpose operator, and where  $I$  represents the identity matrix. Equation 3.145 can be rewritten as

$$\text{Re} (S_I^\dagger S_V) = I, \quad (3.146)$$

where the superscript  $\dagger$  denotes the Hermite operation, i.e., transpose and complex conjugate. Note that

$$S_I^\dagger S_V = S_I^{N\dagger} S_V^N, \quad (3.147)$$

which justifies the definition of the power wave generalized scattering matrix. If we calculate  $\text{Re}(S_I^\dagger S_V)$  for the simple basic structure described at the end of section 3.9.3, we find

$$\begin{aligned} \text{Re}(S_I^\dagger S_V) &= \frac{1}{|Y_\infty^{(1)} + Y_\infty^{(2)}|^2} \\ \text{Re} \left( \begin{array}{cc} |Y_\infty^{(1)} - Y_\infty^{(2)}|^2 + 4Y_\infty^{(1)} Y_\infty^{(2)*} & 2(Y_\infty^{(1)*} Y_\infty^{(2)} - Y_\infty^{(1)} Y_\infty^{(2)*}) \\ 2(Y_\infty^{(1)} Y_\infty^{(2)*} - Y_\infty^{(1)*} Y_\infty^{(2)}) & |Y_\infty^{(2)} - Y_\infty^{(1)}|^2 + 4Y_\infty^{(1)*} Y_\infty^{(2)} \end{array} \right), \end{aligned} \quad (3.148)$$

which reduces to

$$\text{Re}(S_I^\dagger S_V) = I, \quad (3.149)$$

since  $\text{Re}(Y_\infty^{(1)*} Y_\infty^{(2)} - Y_\infty^{(1)} Y_\infty^{(2)*}) = 0$ . Finally, it should be remarked that the energy conservation for lossless basic structures discussed in this section can be generalized to multi-mode probes.

### 3.9.5 Direct Measure for Energy

When we consider the multi-mode case where both propagating and evanescent modes are present at both probing interfaces, the corresponding generalized scattering matrices  $S_V$ ,  $S_I$ ,  $S_V^N$  and  $S_I^N$  cannot be used individually as a measure of transmitted or reflected energy [49].

To overcome this problem, we define a specific energy related quantity  $S_{VI}$  as the point-wise multiplication of  $S_V$  and  $S_I^*$ . Subsequently, by using the definition of complex Poynting flux  $P = VI^*/2$ ,  $S_{VI}$  can be written as

$$S_{VI} = \begin{pmatrix} \frac{V_1^- I_1^{-*}}{V_1^+ I_1^{+*}} & \frac{V_1^- I_1^{-*}}{V_2^- I_2^{-*}} \\ \frac{V_2^+ I_2^{+*}}{V_1^+ I_1^{+*}} & \frac{V_2^+ I_2^{+*}}{V_2^- I_2^{-*}} \end{pmatrix} = \begin{pmatrix} P_1^-/P_1^+ & P_1^-/P_2^- \\ P_2^+/P_1^+ & P_2^+/P_2^- \end{pmatrix}. \quad (3.150)$$

The elements of  $S_{VI}$  can be interpreted as a direct measure of reflected (diagonal elements) and transmitted (anti-diagonal elements) complex power related to the incident complex power. Finally, if we calculate  $S_{VI}$  for the simple basic structure described at the end of section 3.9.3, we find

$$S_{VI} = \frac{1}{|Y_\infty^{(1)} + Y_\infty^{(2)}|^2} \begin{pmatrix} |Y_\infty^{(1)} - Y_\infty^{(2)}|^2 & 4Y_\infty^{(1)*} Y_\infty^{(2)} \\ 4Y_\infty^{(1)} Y_\infty^{(2)*} & |Y_\infty^{(2)} - Y_\infty^{(1)}|^2 \end{pmatrix}, \quad (3.151)$$

which reduces to  $S_{VI} = S_V^{N2} = S_I^{N2}$  if we consider propagating modes only at the probes. This means that  $Y_\infty^{(1)}$  and  $Y_\infty^{(2)}$  are real-valued.

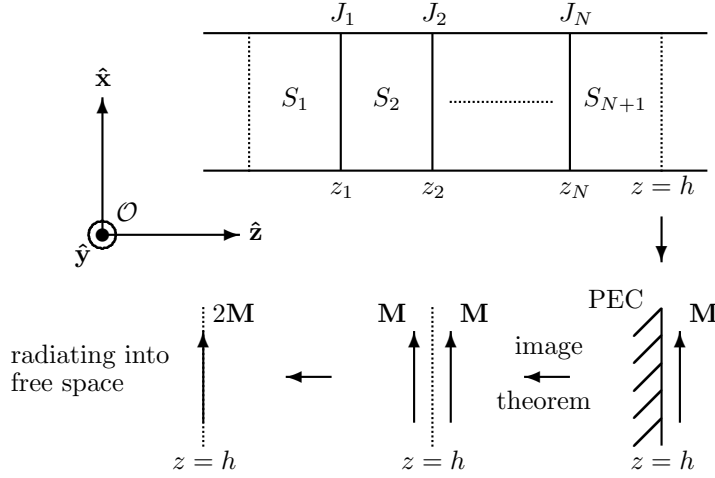


Figure 3.19: The process to obtain an equivalent field configuration for  $z > h$  for an arbitrary basic structure with  $N + 1$  segments  $S_n$  separated by  $N$  junctions  $J_n$  positioned at  $z = z_n$  for a given integer  $N$ .

### 3.10 Calculation of the Far Field

In this section we derive two different expressions for the far field of the radiating part of the basic structure. First we assume that the total electromagnetic field in the basic structure is determined by solving the coupled field integral equation with the method of moments, and that the electric field can be calculated at an interface at  $z = h$  located at a finite distance at the right side of the radiating part of the basic structure. Then we use the field equivalence principle to formulate an equivalent field configuration for  $z > h$  where only a magnetic surface current is replacing the total basic structure, and is radiating an electromagnetic field into free space which is characterized by  $\epsilon_r = 1$ . We assume the basic structure to be lossless, i.e.,  $\sigma = \alpha = 0$ . Further we consider a steady-state analysis, i.e.  $s = j\omega$ . Then we can make the following substitutions  $\gamma = jk$ ,  $\eta = j\omega\epsilon$ ,  $\xi = j\omega\mu$ , and  $k^2 = \omega^2\epsilon\mu$ . We define  $\mathbf{k} = k\hat{\mathbf{r}}$  and  $r = \|\mathbf{r}\|$ . By using the field equivalence principle, the total electric field at an arbitrary transverse interface at  $z = h$  above the radiating part of the basic structure can be expressed in terms of an equivalent magnetic surface current as

$$\mathbf{M}(\mathbf{r}) = 2\delta(z - h)[\mathbf{E}(\boldsymbol{\rho}, h) \times \hat{\mathbf{z}}]. \quad (3.152)$$

The equivalent field configuration is schematized in figure 3.19 and explains that the factor of two comes from the elimination of the PEC plane via the image theorem. In the next two sections we describe two different techniques for defining the far-field region and for evaluating the electromagnetic field in this region.

### 3.10.1 Far Away from a Transverse Plane

The first technique defines the far-field region as the region of observation  $\mathbf{r}$  for which  $h < z \rightarrow \infty$ . The electromagnetic field is then evaluated within this plane by using the field representations 2.167 and 2.168 given by

$$\mathbf{E}_t(\boldsymbol{\rho}, z) = \frac{1}{2} \sum_{\alpha} \int V^{\alpha}(\mathbf{k}_t, z) \mathbf{e}_t^{\alpha}(\mathbf{k}_t, \boldsymbol{\rho}) d\mathbf{k}_t, \quad (3.153)$$

$$\mathbf{H}_t(\boldsymbol{\rho}, z) = \frac{1}{2} \sum_{\alpha} \int I^{\alpha}(\mathbf{k}_t, z) \mathbf{h}_t^{\alpha}(\mathbf{k}_t, \boldsymbol{\rho}) d\mathbf{k}_t. \quad (3.154)$$

Since the magnetic surface current at  $z = h$  is radiating an electromagnetic field into free space characterized by  $\{Y_{\infty}^{\alpha}, k_z\}$ , we can use the solution for the transmission line for a dielectric junction with source described in appendix B.1. This leads to

$$V^{\alpha}(\mathbf{k}_t, z) = - \langle \mathbf{M}_t^{\text{eff}}(\boldsymbol{\rho}) | \mathbf{h}_t^{\alpha}(\mathbf{k}_t, \boldsymbol{\rho}) \rangle \exp(-jk_z[z - h]), \quad (3.155)$$

$$I^{\alpha}(\mathbf{k}_t, z) = - \langle \mathbf{M}_t^{\text{eff}}(\boldsymbol{\rho}) | \mathbf{h}_t^{\alpha}(\mathbf{k}_t, \boldsymbol{\rho}) \rangle Y_{\infty}^{\alpha}(\mathbf{k}_t) \exp(-jk_z[z - h]), \quad (3.156)$$

for  $z > h$ . When we substitute expression 3.152 for the equivalent magnetic surface current in equations 3.155 and 3.156, we obtain

$$V^{\alpha}(\mathbf{k}_t, z) = V^{\alpha}(\mathbf{k}_t, h) \exp(-jk_z[z - h]), \quad (3.157)$$

$$I^{\alpha}(\mathbf{k}_t, z) = V^{\alpha}(\mathbf{k}_t, h) Y_{\infty}^{\alpha}(\mathbf{k}_t) \exp(-jk_z[z - h]), \quad (3.158)$$

where we have used equation 2.199. Combining equations 3.153 and 3.154 with equations 3.157 and 3.158 leads to

$$\mathbf{E}_t(\boldsymbol{\rho}, z) = \sum_{\alpha} \int V^{\alpha}(\mathbf{k}_t, h) \exp(-jk_z[z - h]) \mathbf{e}_t^{\alpha}(\mathbf{k}_t, \boldsymbol{\rho}) d\mathbf{k}_t, \quad (3.159)$$

$$\mathbf{H}_t(\boldsymbol{\rho}, z) = \sum_{\alpha} \int V^{\alpha}(\mathbf{k}_t, h) Y_{\infty}^{\alpha}(\mathbf{k}_t) \exp(-jk_z[z - h]) \mathbf{h}_t^{\alpha}(\mathbf{k}_t, \boldsymbol{\rho}) d\mathbf{k}_t. \quad (3.160)$$

By using these radiated field approximations<sup>8</sup> of  $\mathbf{E}_t$  and  $\mathbf{H}_t$ , we can express the time average energy flow transferred across an arbitrary transverse plane, given by equation 3.132, as

$$\int \langle \mathcal{S} \rangle_T \cdot \hat{\mathbf{z}} dA = \sum_{\alpha} \int |V^{\alpha}(\mathbf{k}_t, h)|^2 \text{Re} \left( Y_{\infty}^{\alpha*}(\mathbf{k}_t) \right) d\mathbf{k}_t. \quad (3.161)$$

From equations 3.159 and 3.160, we conclude that only propagating plane waves are present in the far field. This is due to an exponentially decaying factor  $\exp(-j|k_z|[z - h])$  as  $z \rightarrow \infty$  for evanescent plane waves. This can also be concluded from equation 3.161 since  $\text{Re} \left( Y_{\infty}^{\alpha*}(\mathbf{k}_t) \right)$  is only non-zero for propagating plane waves. This means that in this region evanescent plane waves do not contribute to time-averaged power flow.

<sup>8</sup>This representation holds for any  $z$  value. The limit for large  $z$  can now be computed. This is easily performed by the stationary phase method or the saddle point method. The result is given by equation 3.173.

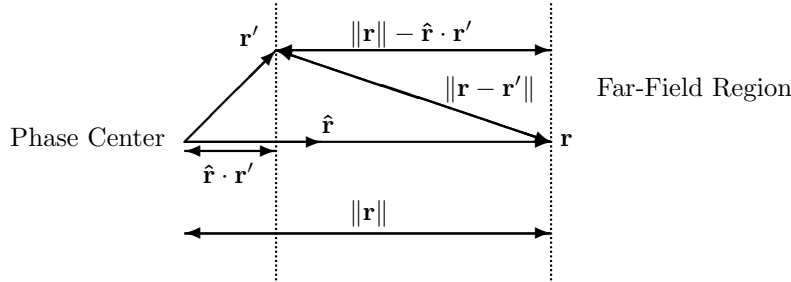


Figure 3.20: Interpretation of the far-field approximation where  $\mathbf{r}$  and  $\mathbf{r}'$  denote the point of observation and location of source distribution, respectively.

### 3.10.2 Far Away from a Finite Volume

The second technique<sup>9</sup> assumes that the source distributions (with spatial dependence  $\mathbf{r}'$ ) are located inside some finite volume. The far-field region is then defined as the region of observation  $\mathbf{r}$  for which  $\|\mathbf{r}\| \rightarrow \infty$ . The electromagnetic field is evaluated within this region by using the field representations described in [35, section 10.7]. It is based on the following two leading order term expansions

$$\|\mathbf{r} - \mathbf{r}'\| = \|\mathbf{r}\| - \hat{\mathbf{r}} \cdot \mathbf{r}' + \text{vanishing terms as } \|\mathbf{r}\| \rightarrow \infty, \quad (3.162)$$

$$\nabla \|\mathbf{r} - \mathbf{r}'\| = \hat{\mathbf{r}} + \text{vanishing terms as } \|\mathbf{r}\| \rightarrow \infty. \quad (3.163)$$

A graphical interpretation of the far-field approximation is given in figure 3.20. The condition for a finite volume of source distributions is in principle not satisfied when we consider the infinite array where we have source distributions of infinite extent in the transverse plane. From a different perspective this means that being infinitely far away from a structure that is infinite in the transverse plane is only possible in the longitudinal direction.

However, we proceed with this technique, since this is what is usually done in the literature. The far-field approximation of  $\mathbf{E}$  and  $\mathbf{H}$  is described in [35, section 10.7], and is given by

$$\{\mathbf{E}, \mathbf{H}\}(\mathbf{r}) \approx \{\mathbf{E}^\infty, \mathbf{H}^\infty\}(\hat{\mathbf{r}})G(\mathbf{r}) \quad \text{as } \|\mathbf{r}\| \rightarrow \infty, \quad (3.164)$$

where  $G(\mathbf{r}) = \frac{\exp(-jkr)}{4\pi r}$  denotes the scalar Green's function and in which

$$\mathbf{E}^\infty = jk\hat{\mathbf{r}} \times \mathbf{F}^\infty, \quad (3.165)$$

$$\mathbf{H}^\infty = -j\omega\epsilon\mathbf{F}^\infty + j\omega\epsilon\hat{\mathbf{r}}(\hat{\mathbf{r}} \cdot \mathbf{F}^\infty), \quad (3.166)$$

and in which

$$\mathbf{F}^\infty(\hat{\mathbf{r}}) = \int_D \mathbf{M}(\mathbf{r}') \exp(jk\hat{\mathbf{r}} \cdot \mathbf{r}') dV', \quad (3.167)$$

<sup>9</sup>This is in principle an artificial distinction. If  $r$  goes to infinity, the two expressions coincide.



where  $dV' \equiv dx'dy'dz'$ . Combining equations 3.164, 3.165, and 3.167 leads to

$$\mathbf{E}(\mathbf{r}) \approx jk \frac{\exp(-jk_r r)}{4\pi r} \hat{\mathbf{r}} \times \int \mathbf{M}(\mathbf{r}') \exp(jk \hat{\mathbf{r}} \cdot \mathbf{r}') dV'. \quad (3.168)$$

When we substitute equation 3.152 for the magnetic surface current in the far-field approximation 3.168, we obtain

$$\mathbf{E}(\mathbf{r}) \approx jk \frac{\exp(-j[kr - k_z h])}{2\pi r} \hat{\mathbf{r}} \times \int \mathbf{E}(\boldsymbol{\rho}', h) \times \hat{\mathbf{z}} \exp(jk \hat{\boldsymbol{\rho}} \cdot \boldsymbol{\rho}') dA', \quad (3.169)$$

where  $\hat{\boldsymbol{\rho}}$  denotes the projection of  $\hat{\mathbf{r}}$  to the  $x, y$ -plane, and where  $dA' \equiv dx'dy'$ . Equation 3.169 can be rewritten as

$$\mathbf{E}(\mathbf{r}) \approx jk \frac{\exp(-j[kr - k_z h])}{r} \hat{\mathbf{r}} \times \left( \frac{1}{2\pi} \int \mathbf{E}(\boldsymbol{\rho}', h) \exp(jk \hat{\boldsymbol{\rho}} \cdot \boldsymbol{\rho}') dA' \right) \times \hat{\mathbf{z}}. \quad (3.170)$$

Using the field representation 2.199 for the layered space mode functions leads to

$$\mathbf{E}(\mathbf{r}) \approx jk \frac{\exp(-j[kr - k_z h])}{r} \hat{\mathbf{r}} \times \mathbf{V}(k \hat{\boldsymbol{\rho}}, h) \times \hat{\mathbf{z}}. \quad (3.171)$$

The modal voltage<sup>10</sup>  $\mathbf{V}$  can be decomposed in terms of TM ( $V'$ ) and TE ( $V''$ ) components as

$$\mathbf{V}(k \hat{\boldsymbol{\rho}}, h) = V'(k \hat{\boldsymbol{\rho}}, h) \hat{\mathbf{k}} + V''(k \hat{\boldsymbol{\rho}}, h) \hat{\boldsymbol{\alpha}}, \quad (3.172)$$

in which  $\hat{\mathbf{k}} = k \hat{\boldsymbol{\rho}} / |k \hat{\boldsymbol{\rho}}|$  and  $\hat{\boldsymbol{\alpha}} = \hat{\mathbf{k}} \times \hat{\mathbf{z}}$ . By using this decomposition for the modal voltage, we can express the far-field approximation<sup>11</sup> of  $\mathbf{E}(\mathbf{r})$  as

$$\mathbf{E}(\mathbf{r}) \approx jk \frac{\exp(-j[kr - k_z h])}{r} \left[ V'(k \hat{\boldsymbol{\rho}}, h) \hat{\boldsymbol{\theta}} - V''(k \hat{\boldsymbol{\rho}}, h) \cos(\theta) \hat{\boldsymbol{\phi}} \right], \quad (3.173)$$

where  $\hat{\mathbf{r}}$ ,  $\hat{\boldsymbol{\theta}}$ , and  $\hat{\boldsymbol{\phi}}$  form a right-handed local coordinate system. In a similar way, we can express the far-field approximation of  $\mathbf{H}(\mathbf{r})$  as

$$\mathbf{H}(\mathbf{r}) \approx j\omega \varepsilon \frac{\exp(-j[kr - k_z h])}{r} \left[ V'(k \hat{\boldsymbol{\rho}}, h) \hat{\boldsymbol{\phi}} + V''(k \hat{\boldsymbol{\rho}}, h) \cos(\theta) \hat{\boldsymbol{\theta}} \right]. \quad (3.174)$$

By using these far-field approximations for  $\mathbf{E}(\mathbf{r})$  and  $\mathbf{H}(\mathbf{r})$ , we can express the time-averaged energy flow, defined by equation 3.115, as

$$\langle \mathcal{S} \rangle_T = \frac{k^2}{2r^2} \text{Re}(Y_\infty) \hat{\mathbf{r}} \left[ |V'(k \hat{\boldsymbol{\rho}}, h)|^2 + |V''(k \hat{\boldsymbol{\rho}}, h)|^2 \cos^2(\theta) \right], \quad (3.175)$$

<sup>10</sup>Note that the dimension of  $V$  is [Vm].

<sup>11</sup>This is the result obtained from equation 3.159 by evaluating the limit for large  $z$  by using the stationary phase method or the saddle point method.

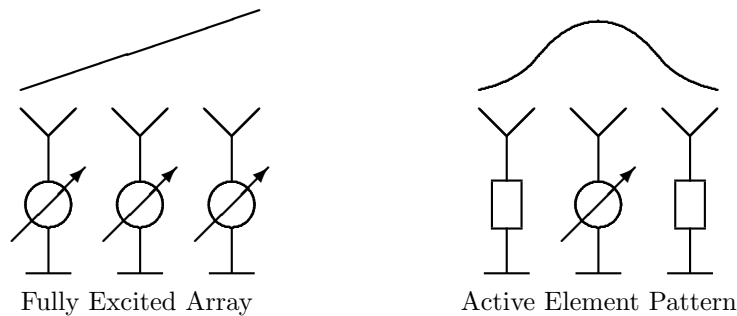


Figure 3.21: Array feeding configurations to obtain the antenna pattern of the fully excited array, and the active element pattern.

where  $Y_\infty = \sqrt{\epsilon/\mu}$  denotes the admittance of free space. To understand the usefulness of this equation let us consider a finite uniform array of identical elements. Ordinary array theory ignores mutual coupling effects between array elements, and expresses the pattern radiated by the array in the well-known pattern multiplication form of an element factor times an array factor. This element factor is identical to the pattern of a single element taken in isolation from the array, and is the same for any element in the array.

Now consider the same array, with the pattern taken with a feed at a single element in the array, and with all other array elements terminated with characteristic loads. The pattern obtained in this case is called the active element pattern of the array. In general this pattern is different from the isolated element pattern because adjacent elements radiate some power due to mutual coupling with the fed element. Also the active element pattern depends on the position of the fed element in the array. For example, edge elements have different active element patterns from elements near the center of the array. If the array is large, however, most of the elements see a uniform neighboring environment, and the active element pattern can be approximated as equal for all elements in the array.

The utility of the active element pattern comes from the fact that, if all the active element factors can be approximated as equal, then the pattern of the fully excited array can be expressed as the product of the active element pattern and the array factor, in an analogous fashion to ordinary array theory. In this case, however, all mutual coupling effects are completely accounted for, including the possibility of scan blindnesses [87]. In fact, the realized gain of the fully excited array at a given scan angle is proportional to the active element pattern gain at this same angle. In addition, the active element pattern at a given angle is also simply related to the magnitude of the active reflection coefficient of the fully excited array scanned at that same angle [86]. The two situations are schematized in figure 3.21

The importance of these results comes from the fact that direct measurement of the scanning characteristics of a large phased array antenna is generally

very expensive, a complete power divider network and a set of phase shifters is required for each element. However direct measurement of an active element pattern is much simpler, involving only a reasonable large portion of the proposed array with characteristic loads on all but one of the elements. Measurements of the active element patterns can thus be used to locate and correct array design problems before a full-scale system is fabricated, which reduces the risk of a costly design failure.

Moreover, comparison of measurement results with infinite-array simulations proves much easier. Equation 3.175 directly gives the radiated power density of the fully excited infinite array steered towards  $\mathbf{k}_t^{\text{inc}}$ . From this analysis, by using the previous mentioned arguments, the active element pattern and the active reflection coefficient are easily obtained. Note that due to the periodicity of the infinite array,  $V'$  and  $V''$  are discrete functions of  $\mathbf{k}_t$ . The contributions consist of a finite number of propagating Floquet modes (plane waves) and an infinite number of evanescent Floquet modes. In the far-field region only the propagating Floquet modes are of interest since the evanescent modes are no longer observed because of their decay. The first propagating Floquet mode at  $\mathbf{k}_t^{\text{inc}}$  represents the broadside plane wave. Higher-order propagating Floquet modes represent so-called grating lobes.

### 3.11 Numerical Implementation

The computational method described in this chapter has been implemented into a matlab computer software package called Luxaflex. The structure of this implementation for each basic structure basically consist of a loop over frequency and angle of incidence and performs the following four functions.

- Assemble the matrix of the linear operator  $L$ .
- Assemble the vector of the forcing vector  $\mathbf{f}$ .
- Solve  $L\mathbf{u} = \mathbf{f}$ .
- Determine the generalized scattering matrices  $S_V$  and  $S_I$ .

In this section we focus on the first two functions and discuss in more detail the numerical computations of the linear operator  $L$  in section 3.11.1, and of the forcing vector  $\mathbf{f}$  calculations in section 3.11.2. Finally, in section 3.11.3 we discuss a simplification to implement a transmission line function for a reversed transmission line.

#### 3.11.1 Implementation of the Matrix Calculation

We have devised a general purpose computational structure to implement equations 3.46, 3.55 and 3.61. This structure supports the idea of linear operator contribution independence, and treats all linear operator contributions to  $L$ , such as for example  $A_{v,r}$ , in the same manner. It does so by requiring the user

to provide a link to the three main ingredients used in the method of moments, i.e.,

1. the inner products (projection matrices) between the expansion and mode functions:  $\langle \mathbf{g}_r | \mathbf{h}_{t;j}^\alpha \rangle$  for the waveguide, and  $\langle \mathbf{g}_r | \mathbf{h}_t^\alpha(\mathbf{k}_t) \rangle$  for the layered space,
2. the link to the specific transmission line function:  $I_j^\alpha(z)$  for the waveguide, and  $I^\alpha(\mathbf{k}_t, z)$  for the layered space,
3. the inner products (projection matrices) between the mode and weighting functions:  $\langle \mathbf{h}_{t;j}^\alpha | \mathbf{g}_v \rangle$  for the waveguide, and  $\langle \mathbf{h}_t^\alpha(\mathbf{k}_t) | \mathbf{g}_v \rangle$  for the layered space.

The computational structure is called the *StampMatrix* function, and has the following interface:

$$\text{function } [L] = \text{StampMatrix}(L, m, n, H, G, F, \text{varargin}).$$

The input parameters are:

1. the matrix  $L$ ,
2. the row and column indices  $m$  and  $n$ , pointing to the specific location of the contribution in  $L$ ,
3. the *NrOfExpansionFunctions* by *NrOfModes* matrix  $F$  with the inner products between the expansion and mode functions,
4. the link  $G$  to the specific transmission line function  $G(i, \dots)$  for a electric-field integral equation (EFIE), and  $G(v, \dots)$  for a magnetic-field integral equation (MFIE),
5. the *NrOfModes* by *NrOfWeightingFunctions* matrix  $H$  with the inner products between the mode and weighting functions,
6. the list of additional parameters *varargin* for the transmission line function. This is a list of variable length, and enables us to select different types of transmission line functions without altering the fundamental behavior of the *StampMatrix* function, i.e., adding matrix contributions such as  $A_{v,r}$  to  $L$ .

The output parameter  $L$  is an updated matrix where the contribution has been added. The computational structure of the *StampMatrix* function<sup>12</sup> is given

<sup>12</sup>Note that a single for-loop is present, which cannot be avoided from a generic code point of view. It therefore reduces the speed of this function.

by

```
function [L] = StampMatrix(L, m, n, H, G, F, varargin)
    for j = 1 : NrOfModes
        L(m, n) = L(m, n) + G(1, varargin{j})[F(:, j)H(j, :)]T;
    endfor;
return.
```

Note that we have used the linearity principle of the transmission line function  $G$  with respect to the sources  $x$ . This obviously means that  $G(x, \dots) = xG(1, \dots)$  and it allows us to write

$$[G(F(:, j), varargin\{j\})H(j, :)]^T = G(1, varargin\{j\})[F(:, j)H(j, :)]^T,$$

which decreases the overall computational time of the *for*-loop within the computational structure of the *StampMatrix* function.

For example, to add the contribution  $A_{v,r}$  to the matrix  $L$  for a given waveguide, we must call the *StampMatrix* function with the following input and output parameters:

$$[L] = \text{StampMatrix}(L, (1 : Q_1), (1 : Q_1), \langle \mathbf{h}_{t;j}^\alpha | \mathbf{g}_v^{(1)} \rangle, \dots, \hat{G}_{I,v}, \langle \mathbf{g}_r^{(1)} | \mathbf{h}_{t;j}^\alpha \rangle, k_{z;j}^\alpha, Y_{\infty;j}^\alpha, z_1^-, z_1^-),$$

where  $Q_1 = \text{NrOfExpansionFunctions} = \text{NrOfWeightingFunctions}$ , and where the computational structure of the transmission line function  $\hat{G}_{I,v}$ , which is the left half space with source described in appendix B.1, is given by

```
function [I] = G_hat_I_v(v, k_z, Y_infinity, a, z)
    I = -vY_infinity exp(jk_z[z - a]);
return.
```

### 3.11.2 Implementation of the Vector Calculation

We have devised a general purpose computational structure to implement equations 3.65, 3.71 and 3.73. This structure supports the idea of forcing vector contribution independence, and treats all forcing vector contributions to  $\mathbf{f}$ , such as for example  $D_v$ , the same. It does so by requiring the user to provide a link to the three main ingredients used in the method of moments, i.e.:

1. the inner products between the incident surface currents and mode functions:  $\langle \mathbf{M}^{\text{inc}} | \mathbf{h}_{t;j}^\alpha \rangle$  for the waveguide, and  $\langle \mathbf{M}^{\text{inc}} | \mathbf{h}_t^\alpha(\mathbf{k}_t) \rangle$  for the layered space,
2. the link to the specific transmission line function:  $I_j^\alpha(z)$  for the waveguide, and  $I^\alpha(\mathbf{k}_t, z)$  for the layered space,

3. the inner products between the mode and weighting functions:  $\langle \mathbf{h}_{t;j}^\alpha | \mathbf{g}_v \rangle$  for the waveguide, and  $\langle \mathbf{h}_t^\alpha(\mathbf{k}_t) | \mathbf{g}_v \rangle$  for the layered space.

The computational structure is called the *StampVector* function, and has the following interface:

$$\text{function } [\mathbf{f}] = \text{StampVector}(\mathbf{f}, m, H, G, F, \text{varargin}).$$

The input parameters are:

1. the vector  $\mathbf{f}$ ,
2. the row index  $m$ , pointing to the specific location of the contribution in  $\mathbf{f}$ ,
3. the 1 by *NrOfModes* matrix  $F$  with the inner products between the incident surface current and mode functions,
4. the link  $G$  to the specific transmission line function  $G(i, \dots)$  for a electric-field integral equation (EFIE), and  $G(v, \dots)$  for a magnetic-field integral equation (MFIE),
5. the *NrOfModes* by *NrOfWeightingFunctions* matrix  $H$  with the inner products between the mode and weighting functions,
6. the list of additional parameters *varargin* for the transmission line function. This is a list of variable length, and enables us to select different types of transmission line functions without altering the fundamental behavior of the *StampVector* function, i.e., adding vector contributions such as  $D_v$  to  $\mathbf{f}$ .

The output parameter  $\mathbf{f}$  is an updated vector where the contribution has been added. The computational structure of the *StampVector* function is given by

$$\begin{aligned} \text{function } [\mathbf{f}] &= \text{StampVector}(\mathbf{f}, m, H, G, F, \text{varargin}) \\ \mathbf{f}(m) &= \mathbf{f}(m) + G(1, \text{varargin})[FH]^T; \\ \text{return.} \end{aligned}$$

Note that we have used the linearity principle of the transmission line function  $G$  with respect to the sources  $x$ . This means that  $G(x, \dots) = xG(1, \dots)$  and it allows us to write

$$[G(F, \text{varargin})H]^T = G(1, \text{varargin})[FH]^T.$$

For example, to add the contribution  $D_v$  to the vector  $\mathbf{f}$  for a given waveguide, we must call the *StampVector* function with the following input and output parameters:

$$\begin{aligned} [\mathbf{f}] &= \text{StampVector}(\mathbf{f}, (1 : Q_1), \langle \mathbf{h}_{t;j}^\alpha | \mathbf{g}_v^{(1)} \rangle, \dots \\ &\quad \hat{G}_{I,v}, - \langle \hat{\mathbf{M}}^{\text{inc}} | \mathbf{h}_{t;j}^\alpha \rangle, k_{z;j}^\alpha, Y_{\infty;j}^\alpha, k_{z;j}^\alpha, Y_{\infty;j}^\alpha, z_L, z_1^-, z_1^-), \end{aligned}$$

where  $Q_1 = NrOfWeightingFunctions$ , where  $z = z_L < z_1^-$  denotes the location of the incident surface current, and where the interface of the transmission line function  $\hat{G}_{I,v}$ , which is the half space with offset source described in appendix B.5, is given by

$$function [I] = \hat{G}_{I,v}(v, k_z^{(1)}, Y_\infty^{(1)}, k_z^{(2)}, Y_\infty^{(2)}, a, b, z).$$

Finally, it is convenient to choose for  $\hat{\mathbf{M}}^{\text{inc}}$  and  $\tilde{\mathbf{M}}^{\text{inc}}$  either waveguide modes or plane waves. For example, if we choose for  $\tilde{\mathbf{M}}^{\text{inc}}$  the waveguide mode  $\mathbf{h}_{t;k}^\beta$ , then  $\langle \hat{\mathbf{M}}^{\text{inc}} | \mathbf{h}_{t;j}^\alpha \rangle$  reduces to  $\delta_{k,j} \delta_{\alpha,\beta}$ .

### 3.11.3 Reversed Transmission Line

Let us consider the transmission line function  $\hat{G}$  for a given transmission line such as for example the left half space with source described in appendix B.1. Suppose it has the following computational structure<sup>13</sup>

$$\begin{aligned} function [V, I] &= \hat{G}(v, i, k_z, Y_\infty, a, z) \\ V &= v \exp(jk_z[z - a]); \\ I &= -vY_\infty \exp(jk_z[z - a]); \\ &return. \end{aligned}$$

The use of the coupled field integral techniques described in the previous sections requires the availability of a transmission line function  $\tilde{G}$  for the corresponding reversed transmission line. The first way to obtain  $\tilde{G}$  is to solve the modal transmission line equations for the reversed structure. However, considerable effort can be saved by using the following substitutions

$$\begin{cases} z \rightarrow -z, \\ v \rightarrow -v, \\ i \rightarrow i, \\ V \rightarrow V, \\ I \rightarrow -I, \end{cases} \quad (3.176)$$

to obtain  $\tilde{G}$ . The idea is based on the identification of the various voltages  $V$ , currents  $I$ , voltage generators  $v$  and current generators  $i$  in the reversed transmission line. This is schematized in figure 3.22, and leads to the following computational structure for  $\tilde{G}$

$$\begin{aligned} function [V, I] &= \tilde{G}(v, i, k_z, Y_\infty, a, z) \\ [V, I] &= \tilde{G}(-v, i, k_z, Y_\infty, -a, -z); \\ I &= -I; \\ &return. \end{aligned}$$

<sup>13</sup>It is also possible to use a local reference plane for which  $a = 0$ .

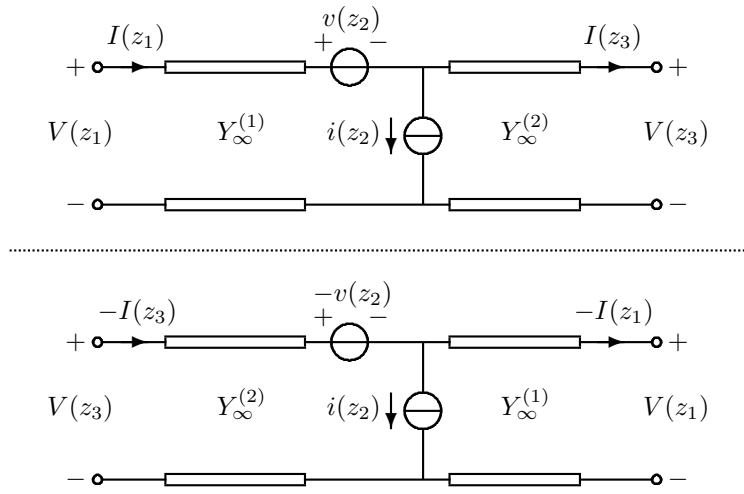


Figure 3.22: Reversing a transmission line in the longitudinal direction.

Note that we can use these substitutions for any available transmission line function to obtain the corresponding transmission line function for the reversed transmission line.





## Chapter 4

# Acceleration Technique

*"Why does this applied science, which saves work and makes life easier, bring us so little happiness? The simple answer runs: Because we have not yet learned to make sensible use of it."* Albert Einstein (1879-1955)

In chapter 3 we have described in full detail the computation of the electromagnetic field within the unit-cell structure. This method is based on the method of moments, and reduces a field integral equation to a matrix equation of the type  $L\mathbf{u} = \mathbf{f}$ .  $L$  and  $\mathbf{f}$  represent the linear operator (a square matrix) and forcing vector of the basic structure under consideration, respectively.  $\mathbf{u}$  represents the unknown that has to be solved.

In this chapter we formulate a new acceleration technique<sup>1</sup> that drastically reduces the computation time needed to calculate the unknown electromagnetic field within the unit-cell structure.

To minimize confusion we define a *series* as an infinite ordered set of *terms* combined together by the addition operator. The term *infinite series* is sometimes used to emphasize the fact that the *series* contains an infinite number of *terms*. A *series* may *converge* to a definite value, or may not, in which case it is called *divergent*. If the *sequence* of *partial sums* converges to a definite value, the *series* is said to *converge*.

The new acceleration technique reduces the assembly time of the linear operator  $L$ , which forms the slowest part in the total computation. To do so, we first show by example in section 4.1, that each element of  $L$  (such as  $A_{v,r}$ ) is a sum of contributions, each of which can be written as a series in the following general form

$$A_{v,r} = \sum_{j,\alpha} g^{(\alpha)}(k_{t;j}) \hat{\gamma}_{v,r}^{(\alpha)}(\mathbf{k}_{t;j}),$$

---

<sup>1</sup>A special word of thanks goes to dr.ir. S.W. Rienstra. He devised in [89] the acceleration procedure as outlined in sections 4.3 and 4.4.1. The implementation and the generalizations outlined in sections 4.3.3, 4.4.2 and following were contributed by the author.

where  $g^{(\alpha)}$  contains the Green's function, and where  $\hat{\gamma}_{v,r}^{(\alpha)}$  contains a combination of the expansion and weighting functions. In order to assemble the complete linear operator  $L$ , these general series have to be evaluated numerically for each contribution.

In section 4.2 we show that these series tend to be asymptotically slowly converging, i.e.,

$$g^{(\alpha)}(k_t) \approx c_1^{(\alpha)} k_t^{-1} + c_2^{(\alpha)} k_t^{-3} + \dots \quad \text{for large } k_t.$$

The new acceleration technique reduces the time needed to evaluate these series and consists of the following three steps.

1. A so-called Kummer transformation [2, section 3.6.26], where the asymptotically slowly converging part of the general series is subtracted (resulting in a fast converging reduced series)

$$A_{v,r} = \sum_j \left[ g^{(\alpha)}(k_{t;j}) - c_1^{(\alpha)} k_{t;j}^{-1} - c_2^{(\alpha)} k_{t;j}^{-3} \right] \hat{\gamma}_{v,r}^{(\alpha)}(\mathbf{k}_{t;j}) + \zeta_{v,r}^{(\alpha)},$$

and added (resulting in a slowly converging correction series)

$$\zeta_{v,r}^{(\alpha)} = \sum_j (c_1^{(\alpha)} k_{t;j}^{-1} + c_2^{(\alpha)} k_{t;j}^{-3}) \hat{\gamma}_{v,r}^{(\alpha)}(\mathbf{k}_{t;j}).$$

This step is described in detail in section 4.2.

2. A so-called Ewald transformation [85, 40], where the asymptotically slowly converging correction series is converted into an integration over  $\tau$  of exponentially fast decaying functions as

$$\zeta_{v,r}^{(\alpha)} = \frac{2\lambda}{\sqrt{\pi}} \int_0^\infty \tau^{\lambda-1} \sum_j (c_1^{(\alpha)} + 2\tau^{2\lambda} c_2^{(\alpha)}) \exp(-k_{t;j}^2 \tau^{2\lambda}) \hat{\gamma}_{v,r}^{(\alpha)}(\mathbf{k}_{t;j}) d\tau.$$

These functions contain an exponentially fast converging series for which the leading-order term is given by  $\exp(-k_t^2 \tau^{2\lambda})$ . This step is described in detail in section 4.3.1.

3. The integration over  $\tau$  is broken up into one for small  $\tau$ , i.e., over the interval  $(0, \tau_1)$ , and one for large  $\tau$ , i.e., over  $(\tau_1, \infty)$ . Then we apply a so-called Poisson transformation step [89, section 6.1] for the integration over small  $\tau$ , where the relatively slow convergence of the series within the exponentially fast decaying function, caused by the behavior of  $\exp(-k_t^2 \tau^{2\lambda})$  for small  $\tau$ , is converted into an exponentially fast converging series. Formally we write

$$\begin{aligned} \zeta_{v,r}^{(\alpha)} &= \frac{2\lambda}{\sqrt{\pi}} \int_{\tau_1}^\infty \tau^{\lambda-1} \sum_j (c_1^{(\alpha)} + 2\tau^{2\lambda} c_2^{(\alpha)}) \exp(-k_{t;j}^2 \tau^{2\lambda}) \hat{\gamma}_{v,r}^{(\alpha)}(\mathbf{k}_{t;j}) d\tau + \\ &|D| \frac{2\lambda}{\sqrt{\pi}} \int_0^{\tau_1} \tau^{\lambda-1} \sum_j (c_1^{(\alpha)} + 2\tau^{2\lambda} c_2^{(\alpha)}) \exp(-j\boldsymbol{\rho}_j \cdot \mathbf{k}_t^{\text{inc}}) \bar{\gamma}_{v,r}^{(\alpha)}(\boldsymbol{\rho}_j, \tau) d\tau. \end{aligned}$$

This is described in detail in section 4.3.2. The leading-order term for the integration over small  $\tau$  is given by  $\exp(-\rho^2/(4\tau^{2\lambda}))$ . The so-called transition point  $\tau_1$  is a compromise between the convergence behavior of the leading-order terms  $\exp(-k_t^2\tau^{2\lambda})$  and  $\exp(-\rho^2/(4\tau^{2\lambda}))$ . This is described in detail in section 4.3.3.

The Poisson transformation step results in the evaluation of  $\bar{\gamma}_{v,r}^{(\alpha)}(\boldsymbol{\rho}, \tau)$ , which is a so-called exponential regularization [53] of  $\hat{\gamma}_{v,r}^{(\alpha)}(\mathbf{k}_t)$ , formally written as

$$\bar{\gamma}_{v,r}^{(\alpha)}(\boldsymbol{\rho}, \tau) = \mathcal{F}^{-1} \left\{ \exp(-k_t^2\tau^{2\lambda}) \hat{\gamma}_{v,r}^{(\alpha)}(\mathbf{k}_t) \right\}.$$

The overall success of this acceleration technique critically depends on the possibility of being able to quickly evaluate  $\bar{\gamma}_{v,r}^{(\alpha)}(\boldsymbol{\rho}, \tau)$ . In section 4.4 we evaluate the exponential regularized functions both for the rooftop and RWG functions.

Finally, in section 4.5 we quantify, compare and discuss the speed improvement of the acceleration technique for the rooftop and RWG expansion functions.

## 4.1 General Series

In this section we show by example that each element of the linear operator  $L$  is a sum of contributions, each of which can be written as a series in a general form. Formally, we write for any contribution  $A_{v,r}$  to  $L$  the following general form

$$A_{v,r} = \sum_{j,\alpha} h^\alpha(k_{t;j}) \hat{\beta}_{v,r}^\alpha(\mathbf{k}_{t;j}). \quad (4.1)$$

The term  $h^\alpha(k_{t;j})$  is dependent on the polarization  $\alpha$  and the mode index  $k_{t;j}$  and, as will be shown later, contains a part of the transmission line function. The term  $\hat{\beta}_{v,r}^\alpha$  is dependent on the polarization  $\alpha$ , the mode index  $k_{t;j}$ , and the indices  $\{v, r\}$  for the expansion and weighting functions. This part, as will be shown later, contains a combination of the inner products of the expansion and weighting functions with the mode functions of the medium.

From now on, we only consider layered space contributions. Waveguide contributions are not considered. This means that we can write the transverse wavevector  $\mathbf{k}_{t;j}$  as

$$\mathbf{k}_{t;j} = R\mathbf{m}_j + \mathbf{k}_t^{\text{inc}}, \quad D^T R = 2\pi I, \quad \mathbf{m}_j = \begin{pmatrix} m_{1,j} \\ m_{2,j} \end{pmatrix}. \quad (4.2)$$

The columns of  $D$  are the basis vectors  $\mathbf{d}_1$  and  $\mathbf{d}_2$  that define the dimensions and periodic arrangement of the unit cells. The matrix  $R$  represents the corresponding reciprocal transverse wavevector lattice. Both indices  $m_{1,j}$  and  $m_{2,j}$  are integers.

Let us for example reconsider the contribution  $A_{v,r} = \langle \hat{\mathbf{H}}_{t,1}(\mathbf{g}_r^{(1)}, \boldsymbol{\rho}) | \mathbf{g}_v^{(1)} \rangle$  to  $L$  (see section 3.5). This represents the self interaction of the magnetic field

strength at the left side of the first interface due to a magnetic surface current at the left side of the first interface.  $A_{v,r}$  can be written as

$$\begin{aligned} A_{v,r} &= \langle \hat{\mathbf{H}}_{t,1}(\mathbf{g}_r, \boldsymbol{\rho}) | \mathbf{g}_v \rangle \\ &= \sum_{j,\alpha} I^\alpha(k_{t,j}, z_1^-) \langle \mathbf{h}_t^\alpha(\mathbf{k}_{t,j}) | \mathbf{g}_v \rangle, \end{aligned} \quad (4.3)$$

in which

$$I^\alpha(k_t, z_1^-) = -Y_\infty^\alpha(k_t) \langle \mathbf{g}_r | \mathbf{h}_t^\alpha(\mathbf{k}_t) \rangle. \quad (4.4)$$

Note that we have used the transmission line function for a left half space with source described in appendix B.1. The general form, i.e., equation 4.1, can be recognized<sup>2</sup> if we take for  $h^\alpha(k_t) = -Y_\infty^\alpha(k_t)$ , and for  $\hat{\beta}_{v,r}^\alpha(\mathbf{k}_t) = \langle \mathbf{g}_r | \mathbf{h}_t^\alpha(\mathbf{k}_t) \rangle \langle \mathbf{h}_t^\alpha(\mathbf{k}_t) | \mathbf{g}_v \rangle$ . Furthermore, if we substitute the layered space mode functions for  $\mathbf{h}_t^\alpha(\mathbf{k}_t)$ , i.e., equations 2.175 and 2.181, we can write  $\hat{\beta}_{v,r}^\alpha(\mathbf{k}_t)$  as

$$\hat{\beta}_{v,r}^\alpha(\mathbf{k}_t) = \begin{cases} \left[ \mathbf{j}\hat{\mathbf{k}} \cdot \hat{\mathbf{g}}_r^*(\mathbf{k}_t) \right] \left[ \mathbf{j}\hat{\mathbf{k}} \cdot \hat{\mathbf{g}}_v(\mathbf{k}_t) \right] + \hat{\mathbf{g}}_r^*(\mathbf{k}_t) \cdot \hat{\mathbf{g}}_v(\mathbf{k}_t) & \text{if } \alpha = \text{TM}, \\ - \left[ \mathbf{j}\hat{\mathbf{k}} \cdot \hat{\mathbf{g}}_r^*(\mathbf{k}_t) \right] \left[ \mathbf{j}\hat{\mathbf{k}} \cdot \hat{\mathbf{g}}_v(\mathbf{k}_t) \right] & \text{if } \alpha = \text{TE}. \end{cases} \quad (4.5)$$

$\hat{\mathbf{k}} = \mathbf{k}_t/k_t$  denotes the unit-length vector in the direction of the transverse wavevector.

As a typical example that we use throughout this chapter, we consider a simple basic structure with a single junction  $J_1$  in between two layered space segments  $S_1$  and  $S_2$ . A graphical representation of this simple basic structure is given in figure 4.1. The dimensions and periodic arrangement of the unit cells is defined by two basis vectors  $\mathbf{d}_1 = 15.8\hat{\mathbf{x}}[\text{mm}]$  and  $\mathbf{d}_2 = 15.8\hat{\mathbf{y}}[\text{mm}]$ . These dimensions correspond to a half wavelength of the excitation. The junction is filled with perfectly electric conducting material. A rectangular hole is made within the unit cell with dimensions: 12.5[mm] length and 1.975[mm] height. The rectangular hole is centered and rotated around the center of the unit cell by 45[deg] with respect to the  $x$ -axis. The hole is meshed in two different ways: with a rectangular and with a triangular mesh. A graphical representation of these two meshes is given in figure 4.1. We define rooftop and RWG functions on the rectangular and triangular mesh, respectively.

The two layered space segments  $S_1$  and  $S_2$  contain vacuum. Two probing interfaces  $P_1$  and  $P_2$  are placed in the vacuum segments  $S_1$  and  $S_2$  at a distance of 1[mm] to the left and 1 [mm] to the right side from the junction interface  $J_1$ , respectively. At both these probing interfaces, only the incident, transmitted and reflected fundamental TM and TE Floquet modes, i.e.,  $\mathbf{m}_j = \mathbf{0}$  are considered since these modes are the only propagating ones.

We characterize the junction interface  $J_1$  as a type II equivalent configuration (see section 3.3). This implies that the unknown magnetic surface currents are

<sup>2</sup>Note that  $h^\alpha$  must not be confused with the magnetic field eigenfunction  $\mathbf{h}_t^\alpha$ .

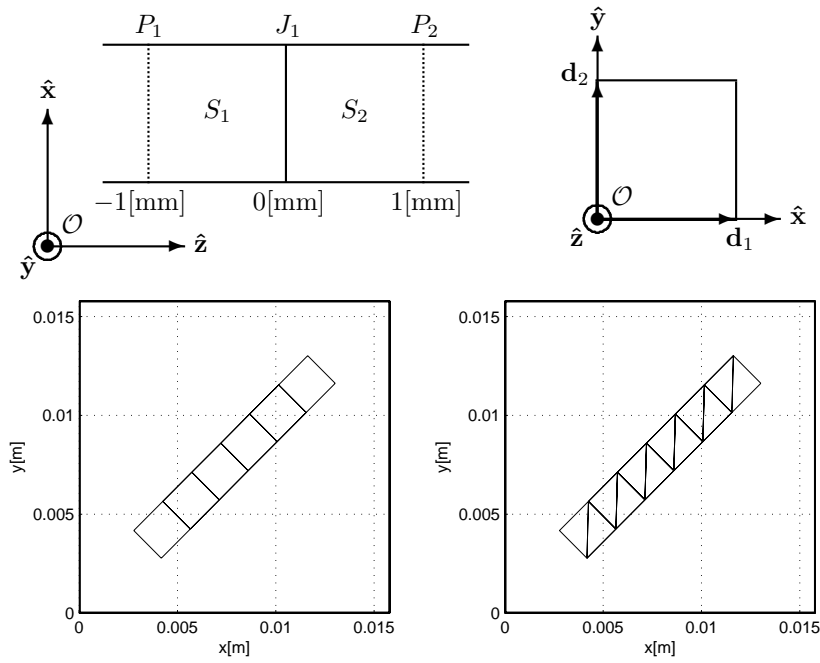


Figure 4.1: A simple basic structure with two segments  $S_m$  separated by a junction  $J_1$  positioned at  $z = 0$  [mm], and enclosed with two probes  $P_1$  and  $P_2$  positioned at  $z = -1$  [mm] and  $z = 1$  [mm], respectively. The unit cell is defined by two basis vectors  $\mathbf{d}_1 = 15.8\hat{x}$  [mm] and  $\mathbf{d}_2 = 15.8\hat{y}$  [mm]. Bottom left figure rectangular mesh and bottom right figure triangular mesh.

solved by means of a magnetic-field integral equation (see section 3.4). Further, the linear operator  $L$  now has two self-interaction contributions  $A_{v,r}$  and  $B_{v,r}$  (see section 3.5).  $A_{v,r} = \langle \hat{\mathbf{H}}_{t,1}(\mathbf{g}_r^{(1)}, \boldsymbol{\rho}) | \mathbf{g}_v^{(1)} \rangle$  represents the self interaction of the magnetic field strength on the left-hand side of interface  $J_1$  due to a magnetic surface current on the left side of this interface.  $B_{v,r} = \langle \tilde{\mathbf{H}}_{t,1}(\mathbf{g}_r^{(1)}, \boldsymbol{\rho}) | \mathbf{g}_v^{(1)} \rangle$  represents the self-interaction of the magnetic field strength on the right-hand side of interface  $J_1$  due to a magnetic surface current on the right side of this interface<sup>3</sup>. We assume a periodical extension of the magnetic surface currents with a staircase phase behavior in between unit cells. Both integer indices  $m_{1,j}$  and  $m_{2,j}$  range independently from  $-30$  to  $30$  for both contributions  $A_{v,r}$  and  $B_{v,r}$ .

The incident plane wave is characterized by fixing the angle of incidence at  $\theta = 5[\text{deg}]$ ,  $\phi = 0[\text{deg}]$ . Further, the frequency is varied from  $8[\text{GHz}]$  to  $16[\text{GHz}]$  in steps of  $200[\text{MHz}]$ . We calculate the reflection coefficient for the two co- and cross-polarization components as a function of the frequency.

## 4.2 Subtraction of Asymptotic Series

In order to assemble the complete linear operator  $L$ , we have to evaluate these general series, equation 4.1, numerically. In this section we show that the series is asymptotically slowly converging. To circumvent this problem, we describe a so-called Kummer transformation [2, section 3.6.26], where the asymptotically slowly converging part of the general series is subtracted (resulting in a fast converging reduced series) and added (resulting in a slowly converging correction series).

Note that, given  $\mathbf{d}_1 = 15.8\hat{\mathbf{x}}[\text{mm}]$  and  $\mathbf{d}_2 = 15.8\hat{\mathbf{y}}[\text{mm}]$ , we have  $\mathbf{k}_1 = (2\pi/15.8)\hat{\mathbf{x}}[\text{mm}^{-1}]$  and  $\mathbf{k}_2 = (2\pi/15.8)\hat{\mathbf{y}}[\text{mm}^{-1}]$ . We can sort the norm of the transverse wavevector  $k_{t,j} = \|\mathbf{k}_t^{inc} + m_{1,j}\mathbf{k}_1 + m_{2,j}\mathbf{k}_2\|$  in such a way that it increases for increasing integer index  $j$ . This means that, for each  $j$ , we have a pair of integers  $(m_{1,j}, m_{2,j})$ . Furthermore, we can compare the sorted norm with the expected relation  $k_{t,j} \sim \sqrt{j}$ . Both actual sorted and expected norms are plotted in figure 4.2 and show a good match. Note the correct slope of  $1/2$ . The rate of convergence is governed by the behavior of  $h^\alpha(k_t)$  for large  $k_t$ . Since  $h^\alpha(k_t) = -Y_\infty^\alpha(k_t)$  for the contribution  $A_{v,r}$  to  $L$  (note that we have used the transmission line function for a left half space with source described in appendix B.1), we can write for an asymptotic expansion for  $h^\alpha(k_t)$  for large  $k_t$

$$h^\alpha(k_t) \approx \tilde{h}^\alpha(k_t) = \begin{cases} c'_1 k_t^{-1} + c'_2 k_t^{-3} + c'_3 k_t^{-5} + \dots & \text{if } \alpha = \text{TM}, \\ c''_1 k_t + c''_2 k_t^{-1} + c''_3 k_t^{-3} + \dots & \text{if } \alpha = \text{TE}, \end{cases} \quad (4.6)$$

<sup>3</sup>Note that  $A_{v,r} = B_{v,r}$  if the two segments  $S_1$  and  $S_2$  are equal.

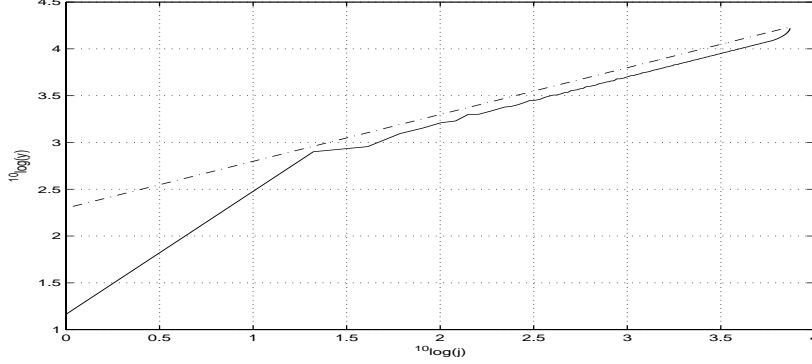


Figure 4.2:  $y = k_{t;j}$  (solid curve) and  $y = \sqrt{j}$  (dashed-dotted curve) as a function of  $j$ .

where

$$c'_1 = -jk_0 \sqrt{\frac{\varepsilon}{\mu}}, \quad c'_2 = -\frac{1}{2}jk_0^3 \sqrt{\frac{\varepsilon}{\mu}}, \quad c'_3 = -\frac{3}{8}jk_0^5 \sqrt{\frac{\varepsilon}{\mu}}, \quad (4.7)$$

$$c''_1 = -\frac{1}{jk_0} \sqrt{\frac{\varepsilon}{\mu}}, \quad c''_2 = -\frac{1}{2}jk_0 \sqrt{\frac{\varepsilon}{\mu}}, \quad c''_3 = -\frac{1}{8}jk_0^3 \sqrt{\frac{\varepsilon}{\mu}}. \quad (4.8)$$

Note that we have used

$$\begin{aligned} k_z &= \sqrt{k^2 - k_t^2} = -j\sqrt{k_t^2 - k^2} = -jk_t \sqrt{1 - \left(\frac{k}{k_t}\right)^2} \\ &\approx -jk_t \left[ 1 - \frac{1}{2} \left(\frac{k}{k_t}\right)^2 - \frac{1}{8} \left(\frac{k}{k_t}\right)^4 - \frac{1}{16} \left(\frac{k}{k_t}\right)^6 - \dots \right] \quad \text{for large } k_t, \end{aligned} \quad (4.9)$$

where the branch [61, section 6.1] of the logarithmic function  $\log(z)$  (used to calculate the square root) was chosen at  $\arg(z) = 0$  ( $-2\pi < \arg(z) \leq 0$ ). Doing this satisfies equation 2.81. Note that the asymptotic expansion of  $k_z$  for large  $k_t$  only contains odd powers of  $1/k_t$ . Similar asymptotic expansions can easily be derived in the case of other types of contributions to  $L$ .

In figure 4.3 we have plotted the convergence behavior of  $h^\alpha(k_{t;j})$ , the two-term asymptotic expansion  $\tilde{h}^\alpha(k_{t;j})$  and the remainder  $h^\alpha(k_{t;j}) - \tilde{h}^\alpha(k_{t;j})$  as a function of  $j$  at frequency = 8[GHz] for the contribution  $A_{v,r}$  to  $L$  on a logarithmic scale. The configuration under consideration is the simple basis structure described in section 4.1. The slopes in this figure are as expected:  $-1/2$  for  $h'$  and  $\tilde{h}'$ ,  $-5/2$  for  $h' - \tilde{h}'$ ,  $1/2$  for  $h''$  and  $\tilde{h}''$ ,  $-3/2$  for  $h'' - \tilde{h}''$ . Note that we have taken into account  $k_{t;j} \sim \sqrt{j}$ .

However, we have an asymmetry in leading order terms between the two polarizations for  $h^\alpha(k_t)$ . To compensate for this asymmetry, we rewrite the general series, equation 4.1, in the following form

$$A_{v,r} = \sum_{j,\alpha} g^{(\alpha)}(k_{t;j}) \hat{\gamma}_{v,r}^{(\alpha)}(\mathbf{k}_{t;j}), \quad (4.10)$$



in which

$$g^{(\alpha)}(k_t) = \begin{cases} k_t^{-2} [h'(k_t) - h''(k_t)] & \text{if } \alpha = 1, \\ h'(k_t) & \text{if } \alpha = 2, \end{cases} \quad (4.11)$$

and in which

$$\hat{\gamma}_{v,r}^{(\alpha)}(\mathbf{k}_t) = \begin{cases} -k_t^2 \hat{\beta}_{v,r}''(\mathbf{k}_t) & \text{if } \alpha = 1, \\ \hat{\beta}_{v,r}'(\mathbf{k}_t) + \hat{\beta}_{v,r}''(\mathbf{k}_t) & \text{if } \alpha = 2. \end{cases} \quad (4.12)$$

Note herein the difference in notation between the superscripts  $\alpha$  and  $(\alpha)$  in equations 4.1 and 4.10, respectively. The superscript  $(\alpha)$  with parenthesis runs over the values  $\{1, 2\}$ , whereas the superscript  $\alpha$  without the parenthesis runs over the type of polarization (TM and TE). By using equation 4.5, we can rewrite equation 4.12 explicitly as

$$\hat{\gamma}_{v,r}^{(\alpha)}(\mathbf{k}_t) = \begin{cases} [\mathbf{j}\mathbf{k}_t \cdot \hat{\mathbf{g}}_r^*(\mathbf{k}_t)] [\mathbf{j}\mathbf{k}_t \cdot \hat{\mathbf{g}}_v(\mathbf{k}_t)] & \text{if } \alpha = 1, \\ \hat{\mathbf{g}}_r^*(\mathbf{k}_t) \cdot \hat{\mathbf{g}}_v(\mathbf{k}_t) & \text{if } \alpha = 2. \end{cases} \quad (4.13)$$

In figure 4.4 we have plotted the convergence behavior of  $\hat{\gamma}_{1,1}^{(\alpha)}(\mathbf{k}_{t;j})$  as a function of  $j$  at frequency = 8[GHz] for the contribution  $A_{v,r}$  to  $L$  for the case of rooftop expansion and weighting functions. The configuration under consideration is the simple basic structure described in section 4.1. The oscillatory behavior is due to the sampling of  $\hat{\gamma}_{1,1}^{(\alpha)}$  in the sorted transverse wavevector  $\mathbf{k}_{t;j}$  where the norm  $k_{t;j}$  increases for increasing integer index  $j$ . Further, the slopes in this figure are as expected:  $-2/2$  for  $\alpha = 1$ , and  $-6/2$  for  $\alpha = 2$ . This result is a combination of equation 4.13, the convergence behavior of  $\hat{\mathbf{g}}_v(\mathbf{k}_t)$  given by

$$\hat{\mathbf{g}}_v(\mathbf{k}_t) \sim \mathcal{O} \left( \frac{1}{(\mathbf{k}_t \cdot \hat{\mathbf{d}}_v)^2 \mathbf{k}_t \cdot (\hat{\mathbf{z}} \times \hat{\mathbf{d}}_v)} \right), \quad (4.14)$$

for large  $k_t$  (described in equation F.9 in appendix F), and of  $k_{t;j} \sim \sqrt{j}$ .

Subsequently, we can write in general for an asymptotic expansion for  $g^{(\alpha)}(k_t)$  for large  $k_t$

$$g^{(\alpha)}(k_t) \approx \tilde{g}^{(\alpha)}(k_t) = c_1^{(\alpha)} k_t^{-1} + c_2^{(\alpha)} k_t^{-3} + c_3^{(\alpha)} k_t^{-5} + \dots, \quad (4.15)$$

where

$$c_1^{(1)} = -c_1'', \quad c_2^{(1)} = (c_1' - c_2''), \quad c_3^{(1)} = (c_2' - c_3''), \quad (4.16)$$

$$c_1^{(2)} = c_1', \quad c_2^{(2)} = c_2', \quad c_3^{(2)} = c_3'. \quad (4.17)$$

In figure 4.5 we have plotted the convergence behavior of  $g^{(\alpha)}(k_{t;j})$ , the two-term asymptotic expansion  $\tilde{g}^{(\alpha)}(k_{t;j})$  and the remainder  $g^{(\alpha)}(k_{t;j}) - \tilde{g}^{(\alpha)}(k_{t;j})$  as a function of  $j$  at frequency = 8[GHz] for the contribution  $A_{v,r}$  to  $L$ . The

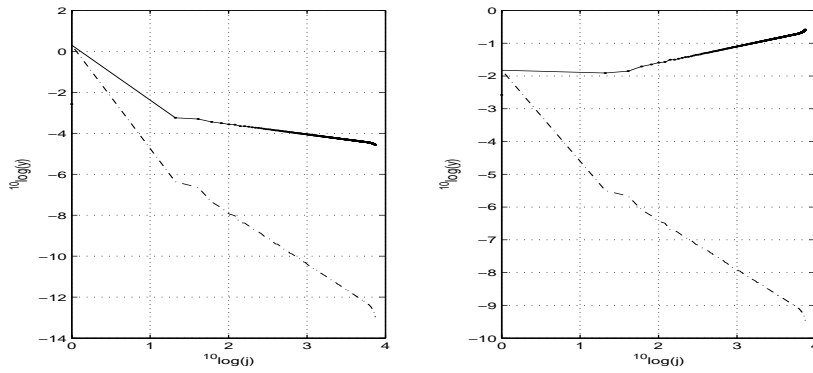


Figure 4.3:  $y = h^\alpha(k_{t;j})$  (solid curve), two-term asymptotic expansion  $y = \tilde{h}^\alpha(k_{t;j})$  (dotted curve superimposed on the solid curve) and remainder  $y = h^\alpha(k_{t;j}) - \tilde{h}^\alpha(k_{t;j})$  (dashed-dotted curve) as a function of  $j$ . Left figure for  $\alpha = \text{TM}$  and right figure for  $\alpha = \text{TE}$ .

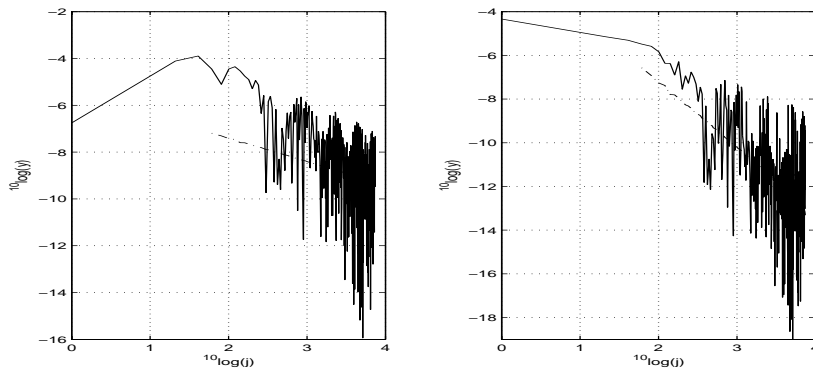


Figure 4.4:  $y = \hat{\gamma}_{1,1}^{(\alpha)}(\mathbf{k}_{t;j})$  (solid curve) and  $y = k_{t;j}^{-4\alpha+2}$  (dashed-dotted curve) as a function of  $j$ . Left figure for  $\alpha = 1$  and right figure for  $\alpha = 2$ .

configuration under consideration is the simple basic structure described in section 4.1. The slopes in this figure are as expected:  $-1/2$  for  $g^{(1)}$  and  $\tilde{g}^{(1)}$ ,  $-5/2$  for  $g^{(1)} - \tilde{g}^{(1)}$ ,  $-1/2$  for  $g^{(2)}$  and  $\tilde{g}^{(2)}$ ,  $-5/2$  for  $g^{(2)} - \tilde{g}^{(2)}$ . Note that we have taken into account  $k_{t;j} \sim \sqrt{j}$ .

From now on, we restrict ourselves to a two-term asymptotic expansion  $\tilde{g}^{(\alpha)}(k_t)$  for  $g^{(\alpha)}(k_t)$ . Subsequently, we subtract and add the two-term asymptotic expansion  $\tilde{g}^{(\alpha)}(k_t)$  from and to the general series. We can formally express these steps as

$$A_{v,r} = \sum_{\alpha} \left[ \xi_{v,r}^{(\alpha)} + \zeta_{v,r}^{(\alpha)} \right], \quad (4.18)$$

in which

$$\xi_{v,r}^{(\alpha)} = \sum_j \left[ g^{(\alpha)}(k_{t;j}) - \tilde{g}^{(\alpha)}(k_{t;j}) \right] \hat{\gamma}_{v,r}^{(\alpha)}(\mathbf{k}_{t;j}), \quad (4.19)$$

and in which

$$\zeta_{v,r}^{(\alpha)} = \sum_j \tilde{g}^{(\alpha)}(k_{t;j}) \hat{\gamma}_{v,r}^{(\alpha)}(\mathbf{k}_{t;j}). \quad (4.20)$$

With the addition and subtraction of a two-term asymptotic expansion, the rate of convergence for the series  $\xi_{v,r}^{(\alpha)}$  is now improved by four orders of  $k_t$ . Note that every additional term for the asymptotic expansion leads to a convergence improvement by two orders in  $k_t$ . However, the series  $\zeta_{v,r}^{(\alpha)}$  is still slowly converging. Its simpler form shows prospects of progress.

The series  $\xi_{v,r}^{(\alpha)}$  is approximated by a summation over a finite number of terms  $n$ , where  $n$  equals the number of terms when the partial sum  $S_n = \sum_{j=1}^n k_{t;j}^{-5}$  has reached a relative error of 0.1[%].  $k_{t;j}^{-5}$  represents the leading-order term of  $g^{(\alpha)}(k_{t;j}) - \tilde{g}^{(\alpha)}(k_{t;j})$  for large  $k_{t;j}$ . The relative error is defined as

$$\text{relative error} = \left| \frac{S_n - S_N}{S_N} \right|, \quad (4.21)$$

$S_N$  denotes the partial sum for a fixed large number of terms  $N \gg n$ , and approximates the result of the infinite series where  $N \rightarrow \infty$ .

We have plotted the convergence behavior of  $[g^{(\alpha)}(k_{t;j}) - \tilde{g}^{(\alpha)}(k_{t;j})] \hat{\gamma}_{1,1}^{(\alpha)}(\mathbf{k}_{t;j})$  in figure 4.6 as a function of  $j$  at frequency = 8[GHz] for the contribution  $A_{v,r}$  to  $L$  for the case of rooftop expansion and weighting functions. The configuration under consideration is the simple basic structure described in section 4.1. The oscillatory behavior is due to the sampling of  $\hat{\gamma}_{1,1}^{(\alpha)}$  in the sorted transverse wavevector  $\mathbf{k}_{t;j}$  where the norm  $k_{t;j}$  increases for increasing integer index  $j$ . The slopes in this figure are as expected:  $(-2 - 5)/2$  for  $\alpha = 1$ , and  $(-6 - 5)/2$  for  $\alpha = 2$ . This result is a combination of figures 4.4 and 4.5. Without the Kummer transformation, the slopes would have been:  $(-2 - 1)/2$  for  $\alpha = 1$ , and  $(-6 - 1)/2$  for  $\alpha = 2$ .

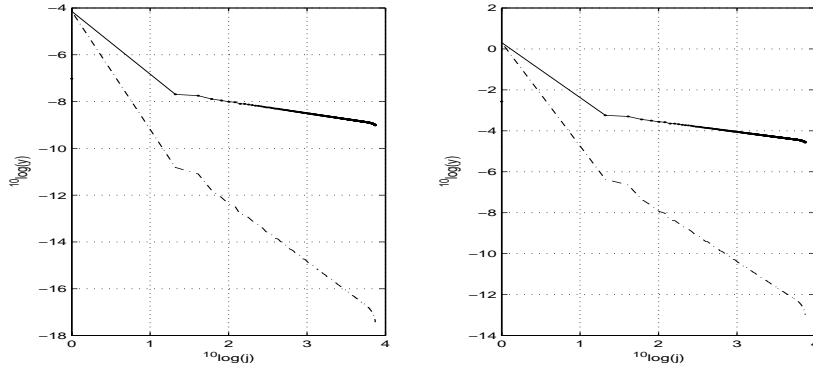


Figure 4.5:  $y = g^{(\alpha)}(k_{t;j})$  (solid curve), two-term asymptotic expansion  $y = \tilde{g}^{(\alpha)}(k_{t;j})$  (dotted curve) and remainder  $y = g^{(\alpha)}(k_{t;j}) - \tilde{g}^{(\alpha)}(k_{t;j})$  (dashed-dotted curve) as a function of  $j$ . Left figure for  $\alpha = 1$  and right figure for  $\alpha = 2$ .

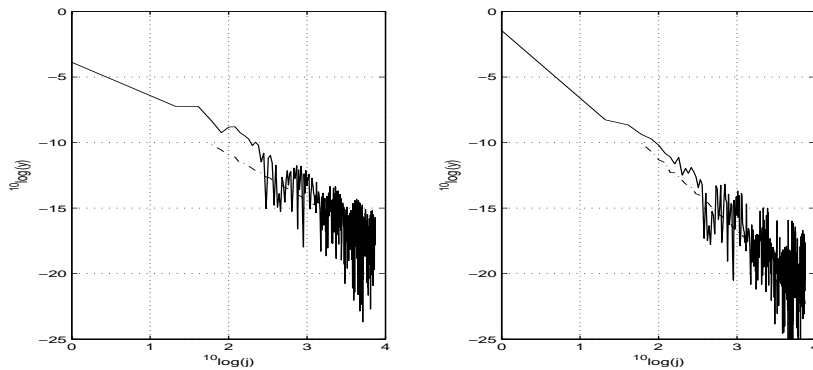


Figure 4.6:  $y = [g^{(\alpha)}(k_{t;j}) - \tilde{g}^{(\alpha)}(k_{t;j})] \hat{\gamma}_{1,1}^{(\alpha)}(\mathbf{k}_{t;j})$  (solid curve) and  $y = k_{t,j}^{-4\alpha-3}$  (dashed-dotted curve) as a function of  $j$ . Left figure for  $\alpha = 1$  and right figure for  $\alpha = 2$ .

Note that we have to be careful with the subtraction and addition of  $\tilde{g}^{(\alpha)}(k_{t;j})$  for  $\mathbf{m}_j = \mathbf{0}$ . If the incident wavevector is chosen almost in parallel with the normal incidence direction,  $k_t^{\text{inc}}$  is small. Correspondingly,  $\tilde{g}^{(\alpha)}(k_{t;j})$  and  $g^{(\alpha)}(k_{t;j})$  significantly differ in magnitude. This causes numerical accuracy problems within equation 4.18.

### 4.3 Evaluation of Asymptotic Series

In this section we describe a so-called Ewald transformation, where the asymptotically slowly converging correction series  $\zeta_{v,r}^{(\alpha)}$  is converted into an integral over  $\tau$  of an exponentially fast decaying function. This function contains an exponentially fast converging series for which the leading-order term is given by  $\exp(-k_t^2 \tau^{2\lambda})$ . Inspired by Ewald's transformation [85, 40], we introduce the identity

$$\frac{1}{k_t^n} = \frac{2\lambda}{\Gamma(n/2)} \int_0^\infty \tau^{\lambda n - 1} \exp(-k_t^2 \tau^{2\lambda}) d\tau, \quad (4.22)$$

where  $\lambda$  is an arbitrary positive parameter (to be selected later).  $\Gamma(x)$  represents the gamma-function. It is defined by the Euler integral [2, formula 6.1.1] as

$$\Gamma(x) = \int_0^\infty t^{x-1} \exp(-t) dt. \quad (4.23)$$

The explicit identities for  $k_t^{-1}$  and  $k_t^{-3}$  are given by

$$\begin{aligned} \frac{1}{k_t} &= \frac{2\lambda}{\sqrt{\pi}} \int_0^\infty \tau^{\lambda-1} \exp(-k_t^2 \tau^{2\lambda}) d\tau, \\ \frac{1}{k_t^3} &= \frac{4\lambda}{\sqrt{\pi}} \int_0^\infty \tau^{3\lambda-1} \exp(-k_t^2 \tau^{2\lambda}) d\tau. \end{aligned} \quad (4.24)$$

We can now rewrite the correction series  $\zeta_{v,r}^{(\alpha)}$  as

$$\zeta_{v,r}^{(\alpha)} = \frac{2\lambda}{\sqrt{\pi}} \int_0^\infty \tau^{\lambda-1} \sum_j (c_1^{(\alpha)} + 2\tau^{2\lambda} c_2^{(\alpha)}) \exp(-k_{t;j}^2 \tau^{2\lambda}) \hat{\gamma}_{v,r}^{(\alpha)}(\mathbf{k}_{t;j}) d\tau, \quad (4.25)$$

where we have interchanged the sum and integral. In figure 4.7 we have plotted the integrand of  $\zeta_{1,1}^{(\alpha)}$  as a function of  $\tau$  with  $\lambda = 3$  at frequency = 8[GHz] for the contribution  $A_{v,r}$  to  $L$  for the case of rooftop expansion and weighting functions. The configuration under consideration is the simple basic structure described in section 4.1. Note the exponential decay of the integrand for large  $\tau$ . Furthermore, this expression has the advantage that the series converges exponentially fast in  $k_t$  for  $\tau > 0$ . Near  $\tau = 0$  the series still needs a relatively large number of terms to converge. In figure 4.8 we have plotted this slow series convergence behavior for small  $\tau$ .

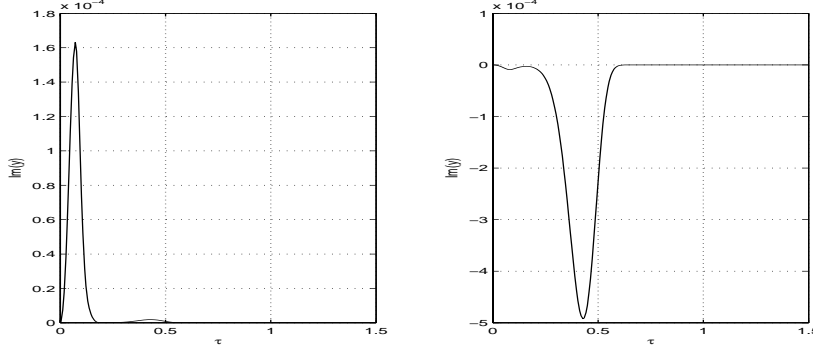


Figure 4.7:  $y = \text{Im}(\text{integrand of } \zeta_{1,1}^{(\alpha)})$  (solid curve) as a function of  $\tau$ . Left figure for  $\alpha = 1$  and right figure for  $\alpha = 2$ .

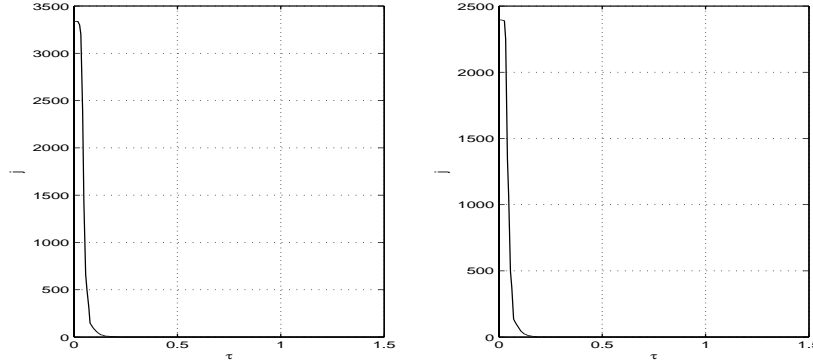


Figure 4.8: Minimum required number of terms for the series in the integrand of  $\zeta_{1,1}^{(\alpha)}$  to converge with a relative error of 1[%] (solid curve) as a function of  $\tau$ . Left figure for  $\alpha = 1$  and right figure for  $\alpha = 2$ .

For this reason, we split the integration interval in  $\zeta_{v,r}^{(\alpha)}$  into two parts around a carefully chosen transition point  $\tau = \tau_1$ : one denoted by  $\zeta_{v,r}^{(\alpha),L}$  for an interval  $[\tau_1, \infty)$  corresponding to large  $\tau$  (explained in section 4.3.1) and one denoted by  $\zeta_{v,r}^{(\alpha),S}$  for an interval  $(0, \tau_1]$  corresponding to small  $\tau$  (explained in section 4.3.2). A good choice for the transition point  $\tau_1$  is proposed in section 4.3.3. Note that  $\zeta_{v,r}^{(\alpha)} = \zeta_{v,r}^{(\alpha),S} + \zeta_{v,r}^{(\alpha),L}$ .

### 4.3.1 Integration for Large Argument

The expression for  $\zeta_{v,r}^{(\alpha),L}$  is given by

$$\zeta_{v,r}^{(\alpha),L} = \frac{2\lambda}{\sqrt{\pi}} \int_{\tau_1}^{\infty} \tau^{\lambda-1} \sum_j (c_1^{(\alpha)} + 2\tau^{2\lambda} c_2^{(\alpha)}) \exp(-k_{t;j}^2 \tau^{2\lambda}) \hat{\gamma}_{v,r}^{(\alpha)}(\mathbf{k}_{t;j}) d\tau. \quad (4.26)$$

The integrand for large argument  $\tau$  decays exponentially at infinity (provided that  $k_{t;j} \neq 0$ ) and can therefore be evaluated numerically very efficiently. However, the  $\mathbf{m}_j = \mathbf{0}$  term slows down the convergence especially if the incident wavevector is chosen almost in parallel with the normal incidence direction. Therefore we separate this term and treat it analytically by rewriting equation 4.26 as

$$\zeta_{v,r}^{(\alpha),L} = \Omega_{v,r}^{(\alpha)}(\mathbf{k}_t^{\text{inc}}, \tau_1, \lambda) + \frac{2\lambda}{\sqrt{\pi}} \int_{\tau_1}^{\infty} \tau^{\lambda-1} \sum_j (c_1^{(\alpha)} + 2\tau^{2\lambda} c_2^{(\alpha)}) \exp(-k_{t;j}^2 \tau^{2\lambda}) \hat{\gamma}_{v,r}^{(\alpha)}(\mathbf{k}_{t;j}) d\tau. \quad (4.27)$$

in which

$$\hat{\gamma}_{v,r}^{(\alpha)}(\mathbf{k}_t) = \begin{cases} \hat{\gamma}_{v,r}^{(\alpha)}(\mathbf{k}_t) & \text{if } \mathbf{k}_t \neq \mathbf{k}_t^{\text{inc}}, \\ 0 & \text{otherwise,} \end{cases} \quad (4.28)$$

and  $\Omega_{v,r}^{(\alpha)}(\mathbf{k}_t^{\text{inc}}, \tau_1, \lambda)$  is given by

$$\frac{2\lambda}{\sqrt{\pi}} \int_{\tau_1}^{\infty} \tau^{\lambda-1} (c_1^{(\alpha)} + 2\tau^{2\lambda} c_2^{(\alpha)}) \exp(-k_t^{\text{inc}2} \tau^{2\lambda}) \hat{\gamma}_{v,r}^{(\alpha)}(\mathbf{k}_t^{\text{inc}}) d\tau. \quad (4.29)$$

The latter can be rewritten as

$$\Omega_{v,r}^{(\alpha)}(\mathbf{k}_t^{\text{inc}}, \tau_1, \lambda) = \hat{\gamma}_{v,r}^{(\alpha)}(\mathbf{k}_t^{\text{inc}}) [c_1^{(\alpha)} \eta(\mathbf{k}_t^{\text{inc}}, \tau_1, \lambda) + c_2^{(\alpha)} \xi(\mathbf{k}_t^{\text{inc}}, \tau_1, \lambda)], \quad (4.30)$$

in which

$$\begin{aligned} \eta(\mathbf{k}_t^{\text{inc}}, \tau_1, \lambda) &= \frac{2\lambda}{\sqrt{\pi}} \int_{\tau_1}^{\infty} \tau^{\lambda-1} \exp(-k_t^{\text{inc}2} \tau^{2\lambda}) d\tau \\ &= \frac{1}{k_t^{\text{inc}}} [1 - \text{erf}(k_t^{\text{inc}} \tau_1^\lambda)], \end{aligned} \quad (4.31)$$

where  $k_t^{\text{inc}} = \|\mathbf{k}_t^{\text{inc}}\|$  and

$$\begin{aligned} \xi(\mathbf{k}_t^{\text{inc}}, \tau_1, \lambda) &= \frac{4\lambda}{\sqrt{\pi}} \int_{\tau_1}^{\infty} \tau^{3\lambda-1} \exp(-k_t^{\text{inc}2} \tau^{2\lambda}) d\tau \\ &= \frac{1}{k_t^{\text{inc}3}} \left[ 1 + \frac{2k_t^{\text{inc}} \tau_1^\lambda}{\sqrt{\pi}} \exp(-k_t^{\text{inc}2} \tau_1^{2\lambda}) - \text{erf}(k_t^{\text{inc}} \tau_1^\lambda) \right]. \end{aligned} \quad (4.32)$$

The error function  $\text{erf}(x)$  of  $x$  is defined as [2, formula 7.1.1]

$$\text{erf}(x) = \frac{2}{\sqrt{\pi}} \int_0^x \exp(-t^2) dt. \quad (4.33)$$

Since the remaining integrand in  $\zeta_{v,r}^{(\alpha),L}$ , i.e., the integrand in the right-hand side of equation 4.27, decays exponentially at infinity, we can reduce the integration interval to a finite interval  $[\tau_1, \tau_2]$ . We use a simple numerical integration scheme

(such as a Simpson or a Gaussian quadrature rule) to perform the integration over  $\tau$ . We can finally write the expression for  $\zeta_{v,r}^{(\alpha),L}$  as

$$\zeta_{v,r}^{(\alpha),L} = \Omega_{v,r}^{(\alpha)}(\mathbf{k}_t^{\text{inc}}, \tau_1, \lambda) + \frac{2\lambda}{\sqrt{\pi}} \int_{\tau_1}^{\tau_2} \tau^{\lambda-1} \sum_j (c_1^{(\alpha)} + 2\tau^{2\lambda} c_2^{(\alpha)}) \exp(-k_{t,j}^2 \tau^{2\lambda}) \check{\gamma}_{v,r}^{(\alpha)}(\mathbf{k}_{t,j}) d\tau. \quad (4.34)$$

The series in the integrand of  $\zeta_{v,r}^{(\alpha),L}$  is reduced to a summation over a finite number of terms  $n$ , where  $n$  equals the number of terms when the partial sum  $S_n = \sum_{j=1}^n \exp(-k_{t,j}^2 \tau_1^{2\lambda})$  has reached a relative error of 0.1 [%].  $\exp(-k_{t,j}^2 \tau_1^{2\lambda})$  represents the worst case leading-order term of the series in the integrand of  $\zeta_{v,r}^{(\alpha),L}$  for large  $k_{t,j}$ . The relative error has been defined in equation 4.21.

### 4.3.2 Integration for Small Argument

The expression for  $\zeta_{v,r}^{(\alpha),S}$  is given by

$$\zeta_{v,r}^{(\alpha),S} = \frac{2\lambda}{\sqrt{\pi}} \int_0^{\tau_1} \tau^{\lambda-1} \sum_j (c_1^{(\alpha)} + 2\tau^{2\lambda} c_2^{(\alpha)}) \exp(-k_{t,j}^2 \tau^{2\lambda}) \hat{\gamma}_{v,r}^{(\alpha)}(\mathbf{k}_{t,j}) d\tau. \quad (4.35)$$

In this section we describe a so-called Poisson transformation step, where the relatively slow convergence of the series within the exponentially fast decaying function, caused by the behavior of  $\exp(-k_t^2 \tau^{2\lambda})$  for small  $\tau$ , is converted into an exponentially fast converging series for which the leading order term is given by  $\exp(-\rho^2/(4\tau^{2\lambda}))$ . We use the following form of Poisson's formula ([79] or [89, section 6.1] with  $\boldsymbol{\xi} = \mathbf{0}$ )

$$\sum_j \hat{\psi}(\mathbf{n}_j) = 4\pi^2 \sum_j \psi(2\pi \mathbf{m}_j), \quad (4.36)$$

in which  $\mathbf{n}_j$  is defined in the reciprocal (Floquet) lattice, in which  $\mathbf{m}_j$  is defined in the direct (Bravais) lattice, and where

$$\hat{\psi}(\mathbf{k}_t) = \mathcal{F}\{\psi(\boldsymbol{\rho})\} = \int \psi(\boldsymbol{\rho}) \exp(-j\boldsymbol{\rho} \cdot \mathbf{k}_t) dA. \quad (4.37)$$

When we apply equation 4.36 to  $\hat{\psi}(\mathbf{n}) = \hat{\phi}(R\mathbf{n} + \mathbf{k}_t^{\text{inc}})$ , we obtain

$$\sum_j \hat{\phi}(R\mathbf{n}_j + \mathbf{k}_t^{\text{inc}}) = |D| \sum_j \exp(-jD\mathbf{m}_j \cdot \mathbf{k}_t^{\text{inc}}) \phi(D\mathbf{m}_j), \quad (4.38)$$

where  $|D|$  denotes the determinant of the matrix  $D$ . Further  $\mathbf{k}_{t,j} \equiv R\mathbf{n}_j + \mathbf{k}_t^{\text{inc}}$  and  $\boldsymbol{\rho}_j \equiv D\mathbf{m}_j$ . Subsequently, when we take  $\hat{\phi}(\mathbf{k}_t) = \exp(-k_t^2 \tau^{2\lambda}) \hat{\gamma}_{v,r}^{(\alpha)}(\mathbf{k}_t)$ , we can rewrite equation 4.38 as

$$\sum_j \exp(-k_{t,j}^2 \tau^{2\lambda}) \hat{\gamma}_{v,r}^{(\alpha)}(\mathbf{k}_{t,j}) = |D| \sum_j \exp(-jD\mathbf{m}_j \cdot \mathbf{k}_t^{\text{inc}}) \check{\gamma}_{v,r}^{(\alpha)}(D\mathbf{m}_j, \tau), \quad (4.39)$$



where

$$\begin{aligned}\bar{\gamma}_{v,r}^{(\alpha)}(\boldsymbol{\rho}, \tau) &= \mathcal{F}^{-1} \left\{ \exp(-k_t^2 \tau^{2\lambda}) \hat{\gamma}_{v,r}^{(\alpha)}(\mathbf{k}_t) \right\} \\ &= \frac{1}{4\pi^2} \int \exp(-k_t^2 \tau^{2\lambda}) \hat{\gamma}_{v,r}^{(\alpha)}(\mathbf{k}_t) \exp(j\mathbf{k}_t \cdot \boldsymbol{\rho}) d\mathbf{k}_t,\end{aligned}\quad (4.40)$$

represents a so-called exponential regularization of  $\hat{\gamma}_{v,r}^{(\alpha)}(\mathbf{k}_t)$ . The series represented by equation 4.39 now converges rapidly for small  $\tau$ . In order to avoid evaluation at  $\tau = 0$ , we select  $\lambda > 1$ . In this case no singularity occurs at  $\tau = 0$ . Further, we use a straight-forward numerical integration scheme (such as a Simpson or a Gaussian quadrature rule) to perform the integration over  $\tau$ . We can finally write the expression for  $\zeta_{v,r}^{(\alpha),S}$  as

$$\begin{aligned}\zeta_{v,r}^{(\alpha),S} &= |D| \frac{2\lambda}{\sqrt{\pi}} \int_0^{\tau_1} \tau^{\lambda-1} \sum_j (c_1^{(\alpha)} + \\ &2\tau^{2\lambda} c_2^{(\alpha)}) \exp(-jD\mathbf{m}_j \cdot \mathbf{k}_t^{\text{inc}}) \bar{\gamma}_{v,r}^{(\alpha)}(D\mathbf{m}_j, \tau) d\tau.\end{aligned}\quad (4.41)$$

The series in the integrand of  $\zeta_{v,r}^{(\alpha),S}$  is reduced to a summation over a finite number of terms  $n$ , where  $n$  equals the number of terms when the partial sum  $S_n = \sum_{j=1}^n \exp(-\rho_j^2/(4\tau_1^{2\lambda}))$  has reached a relative error of 0.1[%].  $\exp(-\rho_j^2/(4\tau_1^{2\lambda}))$  represents the worst case leading-order term of the series in the integrand of  $\zeta_{v,r}^{(\alpha),S}$  for large  $\rho_j$ . The relative error has been defined in equation 4.21.

### 4.3.3 Determination of the Transition Point

The new acceleration technique described in the previous sections comes with a number of freely selectable parameters. Its performance will only be optimal if they are chosen in the right way. Most of these parameters (such as  $\lambda$ ,  $\tau_2$ , the truncation of the reduced series  $\xi_{v,r}^{(\alpha)}$  and the series in  $\zeta_{v,r}^{(\alpha),S}$  and  $\zeta_{v,r}^{(\alpha),L}$ ) have been discussed in the previous sections. The choice of an optimal transition point  $\tau_1$  is described in this section.

The transition point  $\tau_1$  is a compromise between the differences in convergence behavior of the series in  $\zeta_{v,r}^{(\alpha),S}$  and  $\zeta_{v,r}^{(\alpha),L}$ , respectively. A good choice for  $\tau_1$  can be obtained by first reconsidering equation 4.39

$$\sum_j \exp(-k_{t;j}^2 \tau^{2\lambda}) \hat{\gamma}_{v,r}^{(\alpha)}(\mathbf{k}_{t;j}) = |D| \sum_j \exp(-jD\mathbf{m}_j \cdot \mathbf{k}_t^{\text{inc}}) \bar{\gamma}_{v,r}^{(\alpha)}(D\mathbf{m}_j, \tau). \quad (4.42)$$

By setting  $\mathbf{k}_t^{\text{inc}} = \mathbf{0}$  and  $\hat{\gamma}_{v,r}^{(\alpha)}(\mathbf{k}_t) = 1$  we obtain for  $\bar{\gamma}_{v,r}^{(\alpha)}$

$$\bar{\gamma}_{v,r}^{(\alpha)}(\boldsymbol{\rho}, \tau) = \frac{1}{4\pi\tau^{2\lambda}} \exp\left(-\frac{\rho^2}{4\tau^{2\lambda}}\right), \quad (4.43)$$

while we can rewrite equation 4.42 as

$$\sum_j \exp(-\|R\mathbf{n}_j\|^2 \tau^{2\lambda}) = \frac{|D|}{4\pi\tau^{2\lambda}} \sum_j \exp\left(-\frac{\|D\mathbf{m}_j\|^2}{4\tau^{2\lambda}}\right). \quad (4.44)$$

This equation shows that the convergence rate of the series in  $\zeta_{v,r}^{(\alpha),S}$  is governed by the leading term

$$\exp\left(-\frac{\|D\mathbf{m}_j\|^2}{4\tau^{2\lambda}}\right), \quad (4.45)$$

and improves for  $\tau < \tau_1$ , while the convergence rate of the series in  $\zeta_{v,r}^{(\alpha),L}$  is governed by the leading term

$$\exp(-\|R\mathbf{n}_j\|^2 \tau^{2\lambda}), \quad (4.46)$$

and improves for  $\tau > \tau_1$ . Consequently,  $\tau_1$  is the compromise between both estimates and is determined by equating these leading order term expressions with

1.  $\|D\mathbf{m}_j\|$  replaced by a characteristic step  $\sqrt{|D|}$ ,
2.  $\|R\mathbf{n}_j\|$  replaced by a characteristic step  $\sqrt{|R|}$ ,

and solving the resulting equation for  $\tau$ . Since  $D^T R = 2\pi I$ , it follows that  $\sqrt{\frac{|D|}{|R|}} = \frac{|D|}{2\pi}$ . The solution for  $\tau_1$  is then given by

$$\tau_1 = \sqrt[2\lambda]{\frac{|D|}{4\pi}}. \quad (4.47)$$

For the special case where  $\mathbf{d}_1 = 15.8\hat{\mathbf{x}}[\text{mm}]$ ,  $\mathbf{d}_2 = 15.8\hat{\mathbf{y}}[\text{mm}]$  and  $\lambda = 3$ , these two curves represented by equation 4.45 and 4.46 are plotted as a function of  $\tau$  in figure 4.9, respectively. At  $\tau = \tau_1 = 0.1646$  the two curves intersect.

## 4.4 Exponential Regularization

In the previous section we have shown that the slow convergence of the original series in  $\zeta_{v,r}^{(\alpha),S}$  can be repaired by using a Poisson transformation that leads to equation 4.41. This step, however, introduces the evaluation of  $\bar{\gamma}_{v,r}^{(\alpha)}(\boldsymbol{\rho}, \tau)$  given by equation 4.40 which is a so-called exponential regularization of  $\hat{\gamma}_{v,r}^{(\alpha)}(\mathbf{k}_t)$  [89].

The overall success of the total acceleration technique critically depends on the availability of a rapid procedure to evaluate  $\bar{\gamma}_{v,r}^{(\alpha)}(\boldsymbol{\rho}, \tau)$ . Equation 4.41 shows us that within the calculation of  $\zeta_{v,r}^{(\alpha),S}$ ,  $\bar{\gamma}_{v,r}^{(\alpha)}(D\mathbf{m}_j, \tau)$  only depends on  $D$ ,  $\tau$ ,  $\mathbf{m}_j$ ,  $v$  and  $r$ . It does not depend on  $\mathbf{k}_t^{\text{inc}}$ , or on any medium parameters. Further we have shown in section 4.3.3 that the transition point  $\tau_1$  only depends on the choice for the elementary dimensions of the periodic structure  $D$  and on  $\lambda$ . This

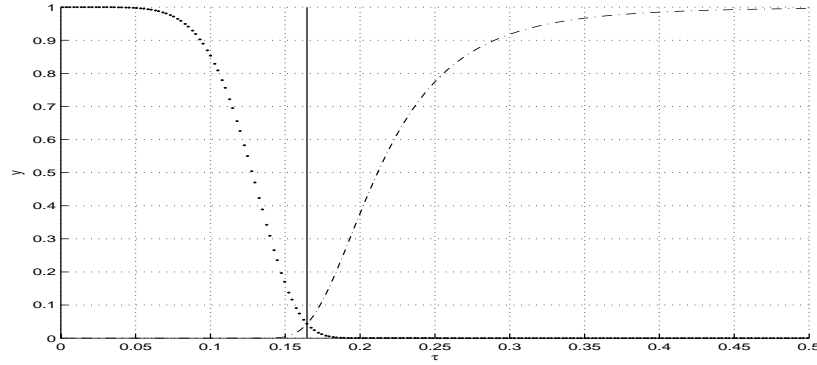


Figure 4.9:  $y = \exp(-\frac{|D|}{4\tau^{2\lambda}})$  (dashed-dotted curve) and  $y = \exp(-|R|\tau^{2\lambda})$  (dotted curve) as a function of  $\tau$ , transition point at  $\tau = \tau_1 = 0.1646$  (vertical solid line).

means that the grid for  $\tau$  (used for a numerical approximation of the integration over  $\tau$  in  $\zeta_{v,r}^{(\alpha),S}$ ) can be fixed at the initialization phase of the computation. We take advantage of this situation by calculating and storing  $\bar{\gamma}_{v,r}^{(\alpha)}(D\mathbf{m}_j, \tau)$  as a function of  $\alpha, v, r, \mathbf{m}_j$  and  $\tau$  at the beginning of the computation. The stored data (lookup table) can then later be used to calculate  $\zeta_{v,r}^{(\alpha),S}$  as a function of  $\mathbf{k}_t^{\text{inc}}$  and of any medium parameter. Note that the grid for small  $\tau$  is fixed and contains a small number of points due to the slowly varying behavior of the integrand. The number of values for  $\mathbf{m}_j$  can be chosen small because of the rapid convergence of the series in  $\zeta_{v,r}^{(\alpha),S}$  for small  $\tau$ .

Further note that  $\bar{\gamma}_{v,r}^{(\alpha)}$  given by equation 4.40 can be considered as an infinitely differentiable regularization [53] of the function  $\gamma_{v,r}^{(\alpha)}$  such that  $\bar{\gamma}_{v,r}^{(\alpha)}(\boldsymbol{\rho}, 0) = \gamma_{v,r}^{(\alpha)}(\boldsymbol{\rho})$ . Note that  $\bar{\gamma}_{v,r}^{(\alpha)}$  satisfies the heat equation

$$\nabla_t^2 \bar{\gamma}_{v,r}^{(\alpha)}(\boldsymbol{\rho}, \tau) = \partial_{\tau^{2\lambda}} \bar{\gamma}_{v,r}^{(\alpha)}(\boldsymbol{\rho}, \tau), \quad (4.48)$$

if we identify  $\tau^{2\lambda}$  to be a time-like variable [89, section 6.2]. We can then interpret  $\bar{\gamma}_{v,r}^{(\alpha)}$  as the temperature profile after a time  $\tau^{2\lambda}$  of the initial profile  $\bar{\gamma}_{v,r}^{(\alpha)}(\boldsymbol{\rho}, 0) = \gamma_{v,r}^{(\alpha)}(\boldsymbol{\rho})$ . Since  $\gamma_{v,r}^{(\alpha)}(\boldsymbol{\rho})$  has a compact support,  $\bar{\gamma}_{v,r}^{(\alpha)}(\boldsymbol{\rho}, \tau)$  has an "almost" compact support, while it decays exponentially for large values of the argument  $\boldsymbol{\rho}$ .

The remaining problem is now to find expressions for  $\bar{\gamma}_{v,r}^{(\alpha)}(\boldsymbol{\rho}, \tau)$  for different choices of expansion and weighting functions. In general, finding an analytical expression appears to be difficult [89, section 6.3]. However in the following three sections we consider three specific choices for these functions that lead to workable analytical solutions and numerical approximations. These cases are:

1. The rooftop function used for both the expansion and weighting functions, and placed in an orthogonal grid. In this case, we can express the  $\bar{\gamma}_{v,r}^{(\alpha)}(\boldsymbol{\rho}, \tau)$

in terms of complementary error functions. We do this in section 4.4.1.

2. The rooftop function used for both the expansion and weighting functions. This case is more general than the previous one; we are not restricted to the placement in the orthogonal grid. In this case, we can express  $\bar{\gamma}_{v,r}^{(\alpha)}(\boldsymbol{\rho}, \tau)$  as a convolution of two analytically known functions, both with "almost" compact support. We do this in section 4.4.2.
3. The RWG function used for both the expansion and weighting functions. In this case, we can express  $\bar{\gamma}_{v,r}^{(\alpha)}(\boldsymbol{\rho}, \tau)$  as a convolution of two numerically approximated functions, both with "almost" compact support. We do this in section 4.4.3.

#### 4.4.1 Rooftop Function Placed in an Orthogonal Grid

In this section, we evaluate  $\bar{\gamma}_{v,r}^{(\alpha)}(\boldsymbol{\rho}, \tau)$  if we use the rooftop function placed in an orthogonal grid for both the expansion and weighting functions. In this case, we can express  $\bar{\gamma}_{v,r}^{(\alpha)}(\boldsymbol{\rho}, \tau)$  in terms of complementary error functions.  $\bar{\gamma}_{v,r}^{(\alpha)}(\boldsymbol{\rho}, \tau)$  is given by equation 4.40

$$\bar{\gamma}_{v,r}^{(\alpha)}(\boldsymbol{\rho}, \tau) = \mathcal{F}^{-1} \left\{ \exp(-k_t^2 \tau^{2\lambda}) \hat{\gamma}_{v,r}^{(\alpha)}(\mathbf{k}_t) \right\}, \quad (4.49)$$

with

$$\hat{\gamma}_{v,r}^{(\alpha)}(\mathbf{k}_t) = \begin{cases} [\mathbf{j}\mathbf{k}_t \cdot \hat{\mathbf{g}}_r^*(\mathbf{k}_t)] [\mathbf{j}\mathbf{k}_t \cdot \hat{\mathbf{g}}_v(\mathbf{k}_t)] & \text{if } \alpha = 1, \\ \hat{\mathbf{g}}_r^*(\mathbf{k}_t) \cdot \hat{\mathbf{g}}_v(\mathbf{k}_t) & \text{if } \alpha = 2. \end{cases} \quad (4.50)$$

Note that  $\hat{\gamma}$  indicates the spatial Fourier transform of  $\gamma$ . Substituting the spectrum of the weighting functions  $\hat{\mathbf{g}}_r(\mathbf{k}_t)$  (equation F.5 in appendix F) given by

$$\hat{\mathbf{g}}_r(\mathbf{k}_t) = \hat{\mathbf{d}}_r \exp(-\mathbf{j}\mathbf{k}_t \cdot \boldsymbol{\rho}_r) \hat{\Lambda}(\mathbf{k}_t \cdot \hat{\mathbf{d}}_r, p_r, q_r) \hat{\Pi}(\mathbf{k}_t \cdot (\hat{\mathbf{z}} \times \hat{\mathbf{d}}_r), w_r), \quad (4.51)$$

and the spectrum of the expansion functions  $\hat{\mathbf{g}}_v(\mathbf{k}_t)$  given by

$$\hat{\mathbf{g}}_v(\mathbf{k}_t) = \hat{\mathbf{d}}_v \exp(-\mathbf{j}\mathbf{k}_t \cdot \boldsymbol{\rho}_v) \hat{\Lambda}(\mathbf{k}_t \cdot \hat{\mathbf{d}}_v, p_v, q_v) \hat{\Pi}(\mathbf{k}_t \cdot (\hat{\mathbf{z}} \times \hat{\mathbf{d}}_v), w_v), \quad (4.52)$$

leads to the following expression for  $\hat{\gamma}_{v,r}^{(1)}(\mathbf{k}_t)$

$$\begin{aligned} \hat{\gamma}_{v,r}^{(1)}(\mathbf{k}_t) &= \exp(\mathbf{j}\mathbf{k}_t \cdot [\boldsymbol{\rho}_r - \boldsymbol{\rho}_v]) \\ &\quad \mathcal{S}(w_r \mathbf{k}_t \cdot (\hat{\mathbf{z}} \times \hat{\mathbf{d}}_r)) \left( \mathcal{T}(q_r \mathbf{k}_t \cdot \hat{\mathbf{d}}_r) - \mathcal{T}(-p_r \mathbf{k}_t \cdot \hat{\mathbf{d}}_r) \right) \\ &\quad \mathcal{S}(w_v \mathbf{k}_t \cdot (\hat{\mathbf{z}} \times \hat{\mathbf{d}}_v)) \left( \mathcal{T}(p_v \mathbf{k}_t \cdot \hat{\mathbf{d}}_v) - \mathcal{T}(-q_v \mathbf{k}_t \cdot \hat{\mathbf{d}}_v) \right), \end{aligned} \quad (4.53)$$

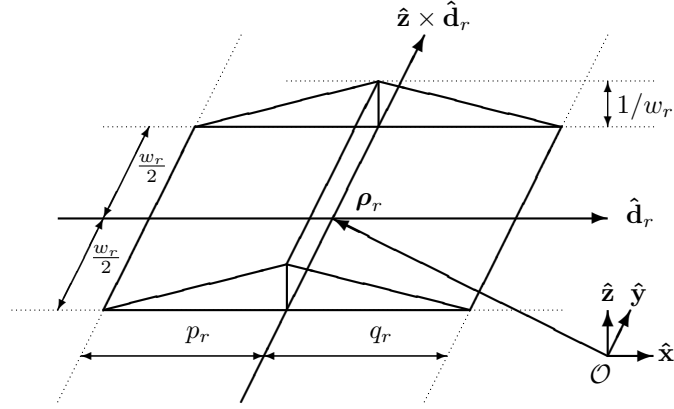


Figure 4.10: Domain, vectors and scalars used in the rooftop function.

and the following expression for  $\hat{\gamma}_{v,r}^{(2)}(\mathbf{k}_t)$

$$\begin{aligned} \hat{\gamma}_{v,r}^{(2)}(\mathbf{k}_t) &= (\hat{\mathbf{d}}_r \cdot \hat{\mathbf{d}}_v) \exp(j\mathbf{k}_t \cdot [\boldsymbol{\rho}_r - \boldsymbol{\rho}_v]) \\ &\mathcal{S}(w_r \mathbf{k}_t \cdot (\hat{\mathbf{z}} \times \hat{\mathbf{d}}_r)) \left( \frac{\mathcal{T}(-p_r \mathbf{k}_t \cdot \hat{\mathbf{d}}_r) - \mathcal{T}(q_r \mathbf{k}_t \cdot \hat{\mathbf{d}}_r)}{\mathbf{k}_t \cdot \hat{\mathbf{d}}_r} \right) \\ &\mathcal{S}(w_v \mathbf{k}_t \cdot (\hat{\mathbf{z}} \times \hat{\mathbf{d}}_v)) \left( \frac{\mathcal{T}(p_v \mathbf{k}_t \cdot \hat{\mathbf{d}}_v) - \mathcal{T}(-q_v \mathbf{k}_t \cdot \hat{\mathbf{d}}_v)}{\mathbf{k}_t \cdot \hat{\mathbf{d}}_v} \right), \end{aligned} \quad (4.54)$$

in which

$$\hat{\Lambda}(k, p, q) = \frac{\mathcal{T}(kp) - \mathcal{T}(-kq)}{jk}, \quad \hat{\Pi}(k, w) = \mathcal{S}(kw), \quad (4.55)$$

and in which

$$\mathcal{T}(z) = \mathcal{S}(z) \exp\left(\frac{jz}{2}\right), \quad \mathcal{S}(z) = \text{sinc}\left(\frac{z}{2}\right). \quad (4.56)$$

See section 3.7.4 for a detailed explanation of the rooftop function. See figure 4.10 for a graphical representation of the domain, vectors and scalars used in the rooftop function.

Subsequently, we fix the rooftop expansion and weighting functions in an orthogonal grid, in which all pairs of  $\hat{\mathbf{d}}_r$  and  $\hat{\mathbf{d}}_v$  are either in parallel or perpendicular. Further, the grid can be rotated around the  $z$ -axis. An example of two expansion functions placed in an orthogonal rotated reference frame is given in figure 4.11. By doing this we create a restriction in the modeling of the unknown surface currents. However most structures do not consist of arbitrarily shaped metal patches and apertures. In most cases the unit-cell structures can be caught in this orthogonal grid. Furthermore, this limitation allows us to express  $\tilde{\gamma}_{v,r}^{(\alpha)}(\boldsymbol{\rho}, \tau)$  in terms of complementary error functions.

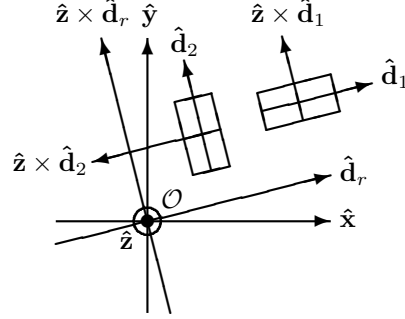


Figure 4.11: Two expansion functions placed in an orthogonal rotated reference frame.

To express  $\bar{\gamma}_{v,r}^{(\alpha)}(\boldsymbol{\rho}, \tau)$  in terms of complementary error functions, let us first define and summarize some properties of these functions, and of related repeated integrals [2, section 7.2]. The complementary error function is denoted by  $\text{erfc}(x)$ , and defined as

$$\text{erfc}(x) = 1 - \text{erf}(x) = \frac{2}{\sqrt{\pi}} \int_x^{\infty} \exp(-t^2) dt. \quad (4.57)$$

The so-called  $n$ 'th repeated integral of  $\text{erfc}(x)$  with  $n = 0, 1, 2, \dots$  (which arises in the study of diffusion and heat conduction) is denoted by  $\text{erfc}(n, x)$ , and is defined as

$$\text{erfc}(n, x) = \int_x^{\infty} \text{erfc}(n-1, t) dt. \quad (4.58)$$

Note that

$$\text{erfc}(-1, x) = \frac{2}{\sqrt{\pi}} \exp(-x^2), \quad \text{erfc}(0, x) = \text{erfc}(x). \quad (4.59)$$

Further  $\text{erfc}(n, x)$  with  $n = 1, 2, 3, \dots$  satisfies the following recurrence relation

$$2n \text{erfc}(n, x) = \text{erfc}(n-2, x) - 2x \text{erfc}(n-1, x). \quad (4.60)$$

Subsequently, we define scalar functions  $f_n(z)$  with  $n = 0, 1, 2, \dots$  that relate to the  $(n-1)$ 'th repeated integral of the complementary error function as follows

$$f_n(z) = (-2)^{n-2} \text{erfc}\left(n-1, \frac{z}{2}\right). \quad (4.61)$$

Note that  $\partial_z f_n(z) = f_{n-1}(z)$ . Explicit forms for the first five functions  $f_n(z)$

are given by

$$f_0(z) = \frac{1}{2\sqrt{\pi}} \exp(-Z^2), \quad (4.62)$$

$$f_1(z) = -\frac{1}{2} \operatorname{erfc}(Z), \quad (4.63)$$

$$f_2(z) = \frac{1}{\sqrt{\pi}} \exp(-Z^2) - Z \operatorname{erfc}(Z), \quad (4.64)$$

$$f_3(z) = \frac{1}{\sqrt{\pi}} Z \exp(-Z^2) - \left(Z^2 + \frac{1}{2}\right) \operatorname{erfc}(Z), \quad (4.65)$$

$$f_4(z) = \frac{2}{3\sqrt{\pi}} (Z^2 + 1) \exp(-Z^2) - Z \left(\frac{2}{3} Z^2 + 1\right) \operatorname{erfc}(Z), \quad (4.66)$$

where  $Z = \frac{1}{2}z$ . Then we define

$$\hat{F}_0(k, w) = \mathcal{S}(kw), \quad (4.67)$$

$$\hat{F}_1(k, w, v) = \mathcal{S}(kw)\mathcal{S}(kv), \quad (4.68)$$

$$\hat{F}_2(k, p, q) = \mathcal{T}(kp) - \mathcal{T}(-kq), \quad (4.69)$$

$$\hat{F}_3(k, w, a, b) = \mathcal{S}(kw)[\mathcal{T}(-ka) - \mathcal{T}(kb)], \quad (4.70)$$

$$\hat{F}_4(k, a, b, p, q) = [\mathcal{T}(-ka) - \mathcal{T}(kb)][\mathcal{T}(kp) - \mathcal{T}(-kq)], \quad (4.71)$$

$$\hat{F}_5(k, a, b, p, q) = k^{-2}[\mathcal{T}(-ka) - \mathcal{T}(kb)][\mathcal{T}(kp) - \mathcal{T}(-kq)], \quad (4.72)$$

$$\hat{F}_6(k, p, q) = k^{-1}[\mathcal{T}(kp) - \mathcal{T}(-kq)]. \quad (4.73)$$

By using the Fourier shift property [55, 111]

$$\frac{1}{2\pi} \int_{-\infty}^{\infty} \hat{F}_n(k) \exp(jk\nu) \exp(-k^2\tau^2\lambda) \exp(jkx) dk = \bar{F}_n(x + \nu, \tau), \quad (4.74)$$

we can find<sup>4</sup> the explicit forms for the exponentially regularized functions  $\bar{F}_n$ :

1.  $\bar{F}_0(x, \tau, w)$  where  $\bar{F}_0(x, 0, w) = \Pi(x, w)$  describes the single rectangle function. This is plotted in figure 4.12 for a number of small values for  $\tau$ .

$$\bar{F}_0(x, \tau, w) = \frac{1}{w} \left[ f_1 \left( \frac{x + \frac{1}{2}w}{\tau} \right) - f_1 \left( \frac{x - \frac{1}{2}w}{\tau} \right) \right], \quad (4.75)$$

<sup>4</sup>These functions could have been derived using a more general approach. However since we are dealing with specific shapes only, we have chosen this approach with efficient and dedicated computational implementations.

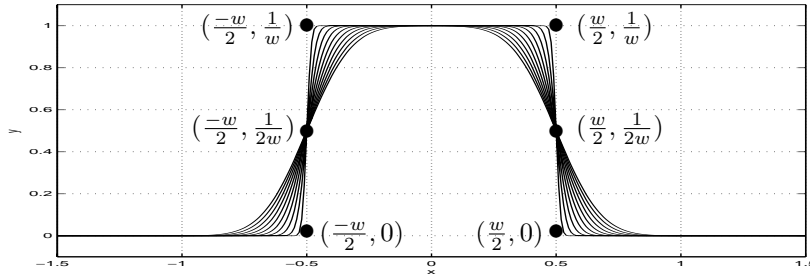


Figure 4.12:  $y = \bar{F}_0(x, \tau, w)$  as a function of  $x$ , with  $w = 1$  and for a number of small values for  $\tau$ .

2.  $\bar{F}_1(x, \tau, w, v)$  where  $\bar{F}_1(x, 0, w, v) = \bar{F}_0(x, 0, w) * \bar{F}_0(x, 0, v)$  describes the single rectangle function with sides of finite slope and can be written as the spatial convolution between two single rectangle functions. This is plotted in figure 4.13 for a number of small values for  $\tau$ .

$$\bar{F}_1(x, \tau, w, v) = \frac{\tau}{wv} \left[ f_2 \left( \frac{x - \frac{1}{2}(v+w)}{\tau} \right) - f_2 \left( \frac{x + \frac{1}{2}(v-w)}{\tau} \right) - f_2 \left( \frac{x - \frac{1}{2}(v-w)}{\tau} \right) + f_2 \left( \frac{x + \frac{1}{2}(v+w)}{\tau} \right) \right], \quad (4.76)$$

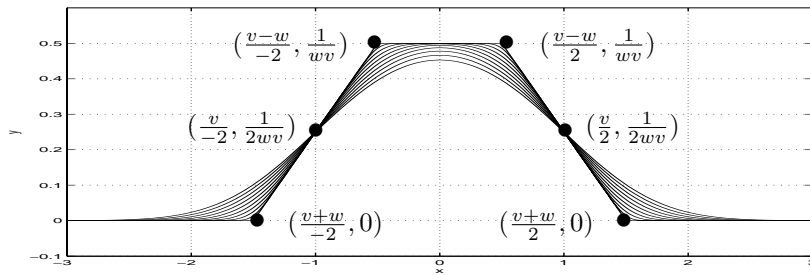


Figure 4.13:  $y = \bar{F}_1(x, \tau, w, v)$  as a function of  $x$ , with  $w = 1$ ,  $v = 2$  and for a number of small values for  $\tau$ .

3.  $\bar{F}_2(x, \tau, p, q)$  where  $\bar{F}_2(x, 0, p, q) = \bar{F}_0(x + \frac{1}{2}p, 0, p) - \bar{F}_0(x - \frac{1}{2}q, 0, q)$  describes the double rectangle function. This is plotted in figure 4.14 for a number of small values for  $\tau$ .

$$\bar{F}_2(x, \tau, p, q) = - \left( \frac{1}{p} + \frac{1}{q} \right) f_1 \left( \frac{x}{\tau} \right) + \frac{1}{p} f_1 \left( \frac{x+p}{\tau} \right) + \frac{1}{q} f_1 \left( \frac{x-q}{\tau} \right), \quad (4.77)$$



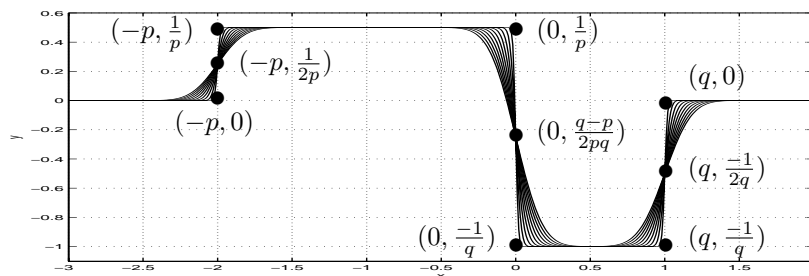


Figure 4.14:  $y = \bar{F}_2(x, \tau, p, q)$  as a function of  $x$ , with  $p = 2$ ,  $q = 1$  and for a number of small values for  $\tau$ .

4.  $\bar{F}_3(x, \tau, w, a, b)$  where  $\bar{F}_3(x, 0, w, a, b) = -\bar{F}_2(x, 0, b, a) * \bar{F}_0(x, 0, w)$  describes a double rectangle function with sides of finite slope and can be written as the spatial convolution between the single and the double rectangle function. This is plotted in figure 4.15 for a number of small values for  $\tau$ .

$$\begin{aligned} \bar{F}_3(x, \tau, w, a, b) = & \frac{\tau}{w} \left[ \left( \frac{1}{a} + \frac{1}{b} \right) f_2 \left( \frac{x + \frac{1}{2}w}{\tau} \right) - \right. \\ & \frac{1}{a} f_2 \left( \frac{x + \frac{1}{2}w - a}{\tau} \right) - \frac{1}{b} f_2 \left( \frac{x + \frac{1}{2}w + b}{\tau} \right) - \left. \left( \frac{1}{a} + \frac{1}{b} \right) \right. \\ & \left. f_2 \left( \frac{x - \frac{1}{2}w}{\tau} \right) + \frac{1}{a} f_2 \left( \frac{x - \frac{1}{2}w - a}{\tau} \right) + \frac{1}{b} f_2 \left( \frac{x - \frac{1}{2}w + b}{\tau} \right) \right], \end{aligned} \quad (4.78)$$

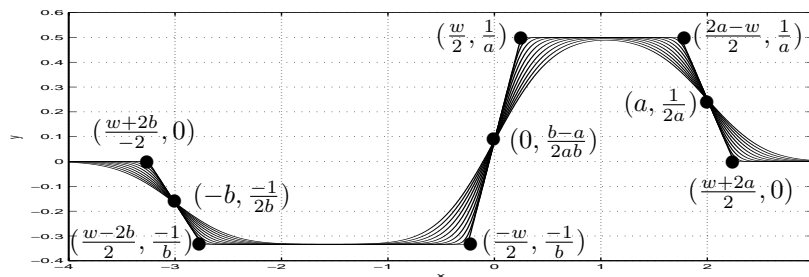


Figure 4.15:  $y = \bar{F}_3(x, \tau, w, a, b)$  as a function of  $x$ , with  $w = 0.5$ ,  $a = 2$ ,  $b = 3$  and for a number of small values for  $\tau$ .

5.  $\bar{F}_4(x, \tau, a, b, p, q)$  where  $\bar{F}_4(x, 0, a, b, p, q) = -\bar{F}_2(x, 0, b, a) * \bar{F}_2(x, 0, p, q)$  describes a piecewise linear function and can be written as the spatial convolution between two double rectangle functions. This is plotted in

figure 4.16 for a number of small values for  $\tau$ .

$$\begin{aligned} \bar{F}_4(x, \tau, a, b, p, q) = -\tau & \left[ \left( \frac{1}{p} + \frac{1}{q} \right) \left[ \left( \frac{1}{a} + \frac{1}{b} \right) f_2 \left( \frac{x}{\tau} \right) - \right. \right. \\ & \frac{1}{a} f_2 \left( \frac{x-a}{\tau} \right) - \frac{1}{b} f_2 \left( \frac{x+b}{\tau} \right) \left. \right] - \frac{1}{p} \left[ \left( \frac{1}{a} + \frac{1}{b} \right) f_2 \left( \frac{x+p}{\tau} \right) - \right. \\ & \frac{1}{a} f_2 \left( \frac{x+p-a}{\tau} \right) - \frac{1}{b} f_2 \left( \frac{x+p+b}{\tau} \right) \left. \right] - \frac{1}{q} \left[ \left( \frac{1}{a} + \frac{1}{b} \right) \right. \\ & \left. \left. f_2 \left( \frac{x-q}{\tau} \right) - \frac{1}{a} f_2 \left( \frac{x-q-a}{\tau} \right) - \frac{1}{b} f_2 \left( \frac{x-q+b}{\tau} \right) \right] \right], \end{aligned} \quad (4.79)$$

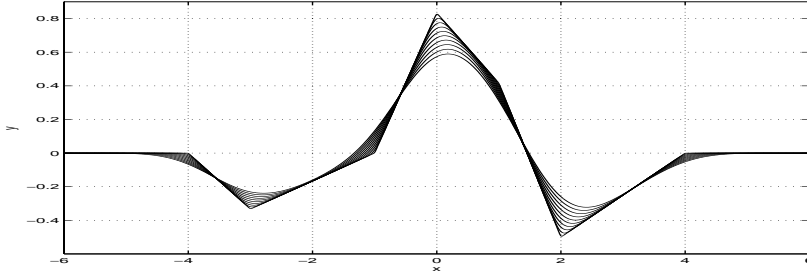


Figure 4.16:  $y = \bar{F}_4(x, \tau, a, b, p, q)$  as a function of  $x$ , with  $a = 2$ ,  $b = 3$ ,  $p = 1$ ,  $q = 2$  and for a number of small values for  $\tau$ .

6.  $\bar{F}_5(x, \tau, a, b, p, q)$  where  $\bar{F}_5(x, 0, a, b, p, q)$  describes a piecewise quadratic function. This is plotted in figure 4.17 for a number of small values for  $\tau$ .

$$\begin{aligned} \bar{F}_5(x, \tau, a, b, p, q) = \tau^3 & \left[ \left( \frac{1}{p} + \frac{1}{q} \right) \left[ \left( \frac{1}{a} + \frac{1}{b} \right) f_4 \left( \frac{x}{\tau} \right) - \right. \right. \\ & \frac{1}{a} f_4 \left( \frac{x-a}{\tau} \right) - \frac{1}{b} f_4 \left( \frac{x+b}{\tau} \right) \left. \right] - \frac{1}{p} \left[ \left( \frac{1}{a} + \frac{1}{b} \right) f_4 \left( \frac{x+p}{\tau} \right) - \right. \\ & \frac{1}{a} f_4 \left( \frac{x+p-a}{\tau} \right) - \frac{1}{b} f_4 \left( \frac{x+p+b}{\tau} \right) \left. \right] - \frac{1}{q} \left[ \left( \frac{1}{a} + \frac{1}{b} \right) \right. \\ & \left. \left. f_4 \left( \frac{x-q}{\tau} \right) - \frac{1}{a} f_4 \left( \frac{x-q-a}{\tau} \right) - \frac{1}{b} f_4 \left( \frac{x-q+b}{\tau} \right) \right] \right], \end{aligned} \quad (4.80)$$

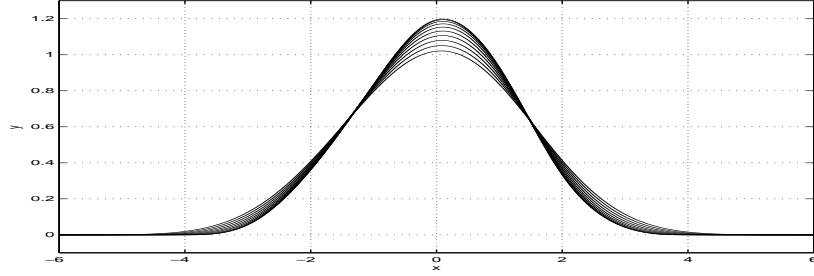


Figure 4.17:  $y = \bar{F}_5(x, \tau, a, b, p, q)$  as a function of  $x$ , with  $a = 2$ ,  $b = 3$ ,  $p = 1$ ,  $q = 2$  and for a number of small values for  $\tau$ .

7.  $\bar{F}_6(x, \tau, p, q)$  where  $\bar{F}_6(x, 0, p, q)$  describes a piecewise linear function. This is plotted in figure 4.18 for a number of small values for  $\tau$ .

$$\bar{F}_6(x, \tau, p, q) = -\tau \left[ \left( \frac{1}{p} + \frac{1}{q} \right) f_2 \left( \frac{x}{\tau} \right) - \frac{1}{p} f_2 \left( \frac{x+p}{\tau} \right) - \frac{1}{q} f_2 \left( \frac{x-q}{\tau} \right) \right]. \quad (4.81)$$

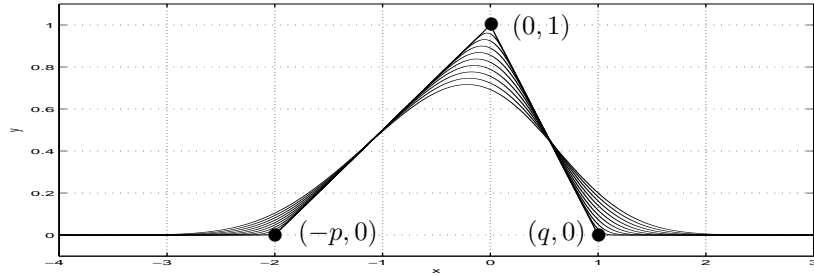


Figure 4.18:  $y = \bar{F}_6(x, \tau, p, q)$  as a function of  $x$ , with  $p = 2$ ,  $q = 1$  and for a number of small values for  $\tau$ .

Subsequently, we use the scalar exponential regularizations  $\bar{F}_n$  of  $\hat{F}_n$  to obtain closed-form expressions for  $\bar{\gamma}_{v,r}^{(\alpha)}$ . We introduce a new rotated frame of spectral coordinates

$$\mathbf{k}'_t = (k'_x, k'_y) = (\mathbf{k}_t \cdot \hat{\mathbf{d}}_r, \mathbf{k}_t \cdot (\hat{\mathbf{z}} \times \hat{\mathbf{d}}_r)). \quad (4.82)$$

Within this frame we can choose for  $\hat{\mathbf{d}}_v$  either  $\hat{\mathbf{d}}_r$ ,  $-\hat{\mathbf{d}}_r$ ,  $\hat{\mathbf{z}} \times \hat{\mathbf{d}}_r$  or  $\hat{\mathbf{d}}_r \times \hat{\mathbf{z}}$ . These choices correspond to the four possible orientations. Further  $d\mathbf{k}'_t = d\mathbf{k}_t$  and

$$\boldsymbol{\rho}' = (x', y') = ((\boldsymbol{\rho} + \boldsymbol{\rho}_r - \boldsymbol{\rho}_v) \cdot \hat{\mathbf{d}}_r, (\boldsymbol{\rho} + \boldsymbol{\rho}_r - \boldsymbol{\rho}_v) \cdot (\hat{\mathbf{z}} \times \hat{\mathbf{d}}_r)). \quad (4.83)$$

We can now recognize the following four different cases for the exponential regularization  $\bar{\gamma}_{v,r}^{(1)}$  of  $\hat{\gamma}_{v,r}^{(1)}$ :

1. If  $\hat{\mathbf{d}}_v = \hat{\mathbf{d}}_r$ , i.e.,  $\hat{\mathbf{d}}_r \parallel \hat{\mathbf{d}}_v$ , then

$$\begin{aligned}\hat{\gamma}_{v,r}^{(1)}(\mathbf{k}_t) &= -\exp(j\mathbf{k}_t \cdot [\boldsymbol{\rho}_r - \boldsymbol{\rho}_v])\hat{F}_1(k'_y, w_r, w_v)\hat{F}_4(k'_x, p_r, q_r, p_v, q_v), \\ \bar{\gamma}_{v,r}^{(1)}(\boldsymbol{\rho}, \tau) &= -\bar{F}_1(y', \tau^\lambda, w_r, w_v)\bar{F}_4(x', \tau^\lambda, p_r, q_r, p_v, q_v).\end{aligned}\quad (4.84)$$

2. If  $\hat{\mathbf{d}}_v = -\hat{\mathbf{d}}_r$ , i.e.,  $\hat{\mathbf{d}}_r \parallel \hat{\mathbf{d}}_v$ , then

$$\begin{aligned}\hat{\gamma}_{v,r}^{(1)}(\mathbf{k}_t) &= \exp(j\mathbf{k}_t \cdot [\boldsymbol{\rho}_r - \boldsymbol{\rho}_v])\hat{F}_1(k'_y, w_r, w_v)\hat{F}_4(k'_x, p_r, q_r, q_v, p_v), \\ \bar{\gamma}_{v,r}^{(1)}(\boldsymbol{\rho}, \tau) &= \bar{F}_1(y', \tau^\lambda, w_r, w_v)\bar{F}_4(x', \tau^\lambda, p_r, q_r, q_v, p_v).\end{aligned}\quad (4.85)$$

3. If  $\hat{\mathbf{d}}_v = \hat{\mathbf{z}} \times \hat{\mathbf{d}}_r$ , i.e.,  $\hat{\mathbf{d}}_r \perp \hat{\mathbf{d}}_v$ , then

$$\begin{aligned}\hat{\gamma}_{v,r}^{(1)}(\mathbf{k}_t) &= \exp(j\mathbf{k}_t \cdot [\boldsymbol{\rho}_r - \boldsymbol{\rho}_v])\hat{F}_3(k'_y, w_r, q_v, p_v)\hat{F}_3(k'_x, w_v, p_r, q_r), \\ \bar{\gamma}_{v,r}^{(1)}(\boldsymbol{\rho}, \tau) &= \bar{F}_3(y', \tau^\lambda, w_r, q_v, p_v)\bar{F}_3(x', \tau^\lambda, w_v, p_r, q_r).\end{aligned}\quad (4.86)$$

4. If  $\hat{\mathbf{d}}_v = \hat{\mathbf{d}}_r \times \hat{\mathbf{z}}$ , i.e.,  $\hat{\mathbf{d}}_r \perp \hat{\mathbf{d}}_v$ , then

$$\begin{aligned}\hat{\gamma}_{v,r}^{(1)}(\mathbf{k}_t) &= -\exp(j\mathbf{k}_t \cdot [\boldsymbol{\rho}_r - \boldsymbol{\rho}_v])\hat{F}_3(k'_y, w_r, p_v, q_v)\hat{F}_3(k'_x, w_v, p_r, q_r), \\ \bar{\gamma}_{v,r}^{(1)}(\boldsymbol{\rho}, \tau) &= -\bar{F}_3(y', \tau^\lambda, w_r, p_v, q_v)\bar{F}_3(x', \tau^\lambda, w_v, p_r, q_r).\end{aligned}\quad (4.87)$$

Further, we can recognize the following two different cases for the exponential regularization  $\bar{\gamma}_{v,r}^{(2)}$  of  $\hat{\gamma}_{v,r}^{(2)}$ :

1. If  $\hat{\mathbf{d}}_v = \hat{\mathbf{d}}_r$ , i.e.,  $\hat{\mathbf{d}}_r \parallel \hat{\mathbf{d}}_v$ , then

$$\begin{aligned}\hat{\gamma}_{v,r}^{(2)}(\mathbf{k}_t) &= \exp(j\mathbf{k}_t \cdot [\boldsymbol{\rho}_r - \boldsymbol{\rho}_v])\hat{F}_1(k'_y, w_r, w_v)\hat{F}_5(k'_x, p_r, q_r, p_v, q_v), \\ \bar{\gamma}_{v,r}^{(2)}(\boldsymbol{\rho}, \tau) &= \bar{F}_1(y', \tau^\lambda, w_r, w_v)\bar{F}_5(x', \tau^\lambda, p_r, q_r, p_v, q_v).\end{aligned}\quad (4.88)$$

2. If  $\hat{\mathbf{d}}_v = -\hat{\mathbf{d}}_r$ , i.e.,  $\hat{\mathbf{d}}_r \parallel \hat{\mathbf{d}}_v$ , then

$$\begin{aligned}\hat{\gamma}_{v,r}^{(2)}(\mathbf{k}_t) &= -\exp(j\mathbf{k}_t \cdot [\boldsymbol{\rho}_r - \boldsymbol{\rho}_v])\hat{F}_1(k'_y, w_r, w_v)\hat{F}_5(k'_x, p_r, q_r, q_v, p_v), \\ \bar{\gamma}_{v,r}^{(2)}(\boldsymbol{\rho}, \tau) &= -\bar{F}_1(y', \tau^\lambda, w_r, w_v)\bar{F}_5(x', \tau^\lambda, p_r, q_r, q_v, p_v).\end{aligned}\quad (4.89)$$

Note that  $\bar{\gamma}_{v,r}^{(2)}(\boldsymbol{\rho}, \tau)$  is zero if  $\hat{\mathbf{d}}_r \perp \hat{\mathbf{d}}_v$ .

## Numerical Results

Finally, we show the numerical results of the complete acceleration technique for this type of regularization. The configuration under consideration is the simple basic structure described in section 4.1. Further we take  $\lambda = 3$ ,  $\tau_1 = 0.1646$  and  $\tau_2 = 1.5$ . The integration over  $\tau$  is performed by using a repeated fourth-order Gaussian quadrature integration rule on 601 subintervals of equal length on the integration interval  $(0, \tau_2]$ . In figure 4.19 we have plotted the integrand

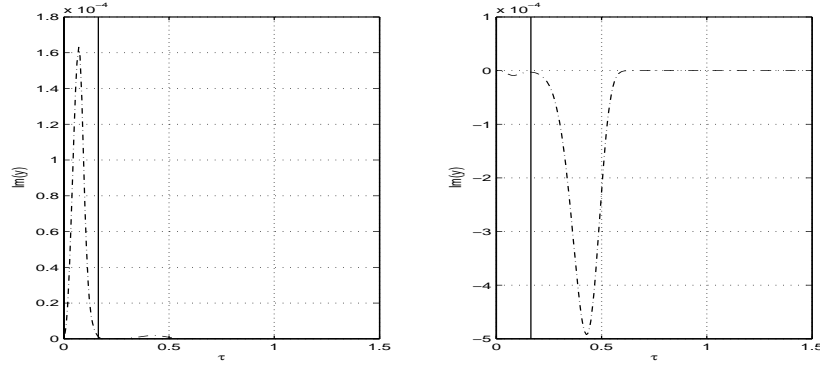


Figure 4.19:  $y = \text{Im}(\text{integrand of } \zeta_{1,1}^{(\alpha)})$  (dashed-dotted curve) as a function of  $\tau$ . Transition point at  $\tau = \tau_1 = 0.1646$  (vertical solid line). Left figure for  $\alpha = 1$  and right figure for  $\alpha = 2$ .

of  $\zeta_{1,1}^{(\alpha)}$  as a function of  $\tau$  at frequency = 8 [GHz] for the contribution  $A_{1,1}$  to  $L$ . The broadside term in the summation for large  $\tau$  has not been separated and not been treated analytically. Note that the integrand decays exponentially for large  $\tau$ , and is continuous at the transition point  $\tau = \tau_1$ , which shows a correct implementation of the evaluation of the integrand for small and large  $\tau$ . In figure 4.20 we have plotted the minimum required index  $j$  for the partial sum in the integrand of  $\zeta_{1,1}^{(\alpha)}$  to converge with a relative error of 0.1[%] as a function of  $\tau$ . These figures show that in general only a single term is needed to obtain the relative error of 0.1[%]. Only near the transition point less than ten terms are needed. In figure 4.21 we have plotted the relative error of  $\xi_{v,r}^{(\alpha)} + \zeta_{v,r}^{(\alpha)}$  as a function of  $\{v, r\}$  at frequency = 8[GHz]. In figure 4.22 we have plotted the relative error of the contribution  $A_{v,r}$  to  $L$  at frequency = 8[GHz]. These relative errors are defined with respect to the single maximum absolute value out of all  $\{v, r\}$ . These figures show that each element for the matrix contribution  $A_{v,r}$  to  $L$  has a low relative error. In figure 4.23 we have plotted the final reflection and transmission coefficients as a function of frequency. Note that there is an excellent agreement between the unaccelerated and the accelerated computational method.

The asymmetry in the relative errors of  $\xi_{v,r}^{(\alpha)} + \zeta_{v,r}^{(\alpha)}$  for  $\alpha = 1$  and  $\alpha = 2$  is caused by the difference of convergence behavior of  $\xi_{v,r}^{(\alpha)}$  for  $\alpha = 1$  and  $\alpha = 2$ , and has already been discussed in section 4.2.

#### 4.4.2 Rooftop Function

In this section we evaluate  $\bar{\gamma}_{v,r}^{(\alpha)}(\boldsymbol{\rho}, \tau)$  if we use the rooftop function for both the expansion and weighting functions. This case is more general than the previous one; we are not restricted to the placement in the orthogonal grid, which allows us to describe more arbitrarily shaped and oriented metal patches and

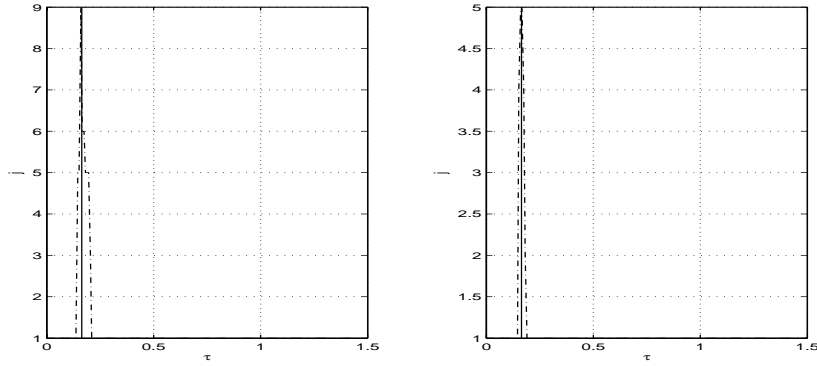


Figure 4.20: Minimum required  $j$  for series in integrand of  $\zeta_{1,1}^{(\alpha)}$  to converge with a relative error of 0.1[%] (dashed-dotted curve) as a function of  $\tau$ . Transition point at  $\tau = \tau_1 = 0.1646$  (vertical solid line). Left figure for  $\alpha = 1$  and right figure for  $\alpha = 2$ .

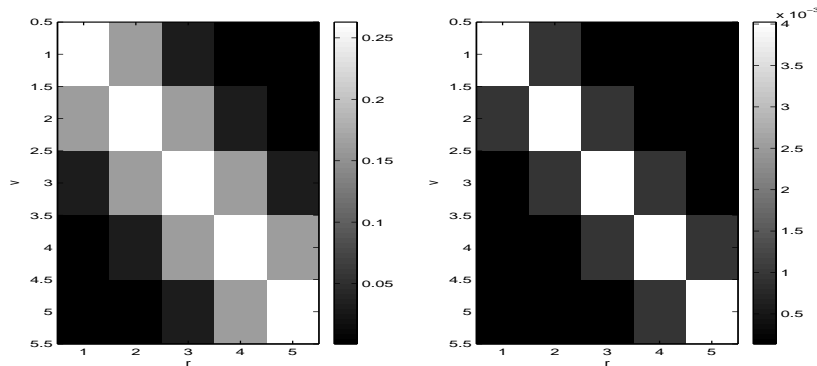


Figure 4.21: Absolute error [%] in  $\xi_{v,r}^{(\alpha)} + \zeta_{v,r}^{(\alpha)}$  as a function of  $\{v, r\}$ . Left figure for  $\alpha = 1$  and right figure for  $\alpha = 2$ .

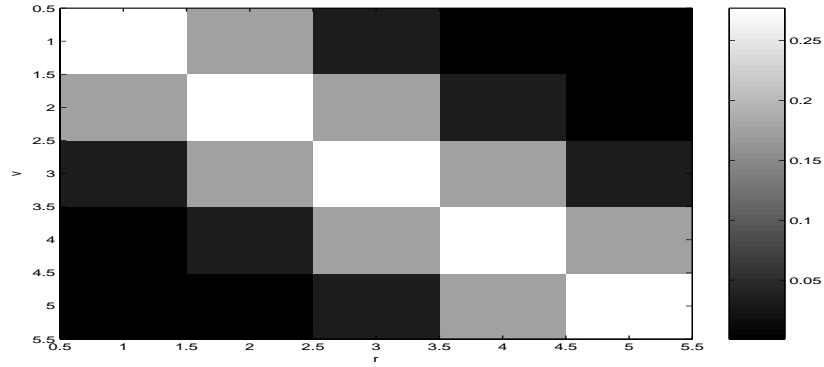


Figure 4.22: Absolute error[%] in the contribution  $A_{v,r}$  as a function of  $\{v, r\}$ .

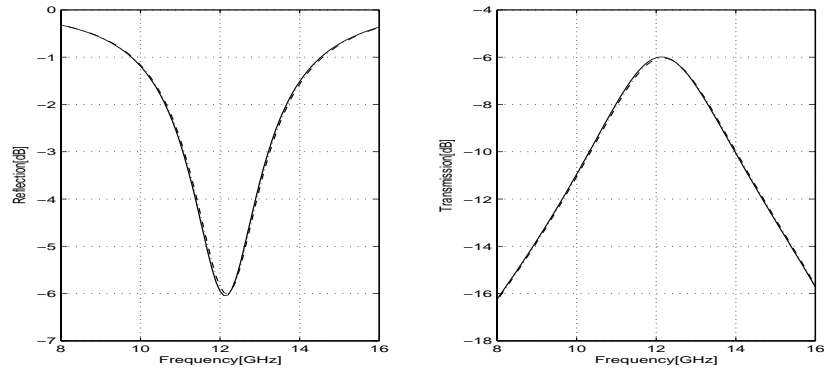


Figure 4.23: Original non-accelerated (solid curve) and accelerated (dashed-dotted curve) as a function of frequency[GHz]. Left figure for power reflection coefficient[dB] and right figure for power transmission coefficient[dB].

apertures. For example we can model the unknown electric surface current on two arbitrarily oriented and separated rectangular patches within a single unit cell. In this case, we can express  $\bar{\gamma}_{v,r}^{(\alpha)}(\boldsymbol{\rho}, \tau)$  as a convolution of two analytically known functions, both with "almost" compact support.  $\bar{\gamma}_{v,r}^{(\alpha)}(\boldsymbol{\rho}, \tau)$  is given by equation 4.40

$$\bar{\gamma}_{v,r}^{(\alpha)}(\boldsymbol{\rho}, \tau) = \mathcal{F}^{-1} \left\{ \exp(-k_t^2 \tau^{2\lambda}) \hat{\gamma}_{v,r}^{(\alpha)}(\mathbf{k}_t) \right\}. \quad (4.90)$$

with

$$\hat{\gamma}_{v,r}^{(\alpha)}(\mathbf{k}_t) = \begin{cases} [\mathbf{j}\mathbf{k}_t \cdot \hat{\mathbf{g}}_r^*(\mathbf{k}_t)] [\mathbf{j}\mathbf{k}_t \cdot \hat{\mathbf{g}}_v(\mathbf{k}_t)] & \text{if } \alpha = 1, \\ \hat{\mathbf{g}}_r^*(\mathbf{k}_t) \cdot \hat{\mathbf{g}}_v(\mathbf{k}_t) & \text{if } \alpha = 2. \end{cases} \quad (4.91)$$

Since  $\mathbf{g}_r(\boldsymbol{\rho})$  is real-valued, the Fourier counterpart of  $\hat{\mathbf{g}}_r^*(\mathbf{k}_t)$  is  $\mathbf{g}_r(-\boldsymbol{\rho})$ . We can now write the expression for  $\bar{\gamma}_{v,r}^{(\alpha)}(\boldsymbol{\rho}, \tau)$  as

$$\bar{\gamma}_{v,r}^{(\alpha)}(\boldsymbol{\rho}, \tau) = \begin{cases} \bar{a}_r(\boldsymbol{\rho}, \tau) * \bar{b}_v(\boldsymbol{\rho}, \tau) & \text{if } \alpha = 1, \\ \bar{\mathbf{c}}_r(\boldsymbol{\rho}, \tau) \cdot * \bar{\mathbf{d}}_v(\boldsymbol{\rho}, \tau) & \text{if } \alpha = 2, \end{cases} \quad (4.92)$$

in which  $\cdot *$  denotes a combination of first an inner product between the vectors  $\bar{\mathbf{c}}_r$  and  $\bar{\mathbf{d}}_v$ , and subsequently a convolution over  $\boldsymbol{\rho}$ . Further

$$\bar{a}_r(\boldsymbol{\rho}, \tau) = -\bar{b}_r(-\boldsymbol{\rho}, \tau), \quad \bar{\mathbf{d}}_v(\boldsymbol{\rho}, \tau) = \mathcal{F}^{-1} \left\{ \hat{\mathbf{g}}_v(\mathbf{k}_t) \exp\left(-\frac{1}{2}k_t^2 \tau^{2\lambda}\right) \right\}, \quad (4.93)$$

and

$$\bar{\mathbf{c}}_r(\boldsymbol{\rho}, \tau) = \bar{\mathbf{d}}_r(-\boldsymbol{\rho}, \tau), \quad \bar{b}_v(\boldsymbol{\rho}, \tau) = \mathcal{F}^{-1} \left\{ \mathbf{j}\mathbf{k}_t \cdot \hat{\mathbf{g}}_v(\mathbf{k}_t) \exp\left(-\frac{1}{2}k_t^2 \tau^{2\lambda}\right) \right\}. \quad (4.94)$$

Note that  $\bar{a}_r$ ,  $\bar{b}_v$ ,  $\bar{\mathbf{c}}_r$  and  $\bar{\mathbf{d}}_v$  are all of "almost" compact support in  $\boldsymbol{\rho}$  for small  $\tau$ . Further, equation 4.92 shows that  $\bar{\gamma}_{v,r}^{(\alpha)}(\boldsymbol{\rho}, \tau)$  can be written as a two-dimensional convolution of two functions. Since these functions are analytically known (as will be shown later on in this section) and both of "almost" compact support, the convolution can be numerically approximated by using two-dimensional fast Fourier transformations (FFT's) [111]. We can rewrite  $\bar{\gamma}_{v,r}^{(1)}(\boldsymbol{\rho}, \tau)$  as

$$\begin{aligned} \bar{\gamma}_{v,r}^{(1)}(\boldsymbol{\rho}', \tau) &= \bar{a}_r(\boldsymbol{\rho}, \tau) * \bar{b}_v(\boldsymbol{\rho}, \tau)|_{\boldsymbol{\rho}=\boldsymbol{\rho}'} \\ &= -\bar{b}_r(-\boldsymbol{\rho}, \tau) * \bar{b}_v(\boldsymbol{\rho}, \tau)|_{\boldsymbol{\rho}=\boldsymbol{\rho}'} \\ &= \bar{a}_r(\boldsymbol{\rho} - \boldsymbol{\rho}_r, \tau) * \bar{b}_v(\boldsymbol{\rho} + \boldsymbol{\rho}_v, \tau)|_{\boldsymbol{\rho}=\boldsymbol{\rho}'+\boldsymbol{\rho}_r-\boldsymbol{\rho}_v} \\ &= -\bar{b}_r(-\boldsymbol{\rho} + \boldsymbol{\rho}_r, \tau) * \bar{b}_v(\boldsymbol{\rho} + \boldsymbol{\rho}_v, \tau)|_{\boldsymbol{\rho}=\boldsymbol{\rho}'+\boldsymbol{\rho}_r-\boldsymbol{\rho}_v}, \end{aligned} \quad (4.95)$$

where  $\boldsymbol{\rho}_r$  and  $\boldsymbol{\rho}_v$  denote the translation vector from the origin to a reference point in the rooftop weighting and expansion function, respectively. Note that

1.  $\bar{a}_r(\boldsymbol{\rho}, \tau) = -\bar{b}_r(-\boldsymbol{\rho}, \tau)$  denotes a mirrored  $\bar{b}_r(\boldsymbol{\rho}, \tau)$ ,



2.  $\bar{a}_r(\boldsymbol{\rho} - \boldsymbol{\rho}_r, \tau) = -\bar{b}_r(-\boldsymbol{\rho} + \boldsymbol{\rho}_r, \tau)$  denotes a shifted and mirrored  $\bar{b}_r(\boldsymbol{\rho}, \tau)$ ,
3.  $\bar{b}_v(\boldsymbol{\rho} + \boldsymbol{\rho}_v, \tau)$  denotes a shifted  $\bar{b}_v(\boldsymbol{\rho}, \tau)$ .

The starting point for the evaluation of  $\bar{\gamma}_{v,r}^{(1)}(\boldsymbol{\rho}', \tau)$  is the knowledge of  $\bar{b}_r(-\boldsymbol{\rho} + \boldsymbol{\rho}_r, \tau)$  and  $\bar{b}_v(\boldsymbol{\rho} + \boldsymbol{\rho}_v, \tau)$ . Similarly, we can rewrite  $\bar{\gamma}_{v,r}^{(2)}(\boldsymbol{\rho}, \tau)$  as

$$\begin{aligned}
\bar{\gamma}_{v,r}^{(2)}(\boldsymbol{\rho}', \tau) &= \bar{\mathbf{c}}_r(\boldsymbol{\rho}, \tau) \cdot * \bar{\mathbf{d}}_v(\boldsymbol{\rho}, \tau) |_{\boldsymbol{\rho}=\boldsymbol{\rho}'} \\
&= \bar{\mathbf{d}}_r(-\boldsymbol{\rho}, \tau) \cdot * \bar{\mathbf{d}}_v(\boldsymbol{\rho}, \tau) |_{\boldsymbol{\rho}=\boldsymbol{\rho}'} \\
&= \bar{\mathbf{c}}_r(\boldsymbol{\rho} - \boldsymbol{\rho}_r, \tau) \cdot * \bar{\mathbf{d}}_v(\boldsymbol{\rho} + \boldsymbol{\rho}_v, \tau) |_{\boldsymbol{\rho}=\boldsymbol{\rho}'+\boldsymbol{\rho}_r-\boldsymbol{\rho}_v} \\
&= \bar{\mathbf{d}}_r(-\boldsymbol{\rho} + \boldsymbol{\rho}_r, \tau) \cdot * \bar{\mathbf{d}}_v(\boldsymbol{\rho} + \boldsymbol{\rho}_v, \tau) |_{\boldsymbol{\rho}=\boldsymbol{\rho}'+\boldsymbol{\rho}_r-\boldsymbol{\rho}_v}.
\end{aligned} \tag{4.96}$$

Note that

1.  $\bar{\mathbf{c}}_r(\boldsymbol{\rho}, \tau) = \bar{\mathbf{d}}_r(-\boldsymbol{\rho}, \tau)$  denotes a mirrored  $\bar{\mathbf{d}}_r(\boldsymbol{\rho}, \tau)$ ,
2.  $\bar{\mathbf{c}}_r(\boldsymbol{\rho} - \boldsymbol{\rho}_r, \tau) = \bar{\mathbf{d}}_r(-\boldsymbol{\rho} + \boldsymbol{\rho}_r, \tau)$  denotes a shifted and mirrored  $\bar{\mathbf{d}}_r(\boldsymbol{\rho}, \tau)$ ,
3.  $\bar{\mathbf{d}}_v(\boldsymbol{\rho} + \boldsymbol{\rho}_v, \tau)$  denotes a shifted  $\bar{\mathbf{d}}_v(\boldsymbol{\rho}, \tau)$ .

The starting point for the evaluation of  $\bar{\gamma}_{v,r}^{(2)}(\boldsymbol{\rho}', \tau)$  is the knowledge of  $\bar{\mathbf{d}}_r(-\boldsymbol{\rho} + \boldsymbol{\rho}_r, \tau)$  and  $\bar{\mathbf{d}}_v(\boldsymbol{\rho} + \boldsymbol{\rho}_v, \tau)$ . Within equations 4.93 and 4.94, the expressions

$$\bar{\mathbf{d}}_v(\boldsymbol{\rho}, \tau) = \mathcal{F}^{-1} \left\{ \hat{\mathbf{g}}_v(\mathbf{k}_t) \exp \left( -\frac{1}{2} k_t^2 \tau^{2\lambda} \right) \right\}, \tag{4.97}$$

and

$$\bar{b}_v(\boldsymbol{\rho}, \tau) = \mathcal{F}^{-1} \left\{ \mathbf{j} \mathbf{k}_t \cdot \hat{\mathbf{g}}_v(\mathbf{k}_t) \exp \left( -\frac{1}{2} k_t^2 \tau^{2\lambda} \right) \right\}, \tag{4.98}$$

remain to be evaluated. To obtain closed form expressions for  $\bar{\mathbf{d}}_v$  and  $\bar{b}_v$ , we use the known spectrum  $\hat{\mathbf{g}}_v(\mathbf{k}_t)$  of a rooftop function (equation F.5 in appendix F) given by

$$\hat{\mathbf{g}}_v(\mathbf{k}_t) = \hat{\mathbf{d}}_v \exp(-\mathbf{j} \mathbf{k}_t \cdot \boldsymbol{\rho}_v) \hat{\Lambda}(\mathbf{k}_t \cdot \hat{\mathbf{d}}_v, p_v, q_v) \hat{\Pi}(\mathbf{k}_t \cdot (\hat{\mathbf{z}} \times \hat{\mathbf{d}}_v), w_v). \tag{4.99}$$

See section 3.7.4 for a detailed explanation of the rooftop function. See figure 4.10 for a graphical representation of the domain, vectors and scalars used in the rooftop function.

Subsequently, by using the functions  $\hat{F}_0$ ,  $\hat{F}_2$  and  $\hat{F}_6$  defined by equations 4.67, 4.69 and 4.73, respectively, in section 4.4.1, we can write  $\mathbf{j} \mathbf{k}_t \cdot \hat{\mathbf{g}}_v(\mathbf{k}_t)$  as

$$\mathbf{j} \mathbf{k}_t \cdot \hat{\mathbf{g}}_v(\mathbf{k}_t) = \exp(-\mathbf{j} \mathbf{k}_t \cdot \boldsymbol{\rho}_v) \hat{F}_2(k'_x, p_v, q_v) \hat{F}_0(k'_y, w_v), \tag{4.100}$$

while we can write  $\hat{\mathbf{g}}_v(\mathbf{k}_t)$  as

$$\hat{\mathbf{g}}_v(\mathbf{k}_t) = \hat{\mathbf{d}}_v \exp(-\mathbf{j} \mathbf{k}_t \cdot \boldsymbol{\rho}_v) \hat{F}_6(k'_x, p_v, q_v) \hat{F}_0(k'_y, w_v), \tag{4.101}$$

with

$$\mathbf{k}'_t = (k'_x, k'_y) = (\mathbf{k}_t \cdot \hat{\mathbf{d}}_v, \mathbf{k}_t \cdot (\hat{\mathbf{z}} \times \hat{\mathbf{d}}_v)). \quad (4.102)$$

By using the corresponding exponential regularizations  $\bar{F}_0$ ,  $\bar{F}_2$  and  $\bar{F}_6$  given by equations 4.75, 4.77 and 4.81, respectively, in section 4.4.1, we can explicitly write  $\bar{b}_v$  as

$$\bar{b}_v(\boldsymbol{\rho}, \tau) = \bar{F}_2 \left( x', \frac{\tau^\lambda}{\sqrt{2}}, p_v, q_v \right) \bar{F}_0 \left( y', \frac{\tau^\lambda}{\sqrt{2}}, w_v \right), \quad (4.103)$$

while we can explicitly write  $\bar{\mathbf{d}}_v$  as

$$\bar{\mathbf{d}}_v(\boldsymbol{\rho}, \tau) = \hat{\mathbf{d}}_v \bar{F}_6 \left( x', \frac{\tau^\lambda}{\sqrt{2}}, p_v, q_v \right) \bar{F}_0 \left( y', \frac{\tau^\lambda}{\sqrt{2}}, w_v \right), \quad (4.104)$$

with

$$\boldsymbol{\rho}' = (x', y') = ((\boldsymbol{\rho} - \boldsymbol{\rho}_v) \cdot \hat{\mathbf{d}}_v, (\boldsymbol{\rho} - \boldsymbol{\rho}_v) \cdot (\hat{\mathbf{z}} \times \hat{\mathbf{d}}_v)). \quad (4.105)$$

The computational structure to calculate  $\bar{\gamma}_{v,r}^{(\alpha)}(D\mathbf{m}_j, \tau)$  has the following form:

```

function Calculate  $\bar{\gamma}_{v,r}^{(\alpha)}(D\mathbf{m}_j, \tau)$ 
  for  $\tau = 0^+ : d\tau : \tau_1$ 
    for  $v = 1 : NrOfExpansionFunctions$ 
      Calculate and Store  $\bar{\mathbf{d}}_v(\boldsymbol{\rho} + \boldsymbol{\rho}_v, \tau)$  on Grid( $\boldsymbol{\rho}$ );
      Calculate and Store  $\bar{b}_v(\boldsymbol{\rho} + \boldsymbol{\rho}_v, \tau)$  on Grid( $\boldsymbol{\rho}$ );
    endfor;
    for  $v = 1 : NrOfExpansionFunctions$ 
      for  $r = 1 : NrOfExpansionFunctions$ 
        Calculate and Store  $\bar{\mathbf{d}}_r(-\boldsymbol{\rho} + \boldsymbol{\rho}_r, \tau) * \bar{\mathbf{d}}_v(\boldsymbol{\rho} + \boldsymbol{\rho}_v, \tau)$ ;
        Calculate and Store  $\bar{b}_r(-\boldsymbol{\rho} + \boldsymbol{\rho}_r, \tau) * \bar{b}_v(\boldsymbol{\rho} + \boldsymbol{\rho}_v, \tau)$ ;
      for  $j = 1 : NrOfModes$ 
         $\boldsymbol{\rho}' = D\mathbf{m}_j + \boldsymbol{\rho}_r - \boldsymbol{\rho}_v$ ;
        Interpolate  $\bar{\gamma}_{v,r}^{(\alpha)}(\boldsymbol{\rho}', \tau)$  from Grid( $\boldsymbol{\rho}$ );
      endfor;
    endfor;
  endfor;
return.

```

### Numerical Results

Finally, we show the numerical results of the complete acceleration technique for this type of regularization. The configuration under consideration is the simple basic structure described in section 4.1. Further we take  $\lambda = 3$ ,  $\tau_1 = 0.1646$  and  $\tau_2 = 1.5$ . The integration over  $\tau$  is performed by using a repeated fourth-order Gaussian quadrature integration rule on 601 subintervals of equal length on the integration interval  $(0, \tau_2]$ . In figure 4.24 we have plotted  $\bar{b}_1(\boldsymbol{\rho}, \tau)$  and  $\bar{\mathbf{d}}_1(\boldsymbol{\rho}, \tau)$  as a function of  $\boldsymbol{\rho} = (x, y)$  with  $\tau \approx 0$ . In figure 4.25 we have plotted  $\bar{\gamma}_{1,1}^{(\alpha)}(\boldsymbol{\rho}, \tau)$  as a function of  $\boldsymbol{\rho} = (x, y)$  with  $\tau \approx 0$ . These figures show that these functions are of "almost" compact support. The numerical convolution is done by using FFT's; we have used a 64 by 64 grid which reaches over a single unit cell. In figure 4.26 we have plotted the integrand of  $\zeta_{1,1}^{(\alpha)}$  as a function of  $\tau$  at frequency = 8[GHz] for the contribution  $A_{1,1}$  to  $L$ . The broadside term in the summation for large  $\tau$  has not been separated and treated analytically. Note that the integrand decreases exponentially for large  $\tau$ , and is continuous at the transition point  $\tau = \tau_1$ , which shows a correct implementation of the evaluation of the integrand for small and large  $\tau$ . For  $\tau \in (0, \tau_1]$  we have only taken into account a single term with index  $(m_{1;j}, m_{2;j}) = (0, 0)$ . In figure 4.27 we have plotted the minimum required index  $j$  for the partial sum in the integrand of  $\zeta_{1,1}^{(\alpha)}$  to converge with a relative error of 0.1[%] as a function of  $\tau$ . For  $\tau \in (0, \tau_1]$  this is set to one in this figure. These figures show that for most  $\tau \in [\tau_1, \tau_2]$  only a single term is needed to obtain the relative error of 0.1[%]. Only near the transition point less than ten terms are needed. In figure 4.28 we have plotted the relative error of  $\xi_{v,r}^{(\alpha)} + \zeta_{v,r}^{(\alpha)}$  as a function of  $\{v, r\}$  at frequency = 8 [GHz]. These figures show that each element of  $\xi_{v,r}^{(\alpha)} + \zeta_{v,r}^{(\alpha)}$  has a low relative error for  $\alpha = 2$  and that some elements have a relatively high relative error of 3.5[%] for  $\alpha = 1$ . In figure 4.29 we have plotted the relative error of the contribution  $A_{v,r}$  to  $L$  at frequency = 8[GHz]. These relative errors are defined with respect to the single maximum absolute value out of all  $\{v, r\}$ . This figure shows that some elements for the matrix contribution  $A_{v,r}$  to  $L$  have a relatively high relative error of 3.5[%]. Despite this high relative error, figure 4.30 shows that for the final reflection and transmission coefficients, as a function of frequency, there is an excellent agreement between the unaccelerated and the accelerated computational method.

The asymmetry in the relative errors of  $\xi_{v,r}^{(\alpha)} + \zeta_{v,r}^{(\alpha)}$  for  $\alpha = 1$  and  $\alpha = 2$  is caused by two effects. The first effect is already described in section 4.2 and is caused by the difference of convergence behavior of  $\xi_{v,r}^{(\alpha)}$  for  $\alpha = 1$  and  $\alpha = 2$ . The second effect is caused by the fact that the outcome of the integration over  $\tau$  for  $\alpha = 1$  is determined by the accuracy for  $\tau < \tau_1$ , whereas for  $\alpha = 2$  by the accuracy for  $\tau > \tau_1$ . This can be seen in figure 4.26. Since we take only into account a single term for  $\tau < \tau_1$ , we lose accuracy compared to the summation for  $\tau > \tau_1$ . Hence,  $\zeta_{v,r}^{(1)}$  is less accurate than  $\zeta_{v,r}^{(2)}$ .

Even though we have limited the summation for  $\tau < \tau_1$  to a single term, we obtain very accurate results for the reflection and transmission coefficients as

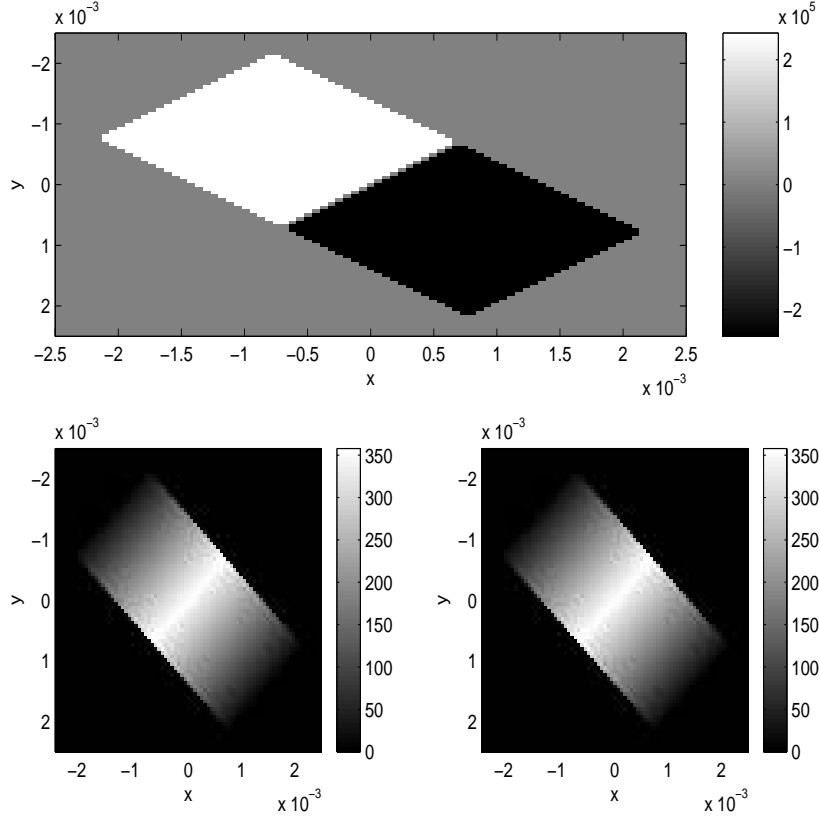


Figure 4.24: Top figure for  $\bar{b}_1(\boldsymbol{\rho}, \tau)$ , bottom left figure for  $\bar{d}_{1,x}(\boldsymbol{\rho}, \tau)$  and bottom right figure for  $\bar{d}_{1,y}(\boldsymbol{\rho}, \tau)$  as a function of  $\boldsymbol{\rho} = (x, y)$  with  $\tau \approx 0$ .

a function of frequency. Taking into account more terms would require larger two-dimensional grids to sample  $\bar{b}_v(\boldsymbol{\rho}, \tau)$  and  $\bar{\mathbf{d}}_v(\boldsymbol{\rho}, \tau)$ . This is not necessary since for small  $\tau$ ,  $\bar{b}_v(\boldsymbol{\rho}, \tau)$  and  $\bar{\mathbf{d}}_v(\boldsymbol{\rho}, \tau)$  have already small bandwidths, i.e., are of "almost" compact support.

#### 4.4.3 RWG Function

In this section, we evaluate  $\bar{\gamma}_{v,r}^{(\alpha)}(\boldsymbol{\rho}, \tau)$  if we use the RWG function for both the expansion and weighting functions. In this case, we can express  $\bar{\gamma}_{v,r}^{(\alpha)}(\boldsymbol{\rho}, \tau)$  as a convolution of two numerically approximated functions both with "almost" compact support.  $\bar{\gamma}_{v,r}^{(\alpha)}(\boldsymbol{\rho}, \tau)$  is given by equation 4.40

$$\bar{\gamma}_{v,r}^{(\alpha)}(\boldsymbol{\rho}, \tau) = \mathcal{F}^{-1} \left\{ \exp(-k_t^2 \tau^{2\lambda}) \hat{\gamma}_{v,r}^{(\alpha)}(\mathbf{k}_t) \right\}, \quad (4.106)$$

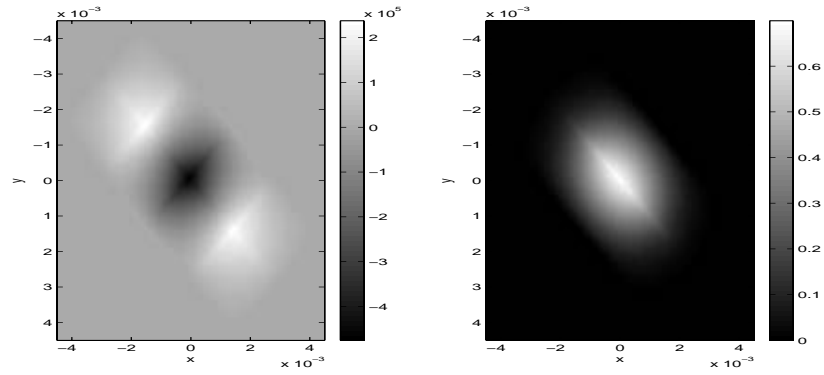


Figure 4.25:  $\bar{\gamma}_{1,1}^{(\alpha)}(\rho, \tau)$  as a function of  $\rho = (x, y)$  with  $\tau \approx 0$ . Left figure for  $\alpha = 1$  and right figure for  $\alpha = 2$ .

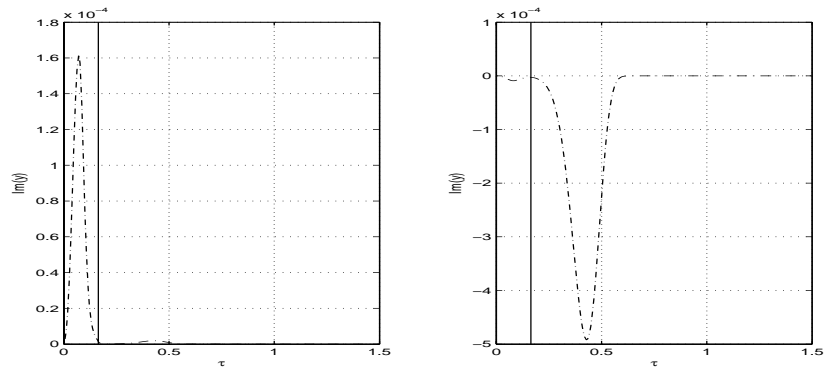


Figure 4.26:  $y = \text{Im}(\text{integrand of } \zeta_{1,1}^{(\alpha)})$  (dashed-dotted curve) as a function of  $\tau$ . Transition point at  $\tau = \tau_1 = 0.1646$  (vertical solid line). Left figure for  $\alpha = 1$  and right figure for  $\alpha = 2$ .

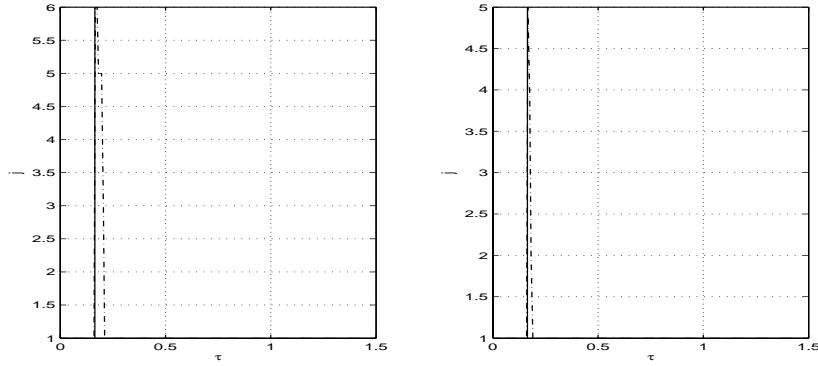


Figure 4.27: Minimum required  $j$  for partial sum in integrand of  $\zeta_{1,1}^{(\alpha)}$  to converge with a relative error of 0.1[%] (dashed-dotted curve) as a function of  $\tau$ . Transition point at  $\tau = \tau_1 = 0.1646$  (vertical solid line). Left figure for  $\alpha = 1$  and right figure for  $\alpha = 2$ .

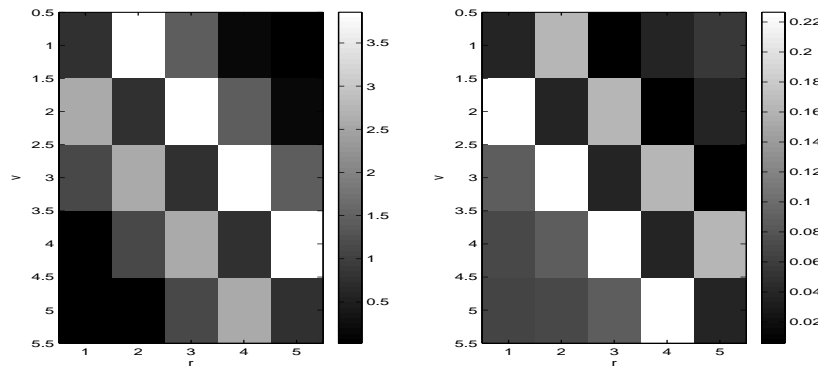


Figure 4.28: Relative error [%] in  $\xi_{v,r}^{(\alpha)} + \zeta_{v,r}^{(\alpha)}$  as a function of  $\{v, r\}$ . Left figure for  $\alpha = 1$  and right figure for  $\alpha = 2$ .

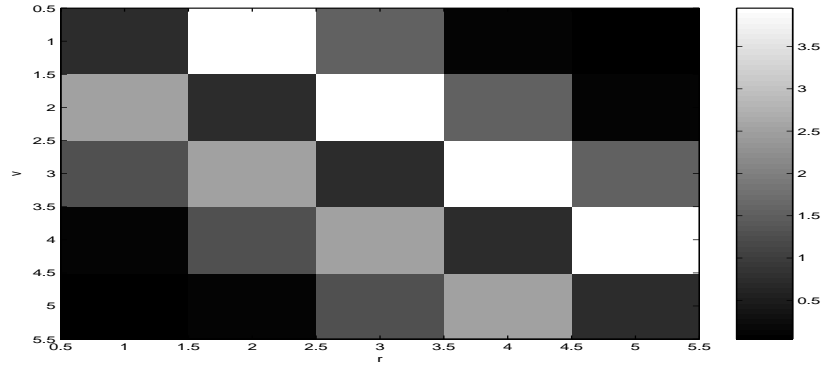


Figure 4.29: Relative error[%] in the contribution  $A_{v,r}$  as a function of  $\{v, r\}$ .

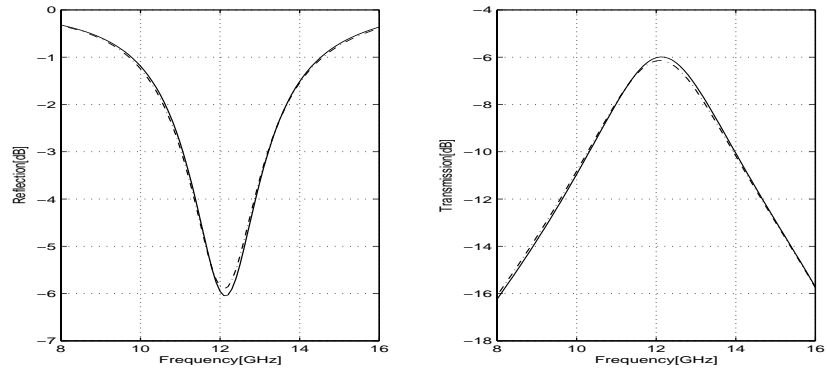


Figure 4.30: Original non-accelerated (solid curve) and accelerated (dashed-dotted curve) as a function of frequency[GHz]. Left figure for power reflection coefficient[dB] and right figure for power transmission coefficient[dB].

with

$$\hat{\gamma}_{v,r}^{(\alpha)}(\mathbf{k}_t) = \begin{cases} [\mathbf{j}\mathbf{k}_t \cdot \hat{\mathbf{g}}_r^*(\mathbf{k}_t)] [\mathbf{j}\mathbf{k}_t \cdot \hat{\mathbf{g}}_v(\mathbf{k}_t)] & \text{if } \alpha = 1, \\ \hat{\mathbf{g}}_r^*(\mathbf{k}_t) \cdot \hat{\mathbf{g}}_v(\mathbf{k}_t) & \text{if } \alpha = 2. \end{cases} \quad (4.107)$$

Since  $\mathbf{g}_r(\boldsymbol{\rho})$  is real-valued, the Fourier counterpart of  $\hat{\mathbf{g}}_r^*(\mathbf{k}_t)$  is  $\mathbf{g}_r(-\boldsymbol{\rho})$ . We can now write the expression for  $\bar{\gamma}_{v,r}^{(\alpha)}(\boldsymbol{\rho}, \tau)$  as

$$\bar{\gamma}_{v,r}^{(\alpha)}(\boldsymbol{\rho}, \tau) = \begin{cases} \bar{a}_r(\boldsymbol{\rho}, \tau) * \bar{b}_v(\boldsymbol{\rho}, \tau) & \text{if } \alpha = 1, \\ \bar{\mathbf{c}}_r(\boldsymbol{\rho}, \tau) \cdot * \bar{\mathbf{d}}_v(\boldsymbol{\rho}, \tau) & \text{if } \alpha = 2, \end{cases} \quad (4.108)$$

in which  $*$  denotes a combination of first an inner product between the vectors  $\bar{\mathbf{c}}_r$ , and  $\bar{\mathbf{d}}_v$  and subsequently a convolution over  $\boldsymbol{\rho}$ . Further

$$\bar{a}_r(\boldsymbol{\rho}, \tau) = \nabla_t \cdot \bar{\mathbf{c}}_r(\boldsymbol{\rho}, \tau), \quad \bar{b}_v(\boldsymbol{\rho}, \tau) = \nabla_t \cdot \bar{\mathbf{d}}_v(\boldsymbol{\rho}, \tau), \quad (4.109)$$

and

$$\bar{\mathbf{c}}_r(\boldsymbol{\rho}, \tau) = \bar{\mathbf{d}}_r(-\boldsymbol{\rho}, \tau), \quad \bar{\mathbf{d}}_v(\boldsymbol{\rho}, \tau) = \mathcal{F}^{-1} \left\{ \hat{\mathbf{g}}_v(\mathbf{k}_t) \exp\left(-\frac{1}{2}k_t^2 \tau^{2\lambda}\right) \right\}. \quad (4.110)$$

Note that  $\bar{a}_r$ ,  $\bar{b}_v$ ,  $\bar{\mathbf{c}}_r$  and  $\bar{\mathbf{d}}_v$  are all of "almost" compact support in  $\boldsymbol{\rho}$  for small  $\tau$ . Further, equation 4.108 shows that  $\bar{\gamma}_{v,r}^{(\alpha)}(\boldsymbol{\rho}, \tau)$  can be written as a two-dimensional convolution of two functions. Since these functions are numerically approximated (as will be shown later on in this section) and both of "almost" compact support, the convolution can be numerically approximated by using two-dimensional fast Fourier transformations (FFT's) [111]. Note that  $\bar{a}_r(\boldsymbol{\rho}, \tau) = -\bar{b}_r(-\boldsymbol{\rho}, \tau)$ . We can rewrite  $\bar{\gamma}_{v,r}^{(1)}(\boldsymbol{\rho}, \tau)$  as

$$\begin{aligned} \bar{\gamma}_{v,r}^{(1)}(\boldsymbol{\rho}', \tau) &= \bar{a}_r(\boldsymbol{\rho}, \tau) * \bar{b}_v(\boldsymbol{\rho}, \tau)|_{\boldsymbol{\rho}=\boldsymbol{\rho}'} \\ &= -\bar{b}_r(-\boldsymbol{\rho}, \tau) * \bar{b}_v(\boldsymbol{\rho}, \tau)|_{\boldsymbol{\rho}=\boldsymbol{\rho}'} \\ &= \bar{a}_r(\boldsymbol{\rho} - \boldsymbol{\rho}_r, \tau) * \bar{b}_v(\boldsymbol{\rho} + \boldsymbol{\rho}_v, \tau)|_{\boldsymbol{\rho}=\boldsymbol{\rho}'+\boldsymbol{\rho}_r-\boldsymbol{\rho}_v} \\ &= -\bar{b}_r(-\boldsymbol{\rho} + \boldsymbol{\rho}_r, \tau) * \bar{b}_v(\boldsymbol{\rho} + \boldsymbol{\rho}_v, \tau)|_{\boldsymbol{\rho}=\boldsymbol{\rho}'+\boldsymbol{\rho}_r-\boldsymbol{\rho}_v}, \end{aligned} \quad (4.111)$$

where  $\boldsymbol{\rho}_r$  and  $\boldsymbol{\rho}_v$  denote the translation vector from the origin to a reference point of the RWG weighting and expansion function, respectively. Note that

1.  $\bar{a}_r(\boldsymbol{\rho}, \tau) = -\bar{b}_r(-\boldsymbol{\rho}, \tau)$  denotes a mirrored  $\bar{b}_r(\boldsymbol{\rho}, \tau)$ ,
2.  $\bar{a}_r(\boldsymbol{\rho} - \boldsymbol{\rho}_r, \tau) = -\bar{b}_r(-\boldsymbol{\rho} + \boldsymbol{\rho}_r, \tau)$  denotes a shifted and mirrored  $\bar{b}_r(\boldsymbol{\rho}, \tau)$ ,
3.  $\bar{b}_v(\boldsymbol{\rho} + \boldsymbol{\rho}_v, \tau)$  denotes a shifted  $\bar{b}_v(\boldsymbol{\rho}, \tau)$ .

The starting point for the evaluation of  $\bar{\gamma}_{v,r}^{(1)}(\boldsymbol{\rho}', \tau)$  is the knowledge of  $\bar{b}_r(-\boldsymbol{\rho} + \boldsymbol{\rho}_r, \tau)$  and  $\bar{b}_v(\boldsymbol{\rho} + \boldsymbol{\rho}_v, \tau)$ . Similarly, we can rewrite  $\bar{\gamma}_{v,r}^{(2)}(\boldsymbol{\rho}, \tau)$  as

$$\begin{aligned} \bar{\gamma}_{v,r}^{(2)}(\boldsymbol{\rho}', \tau) &= \bar{\mathbf{c}}_r(\boldsymbol{\rho}, \tau) \cdot * \bar{\mathbf{d}}_v(\boldsymbol{\rho}, \tau)|_{\boldsymbol{\rho}=\boldsymbol{\rho}'} \\ &= \bar{\mathbf{d}}_r(-\boldsymbol{\rho}, \tau) \cdot * \bar{\mathbf{d}}_v(\boldsymbol{\rho}, \tau)|_{\boldsymbol{\rho}=\boldsymbol{\rho}'} \\ &= \bar{\mathbf{c}}_r(\boldsymbol{\rho} - \boldsymbol{\rho}_r, \tau) \cdot * \bar{\mathbf{d}}_v(\boldsymbol{\rho} + \boldsymbol{\rho}_v, \tau)|_{\boldsymbol{\rho}=\boldsymbol{\rho}'+\boldsymbol{\rho}_r-\boldsymbol{\rho}_v} \\ &= \bar{\mathbf{d}}_r(-\boldsymbol{\rho} + \boldsymbol{\rho}_r, \tau) \cdot * \bar{\mathbf{d}}_v(\boldsymbol{\rho} + \boldsymbol{\rho}_v, \tau)|_{\boldsymbol{\rho}=\boldsymbol{\rho}'+\boldsymbol{\rho}_r-\boldsymbol{\rho}_v}. \end{aligned} \quad (4.112)$$



Note that

1.  $\bar{\mathbf{c}}_r(\boldsymbol{\rho}, \tau) = \bar{\mathbf{d}}_r(-\boldsymbol{\rho}, \tau)$  denotes a mirrored  $\bar{\mathbf{d}}_r(\boldsymbol{\rho}, \tau)$ ,
2.  $\bar{\mathbf{c}}_r(\boldsymbol{\rho} - \boldsymbol{\rho}_r, \tau) = \bar{\mathbf{d}}_r(-\boldsymbol{\rho} + \boldsymbol{\rho}_r, \tau)$  denotes a shifted and mirrored  $\bar{\mathbf{d}}_r(\boldsymbol{\rho}, \tau)$ ,
3.  $\bar{\mathbf{d}}_v(\boldsymbol{\rho} + \boldsymbol{\rho}_v, \tau)$  denotes a shifted  $\bar{\mathbf{d}}_v(\boldsymbol{\rho}, \tau)$ .

The starting point for the evaluation of  $\bar{\gamma}_{v,r}^{(2)}(\boldsymbol{\rho}', \tau)$  is the knowledge of  $\bar{\mathbf{d}}_r(-\boldsymbol{\rho} + \boldsymbol{\rho}_r, \tau)$  and  $\bar{\mathbf{d}}_v(\boldsymbol{\rho} + \boldsymbol{\rho}_v, \tau)$ . Within equations 4.109 and 4.110, the expression

$$\bar{\mathbf{d}}_v(\boldsymbol{\rho}, \tau) = \mathcal{F}^{-1} \left\{ \hat{\mathbf{g}}_v(\mathbf{k}_t) \exp \left( -\frac{1}{2} k_t^2 \tau^{2\lambda} \right) \right\}, \quad (4.113)$$

and its corresponding transverse divergence  $\bar{b}_v(\boldsymbol{\rho}, \tau) = \nabla_t \cdot \bar{\mathbf{d}}_v(\boldsymbol{\rho}, \tau)$  remain to be evaluated. To obtain closed form expressions for  $\bar{\mathbf{d}}_v$  and  $\bar{b}_v$ , we first substitute the spectrum  $\hat{\mathbf{g}}_v(\mathbf{k}_t)$  of a RWG function (equation H.12 in appendix H) given by

$$\hat{\mathbf{g}}_v(\mathbf{k}_t) = \frac{l_v}{2A_v^+} [\mathbf{j}\nabla_k - \boldsymbol{\rho}_v^+] h_v^+(\mathbf{k}_t) + \frac{l_v}{2A_v^-} [\boldsymbol{\rho}_v^- - \mathbf{j}\nabla_k] h_v^-(\mathbf{k}_t), \quad (4.114)$$

in which

$$h_v^\pm(\mathbf{k}_t) = \int_{T_v^\pm} \exp(-\mathbf{j}\mathbf{k}_t \cdot \boldsymbol{\rho}) dA = \mathcal{F} \{ T_v^\pm(\boldsymbol{\rho}) \}, \quad (4.115)$$

in equation 4.113. This leads to

$$\begin{aligned} \bar{\mathbf{d}}_v(\boldsymbol{\rho}, \tau) = & \frac{\mathbf{j}l_v}{2A_v^+} \mathcal{F}^{-1} \left\{ \exp \left( -\frac{1}{2} k_t^2 \tau^{2\lambda} \right) \nabla_k h_v^+(\mathbf{k}_t) \right\} - \\ & \frac{l_v \boldsymbol{\rho}_v^+}{2A_v^+} \mathcal{F}^{-1} \left\{ \exp \left( -\frac{1}{2} k_t^2 \tau^{2\lambda} \right) h_v^+(\mathbf{k}_t) \right\} + \\ & \frac{l_v \boldsymbol{\rho}_v^-}{2A_v^-} \mathcal{F}^{-1} \left\{ \exp \left( -\frac{1}{2} k_t^2 \tau^{2\lambda} \right) h_v^-(\mathbf{k}_t) \right\} - \\ & \frac{\mathbf{j}l_v}{2A_v^-} \mathcal{F}^{-1} \left\{ \exp \left( -\frac{1}{2} k_t^2 \tau^{2\lambda} \right) \nabla_k h_v^-(\mathbf{k}_t) \right\}, \end{aligned} \quad (4.116)$$

which by using differentiation by parts can be rewritten as

$$\begin{aligned} \bar{\mathbf{d}}_v(\boldsymbol{\rho}, \tau) = & \frac{\mathbf{j}l_v}{2A_v^+} \mathcal{F}^{-1} \left\{ (\mathbf{k}_t \tau^{2\lambda} + \nabla_k) \left[ h_v^+(\mathbf{k}_t) \exp \left( -\frac{1}{2} k_t^2 \tau^{2\lambda} \right) \right] \right\} - \\ & \frac{l_v \boldsymbol{\rho}_v^+}{2A_v^+} \mathcal{F}^{-1} \left\{ \exp \left( -\frac{1}{2} k_t^2 \tau^{2\lambda} \right) h_v^+(\mathbf{k}_t) \right\} + \\ & \frac{l_v \boldsymbol{\rho}_v^-}{2A_v^-} \mathcal{F}^{-1} \left\{ \exp \left( -\frac{1}{2} k_t^2 \tau^{2\lambda} \right) h_v^-(\mathbf{k}_t) \right\} - \\ & \frac{\mathbf{j}l_v}{2A_v^-} \mathcal{F}^{-1} \left\{ (\mathbf{k}_t \tau^{2\lambda} + \nabla_k) \left[ h_v^-(\mathbf{k}_t) \exp \left( -\frac{1}{2} k_t^2 \tau^{2\lambda} \right) \right] \right\}. \end{aligned} \quad (4.117)$$

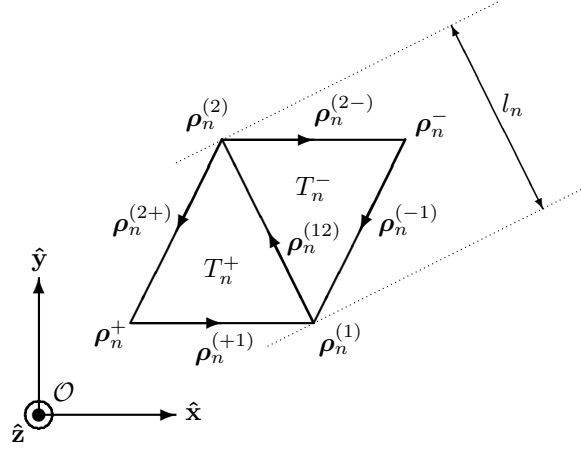


Figure 4.31: Domain, vectors and scalars used in the RWG function.

See section 3.7.5 for a detailed explanation of the RWG function. See figure 4.31 for a graphical representation of the domain, vectors and scalars used in the RWG function. Note that we have defined the reference point as  $\boldsymbol{\rho}_n = (\boldsymbol{\rho}_n^{(1)} + \boldsymbol{\rho}_n^{(2)})/2$ , i.e., the center of the common interface between two adjoining triangles. Now collecting similar terms within equation 4.117 leads to

$$\begin{aligned} \bar{\mathbf{d}}_v(\boldsymbol{\rho}, \tau) = & \frac{l_v}{2A_v^+} [\boldsymbol{\rho} - \boldsymbol{\rho}_v^+ + \tau^{2\lambda} \nabla_t] \eta_v^+(\tau, \lambda, \boldsymbol{\rho}) + \\ & \frac{l_v}{2A_v^-} [\boldsymbol{\rho}_v^- - \boldsymbol{\rho} - \tau^{2\lambda} \nabla_t] \eta_v^-(\tau, \lambda, \boldsymbol{\rho}), \end{aligned} \quad (4.118)$$

where

$$\eta_v^\pm(\tau, \lambda, \boldsymbol{\rho}) = \mathcal{F}^{-1} \left\{ \exp \left( -\frac{1}{2} k_t^2 \tau^{2\lambda} \right) h_v^\pm(\mathbf{k}_t) \right\}. \quad (4.119)$$

The corresponding transverse divergence is given by

$$\begin{aligned} \bar{b}_v(\boldsymbol{\rho}, \tau) = & \frac{l_v}{2A_v^+} [2 + (\boldsymbol{\rho} - \boldsymbol{\rho}_v^+) \cdot \nabla_t + \tau^{2\lambda} \nabla_t \cdot \nabla_t] \eta_v^+(\tau, \lambda, \boldsymbol{\rho}) + \\ & \frac{l_v}{2A_v^-} [(\boldsymbol{\rho}_v^- - \boldsymbol{\rho}) \cdot \nabla_t - 2 - \tau^{2\lambda} \nabla_t \cdot \nabla_t] \eta_v^-(\tau, \lambda, \boldsymbol{\rho}). \end{aligned} \quad (4.120)$$

Now, we are left with the evaluation of  $\eta_v^\pm(\tau, \lambda, \boldsymbol{\rho})$ ,  $\nabla_t \eta_v^\pm(\tau, \lambda, \boldsymbol{\rho})$  and  $\nabla_t \cdot \nabla_t \eta_v^\pm(\tau, \lambda, \boldsymbol{\rho})$ . We can write the expression for  $\eta_v^\pm(\tau, \lambda, \boldsymbol{\rho})$  as

$$\begin{aligned} \eta_v^\pm(\tau, \lambda, \boldsymbol{\rho}) &= T_v^\pm(\boldsymbol{\rho}) * \frac{1}{2\pi\tau^{2\lambda}} \exp\left(-\frac{\boldsymbol{\rho}^2}{2\tau^{2\lambda}}\right) \\ &= \int T_v^\pm(\boldsymbol{\rho}') \frac{1}{2\pi\tau^{2\lambda}} \exp\left(-\frac{\|\boldsymbol{\rho} - \boldsymbol{\rho}'\|^2}{2\tau^{2\lambda}}\right) dA' \\ &= \frac{1}{2\pi\tau^{2\lambda}} \Lambda_v^\pm(\tau, \lambda, \boldsymbol{\rho}), \end{aligned} \quad (4.121)$$

where

$$\Lambda_v^\pm(\tau, \lambda, \boldsymbol{\rho}) = \int_{T_v^\pm} \exp\left(-\frac{\|\boldsymbol{\rho} - \boldsymbol{\rho}'\|^2}{2\tau^{2\lambda}}\right) dA'. \quad (4.122)$$

We can write the expression for  $\nabla_t \eta_v^\pm(\tau, \lambda, \boldsymbol{\rho})$  as

$$\begin{aligned} \nabla_t \eta_v^\pm(\tau, \lambda, \boldsymbol{\rho}) &= \frac{1}{2\pi\tau^{2\lambda}} \int_{T_v^\pm} \nabla_t \left\{ \exp\left(-\frac{\|\boldsymbol{\rho} - \boldsymbol{\rho}'\|^2}{2\tau^{2\lambda}}\right) \right\} dA' \\ &= -\frac{1}{2\pi\tau^{2\lambda}} \int_{T_v^\pm} \frac{\boldsymbol{\rho} - \boldsymbol{\rho}'}{\tau^{2\lambda}} \exp\left(-\frac{\|\boldsymbol{\rho} - \boldsymbol{\rho}'\|^2}{2\tau^{2\lambda}}\right) dA' \\ &= -\frac{1}{2\pi\tau^{4\lambda}} \Phi_v^\pm(\tau, \lambda, \boldsymbol{\rho}), \end{aligned} \quad (4.123)$$

where

$$\Phi_v^\pm(\tau, \lambda, \boldsymbol{\rho}) = \int_{T_v^\pm} (\boldsymbol{\rho} - \boldsymbol{\rho}') \exp\left(-\frac{\|\boldsymbol{\rho} - \boldsymbol{\rho}'\|^2}{2\tau^{2\lambda}}\right) dA'. \quad (4.124)$$

We can write the expression for  $\nabla_t \cdot \nabla_t \eta_v^\pm(\tau, \lambda, \boldsymbol{\rho})$  as

$$\begin{aligned} \nabla_t \cdot \nabla_t \eta_v^\pm(\tau, \lambda, \boldsymbol{\rho}) &= \frac{1}{2\pi\tau^{2\lambda}} \int_{T_v^\pm} \nabla_t \cdot \nabla_t \left\{ \exp\left(-\frac{\|\boldsymbol{\rho} - \boldsymbol{\rho}'\|^2}{2\tau^{2\lambda}}\right) \right\} dA' \\ &= \frac{1}{2\pi\tau^{2\lambda}} \int_{T_v^\pm} \frac{1}{\tau^{2\lambda}} \left( \frac{\|\boldsymbol{\rho} - \boldsymbol{\rho}'\|^2}{\tau^{2\lambda}} - 2 \right) \exp\left(-\frac{\|\boldsymbol{\rho} - \boldsymbol{\rho}'\|^2}{2\tau^{2\lambda}}\right) dA' \\ &= \frac{1}{2\pi\tau^{6\lambda}} \Psi_v^\pm(\tau, \lambda, \boldsymbol{\rho}) - \frac{1}{\pi\tau^{4\lambda}} \Lambda_v^\pm(\tau, \lambda, \boldsymbol{\rho}), \end{aligned} \quad (4.125)$$

where

$$\Psi_v^\pm(\tau, \lambda, \boldsymbol{\rho}) = \int_{T_v^\pm} \|\boldsymbol{\rho} - \boldsymbol{\rho}'\|^2 \exp\left(-\frac{\|\boldsymbol{\rho} - \boldsymbol{\rho}'\|^2}{2\tau^{2\lambda}}\right) dA'. \quad (4.126)$$

By using equations 4.121 and 4.123, we can write the expression for  $\bar{\mathbf{d}}_v$  as

$$\begin{aligned} \bar{\mathbf{d}}_v(\boldsymbol{\rho}, \tau) &= \frac{l_v}{4\pi A_v^+ \tau^{2\lambda}} [(\boldsymbol{\rho} - \boldsymbol{\rho}_v^+) \Lambda_v^+(\tau, \lambda, \boldsymbol{\rho}) - \Phi_v^+(\tau, \lambda, \boldsymbol{\rho})] + \\ &\quad \frac{l_v}{4\pi A_v^- \tau^{2\lambda}} [(\boldsymbol{\rho}_v^- - \boldsymbol{\rho}) \Lambda_v^-(\tau, \lambda, \boldsymbol{\rho}) + \Phi_v^-(\tau, \lambda, \boldsymbol{\rho})]. \end{aligned} \quad (4.127)$$

By using equations 4.121, 4.123 and 4.125, we can write the expression for  $\bar{b}_v$  as

$$\begin{aligned} \bar{b}_v(\boldsymbol{\rho}, \tau) = & \frac{l_v}{4\pi A_v^+ \tau^{4\lambda}} [(\boldsymbol{\rho}_v^+ - \boldsymbol{\rho}) \cdot \boldsymbol{\Phi}_v^+(\tau, \lambda, \boldsymbol{\rho}) + \Psi_v^+(\tau, \lambda, \boldsymbol{\rho})] + \\ & \frac{l_v}{4\pi A_v^- \tau^{4\lambda}} [(\boldsymbol{\rho} - \boldsymbol{\rho}_v^-) \cdot \boldsymbol{\Phi}_v^-(\tau, \lambda, \boldsymbol{\rho}) - \Psi_v^-(\tau, \lambda, \boldsymbol{\rho})]. \end{aligned} \quad (4.128)$$

We stress that equations 4.127 and 4.128 are an important result to evaluate the exponential regularized RWG function. What finally remains to be done is to find closed-form expressions (or at least sufficiently accurate numerical approximations) for  $\Lambda_v^\pm$ ,  $\boldsymbol{\Phi}_v^\pm$  and  $\Psi_v^\pm$ . By using the substitutions

$$\alpha = \frac{1}{2\tau^{2\lambda}}, \quad \mathbf{u} = \boldsymbol{\rho} - \boldsymbol{\rho}', \quad T_v^\pm(\boldsymbol{\rho}') = T_v^\pm(\boldsymbol{\rho} - \mathbf{u}), \quad (4.129)$$

$$dA' \equiv dA(\boldsymbol{\rho}') = -dA(\mathbf{u}) \equiv -dA, \quad (4.130)$$

we can write

$$\Lambda_v^\pm(\tau, \lambda, \boldsymbol{\rho}) = - \int_{T_v^\pm} \exp(-\alpha u^2) dA, \quad (4.131)$$

$$\boldsymbol{\Phi}_v^\pm(\tau, \lambda, \boldsymbol{\rho}) = - \int_{T_v^\pm} \mathbf{u} \exp(-\alpha u^2) dA, \quad (4.132)$$

$$\Psi_v^\pm(\tau, \lambda, \boldsymbol{\rho}) = - \int_{T_v^\pm} u^2 \exp(-\alpha u^2) dA. \quad (4.133)$$

We use Stokes' theorem (equation 2.7) to reduce the surface integrations in  $\Lambda_v^\pm$  and  $\Psi_v^\pm$  to contour integrations. If we express the vector field  $\mathbf{A}$  in Stokes' theorem in terms of cylinder coordinates  $\{u, \phi, z\}$  where  $x = u \cos(\phi)$  and  $y = u \sin(\phi)$ , we can write for the curl of  $\mathbf{A}$

$$\begin{aligned} \nabla \times \mathbf{A} = & \hat{\mathbf{u}} (u^{-1} \partial_u A_z - \partial_z A_\phi) + \\ & \hat{\boldsymbol{\phi}} (\partial_z A_u - \partial_u A_z) + \hat{\mathbf{z}} u^{-1} (\partial_u (u A_\phi) - \partial_\phi A_u). \end{aligned} \quad (4.134)$$

For a piecewise smooth surface  $S$ , we choose a flat surface (the triangle  $T_v^\pm$ ) and place it in the plane  $z = 0$ . Further, we choose a simple parametrization  $\mathbf{S}(x, y) = x\hat{\mathbf{x}} + y\hat{\mathbf{y}}$  and an orientation  $\hat{\boldsymbol{\nu}} = \hat{\mathbf{z}}$  for  $S$ . This means that  $\hat{\boldsymbol{\nu}} dA = \hat{\mathbf{z}} dA$ . Finally, if we assume that

$$\mathbf{A} = \mathbf{A}(u, \phi, z) = \hat{\boldsymbol{\phi}} A_\phi(u), \quad (4.135)$$

the curl of  $\mathbf{A}$  assumes the following expression

$$\nabla \times \mathbf{A} = \hat{\mathbf{z}} u^{-1} \partial_u (u A_\phi). \quad (4.136)$$

Stokes' theorem for this specific vector field  $\mathbf{A}$  now reads

$$\int_S u^{-1} \partial_u (u A_\phi) dA = \oint_C A_\phi(u) \hat{\boldsymbol{\phi}} \cdot \hat{\boldsymbol{\tau}} dl. \quad (4.137)$$

**Evaluation of  $\Lambda_v^\pm(\tau, \lambda, \boldsymbol{\rho})$** 

We can now simplify the expression for  $\Lambda_v^\pm(\tau, \lambda, \boldsymbol{\rho})$ , equation 4.131, by choosing

$$\nabla \times \mathbf{A} = -\hat{\mathbf{z}} \exp(-\alpha u^2). \quad (4.138)$$

This implies that

$$u^{-1} \partial_u (u A_\phi) = -\exp(-\alpha u^2). \quad (4.139)$$

When we solve for  $A_\phi(u)$ , we obtain

$$A_\phi(u) = \frac{1}{2\alpha} \left[ \frac{\exp(-\alpha u^2)}{u} - \frac{C}{u} \right]. \quad (4.140)$$

Note that  $C = 1$  if  $\mathbf{0} \in T_v^\pm(\boldsymbol{\rho} - \mathbf{u})$ , otherwise  $C = 0$ . In this way we extract the singularity for  $1/u$  at  $u = 0$  if  $\mathbf{0} \in T_v^\pm(\boldsymbol{\rho} - \mathbf{u})$ . Combining this result for  $A_\phi(u)$  with Stokes' theorem, given by equation 4.137, leads to

$$-\int_{T_v^\pm} \exp(-\alpha u^2) dA = \frac{1}{2\alpha} \oint_{\partial T_v^\pm} \left[ \frac{\exp(-\alpha u^2) - C}{u} \right] \hat{\boldsymbol{\phi}} \cdot \hat{\boldsymbol{\tau}} d\ell. \quad (4.141)$$

The triangular contour integration over  $\partial T_v^\pm$  is the sum of three separate straight-line contributions. Each of them is represented by  $\xi_\Lambda(\alpha, \mathbf{u}_A, \mathbf{u}_B)$  with  $\mathbf{u}_A$  and  $\mathbf{u}_B$  denoting the starting and ending vertex of that particular side of the triangle, respectively. A graphical representation of the definition of the vectors is given in figure 4.32.  $\xi_\Lambda(\alpha, \mathbf{u}_A, \mathbf{u}_B)$  can be written using a simple straight line parametrization  $\mathbf{u}(t) = \mathbf{u}_A + \mathbf{u}_{AB}t$  with  $\mathbf{u}_{AB} = \mathbf{u}_B - \mathbf{u}_A$  as

$$\begin{aligned} \xi_\Lambda(\alpha, \mathbf{u}_A, \mathbf{u}_B) &= \frac{1}{2\alpha} \int_{\mathbf{u}_A}^{\mathbf{u}_B} \left[ \frac{\exp(-\alpha u^2) - C}{u} \right] \hat{\boldsymbol{\phi}} \cdot \hat{\boldsymbol{\tau}} d\ell \\ &= \frac{(\mathbf{u}_{AB} \times \hat{\mathbf{z}}) \cdot \mathbf{u}_A}{2\alpha} \int_0^1 \frac{\exp(-\alpha \|\mathbf{u}(t)\|^2) - C}{\|\mathbf{u}(t)\|^2} dt, \end{aligned} \quad (4.142)$$

where we have used

$$\hat{\boldsymbol{\phi}} \cdot \hat{\boldsymbol{\tau}} d\ell = \frac{(\mathbf{u}_{AB} \times \hat{\mathbf{z}}) \cdot \mathbf{u}_A}{\|\mathbf{u}(t)\|} dt. \quad (4.143)$$

We use the following change of parametrization from  $t$  to  $\ell$

$$t(\ell) = \frac{\ell - \ell_A}{\ell_B - \ell_A}, \quad (4.144)$$

where  $\ell$  ranges from  $\ell_A$  for which  $t(\ell_A) = 0$  to  $\ell_B$  for which  $t(\ell_B) = 1$  and where

$$\begin{aligned} \ell_A &= \mathbf{u}_A \cdot \hat{\boldsymbol{\tau}}_{AB}, \\ \ell_B &= \|\mathbf{u}_{AB}\| + \mathbf{u}_A \cdot \hat{\boldsymbol{\tau}}_{AB}. \end{aligned} \quad (4.145)$$

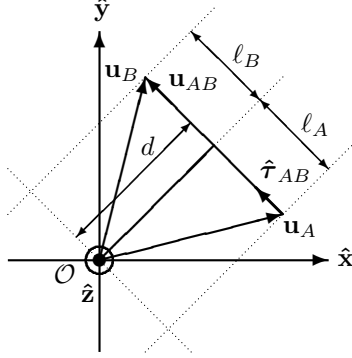


Figure 4.32: Definition of the vectors and scalars used in the two different straight line parametrizations. Note that the parametrization holds for arbitrary  $\mathbf{u}_A$  and  $\mathbf{u}_B$ .

Note that  $\ell_B - \ell_A = \|\mathbf{u}_{AB}\|$  and  $\hat{\boldsymbol{\tau}}_{AB} = \mathbf{u}_{AB} / \|\mathbf{u}_{AB}\|$ . A graphical representation of the definition of the vectors and scalars used in these two different types of straight line parametrizations is also given in figure 4.32. By using this change of parametrization, we can rewrite the Euclidean distance  $\|\mathbf{u}(t)\|$  into a simple Pythagoras distance  $\sqrt{d^2 + \ell^2}$  for a triangle with two perpendicular sides. This simplifies equation 4.142 to

$$\begin{aligned} \xi_\Lambda(\alpha, \mathbf{u}_A, \mathbf{u}_B) = & \frac{d}{2\alpha} \int_{\ell_A}^{\ell_B} \frac{1}{\ell^2 + d^2} \exp(-\alpha[\ell^2 + d^2]) d\ell - \\ & \frac{C}{2\alpha} \left[ \arctan\left(\frac{\ell_B}{d}\right) - \arctan\left(\frac{\ell_A}{d}\right) \right], \end{aligned} \quad (4.146)$$

where

$$d = (\hat{\boldsymbol{\tau}}_{AB} \times \hat{\mathbf{z}}) \cdot \mathbf{u}_A, \quad (4.147)$$

denotes the (signed) length of the vector starting from the origin and ending at the perpendicular intersection of the vector  $\mathbf{u}_{AB}$ . Note that the sign of  $d$  is important and represents an oriented distance. Now if  $\mathbf{u}_B = \beta \mathbf{u}_A$  for some  $\beta \in \mathbb{R}$ , i.e.,  $\mathbf{u}_A$  and  $\mathbf{u}_B$  are in line with the origin, then  $\mathbf{u}_B \times \mathbf{u}_A = \mathbf{0}$  and  $d = 0$ . This means that  $\xi_\Lambda(\alpha, \mathbf{u}_A, \mathbf{u}_B) = 0$ . However, if  $\mathbf{u}_A$  and  $\mathbf{u}_B$  are not in line with the origin, then  $d \neq 0$  and we have to evaluate the integral

$$\exp(-\alpha d^2) \int_{\ell_A}^{\ell_B} \frac{1}{\ell^2 + d^2} \exp(-\alpha \ell^2) d\ell, \quad (4.148)$$

In the present straightforward implementation, this so-called regularization integral is evaluated by a standard numerical integration rule, which is very time consuming if  $\alpha$  is large. A more elaborate technique to evaluate the regularization integral for large  $\alpha$  is described in full detail in appendix A. This technique

has been implemented in a stand-alone application to prove a correct functioning. However, due to lack of time it has not yet been implemented to generate  $\bar{b}_v(\boldsymbol{\rho}, \tau)$  and  $\bar{\mathbf{d}}_v(\boldsymbol{\rho}, \tau)$ .

Finally, by recalling that  $\mathbf{u} = \boldsymbol{\rho} - \boldsymbol{\rho}'$ , equation 4.131 can be written as

$$\begin{aligned} \Lambda_v^\pm(\tau, \lambda, \boldsymbol{\rho}) = & \xi_\Lambda(\alpha, \boldsymbol{\rho} - \boldsymbol{\rho}_A, \boldsymbol{\rho} - \boldsymbol{\rho}_B) + \\ & \xi_\Lambda(\alpha, \boldsymbol{\rho} - \boldsymbol{\rho}_B, \boldsymbol{\rho} - \boldsymbol{\rho}_C) + \xi_\Lambda(\alpha, \boldsymbol{\rho} - \boldsymbol{\rho}_C, \boldsymbol{\rho} - \boldsymbol{\rho}_A), \end{aligned} \quad (4.149)$$

where  $\boldsymbol{\rho}_A$ ,  $\boldsymbol{\rho}_B$  and  $\boldsymbol{\rho}_C$  denote the vertices of the triangle  $T_v^\pm$ , in counter-clockwise order.

### Evaluation of $\Phi_v^\pm(\tau, \lambda, \boldsymbol{\rho})$

The surface integration over  $T_v^\pm$  within  $\Phi_v^\pm(\tau, \lambda, \boldsymbol{\rho})$ , equation 4.132, can be reduced to a contour integration over  $\partial T_v^\pm$  by first noting that

$$\mathbf{u} \exp(-\alpha u^2) = -\frac{1}{2\alpha} \nabla_t \exp(-\alpha u^2), \quad (4.150)$$

where  $\nabla_t$  is defined with respect to  $\mathbf{u} = \boldsymbol{\rho} - \boldsymbol{\rho}'$ . Subsequently, if we combine this result with the reduced version of Gauss' theorem given by equation 2.6, we obtain

$$-\int_{T_v^\pm} \mathbf{u} \exp(-\alpha u^2) dA = \frac{1}{2\alpha} \oint_{\partial T_v^\pm} \exp(-\alpha u^2) \hat{\nu} d\ell. \quad (4.151)$$

The triangular contour integration over  $\partial T_v^\pm$  is the sum of three separate straight-line contributions. Each of these contributions is represented by  $\xi_\Phi(\alpha, \mathbf{u}_A, \mathbf{u}_B)$  with  $\mathbf{u}_A$  and  $\mathbf{u}_B$  denoting the starting and ending vertex of that particular side of the triangle, respectively.  $\xi_\Phi(\alpha, \mathbf{u}_A, \mathbf{u}_B)$  can be written using a simple straight line parametrization  $\mathbf{u}(t) = \mathbf{u}_A + \mathbf{u}_{AB}t$  with  $\mathbf{u}_{AB} = \mathbf{u}_B - \mathbf{u}_A$  as

$$\begin{aligned} \xi_\Phi(\alpha, \mathbf{u}_A, \mathbf{u}_B) &= \frac{1}{2\alpha} \int_{\mathbf{u}_A}^{\mathbf{u}_B} \exp(-\alpha u^2) \hat{\nu} d\ell \\ &= \frac{\mathbf{u}_{AB} \times \hat{\mathbf{z}}}{2\alpha} \int_0^1 \exp(-\alpha \|\mathbf{u}(t)\|^2) dt. \end{aligned} \quad (4.152)$$

We can express  $\xi_\Phi$  in closed form as

$$\xi_\Phi(\alpha, \mathbf{u}_A, \mathbf{u}_B) = \frac{\hat{\nu}_{AB}}{4\alpha} \sqrt{\frac{\pi}{\alpha}} \exp(-\alpha d^2) [\operatorname{erf}(\ell_B \sqrt{\alpha}) - \operatorname{erf}(\ell_A \sqrt{\alpha})], \quad (4.153)$$

where  $\ell_A$ ,  $\ell_B$  and  $d$  are given by equations 4.145 and 4.147. Finally, by recalling that  $\mathbf{u} = \boldsymbol{\rho} - \boldsymbol{\rho}'$ , equation 4.132 can be written as

$$\begin{aligned} \Phi_v^\pm(\tau, \lambda, \boldsymbol{\rho}) = & \xi_\Phi(\alpha, \boldsymbol{\rho} - \boldsymbol{\rho}_A, \boldsymbol{\rho} - \boldsymbol{\rho}_B) + \\ & \xi_\Phi(\alpha, \boldsymbol{\rho} - \boldsymbol{\rho}_B, \boldsymbol{\rho} - \boldsymbol{\rho}_C) + \xi_\Phi(\alpha, \boldsymbol{\rho} - \boldsymbol{\rho}_C, \boldsymbol{\rho} - \boldsymbol{\rho}_A), \end{aligned} \quad (4.154)$$

where  $\boldsymbol{\rho}_A$ ,  $\boldsymbol{\rho}_B$  and  $\boldsymbol{\rho}_C$  denote the vertices of the triangle  $T_v^\pm$ , in counter-clockwise order.

**Evaluation of  $\Psi_v^\pm(\tau, \lambda, \boldsymbol{\rho})$** 

The expression for  $\Psi_v^\pm(\tau, \lambda, \boldsymbol{\rho})$ , equation 4.133, can be simplified by choosing

$$\nabla \times \mathbf{A} = -\hat{\mathbf{z}}u^2 \exp(-\alpha u^2). \quad (4.155)$$

This implies that

$$u^{-1} \partial_u (u A_\phi) = -u^2 \exp(-\alpha u^2). \quad (4.156)$$

When we solve for  $A_\phi(u)$ , we obtain

$$A_\phi(u) = \frac{1}{2\alpha} \left[ \exp(-\alpha u^2) \left( u + \frac{1}{\alpha u} \right) - \frac{C}{\alpha u} \right]. \quad (4.157)$$

Note that  $C = 1$  if  $\mathbf{0} \in T_v^\pm(\boldsymbol{\rho} - \mathbf{u})$ , otherwise  $C = 0$ . If we combine this result for  $A_\phi(\boldsymbol{\rho})$  with Stokes' theorem, given by equation 4.137, this leads us to

$$- \int_{T_v^\pm} u^2 \exp(-\alpha u^2) dA = \frac{1}{2\alpha} \oint_{\partial T_v^\pm} \left[ \exp(-\alpha u^2) \left( u + \frac{1}{\alpha u} \right) - \frac{C}{\alpha u} \right] \hat{\boldsymbol{\phi}} \cdot \hat{\boldsymbol{\tau}} d\ell. \quad (4.158)$$

The triangular contour integration over  $\partial T_v^\pm$  is the sum of three separate straight-line contributions. Each line integral is represented by  $\xi_\Psi(\alpha, \mathbf{u}_A, \mathbf{u}_B)$  with  $\mathbf{u}_A$  and  $\mathbf{u}_B$  denoting the starting and ending vertex of that particular side of the triangle, respectively.  $\xi_\Psi(\alpha, \mathbf{u}_A, \mathbf{u}_B)$  can be written using a simple straight line parametrization  $\mathbf{u}(t) = \mathbf{u}_A + \mathbf{u}_{AB}t$  with  $\mathbf{u}_{AB} = \mathbf{u}_B - \mathbf{u}_A$  as

$$\begin{aligned} \xi_\Psi(\alpha, \mathbf{u}_A, \mathbf{u}_B) &= \frac{1}{2\alpha} \int_{\mathbf{u}_A}^{\mathbf{u}_B} \left[ \exp(-\alpha u^2) \left( u + \frac{1}{\alpha u} \right) - \frac{C}{\alpha u} \right] \hat{\boldsymbol{\phi}} \cdot \hat{\boldsymbol{\tau}} d\ell \\ &= \frac{(\mathbf{u}_{AB} \times \hat{\mathbf{z}}) \cdot \mathbf{u}_A}{2\alpha} \int_0^1 \left[ \exp(-\alpha \|\mathbf{u}(t)\|^2) + \left( \frac{\exp(-\alpha \|\mathbf{u}(t)\|^2) - C}{\alpha \|\mathbf{u}(t)\|^2} \right) \right] dt \\ &= \mathbf{u}_A \cdot \boldsymbol{\xi}_\Phi(\alpha, \mathbf{u}_A, \mathbf{u}_B) + \frac{\xi_\Lambda(\alpha, \mathbf{u}_A, \mathbf{u}_B)}{\alpha}. \end{aligned} \quad (4.159)$$

Finally, by recalling that  $\mathbf{u} = \boldsymbol{\rho} - \boldsymbol{\rho}'$ , we can write equation 4.133 as

$$\begin{aligned} \Psi_v^\pm(\tau, \lambda, \boldsymbol{\rho}) &= \xi_\Psi(\alpha, \boldsymbol{\rho} - \boldsymbol{\rho}_A, \boldsymbol{\rho} - \boldsymbol{\rho}_B) + \\ &\quad \xi_\Psi(\alpha, \boldsymbol{\rho} - \boldsymbol{\rho}_B, \boldsymbol{\rho} - \boldsymbol{\rho}_C) + \xi_\Psi(\alpha, \boldsymbol{\rho} - \boldsymbol{\rho}_C, \boldsymbol{\rho} - \boldsymbol{\rho}_A), \end{aligned} \quad (4.160)$$

where  $\boldsymbol{\rho}_A$ ,  $\boldsymbol{\rho}_B$  and  $\boldsymbol{\rho}_C$  denote the vertices of the triangle  $T_v^\pm$ , in counter-clockwise order.



**Evaluation of  $\bar{\mathbf{d}}_v(\boldsymbol{\rho}, \tau)$  for  $\tau \downarrow 0$** 

To verify the correctness of equation 4.127 we evaluate  $\bar{\mathbf{d}}_v(\boldsymbol{\rho}, \tau)$  for  $\tau \downarrow 0$ . By using  $\alpha = \frac{1}{2\tau^2\lambda}$ ,  $\bar{\mathbf{d}}_v$  can be rewritten as

$$\begin{aligned} \bar{\mathbf{d}}_v(\boldsymbol{\rho}, \tau) &= \frac{l_v}{2A_v^+} \frac{\alpha}{\pi} [(\boldsymbol{\rho} - \boldsymbol{\rho}_v^+) \Lambda_v^+(\tau, \lambda, \boldsymbol{\rho}) - \Phi_v^+(\tau, \lambda, \boldsymbol{\rho})] + \\ &\quad \frac{l_v}{2A_v^-} \frac{\alpha}{\pi} [(\boldsymbol{\rho}_v^- - \boldsymbol{\rho}) \Lambda_v^-(\tau, \lambda, \boldsymbol{\rho}) + \Phi_v^-(\tau, \lambda, \boldsymbol{\rho})]. \end{aligned} \quad (4.161)$$

Note that  $\tau \downarrow 0$  is equivalent to  $\alpha \rightarrow \infty$ . Then  $\lim_{\alpha \rightarrow \infty} [\alpha \Phi_v^\pm(\tau, \lambda, \boldsymbol{\rho})] = 0$  since  $\lim_{\alpha \rightarrow \infty} [\alpha \xi_{\Phi}(\alpha, \mathbf{u}_A, \mathbf{u}_B)] = 0$  for any  $\mathbf{u}_A$  and  $\mathbf{u}_B$ . Further

$$\lim_{\alpha \rightarrow \infty} \int_{\ell_A}^{\ell_B} \frac{1}{\ell^2 + d^2} \exp(-\alpha[\ell^2 + d^2]) d\ell = 0. \quad (4.162)$$

To evaluate  $\bar{\mathbf{d}}_v$  for  $\tau \downarrow 0$ , we first consider  $\boldsymbol{\rho} \notin T_v^\pm$ . In this case  $\mathbf{0} \notin T_v^\pm(\boldsymbol{\rho} - \mathbf{u})$ , and accordingly  $C = 0$ . This implies that  $\lim_{\alpha \rightarrow \infty} [\alpha \xi_\Lambda(\alpha, \mathbf{u}_A, \mathbf{u}_B)] = 0$ , and thus  $\lim_{\alpha \rightarrow \infty} [\alpha \Lambda_v^\pm(\tau, \lambda, \boldsymbol{\rho})] = 0$ . For this case, we thus arrive at  $\lim_{\tau \downarrow 0} \bar{\mathbf{d}}_v(\boldsymbol{\rho}, \tau) = \mathbf{0}$ . Subsequently, we consider  $\boldsymbol{\rho} \in T_v^\pm$ . In this case  $\mathbf{0} \in T_v^\pm(\boldsymbol{\rho} - \mathbf{u})$ , and accordingly  $C = 1$ . This implies that

$$\lim_{\alpha \rightarrow \infty} \left[ \frac{\alpha}{\pi} \xi_\Lambda(\alpha, \mathbf{u}_A, \mathbf{u}_B) \right] = \frac{1}{2\pi} \left[ \arctan \left( \frac{\ell_B}{d} \right) - \arctan \left( \frac{\ell_A}{d} \right) \right], \quad (4.163)$$

which equals the  $2\pi$ -normalized angle between  $\mathbf{u}_A$  and  $\mathbf{u}_B$ . The sum of the three angles between  $\mathbf{u}_A$  and  $\mathbf{u}_B$ , between  $\mathbf{u}_B$  and  $\mathbf{u}_C$  and between  $\mathbf{u}_C$  and  $\mathbf{u}_A$ , respectively, equals  $2\pi$ . This leads us to

$$\lim_{\alpha \rightarrow \infty} \left[ \frac{\alpha}{\pi} \Lambda_v^\pm(\tau, \lambda, \boldsymbol{\rho}) \right] = 1. \quad (4.164)$$

Combining these results gives us

$$\lim_{\tau \downarrow 0} \bar{\mathbf{d}}_v(\boldsymbol{\rho}, \tau) = \begin{cases} \frac{l_v}{2A_v^+} (\boldsymbol{\rho} - \boldsymbol{\rho}_v^+) & \text{if } \boldsymbol{\rho} \in T_v^+, \\ \frac{l_v}{2A_v^-} (\boldsymbol{\rho}_v^- - \boldsymbol{\rho}) & \text{if } \boldsymbol{\rho} \in T_v^-, \\ \mathbf{0} & \text{otherwise,} \end{cases} \quad (4.165)$$

which equals the definition of the RWG function, equation 3.90 in section 3.7.5.

**Evaluation of  $\bar{b}_v(\boldsymbol{\rho}, \tau)$  for  $\tau \downarrow 0$** 

To verify the correctness of equation 4.128 we evaluate  $\bar{b}_v(\boldsymbol{\rho}, \tau)$  for  $\tau \downarrow 0$ . By using  $\alpha = \frac{1}{2\tau^2\lambda}$ ,  $\bar{b}_v$  can be rewritten as

$$\begin{aligned} \bar{b}_v(\boldsymbol{\rho}, \tau) &= \frac{l_v}{A_v^+} \frac{\alpha^2}{\pi} [(\boldsymbol{\rho}_v^+ - \boldsymbol{\rho}) \cdot \Phi_v^+(\tau, \lambda, \boldsymbol{\rho}) + \Psi_v^+(\tau, \lambda, \boldsymbol{\rho})] + \\ &\quad \frac{l_v}{A_v^-} \frac{\alpha^2}{\pi} [(\boldsymbol{\rho} - \boldsymbol{\rho}_v^-) \cdot \Phi_v^-(\tau, \lambda, \boldsymbol{\rho}) - \Psi_v^-(\tau, \lambda, \boldsymbol{\rho})]. \end{aligned} \quad (4.166)$$

Note that  $\lim_{\alpha \rightarrow \infty} [\alpha^2 \Phi_v^\pm(\tau, \lambda, \boldsymbol{\rho})] = 0$  since  $\lim_{\alpha \rightarrow \infty} [\alpha^2 \xi_{\Phi}(\alpha, \mathbf{u}_A, \mathbf{u}_B)] = 0$  for any  $\mathbf{u}_A$  and  $\mathbf{u}_B$ . To evaluate  $\bar{b}_v$  for  $\tau \downarrow 0$ , we first consider  $\boldsymbol{\rho} \notin T_v^\pm$ . In this case  $\mathbf{0} \notin T_v^\pm(\boldsymbol{\rho} - \mathbf{u})$ , and accordingly  $C = 0$ . By also making use of equation 4.159, this implies that  $\lim_{\alpha \rightarrow \infty} [\alpha^2 \xi_{\Psi}(\alpha, \mathbf{u}_A, \mathbf{u}_B)] = 0$ , and thus  $\lim_{\alpha \rightarrow \infty} [\alpha^2 \Psi_v^\pm(\tau, \lambda, \boldsymbol{\rho})] = 0$ . For this case, we thus find  $\lim_{\tau \downarrow 0} \bar{b}_v(\boldsymbol{\rho}, \tau) = 0$ .

Subsequently, we consider  $\boldsymbol{\rho} \in T_v^\pm$ . In this case  $\mathbf{0} \in T_v^\pm(\boldsymbol{\rho} - \mathbf{u})$ , and accordingly  $C = 1$ . By making use of equation 4.163, we find

$$\begin{aligned} \lim_{\alpha \rightarrow \infty} \left[ \frac{\alpha^2}{\pi} \xi_{\Psi}(\alpha, \mathbf{u}_A, \mathbf{u}_B) \right] &= \lim_{\alpha \rightarrow \infty} \left[ \frac{\alpha}{\pi} \xi_{\Lambda}(\alpha, \mathbf{u}_A, \mathbf{u}_B) \right] \\ &= \frac{1}{2\pi} \left[ \arctan \left( \frac{\ell_B}{d} \right) - \arctan \left( \frac{\ell_A}{d} \right) \right], \end{aligned} \quad (4.167)$$

which equals the  $2\pi$ -normalized angle between  $\mathbf{u}_A$  and  $\mathbf{u}_B$ . The sum of the three angles between  $\mathbf{u}_A$  and  $\mathbf{u}_B$ , between  $\mathbf{u}_B$  and  $\mathbf{u}_C$  and between  $\mathbf{u}_C$  and  $\mathbf{u}_A$ , respectively, equals  $2\pi$ . This leads us to

$$\lim_{\alpha \rightarrow \infty} \left[ \frac{\alpha^2}{\pi} \Psi_v^\pm(\tau, \lambda, \boldsymbol{\rho}) \right] = 1. \quad (4.168)$$

Combining these results gives us

$$\lim_{\tau \downarrow 0} \bar{b}_v(\boldsymbol{\rho}, \tau) = \begin{cases} \frac{l_v}{A_v^+} & \text{if } \boldsymbol{\rho} \in T_v^+, \\ -\frac{l_v}{A_v^-} & \text{if } \boldsymbol{\rho} \in T_v^-, \\ 0 & \text{otherwise,} \end{cases} \quad (4.169)$$

which can be identified as the divergence of the RWG function, equation 3.91 in section 3.7.5.

The computational structure to calculate  $\bar{\gamma}_{v,r}^{(\alpha)}(D\mathbf{m}_j, \tau)$  has a similar form as the one given in section 4.4.2.

## Numerical Results

Finally, we show the numerical results of the complete acceleration technique for this type of regularization. The configuration under consideration is the simple basic structure described in section 4.1. Further we take  $\lambda = 3$ ,  $\tau_1 = 0.1646$  and  $\tau_2 = 1.5$ . The integration over  $\tau$  is performed by using a repeated second-order Gaussian quadrature integration rule on 151 subintervals of equal length on the integration interval  $(0, \tau_2]$ . In figure 4.33 we have plotted  $\bar{b}_1(\boldsymbol{\rho}, \tau)$  and  $\bar{\mathbf{d}}_1(\boldsymbol{\rho}, \tau)$  as a function of  $\boldsymbol{\rho} = (x, y)$  with  $\tau \approx 0$ . In figure 4.34 we have plotted  $\bar{\gamma}_{1,1}^{(\alpha)}(\boldsymbol{\rho}, \tau)$  as a function of  $\boldsymbol{\rho} = (x, y)$  with  $\tau \approx 0$ . These figures show that these functions are of "almost" compact support. The numerical convolution is done by using FFT's; we have used a 64 by 64 grid which reaches over a quarter of a single unit cell. The regularization integral is evaluated with a repeated fourth-order Gaussian quadrature integration rule on 101 subintervals of equal length on each separate line integral which is part of the triangular contour

integration. In figure 4.35 we have plotted the integrand of  $\zeta_{1,1}^{(\alpha)}$  as a function of  $\tau$  at frequency = 8[GHz] for the contribution  $A_{1,1}$  to  $L$ . The broadside term in the summation for large  $\tau$  has not been separated and treated analytically. Note that the integrand decays exponentially for large  $\tau$ , and is continuous at the transition point  $\tau = \tau_1$ , which shows a correct implementation of the evaluation of the integrand for small and large  $\tau$ . For  $\tau \in (0, \tau_1]$  we have only taken into account a single term with index  $(m_{1;j}, m_{2;j}) = (0, 0)$ . In figure 4.36 we have plotted the minimum required summation index  $j$  for the series in the integrand of  $\zeta_{1,1}^{(\alpha)}$  to converge with a relative error of 0.1[%] as a function of  $\tau$ . For  $\tau \in (0, \tau_1]$  this is set to one in this figure. These figures show that for most  $\tau \in [\tau_1, \tau_2]$  only a single term is needed to obtain the relative error of 0.1[%]. Only near the transition point less than ten terms are needed. In figure 4.37 we have plotted the relative error of  $\xi_{v,r}^{(\alpha)} + \zeta_{v,r}^{(\alpha)}$  as a function of  $\{v, r\}$  at frequency = 8[GHz]. These figures show that each element of  $\xi_{v,r}^{(\alpha)} + \zeta_{v,r}^{(\alpha)}$  has a low relative error for  $\alpha = 2$  and that some elements have a relatively high relative error of 6[%] for  $\alpha = 1$ . In figure 4.38 we have plotted the relative error of the contribution  $A_{v,r}$  to  $L$  at frequency = 8 [GHz]. These relative errors are defined with respect to the single maximum absolute value out of all  $\{v, r\}$ . This figure shows that some elements for the matrix contribution  $A_{v,r}$  to  $L$  have a relatively high relative error of 6[%]. Figure 4.39 shows the final reflection and transmission coefficients as a function of frequency, for which there is an excellent agreement between the unaccelerated and the accelerated, despite of this high relative error, computational method.

The asymmetry in relative errors of  $\xi_{v,r}^{(\alpha)} + \zeta_{v,r}^{(\alpha)}$  for  $\alpha = 1$  and  $\alpha = 2$  is caused by two effects. The first effect is already described in section 4.2 and corresponds to the difference of convergence behavior of  $\xi_{v,r}^{(\alpha)}$  for  $\alpha = 1$  and  $\alpha = 2$ . The second effect is caused by the fact that the result of the integration over  $\tau$  for  $\alpha = 1$  is determined by the accuracy for  $\tau < \tau_1$ , whereas for  $\alpha = 2$  by  $\tau > \tau_1$ . This can be seen in figure 4.35. Since we take only into account a single term for  $\tau < \tau_1$ , we lose accuracy compared to  $\tau > \tau_1$ . Hence,  $\zeta_{v,r}^{(1)}$  is less accurate than  $\zeta_{v,r}^{(2)}$ .

Even though we have limited the summation for  $\tau < \tau_1$  to a single term, we obtain very accurate results for the reflection and transmission coefficients as a function of frequency. Taking into account more terms would require larger two-dimensional grids to sample  $\bar{b}_v(\boldsymbol{\rho}, \tau)$  and  $\bar{\mathbf{d}}_v(\boldsymbol{\rho}, \tau)$ . This is not necessary since, for small  $\tau$ ,  $\bar{b}_v(\boldsymbol{\rho}, \tau)$  and  $\bar{\mathbf{d}}_v(\boldsymbol{\rho}, \tau)$  have already small bandwidths, i.e., are of "almost" compact support.

## 4.5 Speed Improvement

The total computation time  $S(n)$  after  $n$  (different frequencies and angles of incidence) steps for the unaccelerated computational method is proportional to

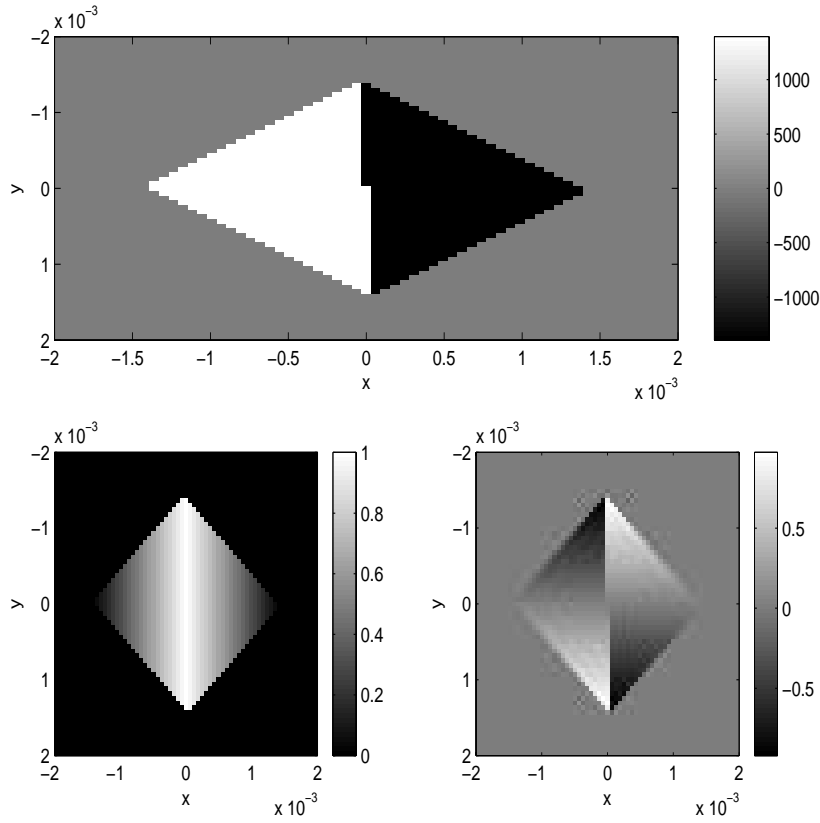


Figure 4.33: Top figure for  $\bar{b}_1(\boldsymbol{\rho}, \tau)$ , bottom left figure for  $\bar{d}_{1,x}(\boldsymbol{\rho}, \tau)$  and bottom right figure for  $\bar{d}_{1,y}(\boldsymbol{\rho}, \tau)$  as a function of  $\boldsymbol{\rho} = (x, y)$  with  $\tau \approx 0$ .

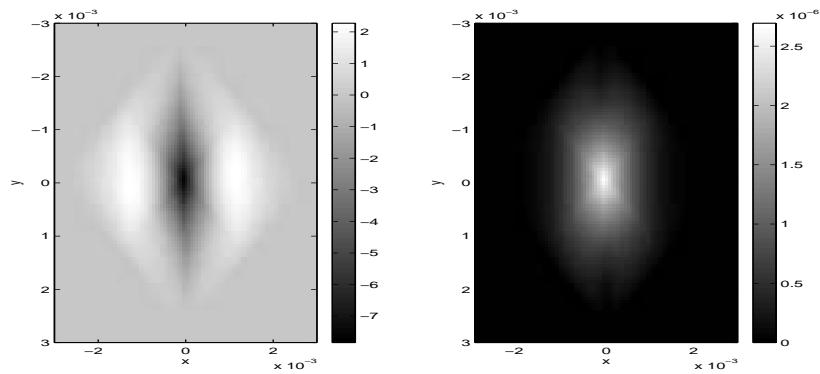


Figure 4.34:  $\bar{\gamma}_{1,1}^{(\alpha)}(\boldsymbol{\rho}, \tau)$  as a function of  $\boldsymbol{\rho} = (x, y)$  with  $\tau \approx 0$ . Left figure for  $\alpha = 1$  and right figure for  $\alpha = 2$ .

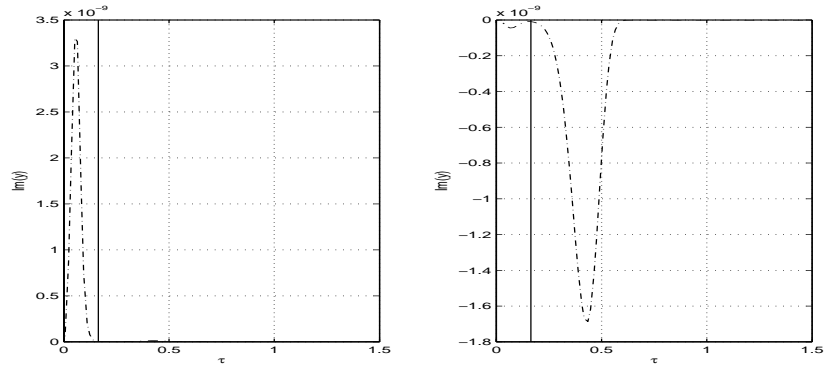


Figure 4.35:  $y = \text{Im}(\text{integrand of } \zeta_{1,1}^{(\alpha)})$  (dashed-dotted curve) as a function of  $\tau$ . Transition point at  $\tau = \tau_1 = 0.1646$  (vertical solid line). Left figure for  $\alpha = 1$  and right figure for  $\alpha = 2$ .

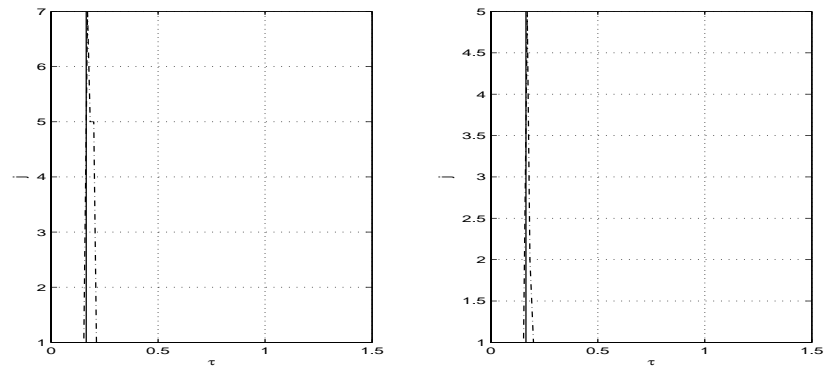


Figure 4.36: Minimum required  $j$  for partial sum in integrand of  $\zeta_{1,1}^{(\alpha)}$  to converge with a relative error of 0.1% (dashed-dotted curve) as a function of  $\tau$ . Transition point at  $\tau = \tau_1 = 0.1646$  (vertical solid line). Left figure for  $\alpha = 1$  and right figure for  $\alpha = 2$ .

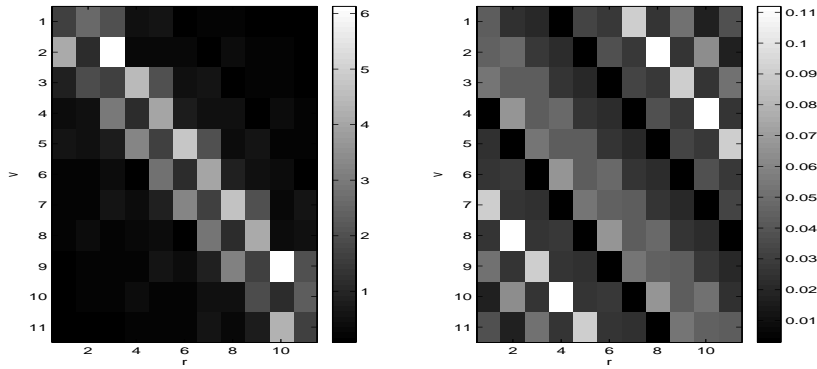


Figure 4.37: Relative error [%] in  $\xi_{v,r}^{(\alpha)} + \zeta_{v,r}^{(\alpha)}$  as a function of  $\{v, r\}$ . Left figure for  $\alpha = 1$  and right figure for  $\alpha = 2$ .

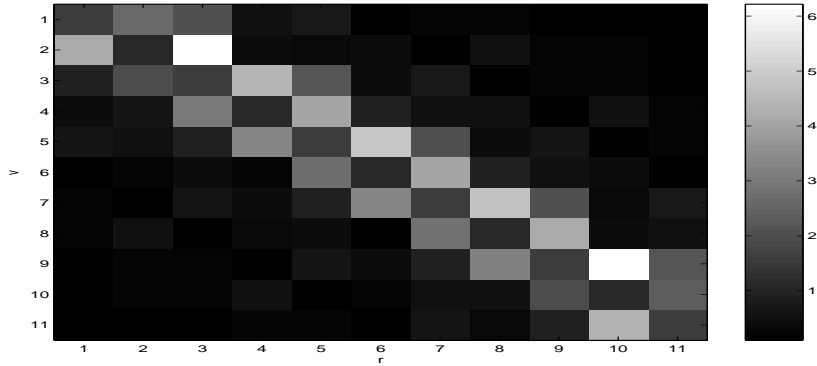


Figure 4.38: Relative error [%] in the contribution  $A_{v,r}$  as a function of  $\{v, r\}$ .

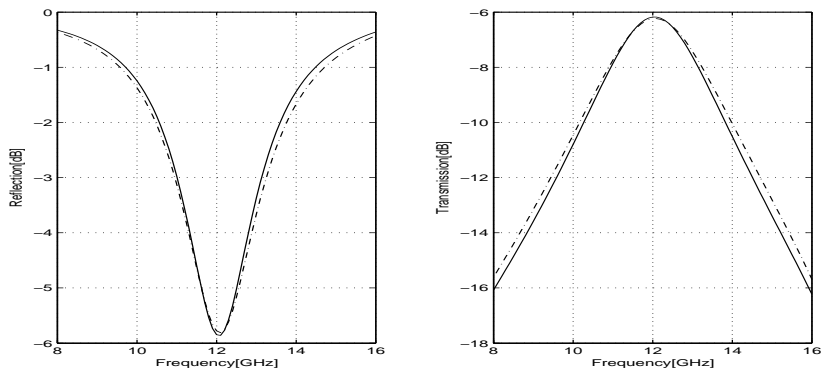


Figure 4.39: Original non-accelerated (solid curve) and accelerated (dashed-dotted curve) as a function of frequency [GHz]. Left figure for power reflection coefficient [dB] and right figure for power transmission coefficient [dB].

the number of steps  $n$ , and is given by

$$S(n) = sn, \quad (4.170)$$

where  $s$  denotes the time per step. It includes the computation time for matrix assembly, matrix inversion and calculation of the scattering parameters. These computation times are assumed constant for each step  $n$ . If matrix inversion is done in full analytical form then this is correct. If however numerical iterative techniques are used for this purpose, then computation times will show a small variation depending on the matrix that has to be inverted. The total computation time  $F(n)$  after  $n$  steps for the accelerated computational method is proportional to the number of steps  $n$  added with a fixed computation time for the generation of the lookup table for  $\bar{\gamma}_{v,r}^{(\alpha)}(\boldsymbol{\rho}, \tau)$ , and is given by

$$F(n) = i + fn, \quad (4.171)$$

where  $i$  denotes the time to generate the lookup table for  $\bar{\gamma}_{v,r}^{(\alpha)}(\boldsymbol{\rho}, \tau)$ , and where  $f$  denotes the time per step. Since the matrix assembly time is reduced when the acceleration technique is used, we have  $f < s$ . Obviously, because of  $i$ , there is a trade off in choosing between the two methods that depends on the number of steps  $n$ . The number of steps where both accelerated and unaccelerated computational method need the same computation time is denoted as the break even point  $n_{\text{bep}}$ , and is given by

$$n_{\text{bep}} = \frac{i}{s - f}, \quad (4.172)$$

and is rounded off to the next nearest integer. Furthermore, we define a so-called relative gain  $G(n)$  as the ratio between  $S(n)$  and  $F(n)$  as

$$G(n) = \frac{S(n)}{F(n)} = \frac{sn}{i + fn}. \quad (4.173)$$

$G(n)$  indicates how much faster the accelerated method is compared to the original method after  $n$  steps. Note that at break even we have

$$G(n_{\text{bep}}) = 1. \quad (4.174)$$

Furthermore, the so-called theoretical relative gain  $G^\infty$  is defined as the gain for which  $n \rightarrow \text{inf}$ , and is given by

$$G^\infty = \lim_{n \rightarrow \text{inf}} G(n) = \frac{s}{f}. \quad (4.175)$$

and is the relative gain where the computation time to generate the lookup table for  $\bar{\gamma}_{v,r}^{(\alpha)}(\boldsymbol{\rho}, \tau)$  is ignored.

The parameters  $i$ ,  $f$  and  $s$  were determined by timing various parts of the total computation. To obtain a good estimation for these parameters, all unimportant parts such as graphical output are switched off. The three different regularization methods that we used were described in detail in sections 4.4.1, 4.4.2 and 4.4.3. The configuration under consideration is the simple basic structure described in section 4.1. We take  $\lambda = 3$ ,  $\tau_1 = 0.1646$  and  $\tau_2 = 0.5$ . Further:

- The first method uses a repeated fourth-order Gaussian quadrature integration rule on 201 subintervals of equal length on the integration interval  $(0, \tau_2]$ .
- The second method uses a repeated fourth-order Gaussian quadrature integration rule on 201 subintervals of equal length on the integration interval  $(0, \tau_2]$ . The numerical convolution is done using a 64 by 64 grid reaching over a single unit cell.
- The third method uses a repeated second-order Gaussian quadrature integration rule on 51 subintervals of equal length on the integration interval  $(0, \tau_2]$ . The numerical convolution is done using a 64 by 64 grid reaching over a quarter of a single unit cell. The regularization integral is evaluated with a repeated fourth-order Gaussian quadrature integration rule on 101 subintervals of equal length on each separate line integral (part of the triangular contour integration).

The broadside term in the summation for large  $\tau$  has been separated and treated analytically. The software was run on a computer with a Pentium 4 running at 2.6[GHz] with 2[Gb] of physical memory. On this computer we obtained the following values for  $i$ ,  $f$  and  $s$ :

- Rooftop expansion functions placed in an orthogonal grid.  $i = 13.32[\text{s}]$ ,  $f = 0.48[\text{s}]$ ,  $s = 3.75[\text{s}]$ ,  $n_{\text{bep}} = 5$ ,  $G^\infty = 7.81$ .
- Arbitrary rooftop expansion functions.  $i = 662.77[\text{s}]$ ,  $f = 0.48[\text{s}]$ ,  $s = 3.75[\text{s}]$ ,  $n_{\text{bep}} = 203$ ,  $G^\infty = 7.81$ .
- Arbitrary RWG expansion functions.  $i = 4410.20[\text{s}]$ ,  $f = 1.32[\text{s}]$ ,  $s = 7.74[\text{s}]$ ,  $n_{\text{bep}} = 687$ ,  $G^\infty = 5.86$ .

In figure 4.40 we have plotted the relative gain  $G(n)$ , the theoretical relative gain  $G^\infty$  and the break even point  $n_{\text{bep}}$  for these three regularization methods.

The first method is the fastest. It has the lowest generation time for the lookup table for  $\bar{\gamma}_{v,r}^{(\alpha)}(\boldsymbol{\rho}, \tau)$  and the time per step is almost eight times smaller compared to the time per step in the unaccelerated method. Break even is already reached from the fifth step onwards.

The second method has a higher generation time for the lookup table for  $\bar{\gamma}_{v,r}^{(\alpha)}(\boldsymbol{\rho}, \tau)$  due to the numerical convolution. The time per step is almost eight times smaller compared to the time per step in the unaccelerated method. Break even is reached at a higher value for  $n$ .

The third method cannot be compared with the previous two methods. This is due to the fact that we have more RWG than rooftop expansion functions, i.e., more unknowns to solve. However, this method has a high generation time for the lookup table for  $\bar{\gamma}_{v,r}^{(\alpha)}(\boldsymbol{\rho}, \tau)$  due to both the numerical convolution and the numerical integration within the generation of  $\bar{b}_v(\boldsymbol{\rho}, \tau)$  and  $\bar{\mathbf{d}}_v(\boldsymbol{\rho}, \tau)$ . Break even is therefore reached at a much higher value for  $n$ . This can be reduced by using the evaluation of the regularization integral described in appendix A.



The time per step is almost six times smaller compared to the time per step in the unaccelerated method.

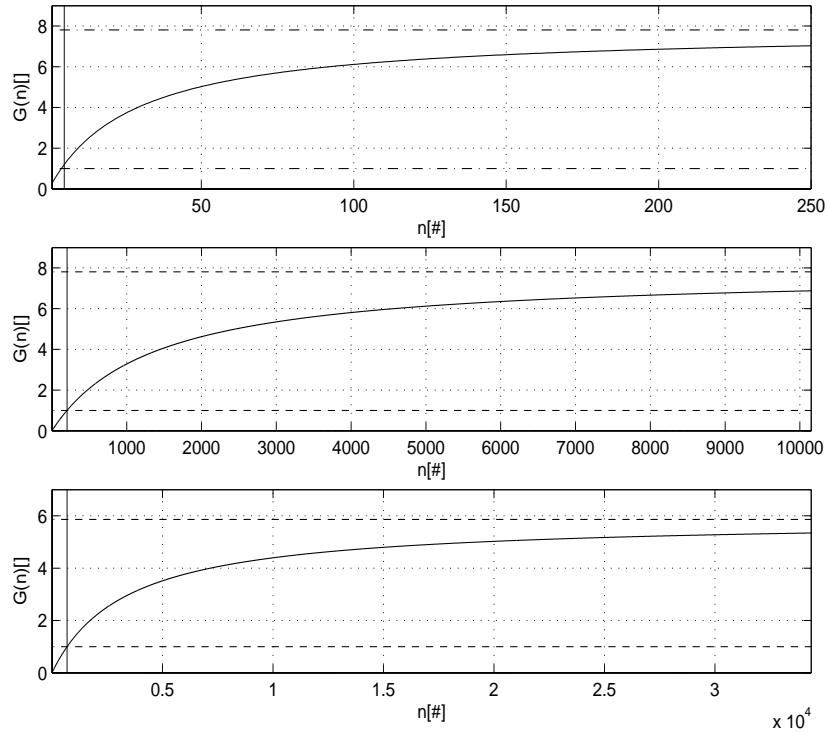


Figure 4.40: Relative gain  $G(n)$  (specified in equation 4.173), theoretical relative gain  $G^\infty$  (specified in equation 4.175) and break even point  $n_{\text{bep}}$  (specified in equation 4.172). Unit relative gain (lower dashed-dotted horizontal line). Theoretical relative gain (upper dashed-dotted horizontal line). Break even point (solid vertical line). Relative gain (solid curve) as a function of the number of steps  $n$ . Top figure for rooftop expansion functions placed in an orthogonal grid. Middle figure for arbitrary rooftop expansion functions. Bottom figure for arbitrary RWG expansion functions.

# Chapter 5

## Validation

*"It doesn't matter how beautiful your theory is, it doesn't matter how smart you are. If it doesn't agree with experiment, it's wrong."*  
Richard Feynman (1918-1988)

In this chapter we validate the outcome of the computational method. We have implemented the computational method in a MATLAB software package called Luxaflex. This software package consists of a collection of individual computational methods for the following types of basic structures.

- Single junction: MFIE and EFIE.
- Two coupled junctions: MFIE-MFIE, EFIE-EFIE and MFIE-EFIE.
- Three coupled junctions: MFIE-MFIE-MFIE and MFIE-EFIE-EFIE.

The individual segments in between the junctions can be chosen arbitrarily, i.e., either waveguide or layered space segments. The individual computational methods make extensive use of a common library of functions. These functions include implementations for transmission line responses, inner products, and routines for adding matrix and vector contributions. The validation is done by using internal consistency checks, by comparing results of Luxaflex with corresponding results obtained with other simulation software packages<sup>1</sup> and with measurements<sup>2</sup>. These various validation techniques are first discussed in section 5.1. Then in section 5.2, we present and validate the numerical results of Luxaflex.

---

<sup>1</sup>A special word of thanks goes to dr.ir. S.M. van den Berg for his contribution to this chapter by supplying me with his insights and with many ©HFSS and Luxaflex simulations.

<sup>2</sup>A special word of thanks goes to ir. J. de Groot for his contribution to this chapter by supplying me with the waveguide simulator measurements.

## 5.1 Overview of Validation Techniques

In this section, we discuss three different validation techniques: internal consistency in section 5.1.1, comparison with commercial software packages in section 5.1.2 and comparison with measurements in section 5.1.3.

### 5.1.1 Internal Consistency

This type of validation is based on the principle of energy conservation and the reciprocity principle. The first principle states that, for a given lossless structure, the incident time-averaged power must be equal to the outgoing time-averaged power. This is easily checked by using the expression 3.146 for the conservation of energy derived in section 3.9.4.

Reciprocity is a necessary condition for any solution to Maxwell's equations [35, chapter 11]. In its most simple form the reciprocity theorem tells us that the measured response of a system to a source is unchanged when the source and measurer are interchanged. To show reciprocity, it is sufficient to show that either the impedance or admittance operator of a linear system is symmetric. This internal consistency check is more thorough compared to the energy conservation check since it takes into account the phase of the response.

### 5.1.2 Commercial Software Packages

This type of validation is based on the idea that different EM computational methods should produce identical results for the same given basic structure. These methods are widely available for a price. Some examples are: ©HFSS [33], ADR2, ©Femlab, and ©CST Mafia. Most of these methods use the finite element method and model the electromagnetic field for a given general complex RF structure in terms of small three-dimensional tetrahedral building blocks. This creates also their weakness. Finite element modeling means large computation times and large memory consumption. However finite element modeling serves as a useful method to validate Luxaflex.

### 5.1.3 Measurement Techniques

This type of validation is based on the idea that our mathematical model approximates the physical reality to some desired level of accuracy. To see if this is true we must first manufacture the basic structure under consideration and then measure its electromagnetic response. This allow us to also test if the modeling assumptions are chosen ideal. There are a number of facilities/devices to do these measurements.

#### Far-Field Range

A modern far-field measurement facility usually consists of a large anechoic chamber where an incident plane wave at a given frequency is created by transmitting a spherical wave from a feeding system to a parabolic mirror. The result

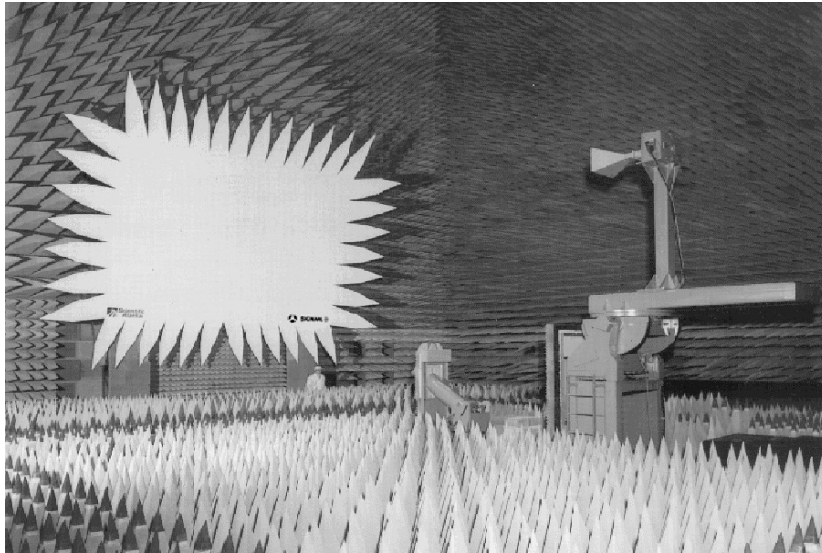


Figure 5.1: Far-Field range.

is a reflected plane wave which is incident on the antenna. Furthermore, the antenna (basic structure) under consideration is placed on a mechanically steered table. By rotating this table around different axes, the response of the antenna with respect to the incident plane wave can be measured. Some examples are shown in figures 5.1 and 5.2. This leads to a characterization of the antenna as a function of frequency and angle of incidence. Furthermore we can measure in a similar way, explained in section 3.10.2, the active antenna pattern. The array finiteness and its effect on mutual coupling between the elements can be studied.

### Near-Field Range

A modern near-field measurement facility usually consists of an anechoic chamber where a probing device is moved mechanically and automatically along a predefined path near the antenna under consideration. The coupling between the probe and the antenna leads to a characterization of the antenna since that of the probe is known. This characterization is very local near the antenna and enables us to see effects (such as reactive near-field effects) which are not seen in the far field. The far field can be obtained by a near-field to far-field transformation.

### Waveguide Simulator Measurement

A waveguide simulator measurement device is a rectangular waveguide in which we place a small number of unit-cell structures. The ends of the waveguide

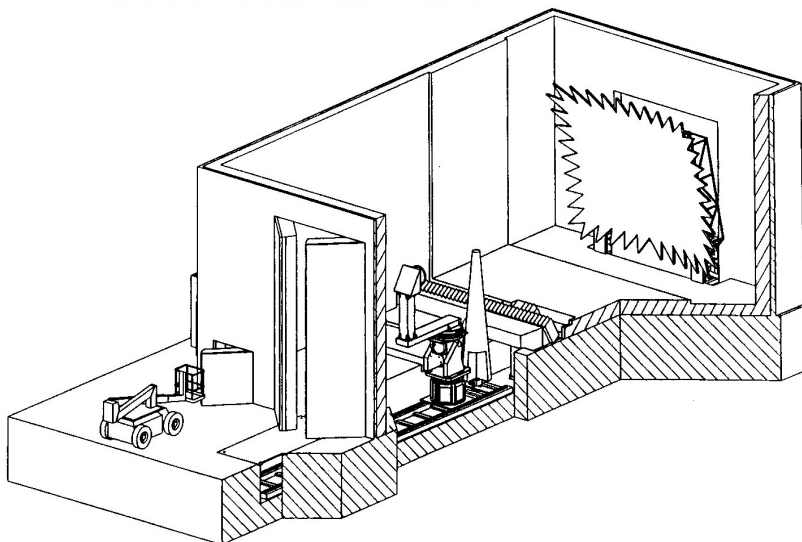


Figure 5.2: Conceptual far-field range.

are connected via a coax-to-waveguide transfer to a two-port measuring device. This device measures the reflection and transmission coefficients as a function of frequency. The waveguide simulator exploits the concept of infinite array theory since it uses the image principle and the notion that any waveguide mode can be written as a sum of two plane waves which are symmetrically oriented with respect to the longitudinal axis of the waveguide.

This means that there is a direct link between this measurement of the finite number of unit cells in the waveguide and the response of the infinite array for the corresponding plane wave. The costs of the manufacturing process are reduced since only a small number of unit cells are needed for this measurement. To this end, we require that the unit cell structure must exhibit a point symmetry in the transverse direction in order for a correct unfolding from a single unit cell to an infinite array of unit cells due to the PEC waveguide walls.

A major disadvantage is that the angle of incidence of the plane wave in the infinite array structure is directly related to the frequency of the incident waveguide mode in the waveguide simulator. This means that frequency and angle of incidence cannot be chosen independently. The freedom of this choice depends on the number of unit cells that are placed inside the waveguide. In addition, we have to ensure that the first propagating waveguide mode can be excited within the frequency range of interest.

For example, let us consider the  $TE(1,0)$  waveguide mode in a rectangular waveguide with a width  $a$  and a height  $b$  for which  $k_t = \pi/a$ . Subsequently we place  $n$  square unit cells with a length and height  $d$  in a row in the waveguide. This means that the waveguide must have dimensions  $a = nd$  and  $b = d$ . Note that  $n$  does not necessarily have to be an integer. We only have to ensure a cor-

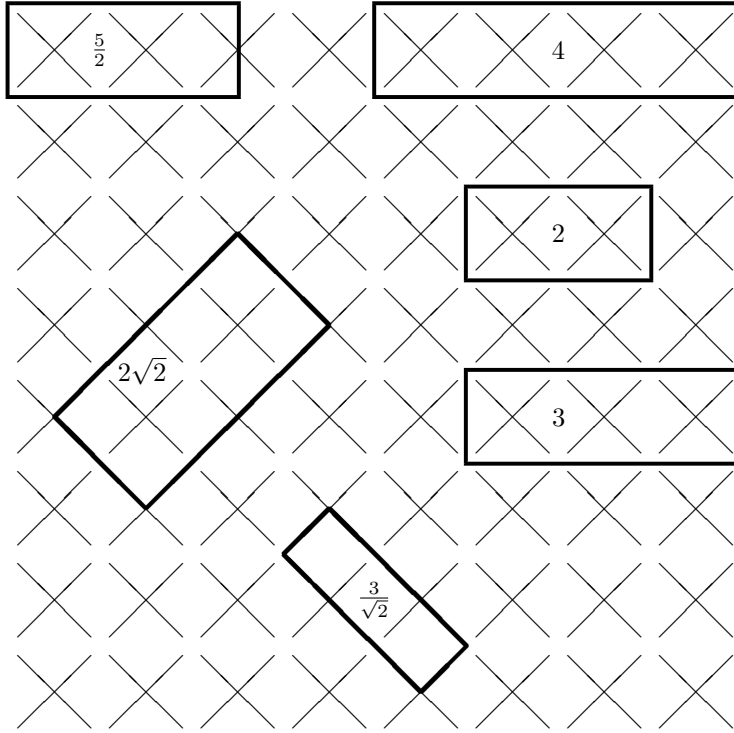


Figure 5.3: Six different ways of placing unit cells inside a waveguide for which  $n = \frac{5}{2}, 4, 2\sqrt{2}, 2, 3, \frac{3}{2}\sqrt{2}$ . Each cross represents a single unit cell. [Source: lecture notes on The Analysis of Frequency Selective Surfaces, R. Orta]

rect unfolding process of the  $n$  unit cells to the infinite array. Now the TE(0,0) Floquet mode in the infinite array corresponds to the TE(1,0) waveguide mode. Consequently, the reflection and transmission coefficients in the waveguide simulator measurement for the TE(1,0) mode are the same for the infinite array with an incident TE(0,0) Floquet mode. The angles of incidence  $\theta$  and  $\phi$  are defined in a polar reference system.  $\theta$  and the frequency  $f$  are related by

$$k_t = \frac{\pi}{a} = k_0 \sin(\theta) \quad \Rightarrow \quad \sin(\theta) = \frac{c}{2nfd}. \quad (5.1)$$

$c$  denotes the speed of light. Furthermore  $\phi = 0$ . Figure 5.3 presents six different ways of placing unit cells inside a waveguide. The corresponding relations between frequency and angle of incidence are given in figure 5.4. Here we have assumed  $d = 8.4[\text{mm}]$ . Note that we have taken into account the cutoff frequency of the TE(1,0) waveguide mode.

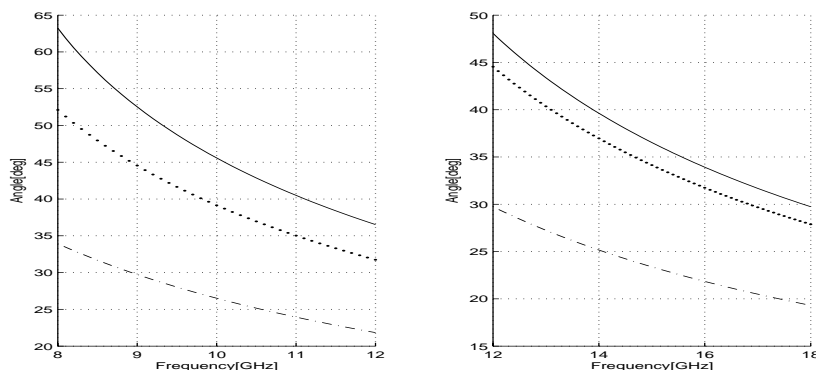


Figure 5.4: Relation between frequency and angle of incidence for the six different ways of placing unit cells inside a waveguide. Left figure for  $n = \frac{5}{2}$  (solid curve),  $n = 4$  (dashed-dotted curve),  $n = 2\sqrt{2}$  (dotted curve). Right figure for  $n = 2$  (solid curve),  $n = 3$  (dashed-dotted curve),  $n = \frac{3}{2}\sqrt{2}$  (dotted curve).

## 5.2 Validation of the Computational Method

In this section, we present and validate the numerical results of Luxaflex for eight different testcases. The first five testcases are concerned with different types of frequency selective surfaces. The last three testcases are concerned with different types of radiators.

### 5.2.1 Horizontal Dipole Frequency Selective Surface

#### Motivation of the Choice for this Structure

With this basic structure we test the computational method for three segments with an EFIE and a dielectric junction. Further, we investigate the independence of the electromagnetic behavior if we choose local rooftop, local RWG and global thin-strip expansion functions to expand the unknown electric surface current on the horizontal<sup>3</sup> dipole.

#### Detailed Description of the Structure

The structure is schematized in figure 5.5. A single horizontal dipole of  $l = 5.95[\text{mm}]$  length and of  $w = 0.15[\text{mm}]$  width is stacked on a kapton layer of  $h = 0.07[\text{mm}]$  thickness with a relative permittivity of  $\epsilon_r = 3.5[]$ . The horizontal dipole and the kapton layer are placed and centered in a square unit cell with sides of  $d = 8.4[\text{mm}]$  length. The unit cells are placed in a rectangular grid with basis vectors  $\mathbf{d}_1 = 8.4\hat{\mathbf{x}}[\text{mm}]$  and  $\mathbf{d}_2 = 8.4\hat{\mathbf{y}}[\text{mm}]$ .

<sup>3</sup>With horizontal we mean an orientation in the transverse plane.

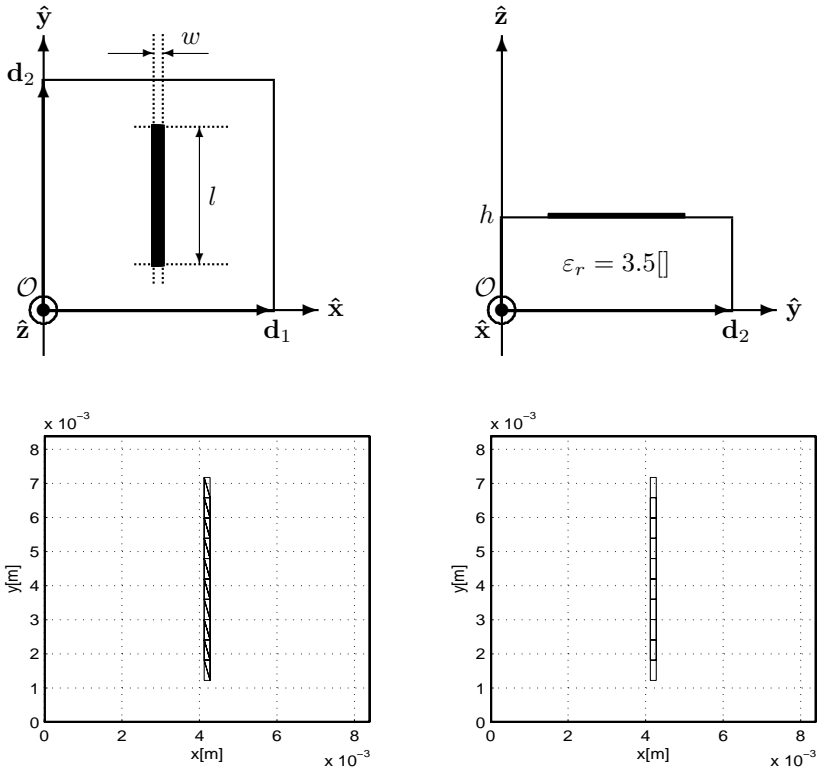


Figure 5.5: Configuration of the horizontal dipole frequency selective surface. Bottom left plot triangular mesh and bottom right plot rectangular mesh.



### Description of the Comparison Techniques

The computational method is based on a Luxaflex model for three segments with a dielectric junction between the first two segments and an EFIE junction between the last two segments.

- A left probing interface is placed in the first (layered space) segment at  $z = -1[\text{mm}]$ .
- The first segment represents the free space behind the kapton layer.
- The first junction at  $z = 0[\text{mm}]$  represents the dielectric junction between the free space and the kapton layer.
- The second segment represents the kapton layer.
- The second junction at  $z = 0.07[\text{mm}]$  represents the horizontal dipole.
- The third segment represents the free space above the horizontal dipole.
- A right probing interface is placed in the last (layered space) segment at  $z = 1.07[\text{mm}]$  (which is  $1[\text{mm}]$  away from the second junction).

This model was used in three different calculations where the unknown electric surface current on the horizontal dipole was expanded using the local RWG, local rooftop and global thin strip expansion functions.

- The first calculation is based on global thin strip expansion functions (first 10 modes).
- The second calculation is based on local rooftop expansion functions defined on a rectangular mesh (given by the right plot in figure 5.5).
- The third calculation is based on local RWG expansion functions defined on a triangular mesh (given by the left plot in figure 5.5).

The reflection coefficient between an incident  $\text{TE}(0,0)$  and an outgoing  $\text{TE}(0,0)$  Floquet plane wave at the right probe is calculated. The transmission coefficient between an incident  $\text{TE}(0,0)$  Floquet plane wave at the right probe and an outgoing  $\text{TE}(0,0)$  Floquet plane wave at the left probe is calculated. The frequency  $f$  is varied from  $7[\text{GHz}]$  to  $30[\text{GHz}]$  in steps of  $100[\text{MHz}]$ . The angle of the incident  $\text{TE}(0,0)$  Floquet plane wave is defined in a polar reference system where the angles  $\theta$  and  $\phi$  vary with the frequency  $f$  given by equation 5.1 with  $n = 3$ .

### Comparison of Results

The results are presented in figure 5.6. The figure shows a very close agreement with the numerical results produced by Luxaflex. The resonance frequency at approximately  $20[\text{GHz}]$  is the same for both methods. This means that the unknown electric surface current on the horizontal dipole can be approximated

in a good way either by using the global thin strip or by using the local rooftop and RWG expansion functions. Furthermore, internal consistency has been checked by using the conservation of energy principle and proved to be correct. This supports a correct functioning of the computational method and of a large part of the library of common functions used in all individual computational methods.

## 5.2.2 Crossed Dipole Frequency Selective Surface

### Motivation of the Choice for this Structure

With this basic structure we test the computational method for three segments with an EFIE and a dielectric junction. Further, we investigate the independence of the electromagnetic behavior if we choose local rooftop and local RWG expansion functions to expand the unknown electric surface current on the crossed dipole. Finally, we compare the response of this basic structure with waveguide simulator measurements.

### Detailed Description of the Structure

The structure is schematized in figure 5.7. Two dipoles each of  $l = 11[\text{mm}]$  length and of  $w = 0.15[\text{mm}]$  width are combined in a cross which is rotated by an angle of  $\alpha = 45[\text{deg}]$  with respect to the  $x$ -axis and stacked on a kapton layer of  $h = 0.07[\text{mm}]$  thickness with a relative permittivity of  $\varepsilon_r = 3.5$ . The two dipoles and the kapton layer are centered in a square unit cell of  $d = 8.4[\text{mm}]$  length. The unit cells are placed in a rectangular grid with basis vectors  $\mathbf{d}_1 = 8.4\hat{\mathbf{x}}[\text{mm}]$  and  $\mathbf{d}_2 = 8.4\hat{\mathbf{y}}[\text{mm}]$ .

### Description of the Comparison Techniques

The computational method is based on a Luxaflex model for three segments with a dielectric junction between the first two segments and an EFIE junction between the last two segments.

- A left probing interface is placed in the first (layered space) segment at  $z = -1[\text{mm}]$ .
- The first segment represents the free space behind the kapton layer.
- The first junction at  $z = 0[\text{mm}]$  represents the dielectric junction between the free space and the kapton layer.
- The second segment represents the kapton layer.
- The second junction at  $z = 0.07[\text{mm}]$  represents the crossed dipole.
- The third segment represents the free space above the crossed dipole.
- A right probing interface is placed in the last (layered space) segment at  $z = 1.07[\text{mm}]$  (which is  $1[\text{mm}]$  away from the second junction).

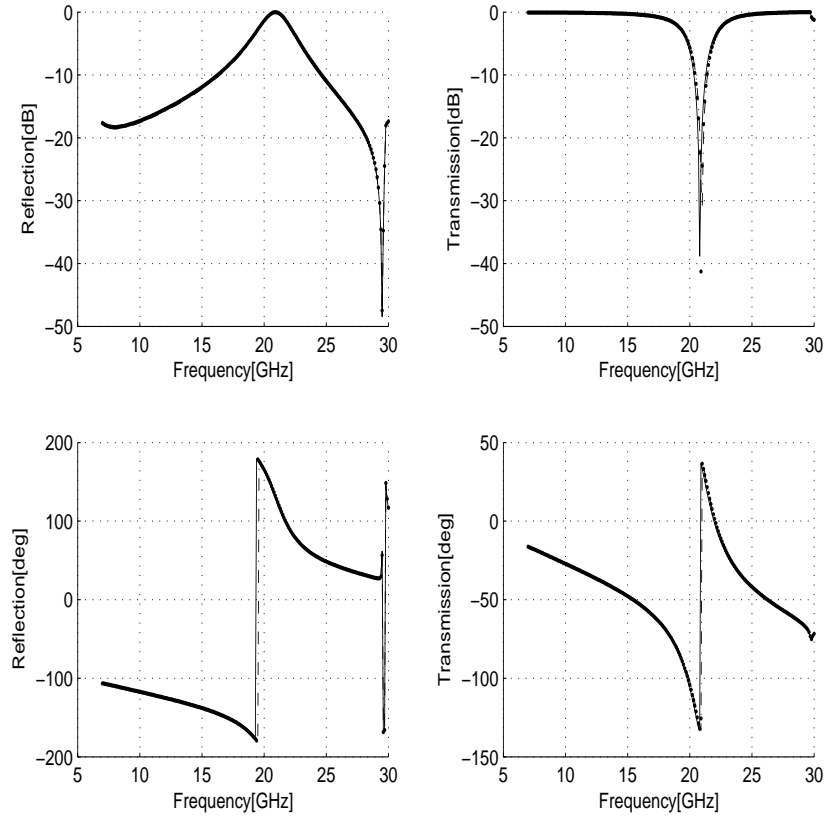


Figure 5.6: Results for horizontal dipole frequency selective surface. Solution based on global thin strip modes (solid curve), local rooftop expansion functions (dashed-dotted curve) and local RWG expansion functions (dotted curve) as a function of frequency  $f$  [GHz]. Top left figure for power reflection coefficient [dB], bottom left figure for phase reflection coefficient [deg]. Top right figure for power transmission coefficient [dB], bottom right figure for phase transmission coefficient [deg].

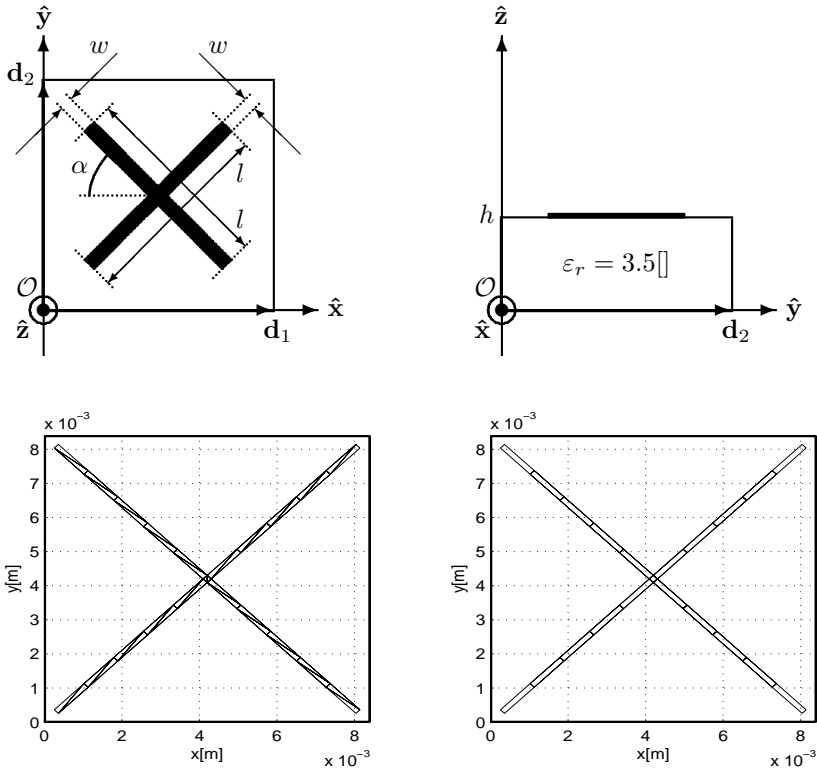


Figure 5.7: Configuration of the crossed dipole frequency selective surface. Bottom left plot triangular mesh and bottom right plot rectangular mesh.

This model was used in three different calculations where the unknown electric surface current on the crossed dipole was expanded using the global thin strip, local RWG and local rooftop expansion functions.

- The first calculation is based on global thin strip expansion functions (first 10 modes).
- The second calculation is based on local rooftop expansion functions defined on a rectangular mesh (given by the right plot in figure 5.7).
- The third calculation is based on local RWG expansion functions defined on a triangular mesh (given by the left plot in figure 5.7).

The reflection coefficient between an incident TE(0,0) and an outgoing TE(0,0) Floquet plane wave at the right probe is calculated. The transmission coefficient between an incident TE(0,0) Floquet plane wave at the right probe and an outgoing TE(0,0) Floquet plane wave at the left probe is calculated. The frequency  $f$  is varied from 7[GHz] to 15[GHz] in steps of 100[MHz]. The angle of the incident TE(0,0) Floquet plane wave is defined in a polar reference system where the angles  $\theta$  and  $\phi$  vary with the frequency  $f$  given by equation 5.1 with  $n = 3$ . This relation establishes a direct link with a waveguide simulator measurement that was carried out where three unit cells in a row were placed in a waveguide with a width of 25.2[mm] and a height of 8.4[mm]. The measured reflection and transmission coefficients of the TE(1,0) waveguide mode can directly be compared with the calculated reflection and transmission coefficients of the TE(0,0) Floquet plane wave as a function of the frequency.

### Comparison of Results

The results are presented in figure 5.8. The figure shows a good agreement between the numerical results produced by Luxaflex, where we used the local expansion functions, and the waveguide simulator measurements. This means that the unknown electric surface current on the crossed dipole can be approximated in a good way either by using the local rooftop or the local RWG expansion functions. The waveguide simulator measurements however show a small approximate 500[MHz] shift to a higher frequency. This is due to a combination of an uncertain value of the permittivity of the kapton layer and the choice of a too simple mesh. Finer meshes lead to smaller frequency shifts with respect to the measurements. At the cross of the two dipoles current must be able to flow around the corner to allow for a coupling between the two dipoles. Further at the edges of the cross we expect a significant singular edge behavior at these corners. With the mesh given in figure 5.7 we can model current flowing around the corner. However this singular edge behavior cannot be modeled properly and will therefore result in an incorrect prediction of the resonance frequency. To see the importance of the fact that current must be able to flow around the corner we have calculated the response of the crossed dipole with the global thin-strip functions. The result, which is also shown in figure 5.8, fails to show

the correct behavior. Finally, internal consistency has been checked by using the conservation of energy principle.

### 5.2.3 Gridded Square Frequency Selective Surface

#### Motivation of the Choice for this Structure

With this basic structure we test the computational method for three segments with an EFIE and a dielectric junction. Further, we investigate the independence of the electromagnetic behavior if we choose local rooftop and local RWG expansion functions to expand the unknown electric surface current on the gridded square. Finally, we compare the response of this basic structure with waveguide simulator measurements. This structure is used within Thales Nederland in a number of research projects. The dimensions and frequencies of operation of this structure are not given for reasons of company confidentiality.

#### Detailed Description of the Structure

The structure is schematized in figure 5.9. Two square rectangular loops are stacked on a kapton layer of thickness  $h$  with a relative permittivity of  $\varepsilon_r$ . The outer rectangular loop has a heart line  $l_o$  and a width  $w_o$ . The inner rectangular loop has a heart line  $l_i$  and a width  $w_i$ . The two loops and the kapton layer are centered in a square unit cell of size  $d$ . The unit cells are placed in a rectangular grid with basis vectors  $\mathbf{d}_1 = d\hat{\mathbf{x}}$  and  $\mathbf{d}_2 = d\hat{\mathbf{y}}$ .

The circumference of a rectangular loop is closely related to a resonance frequency of the complete structure. In the case of a loop this occurs when the wavelength of the incident wave equals the circumference. However since there are two loops there is interference between them which disturbs this relation. Within Thales Nederland we have used simple lumped circuit models to describe this coupling and to predict the new resonance frequency for given dimensions of the rectangular loops.

#### Description of the Comparison Techniques

The computational method is based on a Luxaflex model for three segments with a dielectric junction between the first two segments and an EFIE junction between the last two segments.

- A left probing interface is placed in the first (layered space) segment.
- The first segment represents the free space behind the kapton layer.
- The first junction represents the dielectric junction between the free space and the kapton layer.
- The second segment represents the kapton layer.
- The second junction represents the gridded square.

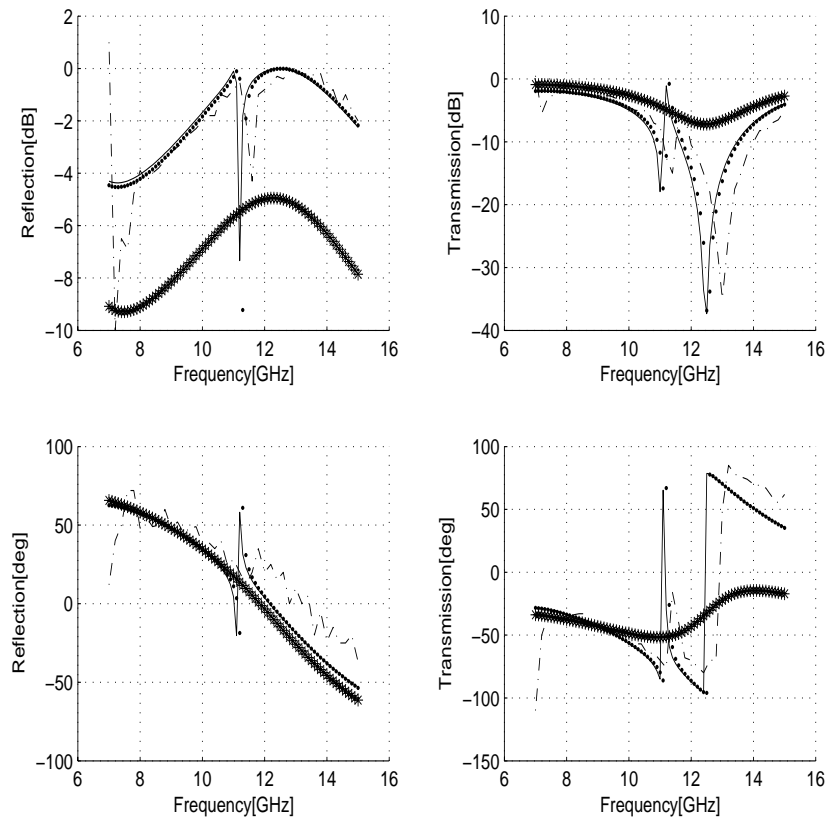


Figure 5.8: Results for crossed dipole frequency selective surface. Solution based on local rooftop expansion functions (solid curve), local RWG expansion functions (dotted curve), global thin-strip expansion functions (artistic curve) and waveguide simulator measurements (dashed-dotted curve) as a function of frequency  $f$ [GHz]. Top left figure for power reflection coefficient[dB], bottom left figure for phase reflection coefficient[deg]. Top right figure for power transmission coefficient[dB], bottom right figure for phase transmission coefficient[deg].

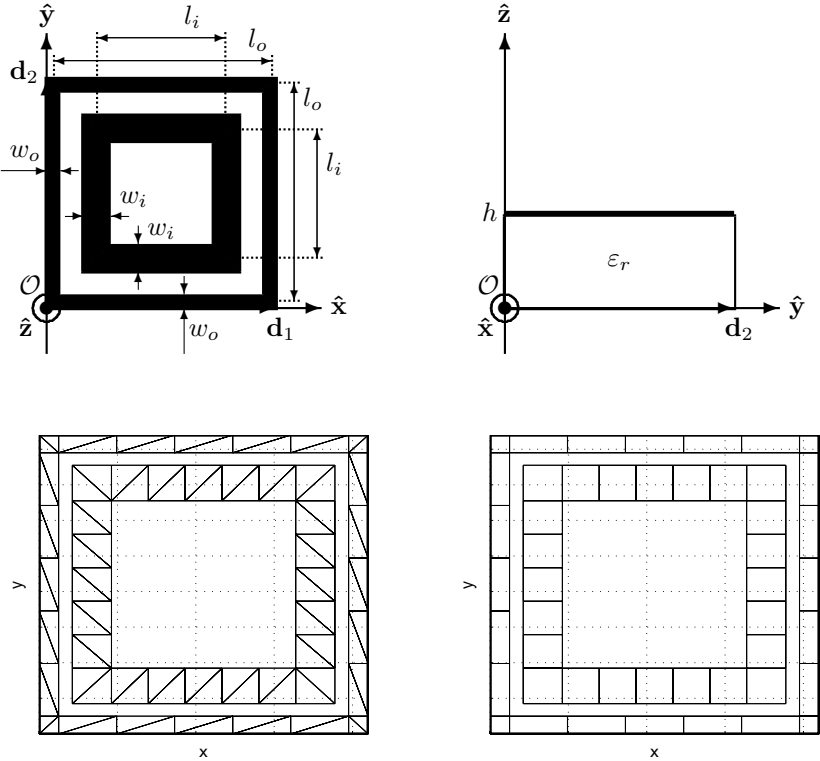


Figure 5.9: Configuration of the gridded square frequency selective surface. Left plot triangular mesh and right plot rectangular mesh.



- The third segment represents the free space above the gridded square.
- A right probing interface is placed in the last (layered space) segment.

This model was used in two different calculations where the unknown electric surface current on the gridded square was expanded using the local RWG and local rooftop expansion functions.

- The first calculation is based on local rooftop expansion functions defined on a rectangular mesh (given by the right plot in figure 5.9).
- The second calculation is based on local RWG expansion functions defined on a triangular mesh (given by the left plot in figure 5.9).

The reflection coefficient between an incident TE(0,0) and an outgoing TE(0,0) Floquet plane wave at the right probe is calculated. The transmission coefficient between an incident TE(0,0) Floquet plane wave at the right probe and an outgoing TE(0,0) Floquet plane wave at the left probe is calculated. The frequency  $f$  is varied. The angle of the incident TE(0,0) Floquet plane wave is defined in a polar reference system where the angles  $\theta$  and  $\phi$  vary with the frequency  $f$  given by equation 5.1 with  $n = 3$ . This relation establishes a direct link with a waveguide simulator measurement that was carried out where three unit cells in a row were placed in a waveguide. The measured reflection and transmission coefficients of the TE(1,0) waveguide mode can directly be compared with the calculated reflection and transmission coefficients of the TE(0,0) Floquet plane wave as a function of the frequency.

### Comparison of Results

The results are presented in figure 5.10. The figure shows a very good agreement between the numerical results produced by Luxaflex and the waveguide simulator measurements. This means that the unknown electric surface current on the gridded square can be approximated in a good way either by using the local rooftop or the local RWG expansion functions. To see the importance of the fact that current must be able to flow around the corner we have calculated the response of the gridded square with the global thin-strip functions. The result completely fails to show a correct behavior and is therefore not shown. Finally, internal consistency has been checked by using the conservation of energy principle.

## 5.2.4 Circular Loop Frequency Selective Surface

### Motivation of the Choice for this Structure

With this basic structure we test the computational method for three segments with an EFIE and a dielectric junction. We compare the response of this basic structure with waveguide simulator measurements.

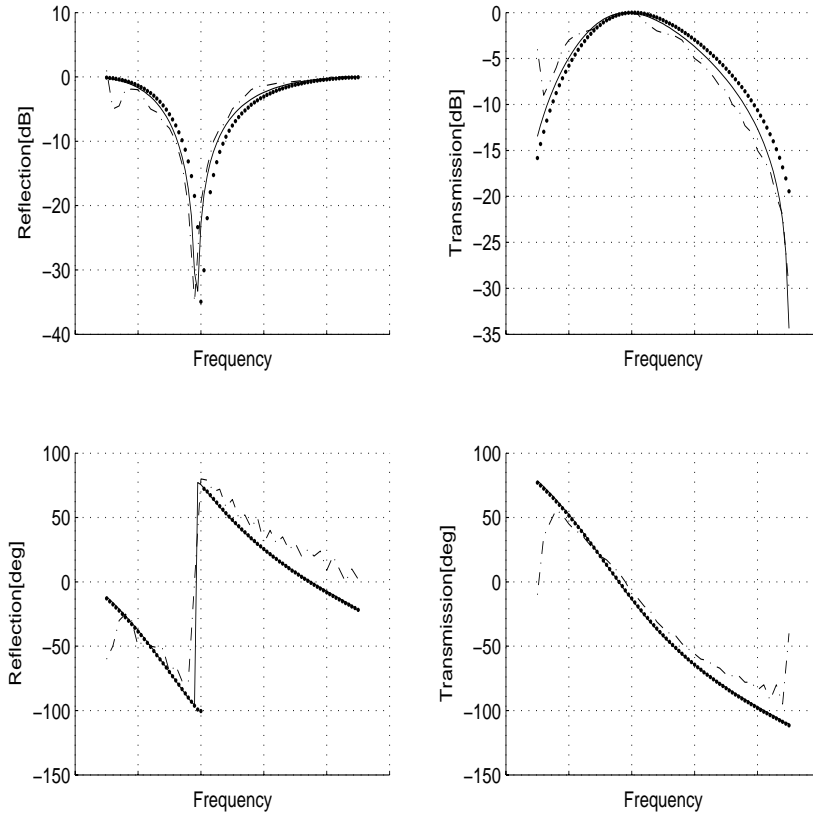


Figure 5.10: Results for gridded square frequency selective surface. Solution based on local rooftop expansion functions (solid curve), local RWG expansion functions (dotted curve) and waveguide simulator measurements (dashed-dotted curve) as a function of frequency. Top left figure for power reflection coefficient[dB], bottom left figure for phase reflection coefficient[deg]. Top right figure for power transmission coefficient[dB], bottom right figure for phase transmission coefficient[deg].

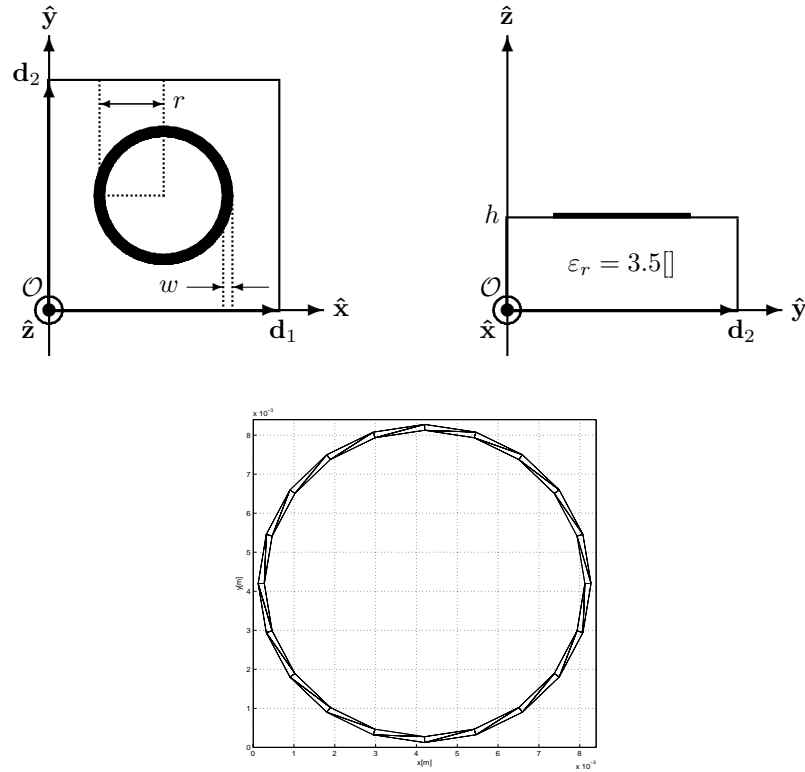


Figure 5.11: Configuration of the circular loop frequency selective surface. Bottom figure triangular mesh.

### Detailed Description of the Structure

The structure is schematized in figure 5.11. A single circular loop with a radius of  $r = 4$ [mm] (from the center to the heart line) and  $w = 1$ [mm] width is stacked on a kapton layer of  $h = 0.07$ [mm] thickness with a relative permittivity of  $\epsilon_r = 3.5$ []. The circular loop and the kapton layer are centered in a square unit cell of  $d = 8.4$ [mm] size. The unit cells are placed in a rectangular grid with basis vectors  $\mathbf{d}_1 = 8.4\hat{\mathbf{x}}$ [mm] and  $\mathbf{d}_2 = 8.4\hat{\mathbf{y}}$ [mm].

### Description of the Comparison Techniques

The computational method is based on a Luxaflex model for three segments with a dielectric junction between the first two segments and an EFIE junction between the last two segments.

- A left probing interface is placed in the first (layered space) segment at  $z = -1$ [mm].

- The first segment represents the free space behind the kapton layer.
- The first junction at  $z = 0$ [mm] represents the dielectric junction between the free space and the kapton layer.
- The second segment represents the kapton layer.
- The second junction at  $z = 0.07$ [mm] represents the circular loop.
- The third segment represents the free space above the circular loop.
- A right probing interface is placed in the last (layered space) segment at  $z = 1.07$ [mm] (which is 1[mm] away from the second junction).

This model was used in a calculation where the unknown electric surface current on the circular loop was expanded using the local RWG expansion functions defined on a triangular mesh (given in figure 5.11). The reflection coefficient between an incident TE(0,0) and an outgoing TE(0,0) Floquet plane wave at the right probe is calculated. The transmission coefficient between an incident TE(0,0) Floquet plane wave at the right probe and an outgoing TE(0,0) Floquet plane wave at the left probe is calculated. The frequency  $f$  is varied from 7[GHz] to 15[GHz] in steps of 100[MHz]. The angle of the incident TE(0,0) Floquet plane wave is defined in a polar reference system where the angles  $\theta$  and  $\phi$  vary with the frequency  $f$  given by equation 5.1 with  $n = 3$ . This relation establishes a direct link with a waveguide simulator measurement that was carried out where three unit cells in a row were placed in a waveguide with a width of 25.2[mm] and a height of 8.4[mm]. The measured reflection and transmission coefficients of the TE(1,0) waveguide mode can directly be compared with the calculated reflection and transmission coefficients of the TE(0,0) Floquet plane wave as a function of the frequency.

### Comparison of Results

The results are presented in figure 5.12. The figure shows a very good agreement between the numerical results produced by Luxaflex and the waveguide simulator measurements. Except in the lower frequency band we see a mismatch between measurement and simulation. This is due to measurement difficulties for frequencies near the cutoff frequency. Furthermore, internal consistency has been checked by using the conservation of energy principle and proved to be correct.

## 5.2.5 Square Patch Frequency Selective Surface

### Motivation of the Choice for this Structure

With this basic structure we test the computational method for two segments with an EFIE junction and a ground plane. Further, we investigate the independence of the electromagnetic behavior if we choose local rooftop, local RWG and global patch expansion functions to expand the unknown electric surface

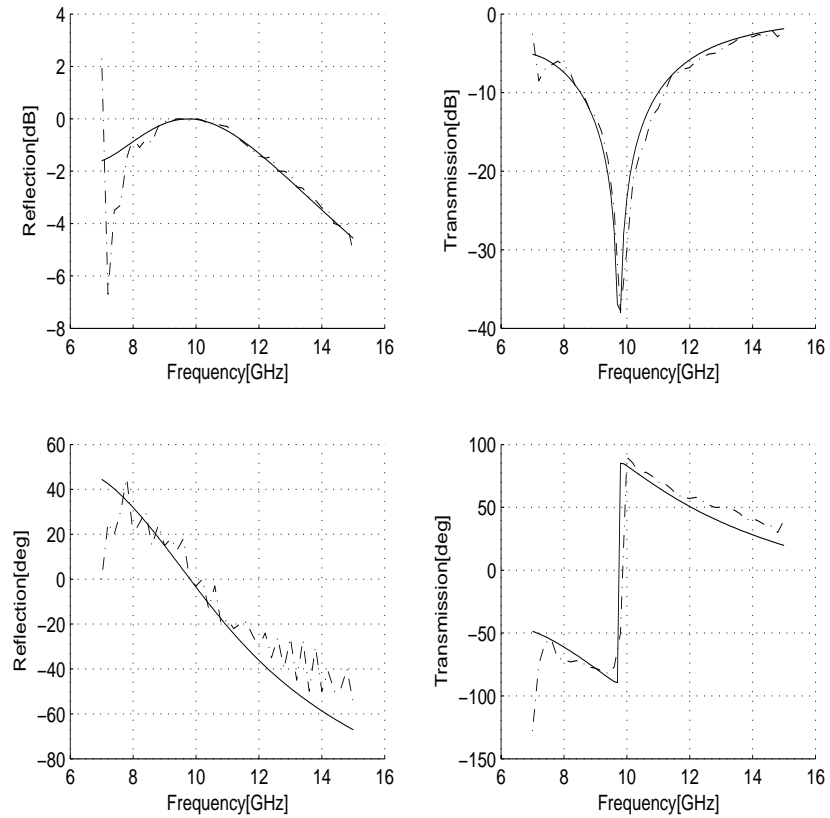


Figure 5.12: Results for circular loop frequency selective surface. Solution based on local RWG expansion functions (solid curve) and waveguide simulator measurements (dashed-dotted curve) as a function of frequency  $f$ [GHz]. Top left figure for power reflection coefficient[dB], bottom left figure for phase reflection coefficient[deg]. Top right figure for power transmission coefficient[dB], bottom right figure for phase transmission coefficient[deg].

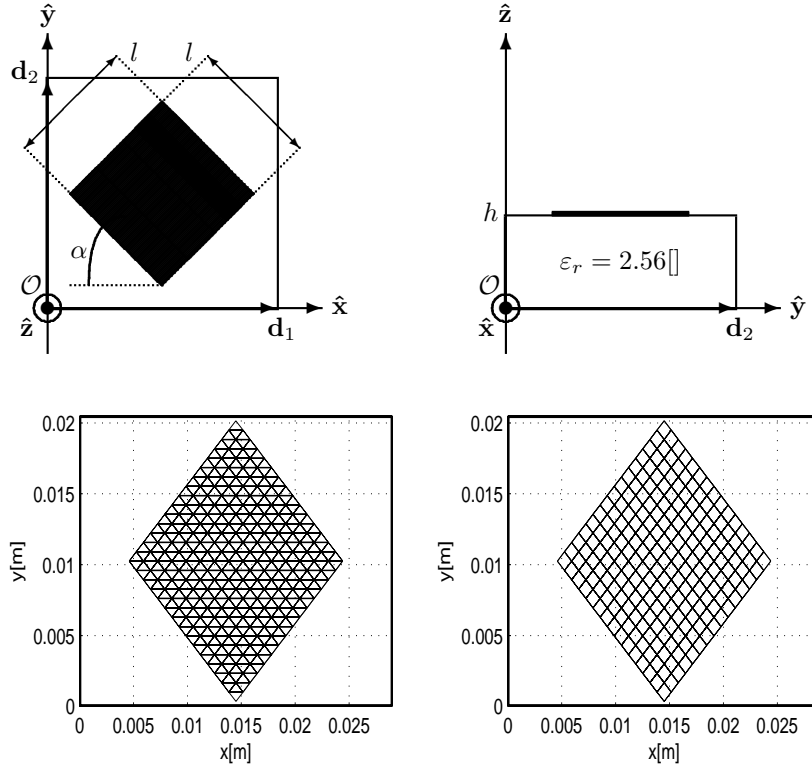


Figure 5.13: Configuration of the square patch frequency selective surface. Bottom left plot triangular mesh and bottom right plot rectangular mesh.

current on the square patch. Finally, we compare the response of this basic structure with results obtained from the literature [1]. Note that the response of this structure has not been measured in the waveguide simulator.

### Detailed Description of the Structure

The structure is schematized in figure 5.13. A square patch of  $l = 14$ [mm] size is stacked on a dielectric layer of  $h = 4.8$  [mm] thickness with a relative permittivity of  $\epsilon_r = 2.56$ []. The patch is rotated by an angle of  $\alpha = 45$ [deg] with respect to the  $x$ -axis. The dielectric layer with the patch is then stacked on a ground plane. The square patch and the dielectric layer are placed and centered in a rectangular unit cell of  $d_x = 29$ [mm] length and  $d_y = 20.5$ [mm] height. The unit cells are placed in a rectangular grid with basis vectors  $\mathbf{d}_1 = 29\hat{\mathbf{x}}$ [mm] and  $\mathbf{d}_2 = 20.5\hat{\mathbf{y}}$ [mm].

### Description of the Comparison Techniques

The computational method is based on a Luxaflex model for three segments with a dielectric junction between the first two segments and an MFIE junction between the last two segments.

- The first segment represents the ground plane below the dielectric layer. The electric conductivity was chosen large enough to represent a ground plane.
- The first junction at  $z = 0$ [mm] represents the dielectric junction between the ground plane and the dielectric layer.
- The second segment represents the dielectric layer.
- The second junction at  $z = 4.8$ [mm] represents the square patch.
- The third segment represents the free space above the square patch.
- A right probing interface is placed in the last (layered space) segment at  $z = 5.8$ [mm].

This model was used in three different calculations where the unknown electric surface current on the patch was expanded using the local RWG, local rooftop and global patch expansion functions.

- The first calculation is based on global patch expansion functions (72 first and second order Chebyshev modes).
- The second calculation is based on local rooftop expansion functions defined on a rectangular mesh (given by the right plot in figure 5.13).
- The third calculation is based on local RWG expansion functions defined on a triangular mesh (given by the left plot in figure 5.13).

The reflection coefficient between an incident TE(0,0) Floquet plane wave and an outgoing TE(0,0) Floquet plane wave at the right probe is calculated. The frequency  $f$  is varied from 8[GHz] to 12[GHz] in steps of 100[MHz]. The angle of the incident TE(0,0) Floquet plane wave is defined in a polar reference system where the angles are fixed at  $\theta = 30$ [deg] and  $\phi = 0$ [deg].

### Comparison of Results

The results are presented in figure 5.14. The figure shows a good agreement between the numerical results produced by Luxaflex. Furthermore these results are in very close agreement with the numerical results presented in [1]. This means that the unknown electric surface current on the square patch can be approximated in a good way either by using the global patch, the local rooftop or the local RWG expansion functions. Furthermore, internal consistency has been checked by using the conservation of energy principle.

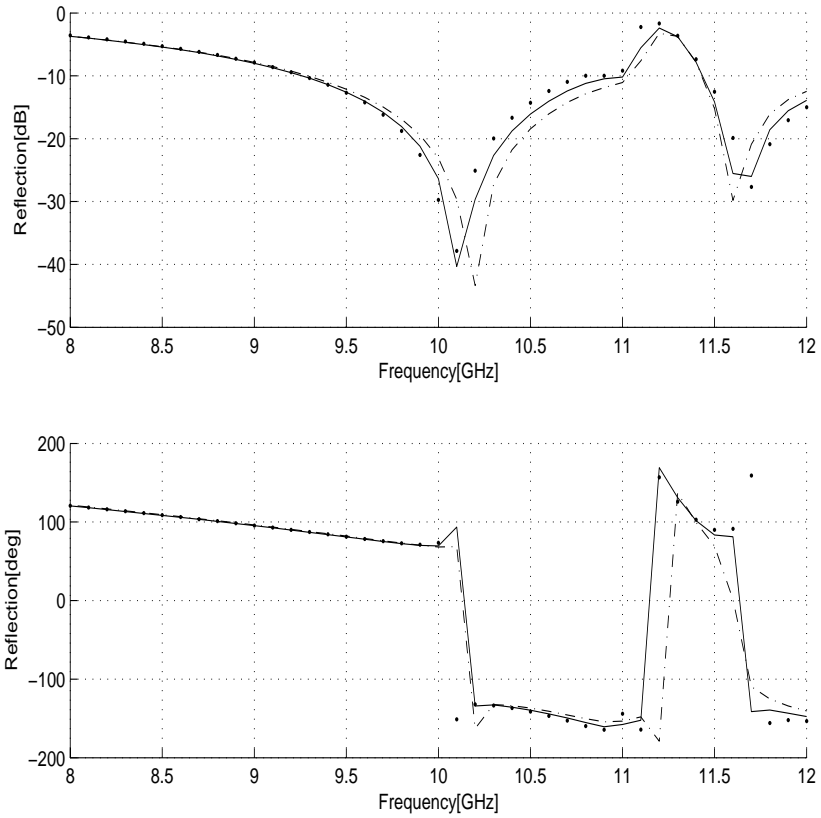


Figure 5.14: Results for square patch frequency selective surface. Solution based on global patch expansion functions (solid curve), local rooftop expansion functions (dashed-dotted curve) and local RWG expansion functions (dotted curve) as a function of frequency  $f$  [GHz]. Top figure for power reflection coefficient [dB], bottom figure for phase reflection coefficient [deg].



## 5.2.6 Cavity Backed Patch Radiator

### Motivation of the Choice for this Structure

With this basic structure we test the computational method for three segments with two coupled MFIE junctions. We use both waveguide and layered space segments. Further, we compare the response of this basic structure with results obtained with ©HFSS. The dimensions and frequencies of operation of this structure are not given for reasons of company confidentiality.

### Detailed Description of the Structure

The structure is schematized in figure 5.15. It consists of three parts: a slot, box and a patch. The slot is a waveguide of width  $w_s$  and of height  $h_s$ . It is filled with a dielectric material with a relative permittivity of  $\epsilon_r$ . The box is a waveguide of width  $w_b$ , of height  $h_b$  and of depth  $h$ . It is filled with the same dielectric material. The patch has a width  $w_p$  and a height  $h_p$ . The patch lies on top of the box on the dielectric material. Above the patch there is free space. The unit cells are placed in a realistic triangular grid with basis vectors  $\mathbf{d}_1$  and  $\mathbf{d}_2$ . In the transverse plane, all parts of this structure are centered within the unit cell.

### Description of the Comparison Techniques

The computational method is based on a Luxaflex model for three segments with MFIE junctions between the segments.

- A left probing interface is placed in the first (waveguide) segment.
- The first segment represents the slot.
- The first junction represents the aperture between the slot and the box.
- The second segment represents the box.
- The second junction represents the interface in which the aperture around the patch is considered.
- The last segment represents the free space above the patch.
- A right probing interface is placed in the last (layered space) segment.

This model was used in a calculation where the unknown magnetic surface currents in both the apertures were expanded using the local RWG expansion functions defined on a triangular mesh (given in figure 5.15). The reflection coefficient between an incident TE(1,0) waveguide mode and an outgoing TE(1,0) waveguide mode at the left probe is calculated. This coefficient is a measure for the mismatch loss of the complete radiating structure. The frequency is varied. The phase shift between the elements in the basic structure is defined in a polar reference system where the angles are fixed at  $\theta = 0[\text{deg}]$  and  $\phi = 0[\text{deg}]$ .

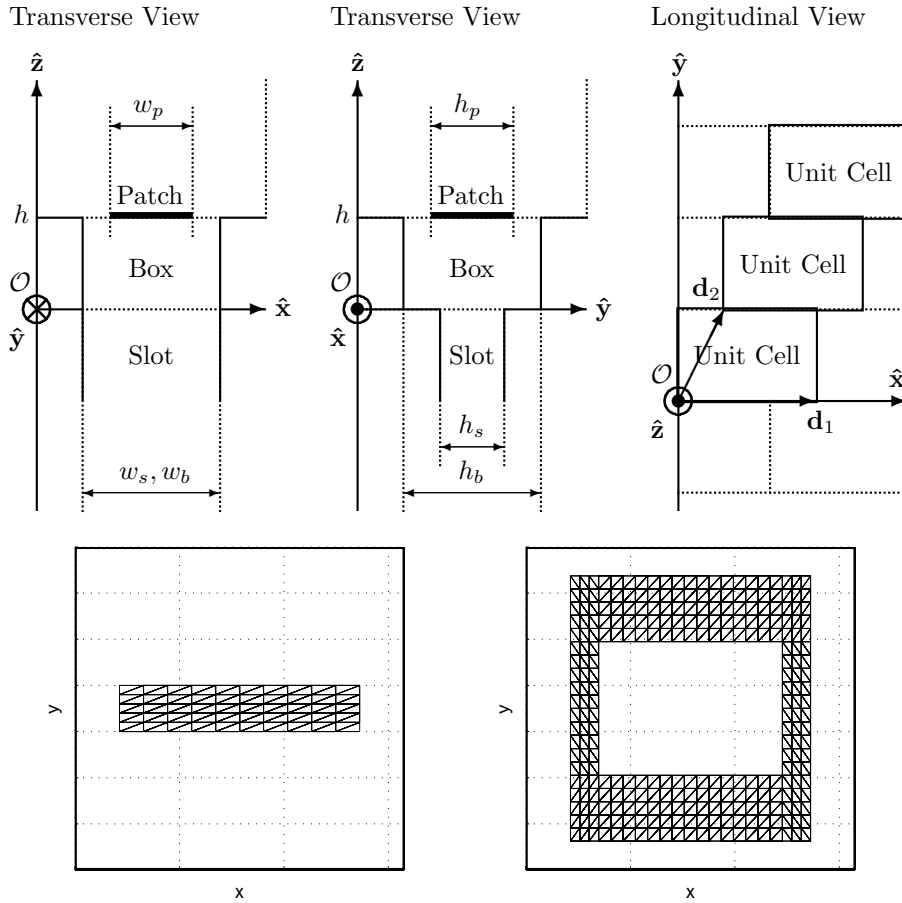


Figure 5.15: Configuration of the cavity backed patch radiator. Triangular mesh. Bottom left plot first aperture and bottom right plot second aperture.

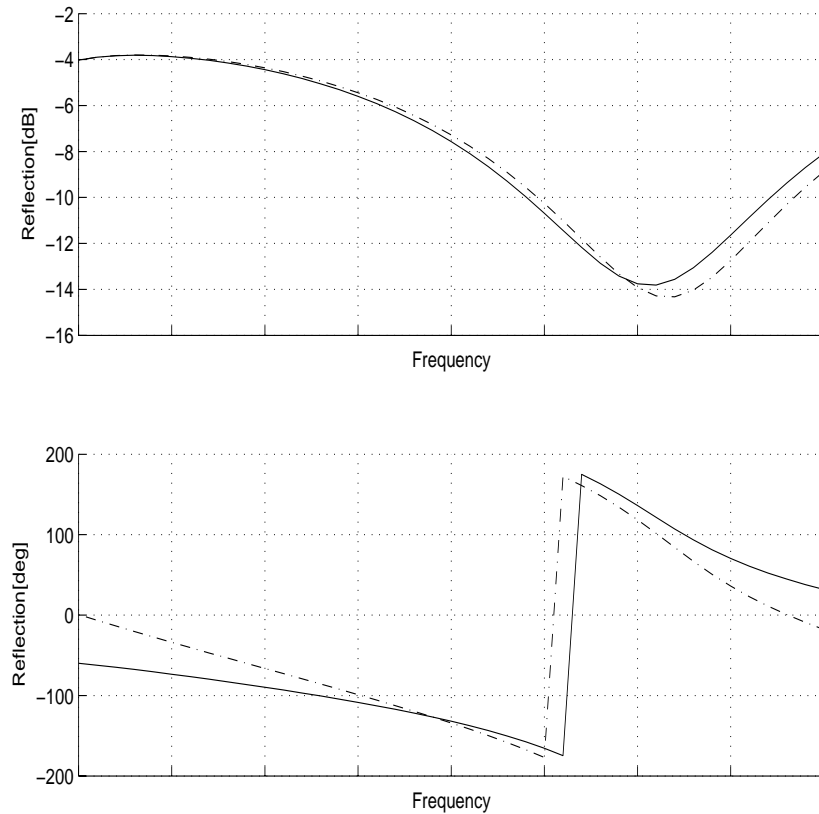


Figure 5.16: Results for cavity backed patch radiator. Solution based on local RWG expansion functions (solid curve) and ©HFSS numerical results (dashed-dotted curve) as a function of frequency. Top figure for power reflection coefficient[dB], bottom figure for phase reflection coefficient[deg].

In a second computation, we have used ©HFSS to obtain numerical results for this configuration for comparison with Luxaflex.

### Comparison of Results

The results are presented in figure 5.16. The figure shows a good agreement between the numerical results produced by Luxaflex and ©HFSS. The simulation times for both ©HFSS and Luxaflex were for this structure an approximate two hours. However we should note that the acceleration technique has not been used in Luxaflex. Further Luxaflex is written in MATLAB which slows down the computation as well. We will come back on this issue in the conclusions and recommendations. Finally, internal consistency has been checked by using the conservation of energy principle and proved to be correct.

### 5.2.7 Open-Ended Waveguide Radiator

#### Motivation of the Choice for this Structure

With this basic structure we test the computational method for five segments with two coupled MFIE junctions and two dielectric junctions. These dielectric junctions constitute a dielectric stacked slab (also referred to as a wide angle impedance matching sheet [59]) on top of the coupled MFIE junctions and improve the scanning properties. We use both waveguide and layered space segments. We investigate the independence of the electromagnetic behavior if we choose local RWG and global waveguide mode expansion functions to expand the unknown magnetic surface current in the apertures. Finally, we compare the response of this basic structure with results obtained from the literature [22, 23, 24, 25, 26, 27, 28, 29]. We note that this type of structure is a representative candidate for a radiator. The dimensions and frequencies of operation of this structure are not given for reasons of company confidentiality.

#### Detailed Description of the Structure

The structure is schematized in figure 5.17. It consists of four parts: a waveguide, iris, foam layer and a so-called waim sheet. The waveguide has a width  $w_w$  and a height  $h_w$ . It is filled with free space. The iris is a waveguide with a width  $w_i$ , a height  $h_i$  and a depth  $d_i$ . It is filled with free space. The foam layer is a layered space which consists of a material with a relative permittivity of  $\epsilon_r$ . It has a thickness of  $d_f$ . The waim sheet is a layered space and consists of a single dielectric layer only. It consists of a material with a relative permittivity of  $\epsilon_r$ . It has a thickness of  $d_w$ . The unit cells are placed in a triangular grid with basis vectors  $\mathbf{d}_1$  and  $\mathbf{d}_2$ . In the transverse direction, all parts of this structure are centered within the unit cell.

#### Description of the Comparison Techniques

The computational method is based on a Luxaflex model for five segments with MFIE junctions between the first and second two segments and dielectric junctions between the third and last two segments.

- A left probing interface is placed in the first (waveguide) segment.
- The first segment represents the waveguide.
- The first junction represents the aperture between the waveguide and the iris.
- The second segment represents the iris.
- The second junction represents the aperture between the iris and the foam segment.
- The third segment represents the foam layer.

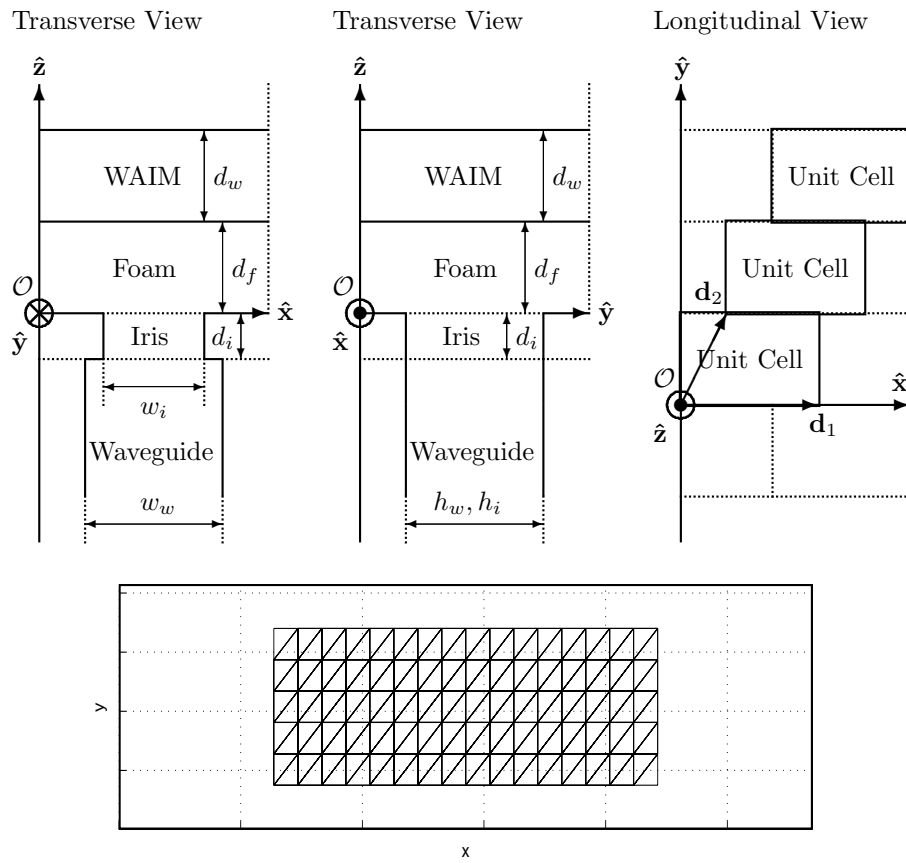


Figure 5.17: Configuration of the open-ended waveguide radiator. Bottom figure triangular mesh.

- The third junction represents the dielectric junction between the foam segment and the waim sheet.
- The fourth layer represents the waim sheet.
- The last junction represents the dielectric junction between the waim sheet and the free space.
- The last segment represents the free space above the waim sheet.
- A right probing interface is placed in the last (layered space) segment.

This model was used in two different calculations where the unknown magnetic surface currents in both apertures were expanded using the local RWG and global waveguide mode expansion functions.

- The first calculation is based on global waveguide mode expansion functions (TM( $m, n$ ) modes with  $m, n = 1, 2, \dots, 10$  and TE( $p, q$ ) modes with  $p, q = 0, 1, 2, \dots, 10$  but  $p = q \neq 0$ ) in both apertures (10 modes are sufficient for convergence).
- The second calculation is based on local RWG expansion functions defined on a triangular mesh (given in figure 5.17) in both apertures.

The reflection coefficient between an incident TE(1,0) waveguide mode and an outgoing TE(1,0) waveguide mode at the left probe is calculated. This coefficient is a measure for the mismatch loss of the complete radiating structure. The phase shift between the elements in the basic structure is defined in a polar reference system where the angle  $\theta$  is varied from 0[deg] to 75[deg] in steps of 1[deg], and where the angle  $\phi$  is fixed. Further the frequency is fixed. Finally, we have used the results from Chan (which are based on a similar but independent computational method) for this configuration for comparison with Luxaflex.

### Comparison of Results

The results are presented in figure 5.18. The figure shows a very close agreement between the numerical results produced by Luxaflex and from the literature [22, 23, 24, 25, 26, 27, 28, 29]. This means that the unknown magnetic surface current in the apertures can be approximated in a good way either by using the global waveguide mode or the local RWG expansion functions. Furthermore, internal consistency has been checked by using the conservation of energy principle.

## 5.2.8 Open-Ended Waveguide with Patch Radiator

### Motivation of the Choice for this Structure

With this basic structure we test the computational method for three segments with a strongly coupled MFIE and EFIE junction. We use both waveguide and layered space segments. We investigate the independence of the electromagnetic behavior if we choose local RWG, global waveguide mode and global

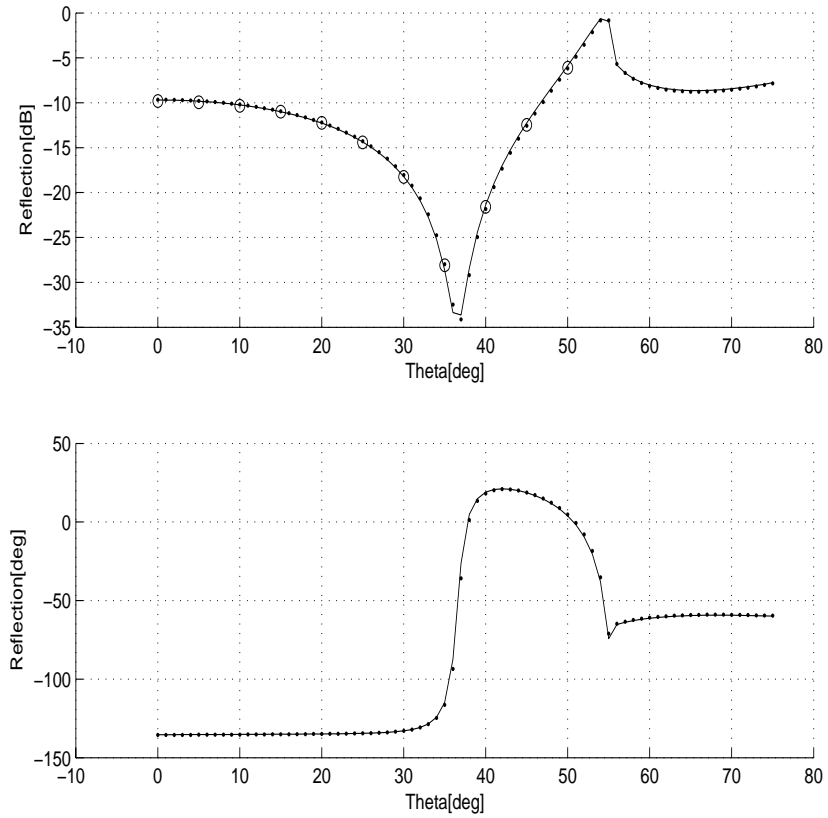


Figure 5.18: Results for open-ended waveguide radiator. Solution based on global waveguide mode expansion functions (solid curve), local RWG expansion functions (dotted curve) and Chan numerical results (circles) as a function of angle of incidence  $\theta$ [deg] for fixed frequency with fixed  $\phi$ . Top figure for power reflection coefficient[dB], bottom figure for phase reflection coefficient[deg].

patch expansion functions to expand the unknown electric and magnetic surface currents on the patch and in the aperture. Furthermore, we compare the response of this basic structure with results obtained from ©HFSS. The dimensions and frequencies of operation of this structure are not given for reasons of company confidentiality.

### Detailed Description of the Structure

The structure is schematized in figure 5.19. It consists of three parts: a slot, a sheet and a patch. The slot is a waveguide of width  $w_s$  and of height  $h_s$ . It is filled with a dielectric material with a relative permittivity of  $\epsilon_r$ . The sheet is a layered space of thickness  $h$ . It is filled with the same dielectric material. The patch has a width  $w_p$  and a height  $h_p$ . The patch lies on top of the sheet. Above the patch there is free space. The unit cells are placed in a triangular grid with basis vectors  $\mathbf{d}_1$  and  $\mathbf{d}_2$ . In the transverse plane, all parts of this structure are centered within the unit cell.

### Description of the Comparison Techniques

The computational method is based on a Luxaflex model for three segments with an MFIE junction between the first two segments, and an EFIE junction between the last two segments.

- A left probing interface is placed in the first (waveguide) segment.
- The first segment represents the slot.
- The first junction represents the aperture between the slot and the sheet.
- The second segment represents the sheet.
- The second junction represents the patch.
- The last segment represents the free space above the patch.
- A right probing interface is placed in the last (layered space) segment.

This model was used in three different calculations where the unknown magnetic surface current in the aperture was expanded using the local RWG and global waveguide mode expansion functions, and where the unknown electric surface current on the patch was expanded using local RWG and global patch expansion functions.

- The first calculation is based on local RWG expansion functions defined on a triangular mesh (given in figure 5.19) in both the aperture and on the patch.
- The second calculation is based on local RWG expansion functions defined on a triangular mesh (given by the left plot in figure 5.19) in the aperture and global patch expansion functions (72 first and second order Chebyshev modes) on the patch.



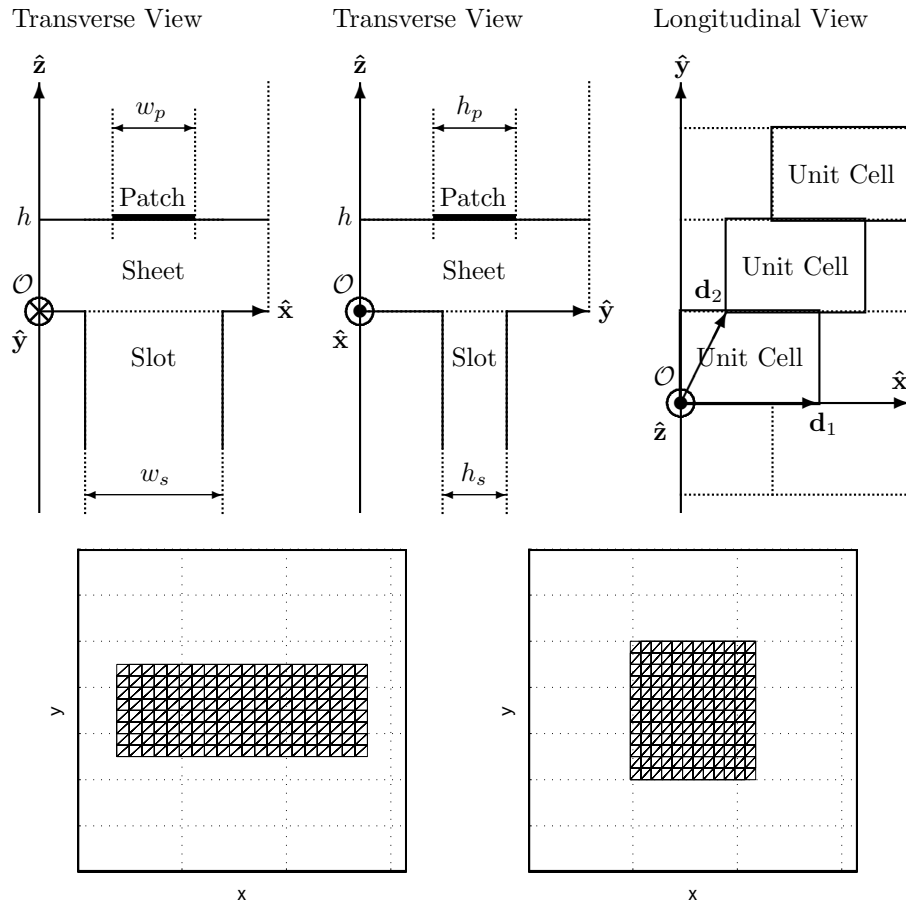


Figure 5.19: Configuration of the open-ended waveguide with patch radiator. Triangular mesh. Bottom left plot for aperture and bottom right plot for patch.

- The third calculation is based on global waveguide mode expansion functions (TM( $m, n$ ) modes with  $m, n = 1, 2, \dots, 10$  and TE( $p, q$ ) modes with  $p, q = 0, 1, 2, \dots, 10$  but  $p = q \neq 0$ ) in the aperture and global patch expansion functions (72 first and second order Chebyshev modes) on the patch.

The reflection coefficient between an incident TE(1,0) waveguide mode and an outgoing TE(1,0) waveguide mode at the left probe is calculated. This coefficient is a measure for the mismatch loss of the complete radiating structure. The frequency is varied. The phase shift between the elements in the basic structure is defined in a polar reference system where the angles are fixed at  $\theta = 30[\text{deg}]$  and  $\phi = 90[\text{deg}]$ .

Finally, we have used ©HFSS to obtain numerical results for this configuration for comparison with Luxaflex.

### Comparison of Results

The results are presented in figure 5.20. The figure shows a very good agreement between the numerical results produced by Luxaflex and ©HFSS. This means that the unknown electric and magnetic surface currents on the patch and in the apertures can be approximated in a good way either by using the global patch or the local RWG expansion functions. For the computation where we use global waveguide mode expansion functions to expand the unknown magnetic surface current in the aperture we have obtained different results. This is caused by a strong interaction due to a short distance between the patch and the aperture. The singular behavior of the  $x$ -directed current at the bottom and top side and the  $y$ -directed current at the left and the right side of the aperture plays a vital role [108]. With the global waveguide mode expansion functions this effect is not taken into account<sup>4</sup>. To see that this is true we have plotted the electric and magnetic surface currents on the patch and in the aperture in figure 5.21, respectively. Furthermore, internal consistency has been checked by using the conservation of energy principle.

---

<sup>4</sup>We would have to use an extremely large number of global waveguide mode expansion functions to catch the right behavior, whereas a small number of RWG expansion functions suffices.

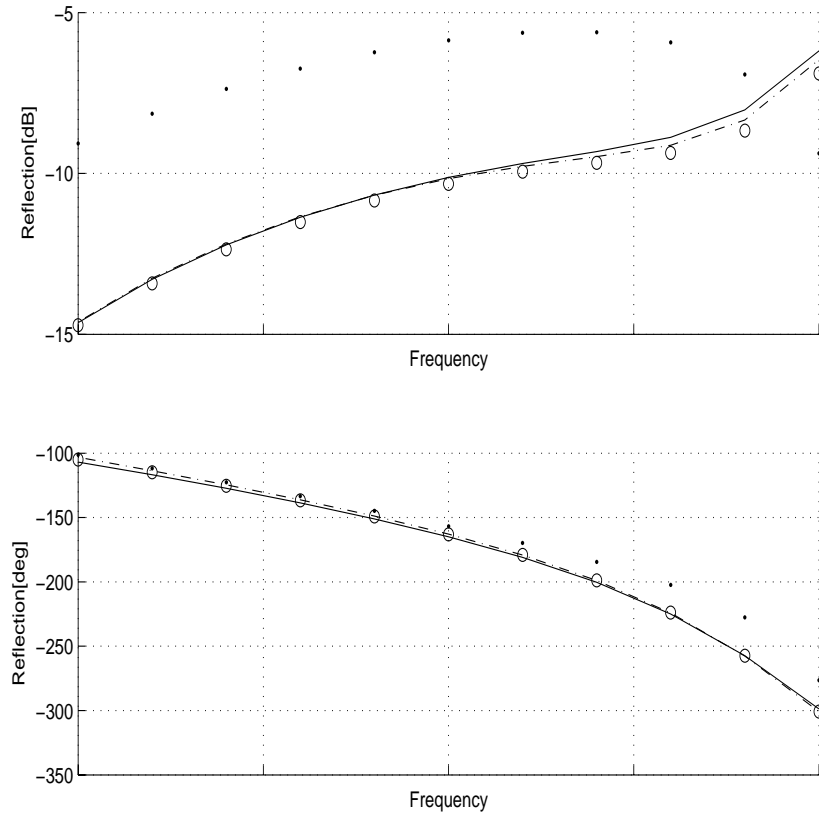


Figure 5.20: Results for open-ended waveguide with patch radiator. Solution based on local RWG expansion functions both in slot and on patch (solid curve), local RWG expansion functions in slot and global patch expansion functions on patch (dashed-dotted curve), global waveguide mode expansion functions in slot and global patch expansion functions on patch (dotted curve) and ©HFSS numerical results (circles) as a function of frequency. Top figure for power reflection coefficient[dB], bottom figure for phase reflection coefficient[deg].

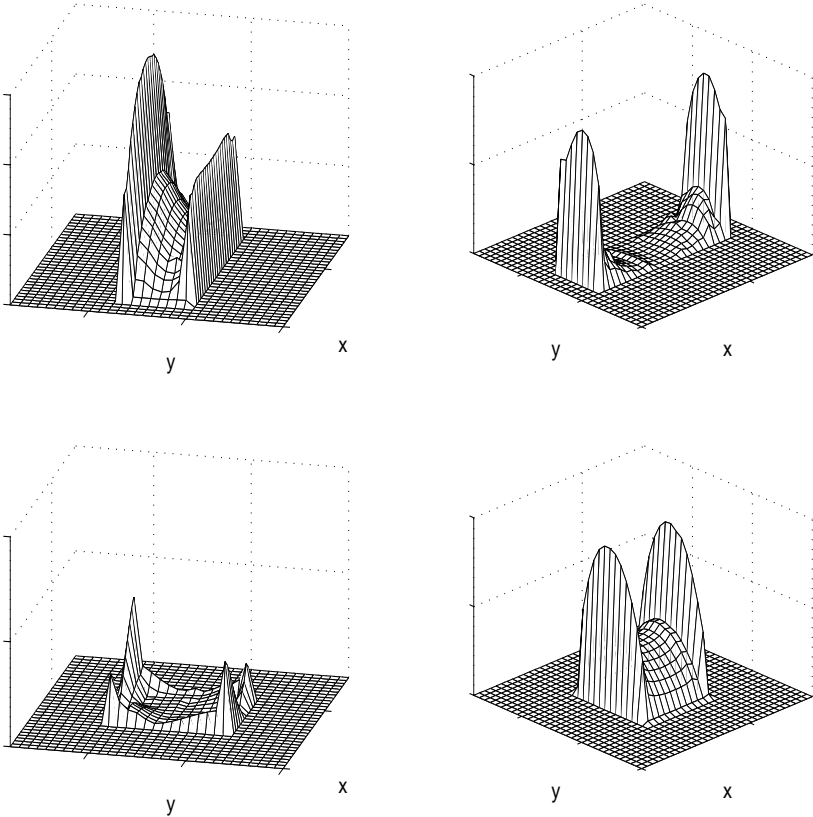


Figure 5.21: Absolute norm of various components of surface currents at fixed frequency. Top left and right figure magnetic surface current in the  $x$ -direction and  $y$ -direction in the aperture, respectively. Bottom left and right figure electric surface current in the  $x$ -direction and  $y$ -direction on the patch, respectively.



## Chapter 6

# Conclusions and Recommendations

In the introduction we have formulated the objectives of the thesis. The first objective was to develop a computational method that can predict the electromagnetic behavior for an arbitrary radiating array structure consisting of waveguide feeding elements, open-ended waveguides, and multilayer frequency selective surfaces. The second objective was to accelerate the computational method to speed up the current and future design process of phased array antennas. In this chapter we reflect on these objectives and give a number of conclusions and recommendations.

### 6.1 Conclusions

We divide the conclusions on the objective of the thesis in three categories: conclusions on the computational method, on the acceleration technique, and on the validation.

#### 6.1.1 Computational Method

In chapter 3 we have developed a computational method (with a software implementation called Luxaflex) that calculates the unknown electromagnetic field within the unit-cell structure. We assumed that within a single radiating element there were parts (basic structures) in which the junctions experienced a significant electromagnetic coupling. We assumed there was low electromagnetic coupling between the basic structures. To determine the total electromagnetic behavior efficiently we have exploited this property, and have separated the total calculation into one for each basic structure, and one for combining them. For the calculation of the electromagnetic behavior within a single basic structure we have formulated the scattering field problem and ensured the existence and uniqueness of a field solution within the basic structure by supplementing proper

boundary conditions which describe the domain where the Maxwell equations are to be solved.

The final objective of the simulation was to compute the field radiated by a given source in a complicated structure. If the Green's function of this structure were known, the computation could be carried out without difficulty and there would be no need to apply the equivalence theorem. On the contrary, by closing some gaps or removing some metal parts, we obtained simpler regions where the Green's function is known, as a modal expansion. The equivalence theorem says that in order to have the same field in the original and the modified structure, it is necessary to introduce suitable current distributions. The actual value of these currents cannot be given explicitly, but can be determined by the solution of an integral equation. Integral, because the relationship between currents and fields is always of integral type, with a kernel which is the Green's function, which is known in each sub-domain.

In the integral formulation, we expressed the unknown electromagnetic fields in terms of unknown electromagnetic surface currents. These unknown surface currents were discretized in terms of expansion functions, such as the rooftop and Rao-Wilton-Glisson (RWG) functions, and subsequently determined by the method of moments. This method converted the integral equation into a matrix equation of the type  $L\mathbf{u} = \mathbf{f}$  with linear operator  $L$ , unknown vector  $\mathbf{u}$ , and forcing vector  $\mathbf{f}$ . The matrix equation was solved by means of simple inversion. After solving the unknown surface currents with the method of moments, we have calculated the total electromagnetic field at any given location within the basic structure. To calculate the electromagnetic behavior of the total unit-cell structure, we have combined the individual electromagnetic behavior of all basic structures. For this purpose we have formulated a so-called generalized scattering matrix, which characterized this behavior for all basic structures individually, by relating the outgoing waves in terms of the incident waves. Then we have formulated a procedure that cascades two generalized scattering matrices. The result was a new generalized scattering matrix that characterizes the electromagnetic behavior of the combination of the two basic structures.

If we consider the case where both propagating and evanescent modes at both probing interfaces are present, the scattering matrices for the electric and magnetic field cannot be used individually as a measure for reflected or transmitted energy. The pointwise multiplication of the scattering matrices for the electric and magnetic field was a good alternative and direct measure for reflected and transmitted energy of a basic structure. Furthermore, and in this case, the cascading procedure must be applied to both scattering matrices for the electric and the magnetic field, respectively.

The stampmatrix/stampvector implementation turns out to be a uniform and cheap way of implementing matrix and vector contributions to the linear operator  $L$ . We have formulated a uniform approach where both waveguide and layered space segments are treated in the same manner. Furthermore, we have created a MATLAB toolbox with code for transmission-line examples, which have been described thoroughly in appendix B. The MATLAB toolbox also incorporates code for the interaction integrals which have been documented in

detail in appendices C-J. These appendices make this thesis a complete manual for Thales Nederland B.V. regarding the theory behind the Luxaflex software implementation. This MATLAB toolbox further allowed for code reusability, reduced the risk for implementation errors, and saved implementation time. This is very important from an industrial point of view. This has become especially apparent in the implementation of a new computational method. Further, by using the reversion technique for transmission lines we have saved half the implementation time for the transmission-line examples.

*We conclude that with this computational method we can predict the electromagnetic behavior for an arbitrary radiating array structure consisting of waveguide feeding elements, open-ended waveguides, and multilayer frequency selective surfaces. The prediction shows convergence when the size of the mesh elements decreases and when the number of waveguide and layered space modes in each segment increases.*

### 6.1.2 Acceleration Technique

Most of the computational effort in the procedure described in chapter 3 is spent in assembling the linear operator  $L$ . In chapter 4 we presented a novel acceleration technique that translated the evaluation of an asymptotically slowly converging series, that needs to be evaluated in assembling  $L$ , into a numerical integration over an exponentially fast converging series. This technique has reduced the time needed to evaluate these series and consists of three steps. The first step is a Kummer transformation, where the asymptotically slowly converging part of the series is subtracted (which results in a rapidly converging reduced series; four orders convergence improvement) and added (which results in a slowly converging correction series). Conventionally, a Kummer transformation is used if the correction series can be evaluated in a fast manner either in closed analytical form or by making use of asymptotical techniques. However this is not the case for the slowly converging correction series. Instead we take a second step where we use an Ewald transformation. This transformation converts the asymptotically slowly converging correction series into an integration over  $\tau$  of exponentially fast decaying functions. These functions contain an exponentially fast converging series for which the leading-order term is given by  $\exp(-k_t^2 \tau^{2\lambda})$ . The third step is to split the integration over  $\tau$  into one for small  $\tau$ , i.e., over the interval  $(0, \tau_1)$ , and one for large  $\tau$ , i.e., over the interval  $(\tau_1, \infty)$ . Then we apply a so-called Poisson transformation for the integration over small  $\tau$ , where the relatively slow convergence of the series within the exponentially fast decaying function, caused by the behavior of  $\exp(-k_t^2 \tau^{2\lambda})$  for small  $\tau$ , is converted into an exponentially fast converging series. The leading-order term for the integration over small  $\tau$  is given by  $\exp(-\rho^2/(4\tau^{2\lambda}))$ . The so-called transition point  $\tau_1$  is a compromise between the convergence behavior of the leading-order terms  $\exp(-k_t^2 \tau^{2\lambda})$  and  $\exp(-\rho^2/(4\tau^{2\lambda}))$ . The Poisson transformation step has resulted in the evaluation of a so-called exponential regularization of (a combination of) the expansion and weighting functions. The



overall success of this acceleration technique is shown to critically depend on the possibility of being able to quickly evaluate the regularization. Since the regularization is independent of angle of incidence, frequency and medium parameters we have calculated it at the beginning of the computation and stored it in a lookup table. This lookup table generation creates a trade-off situation where we can decide whether or not we use the acceleration technique. Since it takes time to generate this lookup table, a critical amount of simulations steps (break-even point) exists where the computational method with the acceleration technique becomes faster than the unaccelerated version.

Furthermore, we have considered three specific choices for the expansion and weighting functions that have led to workable analytical solutions and numerical approximations for the exponential regularization. The first case is the rooftop function defined in an orthogonal grid, which created a restriction in the modeling of the unknown surface currents. However most structures do not consist of arbitrarily shaped metal patches and apertures, and can therefore be captured in this orthogonal grid. An advantage of this grid is that we are able to express the exponential regularization in terms of complementary error functions. This method is the fastest for a given testcase when compared with the other two methods. It has the lowest lookup table generation time and the time per step is almost eight times smaller compared to the time per step in the unaccelerated method. Break-even is already reached from the fifth step onwards. In some cases where the unit-cell structure cannot be captured in an orthogonal grid we use the second case where the rooftop function is defined in an arbitrary grid. In this case, we express the exponential regularization as a convolution of two analytically known functions both with "almost" compact support. This method has a higher lookup table generation time due to the numerical convolution. The time per step is almost eight times smaller compared to the time per step in the unaccelerated method. Break-even is reached at a higher number of steps. The third case is the more general Rao-Wilton-Glisson function. With this triangular expansion function we can model the unknown currents in the most arbitrary way. In this case, we express the exponential regularization as a convolution of two numerically approximated functions both with "almost" compact support. This method has a high lookup table generation time due to both the numerical convolution and the numerical integration within the regularization integral. An analytical alternative has been given for the numerical integration, but due to time limitations has not yet been included in the implementation. Break-even is reached at a much higher number of steps. The time per step is almost six times smaller compared to the time per step in the unaccelerated method.

*Using the acceleration technique leads to the conclusion that the computational method is fast and produces equally accurate results (within tenths of dB's in power) compared to the unaccelerated method.*

### 6.1.3 Validation

In chapter 5 we have validated the capabilities of Luxaflex. We have validated our computational method against available commercial software tools (such as the finite-element code ©HFSS), and (some of them) against waveguide simulator measurements. We have done this for eight different radiating structures, of which the first five structures represented different types of frequency selective surfaces, and where the last three structures were concerned with different types of realistic radiators.

The results showed a close agreement between Luxaflex, ©HFSS, the literature, and the waveguide simulator measurements. A key point in this success was that we have been able to model the unknown electromagnetic current behavior in a good way. We allowed for current flowing around corners and for singular behavior of current near edges in junction structures. Internal consistency has further been checked by verifying conservation of energy. The open-ended waveguide with patch example showed that a good understanding is required to properly model the unknown surface currents in highly coupled junctions. In this case, the insufficient use of global expansion functions in the slot led to an incorrect reflection and transmission behavior as a function of the frequency. Instead we used local expansion functions to correctly model the singular behavior on the edges of the open-ended waveguide.

The waveguide simulator is an inexpensive alternative to validate infinite array theory. A disadvantage of such a device is a coupling between frequency and angle of incidence. This can partly be solved by placing a different number of unit cells inside the waveguide. In this case there is still a limitation in the use of the device due to the cutoff frequency of the waveguide.

*The validation has led to the conclusion that the computational method is accurate for a number of realistic examples (within tenths of dB's) compared to simulations with other software packages and with measurements. The accuracy increases when the size of the mesh elements decreases and when the number of waveguide and layered space modes in each segment increases.*

### 6.1.4 Applications

In this section we express our opinion on the value of the work done in this thesis for the industry. First, we would like to stress that, with the computational method described in this thesis, we have been able to calculate the electromagnetic behavior for a number of realistic radiating structures. These complicated structures consisted of multilayer parts such as feeding slots, cavities and frequency selective surfaces.

To be able to do these calculations, we have developed a large software package, called Luxaflex, which is setup using professional industry standards. Luxaflex has been extensively validated and is now used within the Thales antenna departments both in Holland and in France, and within a number of external research institutes such as TNO and IRCTR. Luxaflex contains easy

and intuitive input file structures and intelligent and innovative post-processing techniques, such as special visualization routines for extracting and plotting the scattering matrix behavior.

What makes Luxaflex advantageous over other commercial software packages is that it is completely transparent and its user completely controls the calculation. Regarding the input of Luxaflex, this means that the user has full control over:

- the separation of the radiating element structure into basic structures,
- the characterization of the segments in terms of permittivity, permeability and electric losses,
- the definition of the probes, i.e., its location and number of modes,
- the choice of the expansion and weighting functions within each junction in which the expected physical behavior can be taken into account,
- the choice of the number of modes for the field expansion within the segments.

Regarding the output of Luxaflex, this means that the user can fully extract and analyze:

- the multimode interactions, both for propagating as well as for evanescent modes,
- the power conservation and field reciprocity,
- the far field for all the electromagnetic field components in all three Ludwig definitions [57],
- the properties of the modes both for waveguide and layered space segments.

Whereas many other commercial software packages operate as a black box, Luxaflex educates, through its transparency, its user. Furthermore, the availability of a complete MATLAB open-source toolbox and build-in object oriented programming principles allows an expansion of Luxaflex in an easy way. This thesis contributes in this by providing a complete theoretical background.

Since Luxaflex is a dedicated tool for planar multilayer periodic structures, it is faster compared to general-purpose commercial software. This is already the case when the acceleration techniques described in this thesis are not used. Using these acceleration techniques can make Luxaflex at least five times faster. Furthermore, the speed improvements presented in this thesis using the acceleration techniques are a bit conservative. By reducing the accuracy requirements we can gain more speed improvement.

Speed improvements become for example important in the analysis of electromagnetic bandgap structures where meshing elements are becoming small

and corresponding spectra become large in bandwidth. The acceleration technique described in this thesis promises a significant reduction of time for these bandgap structures.

By combining the strengths of different dedicated electromagnetic computational methods, Luxaflex can be linked through its transparency with other such software packages to form an integrated computational method which can be used to analyze larger complex structures. Finally, since Luxaflex is fast and transparent, it can be embedded in an iterative design method.

## 6.2 Recommendations

We divide the recommendations in three categories: recommendations for the computational method, for the acceleration technique and for the validation.

### 6.2.1 Computational Method

It would be useful to incorporate the circular waveguide segment and TEM mode functions. This would enable us to take into account segments with inner perfect electric conductors such as coaxial feeding lines. We recommend an evaluation and implementation of the inner product between a waveguide mode and a global patch expansion function, and between a waveguide mode and a global thin strip expansion function. Doing this would allow us to use these global expansion functions within waveguide segments. A further increase of the computational speed can be achieved by implementing the core of the computational method (kernel) in a higher programming language such as Fortran. We recommend to keep the data postprocessing of luxaflex in MATLAB.

### 6.2.2 Acceleration Technique

We first recommend an implementation of the evaluation of the regularization integral as described in appendix A. This will reduce the computation time of the exponential regularization lookup table for the Rao-Wilton-Glisson expansion function considerably. The acceleration technique has further been implemented and demonstrated for a magnetic-field integral equation (MFIE) and for self-interaction terms only such as  $A_{v,\tau}$  of  $L$ . It would be useful to also implement the acceleration technique for the electric-field integral equation (EFIE) and for the coupling terms between different junctions such as  $C_{v,s}$  to  $L$  (see section 3.5).

For the Rao-Wilton-Glisson and for the arbitrary rooftop expansion function, the summation for small  $\tau$  is currently done over a single term only. We recommend an extension of the summation to more terms for both expansion functions. This will increase the accuracy of the summation for small  $\tau$ , and will consequently increase the accuracy of the correction series. This can only be achieved by allowing for larger FFT grids within the numerical convolution of two exponentially regularized functions.

### 6.2.3 Validation

Using multimode waveguide simulators would further reduce the limitations of single-mode waveguide simulators. Multimode waveguide simulators allow for higher angles of incidence in the given frequency range of the waveguide. Note that in this case a special multimode calibration technique is required.

### 6.2.4 Applications

In this section we give our opinion on the added value of these recommendations for the industry. Put in other words: what do we foresee for the future for Luxaflex and its applications within the industry.

Obviously we will get a faster Luxaflex due to optimization of both the current method of moment algorithm and the acceleration techniques. This will be even more supported by an implementation of the kernel in a higher programming language. The implementation in Fortran alone will already improve the speed by at least a factor five. This facilitates a faster and cheaper phased array antenna design period.

A fast Luxaflex supports and can easily be embedded in an iterative design process. Furthermore, new synthesis techniques based on multimode filter theory are coming into play and require fast computations of electromagnetic responses. These techniques further support and make use of the idea of constructing a radiating element in terms of segments and junctions as described in this thesis.

New innovative interpolation techniques can easily be incorporated in Luxaflex as an alternative acceleration method. These methods support a fast computation of the electromagnetic response for a given number of design parameter variations without having to perform a complete method of moments calculation for each variation. The matrix equation  $L\mathbf{u} = \mathbf{f}$  for the method of moment solution technique is solved for  $\mathbf{u}$  taking into account the dependence of  $L$  and  $\mathbf{f}$  on the design parameters.

The incorporation of TEM modes in strip-lines and coaxial feeds into Luxaflex will enable us to handle more complex structures. Today we tackle this problem by using other packages to simulate these difficult parts and subsequently combining the results, which slows down and complicates the complete analysis. This has especially become apparent when we connected two structures where evanescent modes play a dominant role at the interface.

For electromagnetic bandgap structures one is interested in the prediction of surface waves and leaky waves. Since Luxaflex is transparent and built on structured programming principles, only minor adjustments and changes are necessary to be able to do these type of predictions. This prediction allows us to understand and design electromagnetic bandgap structures that forbid unwanted surface waves in certain bandwidths. The goal would be to reduce mutual coupling and corresponding unwanted performance degradations in phased array antennas by designing appropriate substrate materials.

# Appendix A

## Evaluation of the Regularization Integral

In this appendix, we will consider the evaluation of the following integral

$$F(\ell_1, \ell_2; \alpha) = \int_{\ell_1}^{\ell_2} \frac{1}{\ell^2 + d^2} \exp(-\alpha \ell^2) d\ell, \quad (\text{A.1})$$

of primary interest<sup>1</sup>, which is used in section 4.4.3 to evaluate parts of the triangular contour integration over a sub-domain of an RWG function. Let  $\alpha$  be real-valued and large. In general, a closed-form expression for the integral given in equation A.1 is not available.

### A.1 Reduction to Standard Integrals

The manner in which this integral is determined depends on the position of the boundaries  $\ell_1$  and  $\ell_2$  with respect to the point  $\ell = 0$ . We distinguish between three cases.

- For  $0 < \ell_1 < \ell_2$ , we write

$$F(\ell_1, \ell_2; \alpha) = F(\ell_1, \infty; \alpha) - F(\ell_2, \infty; \alpha). \quad (\text{A.2})$$

- For  $\ell_1 < 0 < \ell_2$ , we write

$$F(\ell_1, \ell_2; \alpha) = F(-\infty, \infty; \alpha) - F(-\ell_1, \infty; \alpha) - F(\ell_2, \infty; \alpha). \quad (\text{A.3})$$

- For  $\ell_1 < \ell_2 < 0$ , we write

$$F(\ell_1, \ell_2; \alpha) = F(-\ell_2, -\ell_1; \alpha). \quad (\text{A.4})$$

---

<sup>1</sup>A special word of thanks goes to prof.dr. A.G. Tijhuis for his help in solving this integral puzzle.

Here, we have twice used the property that the integrand is an even function of the integration variable  $\ell$ .

This leaves the evaluation of  $F(-\infty, \infty; \alpha)$  and  $F(\ell_1, \infty; \alpha)$ , where  $\ell_1 > 0$ . Once these integrals are available, the symmetry relations A.2–A.4 can be used to evaluate the integrals, as long as  $\alpha\ell_1^2 \gg 1$  and  $\alpha\ell_2^2 \gg 1$ .

## A.2 Integral over $-\infty < \ell < \infty$

We write the integral over the real line as

$$F(-\infty, \infty; \alpha) = \exp(\alpha d^2) \int_{-\infty}^{\infty} \frac{1}{\ell^2 + d^2} \exp(-\alpha[\ell^2 + d^2]) d\ell, \quad (\text{A.5})$$

and use the identity

$$\frac{1}{\ell^2 + d^2} \exp(-\alpha[\ell^2 + d^2]) = \int_{\alpha}^{\infty} \exp(-\beta[\ell^2 + d^2]) d\beta. \quad (\text{A.6})$$

We thus end up with

$$\begin{aligned} F(-\infty, \infty; \alpha) &= \exp(\alpha d^2) \int_{\alpha}^{\infty} \exp(-\beta d^2) \int_{-\infty}^{\infty} \exp(-\beta \ell^2) d\ell d\beta \\ &= \exp(\alpha d^2) \int_{\alpha}^{\infty} \sqrt{\frac{\pi}{\beta}} \exp(-\beta d^2) d\beta \\ &= 2\sqrt{\pi} \exp(\alpha d^2) \int_{\alpha}^{\infty} \exp(-\beta d^2) d\sqrt{\beta}. \end{aligned} \quad (\text{A.7})$$

Now we use the change of variables  $p = d\sqrt{\beta}$  to rewrite this result as

$$\begin{aligned} F(-\infty, \infty; \alpha) &= \frac{2\sqrt{\pi}}{d} \exp(\alpha d^2) \int_{d\sqrt{\alpha}}^{\infty} \exp(-p^2) dp \\ &= \frac{\pi}{d} \exp(\alpha d^2) \operatorname{erfc}(d\sqrt{\alpha}), \end{aligned} \quad (\text{A.8})$$

which, apart from a multiplicative constant, is the complement of the error function with the leading exponential factored out. By using the property that the integrand of equation A.1 is an even function of  $\ell$ , we find [45, section 3.466]

$$F(-\infty, 0; \alpha) = F(0, \infty; \alpha) = \frac{1}{2} F(-\infty, \infty; \alpha). \quad (\text{A.9})$$

## A.3 Integral over $\ell_1 < \ell < \infty$

Next, we consider the integral over the interval  $\ell_1 < \ell < \infty$ , where we assume that  $\alpha\ell_1^2 \gg 1$ . This integral is evaluated by repeated integration by parts. We

carry out the first step:

$$\begin{aligned} F(\ell_1, \infty; \alpha) &= \int_{\ell_1}^{\infty} \frac{1}{(\ell^2 + d^2)} \frac{1}{(-2\alpha\ell)} d \exp(-\alpha\ell^2) \\ &= \frac{\exp(-\alpha\ell_1^2)}{2\alpha\ell_1(\ell_1^2 + d^2)} - \frac{1}{2\alpha} \int_{\ell_1}^{\infty} \frac{(3\ell^2 + d^2) \exp(-\alpha\ell^2)}{\ell^2(\ell^2 + d^2)^2} d\ell. \end{aligned} \quad (\text{A.10})$$

This inspires us to consider the evaluation of the integral:

$$\int_{\ell_1}^{\infty} \frac{P_n(\ell^2) \exp(-\alpha\ell^2)}{\ell^{2n}(\ell^2 + d^2)^{n+1}} d\ell, \quad (\text{A.11})$$

where  $P_n(x)$  is a polynomial of degree  $n$  whose coefficients may still depend on  $d^2$ . Using the same procedure, we have

$$\begin{aligned} -\frac{1}{2\alpha} \int_{\ell_1}^{\infty} \frac{P_n(\ell^2)}{\ell^{2n+1}(\ell^2 + d^2)^{n+1}} d \exp(-\alpha\ell^2) &= \\ \frac{1}{2\alpha} \frac{P_n(\ell_1^2) \exp(-\alpha\ell_1^2)}{\ell_1^{2n+1}(\ell_1^2 + d^2)^{n+1}} - \frac{1}{2\alpha} \int_{\ell_1}^{\infty} \frac{P_{n+1}(\ell^2) \exp(-\alpha\ell^2)}{\ell^{2n+2}(\ell^2 + d^2)^{n+2}} d\ell, \end{aligned} \quad (\text{A.12})$$

with

$$P_{n+1}(x) = [(4n + 3)x + (2n + 1)d^2] P_n(x) - 2x(x + d^2) P'_n(x), \quad (\text{A.13})$$

where the prime indicates differentiation with respect to  $x$ . Now, from equation A.10, we observe that  $P_0(x) = 1$ . By induction, it then follows that after  $N + 1$  steps the following approximation is obtained:

$$F(\ell_1, \infty; \alpha) \approx \sum_{n=0}^N \frac{(-1)^n P_n(\ell_1^2) \exp(-\alpha\ell_1^2)}{(2\alpha)^{n+1} (\ell_1^2 + d^2)^{n+1} \ell_1^{2n+1}}, \quad (\text{A.14})$$

where the first five polynomials are given by

$$\begin{aligned} P_0(x) &= 1, \\ P_1(x) &= 3x + d^2, \\ P_2(x) &= 15x^2 + 10xd^2 + 3d^4, \\ P_3(x) &= 105x^3 + 105x^2d^2 + 63xd^4 + 15d^6, \\ P_4(x) &= 945x^4 + 1260x^3d^2 + 1134x^2d^4 + 540xd^6 + 105d^8. \end{aligned} \quad (\text{A.15})$$

A special case arises for  $\ell_1 = d$ . In [2, formula 7.4.12] we find

$$F(0, d; \alpha) = \frac{\pi}{4d} \exp(\alpha d^2) [1 - \operatorname{erf}^2(d\sqrt{\alpha})], \quad (\text{A.16})$$

which leads to

$$F(d, \infty; \alpha) = \frac{\pi}{4d} \exp(\alpha d^2) [1 - \operatorname{erf}(d\sqrt{\alpha}) (2 - \operatorname{erf}(d\sqrt{\alpha}))], \quad (\text{A.17})$$

where we have used equation A.9.



## A.4 Convergence of Series

To estimate the magnitude of  $P_n(x)$ , we consider the coefficients of  $x^n$  and  $d^{2n}$ . This seems sufficient, since one of these terms will dominate the polynomial as  $n$  becomes large. We consider the recurrence from  $P_n(x)$  to  $P_{n+1}(x)$ .

- The term  $x^n$  is replaced by:

$$[(4n + 3)x + (2n + 1)d^2]x^n - 2x(x + d^2)nx^{n-1} = (2n + 3)x^{n+1} + \mathcal{O}(x^n).$$

- The term  $d^{2n}$  is replaced by:  $(2n + 1)d^{2n+2}$ .

This means that the numerator in equation A.14 approximately increases in magnitude by a factor of  $2n(\ell_1^2 + d^2)$ . Hence, the entire term is approximately multiplied by a factor of  $-n/(\alpha\ell_1^2)$ , which means that we have a *diverging, alternating* asymptotic series that should be truncated before  $N \approx \alpha\ell_1^2$ . The error term can then be estimated from the integral that is left after integrating by parts.

When  $\alpha\ell_1^2$  is too small to obtain sufficient accuracy in this manner, the exponent  $\exp(-\alpha\ell^2)$  decreases slowly enough over at least part of the integration interval to allow for an efficient brute-force numerical integration. For this case we can assume that there is a  $\ell_2 > \ell_1$  for which  $\alpha\ell_2^2 \gg 1$ . Then we write

$$F(\ell_1, \infty; \alpha) = F(\ell_1, \ell_2; \alpha) + F(\ell_2, \infty; \alpha), \quad (\text{A.18})$$

where the first part  $F(\ell_1, \ell_2; \alpha)$  will be done by the brute-force numerical integration, and the second part  $F(\ell_2, \infty; \alpha)$  by the method described in this appendix. However, it is expected that this more complicated procedure is required only for a few integrals in the determination of the exponential regularization of the RWG functions.

# Appendix B

## Transmission Line Examples

In this appendix we will solve the modal transmission line equations, 2.197 and 2.198, derived in section 2.4.4 for six standard configurations. These equations are used as part of the field representation in section 3.6 where we calculate the linear operator  $L$  and the forcing vector  $\mathbf{f}$ , and in section 3.8 where we calculate the total electromagnetic field. To improve readability, we will omit the polarization index  $\alpha$ . This means that  $V^\alpha, I^\alpha, Y_\infty^\alpha, Z_\infty^\alpha, k_z^\alpha, v^\alpha, i^\alpha, \mathbf{e}_t^\alpha$  and  $\mathbf{h}_t^\alpha$  will be written as  $V, I, Y_\infty, Z_\infty, k_z, v, i, \mathbf{e}_t$  and  $\mathbf{h}_t$ , respectively.

### B.1 Dielectric Junction with Source

In this example we will solve the modal transmission line equations, 2.197 and 2.198, for the configuration shown<sup>1</sup> in figure B.1. This transmission line is used for a single EFIE junction to calculate the matrix contribution for the self interaction. It is further used as a building block for the other transmission lines in this appendix.

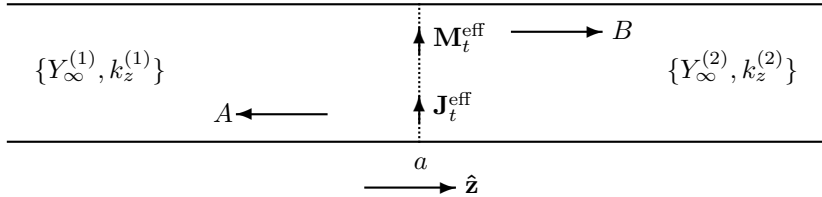


Figure B.1: Dielectric junction with source.

<sup>1</sup>Note that the figures in this appendix are hybrid ones, i.e., a mixture between a physical waveguide description and a modal transmission line concept with corresponding propagation constants and characteristic admittances both of which are modal parameters.

Effective transverse electric  $\mathbf{J}_t^{\text{eff}}$  and magnetic  $\mathbf{M}_t^{\text{eff}}$  surface current distributions are positioned at  $z = a$ . The medium for  $z < a$  is characterized by  $\{\eta^{(1)}, \xi^{(1)}\}$ , and for  $z > a$  by  $\{\eta^{(2)}, \xi^{(2)}\}$ . The current distributions are defined as

$$\mathbf{J}_t^{\text{eff}}(\boldsymbol{\rho}, z) = \mathbf{J}_t^{\text{eff}}(\boldsymbol{\rho})\delta(z - a), \quad (\text{B.1})$$

$$\mathbf{M}_t^{\text{eff}}(\boldsymbol{\rho}, z) = \mathbf{M}_t^{\text{eff}}(\boldsymbol{\rho})\delta(z - a). \quad (\text{B.2})$$

For this configuration, the radiation conditions at  $z = \pm\infty$  prescribe the following form for the unknown  $V(z)$

$$V(z) = \begin{cases} A \exp(jk_z^{(1)}[z - a]) & \text{if } z < a, \\ B \exp(-jk_z^{(2)}[z - a]) & \text{if } z > a. \end{cases} \quad (\text{B.3})$$

If we substitute equation B.3 in equation 2.197 with  $v^\alpha(z) = 0$ , we obtain for  $I(z)$

$$I(z) = \begin{cases} -AY_\infty^{(1)} \exp(jk_z^{(1)}[z - a]) & \text{if } z < a, \\ BY_\infty^{(2)} \exp(-jk_z^{(2)}[z - a]) & \text{if } z > a. \end{cases} \quad (\text{B.4})$$

If we combine equations B.3 and B.4 with equations 2.205 and 2.206, we find the following boundary conditions for  $V(z)$  and  $I(z)$  at  $z = a$

$$\begin{cases} V(a^-) - V(a^+) = v = \langle \mathbf{M}_t^{\text{eff}}(\boldsymbol{\rho}) | \mathbf{h}_t(\boldsymbol{\rho}) \rangle, \\ I(a^-) - I(a^+) = i = \langle \mathbf{J}_t^{\text{eff}}(\boldsymbol{\rho}) | \mathbf{e}_t(\boldsymbol{\rho}) \rangle. \end{cases} \quad (\text{B.5})$$

$V(z)$  is discontinuous at  $z = a$  if  $\mathbf{M}_t^{\text{eff}}$  is non-vanishing.  $I(z)$  has a discontinuity at  $z = a$  if  $\mathbf{J}_t^{\text{eff}}$  is non-vanishing. If we solve for the unknowns  $A$  and  $B$ , we obtain

$$A = \frac{-i + Y_\infty^{(2)}v}{Y_\infty^{(1)} + Y_\infty^{(2)}}, \quad (\text{B.6})$$

$$B = -\frac{i + Y_\infty^{(1)}v}{Y_\infty^{(1)} + Y_\infty^{(2)}}. \quad (\text{B.7})$$

If the medium for  $z > a$  becomes perfectly electric conducting, i.e.,  $Y_\infty^{(2)} \rightarrow \infty$ , the unknown  $A$  reduces to

$$A = v, \quad (\text{B.8})$$

and characterizes the solution for a left half space with source shown in figure B.2.

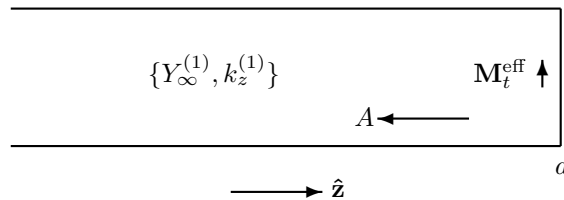


Figure B.2: Left half space with source.

If the medium for  $z < a$  becomes perfectly electric conducting, i.e.,  $Y_\infty^{(1)} \rightarrow \infty$ , the unknown  $B$  reduces to

$$B = -v, \tag{B.9}$$

and characterizes the solution for a right half space with source shown in figure B.3.

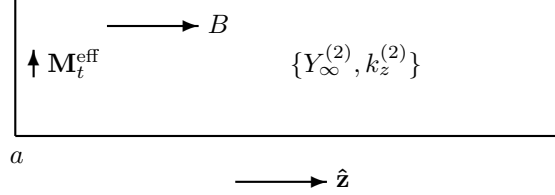


Figure B.3: Right half space with source.

## B.2 Dielectric Junction with Incident Wave

In this example we will solve the modal transmission line equations, 2.197 and 2.198, for the configuration shown in figure B.4 [16, chapter 4]. This transmission line is used as a building block for the other transmission lines in this appendix.

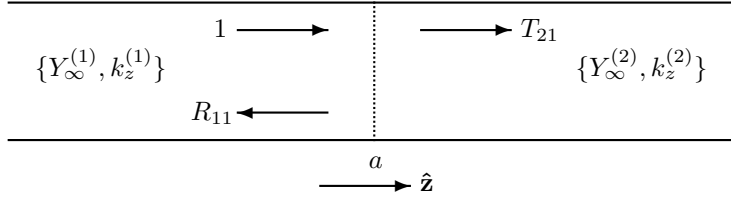


Figure B.4: Dielectric junction with left incident wave.

The medium for  $z < a$  is characterized by  $\{\eta^{(1)}, \xi^{(1)}\}$ , and for  $z > a$  by  $\{\eta^{(2)}, \xi^{(2)}\}$ . First, we consider a wave with unit amplitude propagating in the positive  $z$ -direction incident from the left side of  $z = a$ . For this configuration, the radiation conditions at  $z = \pm\infty$  prescribe the following form for the unknown  $V(z)$

$$V(z) = \begin{cases} \exp(-jk_z^{(1)}[z - a]) + R_{11} \exp(jk_z^{(1)}[z - a]) & \text{if } z < a, \\ T_{21} \exp(-jk_z^{(2)}[z - a]) & \text{if } z > a. \end{cases} \tag{B.10}$$

If we substitute equation B.10 into equation 2.197 with  $v^\alpha(z) = 0$ , we obtain for  $I(z)$

$$I(z) = \begin{cases} Y_\infty^{(1)} \exp(-jk_z^{(1)}[z - a]) - R_{11} Y_\infty^{(1)} \exp(jk_z^{(1)}[z - a]) & \text{if } z < a, \\ T_{21} Y_\infty^{(2)} \exp(-jk_z^{(2)}[z - a]) & \text{if } z > a. \end{cases} \tag{B.11}$$

If we combine equations B.10 and B.11 with equations 2.205 and 2.206, the following boundary conditions must be satisfied at  $z = a$

$$\begin{cases} V(a^-) - V(a^+) = 0, \\ I(a^-) - I(a^+) = 0. \end{cases} \quad (\text{B.12})$$

If we solve for the unknowns  $R_{11}$  and  $T_{21}$ , we obtain

$$R_{11} = \frac{Y_\infty^{(1)} - Y_\infty^{(2)}}{Y_\infty^{(1)} + Y_\infty^{(2)}}, \quad (\text{B.13})$$

$$T_{21} = \frac{2Y_\infty^{(1)}}{Y_\infty^{(1)} + Y_\infty^{(2)}}. \quad (\text{B.14})$$

If the medium for  $z > a$  becomes perfectly electric conducting, i.e.,  $Y_\infty^{(2)} \rightarrow \infty$ , the unknown  $R_{11}$  reduces to

$$R_{11} = -1, \quad (\text{B.15})$$

and represents the solution for a left half space with incident wave shown in figure B.5.

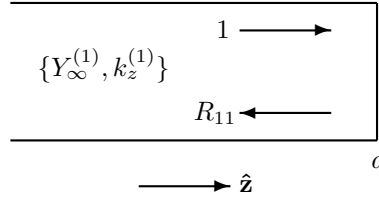


Figure B.5: Left half space with incident wave.

Subsequently, we consider the same configuration with a wave with unit amplitude propagating in the negative  $z$ -direction incident at the right side of  $z = a$ . This is shown in figure B.6.

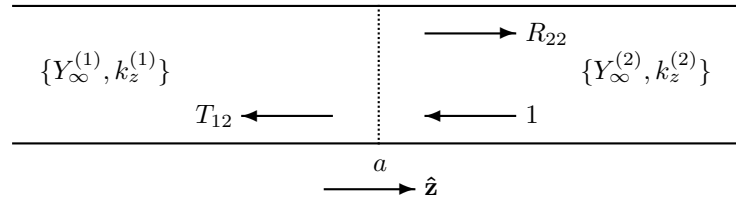


Figure B.6: Dielectric junction with right incident wave.

For this configuration, the radiation conditions at  $z = \pm\infty$  prescribe the following form for the unknown  $V(z)$

$$V(z) = \begin{cases} T_{12} \exp(jk_z^{(1)}[z - a]) & \text{if } z < a, \\ \exp(jk_z^{(2)}[z - a]) + R_{22} \exp(-jk_z^{(2)}[z - a]) & \text{if } z > a. \end{cases} \quad (\text{B.16})$$

Following the same steps used for the left incident wave, we obtain

$$R_{22} = \frac{Y_\infty^{(2)} - Y_\infty^{(1)}}{Y_\infty^{(1)} + Y_\infty^{(2)}}, \quad (\text{B.17})$$

$$T_{12} = \frac{2Y_\infty^{(2)}}{Y_\infty^{(1)} + Y_\infty^{(2)}}. \quad (\text{B.18})$$

If the medium for  $z < a$  becomes perfectly electric conducting, i.e.,  $Y_\infty^{(1)} \rightarrow \infty$ , the unknown  $R_{22}$  reduces to

$$R_{22} = -1, \quad (\text{B.19})$$

and represents the solution for a right half space with incident wave shown in figure B.7.

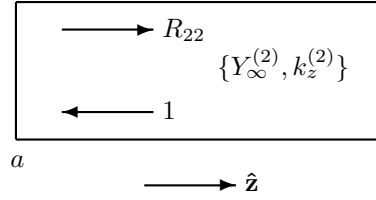


Figure B.7: Right half space with incident wave.

$R_{ij}$  and  $T_{ij}$  denote the reflection and transmission coefficient and relate the exiting wave in medium  $i$  to the incident wave with unit amplitude in medium  $j$ , respectively.

### B.3 Dielectric Junction with Offset Source

In this example we will solve the modal transmission line equations, 2.197 and 2.198, for the configuration shown in figure B.8. This transmission line is used for a single EFIE junction with a dielectric slab to calculate the vector contribution for an incident field on the EFIE junction.

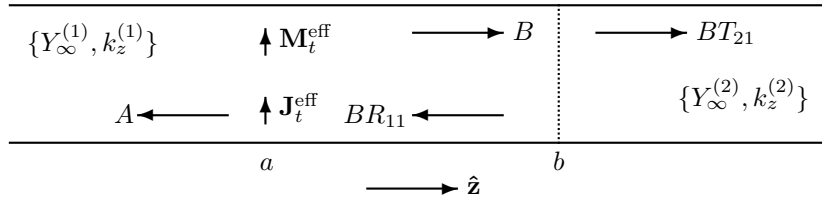


Figure B.8: Dielectric junction with offset source.

Effective transverse electric  $\mathbf{J}_t^{\text{eff}}$  and magnetic  $\mathbf{M}_t^{\text{eff}}$  surface current distributions are positioned at  $z = a < b$ . The medium for  $z < b$  is characterized by

$\{\eta^{(1)}, \xi^{(1)}\}$ . The medium for  $z > b$  is characterized by  $\{\eta^{(2)}, \xi^{(2)}\}$ . The current distributions are defined as

$$\mathbf{J}_t^{\text{eff}}(\boldsymbol{\rho}, z) = \mathbf{J}_t^{\text{eff}}(\boldsymbol{\rho})\delta(z - a), \quad (\text{B.20})$$

$$\mathbf{M}_t^{\text{eff}}(\boldsymbol{\rho}, z) = \mathbf{M}_t^{\text{eff}}(\boldsymbol{\rho})\delta(z - a). \quad (\text{B.21})$$

For this configuration, the radiation conditions at  $z = \pm\infty$  prescribe the following form for the unknown  $V(z)$

$$V(z) = \begin{cases} A \exp(jk_z^{(1)}[z - a]) & \text{if } z < a, \\ B \exp(-jk_z^{(1)}[z - a]) + BR_{11} \exp(jk_z^{(1)}[z - b]) & \text{if } a < z < b, \\ BT_{21} \exp(-jk_z^{(2)}[z - b]) & \text{if } z > b, \end{cases} \quad (\text{B.22})$$

with

$$R_{11} = \frac{Y_\infty^{(1)} - Y_\infty^{(2)}}{Y_\infty^{(1)} + Y_\infty^{(2)}}, \quad (\text{B.23})$$

$$T_{21} = \frac{2Y_\infty^{(1)}}{Y_\infty^{(1)} + Y_\infty^{(2)}}. \quad (\text{B.24})$$

Note that we have used the solution for the dielectric junction with a left incident wave. If we substitute equation B.22 into equation 2.197 with  $v^\alpha(z) = 0$ , we obtain for  $I(z)$

$$I(z) = \begin{cases} -AY_\infty^{(1)} \exp(jk_z^{(1)}[z - a]) & \text{if } z < a, \\ BY_\infty^{(1)} [\exp(-jk_z^{(1)}[z - a]) - R_{11} \exp(jk_z^{(1)}[z - b])] & \text{if } a < z < b, \\ BT_{21}Y_\infty^{(2)} \exp(-jk_z^{(2)}[z - b]) & \text{if } z > b. \end{cases} \quad (\text{B.25})$$

If we combine equations B.22 and B.25 with equations 2.205 and 2.206, the following boundary conditions must be satisfied at  $z = a$

$$\begin{cases} V(a^-) - V(a^+) = v = \langle \mathbf{M}_t^{\text{eff}}(\boldsymbol{\rho}) | \mathbf{h}_t(\boldsymbol{\rho}) \rangle, \\ I(a^-) - I(a^+) = i = \langle \mathbf{J}_t^{\text{eff}}(\boldsymbol{\rho}) | \mathbf{e}_t(\boldsymbol{\rho}) \rangle. \end{cases} \quad (\text{B.26})$$

$V(z)$  is discontinuous at  $z = a$  if  $\mathbf{M}_t^{\text{eff}}$  is non-vanishing.  $I(z)$  has a discontinuity at  $z = a$  if  $\mathbf{J}_t^{\text{eff}}$  is non-vanishing. When we solve for the unknowns  $A$  and  $B$ , we obtain

$$A = -\frac{1}{2} \left( v + \frac{i}{Y_\infty^{(1)}} \right) R_{11} \exp(jk_z^{(1)}[a - b]) + \frac{1}{2} \left( v - \frac{i}{Y_\infty^{(1)}} \right), \quad (\text{B.27})$$

$$B = -\frac{1}{2} \left( v + \frac{i}{Y_\infty^{(1)}} \right). \quad (\text{B.28})$$

## B.4 Half Space with Dielectric Junction and Source

In this example we will solve the modal transmission line equations, 2.197 and 2.198, for the configuration shown in figure B.9. This transmission line is used for a single MFIE junction with a dielectric slab to calculate the matrix contribution for the self interaction.

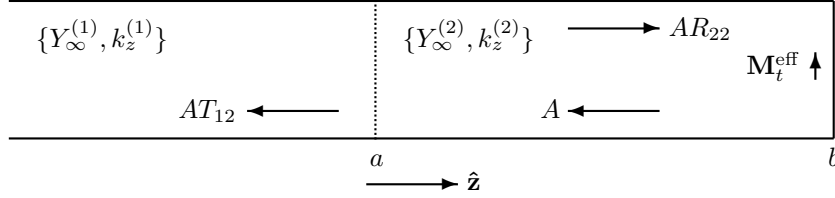


Figure B.9: Half space with dielectric junction and source.

The configuration is closed with a perfectly electric conducting wall at  $z = b$ . An effective transverse magnetic  $\mathbf{M}_t^{\text{eff}}$  surface current distribution is positioned at an infinitesimal distance from this wall. The medium for  $z < a$  is characterized by  $\{\eta^{(1)}, \xi^{(1)}\}$ , and for  $a < z < b$  by  $\{\eta^{(2)}, \xi^{(2)}\}$ . The current distribution is defined as

$$\mathbf{M}_t^{\text{eff}}(\boldsymbol{\rho}, z) = \mathbf{M}_t^{\text{eff}}(\boldsymbol{\rho})\delta(z - b). \quad (\text{B.29})$$

For this configuration, the radiation conditions at  $z = \pm\infty$  prescribe the following form for the unknown  $V(z)$

$$V(z) = \begin{cases} AT_{12} \exp(jk_z^{(1)}[z - a]) & \text{if } z < a, \\ AR_{22} \exp(-jk_z^{(2)}[z - a]) + A \exp(jk_z^{(2)}[z - b]) & \text{if } a < z < b, \end{cases} \quad (\text{B.30})$$

with

$$R_{22} = \frac{Y_\infty^{(2)} - Y_\infty^{(1)}}{Y_\infty^{(1)} + Y_\infty^{(2)}}, \quad (\text{B.31})$$

$$T_{12} = \frac{2Y_\infty^{(2)}}{Y_\infty^{(1)} + Y_\infty^{(2)}}. \quad (\text{B.32})$$

Note that we have used the solution for the dielectric junction with a wave incident from the right. If we substitute equation B.30 into equation 2.197 with  $v^\alpha(z) = 0$ , we obtain for  $I(z)$

$$I(z) = \begin{cases} -AY_\infty^{(1)}T_{12} \exp(jk_z^{(1)}[z - a]) & \text{if } z < a, \\ AY_\infty^{(2)}[R_{22} \exp(-jk_z^{(2)}[z - a]) - \exp(jk_z^{(2)}[z - b])] & \text{if } a < z < b. \end{cases} \quad (\text{B.33})$$

If we combine equations B.30 and B.32 with equations 2.205 and 2.206, the following boundary condition must be satisfied at  $z = b$

$$V(b^-) = v = \langle \mathbf{M}_t^{\text{eff}}(\boldsymbol{\rho}) | \mathbf{h}_t(\boldsymbol{\rho}) \rangle. \quad (\text{B.34})$$



When we solve for the unknown  $A$ , we obtain

$$A = \frac{v}{1 + R_{22} \exp(-jk_z^{(2)}[b - a])}. \quad (\text{B.35})$$

## B.5 Half Space with Offset Source

In this example we will solve the modal transmission line equations, 2.197 and 2.198, for the configuration shown in figure B.10. This transmission line is used for a single MFIE junction with a dielectric slab to calculate the vector contribution for an incident field on the MFIE junction.

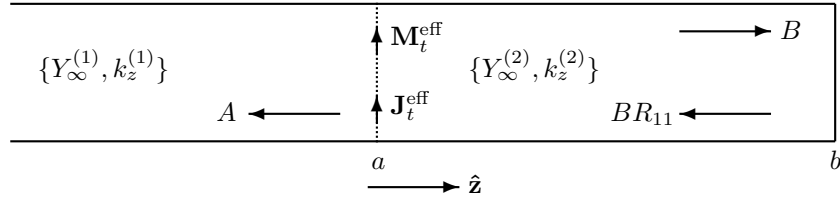


Figure B.10: Half space with offset source.

The configuration is closed with a perfectly electric conducting wall at  $z = b$ . Effective transverse electric  $\mathbf{J}_t^{\text{eff}}$  and magnetic  $\mathbf{M}_t^{\text{eff}}$  surface current distributions are positioned at  $z = a < b$ . The medium for  $z < a$  is characterized by  $\{\eta^{(1)}, \xi^{(1)}\}$ , and for  $a < z < b$  by  $\{\eta^{(2)}, \xi^{(2)}\}$ . The current distributions are defined as

$$\mathbf{J}_t^{\text{eff}}(\boldsymbol{\rho}, z) = \mathbf{J}_t^{\text{eff}}(\boldsymbol{\rho})\delta(z - a), \quad (\text{B.36})$$

$$\mathbf{M}_t^{\text{eff}}(\boldsymbol{\rho}, z) = \mathbf{M}_t^{\text{eff}}(\boldsymbol{\rho})\delta(z - a). \quad (\text{B.37})$$

For this configuration, the radiation conditions at  $z = \pm\infty$  prescribe the following form for the unknown  $V(z)$

$$V(z) = \begin{cases} A \exp(jk_z^{(1)}[z - a]) & \text{if } z < a, \\ B \exp(-jk_z^{(2)}[z - a]) + BR_{11} \exp(jk_z^{(2)}[z - b]) & \text{if } a < z < b. \end{cases} \quad (\text{B.38})$$

with

$$R_{11} = -1. \quad (\text{B.39})$$

Note that we have used the solution for the left half space with an incident wave. If we substitute equation B.38 into equation 2.197 with  $v^\alpha(z) = 0$ , we obtain for  $I(z)$

$$I(z) = \begin{cases} -AY_\infty^{(1)} \exp(jk_z^{(1)}[z - a]) & \text{if } z < a, \\ BY_\infty^{(2)} [\exp(-jk_z^{(2)}[z - a]) - R_{11} \exp(jk_z^{(2)}[z - b])] & \text{if } a < z < b. \end{cases} \quad (\text{B.40})$$

Combining equations B.38 and B.40 with equations 2.205 and 2.206 leads to the following boundary conditions for  $V(z)$  and  $I(z)$  at  $z = a$

$$\begin{cases} V(a^-) - V(a^+) = v = \langle \mathbf{M}_t^{\text{eff}}(\boldsymbol{\rho}) | \mathbf{h}_t(\boldsymbol{\rho}) \rangle, \\ I(a^-) - I(a^+) = i = \langle \mathbf{J}_t^{\text{eff}}(\boldsymbol{\rho}) | \mathbf{e}_t(\boldsymbol{\rho}) \rangle. \end{cases} \quad (\text{B.41})$$

$V(z)$  is discontinuous at  $z = a$  if  $\mathbf{M}_t^{\text{eff}}$  is non-vanishing.  $I(z)$  has a discontinuity at  $z = a$  if  $\mathbf{J}_t^{\text{eff}}$  is non-vanishing. When we solve for the unknowns  $A$  and  $B$ , we obtain

$$A = \frac{vY_\infty^{(2)}(1 + \exp(jk_z^{(2)}[a - b])) - i(1 - \exp(jk_z^{(2)}[a - b]))}{Y_\infty^{(1)}(1 - \exp(jk_z^{(2)}[a - b])) + Y_\infty^{(2)}(1 + \exp(jk_z^{(2)}[a - b]))}, \quad (\text{B.42})$$

$$B = \frac{-(i + vY_\infty^{(1)})}{Y_\infty^{(1)}(1 - \exp(jk_z^{(2)}[a - b])) + Y_\infty^{(2)}(1 + \exp(jk_z^{(2)}[a - b]))}. \quad (\text{B.43})$$

## B.6 Cavity with Source

In this example we will solve the modal transmission line equations, 2.197 and 2.198, for the configuration shown in figure B.11. This transmission line is used for a double MFIE junction to calculate the matrix contribution for the self interaction and the coupling between the two MFIE junctions.

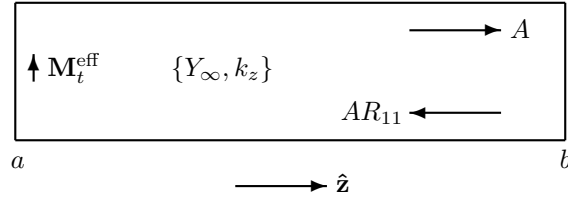


Figure B.11: Cavity with source.

Both at  $z = a < b$  and  $z = b$  the configuration is closed with perfectly electric conducting walls. An effective transverse magnetic  $\mathbf{M}_t^{\text{eff}}$  surface current distribution is positioned at an infinitesimal distance from the left wall. The medium for  $a < z < b$  is characterized by  $\{\eta, \xi\}$ . The current distribution is defined as

$$\mathbf{M}_t^{\text{eff}}(\boldsymbol{\rho}, z) = \mathbf{M}_t^{\text{eff}}(\boldsymbol{\rho})\delta(z - a). \quad (\text{B.44})$$

For this configuration, the radiation conditions at  $z = \pm\infty$  prescribe the following form for the unknown  $V(z)$

$$V(z) = A \exp(-jk_z[z - a]) + AR_{11} \exp(jk_z[z - b]) \quad \text{if } a < z < b. \quad (\text{B.45})$$

with

$$R_{11} = -1. \quad (\text{B.46})$$

Note that we have used the solution for the left half space with an incident wave. When we substitute equation B.45 in equation 2.197 with  $v^\alpha(z) = 0$ , we obtain for  $I(z)$

$$I(z) = AY_\infty[\exp(-jk_z[z - a]) - R_{11} \exp(jk_z[z - b])] \quad \text{if } a < z < b. \quad (\text{B.47})$$

Combining equations B.45 and B.47 with equations 2.205 and 2.206 results in a following boundary condition for  $V(z)$  at  $z = a$

$$-V(a^+) = v = \langle \mathbf{M}_t^{\text{eff}}(\boldsymbol{\rho}) | \mathbf{h}_t(\boldsymbol{\rho}) \rangle. \quad (\text{B.48})$$

When we solve for the unknown  $A$ , we obtain

$$A = \frac{-v}{1 - \exp(jk_z[a - b])}. \quad (\text{B.49})$$

## Appendix C

# Interaction between Two Waveguides

In this appendix, we evaluate<sup>1</sup> the inner product between the electric and magnetic modal fields for two different overlapping rectangular waveguides. This inner product is used in section 3.6 where we calculate the linear operator  $L$  and the forcing vector  $\mathbf{f}$ . The two waveguides are specified in figure C.1.

The first waveguide has a cross section  $A^{(1)}$  with a boundary  $\partial A^{(1)}$ . The cross section is rectangular in shape with length  $a$  and height  $b$ . The lower left corner of this waveguide is shifted from the origin towards  $x = e$  and  $y = f$ .

The electric and magnetic modal fields within this waveguide can be written in terms of square integrable and normalized scalar generating functions  $\Phi_m^{(1)}$  and  $\Psi_m^{(1)}$ , given by equations 2.137, 2.138, 2.162 and 2.163. Further,  $\Phi_m^{(1)}$  and  $\Psi_m^{(1)}$  satisfy equations 2.134 and 2.159, respectively. For this special case of a rectangular waveguide, we can solve these equations in closed form. This has been done in section 3.7.1. The result is given by equations 3.74 and 3.75 for  $\Phi_m^{(1)}$ , and by equations 3.76 and 3.77 for  $\Psi_m^{(1)}$ , with substitutions  $\Phi_m \rightarrow \Phi_m^{(1)}$ ,  $k'_{t;m} \rightarrow k'^{(1)}_{t;m}$ ,  $\Psi_m \rightarrow \Psi_m^{(1)}$ ,  $k''_{t;m} \rightarrow k''^{(1)}_{t;m}$ , and  $A \rightarrow A^{(1)}$ .

The second waveguide has a cross-section  $A^{(2)}$  with a boundary  $\partial A^{(2)}$ . The cross section of this waveguide is overlapped by the cross section of the first waveguide, i.e.,  $A^{(2)} \subset A^{(1)}$ . The cross-section is rectangular in shape with length  $c$  and height  $d$ . The lower left corner of this waveguide is shifted from the origin towards  $x = g$  and  $y = h$ . The condition  $A^{(2)} \subset A^{(1)}$  is equivalent to the following conditions

$$e < g < g + c < e + a \quad \text{and} \quad f < h < h + d < f + b. \quad (\text{C.1})$$

The electric and magnetic modal fields within this waveguide can be written in terms of square integrable and normalized scalar generating functions  $\Phi_n^{(2)}$  and

---

<sup>1</sup>Computation of the projection matrix between two rectangular waveguide modes.

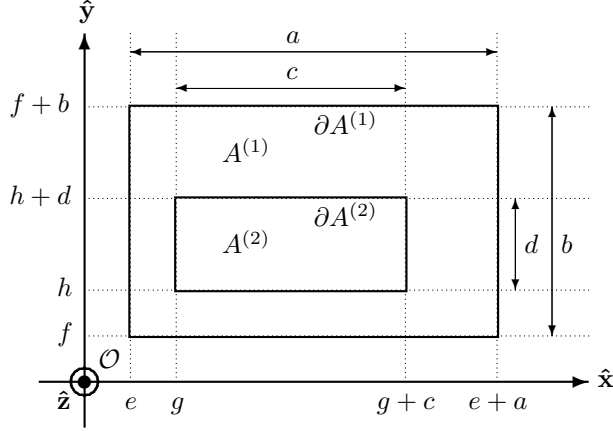


Figure C.1: Two overlapping rectangular waveguides.

$\Psi_n^{(2)}$  given by equations 2.137, 2.138, 2.162 and 2.163. Using equations 3.74-3.77 with substitutions  $\Phi_m \rightarrow \Phi_n^{(2)}$ ,  $k'_{t;m} \rightarrow k'_{t;n}$ ,  $\Psi_m \rightarrow \Psi_n^{(2)}$ ,  $k''_{t;m} \rightarrow k''_{t;n}$ ,  $m \rightarrow p$ ,  $n \rightarrow q$ ,  $a \rightarrow c$ ,  $b \rightarrow d$ ,  $e \rightarrow g$ ,  $f \rightarrow h$ , and  $A \rightarrow A^{(2)}$ , we directly obtain expressions for  $\Phi_n^{(2)}$  and  $\Psi_n^{(2)}$ . Note that for this case we have replaced the single index  $n$  with an index pair  $(p, q)$ . Note that we can place the lower-left corner of one of the two waveguides in the origin, since the interaction will depend on  $g - e$  and  $h - f$ . We define

$$\alpha(M, P, c, e, g) \equiv \int_g^{g+c} \sin(M(x-e)) \sin(P(x-g)) dx, \quad (\text{C.2})$$

which has the following analytical form

$$\alpha(M, P, c, e, g) = \frac{c}{2} \text{sinc} \left( \frac{c}{2}(M-P) \right) \cos \left( M(e-g) - \frac{c}{2}(M-P) \right) - \frac{c}{2} \text{sinc} \left( \frac{c}{2}(M+P) \right) \cos \left( M(e-g) - \frac{c}{2}(M+P) \right). \quad (\text{C.3})$$

We define

$$\beta(M, P, c, e, g) \equiv \int_g^{g+c} \cos(M(x-e)) \cos(P(x-g)) dx, \quad (\text{C.4})$$

which has the following analytical form

$$\beta(M, P, c, e, g) = \frac{c}{2} \text{sinc} \left( \frac{c}{2}(M-P) \right) \cos \left( M(e-g) - \frac{c}{2}(M-P) \right) + \frac{c}{2} \text{sinc} \left( \frac{c}{2}(M+P) \right) \cos \left( M(e-g) - \frac{c}{2}(M+P) \right). \quad (\text{C.5})$$

We define

$$\gamma(M, P, c, e, g) \equiv \int_g^{g+c} \cos(M(x-e)) \sin(P(x-g)) dx, \quad (\text{C.6})$$

which has the following analytical form

$$\begin{aligned} \gamma(M, P, c, e, g) = & \frac{c}{2} \text{sinc} \left( \frac{c}{2}(M-P) \right) \sin \left( M(e-g) - \frac{c}{2}(M-P) \right) + \\ & \frac{c}{2} \text{sinc} \left( \frac{c}{2}(M+P) \right) \sin \left( M(g-e) + \frac{c}{2}(M+P) \right). \end{aligned} \quad (\text{C.7})$$

We define

$$\delta(M, P, c, e, g) \equiv \int_g^{g+c} \sin(M(x-e)) \cos(P(x-g)) dx, \quad (\text{C.8})$$

which has the following analytical form

$$\begin{aligned} \delta(M, P, c, e, g) = & \frac{c}{2} \text{sinc} \left( \frac{c}{2}(M-P) \right) \sin \left( M(g-e) + \frac{c}{2}(M-P) \right) + \\ & \frac{c}{2} \text{sinc} \left( \frac{c}{2}(M+P) \right) \sin \left( M(g-e) + \frac{c}{2}(M+P) \right). \end{aligned} \quad (\text{C.9})$$

Further we define

$$M = \frac{m\pi}{a}, \quad N = \frac{n\pi}{b}, \quad P = \frac{p\pi}{c}, \quad Q = \frac{q\pi}{d}. \quad (\text{C.10})$$

In the next four sections, we will evaluate four different possible combinations of inner products.

## C.1 TM Mode in Waveguide 1, TM Mode in Waveguide 2

First we substitute the expressions for the two TM modal fields, i.e., equations 2.137 and 2.138, in the inner product. We obtain

$$\begin{aligned} \langle \mathbf{e}'_{t;m}{}^{(1)} | \mathbf{e}'_{t;n}{}^{(2)} \rangle &= \langle \mathbf{h}'_{t;m}{}^{(1)} | \mathbf{h}'_{t;n}{}^{(2)} \rangle \\ &= \frac{1}{k'_{t;m}{}^{(1)} k'_{t;n}{}^{(2)}} \langle \nabla_t \Phi_m^{(1)} | \nabla_t \Phi_n^{(2)} \rangle. \end{aligned} \quad (\text{C.11})$$

We can simplify the inner product on the right-hand side by using the chain rule for differentiation by parts

$$\begin{aligned} (\nabla_t \Phi_n^{(2)*}) \cdot \nabla_t \Phi_m^{(1)} &= \\ &= \nabla_t \cdot (\Phi_n^{(2)*} \nabla_t \Phi_m^{(1)}) - \Phi_n^{(2)*} \nabla_t^2 \Phi_m^{(1)} \\ &= \nabla_t \cdot (\Phi_n^{(2)*} \nabla_t \Phi_m^{(1)}) + (k'_{t;m}{}^{(1)})^2 \Phi_n^{(2)*} \Phi_m^{(1)}, \end{aligned} \quad (\text{C.12})$$

(since  $\Phi_m^{(1)}$  satisfies equation 2.134 and since  $k_{t;m}^{\prime(1)}$  is real-valued) and by applying Gauss' divergence theorem. This leads to

$$\frac{1}{k_{t;m}^{\prime(1)} k_{t;n}^{\prime(2)}} \oint_{\partial A^{(2)}} \Phi_n^{(2)*} \partial_\nu \Phi_m^{(1)} d\ell + \frac{k_{t;m}^{\prime(1)}}{k_{t;n}^{\prime(2)}} \langle \Phi_m^{(1)} | \Phi_n^{(2)} \rangle. \quad (\text{C.13})$$

In equation C.13, the contour integral vanishes due to the boundary condition 2.135. This means that we are left with the second term. When we substitute the analytical solutions for  $\Phi_m^{(1)}$  and  $\Phi_n^{(2)}$  for the rectangular waveguides in equation C.13, and if we use the definition C.2, we arrive at

$$\begin{aligned} \langle \mathbf{e}_{t;m}^{\prime(1)} | \mathbf{e}_{t;n}^{\prime(2)} \rangle &= \langle \mathbf{h}_{t;m}^{\prime(1)} | \mathbf{h}_{t;n}^{\prime(2)} \rangle \\ &= \frac{4}{\sqrt{abcd}} \sqrt{\frac{M^2 + N^2}{P^2 + Q^2}} \alpha(M, P, c, e, g) \alpha(N, Q, d, f, h). \end{aligned} \quad (\text{C.14})$$

Subsequently, we substitute the expressions for the two TM modal fields, i.e., equations 2.137 and 2.138, in the inner product. We obtain

$$\begin{aligned} \langle \mathbf{h}_{t;m}^{\prime(1)} | \mathbf{e}_{t;n}^{\prime(2)} \rangle &= - \langle \mathbf{e}_{t;m}^{\prime(1)} | \mathbf{h}_{t;n}^{\prime(2)} \rangle \\ &= \frac{1}{k_{t;m}^{\prime(1)} k_{t;n}^{\prime(2)}} \langle \hat{\mathbf{z}} \times \nabla_t \Phi_m^{(1)} | \nabla_t \Phi_n^{(2)} \rangle. \end{aligned} \quad (\text{C.15})$$

We can simplify the inner product on the right-hand side by using the chain rule for differentiation by parts

$$\begin{aligned} (\nabla_t \Phi_n^{(2)*}) \cdot (\hat{\mathbf{z}} \times \nabla_t \Phi_m^{(1)}) &= \\ &= \nabla_t \cdot (\Phi_n^{(2)*} \hat{\mathbf{z}} \times \nabla_t \Phi_m^{(1)}) - \Phi_n^{(2)*} \nabla_t \cdot (\hat{\mathbf{z}} \times \nabla_t \Phi_m^{(1)}) \\ &= \nabla_t \cdot (\Phi_n^{(2)*} \hat{\mathbf{z}} \times \nabla_t \Phi_m^{(1)}), \end{aligned} \quad (\text{C.16})$$

and by applying Gauss' divergence theorem. This leads to

$$\begin{aligned} \langle \mathbf{h}_{t;m}^{\prime(1)} | \mathbf{e}_{t;n}^{\prime(2)} \rangle &= - \langle \mathbf{e}_{t;m}^{\prime(1)} | \mathbf{h}_{t;n}^{\prime(2)} \rangle \\ &= \frac{-1}{k_{t;m}^{\prime(1)} k_{t;n}^{\prime(2)}} \oint_{\partial A^{(2)}} \Phi_n^{(2)*} \partial_\tau \Phi_m^{(1)} d\ell. \end{aligned} \quad (\text{C.17})$$

In equation C.17, the contour integral vanishes due to the boundary condition 2.135. With this result, the right-hand side of equation C.17 reduces to zero. At this type of junction, where these two (arbitrary shaped) waveguide apertures meet, this relation holds, when the second aperture is completely covered by the first one, and when TM modes are considered for both apertures.

## C.2 TM Mode in Waveguide 1, TE Mode in Waveguide 2

First we substitute the expressions for the TM and TE modal fields, i.e., equations 2.137, 2.138, 2.162 and 2.163, in the inner product. We obtain

$$\begin{aligned} \langle \mathbf{e}'_{t;m} | \mathbf{e}''_{t;n} \rangle &= \langle \mathbf{h}'_{t;m} | \mathbf{h}''_{t;n} \rangle \\ &= \frac{1}{k'_{t;m} k''_{t;n}} \langle \hat{\mathbf{z}} \times \nabla_t \Phi_m^{(1)} | \nabla_t \Psi_n^{(2)} \rangle. \end{aligned} \quad (\text{C.18})$$

We can simplify the inner product on the right-hand side by using the chain rule for differentiation by parts

$$\begin{aligned} (\nabla_t \Phi_m^{(1)}) \cdot (\nabla_t \Psi_n^{(2)*} \times \hat{\mathbf{z}}) &= \\ &= \nabla_t \cdot (\Phi_m^{(1)} \nabla_t \Psi_n^{(2)*} \times \hat{\mathbf{z}}) - \Phi_m^{(1)} \nabla_t \cdot (\nabla_t \Psi_n^{(2)*} \times \hat{\mathbf{z}}) \\ &= \nabla_t \cdot (\Phi_m^{(1)} \nabla_t \Psi_n^{(2)*} \times \hat{\mathbf{z}}), \end{aligned} \quad (\text{C.19})$$

and by applying Gauss' divergence theorem. This leads to

$$\frac{1}{k'_{t;m} k''_{t;n}} \oint_{\partial A^{(2)}} \Phi_m^{(1)} \partial_\tau \Psi_n^{(2)*} d\ell. \quad (\text{C.20})$$

When we substitute the analytical solutions for  $\Phi_m^{(1)}$  and  $\Psi_n^{(2)}$  for the rectangular waveguides in equation C.20, and if we use the definitions C.2 and C.4, we arrive at

$$\begin{aligned} \langle \mathbf{e}'_{t;m} | \mathbf{e}''_{t;n} \rangle &= \langle \mathbf{h}'_{t;m} | \mathbf{h}''_{t;n} \rangle \\ &= \frac{2}{\sqrt{(M^2 + N^2)(P^2 + Q^2)}} \sqrt{\frac{\epsilon_p \epsilon_q}{abcd}} \\ &\quad [NP\alpha(M, P, c, e, g) \beta(N, Q, d, f, h) - \\ &\quad MQ\beta(M, P, c, e, g) \alpha(N, Q, d, f, h)]. \end{aligned} \quad (\text{C.21})$$

Subsequently, we substitute the expressions for the TM and TE modal fields, i.e., equations 2.137, 2.138, 2.162 and 2.163, in the inner product. We obtain

$$\begin{aligned} \langle \mathbf{h}'_{t;m} | \mathbf{e}''_{t;n} \rangle &= - \langle \mathbf{e}'_{t;m} | \mathbf{h}''_{t;n} \rangle \\ &= \frac{-1}{k'_{t;m} k''_{t;n}} \langle \nabla_t \Phi_m^{(1)} | \nabla_t \Psi_n^{(2)} \rangle. \end{aligned} \quad (\text{C.22})$$

If we substitute the analytical solutions for  $\Phi_m^{(1)}$  and  $\Psi_n^{(2)}$  for the rectangular waveguides in equation C.22, and if we use the definitions C.6 and C.8, we arrive



at

$$\begin{aligned}
\langle \mathbf{h}_{t;m}^{(1)} | \mathbf{e}_{t;n}^{(2)} \rangle &= - \langle \mathbf{e}_{t;m}^{(1)} | \mathbf{h}_{t;n}^{(2)} \rangle \\
&= \frac{2}{\sqrt{(M^2 + N^2)(P^2 + Q^2)}} \sqrt{\frac{\epsilon_p \epsilon_q}{abcd}} \\
&\quad [MP\gamma(M, P, c, e, g) \delta(N, Q, d, f, h) + \\
&\quad NQ\delta(M, P, c, e, g) \gamma(N, Q, d, f, h)].
\end{aligned} \tag{C.23}$$

### C.3 TE Mode in Waveguide 1, TM Mode in Waveguide 2

First we substitute the expressions for the TE and TM modal fields, i.e., equations 2.137, 2.138, 2.162 and 2.163, in the inner product. We obtain

$$\begin{aligned}
\langle \mathbf{e}_{t;m}^{(1)} | \mathbf{e}_{t;n}^{(2)} \rangle &= \langle \mathbf{h}_{t;m}^{(1)} | \mathbf{h}_{t;n}^{(2)} \rangle \\
&= \frac{1}{k_{t;m}^{(1)} k_{t;n}^{(2)}} \langle \nabla_t \Psi_m^{(1)} | \hat{\mathbf{z}} \times \nabla_t \Phi_n^{(2)} \rangle.
\end{aligned} \tag{C.24}$$

We can simplify the inner product on the right-hand side by using the chain rule for differentiation by parts

$$\begin{aligned}
(\nabla_t \Psi_m^{(1)}) \cdot (\hat{\mathbf{z}} \times \nabla_t \Phi_n^{(2)*}) &= \\
&= \nabla_t \cdot (\Psi_m^{(1)} \hat{\mathbf{z}} \times \nabla_t \Phi_n^{(2)*}) - \Psi_m^{(1)} \nabla_t \cdot (\hat{\mathbf{z}} \times \nabla_t \Phi_n^{(2)*}) \\
&= \nabla_t \cdot (\Psi_m^{(1)} \hat{\mathbf{z}} \times \nabla_t \Phi_n^{(2)*}),
\end{aligned} \tag{C.25}$$

and by applying Gauss' divergence theorem. This leads to

$$\begin{aligned}
\langle \mathbf{e}_{t;m}^{(1)} | \mathbf{e}_{t;n}^{(2)} \rangle &= \langle \mathbf{h}_{t;m}^{(1)} | \mathbf{h}_{t;n}^{(2)} \rangle \\
&= \frac{-1}{k_{t;m}^{(1)} k_{t;n}^{(2)}} \oint_{\partial A^{(2)}} \Psi_m^{(1)} \partial_\tau \Phi_n^{(2)*} d\ell.
\end{aligned} \tag{C.26}$$

Furthermore, the contour integral vanishes due to the boundary condition 2.135. With this result, the inner products given in equation C.26 reduce to zero. At this type of junction, where these two (arbitrarily shaped) waveguide apertures meet, this relation holds, provided that the second aperture is completely covered by the first aperture, when TE modes are considered for the first aperture, and TM modes for the second aperture.

Subsequently, we substitute the expressions for the TE and TM modal fields, i.e., equations 2.137, 2.138, 2.162 and 2.163, in the inner product. We obtain

$$\begin{aligned}
\langle \mathbf{h}_{t;m}^{(1)} | \mathbf{e}_{t;n}^{(2)} \rangle &= - \langle \mathbf{e}_{t;m}^{(1)} | \mathbf{h}_{t;n}^{(2)} \rangle \\
&= \frac{1}{k_{t;m}^{(1)} k_{t;n}^{(2)}} \langle \nabla_t \Psi_m^{(1)} | \nabla_t \Phi_n^{(2)} \rangle.
\end{aligned} \tag{C.27}$$

We can simplify the inner product on the right-hand side by using the chain rule for differentiation by parts

$$\begin{aligned} (\nabla_t \Psi_m^{(1)}) \cdot \nabla_t \Phi_n^{(2)*} &= \\ &= \nabla_t \cdot (\Phi_n^{(2)*} \nabla_t \Psi_m^{(1)}) - \Phi_n^{(2)*} \nabla_t^2 \Psi_m^{(1)} \\ &= \nabla_t \cdot (\Phi_n^{(2)*} \nabla_t \Psi_m^{(1)}) + (k_{t;m}''^{(1)})^2 \Phi_n^{(2)*} \Psi_m^{(1)}, \end{aligned} \quad (\text{C.28})$$

(since  $\Psi_m^{(1)}$  satisfies equation 2.159 and since  $k_{t;m}''^{(1)}$  is real) and by applying Gauss' divergence theorem. This leads to

$$\frac{1}{k_{t;m}''^{(1)} k_{t;n}''^{(2)}} \oint_{\partial A^{(2)}} \Phi_n^{(2)*} \partial_\nu \Psi_m^{(1)} d\ell + \frac{k_{t;m}''^{(1)}}{k_{t;n}''^{(2)}} \langle \Psi_m^{(1)} | \Phi_n^{(2)} \rangle. \quad (\text{C.29})$$

In equation C.29, the contour integral vanishes due to boundary condition 2.135. This leaves us with the second term in equation C.29. If we substitute the analytical solutions for  $\Psi_m^{(1)}$  and  $\Phi_n^{(2)}$  for the rectangular waveguides in equation C.29, and if we use the definition C.6, we arrive at

$$\begin{aligned} \langle \mathbf{h}_{t;m}''^{(1)} | \mathbf{e}_{t;n}''^{(2)} \rangle &= - \langle \mathbf{e}_{t;m}''^{(1)} | \mathbf{h}_{t;n}''^{(2)} \rangle \\ &= 2 \sqrt{\frac{\epsilon_m \epsilon_n}{abcd}} \sqrt{\frac{M^2 + N^2}{P^2 + Q^2}} \gamma(M, P, c, e, g) \gamma(N, Q, d, f, h). \end{aligned} \quad (\text{C.30})$$

## C.4 TE Mode in Waveguide 1, TE Mode in Waveguide 2

First we substitute the expressions for the two TE modal fields, i.e., equations 2.162 and 2.163, in the inner product. We obtain

$$\begin{aligned} \langle \mathbf{e}_{t;m}''^{(1)} | \mathbf{e}_{t;n}''^{(2)} \rangle &= \langle \mathbf{h}_{t;m}''^{(1)} | \mathbf{h}_{t;n}''^{(2)} \rangle \\ &= \frac{1}{k_{t;m}''^{(1)} k_{t;n}''^{(2)}} \langle \nabla_t \Psi_m^{(1)} | \nabla_t \Psi_n^{(2)} \rangle. \end{aligned} \quad (\text{C.31})$$

We can simplify the inner product on the right-hand side by using the chain rule for differentiation by parts

$$\begin{aligned} (\nabla_t \Psi_m^{(1)}) \cdot \nabla_t \Psi_n^{(2)*} &= \\ &= \nabla_t \cdot (\Psi_m^{(1)} \nabla_t \Psi_n^{(2)*}) - \Psi_m^{(1)} \nabla_t^2 \Psi_n^{(2)*} \\ &= \nabla_t \cdot (\Psi_m^{(1)} \nabla_t \Psi_n^{(2)*}) + (k_{t;n}''^{(2)})^2 \Psi_m^{(1)} \Psi_n^{(2)*}, \end{aligned} \quad (\text{C.32})$$

(since  $\Psi_n^{(2)}$  satisfies equation 2.159 and since  $k_{t;n}''^{(2)}$  is real) and by applying Gauss' divergence theorem. This leads to

$$\frac{1}{k_{t;m}''^{(1)} k_{t;n}''^{(2)}} \oint_{\partial A^{(2)}} \Psi_m^{(1)} \partial_\nu \Psi_n^{(2)*} d\ell + \frac{k_{t;n}''^{(2)}}{k_{t;m}''^{(1)}} \langle \Psi_m^{(1)} | \Psi_n^{(2)} \rangle. \quad (\text{C.33})$$

Furthermore, the contour integral vanishes due to boundary condition 2.135. This leaves only the second term in equation C.33. When we substitute the analytical solutions for  $\Psi_m^{(1)}$  and  $\Psi_n^{(2)}$  for the rectangular waveguides in equation C.33, and if we use the definition C.4, we arrive at

$$\begin{aligned} \langle \mathbf{e}_{t;m}^{\prime\prime(1)} | \mathbf{e}_{t;n}^{\prime\prime(2)} \rangle &= \langle \mathbf{h}_{t;m}^{\prime\prime(1)} | \mathbf{h}_{t;n}^{\prime\prime(2)} \rangle \\ &= \sqrt{\frac{\epsilon_m \epsilon_n \epsilon_p \epsilon_q}{abcd}} \sqrt{\frac{P^2 + Q^2}{M^2 + N^2}} \\ &\quad \beta(M, P, c, e, g) \beta(N, Q, d, f, h). \end{aligned} \quad (\text{C.34})$$

Subsequently, we substitute the expressions for the two TE modal fields, i.e., equations 2.162 and 2.163, in the inner product. We obtain

$$\begin{aligned} \langle \mathbf{h}_{t;m}^{\prime\prime(1)} | \mathbf{e}_{t;n}^{\prime\prime(2)} \rangle &= - \langle \mathbf{e}_{t;m}^{\prime\prime(1)} | \mathbf{h}_{t;n}^{\prime\prime(2)} \rangle \\ &= \frac{1}{k_{t;m}^{\prime\prime(1)} k_{t;n}^{\prime\prime(2)}} \langle \nabla_t \Psi_m^{(1)} | \nabla_t \Psi_n^{(2)} \times \hat{\mathbf{z}} \rangle. \end{aligned} \quad (\text{C.35})$$

If we substitute the analytical solutions for  $\Psi_m^{(1)}$  and  $\Psi_n^{(2)}$  for the rectangular waveguides in equation C.35, and if we use the definitions C.6 and C.8, we arrive at

$$\begin{aligned} \langle \mathbf{h}_{t;m}^{\prime\prime(1)} | \mathbf{e}_{t;n}^{\prime\prime(2)} \rangle &= - \langle \mathbf{e}_{t;m}^{\prime\prime(1)} | \mathbf{h}_{t;n}^{\prime\prime(2)} \rangle \\ &= \frac{1}{\sqrt{(M^2 + N^2)(P^2 + Q^2)}} \sqrt{\frac{\epsilon_m \epsilon_n \epsilon_p \epsilon_q}{abcd}} \\ &\quad [MQ\delta(M, P, c, e, g) \gamma(N, Q, d, f, h) - \\ &\quad NP\gamma(M, P, c, e, g) \delta(N, Q, d, f, h)]. \end{aligned} \quad (\text{C.36})$$

## C.5 Summary

In this appendix we have obtained the following interaction integrals between modes in two waveguides. For the coupling between two TM modes, we have

$$\begin{aligned} \langle \mathbf{e}_{t;m}^{\prime(1)} | \mathbf{e}_{t;n}^{\prime(2)} \rangle &= \langle \mathbf{h}_{t;m}^{\prime(1)} | \mathbf{h}_{t;n}^{\prime(2)} \rangle \\ &= \frac{4}{\sqrt{abcd}} \sqrt{\frac{M^2 + N^2}{P^2 + Q^2}} \alpha(M, P, c, e, g) \alpha(N, Q, d, f, h), \end{aligned} \quad (\text{C.37})$$

and

$$\langle \mathbf{h}_{t;m}^{\prime(1)} | \mathbf{e}_{t;n}^{\prime(2)} \rangle = - \langle \mathbf{e}_{t;m}^{\prime(1)} | \mathbf{h}_{t;n}^{\prime(2)} \rangle = 0. \quad (\text{C.38})$$

For the coupling between a TM mode in the first waveguide and a TE mode in the second waveguide, we have

$$\begin{aligned}
\langle \mathbf{e}_{t;m}^{(1)} | \mathbf{e}_{t;n}^{(2)} \rangle &= \langle \mathbf{h}_{t;m}^{(1)} | \mathbf{h}_{t;n}^{(2)} \rangle \\
&= \frac{2}{\sqrt{(M^2 + N^2)(P^2 + Q^2)}} \sqrt{\frac{\epsilon_p \epsilon_q}{abcd}} \\
&\quad [NP\alpha(M, P, c, e, g) \beta(N, Q, d, f, h) - \\
&\quad MQ\beta(M, P, c, e, g) \alpha(N, Q, d, f, h)],
\end{aligned} \tag{C.39}$$

and

$$\begin{aligned}
\langle \mathbf{h}_{t;m}^{(1)} | \mathbf{e}_{t;n}^{(2)} \rangle &= - \langle \mathbf{e}_{t;m}^{(1)} | \mathbf{h}_{t;n}^{(2)} \rangle \\
&= \frac{2}{\sqrt{(M^2 + N^2)(P^2 + Q^2)}} \sqrt{\frac{\epsilon_p \epsilon_q}{abcd}} \\
&\quad [MP\gamma(M, P, c, e, g) \delta(N, Q, d, f, h) + \\
&\quad NQ\delta(M, P, c, e, g) \gamma(N, Q, d, f, h)].
\end{aligned} \tag{C.40}$$

For the coupling between a TE mode in the first waveguide and a TM mode in the second waveguide, we have

$$\langle \mathbf{e}_{t;m}^{(1)} | \mathbf{e}_{t;n}^{(2)} \rangle = \langle \mathbf{h}_{t;m}^{(1)} | \mathbf{h}_{t;n}^{(2)} \rangle = 0, \tag{C.41}$$

and

$$\begin{aligned}
\langle \mathbf{h}_{t;m}^{(1)} | \mathbf{e}_{t;n}^{(2)} \rangle &= - \langle \mathbf{e}_{t;m}^{(1)} | \mathbf{h}_{t;n}^{(2)} \rangle \\
&= 2\sqrt{\frac{\epsilon_m \epsilon_n}{abcd}} \sqrt{\frac{M^2 + N^2}{P^2 + Q^2}} \gamma(M, P, c, e, g) \gamma(N, Q, d, f, h).
\end{aligned} \tag{C.42}$$

For the coupling between two TE modes we have

$$\begin{aligned}
\langle \mathbf{e}_{t;m}^{(1)} | \mathbf{e}_{t;n}^{(2)} \rangle &= \langle \mathbf{h}_{t;m}^{(1)} | \mathbf{h}_{t;n}^{(2)} \rangle \\
&= \sqrt{\frac{\epsilon_m \epsilon_n \epsilon_p \epsilon_q}{abcd}} \sqrt{\frac{P^2 + Q^2}{M^2 + N^2}} \\
&\quad \beta(M, P, c, e, g) \beta(N, Q, d, f, h),
\end{aligned} \tag{C.43}$$

and

$$\begin{aligned}
\langle \mathbf{h}_{t;m}^{(1)} | \mathbf{e}_{t;n}^{(2)} \rangle &= - \langle \mathbf{e}_{t;m}^{(1)} | \mathbf{h}_{t;n}^{(2)} \rangle \\
&= \frac{1}{\sqrt{(M^2 + N^2)(P^2 + Q^2)}} \sqrt{\frac{\epsilon_m \epsilon_n \epsilon_p \epsilon_q}{abcd}} \\
&\quad [MQ\delta(M, P, c, e, g) \gamma(N, Q, d, f, h) - \\
&\quad NP\gamma(M, P, c, e, g) \delta(N, Q, d, f, h)].
\end{aligned} \tag{C.44}$$



## Appendix D

# Interaction between a Waveguide and a Layered Space

In this appendix, we will evaluate<sup>1</sup> the inner product between the electric and magnetic modal fields for a layered space and a rectangular waveguide. This waveguide is specified in figure D.1.

The waveguide has a cross section  $A$  with a boundary  $\partial A$ . The cross section is rectangular in shape with length  $a$  and height  $b$ . The lower left corner of this waveguide is shifted from the origin towards  $x = e$  and  $y = f$ .

The electric and magnetic modal fields within this waveguide can be written in terms of square integrable and normalized scalar generating functions  $\Phi_m$

---

<sup>1</sup>Computation of the projection matrix between a rectangular waveguide mode and a layered space mode.

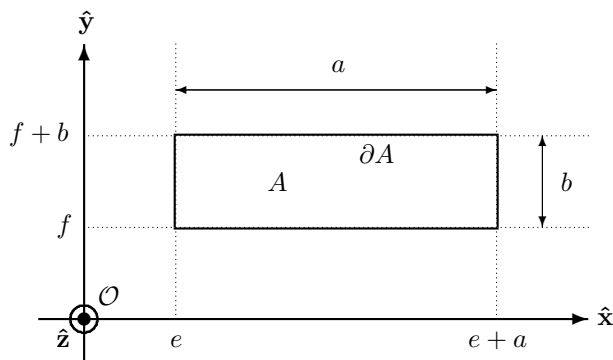


Figure D.1: Rectangular waveguide.

and  $\Psi_m$ , given by equations 2.137, 2.138, 2.162 and 2.163. Further,  $\Phi_m$  and  $\Psi_m$  satisfy the Helmholtz equations 2.134 and 2.159, respectively. Given the rectangular shape of the waveguide, we can solve these equations in closed form. This has been done in section 3.7.1. The result is given by equations 3.74 and 3.75 for  $\Phi_m$ , and by equations 3.76 and 3.77 for  $\Psi_m$ .

The electric and magnetic modal fields within the layered space are given by equations 2.174, 2.175, 2.181 and 2.182. We define

$$\alpha(M, k_x, a, e) \equiv \int_e^{e+a} \sin(M(x-e)) \exp(-jk_x x) dx, \quad (\text{D.1})$$

which has the following analytical form

$$\begin{aligned} \alpha(M, k_x, a, e) = & \frac{ja}{2} \text{sinc} \left( \frac{a}{2} [M + k_x] \right) \exp \left( -\frac{ja}{2} [M + k_x] - jk_x e \right) - \\ & \frac{ja}{2} \text{sinc} \left( \frac{a}{2} [M - k_x] \right) \exp \left( \frac{ja}{2} [M - k_x] - jk_x e \right). \end{aligned} \quad (\text{D.2})$$

We define

$$\beta(M, k_x, a, e) \equiv \int_e^{e+a} \cos(M(x-e)) \exp(-jk_x x) dx, \quad (\text{D.3})$$

which has the following analytical form

$$\begin{aligned} \beta(M, k_x, a, e) = & \frac{a}{2} \text{sinc} \left( \frac{a}{2} [M + k_x] \right) \exp \left( -\frac{ja}{2} [M + k_x] - jk_x e \right) + \\ & \frac{a}{2} \text{sinc} \left( \frac{a}{2} [M - k_x] \right) \exp \left( \frac{ja}{2} [M - k_x] - jk_x e \right). \end{aligned} \quad (\text{D.4})$$

Further we define

$$M = \frac{m\pi}{a}, \quad N = \frac{n\pi}{b}. \quad (\text{D.5})$$

In the next four sections, we will evaluate four different possible combinations of inner products.

## D.1 TM Mode in Waveguide, TM Mode in Layered Space

First we substitute the expressions for the two TM modal fields, i.e., equations 2.137, 2.138, 2.174 and 2.175, in the inner product. We obtain

$$\begin{aligned} \langle \mathbf{e}'_t(\mathbf{k}_t) | \mathbf{e}'_{t;m} \rangle &= \langle \mathbf{h}'_t(\mathbf{k}_t) | \mathbf{h}'_{t;m} \rangle \\ &= -\frac{j}{2\pi k'_{t;m}} \langle \hat{\mathbf{k}} \exp(-j\mathbf{k}_t \cdot \boldsymbol{\rho}) | \nabla_t \Phi_m \rangle. \end{aligned} \quad (\text{D.6})$$

We can simplify the inner product on the right-hand side by using the chain rule for differentiation by parts

$$\begin{aligned} (\hat{\mathbf{k}} \exp(-j\mathbf{k}_t \cdot \boldsymbol{\rho})) \cdot \nabla_t \Phi_m &= \nabla_t \cdot (\hat{\mathbf{k}} \exp(-j\mathbf{k}_t \cdot \boldsymbol{\rho}) \Phi_m) - \\ &\Phi_m \nabla_t \cdot (\hat{\mathbf{k}} \exp(-j\mathbf{k}_t \cdot \boldsymbol{\rho})), \end{aligned} \quad (\text{D.7})$$

and by applying Gauss' divergence theorem. This leads to

$$\begin{aligned} -\frac{j}{2\pi k'_{t,m}} \oint_{\partial V} \hat{\mathbf{k}} \exp(-j\mathbf{k}_t \cdot \boldsymbol{\rho}) \Phi_m^* \cdot \hat{\nu} d\ell + \\ \frac{j}{2\pi k'_{t,m}} \langle \nabla_t \cdot (\hat{\mathbf{k}} \exp(-j\mathbf{k}_t \cdot \boldsymbol{\rho})) | \Phi_m \rangle. \end{aligned} \quad (\text{D.8})$$

In equation D.8, the contour integral vanishes due to the boundary condition 2.135. With this result, equation D.8 reduces to

$$\frac{k_t}{2\pi k'_{t,m}} \langle \exp(-j\mathbf{k}_t \cdot \boldsymbol{\rho}) | \Phi_m \rangle. \quad (\text{D.9})$$

If we substitute the analytical solution for  $\Phi_m$  for the rectangular waveguide into equation D.9, and if we make use of definition D.1, we arrive at

$$\begin{aligned} \langle \mathbf{e}'_t(\mathbf{k}_t) | \mathbf{e}'_{t,m} \rangle &= \langle \mathbf{h}'_t(\mathbf{k}_t) | \mathbf{h}'_{t,m} \rangle \\ &= \frac{k_t}{\pi \sqrt{(M^2 + N^2)ab}} \alpha(M, k_x, a, e) \alpha(N, k_y, b, f). \end{aligned} \quad (\text{D.10})$$

Finally, note that

$$\langle \mathbf{h}''_t(\mathbf{k}_t) | \mathbf{e}'_{t,m} \rangle = - \langle \mathbf{e}''_t(\mathbf{k}_t) | \mathbf{h}'_{t,m} \rangle = \langle \mathbf{e}'_t(\mathbf{k}_t) | \mathbf{e}'_{t,m} \rangle. \quad (\text{D.11})$$

## D.2 TM Mode in Waveguide, TE Mode in Layered Space

First we substitute the expressions for the TM and TE modal fields, i.e., equations 2.137, 2.138, 2.181 and 2.182, in the inner product. We obtain

$$\begin{aligned} \langle \mathbf{e}''_t(\mathbf{k}_t) | \mathbf{e}'_{t,m} \rangle &= \langle \mathbf{h}''_t(\mathbf{k}_t) | \mathbf{h}'_{t,m} \rangle \\ &= -\frac{j}{2\pi k'_{t,m}} \langle \hat{\boldsymbol{\alpha}} \exp(-j\mathbf{k}_t \cdot \boldsymbol{\rho}) | \nabla_t \Phi_m \rangle. \end{aligned} \quad (\text{D.12})$$

We can simplify the inner product on the right-hand side by using the chain rule for differentiation by parts

$$\begin{aligned} (\hat{\boldsymbol{\alpha}} \exp(-j\mathbf{k}_t \cdot \boldsymbol{\rho})) \cdot \nabla_t \Phi_m &= \nabla_t \cdot (\hat{\boldsymbol{\alpha}} \exp(-j\mathbf{k}_t \cdot \boldsymbol{\rho}) \Phi_m) - \\ &\Phi_m \nabla_t \cdot (\hat{\boldsymbol{\alpha}} \exp(-j\mathbf{k}_t \cdot \boldsymbol{\rho})), \end{aligned} \quad (\text{D.13})$$



and by applying Gauss' divergence theorem. This leads to

$$-\frac{j}{2\pi k'_{t;m}} \oint_{\partial V} \hat{\alpha} \exp(-j\mathbf{k}_t \cdot \boldsymbol{\rho}) \Phi_m^* \cdot \hat{\nu} dl + \frac{j}{2\pi k'_{t;m}} \langle \nabla_t \cdot (\hat{\alpha} \exp(-j\mathbf{k}_t \cdot \boldsymbol{\rho})) | \Phi_m \rangle. \quad (\text{D.14})$$

In equation D.14, the contour integral vanishes due to the boundary condition 2.135. With this result, equation D.14 reduces to

$$\begin{aligned} \langle \mathbf{e}'_t(\mathbf{k}_t) | \mathbf{e}'_{t;m} \rangle &= \langle \mathbf{h}''_t(\mathbf{k}_t) | \mathbf{h}'_{t;m} \rangle \\ &= \frac{j}{2\pi k'_{t;m}} \langle \nabla_t \cdot (\hat{\alpha} \exp(-j\mathbf{k}_t \cdot \boldsymbol{\rho})) | \Phi_m \rangle \\ &= -\frac{j\mathbf{k}_t \cdot (\mathbf{k}_t \times \hat{\mathbf{z}})}{2\pi k'_{t;m} k_t} \langle \exp(-j\mathbf{k}_t \cdot \boldsymbol{\rho}) | \Phi_m \rangle = 0, \end{aligned} \quad (\text{D.15})$$

where we have used  $\mathbf{k}_t \cdot (\mathbf{k}_t \times \hat{\mathbf{z}})$ . At this type of junction where this (arbitrary shaped) waveguide meets the layered space, this relation holds, if TM modes are considered for the waveguide, and if TE modes are considered for the layered space. Finally, note that

$$\langle \mathbf{e}'_t(\mathbf{k}_t) | \mathbf{h}'_{t;m} \rangle = -\langle \mathbf{h}'_t(\mathbf{k}_t) | \mathbf{e}'_{t;m} \rangle = \langle \mathbf{e}''_t(\mathbf{k}_t) | \mathbf{h}'_{t;m} \rangle = 0. \quad (\text{D.16})$$

### D.3 TE Mode in Waveguide, TM Mode in Layered Space

First we substitute the expressions for the TE and TM modal fields, i.e., equations 2.162, 2.163, 2.174 and 2.175, in the inner product. We obtain

$$\begin{aligned} \langle \mathbf{e}'_t(\mathbf{k}_t) | \mathbf{e}''_{t;m} \rangle &= \langle \mathbf{h}'_t(\mathbf{k}_t) | \mathbf{h}''_{t;m} \rangle \\ &= \frac{j}{2\pi k''_{t;m}} \langle \hat{\alpha} \exp(-j\mathbf{k}_t \cdot \boldsymbol{\rho}) | \nabla_t \Psi_m \rangle. \end{aligned} \quad (\text{D.17})$$

This equation can be simplified by expanding the inner product. This results in

$$\begin{aligned} \frac{jk_y}{2\pi k''_{t;m} k_t} \langle \exp(-j\mathbf{k}_t \cdot \boldsymbol{\rho}) | \partial_x \Psi_m \rangle - \frac{jk_x}{2\pi k''_{t;m} k_t} \langle \exp(-j\mathbf{k}_t \cdot \boldsymbol{\rho}) | \partial_y \Psi_m \rangle. \end{aligned} \quad (\text{D.18})$$

If we substitute the analytical solution for  $\Psi_m$  for the rectangular waveguide into equation D.18, and if we make use of definitions D.1 and D.3, we arrive at

$$\begin{aligned} \langle \mathbf{e}'_t(\mathbf{k}_t) | \mathbf{e}''_{t;m} \rangle &= \langle \mathbf{h}'_t(\mathbf{k}_t) | \mathbf{h}''_{t;m} \rangle \\ &= \frac{j}{2\pi k_t} \sqrt{\frac{\epsilon_m \epsilon_n}{(M^2 + N^2)ab}} \\ &\quad [-k_y M \alpha(M, k_x, a, e) \beta(N, k_y, b, f) + k_x N \beta(M, k_x, a, e) \alpha(N, k_y, b, f)]. \end{aligned} \quad (\text{D.19})$$

Finally, note that

$$\langle \mathbf{h}_t''(\mathbf{k}_t) | \mathbf{e}_{t;m}'' \rangle = - \langle \mathbf{e}_t''(\mathbf{k}_t) | \mathbf{h}_{t;m}'' \rangle = \langle \mathbf{e}_t'(\mathbf{k}_t) | \mathbf{e}_{t;m}'' \rangle . \quad (\text{D.20})$$

## D.4 TE Mode in Waveguide, TE Mode in Layered Space

First we substitute the expressions for the two TE modal fields, i.e., equations 2.162, 2.163, 2.181 and 2.182, in the inner product. We obtain

$$\begin{aligned} \langle \mathbf{e}_t''(\mathbf{k}_t) | \mathbf{e}_{t;m}'' \rangle &= \langle \mathbf{h}_t''(\mathbf{k}_t) | \mathbf{h}_{t;m}'' \rangle \\ &= - \frac{j}{2\pi k_{t;m}''} \langle \hat{\mathbf{k}} \exp(-j\mathbf{k}_t \cdot \boldsymbol{\rho}) | \nabla_t \Psi_m \rangle . \end{aligned} \quad (\text{D.21})$$

This equation will be simplified by expanding the inner product. This results in

$$\begin{aligned} - \frac{j k_x}{2\pi k_{t;m}'' k_t} \langle \exp(-j\mathbf{k}_t \cdot \boldsymbol{\rho}) | \partial_x \Psi_m \rangle - \\ \frac{j k_y}{2\pi k_{t;m}'' k_t} \langle \exp(-j\mathbf{k}_t \cdot \boldsymbol{\rho}) | \partial_y \Psi_m \rangle . \end{aligned} \quad (\text{D.22})$$

If we substitute the analytical solution for  $\Psi_m$  for the rectangular waveguide in equation D.22, and if we make use of definitions D.1 and D.3, we arrive at

$$\begin{aligned} \langle \mathbf{e}_t''(\mathbf{k}_t) | \mathbf{e}_{t;m}'' \rangle &= \langle \mathbf{h}_t''(\mathbf{k}_t) | \mathbf{h}_{t;m}'' \rangle \\ &= \frac{j}{2\pi k_t} \sqrt{\frac{\epsilon_m \epsilon_n}{(M^2 + N^2)ab}} \\ &\quad [k_x M \alpha(M, k_x, a, e) \beta(N, k_y, b, f) + \\ &\quad k_y N \beta(M, k_x, a, e) \alpha(N, k_y, b, f)] . \end{aligned} \quad (\text{D.23})$$

Finally, note that

$$\langle \mathbf{e}_t'(\mathbf{k}_t) | \mathbf{h}_{t;m}'' \rangle = - \langle \mathbf{h}_t'(\mathbf{k}_t) | \mathbf{e}_{t;m}'' \rangle = \langle \mathbf{e}_t''(\mathbf{k}_t) | \mathbf{e}_{t;m}'' \rangle . \quad (\text{D.24})$$

## D.5 Summary

In this appendix we have obtained the following interaction integrals between modes in a waveguide and a layered space. For the coupling between two TM modes, we have

$$\begin{aligned} \langle \mathbf{e}_t'(\mathbf{k}_t) | \mathbf{e}_{t;m}' \rangle &= \langle \mathbf{h}_t'(\mathbf{k}_t) | \mathbf{h}_{t;m}' \rangle \\ &= \frac{k_t}{\pi \sqrt{(M^2 + N^2)ab}} \alpha(M, k_x, a, e) \alpha(N, k_y, b, f) , \end{aligned} \quad (\text{D.25})$$

and

$$\langle \mathbf{h}_t''(\mathbf{k}_t) | \mathbf{e}_{t;m}' \rangle = - \langle \mathbf{e}_t''(\mathbf{k}_t) | \mathbf{h}_{t;m}' \rangle = \langle \mathbf{e}_t'(\mathbf{k}_t) | \mathbf{e}_{t;m}' \rangle. \quad (\text{D.26})$$

For the coupling between a TM mode in the waveguide and a TE mode in the layered space, we have

$$\begin{aligned} \langle \mathbf{e}_t''(\mathbf{k}_t) | \mathbf{e}_{t;m}' \rangle &= \langle \mathbf{h}_t''(\mathbf{k}_t) | \mathbf{h}_{t;m}' \rangle \\ &= \frac{j}{2\pi k_{t;m}'} \langle \nabla_t \cdot (\hat{\alpha} \exp(-j\mathbf{k}_t \cdot \boldsymbol{\rho})) | \Phi_m \rangle \\ &= -\frac{j\mathbf{k}_t \cdot (\mathbf{k}_t \times \hat{\mathbf{z}})}{2\pi k_{t;m}' k_t} \langle \exp(-j\mathbf{k}_t \cdot \boldsymbol{\rho}) | \Phi_m \rangle = 0, \end{aligned} \quad (\text{D.27})$$

and

$$\langle \mathbf{e}_t'(\mathbf{k}_t) | \mathbf{h}_{t;m}' \rangle = - \langle \mathbf{h}_t'(\mathbf{k}_t) | \mathbf{e}_{t;m}' \rangle = \langle \mathbf{e}_t''(\mathbf{k}_t) | \mathbf{h}_{t;m}' \rangle = 0. \quad (\text{D.28})$$

For the coupling between a TE mode in the waveguide and a TM mode in the layered space, we have

$$\begin{aligned} \langle \mathbf{e}_t'(\mathbf{k}_t) | \mathbf{e}_{t;m}'' \rangle &= \langle \mathbf{h}_t'(\mathbf{k}_t) | \mathbf{h}_{t;m}'' \rangle \\ &= \frac{j}{2\pi k_t} \sqrt{\frac{\epsilon_m \epsilon_n}{(M^2 + N^2)ab}} \\ &\quad [-k_y M \alpha(M, k_x, a, e) \beta(N, k_y, b, f) + \\ &\quad k_x N \beta(M, k_x, a, e) \alpha(N, k_y, b, f)], \end{aligned} \quad (\text{D.29})$$

and

$$\langle \mathbf{h}_t''(\mathbf{k}_t) | \mathbf{e}_{t;m}'' \rangle = - \langle \mathbf{e}_t''(\mathbf{k}_t) | \mathbf{h}_{t;m}'' \rangle = \langle \mathbf{e}_t'(\mathbf{k}_t) | \mathbf{e}_{t;m}'' \rangle. \quad (\text{D.30})$$

For the coupling between two TE modes we have

$$\begin{aligned} \langle \mathbf{e}_t''(\mathbf{k}_t) | \mathbf{e}_{t;m}'' \rangle &= \langle \mathbf{h}_t''(\mathbf{k}_t) | \mathbf{h}_{t;m}'' \rangle \\ &= \frac{j}{2\pi k_t} \sqrt{\frac{\epsilon_m \epsilon_n}{(M^2 + N^2)ab}} \\ &\quad [k_x M \alpha(M, k_x, a, e) \beta(N, k_y, b, f) + \\ &\quad k_y N \beta(M, k_x, a, e) \alpha(N, k_y, b, f)], \end{aligned} \quad (\text{D.31})$$

and

$$\langle \mathbf{e}_t'(\mathbf{k}_t) | \mathbf{h}_{t;m}'' \rangle = - \langle \mathbf{h}_t'(\mathbf{k}_t) | \mathbf{e}_{t;m}'' \rangle = \langle \mathbf{e}_t''(\mathbf{k}_t) | \mathbf{e}_{t;m}'' \rangle. \quad (\text{D.32})$$

## Appendix E

# Interaction between a Rooftop and a Waveguide

In this appendix, we will evaluate<sup>1</sup> the inner product between the electric and magnetic modal fields for a rectangular waveguide and a rooftop function. This waveguide is drawn in figure E.1. The waveguide has a cross section  $A$  with a boundary  $\partial A$ . The cross section is rectangular in shape with length  $a$  and height  $b$ . The lower left corner of this waveguide is shifted from the origin towards  $x = e$  and  $y = f$ .

The electric and magnetic modal fields within this waveguide can be written in terms of square integrable and normalized scalar generating functions  $\Phi_m$  and  $\Psi_m$ , given by equations 2.137, 2.138, 2.162 and 2.163. Further,  $\Phi_m$  and  $\Psi_m$  satisfy the Helmholtz equations 2.134 and 2.159, respectively. Given the rectangular shape of the waveguide, we can solve these equations. This has been

---

<sup>1</sup>Computation of the projection matrix between a rooftop function and a rectangular waveguide mode.

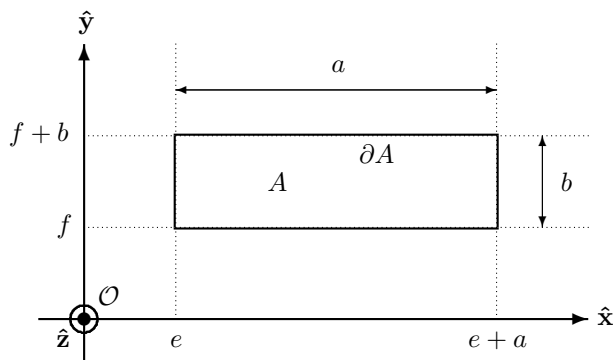


Figure E.1: Rectangular waveguide.

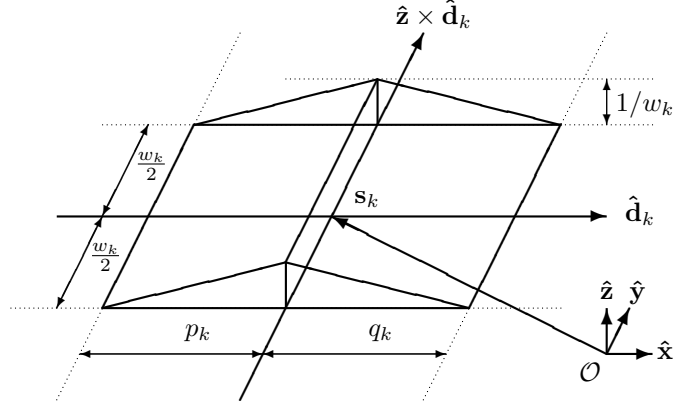


Figure E.2: Domain, vectors and scalars used in the rooftop function.

done in section 3.7.1. The result is given by equations 3.74 and 3.75 for  $\Phi_m$ , and by equations 3.76 and 3.77 for  $\Psi_m$ .

The rooftop function has been defined by equation 3.86 as [104]

$$\mathbf{f}_k(\boldsymbol{\rho}) = \hat{\mathbf{d}}_k \Lambda((\boldsymbol{\rho} - \mathbf{s}_k) \cdot \hat{\mathbf{d}}_k, p_k, q_k) \Pi((\boldsymbol{\rho} - \mathbf{s}_k) \cdot (\hat{\mathbf{z}} \times \hat{\mathbf{d}}_k), w_k). \quad (\text{E.1})$$

See section 3.7.4 for a detailed explanation of the rooftop function. See figure E.2 for a graphical representation of the domain, vectors and scalars used in the rooftop function. Further,  $\hat{\mathbf{d}}_k$  is determined by the angle  $\alpha_k$  as

$$\hat{\mathbf{d}}_k = \begin{pmatrix} \cos(\alpha_k) \\ \sin(\alpha_k) \end{pmatrix}. \quad (\text{E.2})$$

Subsequently, we define a new right-handed Cartesian reference frame  $\mathcal{O}_\sigma$  with coordinates  $\boldsymbol{\sigma} = (u, v)$  with respect to the original right-handed Cartesian reference frame  $\mathcal{O}_\rho$  with coordinates  $\boldsymbol{\rho} = (x, y)$ . The origin of this new frame is translated by the vector  $\mathbf{s}_k$  to the center of the rooftop function  $\mathbf{f}_k(\boldsymbol{\rho})$ . Further, it is rotated by  $\alpha_k$  such that  $\hat{\mathbf{u}}$  is parallel to  $\hat{\mathbf{d}}_k$ , and  $\hat{\mathbf{v}}$  is parallel to  $\hat{\mathbf{z}} \times \hat{\mathbf{d}}_k$ . The transformation law between the two reference frames  $\mathcal{O}_\rho$  and  $\mathcal{O}_\sigma$  is given by

$$\boldsymbol{\rho}(\boldsymbol{\sigma}) = \mathbf{s}_k + R\boldsymbol{\sigma}, \quad \boldsymbol{\sigma}(\boldsymbol{\rho}) = R^T(\boldsymbol{\rho} - \mathbf{s}_k), \quad (\text{E.3})$$

with

$$R = \begin{pmatrix} \cos(\alpha_k) & -\sin(\alpha_k) \\ \sin(\alpha_k) & \cos(\alpha_k) \end{pmatrix}. \quad (\text{E.4})$$

We define

$$\alpha(a, b, c, d, e, f, w, p, q) \equiv \int_{-p}^q \int_{-\frac{w}{2}}^{\frac{w}{2}} \Lambda(u, p, q) \Pi(v, w) \cos(a + bu + cv) \sin(d + eu + fv) dv du, \quad (\text{E.5})$$

which has the following analytical form

$$\alpha(a, b, c, d, e, f, w, p, q) = \theta(a + d, a - d, b + e, b - e, c + f, c - f, w, p) - \theta(a + d, a - d, b + e, b - e, c + f, c - f, w, -q), \quad (\text{E.6})$$

in which

$$\begin{aligned} \theta(a, b, c, d, e, f, w, p) = & \frac{1}{2} \text{sinc} \left( \frac{1}{2} w f \right) \left[ -p \text{sinc} \left( \frac{1}{2} p d \right) \right. \\ & \left. \sin \left( b - \frac{1}{2} p d \right) + \frac{\phi(d, b, p)}{p} \right] + \frac{1}{2} \text{sinc} \left( \frac{1}{2} w e \right) \\ & \left[ p \text{sinc} \left( \frac{1}{2} p c \right) \sin \left( a - \frac{1}{2} p c \right) - \frac{\phi(c, a, p)}{p} \right], \end{aligned} \quad (\text{E.7})$$

and in which

$$\phi(g, h, p) = \frac{p g \cos(h - p g) - \sin(h) + \sin(h - p g)}{g^2}. \quad (\text{E.8})$$

Note that

$$\lim_{g \rightarrow 0} \phi(g, h, p) = \frac{1}{2} p^2 \sin(h). \quad (\text{E.9})$$

Further, we introduce the short notation

$$M = \frac{m\pi}{a}, \quad N = \frac{n\pi}{b}, \quad (\text{E.10})$$

and

$$\begin{aligned} A_k &= M(s_{k,x} - e), & B_k &= M \cos(\alpha_k), & C_k &= -M \sin(\alpha_k), \\ D_k &= M(s_{k,y} - f), & E_k &= N \sin(\alpha_k), & F_k &= N \cos(\alpha_k). \end{aligned} \quad (\text{E.11})$$

In the next four sections, we will evaluate four possible combinations of inner products.

## E.1 Magnetic TM Mode in Waveguide

First, we substitute the expression for the magnetic TM modal field, i.e., equation 2.138, in the inner product. We obtain

$$\langle \mathbf{h}'_{t;m} | \mathbf{f}_k \rangle = -\frac{1}{k'_{t;m}} \langle \nabla_t \Phi_m | \mathbf{f}_k \times \hat{\mathbf{z}} \rangle. \quad (\text{E.12})$$

If we use the coordinate transformation from  $\mathcal{O}_\rho$  to  $\mathcal{O}_\sigma$ , we can elaborate equation E.12 as

$$\langle \mathbf{h}'_{t;m} | \mathbf{f}_k \rangle = -\frac{1}{k'_{t;m}} \int [\mathbf{f}_k(\boldsymbol{\sigma}) \times \hat{\mathbf{z}}] \cdot \nabla_t \Phi_m(\boldsymbol{\sigma}) \left| \frac{\partial \rho}{\partial \boldsymbol{\sigma}} \right| dA(\boldsymbol{\sigma}), \quad (\text{E.13})$$

which reduces to

$$\langle \mathbf{h}'_{t;m} | \mathbf{f}_k \rangle = -\frac{1}{k'_{t;m}} \int [\mathbf{f}_k(\boldsymbol{\sigma}) \times \hat{\mathbf{z}}] \cdot \nabla_t \Phi_m(\mathbf{s}_k + R\boldsymbol{\sigma}) dA(\boldsymbol{\sigma}). \quad (\text{E.14})$$

If we substitute the expressions for  $\mathbf{f}_k$ , equation E.1, and the analytical solution for  $\Phi_m$  for the rectangular waveguide into the previous equation, we arrive at

$$\begin{aligned} \langle \mathbf{h}'_{t;m} | \mathbf{f}_k \rangle = & \frac{2C_k}{k'_{t;m} \sqrt{ab}} \int_{-p_k}^{q_k} \int_{-\frac{w_k}{2}}^{\frac{w_k}{2}} \Lambda(u, p_k, q_k) \Pi(v, w_k) \\ & \cos(A_k + B_k u + C_k v) \sin(D_k + E_k u + F_k v) dv du + \\ & \frac{2F_k}{k'_{t;m} \sqrt{ab}} \int_{-p_k}^{q_k} \int_{-\frac{w_k}{2}}^{\frac{w_k}{2}} \Lambda(u, p_k, q_k) \Pi(v, w_k) \\ & \sin(A_k + B_k u + C_k v) \cos(D_k + E_k u + F_k v) dv du. \end{aligned} \quad (\text{E.15})$$

Finally, using definitions E.5, E.10 and E.11, we can rewrite equation E.15 as

$$\begin{aligned} \langle \mathbf{h}'_{t;m} | \mathbf{f}_k \rangle = & \frac{2C_k}{\sqrt{ab(M^2 + N^2)}} \alpha(A_k, B_k, C_k, D_k, E_k, F_k, w_k, p_k, q_k) + \\ & \frac{2F_k}{\sqrt{ab(M^2 + N^2)}} \alpha(D_k, E_k, F_k, A_k, B_k, C_k, w_k, p_k, q_k). \end{aligned} \quad (\text{E.16})$$

## E.2 Magnetic TE Mode in Waveguide

First, we substitute the expression for the magnetic TE modal field, equation 2.162, in the inner product. We obtain

$$\langle \mathbf{h}''_{t;m} | \mathbf{f}_k \rangle = -\frac{1}{k''_{t;m}} \langle \nabla_t \Psi_m | \mathbf{f}_k \rangle. \quad (\text{E.17})$$

With the aid of the coordinate transformation from  $\mathcal{O}_\rho$  to  $\mathcal{O}_\sigma$ , we can write equation E.17 as

$$\langle \mathbf{h}''_{t;m} | \mathbf{f}_k \rangle = -\frac{1}{k''_{t;m}} \int \mathbf{f}_k(\boldsymbol{\rho}(\boldsymbol{\sigma})) \cdot \nabla_t \Psi_m(\boldsymbol{\rho}(\boldsymbol{\sigma})) \left| \frac{\partial \boldsymbol{\rho}}{\partial \boldsymbol{\sigma}} \right| dA(\boldsymbol{\sigma}), \quad (\text{E.18})$$

which reduces to

$$\langle \mathbf{h}''_{t;m} | \mathbf{f}_k \rangle = -\frac{1}{k''_{t;m}} \int \mathbf{f}_k(\boldsymbol{\sigma}) \cdot \nabla_t \Psi_m(\mathbf{s}_k + R\boldsymbol{\sigma}) dA(\boldsymbol{\sigma}). \quad (\text{E.19})$$

Upon substitution of the expressions for  $\mathbf{f}_k$  given in equation E.1 and the analytical solution for  $\Psi_m$  for the rectangular waveguide in the previous equation,

we arrive at

$$\begin{aligned}
\langle \mathbf{h}''_{t;m} | \mathbf{f}_k \rangle = & \frac{B_k \sqrt{\epsilon_m \epsilon_n}}{k'_{t;m} \sqrt{ab}} \int_{-p_k}^{q_k} \int_{-\frac{w_k}{2}}^{\frac{w_k}{2}} \Lambda(u, p_k, q_k) \Pi(v, w_k) \\
& \sin(A_k + B_k u + C_k v) \cos(D_k + E_k u + F_k v) dv du + \\
& \frac{E_k \sqrt{\epsilon_m \epsilon_n}}{k'_{t;m} \sqrt{ab}} \int_{-p_k}^{q_k} \int_{-\frac{w_k}{2}}^{\frac{w_k}{2}} \Lambda(u, p_k, q_k) \Pi(v, w_k) \\
& \cos(A_k + B_k u + C_k v) \sin(D_k + E_k u + F_k v) dv du.
\end{aligned} \tag{E.20}$$

Finally, using definitions E.5, E.10 and E.11, we rewrite equation E.20 as

$$\begin{aligned}
\langle \mathbf{h}''_{t;m} | \mathbf{f}_k \rangle = & \frac{B_k \sqrt{\epsilon_m \epsilon_n}}{\sqrt{ab(M^2 + N^2)}} \alpha(D_k, E_k, F_k, A_k, B_k, C_k, w_k, p_k, q_k) + \\
& \frac{E_k \sqrt{\epsilon_m \epsilon_n}}{\sqrt{ab(M^2 + N^2)}} \alpha(A_k, B_k, C_k, D_k, E_k, F_k, w_k, p_k, q_k).
\end{aligned} \tag{E.21}$$

### E.3 Electric TM Mode in Waveguide

First, we substitute the expression for the electric TM modal field given in equation 2.137, in the inner product. We obtain

$$\langle \mathbf{e}'_{t;m} | \mathbf{f}_k \rangle = -\frac{1}{k'_{t;m}} \langle \nabla_t \Phi_m | \mathbf{f}_k \rangle. \tag{E.22}$$

With the aid of the coordinate transformation from  $\mathcal{O}_\rho$  to  $\mathcal{O}_\sigma$ , we write equation E.22 as

$$\langle \mathbf{e}'_{t;m} | \mathbf{f}_k \rangle = -\frac{1}{k'_{t;m}} \int \mathbf{f}_k(\boldsymbol{\rho}(\boldsymbol{\sigma})) \cdot \nabla_t \Phi_m(\boldsymbol{\rho}(\boldsymbol{\sigma})) \left| \frac{\partial \boldsymbol{\rho}}{\partial \boldsymbol{\sigma}} \right| dA(\boldsymbol{\sigma}), \tag{E.23}$$

which reduces to

$$\langle \mathbf{e}'_{t;m} | \mathbf{f}_k \rangle = -\frac{1}{k'_{t;m}} \int \mathbf{f}_k(\boldsymbol{\sigma}) \cdot \nabla_t \Phi_m(\mathbf{s}_k + R\boldsymbol{\sigma}) dA(\boldsymbol{\sigma}). \tag{E.24}$$

Upon substitution of the expressions for  $\mathbf{f}_k$  given in equation E.1 and the analytical solution for  $\Phi_m$  for the rectangular waveguide in the previous equation, we arrive at

$$\begin{aligned}
\langle \mathbf{e}'_{t;m} | \mathbf{f}_k \rangle = & -\frac{2B_k}{k'_{t;m} \sqrt{ab}} \int_{-p_k}^{q_k} \int_{-\frac{w_k}{2}}^{\frac{w_k}{2}} \Lambda(u, p_k, q_k) \Pi(v, w_k) \\
& \cos(A_k + B_k u + C_k v) \sin(D_k + E_k u + F_k v) dv du + \\
& -\frac{2E_k}{k'_{t;m} \sqrt{ab}} \int_{-p_k}^{q_k} \int_{-\frac{w_k}{2}}^{\frac{w_k}{2}} \Lambda(u, p_k, q_k) \Pi(v, w_k) \\
& \sin(A_k + B_k u + C_k v) \cos(D_k + E_k u + F_k v) dv du.
\end{aligned} \tag{E.25}$$



Finally, using definitions E.5, E.10 and E.11, we rewrite equation E.25 as

$$\begin{aligned} \langle \mathbf{e}'_{t;m} | \mathbf{f}_k \rangle = & \frac{-2B_k}{\sqrt{ab(M^2 + N^2)}} \alpha(A_k, B_k, C_k, D_k, E_k, F_k, w_k, p_k, q_k) + \\ & \frac{-2E_k}{\sqrt{ab(M^2 + N^2)}} \alpha(D_k, E_k, F_k, A_k, B_k, C_k, w_k, p_k, q_k). \end{aligned} \quad (\text{E.26})$$

## E.4 Electric TE Mode in Waveguide

First, we substitute the expression for the electric TE modal field, equation 2.163, in the inner product. We obtain

$$\langle \mathbf{e}''_{t;m} | \mathbf{f}_k \rangle = \frac{1}{k''_{t;m}} \langle \nabla_t \Psi_m | \mathbf{f}_k \times \hat{\mathbf{z}} \rangle, \quad (\text{E.27})$$

With the aid of the coordinate transformation from  $\mathcal{O}_\rho$  to  $\mathcal{O}_\sigma$ , we write equation E.27 as

$$\langle \mathbf{e}''_{t;m} | \mathbf{f}_k \rangle = \frac{1}{k''_{t;m}} \int [\mathbf{f}_k(\boldsymbol{\rho}(\boldsymbol{\sigma})) \times \hat{\mathbf{z}}] \cdot \nabla_t \Psi_m(\boldsymbol{\rho}(\boldsymbol{\sigma})) \left| \frac{\partial \boldsymbol{\rho}}{\partial \boldsymbol{\sigma}} \right| dA(\boldsymbol{\sigma}), \quad (\text{E.28})$$

which reduces to

$$\langle \mathbf{e}''_{t;m} | \mathbf{f}_k \rangle = \frac{1}{k''_{t;m}} \int [\mathbf{f}_k(\boldsymbol{\sigma}) \times \hat{\mathbf{z}}] \cdot \nabla_t \Psi_m(\mathbf{s}_k + R\boldsymbol{\sigma}) dA(\boldsymbol{\sigma}). \quad (\text{E.29})$$

After substituting the expressions for  $\mathbf{f}_k$  given in equation E.1, and the analytical solution for  $\Psi_m$  for the rectangular waveguide into the previous equation, we arrive at

$$\begin{aligned} \langle \mathbf{e}''_{t;m} | \mathbf{f}_k \rangle = & \frac{C_k \sqrt{\epsilon_m \epsilon_n}}{k''_{t;m} \sqrt{ab}} \int_{-p_k}^{q_k} \int_{-\frac{w_k}{2}}^{\frac{w_k}{2}} \Lambda(u, p_k, q_k) \Pi(v, w_k) \\ & \sin(A_k + B_k u + C_k v) \cos(D_k + E_k u + F_k v) dv du + \\ & \frac{F_k \sqrt{\epsilon_m \epsilon_n}}{k''_{t;m} \sqrt{ab}} \int_{-p_k}^{q_k} \int_{-\frac{w_k}{2}}^{\frac{w_k}{2}} \Lambda(u, p_k, q_k) \Pi(v, w_k) \\ & \cos(A_k + B_k u + C_k v) \sin(D_k + E_k u + F_k v) dv du. \end{aligned} \quad (\text{E.30})$$

Finally, using definitions E.5, E.10 and E.11, we rewrite equation E.30 as

$$\begin{aligned} \langle \mathbf{e}''_{t;m} | \mathbf{f}_k \rangle = & \frac{C_k \sqrt{\epsilon_m \epsilon_n}}{\sqrt{ab(M^2 + N^2)}} \alpha(D_k, E_k, F_k, A_k, B_k, C_k, w_k, p_k, q_k) + \\ & \frac{F_k \sqrt{\epsilon_m \epsilon_n}}{\sqrt{ab(M^2 + N^2)}} \alpha(A_k, B_k, C_k, D_k, E_k, F_k, w_k, p_k, q_k). \end{aligned} \quad (\text{E.31})$$

## E.5 Summary

In this appendix we have obtained the following interaction integrals between a rooftop function and a waveguide mode. For the coupling between a rooftop function and a magnetic TM mode in the waveguide, we have

$$\begin{aligned} \langle \mathbf{h}'_{t;m} | \mathbf{f}_k \rangle = & \frac{2C_k}{\sqrt{ab(M^2 + N^2)}} \alpha(A_k, B_k, C_k, D_k, E_k, F_k, w_k, p_k, q_k) + \\ & \frac{2F_k}{\sqrt{ab(M^2 + N^2)}} \alpha(D_k, E_k, F_k, A_k, B_k, C_k, w_k, p_k, q_k). \end{aligned} \quad (\text{E.32})$$

For the coupling between a rooftop function and a magnetic TE mode in the waveguide, we have

$$\begin{aligned} \langle \mathbf{h}''_{t;m} | \mathbf{f}_k \rangle = & \frac{B_k \sqrt{\epsilon_m \epsilon_n}}{\sqrt{ab(M^2 + N^2)}} \alpha(D_k, E_k, F_k, A_k, B_k, C_k, w_k, p_k, q_k) + \\ & \frac{E_k \sqrt{\epsilon_m \epsilon_n}}{\sqrt{ab(M^2 + N^2)}} \alpha(A_k, B_k, C_k, D_k, E_k, F_k, w_k, p_k, q_k). \end{aligned} \quad (\text{E.33})$$

For the coupling between a rooftop function and an electric TM mode in the waveguide, we have

$$\begin{aligned} \langle \mathbf{e}'_{t;m} | \mathbf{f}_k \rangle = & \frac{-2B_k}{\sqrt{ab(M^2 + N^2)}} \alpha(A_k, B_k, C_k, D_k, E_k, F_k, w_k, p_k, q_k) + \\ & \frac{-2E_k}{\sqrt{ab(M^2 + N^2)}} \alpha(D_k, E_k, F_k, A_k, B_k, C_k, w_k, p_k, q_k). \end{aligned} \quad (\text{E.34})$$

For the coupling between a rooftop function and an electric TE mode in the waveguide, we have

$$\begin{aligned} \langle \mathbf{e}''_{t;m} | \mathbf{f}_k \rangle = & \frac{C_k \sqrt{\epsilon_m \epsilon_n}}{\sqrt{ab(M^2 + N^2)}} \alpha(D_k, E_k, F_k, A_k, B_k, C_k, w_k, p_k, q_k) + \\ & \frac{F_k \sqrt{\epsilon_m \epsilon_n}}{\sqrt{ab(M^2 + N^2)}} \alpha(A_k, B_k, C_k, D_k, E_k, F_k, w_k, p_k, q_k). \end{aligned} \quad (\text{E.35})$$



## Appendix F

# Interaction between a Rooftop and a Layered Space

In this appendix, we evaluate<sup>1</sup> the inner product between the electric and magnetic modal fields for a layered space and a rooftop function.

The electric and magnetic modal fields within the layered space are given by equations 2.174, 2.175, 2.181 and 2.182. The rooftop function has been defined by equation 3.86 as [104, 89]

$$\mathbf{f}_n(\boldsymbol{\rho}) = \hat{\mathbf{d}}_n \Lambda((\boldsymbol{\rho} - \mathbf{s}_n) \cdot \hat{\mathbf{d}}_n, p_n, q_n) \Pi((\boldsymbol{\rho} - \mathbf{s}_n) \cdot (\hat{\mathbf{z}} \times \hat{\mathbf{d}}_n), w_n). \quad (\text{F.1})$$

See section 3.7.4 for a detailed description of the rooftop function. See figure F.1 for a graphical representation of the domain, vectors and scalars used in the rooftop function. If we use the expressions for the electric and magnetic modal fields within the layered space, i.e., equations 2.174, 2.175, 2.181 and 2.182, we can distinguish the following four possible combinations of inner products

$$\langle \mathbf{e}'_t(\mathbf{k}_t) | \mathbf{f}_n \rangle = \frac{j}{2\pi} \hat{\mathbf{k}} \cdot \hat{\mathbf{f}}_n(\mathbf{k}_t), \quad \langle \mathbf{e}''_t(\mathbf{k}_t) | \mathbf{f}_n \rangle = \frac{j}{2\pi} \hat{\boldsymbol{\alpha}} \cdot \hat{\mathbf{f}}_n(\mathbf{k}_t), \quad (\text{F.2})$$

$$\langle \mathbf{h}'_t(\mathbf{k}_t) | \mathbf{f}_n \rangle = -\frac{j}{2\pi} \hat{\boldsymbol{\alpha}} \cdot \hat{\mathbf{f}}_n(\mathbf{k}_t), \quad \langle \mathbf{h}''_t(\mathbf{k}_t) | \mathbf{f}_n \rangle = \frac{j}{2\pi} \hat{\mathbf{k}} \cdot \hat{\mathbf{f}}_n(\mathbf{k}_t), \quad (\text{F.3})$$

in which the so-called spectrum of a rooftop function is given by

$$\hat{\mathbf{f}}_n(\mathbf{k}_t) = \langle \exp(-j\mathbf{k}_t \cdot \boldsymbol{\rho}) | \mathbf{f}_n \rangle. \quad (\text{F.4})$$

Therefore, it suffices to evaluate  $\hat{\mathbf{f}}_n(\mathbf{k}_t)$ . If we substitute the expression for the rooftop function given in F.1, in equation F.4, we arrive at

$$\hat{\mathbf{f}}_n(\mathbf{k}_t) = \hat{\mathbf{d}}_n \exp(-j\mathbf{k}_t \cdot \mathbf{s}_n) \hat{\Lambda}(\mathbf{k}_t \cdot \hat{\mathbf{d}}_n, p_n, q_n) \hat{\Pi}(\mathbf{k}_t \cdot (\hat{\mathbf{z}} \times \hat{\mathbf{d}}_n), w_n), \quad (\text{F.5})$$

<sup>1</sup>Computation of the projection matrix between a rooftop function and a layered space mode.

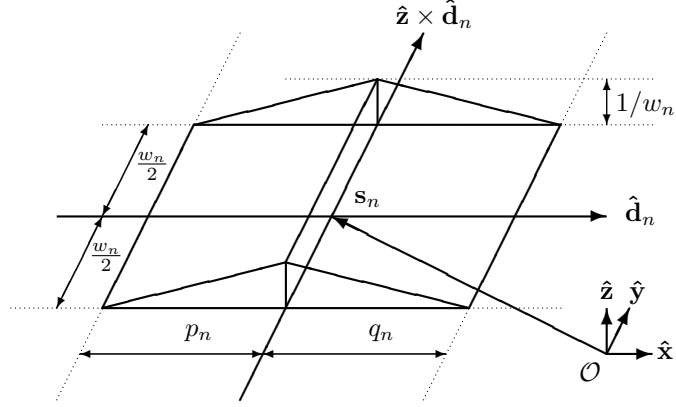


Figure F.1: Domain, vectors and scalars used in the rooftop function.

in which

$$\hat{\Lambda}(k, p, q) = \frac{\mathcal{T}(kp) - \mathcal{T}(-kq)}{jk}, \quad \hat{\Pi}(k, w) = \mathcal{S}(kw), \quad (\text{F.6})$$

and in which

$$\mathcal{T}(z) = \mathcal{S}(z) \exp\left(\frac{jz}{2}\right), \quad \mathcal{S}(z) = \text{sinc}\left(\frac{z}{2}\right). \quad (\text{F.7})$$

Note that

$$\lim_{k \rightarrow 0} \hat{\Lambda}(k, p, q) = \frac{1}{2}(p + q). \quad (\text{F.8})$$

Finally, note that

$$\hat{\mathbf{f}}_n(\mathbf{k}_t) \sim \mathcal{O}\left(\frac{1}{(\mathbf{k}_t \cdot \hat{\mathbf{d}}_n)^2 \mathbf{k}_t \cdot (\hat{\mathbf{z}} \times \hat{\mathbf{d}}_n)}\right), \quad (\text{F.9})$$

for large  $k_t$ , since

$$\hat{\Lambda}(k, p, q) \sim \mathcal{O}\left(\frac{1}{k^2}\right), \quad \hat{\Pi}(k, w) \sim \mathcal{O}\left(\frac{1}{k}\right), \quad (\text{F.10})$$

for large  $k$ .

## Appendix G

# Interaction between an RWG and a Waveguide

In this appendix, we will evaluate<sup>1</sup> the inner product between the electric and magnetic modal fields for a rectangular waveguide and an RWG function. This waveguide is shown in figure G.1.

The waveguide has a cross section  $A$  with a boundary  $\partial A$ . The cross section is rectangular in shape with length  $a$  and height  $b$ . The lower left corner of this waveguide is shifted from the origin towards  $x = e$  and  $y = f$ .

The electric and magnetic modal fields within this waveguide can be written in terms of square integrable and normalized scalar generating functions  $\Phi_m$  and  $\Psi_m$ , given by equations 2.137, 2.138, 2.162 and 2.163. Further,  $\Phi_m$  and  $\Psi_m$  satisfy the Helmholtz equations 2.134 and 2.159, respectively. Given the rectangular shape of the waveguide, we can solve these equations in closed form.

---

<sup>1</sup>Computation of the projection matrix between an RWG function and a rectangular waveguide mode.

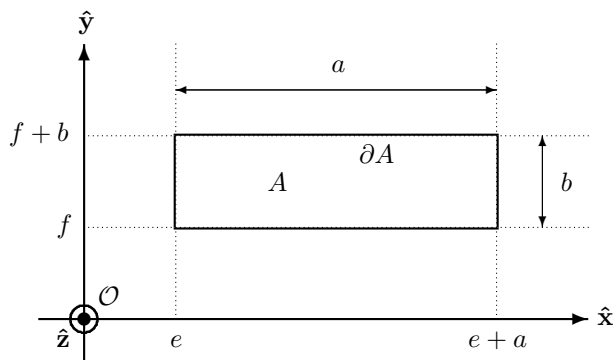


Figure G.1: Rectangular waveguide.

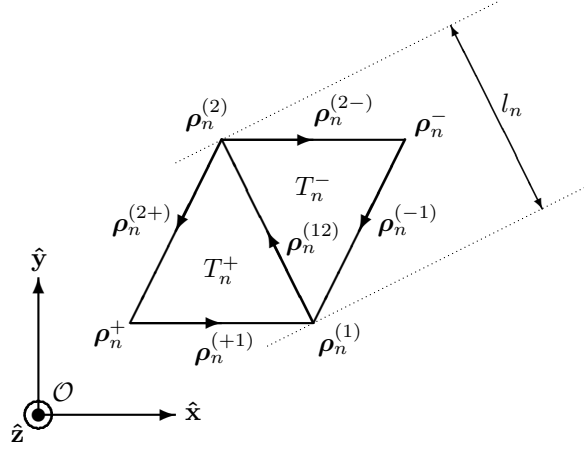


Figure G.2: Domain, vectors and scalars used in the RWG function.

This has been done in section 3.7.1. The result is given by equations 3.74 and 3.75 for  $\Phi_m$ , and by equations 3.76 and 3.77 for  $\Psi_m$ .

The RWG function has been defined by equation 3.90 as [88]

$$\mathbf{f}_k(\boldsymbol{\rho}) = \begin{cases} \frac{l_k}{2A_k^+}(\boldsymbol{\rho} - \boldsymbol{\rho}_k^+) & \text{if } \boldsymbol{\rho} \in T_k^+, \\ \frac{l_k}{2A_k^-}(\boldsymbol{\rho}_k^- - \boldsymbol{\rho}) & \text{if } \boldsymbol{\rho} \in T_k^-, \\ \mathbf{0} & \text{otherwise.} \end{cases} \quad (\text{G.1})$$

See section 3.7.5 for a detailed discussion of the RWG function. See figure G.2 for a graphical representation of the domain, vectors and scalars used in the RWG function. Note that the divergence of  $\mathbf{f}_k(\boldsymbol{\rho})$  reduces to

$$\nabla_t \cdot \mathbf{f}_k(\boldsymbol{\rho}) = \begin{cases} \frac{l_k}{A_k^+} & \text{if } \boldsymbol{\rho} \in T_k^+, \\ -\frac{l_k}{A_k^-} & \text{if } \boldsymbol{\rho} \in T_k^-, \\ 0 & \text{otherwise,} \end{cases} \quad (\text{G.2})$$

and that the curl of  $\mathbf{f}_k(\boldsymbol{\rho})$  reduces to

$$\nabla_t \times \mathbf{f}_k(\boldsymbol{\rho}) = \mathbf{0}. \quad (\text{G.3})$$

We define

$$\omega(\alpha, \beta, \gamma, \delta) \equiv \int_0^1 \cos(\alpha + \beta t) \cos(\gamma + \delta t) t dt, \quad (\text{G.4})$$

which has the following analytical form

$$\omega(\alpha, \beta, \gamma, \delta) = \omega_1(\alpha, \beta, \gamma, \delta) + \omega_2(\alpha, \beta, \gamma, \delta), \quad (\text{G.5})$$

in which

$$\omega_1(\alpha, \beta, \gamma, \delta) = \frac{\cos(\alpha + \gamma + \beta + \delta) - \cos(\alpha + \gamma)}{2(\beta + \delta)^2} + \frac{\sin(\alpha + \gamma + \beta + \delta)}{2(\beta + \delta)}, \quad (\text{G.6})$$

and in which

$$\omega_2(\alpha, \beta, \gamma, \delta) = \frac{\cos(\alpha - \gamma + \beta - \delta) - \cos(\alpha - \gamma)}{2(\beta - \delta)^2} + \frac{\sin(\alpha - \gamma + \beta - \delta)}{2(\beta - \delta)}. \quad (\text{G.7})$$

Note that

$$\begin{aligned} \lim_{(\beta+\delta) \rightarrow 0} \omega_1(\alpha, \beta, \gamma, \delta) &= \frac{1}{4} \cos(\alpha + \gamma), \\ \lim_{(\beta-\delta) \rightarrow 0} \omega_2(\alpha, \beta, \gamma, \delta) &= \frac{1}{4} \cos(\alpha - \gamma). \end{aligned} \quad (\text{G.8})$$

We define

$$\lambda(\alpha, \beta, \gamma, \delta) \equiv \int_0^1 \sin(\alpha + \beta t) \sin(\gamma + \delta t) t dt, \quad (\text{G.9})$$

which has the following analytical form

$$\lambda(\alpha, \beta, \gamma, \delta) = -\lambda_1(\alpha, \beta, \gamma, \delta) + \lambda_2(\alpha, \beta, \gamma, \delta), \quad (\text{G.10})$$

in which

$$\begin{aligned} \lambda_1(\alpha, \beta, \gamma, \delta) &= \frac{1}{4} \cos\left(\alpha + \gamma + \frac{\beta + \delta}{2}\right) \operatorname{sinc}\left(\frac{\beta + \delta}{2}\right) + \\ &\frac{1}{4} \sin\left(\alpha + \gamma + \frac{\beta + \delta}{2}\right) \operatorname{sinc}'\left(\frac{\beta + \delta}{2}\right), \end{aligned} \quad (\text{G.11})$$

and in which

$$\begin{aligned} \lambda_2(\alpha, \beta, \gamma, \delta) &= \frac{1}{4} \cos\left(\alpha - \gamma + \frac{\beta - \delta}{2}\right) \operatorname{sinc}\left(\frac{\beta - \delta}{2}\right) + \\ &\frac{1}{4} \sin\left(\alpha - \gamma + \frac{\beta - \delta}{2}\right) \operatorname{sinc}'\left(\frac{\beta - \delta}{2}\right). \end{aligned} \quad (\text{G.12})$$

Note that

$$\begin{aligned} \lim_{(\beta+\delta) \rightarrow 0} \lambda_1(\alpha, \beta, \gamma, \delta) &= \frac{1}{4} \cos(\alpha + \gamma), \\ \lim_{(\beta-\delta) \rightarrow 0} \lambda_2(\alpha, \beta, \gamma, \delta) &= \frac{1}{4} \cos(\alpha - \gamma). \end{aligned} \quad (\text{G.13})$$



We define

$$\kappa(\alpha, \beta, \gamma, \delta) \equiv \int_0^1 \sin(\alpha + \beta t) \sin(\gamma + \delta t) dt, \quad (\text{G.14})$$

which has the following analytical form

$$\begin{aligned} \kappa(\alpha, \beta, \gamma, \delta) = & \frac{1}{2} \text{sinc} \left( \frac{\beta - \delta}{2} \right) \cos \left( \alpha - \gamma + \frac{\beta - \delta}{2} \right) - \\ & \frac{1}{2} \text{sinc} \left( \frac{\beta + \delta}{2} \right) \cos \left( \alpha + \gamma + \frac{\beta + \delta}{2} \right). \end{aligned} \quad (\text{G.15})$$

We define

$$\mu(\alpha, \beta, \gamma, \delta) \equiv \int_0^1 \cos(\alpha + \beta t) \sin(\gamma + \delta t) dt, \quad (\text{G.16})$$

which has the following analytical form

$$\begin{aligned} \mu(\alpha, \beta, \gamma, \delta) = & \frac{1}{2} \text{sinc} \left( \frac{\beta + \delta}{2} \right) \sin \left( \alpha + \gamma + \frac{\beta + \delta}{2} \right) - \\ & \frac{1}{2} \text{sinc} \left( \frac{\beta - \delta}{2} \right) \sin \left( \alpha - \gamma + \frac{\beta - \delta}{2} \right). \end{aligned} \quad (\text{G.17})$$

We define

$$\nu(\alpha, \beta, \gamma, \delta) \equiv \int_0^1 \cos(\alpha + \beta t) \cos(\gamma + \delta t) dt, \quad (\text{G.18})$$

which has the following analytical form

$$\begin{aligned} \nu(\alpha, \beta, \gamma, \delta) = & \frac{1}{2} \text{sinc} \left( \frac{\beta + \delta}{2} \right) \cos \left( \alpha + \gamma + \frac{\beta + \delta}{2} \right) + \\ & \frac{1}{2} \text{sinc} \left( \frac{\beta - \delta}{2} \right) \cos \left( \alpha - \gamma + \frac{\beta - \delta}{2} \right). \end{aligned} \quad (\text{G.19})$$

In the next four sections, we will evaluate four possible combinations of coupling integrals (inner products).

## G.1 Magnetic TM Mode in Waveguide

First we substitute the expression for the magnetic TM modal field, i.e., equation 2.138, in the inner product. We obtain

$$\langle \mathbf{h}'_{t;m} | \mathbf{f}_k \rangle = \frac{1}{k'_{t;m}} \langle \nabla_t \Phi_m | \hat{\mathbf{z}} \times \mathbf{f}_k \rangle. \quad (\text{G.20})$$

By using the definition of the RWG function, i.e., equation G.1, the right-hand side can be rewritten as

$$\frac{1}{k'_{t;m}} \int_{T_k^+} (\nabla_t \Phi_m) \cdot (\hat{\mathbf{z}} \times \mathbf{f}_k) dA + \frac{1}{k'_{t;m}} \int_{T_k^-} (\nabla_t \Phi_m) \cdot (\hat{\mathbf{z}} \times \mathbf{f}_k) dA. \quad (\text{G.21})$$

We simplify the previous equation by using the chain rule for differentiation by parts

$$(\nabla_t \Phi_m) \cdot (\hat{\mathbf{z}} \times \mathbf{f}_k) = \nabla_t \cdot (\Phi_m \hat{\mathbf{z}} \times \mathbf{f}_k) - \Phi_m \nabla_t \cdot (\hat{\mathbf{z}} \times \mathbf{f}_k), \quad (\text{G.22})$$

and by applying Gauss' divergence theorem. This leads to

$$\begin{aligned} & \frac{1}{k'_{t;m}} \int_{T_k^+} \Phi_m \hat{\mathbf{z}} \cdot (\nabla_t \times \mathbf{f}_k) dA - \frac{1}{k'_{t;m}} \oint_{\partial T_k^+} \Phi_m \mathbf{f}_k \cdot \hat{\boldsymbol{\tau}} dl + \\ & \frac{1}{k'_{t;m}} \int_{T_k^-} \Phi_m \hat{\mathbf{z}} \cdot (\nabla_t \times \mathbf{f}_k) dA - \frac{1}{k'_{t;m}} \oint_{\partial T_k^-} \Phi_m \mathbf{f}_k \cdot \hat{\boldsymbol{\tau}} dl. \end{aligned} \quad (\text{G.23})$$

The application of Gauss' divergence theorem is allowed here since the integrands are continuous differentiable within the area of support. Furthermore, the boundary integral vanishes due to equation G.3. With this result, equation G.23 reduces to

$$-\frac{1}{k'_{t;m}} \oint_{\partial T_k^+} \Phi_m \mathbf{f}_k \cdot \hat{\boldsymbol{\tau}} dl - \frac{1}{k'_{t;m}} \oint_{\partial T_k^-} \Phi_m \mathbf{f}_k \cdot \hat{\boldsymbol{\tau}} dl. \quad (\text{G.24})$$

If we substitute the expression for the RWG function, i.e., equation G.1, in equation G.24, we arrive at

$$\begin{aligned} \langle \mathbf{h}'_{t;m} | \mathbf{f}_k \rangle = & -\frac{l_k}{2A_k^+ k'_{t;m}} \oint_{\partial T_k^+} \Phi_m(\boldsymbol{\rho})(\boldsymbol{\rho} - \boldsymbol{\rho}_k^+) \cdot \hat{\boldsymbol{\tau}} dl + \\ & -\frac{l_k}{2A_k^- k'_{t;m}} \oint_{\partial T_k^-} \Phi_m(\boldsymbol{\rho})(\boldsymbol{\rho}_k^- - \boldsymbol{\rho}) \cdot \hat{\boldsymbol{\tau}} dl. \end{aligned} \quad (\text{G.25})$$

If we split the contour integrals in the previous equation into separate integrals along the straight edges, we obtain

$$\begin{aligned} \langle \mathbf{h}'_{t;m} | \mathbf{f}_k \rangle = & -\frac{l_k}{2A_k^+ k'_{t;m}} \int_{\boldsymbol{\rho}_k^{(1)}}^{\boldsymbol{\rho}_k^{(2)}} \mathbf{f} \cdot \hat{\boldsymbol{\tau}}_{12} dl - \frac{l_k}{2A_k^+ k'_{t;m}} \int_{\boldsymbol{\rho}_k^{(2)}}^{\boldsymbol{\rho}_k^+} \mathbf{f} \cdot \hat{\boldsymbol{\tau}}_{2+} dl + \\ & -\frac{l_k}{2A_k^+ k'_{t;m}} \int_{\boldsymbol{\rho}_k^+}^{\boldsymbol{\rho}_k^{(1)}} \mathbf{f} \cdot \hat{\boldsymbol{\tau}}_{+1} dl - \frac{l_k}{2A_k^- k'_{t;m}} \int_{\boldsymbol{\rho}_k^{(1)}}^{\boldsymbol{\rho}_k^{(2)}} \mathbf{g} \cdot \hat{\boldsymbol{\tau}}_{12} dl + \\ & -\frac{l_k}{2A_k^- k'_{t;m}} \int_{\boldsymbol{\rho}_k^{(1)}}^{\boldsymbol{\rho}_k^-} \mathbf{g} \cdot \hat{\boldsymbol{\tau}}_{-1} dl - \frac{l_k}{2A_k^- k'_{t;m}} \int_{\boldsymbol{\rho}_k^-}^{\boldsymbol{\rho}_k^{(2)}} \mathbf{g} \cdot \hat{\boldsymbol{\tau}}_{2-} dl, \end{aligned} \quad (\text{G.26})$$

in which

$$\begin{aligned}\mathbf{f}(\boldsymbol{\rho}) &= \Phi_m(\boldsymbol{\rho})(\boldsymbol{\rho} - \boldsymbol{\rho}_k^+) \\ &= \frac{2}{\sqrt{ab}} \sin\left(\frac{m\pi}{a}(x - e)\right) \sin\left(\frac{n\pi}{b}(y - f)\right) (\boldsymbol{\rho} - \boldsymbol{\rho}_k^+),\end{aligned}\quad (\text{G.27})$$

and in which

$$\begin{aligned}\mathbf{g}(\boldsymbol{\rho}) &= \Phi_m(\boldsymbol{\rho})(\boldsymbol{\rho}_k^- - \boldsymbol{\rho}) \\ &= \frac{2}{\sqrt{ab}} \sin\left(\frac{m\pi}{a}(x - e)\right) \sin\left(\frac{n\pi}{b}(y - f)\right) (\boldsymbol{\rho}_k^- - \boldsymbol{\rho}).\end{aligned}\quad (\text{G.28})$$

Note that we have reversed the direction of integration over the contour  $\partial T_k^-$ . Furthermore, we can write for each separate integration of  $\mathbf{f}(\boldsymbol{\rho})$  along a straight line

$$\begin{aligned}\tau_{\mathbf{f},\Phi}(\boldsymbol{\rho}_k^A, \boldsymbol{\rho}_k^{AB}, \boldsymbol{\rho}_k^+) &= \int_{\boldsymbol{\rho}_k^A}^{\boldsymbol{\rho}_k^B} \mathbf{f} \cdot \hat{\boldsymbol{\tau}}_{AB} d\ell \\ &= \int_0^1 \mathbf{f}(\mathbf{c}(t)) \cdot \hat{\boldsymbol{\tau}}_{AB} \|\mathbf{c}'(t)\| dt \\ &= \int_0^1 \mathbf{f}(\boldsymbol{\rho}_k^A + t\boldsymbol{\rho}_k^{AB}) \cdot \boldsymbol{\rho}_k^{AB} dt,\end{aligned}\quad (\text{G.29})$$

in which

$$\mathbf{c}(t) = \boldsymbol{\rho}_k^A + t\boldsymbol{\rho}_k^{AB}, \quad \boldsymbol{\rho}_k^{AB} = \boldsymbol{\rho}_k^B - \boldsymbol{\rho}_k^A, \quad \hat{\boldsymbol{\tau}}_{AB} = \frac{\boldsymbol{\rho}_k^{AB}}{\|\boldsymbol{\rho}_k^{AB}\|}, \quad (\text{G.30})$$

where  $\boldsymbol{\rho}_k^A$  and  $\boldsymbol{\rho}_k^B$  denote the starting and ending vertex, respectively. Elaborating the integrands in equation G.29 results in

$$\begin{aligned}\tau_{\mathbf{f},\Phi}(\boldsymbol{\rho}_k^A, \boldsymbol{\rho}_k^{AB}, \boldsymbol{\rho}_k^+) &= \frac{2A_f}{\sqrt{ab}} \int_0^1 \sin(\alpha_f + \beta_f t) \sin(\gamma_f + \delta_f t) dt + \\ &\quad \frac{2B_f}{\sqrt{ab}} \int_0^1 \sin(\alpha_f + \beta_f t) \sin(\gamma_f + \delta_f t) t dt,\end{aligned}\quad (\text{G.31})$$

in which

$$\begin{aligned}A_f &= (\boldsymbol{\rho}_k^A - \boldsymbol{\rho}_k^+) \cdot \boldsymbol{\rho}_k^{AB}, & B_f &= \|\boldsymbol{\rho}_k^{AB}\|^2, \\ \alpha_f &= \left(\frac{m\pi}{a}\right) (\rho_{k,x}^A - e), & \beta_f &= \left(\frac{m\pi}{a}\right) \rho_{k,x}^{AB}, \\ \gamma_f &= \left(\frac{n\pi}{b}\right) (\rho_{k,y}^A - f), & \delta_f &= \left(\frac{n\pi}{b}\right) \rho_{k,y}^{AB}.\end{aligned}\quad (\text{G.32})$$

If we now use definitions G.9 and G.14, we can rewrite equation G.31 as

$$\tau_{\mathbf{f},\Phi}(\boldsymbol{\rho}_k^A, \boldsymbol{\rho}_k^{AB}, \boldsymbol{\rho}_k^+) = \frac{2}{\sqrt{ab}} [A_f \kappa(\alpha_f, \beta_f, \gamma_f, \delta_f) + B_f \lambda(\alpha_f, \beta_f, \gamma_f, \delta_f)]. \quad (\text{G.33})$$

Furthermore, we can write for each separate integration of  $\mathbf{g}(\boldsymbol{\rho})$  along a straight line

$$\begin{aligned}\tau_{\mathbf{g},\Phi}(\boldsymbol{\rho}_k^A, \boldsymbol{\rho}_k^{AB}, \boldsymbol{\rho}_k^-) &= \int_{\boldsymbol{\rho}_k^A}^{\boldsymbol{\rho}_k^B} \mathbf{g} \cdot \hat{\boldsymbol{\tau}}_{AB} d\ell \\ &= \int_0^1 \mathbf{g}(\mathbf{c}(t)) \cdot \hat{\boldsymbol{\tau}}_{AB} \|\mathbf{c}'(t)\| dt \\ &= \int_0^1 \mathbf{g}(\boldsymbol{\rho}_k^A + t\boldsymbol{\rho}_k^{AB}) \cdot \boldsymbol{\rho}_k^{AB} dt,\end{aligned}\quad (\text{G.34})$$

which reduces to

$$\begin{aligned}\tau_{\mathbf{g},\Phi}(\boldsymbol{\rho}_k^A, \boldsymbol{\rho}_k^{AB}, \boldsymbol{\rho}_k^-) &= \frac{2A_g}{\sqrt{ab}} \int_0^1 \sin(\alpha_g + \beta_g t) \sin(\gamma_g + \delta_g t) dt + \\ &\quad \frac{2B_g}{\sqrt{ab}} \int_0^1 \sin(\alpha_g + \beta_g t) \sin(\gamma_g + \delta_g t) t dt,\end{aligned}\quad (\text{G.35})$$

in which

$$\begin{aligned}A_g &= (\boldsymbol{\rho}_k^- - \boldsymbol{\rho}_k^A) \cdot \boldsymbol{\rho}_k^{AB}, & B_g &= -\|\boldsymbol{\rho}_k^{AB}\|^2, \\ \alpha_g &= \left(\frac{m\pi}{a}\right) (\rho_{k,x}^A - e), & \beta_g &= \left(\frac{m\pi}{a}\right) \rho_{k,x}^{AB}, \\ \gamma_g &= \left(\frac{n\pi}{b}\right) (\rho_{k,y}^A - f), & \delta_g &= \left(\frac{n\pi}{b}\right) \rho_{k,y}^{AB}.\end{aligned}\quad (\text{G.36})$$

If we now use definitions G.9 and G.14, we can rewrite equation G.35 as

$$\tau_{\mathbf{g},\Phi}(\boldsymbol{\rho}_k^A, \boldsymbol{\rho}_k^{AB}, \boldsymbol{\rho}_k^-) = \frac{2}{\sqrt{ab}} [A_g \kappa(\alpha_g, \beta_g, \gamma_g, \delta_g) + B_g \lambda(\alpha_g, \beta_g, \gamma_g, \delta_g)]. \quad (\text{G.37})$$

Finally, combining equations G.26, G.33 and G.37, we arrive at

$$\begin{aligned}\langle \mathbf{h}'_{t;m} | \mathbf{f}_k \rangle &= \frac{-l_k}{2A_k^+ k'_{t;m}} [\tau_{\mathbf{f},\Phi}(\boldsymbol{\rho}_k^{(1)}, \boldsymbol{\rho}_k^{(12)}, \boldsymbol{\rho}_k^+) + \tau_{\mathbf{f},\Phi}(\boldsymbol{\rho}_k^{(2)}, \boldsymbol{\rho}_k^{(2+)}, \boldsymbol{\rho}_k^+) + \\ &\quad \tau_{\mathbf{f},\Phi}(\boldsymbol{\rho}_k^+, \boldsymbol{\rho}_k^{(+1)}, \boldsymbol{\rho}_k^+)] + \frac{l_k}{2A_k^- k'_{t;m}} [\tau_{\mathbf{g},\Phi}(\boldsymbol{\rho}_k^{(1)}, \boldsymbol{\rho}_k^{(12)}, \boldsymbol{\rho}_k^-) + \\ &\quad \tau_{\mathbf{g},\Phi}(\boldsymbol{\rho}_k^-, \boldsymbol{\rho}_k^{(-1)}, \boldsymbol{\rho}_k^-) + \tau_{\mathbf{g},\Phi}(\boldsymbol{\rho}_k^{(2)}, \boldsymbol{\rho}_k^{(2-)}, \boldsymbol{\rho}_k^-)].\end{aligned}\quad (\text{G.38})$$

## G.2 Magnetic TE Mode in Waveguide

First, we substitute the expression for the magnetic TE modal field, i.e. equation 2.162, in the inner product. We obtain

$$\langle \mathbf{h}''_{t;m} | \mathbf{f}_k \rangle = -\frac{1}{k''_{t;m}} \langle \nabla_t \Psi_m | \mathbf{f}_k \rangle, \quad (\text{G.39})$$

which, by using the definition of the RWG function, equation G.1, can be rewritten as

$$-\frac{1}{k''_{t;m}} \int_{T_k^+} (\nabla_t \Psi_m) \cdot \mathbf{f}_k dA - \frac{1}{k''_{t;m}} \int_{T_k^-} (\nabla_t \Psi_m) \cdot \mathbf{f}_k dA. \quad (\text{G.40})$$

We simplify this result by using the chain rule for differentiation by parts

$$(\nabla_t \Psi_m) \cdot \mathbf{f}_k = \nabla_t \cdot (\Psi_m \mathbf{f}_k) - \Psi_m \nabla_t \cdot \mathbf{f}_k, \quad (\text{G.41})$$

and by applying Gauss' divergence theorem. This leads to

$$\begin{aligned} & -\frac{1}{k''_{t;m}} \oint_{\partial T_k^+} \Psi_m \mathbf{f}_k \cdot \hat{\nu} dl - \frac{1}{k''_{t;m}} \int_{T_k^+} \Psi_m \nabla_t \cdot \mathbf{f}_k dA + \\ & -\frac{1}{k''_{t;m}} \oint_{\partial T_k^-} \Psi_m \mathbf{f}_k \cdot \hat{\nu} dl - \frac{1}{k''_{t;m}} \int_{T_k^-} \Psi_m \nabla_t \cdot \mathbf{f}_k dA. \end{aligned} \quad (\text{G.42})$$

The application of Gauss' divergence theorem is allowed here since the integrands are continuous differentiable within the area of support. Furthermore, we rewrite equation G.42 by using equation G.2, as

$$\begin{aligned} & \frac{\nabla_t \cdot \mathbf{f}_k}{k''_{t;m}} \int_{T_k^+} \Psi_m dA - \frac{1}{k''_{t;m}} \oint_{\partial T_k^+} \Psi_m \mathbf{f}_k \cdot \hat{\nu} dl + \\ & \frac{\nabla_t \cdot \mathbf{f}_k}{k''_{t;m}} \int_{T_k^-} \Psi_m dA - \frac{1}{k''_{t;m}} \oint_{\partial T_k^-} \Psi_m \mathbf{f}_k \cdot \hat{\nu} dl. \end{aligned} \quad (\text{G.43})$$

Note that

$$(\nabla_t^2 + k''_{t;m}) \Psi_m = 0 \quad \Leftrightarrow \quad \Psi_m = -\frac{1}{k''_{t;m}} \nabla_t \cdot (\nabla_t \Psi_m). \quad (\text{G.44})$$

If we use equation G.44 and Gauss' divergence theorem, we can therefore rewrite equation G.43 as

$$\begin{aligned} & -\frac{\nabla_t \cdot \mathbf{f}_k}{k''_{t;m}} \oint_{\partial T_k^+} (\nabla_t \Psi_m) \cdot \hat{\nu} dl - \frac{1}{k''_{t;m}} \oint_{\partial T_k^+} \Psi_m \mathbf{f}_k \cdot \hat{\nu} dl + \\ & -\frac{\nabla_t \cdot \mathbf{f}_k}{k''_{t;m}} \oint_{\partial T_k^-} (\nabla_t \Psi_m) \cdot \hat{\nu} dl - \frac{1}{k''_{t;m}} \oint_{\partial T_k^-} \Psi_m \mathbf{f}_k \cdot \hat{\nu} dl. \end{aligned} \quad (\text{G.45})$$

When we substitute the expression for the RWG function, i.e., equation G.1, in equation G.45, we arrive at

$$\begin{aligned} \langle \mathbf{h}''_{t;m} | \mathbf{f}_k \rangle = & -\frac{l_k}{A_k^+ k''_{t;m}} \oint_{\partial T_k^+} (\nabla_t \Psi_m) \cdot \hat{\nu} dl + \\ & -\frac{l_k}{2A_k^+ k''_{t;m}} \oint_{\partial T_k^+} \Psi_m(\boldsymbol{\rho})(\boldsymbol{\rho} - \boldsymbol{\rho}_k^+) \cdot \hat{\nu} dl + \\ & \frac{l_k}{A_k^- k''_{t;m}} \oint_{\partial T_k^-} (\nabla_t \Psi_m) \cdot \hat{\nu} dl + \\ & -\frac{l_k}{2A_k^- k''_{t;m}} \oint_{\partial T_k^-} \Psi_m(\boldsymbol{\rho})(\boldsymbol{\rho}_k^- - \boldsymbol{\rho}) \cdot \hat{\nu} dl. \end{aligned} \quad (\text{G.46})$$

If we split the contour integrals in the previous equation into separate contributions from straight lines, we obtain

$$\begin{aligned}
\langle \mathbf{h}''_{t;m} | \mathbf{f}_k \rangle = & -\frac{l_k}{A_k^+ k_{t;m}''3} \int_{\rho_k^{(1)}}^{\rho_k^{(2)}} \mathbf{f} \cdot \hat{\nu}_{12} d\ell - \frac{l_k}{A_k^+ k_{t;m}''3} \int_{\rho_k^{(2)}}^{\rho_k^+} \mathbf{f} \cdot \hat{\nu}_{2+} d\ell + \\
& -\frac{l_k}{A_k^+ k_{t;m}''3} \int_{\rho_k^+}^{\rho_k^{(1)}} \mathbf{f} \cdot \hat{\nu}_{+1} d\ell - \frac{l_k}{2A_k^+ k_{t;m}''} \int_{\rho_k^{(1)}}^{\rho_k^{(2)}} \mathbf{g} \cdot \hat{\nu}_{12} d\ell + \\
& -\frac{l_k}{A_k^- k_{t;m}''3} \int_{\rho_k^{(1)}}^{\rho_k^{(2)}} \mathbf{f} \cdot \hat{\nu}_{12} d\ell - \frac{l_k}{A_k^- k_{t;m}''3} \int_{\rho_k^-}^{\rho_k^{(1)}} \mathbf{f} \cdot \hat{\nu}_{-1} d\ell + \\
& -\frac{l_k}{A_k^- k_{t;m}''3} \int_{\rho_k^{(2)}}^{\rho_k^-} \mathbf{f} \cdot \hat{\nu}_{2-} d\ell + \frac{l_k}{2A_k^- k_{t;m}''} \int_{\rho_k^{(1)}}^{\rho_k^{(2)}} \mathbf{h} \cdot \hat{\nu}_{12} d\ell,
\end{aligned} \tag{G.47}$$

in which

$$\begin{aligned}
\mathbf{f}(\boldsymbol{\rho}) = & \nabla_t \Psi_m(\boldsymbol{\rho}) \\
= & -\hat{\mathbf{x}} \sqrt{\frac{\epsilon_m \epsilon_n}{ab}} \left( \frac{m\pi}{a} \right) \sin \left( \frac{m\pi}{a} (x-e) \right) \cos \left( \frac{n\pi}{b} (y-f) \right) + \\
& -\hat{\mathbf{y}} \sqrt{\frac{\epsilon_m \epsilon_n}{ab}} \left( \frac{n\pi}{b} \right) \cos \left( \frac{m\pi}{a} (x-e) \right) \sin \left( \frac{n\pi}{b} (y-f) \right),
\end{aligned} \tag{G.48}$$

and

$$\begin{aligned}
\mathbf{g}(\boldsymbol{\rho}) = & \Psi_m(\boldsymbol{\rho})(\boldsymbol{\rho} - \rho_k^+) \\
= & \sqrt{\frac{\epsilon_m \epsilon_n}{ab}} \cos \left( \frac{m\pi}{a} (x-e) \right) \cos \left( \frac{n\pi}{b} (y-f) \right) (\boldsymbol{\rho} - \rho_k^+),
\end{aligned} \tag{G.49}$$

and

$$\begin{aligned}
\mathbf{h}(\boldsymbol{\rho}) = & \Psi_m(\boldsymbol{\rho})(\rho_k^- - \boldsymbol{\rho}) \\
= & \sqrt{\frac{\epsilon_m \epsilon_n}{ab}} \cos \left( \frac{m\pi}{a} (x-e) \right) \cos \left( \frac{n\pi}{b} (y-f) \right) (\rho_k^- - \boldsymbol{\rho}).
\end{aligned} \tag{G.50}$$

Note that we have reversed the direction of integration along the contour  $\partial T_k^-$ . Furthermore, we can write for each separate integral of  $\mathbf{f}(\boldsymbol{\rho})$  along a straight line

$$\begin{aligned}
\nu_{\mathbf{f}, \Psi}(\rho_k^A, \rho_k^{AB}) = & \int_{\rho_k^A}^{\rho_k^B} \mathbf{f} \cdot \hat{\nu}_{AB} d\ell \\
= & \int_0^1 \mathbf{f}(\mathbf{c}(t)) \cdot \hat{\nu}_{AB} \|\mathbf{c}'(t)\| dt \\
= & \int_0^1 \mathbf{f}(\rho_k^A + t\rho_k^{AB}) \cdot (\rho_k^{AB} \times \hat{\mathbf{z}}) dt,
\end{aligned} \tag{G.51}$$

in which

$$\mathbf{c}(t) = \boldsymbol{\rho}_k^A + t\boldsymbol{\rho}_k^{AB}, \quad \boldsymbol{\rho}_k^{AB} = \boldsymbol{\rho}_k^B - \boldsymbol{\rho}_k^A, \quad \hat{\boldsymbol{\tau}}_{AB} = \frac{\boldsymbol{\rho}_k^{AB}}{\|\boldsymbol{\rho}_k^{AB}\|}, \quad (\text{G.52})$$

where  $\boldsymbol{\rho}_k^A$  and  $\boldsymbol{\rho}_k^B$  denote the starting and ending vertex, respectively. Equation G.51 reduces to

$$\begin{aligned} \nu_{\mathbf{f},\Psi}(\boldsymbol{\rho}_k^A, \boldsymbol{\rho}_k^{AB}) &= A_f \sqrt{\frac{\epsilon_m \epsilon_n}{ab}} \int_0^1 \cos(\alpha_f + \beta_f t) \sin(\gamma_f + \delta_f t) dt + \\ & B_f \sqrt{\frac{\epsilon_m \epsilon_n}{ab}} \int_0^1 \sin(\alpha_f + \beta_f t) \cos(\gamma_f + \delta_f t) dt, \end{aligned} \quad (\text{G.53})$$

in which

$$\begin{aligned} A_f &= \left(\frac{n\pi}{b}\right) \rho_{k,x}^{AB}, & B_f &= -\left(\frac{m\pi}{a}\right) \rho_{k,y}^{AB}, \\ \alpha_f &= \left(\frac{m\pi}{a}\right) (\rho_{k,x}^A - e), & \beta_f &= \left(\frac{m\pi}{a}\right) \rho_{k,x}^{AB}, \\ \gamma_f &= \left(\frac{n\pi}{b}\right) (\rho_{k,y}^A - f), & \delta_f &= \left(\frac{n\pi}{b}\right) \rho_{k,y}^{AB}. \end{aligned} \quad (\text{G.54})$$

Using definition G.16, we rewrite equation G.53 as

$$\nu_{\mathbf{f},\Psi}(\boldsymbol{\rho}_k^A, \boldsymbol{\rho}_k^{AB}) = \sqrt{\frac{\epsilon_m \epsilon_n}{ab}} [A_f \mu(\alpha_f, \beta_f, \gamma_f, \delta_f) + B_f \mu(\gamma_f, \delta_f, \alpha_f, \beta_f)]. \quad (\text{G.55})$$

Furthermore, we can write for each separate integral of  $\mathbf{g}(\boldsymbol{\rho})$  along a straight line

$$\begin{aligned} \nu_{\mathbf{g},\Psi}(\boldsymbol{\rho}_k^A, \boldsymbol{\rho}_k^{AB}, \boldsymbol{\rho}_k^+) &= \int_{\boldsymbol{\rho}_k^A}^{\boldsymbol{\rho}_k^+} \mathbf{g} \cdot \hat{\boldsymbol{\nu}}_{AB} d\ell \\ &= \int_0^1 \mathbf{g}(\mathbf{c}(t)) \cdot \hat{\boldsymbol{\nu}}_{AB} \|\mathbf{c}'(t)\| dt \\ &= \int_0^1 \mathbf{g}(\boldsymbol{\rho}_k^A + t\boldsymbol{\rho}_k^{AB}) \cdot (\boldsymbol{\rho}_k^{AB} \times \hat{\mathbf{z}}) dt, \end{aligned} \quad (\text{G.56})$$

which reduces to

$$\nu_{\mathbf{g},\Psi}(\boldsymbol{\rho}_k^A, \boldsymbol{\rho}_k^{AB}, \boldsymbol{\rho}_k^+) = A_g \sqrt{\frac{\epsilon_m \epsilon_n}{ab}} \int_0^1 \cos(\alpha_g + \beta_g t) \cos(\gamma_g + \delta_g t) dt, \quad (\text{G.57})$$

in which

$$\begin{aligned} A_g &= (\boldsymbol{\rho}_k^A - \boldsymbol{\rho}_k^+) \cdot (\boldsymbol{\rho}_k^{AB} \times \hat{\mathbf{z}}), \\ \alpha_g &= \left(\frac{m\pi}{a}\right) (\rho_{k,x}^A - e), & \beta_g &= \left(\frac{m\pi}{a}\right) \rho_{k,x}^{AB} \\ \gamma_g &= \left(\frac{n\pi}{b}\right) (\rho_{k,y}^A - f), & \delta_g &= \left(\frac{n\pi}{b}\right) \rho_{k,y}^{AB}. \end{aligned} \quad (\text{G.58})$$

Using definition G.18, we rewrite equation G.57 as

$$\nu_{\mathbf{g},\Psi}(\boldsymbol{\rho}_k^A, \boldsymbol{\rho}_k^{AB}, \boldsymbol{\rho}_k^+) = A_g \sqrt{\frac{\epsilon_m \epsilon_n}{ab}} \nu(\alpha_g, \beta_g, \gamma_g, \delta_g). \quad (\text{G.59})$$

Furthermore, we can write for each separate integral of  $\mathbf{h}(\boldsymbol{\rho})$  along a straight line

$$\begin{aligned} \nu_{\mathbf{h},\Psi}(\boldsymbol{\rho}_k^A, \boldsymbol{\rho}_k^{AB}, \boldsymbol{\rho}_k^-) &= \int_{\boldsymbol{\rho}_k^A}^{\boldsymbol{\rho}_k^B} \mathbf{h} \cdot \hat{\boldsymbol{\nu}}_{AB} d\ell \\ &= \int_0^1 \mathbf{h}(\mathbf{c}(t)) \cdot \hat{\boldsymbol{\nu}}_{AB} \|\mathbf{c}'(t)\| dt \\ &= \int_0^1 \mathbf{h}(\boldsymbol{\rho}_k^A + t\boldsymbol{\rho}_k^{AB}) \cdot (\boldsymbol{\rho}_k^{AB} \times \hat{\mathbf{z}}) dt, \end{aligned} \quad (\text{G.60})$$

which reduces to

$$\nu_{\mathbf{h},\Psi}(\boldsymbol{\rho}_k^A, \boldsymbol{\rho}_k^{AB}, \boldsymbol{\rho}_k^-) = A_h \sqrt{\frac{\epsilon_m \epsilon_n}{ab}} \int_0^1 \cos(\alpha_h + \beta_h t) \cos(\gamma_h + \delta_h t) dt, \quad (\text{G.61})$$

in which

$$\begin{aligned} A_h &= (\boldsymbol{\rho}_k^- - \boldsymbol{\rho}_k^A) \cdot (\boldsymbol{\rho}_k^{AB} \times \hat{\mathbf{z}}), \\ \alpha_h &= \left(\frac{m\pi}{a}\right) (\rho_{k,x}^A - e), \quad \beta_h = \left(\frac{m\pi}{a}\right) \rho_{k,x}^{AB} \\ \gamma_h &= \left(\frac{n\pi}{b}\right) (\rho_{k,y}^A - f), \quad \delta_h = \left(\frac{n\pi}{b}\right) \rho_{k,y}^{AB}. \end{aligned} \quad (\text{G.62})$$

With the aid of definition G.18, we rewrite equation G.61 as

$$\nu_{\mathbf{h},\Psi}(\boldsymbol{\rho}_k^A, \boldsymbol{\rho}_k^{AB}, \boldsymbol{\rho}_k^-) = A_h \sqrt{\frac{\epsilon_m \epsilon_n}{ab}} \nu(\alpha_h, \beta_h, \gamma_h, \delta_h). \quad (\text{G.63})$$

Finally, combining equations G.47, G.55, G.59 and G.63, we arrive at

$$\begin{aligned} \langle \mathbf{h}_{t;m}'' | \mathbf{f}_k \rangle &= -\frac{l_k}{A_k^+ k_{t;m}''} [\nu_{\mathbf{f},\Psi}(\boldsymbol{\rho}_k^{(1)}, \boldsymbol{\rho}_k^{(12)}) + \nu_{\mathbf{f},\Psi}(\boldsymbol{\rho}_k^{(2)}, \boldsymbol{\rho}_k^{(2+)}) + \\ &\quad \nu_{\mathbf{f},\Psi}(\boldsymbol{\rho}_k^+, \boldsymbol{\rho}_k^{(+1)})] - \frac{l_k}{2A_k^+ k_{t;m}''} \nu_{\mathbf{g},\Psi}(\boldsymbol{\rho}_k^{(1)}, \boldsymbol{\rho}_k^{(12)}, \boldsymbol{\rho}_k^+) + \\ &\quad -\frac{l_k}{A_k^- k_{t;m}''} [\nu_{\mathbf{f},\Psi}(\boldsymbol{\rho}_k^{(1)}, \boldsymbol{\rho}_k^{(12)}) + \nu_{\mathbf{f},\Psi}(\boldsymbol{\rho}_k^-, \boldsymbol{\rho}_k^{(-1)}) + \\ &\quad \nu_{\mathbf{f},\Psi}(\boldsymbol{\rho}_k^{(2)}, \boldsymbol{\rho}_k^{(2-)})] + \frac{l_k}{2A_k^- k_{t;m}''} \nu_{\mathbf{h},\Psi}(\boldsymbol{\rho}_k^{(1)}, \boldsymbol{\rho}_k^{(12)}, \boldsymbol{\rho}_k^-). \end{aligned} \quad (\text{G.64})$$

### G.3 Electric TM Mode in Waveguide

First, we substitute the expression for the electric TM modal field, i.e., equation 2.137, in the inner product. We obtain

$$\langle \mathbf{e}'_{t;m} | \mathbf{f}_k \rangle = -\frac{1}{k'_{t;m}} \langle \nabla_t \Phi_m | \mathbf{f}_k \rangle, \quad (\text{G.65})$$



which, by using the definition of the RWG function, equation G.1, can be rewritten as

$$-\frac{1}{k'_{t;m}} \int_{T_k^+} (\nabla_t \Phi_m) \cdot \mathbf{f}_k dA - \frac{1}{k'_{t;m}} \int_{T_k^-} (\nabla_t \Phi_m) \cdot \mathbf{f}_k dA. \quad (\text{G.66})$$

We simplify the previous equation by using the chain rule for differentiation by parts

$$(\nabla_t \Phi_m) \cdot \mathbf{f}_k = \nabla_t \cdot (\Phi_m \mathbf{f}_k) - \Phi_m \nabla_t \cdot \mathbf{f}_k, \quad (\text{G.67})$$

and by applying Gauss' divergence theorem. This leads to

$$\begin{aligned} & -\frac{1}{k'_{t;m}} \oint_{\partial T_k^+} \Phi_m \mathbf{f}_k \cdot \hat{\nu} dl - \frac{1}{k'_{t;m}} \int_{T_k^+} \Phi_m \nabla_t \cdot \mathbf{f}_k dA + \\ & -\frac{1}{k'_{t;m}} \oint_{\partial T_k^-} \Phi_m \mathbf{f}_k \cdot \hat{\nu} dl - \frac{1}{k'_{t;m}} \int_{T_k^-} \Phi_m \nabla_t \cdot \mathbf{f}_k dA. \end{aligned} \quad (\text{G.68})$$

The application of Gauss' divergence theorem is allowed here since the integrands are continuous differentiable within the area of support. Next, we use equation G.2 to rewrite equation G.68 as

$$\begin{aligned} & \frac{\nabla_t \cdot \mathbf{f}_k}{k'_{t;m}} \int_{T_k^+} \Phi_m dA - \frac{1}{k'_{t;m}} \oint_{\partial T_k^+} \Phi_m \mathbf{f}_k \cdot \hat{\nu} dl + \\ & \frac{\nabla_t \cdot \mathbf{f}_k}{k'_{t;m}} \int_{T_k^-} \Phi_m dA - \frac{1}{k'_{t;m}} \oint_{\partial T_k^-} \Phi_m \mathbf{f}_k \cdot \hat{\nu} dl. \end{aligned} \quad (\text{G.69})$$

Note that

$$(\nabla_t^2 + k'^2_{t;m})\Phi_m = 0 \quad \Leftrightarrow \quad \Phi_m = -\frac{1}{k'^2_{t;m}} \nabla_t \cdot (\nabla_t \Phi_m). \quad (\text{G.70})$$

With equation G.70 and Gauss' divergence theorem, we rewrite equation G.69 as

$$\begin{aligned} & -\frac{\nabla_t \cdot \mathbf{f}_k}{k'^3_{t;m}} \oint_{\partial T_k^+} (\nabla_t \Phi_m) \cdot \hat{\nu} dl - \frac{1}{k'_{t;m}} \oint_{\partial T_k^+} \Phi_m \mathbf{f}_k \cdot \hat{\nu} dl + \\ & -\frac{\nabla_t \cdot \mathbf{f}_k}{k'^3_{t;m}} \oint_{\partial T_k^-} (\nabla_t \Phi_m) \cdot \hat{\nu} dl - \frac{1}{k'_{t;m}} \oint_{\partial T_k^-} \Phi_m \mathbf{f}_k \cdot \hat{\nu} dl. \end{aligned} \quad (\text{G.71})$$

When we substitute the expression for the RWG function, i.e., equation G.1, in equation G.71, we arrive at

$$\begin{aligned} \langle \mathbf{e}'_{t;m} | \mathbf{f}_k \rangle = & -\frac{l_k}{A_k^+ k'^3_{t;m}} \oint_{\partial T_k^+} (\nabla_t \Phi_m) \cdot \hat{\nu} dl + \\ & -\frac{l_k}{2A_k^+ k'_{t;m}} \oint_{\partial T_k^+} \Phi_m(\boldsymbol{\rho})(\boldsymbol{\rho} - \boldsymbol{\rho}_k^+) \cdot \hat{\nu} dl + \\ & \frac{l_k}{A_k^- k'^3_{t;m}} \oint_{\partial T_k^-} (\nabla_t \Phi_m) \cdot \hat{\nu} dl + \\ & -\frac{l_k}{2A_k^- k'_{t;m}} \oint_{\partial T_k^-} \Phi_m(\boldsymbol{\rho})(\boldsymbol{\rho}_k^- - \boldsymbol{\rho}) \cdot \hat{\nu} dl. \end{aligned} \quad (\text{G.72})$$

If we split the contour integrals in the previous equation into separate contributions from straight lines, we obtain

$$\begin{aligned}
\langle \mathbf{e}'_{t;m} | \mathbf{f}_k \rangle = & -\frac{l_k}{A_k^+ k'^3_{t;m}} \int_{\rho_k^{(1)}}^{\rho_k^{(2)}} \mathbf{f} \cdot \hat{\nu}_{12} d\ell - \frac{l_k}{A_k^+ k'^3_{t;m}} \int_{\rho_k^{(2)}}^{\rho_k^+} \mathbf{f} \cdot \hat{\nu}_{2+} d\ell + \\
& -\frac{l_k}{A_k^+ k'^3_{t;m}} \int_{\rho_k^+}^{\rho_k^{(1)}} \mathbf{f} \cdot \hat{\nu}_{+1} d\ell - \frac{l_k}{2A_k^+ k'^3_{t;m}} \int_{\rho_k^{(1)}}^{\rho_k^{(2)}} \mathbf{g} \cdot \hat{\nu}_{12} d\ell + \\
& -\frac{l_k}{A_k^- k'^3_{t;m}} \int_{\rho_k^{(1)}}^{\rho_k^{(2)}} \mathbf{f} \cdot \hat{\nu}_{12} d\ell - \frac{l_k}{A_k^- k'^3_{t;m}} \int_{\rho_k^-}^{\rho_k^{(1)}} \mathbf{f} \cdot \hat{\nu}_{-1} d\ell + \\
& -\frac{l_k}{A_k^- k'^3_{t;m}} \int_{\rho_k^{(2)}}^{\rho_k^-} \mathbf{f} \cdot \hat{\nu}_{2-} d\ell + \frac{l_k}{2A_k^- k'^3_{t;m}} \int_{\rho_k^{(1)}}^{\rho_k^{(2)}} \mathbf{h} \cdot \hat{\nu}_{12} d\ell,
\end{aligned} \tag{G.73}$$

in which

$$\begin{aligned}
\mathbf{f}(\boldsymbol{\rho}) &= \nabla_t \Phi_m(\boldsymbol{\rho}) \\
&= \hat{\mathbf{x}} \frac{2}{\sqrt{ab}} \left( \frac{m\pi}{a} \right) \cos \left( \frac{m\pi}{a} (x - e) \right) \sin \left( \frac{n\pi}{b} (y - f) \right) + \\
&\quad \hat{\mathbf{y}} \frac{2}{\sqrt{ab}} \left( \frac{n\pi}{b} \right) \sin \left( \frac{m\pi}{a} (x - e) \right) \cos \left( \frac{n\pi}{b} (y - f) \right),
\end{aligned} \tag{G.74}$$

and

$$\begin{aligned}
\mathbf{g}(\boldsymbol{\rho}) &= \Phi_m(\boldsymbol{\rho})(\boldsymbol{\rho} - \rho_k^+) \\
&= \frac{2}{\sqrt{ab}} \sin \left( \frac{m\pi}{a} (x - e) \right) \sin \left( \frac{n\pi}{b} (y - f) \right) (\boldsymbol{\rho} - \rho_k^+),
\end{aligned} \tag{G.75}$$

and

$$\begin{aligned}
\mathbf{h}(\boldsymbol{\rho}) &= \Phi_m(\boldsymbol{\rho})(\rho_k^- - \boldsymbol{\rho}) \\
&= \frac{2}{\sqrt{ab}} \sin \left( \frac{m\pi}{a} (x - e) \right) \sin \left( \frac{n\pi}{b} (y - f) \right) (\rho_k^- - \boldsymbol{\rho}).
\end{aligned} \tag{G.76}$$

Note that we have reversed the direction of integration along the contour  $\partial T_k^-$ . Furthermore, we can write for each separate integral of  $\mathbf{f}(\boldsymbol{\rho})$  along a straight line

$$\begin{aligned}
\nu_{\mathbf{f},\Phi}(\rho_k^A, \rho_k^{AB}) &= \int_{\rho_k^A}^{\rho_k^{AB}} \mathbf{f} \cdot \hat{\nu}_{AB} d\ell \\
&= \int_0^1 \mathbf{f}(\mathbf{c}(t)) \cdot \hat{\nu}_{AB} \|\mathbf{c}'(t)\| dt \\
&= \int_0^1 \mathbf{f}(\rho_k^A + t\rho_k^{AB}) \cdot (\rho_k^{AB} \times \hat{\mathbf{z}}) dt,
\end{aligned} \tag{G.77}$$

in which

$$\mathbf{c}(t) = \boldsymbol{\rho}_k^A + t\boldsymbol{\rho}_k^{AB}, \quad \boldsymbol{\rho}_k^{AB} = \boldsymbol{\rho}_k^B - \boldsymbol{\rho}_k^A, \quad \hat{\boldsymbol{\tau}}_{AB} = \frac{\boldsymbol{\rho}_k^{AB}}{\|\boldsymbol{\rho}_k^{AB}\|}, \quad (\text{G.78})$$

where  $\boldsymbol{\rho}_k^A$  and  $\boldsymbol{\rho}_k^B$  denote the starting and ending vertex, respectively. Equation G.77 reduces to

$$\begin{aligned} \nu_{\mathbf{f},\Phi}(\boldsymbol{\rho}_k^A, \boldsymbol{\rho}_k^{AB}) &= A_f \frac{2}{\sqrt{ab}} \int_0^1 \cos(\alpha_f + \beta_f t) \sin(\gamma_f + \delta_f t) dt + \\ & B_f \frac{2}{\sqrt{ab}} \int_0^1 \sin(\alpha_f + \beta_f t) \cos(\gamma_f + \delta_f t) dt, \end{aligned} \quad (\text{G.79})$$

in which

$$\begin{aligned} A_f &= \left(\frac{m\pi}{a}\right) \rho_{k,y}^{AB}, & B_f &= -\left(\frac{n\pi}{b}\right) \rho_{k,x}^{AB}, \\ \alpha_f &= \left(\frac{m\pi}{a}\right) (\rho_{k,x}^A - e), & \beta_f &= \left(\frac{m\pi}{a}\right) \rho_{k,x}^{AB}, \\ \gamma_f &= \left(\frac{n\pi}{b}\right) (\rho_{k,y}^A - f), & \delta_f &= \left(\frac{n\pi}{b}\right) \rho_{k,y}^{AB}. \end{aligned} \quad (\text{G.80})$$

By using definition G.16, we rewrite equation G.79 as

$$\nu_{\mathbf{f},\Phi}(\boldsymbol{\rho}_k^A, \boldsymbol{\rho}_k^{AB}) = \frac{2}{\sqrt{ab}} [A_f \mu(\alpha_f, \beta_f, \gamma_f, \delta_f) + B_f \mu(\gamma_f, \delta_f, \alpha_f, \beta_f)]. \quad (\text{G.81})$$

Furthermore, we can write for each separate integral of  $\mathbf{g}(\boldsymbol{\rho})$  along a straight line

$$\begin{aligned} \nu_{\mathbf{g},\Phi}(\boldsymbol{\rho}_k^A, \boldsymbol{\rho}_k^{AB}, \boldsymbol{\rho}_k^+) &= \int_{\boldsymbol{\rho}_k^A}^{\boldsymbol{\rho}_k^+} \mathbf{g} \cdot \hat{\boldsymbol{\nu}}_{AB} d\ell \\ &= \int_0^1 \mathbf{g}(\mathbf{c}(t)) \cdot \hat{\boldsymbol{\nu}}_{AB} \|\mathbf{c}'(t)\| dt \\ &= \int_0^1 \mathbf{g}(\boldsymbol{\rho}_k^A + t\boldsymbol{\rho}_k^{AB}) \cdot (\boldsymbol{\rho}_k^{AB} \times \hat{\mathbf{z}}) dt, \end{aligned} \quad (\text{G.82})$$

which reduces to

$$\nu_{\mathbf{g},\Phi}(\boldsymbol{\rho}_k^A, \boldsymbol{\rho}_k^{AB}, \boldsymbol{\rho}_k^+) = A_g \frac{2}{\sqrt{ab}} \int_0^1 \sin(\alpha_g + \beta_g t) \sin(\gamma_g + \delta_g t) dt, \quad (\text{G.83})$$

in which

$$\begin{aligned} A_g &= (\boldsymbol{\rho}_k^A - \boldsymbol{\rho}_k^+) \cdot (\boldsymbol{\rho}_k^{AB} \times \hat{\mathbf{z}}), \\ \alpha_g &= \left(\frac{m\pi}{a}\right) (\rho_{k,x}^A - e), & \beta_g &= \left(\frac{m\pi}{a}\right) \rho_{k,x}^{AB} \\ \gamma_g &= \left(\frac{n\pi}{b}\right) (\rho_{k,y}^A - f), & \delta_g &= \left(\frac{n\pi}{b}\right) \rho_{k,y}^{AB}. \end{aligned} \quad (\text{G.84})$$

With the aid of definition G.14, we rewrite equation G.83 as

$$\nu_{\mathbf{g},\Phi}(\boldsymbol{\rho}_k^A, \boldsymbol{\rho}_k^{AB}, \boldsymbol{\rho}_k^+) = A_g \frac{2}{\sqrt{ab}} \kappa(\alpha_g, \beta_g, \gamma_g, \delta_g). \quad (\text{G.85})$$

Furthermore, we can write for each separate integral of  $\mathbf{h}(\boldsymbol{\rho})$  along a straight line

$$\begin{aligned} \nu_{\mathbf{h},\Phi}(\boldsymbol{\rho}_k^A, \boldsymbol{\rho}_k^{AB}, \boldsymbol{\rho}_k^-) &= \int_{\boldsymbol{\rho}_k^A}^{\boldsymbol{\rho}_k^B} \mathbf{h} \cdot \hat{\boldsymbol{\nu}}_{AB} d\ell \\ &= \int_0^1 \mathbf{h}(\mathbf{c}(t)) \cdot \hat{\boldsymbol{\nu}}_{AB} \|\mathbf{c}'(t)\| dt \\ &= \int_0^1 \mathbf{h}(\boldsymbol{\rho}_k^A + t\boldsymbol{\rho}_k^{AB}) \cdot (\boldsymbol{\rho}_k^{AB} \times \hat{\mathbf{z}}) dt, \end{aligned} \quad (\text{G.86})$$

which reduces to

$$\nu_{\mathbf{h},\Phi}(\boldsymbol{\rho}_k^A, \boldsymbol{\rho}_k^{AB}, \boldsymbol{\rho}_k^-) = A_h \frac{2}{\sqrt{ab}} \int_0^1 \sin(\alpha_h + \beta_h t) \sin(\gamma_h + \delta_h t) dt, \quad (\text{G.87})$$

in which

$$\begin{aligned} A_h &= (\boldsymbol{\rho}_k^- - \boldsymbol{\rho}_k^A) \cdot (\boldsymbol{\rho}_k^{AB} \times \hat{\mathbf{z}}), \\ \alpha_h &= \left(\frac{m\pi}{a}\right) (\rho_{k,x}^A - e), \quad \beta_h = \left(\frac{m\pi}{a}\right) \rho_{k,x}^{AB} \\ \gamma_h &= \left(\frac{n\pi}{b}\right) (\rho_{k,y}^A - f), \quad \delta_h = \left(\frac{n\pi}{b}\right) \rho_{k,y}^{AB}. \end{aligned} \quad (\text{G.88})$$

In view of definition G.14, equation G.87 is rewritten as

$$\nu_{\mathbf{h},\Phi}(\boldsymbol{\rho}_k^A, \boldsymbol{\rho}_k^{AB}, \boldsymbol{\rho}_k^-) = A_h \frac{2}{\sqrt{ab}} \kappa(\alpha_h, \beta_h, \gamma_h, \delta_h). \quad (\text{G.89})$$

Finally, by combining equations G.73, G.81, G.85 and G.89, we end up with

$$\begin{aligned} \langle \mathbf{e}'_{t;m} | \mathbf{f}_k \rangle &= -\frac{l_k}{A_k^+ k'_{t;m}} [\nu_{\mathbf{f},\Phi}(\boldsymbol{\rho}_k^{(1)}, \boldsymbol{\rho}_k^{(12)}) + \nu_{\mathbf{f},\Phi}(\boldsymbol{\rho}_k^{(2)}, \boldsymbol{\rho}_k^{(2+)}) + \\ &\quad \nu_{\mathbf{f},\Phi}(\boldsymbol{\rho}_k^+, \boldsymbol{\rho}_k^{(+1)})] - \frac{l_k}{2A_k^+ k'_{t;m}} \nu_{\mathbf{g},\Phi}(\boldsymbol{\rho}_k^{(1)}, \boldsymbol{\rho}_k^{(12)}, \boldsymbol{\rho}_k^+) + \\ &\quad -\frac{l_k}{A_k^- k'_{t;m}} [\nu_{\mathbf{f},\Phi}(\boldsymbol{\rho}_k^{(1)}, \boldsymbol{\rho}_k^{(12)}) + \nu_{\mathbf{f},\Phi}(\boldsymbol{\rho}_k^-, \boldsymbol{\rho}_k^{(-1)}) + \\ &\quad \nu_{\mathbf{f},\Phi}(\boldsymbol{\rho}_k^{(2)}, \boldsymbol{\rho}_k^{(2-)})] + \frac{l_k}{2A_k^- k'_{t;m}} \nu_{\mathbf{h},\Phi}(\boldsymbol{\rho}_k^{(1)}, \boldsymbol{\rho}_k^{(12)}, \boldsymbol{\rho}_k^-). \end{aligned} \quad (\text{G.90})$$

## G.4 Electric TE Mode in Waveguide

First, we substitute the expression for the electric TE modal field, i.e., equation 2.163, in the inner product. We obtain

$$\langle \mathbf{e}''_{t;m} | \mathbf{f}_k \rangle = -\frac{1}{k''_{t;m}} \langle \nabla_t \Psi_m | \hat{\mathbf{z}} \times \mathbf{f}_k \rangle, \quad (\text{G.91})$$

which by using the definition of the RWG function, equation G.1, can be rewritten as

$$-\frac{1}{k''_{t;m}} \int_{T_k^+} (\nabla_t \Psi_m) \cdot (\hat{\mathbf{z}} \times \mathbf{f}_k) dA - \frac{1}{k''_{t;m}} \int_{T_k^-} (\nabla_t \Psi_m) \cdot (\hat{\mathbf{z}} \times \mathbf{f}_k) dA. \quad (\text{G.92})$$

We simplify these expressions by using the chain rule for differentiation by parts

$$(\nabla_t \Psi_m) \cdot (\hat{\mathbf{z}} \times \mathbf{f}_k) = \nabla_t \cdot (\Psi_m \hat{\mathbf{z}} \times \mathbf{f}_k) - \Psi_m \nabla_t \cdot (\hat{\mathbf{z}} \times \mathbf{f}_k), \quad (\text{G.93})$$

and by applying Gauss' divergence theorem. This leads to

$$\begin{aligned} & \frac{1}{k''_{t;m}} \int_{T_k^+} \Psi_m \hat{\mathbf{z}} \cdot (\nabla_t \times \mathbf{f}_k) dA - \frac{1}{k''_{t;m}} \oint_{\partial T_k^+} \Psi_m \mathbf{f}_k \cdot \hat{\boldsymbol{\tau}} dl + \\ & \frac{1}{k''_{t;m}} \int_{T_k^-} \Psi_m \hat{\mathbf{z}} \cdot (\nabla_t \times \mathbf{f}_k) dA - \frac{1}{k''_{t;m}} \oint_{\partial T_k^-} \Psi_m \mathbf{f}_k \cdot \hat{\boldsymbol{\tau}} dl. \end{aligned} \quad (\text{G.94})$$

The application of Gauss' divergence theorem is allowed here since the integrands are continuous differentiable within the area of support. Furthermore, the surface integration vanishes due to equation G.3. With this result, equation G.94 reduces to

$$-\frac{1}{k''_{t;m}} \oint_{\partial T_k^+} \Psi_m \mathbf{f}_k \cdot \hat{\boldsymbol{\tau}} dl - \frac{1}{k''_{t;m}} \oint_{\partial T_k^-} \Psi_m \mathbf{f}_k \cdot \hat{\boldsymbol{\tau}} dl. \quad (\text{G.95})$$

After substituting the expression for the RWG function, equation G.1, in equation G.95, we arrive at

$$\begin{aligned} \langle \mathbf{e}''_{t;m} | \mathbf{f}_k \rangle = & -\frac{l_k}{2A_k^+ k''_{t;m}} \oint_{\partial T_k^+} \Psi_m(\boldsymbol{\rho})(\boldsymbol{\rho} - \boldsymbol{\rho}_k^+) \cdot \hat{\boldsymbol{\tau}} dl + \\ & -\frac{l_k}{2A_k^- k''_{t;m}} \oint_{\partial T_k^-} \Psi_m(\boldsymbol{\rho})(\boldsymbol{\rho}_k^- - \boldsymbol{\rho}) \cdot \hat{\boldsymbol{\tau}} dl. \end{aligned} \quad (\text{G.96})$$

If we split the contour integrals in this equation into separate integrals along straight lines, we obtain

$$\begin{aligned} \langle \mathbf{e}''_{t;m} | \mathbf{f}_k \rangle = & -\frac{l_k}{2A_k^+ k''_{t;m}} \int_{\boldsymbol{\rho}_k^{(1)}}^{\boldsymbol{\rho}_k^{(2)}} \mathbf{f} \cdot \hat{\boldsymbol{\tau}}_{12} dl - \frac{l_k}{2A_k^+ k''_{t;m}} \int_{\boldsymbol{\rho}_k^{(2)}}^{\boldsymbol{\rho}_k^+} \mathbf{f} \cdot \hat{\boldsymbol{\tau}}_{2+} dl + \\ & -\frac{l_k}{2A_k^+ k''_{t;m}} \int_{\boldsymbol{\rho}_k^+}^{\boldsymbol{\rho}_k^{(1)}} \mathbf{f} \cdot \hat{\boldsymbol{\tau}}_{+1} dl - \frac{l_k}{2A_k^- k''_{t;m}} \int_{\boldsymbol{\rho}_k^{(1)}}^{\boldsymbol{\rho}_k^{(2)}} \mathbf{g} \cdot \hat{\boldsymbol{\tau}}_{12} dl + \\ & -\frac{l_k}{2A_k^- k''_{t;m}} \int_{\boldsymbol{\rho}_k^-}^{\boldsymbol{\rho}_k^{(1)}} \mathbf{g} \cdot \hat{\boldsymbol{\tau}}_{-1} dl - \frac{l_k}{2A_k^- k''_{t;m}} \int_{\boldsymbol{\rho}_k^{(2)}}^{\boldsymbol{\rho}_k^-} \mathbf{g} \cdot \hat{\boldsymbol{\tau}}_{-2} dl, \end{aligned} \quad (\text{G.97})$$

in which

$$\begin{aligned} \mathbf{f}(\boldsymbol{\rho}) &= \Psi_m(\boldsymbol{\rho})(\boldsymbol{\rho} - \boldsymbol{\rho}_k^+) \\ &= \sqrt{\frac{\epsilon_m \epsilon_n}{ab}} \cos\left(\frac{m\pi}{a}(x - e)\right) \cos\left(\frac{n\pi}{b}(y - f)\right) (\boldsymbol{\rho} - \boldsymbol{\rho}_k^+), \end{aligned} \quad (\text{G.98})$$

and in which

$$\begin{aligned} \mathbf{g}(\boldsymbol{\rho}) &= \Psi_m(\boldsymbol{\rho})(\boldsymbol{\rho}_k^- - \boldsymbol{\rho}) \\ &= \sqrt{\frac{\epsilon_m \epsilon_n}{ab}} \cos\left(\frac{m\pi}{a}(x - e)\right) \cos\left(\frac{n\pi}{b}(y - f)\right) (\boldsymbol{\rho}_k^- - \boldsymbol{\rho}). \end{aligned} \quad (\text{G.99})$$

Note that we have reversed the direction of integration over the contour  $\partial T_k^-$ . Furthermore, we can write for each separate integral of  $\mathbf{f}(\boldsymbol{\rho})$  along a straight line

$$\begin{aligned} \tau_{\mathbf{f}, \Psi}(\boldsymbol{\rho}_k^A, \boldsymbol{\rho}_k^{AB}, \boldsymbol{\rho}_k^+) &= \int_{\boldsymbol{\rho}_k^A}^{\boldsymbol{\rho}_k^B} \mathbf{f} \cdot \hat{\boldsymbol{\tau}}_{AB} d\ell \\ &= \int_0^1 \mathbf{f}(\mathbf{c}(t)) \cdot \hat{\boldsymbol{\tau}}_{AB} \|\mathbf{c}'(t)\| dt \\ &= \int_0^1 \mathbf{f}(\boldsymbol{\rho}_k^A + t\boldsymbol{\rho}_k^{AB}) \cdot \boldsymbol{\rho}_k^{AB} dt, \end{aligned} \quad (\text{G.100})$$

in which

$$\mathbf{c}(t) = \boldsymbol{\rho}_k^A + t\boldsymbol{\rho}_k^{AB}, \quad \boldsymbol{\rho}_k^{AB} = \boldsymbol{\rho}_k^B - \boldsymbol{\rho}_k^A, \quad \hat{\boldsymbol{\tau}}_{AB} = \frac{\boldsymbol{\rho}_k^{AB}}{\|\boldsymbol{\rho}_k^{AB}\|}, \quad (\text{G.101})$$

where  $\boldsymbol{\rho}_k^A$  and  $\boldsymbol{\rho}_k^B$  denote the starting and ending vertex, respectively. Equation G.100 reduces to

$$\begin{aligned} \tau_{\mathbf{f}, \Psi}(\boldsymbol{\rho}_k^A, \boldsymbol{\rho}_k^{AB}, \boldsymbol{\rho}_k^+) &= A_f \sqrt{\frac{\epsilon_m \epsilon_n}{ab}} \int_0^1 \cos(\alpha_f + \beta_f t) \cos(\gamma_f + \delta_f t) dt + \\ &B_f \sqrt{\frac{\epsilon_m \epsilon_n}{ab}} \int_0^1 \cos(\alpha_f + \beta_f t) \cos(\gamma_f + \delta_f t) t dt, \end{aligned} \quad (\text{G.102})$$

in which

$$\begin{aligned} A_f &= (\boldsymbol{\rho}_k^A - \boldsymbol{\rho}_k^+) \cdot \boldsymbol{\rho}_k^{AB}, & B_f &= \|\boldsymbol{\rho}_k^{AB}\|^2, \\ \alpha_f &= \left(\frac{m\pi}{a}\right) (\rho_{k,x}^A - e), & \beta_f &= \left(\frac{m\pi}{a}\right) \rho_{k,x}^{AB}, \\ \gamma_f &= \left(\frac{n\pi}{b}\right) (\rho_{k,y}^A - f), & \delta_f &= \left(\frac{n\pi}{b}\right) \rho_{k,y}^{AB}. \end{aligned} \quad (\text{G.103})$$

By using definitions G.4 and G.18, we rewrite equation G.102 as

$$\tau_{\mathbf{f}, \Psi}(\boldsymbol{\rho}_k^A, \boldsymbol{\rho}_k^{AB}, \boldsymbol{\rho}_k^+) = \sqrt{\frac{\epsilon_m \epsilon_n}{ab}} [A_f \nu(\alpha_f, \beta_f, \gamma_f, \delta_f) + B_f \omega(\alpha_f, \beta_f, \gamma_f, \delta_f)]. \quad (\text{G.104})$$

Furthermore, we write for each separate integral of  $\mathbf{g}(\boldsymbol{\rho})$  along a straight line

$$\begin{aligned}\tau_{\mathbf{g},\Psi}(\boldsymbol{\rho}_k^A, \boldsymbol{\rho}_k^{AB}, \boldsymbol{\rho}_k^-) &= \int_{\boldsymbol{\rho}_k^A}^{\boldsymbol{\rho}_k^B} \mathbf{g} \cdot \hat{\boldsymbol{\tau}}_{AB} d\ell \\ &= \int_0^1 \mathbf{g}(\mathbf{c}(t)) \cdot \hat{\boldsymbol{\tau}}_{AB} \|\mathbf{c}'(t)\| dt \\ &= \int_0^1 \mathbf{g}(\boldsymbol{\rho}_k^A + t\boldsymbol{\rho}_k^{AB}) \cdot \boldsymbol{\rho}_k^{AB} dt,\end{aligned}\quad (\text{G.105})$$

which reduces to

$$\begin{aligned}\tau_{\mathbf{g},\Psi}(\boldsymbol{\rho}_k^A, \boldsymbol{\rho}_k^{AB}, \boldsymbol{\rho}_k^-) &= A_g \sqrt{\frac{\epsilon_m \epsilon_n}{ab}} \int_0^1 \cos(\alpha_g + \beta_g t) \cos(\gamma_g + \delta_g t) dt + \\ &B_g \sqrt{\frac{\epsilon_m \epsilon_n}{ab}} \int_0^1 \cos(\alpha_g + \beta_g t) \cos(\gamma_g + \delta_g t) t dt,\end{aligned}\quad (\text{G.106})$$

in which

$$\begin{aligned}A_g &= (\boldsymbol{\rho}_k^- - \boldsymbol{\rho}_k^A) \cdot \boldsymbol{\rho}_k^{AB}, & B_g &= -\|\boldsymbol{\rho}_k^{AB}\|^2, \\ \alpha_g &= \left(\frac{m\pi}{a}\right) (\rho_{k,x}^A - e), & \beta_g &= \left(\frac{m\pi}{a}\right) \rho_{k,x}^{AB}, \\ \gamma_g &= \left(\frac{n\pi}{b}\right) (\rho_{k,y}^A - f), & \delta_g &= \left(\frac{n\pi}{b}\right) \rho_{k,y}^{AB}.\end{aligned}\quad (\text{G.107})$$

By virtue of definitions G.4 and G.18, we can rewrite equation G.106 as

$$\tau_{\mathbf{g},\Psi}(\boldsymbol{\rho}_k^A, \boldsymbol{\rho}_k^{AB}, \boldsymbol{\rho}_k^-) = \sqrt{\frac{\epsilon_m \epsilon_n}{ab}} [A_g \nu(\alpha_g, \beta_g, \gamma_g, \delta_g) + B_g \omega(\alpha_g, \beta_g, \gamma_g, \delta_g)]. \quad (\text{G.108})$$

Finally, when we combine equations G.97, G.104 and G.108, we arrive at

$$\begin{aligned}\langle \mathbf{e}_{t;m}'' | \mathbf{f}_k \rangle &= \frac{l_k}{2A_k^+ k_{t;m}''} [\tau_{\mathbf{f},\Psi}(\boldsymbol{\rho}_k^{(1)}, \boldsymbol{\rho}_k^{(12)}, \boldsymbol{\rho}_k^+) + \tau_{\mathbf{f},\Psi}(\boldsymbol{\rho}_k^{(2)}, \boldsymbol{\rho}_k^{(2+)}, \boldsymbol{\rho}_k^+) + \\ &\tau_{\mathbf{f},\Psi}(\boldsymbol{\rho}_k^+, \boldsymbol{\rho}_k^{(+1)}, \boldsymbol{\rho}_k^+)] - \frac{l_k}{2A_k^- k_{t;m}''} [\tau_{\mathbf{g},\Psi}(\boldsymbol{\rho}_k^{(1)}, \boldsymbol{\rho}_k^{(12)}, \boldsymbol{\rho}_k^-) + \\ &\tau_{\mathbf{g},\Psi}(\boldsymbol{\rho}_k^-, \boldsymbol{\rho}_k^{(-1)}, \boldsymbol{\rho}_k^-) + \tau_{\mathbf{g},\Psi}(\boldsymbol{\rho}_k^{(2)}, \boldsymbol{\rho}_k^{(2-)}, \boldsymbol{\rho}_k^-)].\end{aligned}\quad (\text{G.109})$$

## G.5 Summary

In this appendix we have obtained the following interaction integrals between an RWG function and a waveguide mode. For the coupling between an RWG

function and a magnetic TM mode in the waveguide, we have

$$\begin{aligned}
\langle \mathbf{h}'_{t;m} | \mathbf{f}_k \rangle = & \frac{-l_k}{2A_k^+ k'_{t;m}} [\tau_{\mathbf{f},\Phi}(\boldsymbol{\rho}_k^{(1)}, \boldsymbol{\rho}_k^{(12)}, \boldsymbol{\rho}_k^+) + \tau_{\mathbf{f},\Phi}(\boldsymbol{\rho}_k^{(2)}, \boldsymbol{\rho}_k^{(2+)}, \boldsymbol{\rho}_k^+) + \\
& \tau_{\mathbf{f},\Phi}(\boldsymbol{\rho}_k^+, \boldsymbol{\rho}_k^{(+1)}, \boldsymbol{\rho}_k^+)] + \frac{l_k}{2A_k^- k'_{t;m}} [\tau_{\mathbf{g},\Phi}(\boldsymbol{\rho}_k^{(1)}, \boldsymbol{\rho}_k^{(12)}, \boldsymbol{\rho}_k^-) + \\
& \tau_{\mathbf{g},\Phi}(\boldsymbol{\rho}_k^-, \boldsymbol{\rho}_k^{(-1)}, \boldsymbol{\rho}_k^-) + \tau_{\mathbf{g},\Phi}(\boldsymbol{\rho}_k^{(2)}, \boldsymbol{\rho}_k^{(2-)}, \boldsymbol{\rho}_k^-)]. \quad (\text{G.110})
\end{aligned}$$

For the coupling between an RWG function and a magnetic TE mode in the waveguide, we have

$$\begin{aligned}
\langle \mathbf{h}''_{t;m} | \mathbf{f}_k \rangle = & -\frac{l_k}{A_k^+ k''_{t;m}} [\nu_{\mathbf{f},\Psi}(\boldsymbol{\rho}_k^{(1)}, \boldsymbol{\rho}_k^{(12)}) + \nu_{\mathbf{f},\Psi}(\boldsymbol{\rho}_k^{(2)}, \boldsymbol{\rho}_k^{(2+)}) + \\
& \nu_{\mathbf{f},\Psi}(\boldsymbol{\rho}_k^+, \boldsymbol{\rho}_k^{(+1)})] - \frac{l_k}{2A_k^+ k''_{t;m}} \nu_{\mathbf{g},\Psi}(\boldsymbol{\rho}_k^{(1)}, \boldsymbol{\rho}_k^{(12)}, \boldsymbol{\rho}_k^+) + \\
& -\frac{l_k}{A_k^- k''_{t;m}} [\nu_{\mathbf{f},\Psi}(\boldsymbol{\rho}_k^{(1)}, \boldsymbol{\rho}_k^{(12)}) + \nu_{\mathbf{f},\Psi}(\boldsymbol{\rho}_k^-, \boldsymbol{\rho}_k^{(-1)}) + \\
& \nu_{\mathbf{f},\Psi}(\boldsymbol{\rho}_k^{(2)}, \boldsymbol{\rho}_k^{(2-)})] + \frac{l_k}{2A_k^- k''_{t;m}} \nu_{\mathbf{h},\Psi}(\boldsymbol{\rho}_k^{(1)}, \boldsymbol{\rho}_k^{(12)}, \boldsymbol{\rho}_k^-). \quad (\text{G.111})
\end{aligned}$$

For the coupling between an RWG function and an electric TM mode in the waveguide, we have

$$\begin{aligned}
\langle \mathbf{e}'_{t;m} | \mathbf{f}_k \rangle = & -\frac{l_k}{A_k^+ k'_{t;m}} [\nu_{\mathbf{f},\Phi}(\boldsymbol{\rho}_k^{(1)}, \boldsymbol{\rho}_k^{(12)}) + \nu_{\mathbf{f},\Phi}(\boldsymbol{\rho}_k^{(2)}, \boldsymbol{\rho}_k^{(2+)}) + \\
& \nu_{\mathbf{f},\Phi}(\boldsymbol{\rho}_k^+, \boldsymbol{\rho}_k^{(+1)})] - \frac{l_k}{2A_k^+ k'_{t;m}} \nu_{\mathbf{g},\Phi}(\boldsymbol{\rho}_k^{(1)}, \boldsymbol{\rho}_k^{(12)}, \boldsymbol{\rho}_k^+) + \\
& -\frac{l_k}{A_k^- k'_{t;m}} [\nu_{\mathbf{f},\Phi}(\boldsymbol{\rho}_k^{(1)}, \boldsymbol{\rho}_k^{(12)}) + \nu_{\mathbf{f},\Phi}(\boldsymbol{\rho}_k^-, \boldsymbol{\rho}_k^{(-1)}) + \\
& \nu_{\mathbf{f},\Phi}(\boldsymbol{\rho}_k^{(2)}, \boldsymbol{\rho}_k^{(2-)})] + \frac{l_k}{2A_k^- k'_{t;m}} \nu_{\mathbf{h},\Phi}(\boldsymbol{\rho}_k^{(1)}, \boldsymbol{\rho}_k^{(12)}, \boldsymbol{\rho}_k^-). \quad (\text{G.112})
\end{aligned}$$

For the coupling between an RWG function and an electric TE mode in the waveguide, we have

$$\begin{aligned}
\langle \mathbf{e}''_{t;m} | \mathbf{f}_k \rangle = & \frac{l_k}{2A_k^+ k''_{t;m}} [\tau_{\mathbf{f},\Psi}(\boldsymbol{\rho}_k^{(1)}, \boldsymbol{\rho}_k^{(12)}, \boldsymbol{\rho}_k^+) + \tau_{\mathbf{f},\Psi}(\boldsymbol{\rho}_k^{(2)}, \boldsymbol{\rho}_k^{(2+)}, \boldsymbol{\rho}_k^+) + \\
& \tau_{\mathbf{f},\Psi}(\boldsymbol{\rho}_k^+, \boldsymbol{\rho}_k^{(+1)}, \boldsymbol{\rho}_k^+)] - \frac{l_k}{2A_k^- k''_{t;m}} [\tau_{\mathbf{g},\Psi}(\boldsymbol{\rho}_k^{(1)}, \boldsymbol{\rho}_k^{(12)}, \boldsymbol{\rho}_k^-) + \\
& \tau_{\mathbf{g},\Psi}(\boldsymbol{\rho}_k^-, \boldsymbol{\rho}_k^{(-1)}, \boldsymbol{\rho}_k^-) + \tau_{\mathbf{g},\Psi}(\boldsymbol{\rho}_k^{(2)}, \boldsymbol{\rho}_k^{(2-)}, \boldsymbol{\rho}_k^-)]. \quad (\text{G.113})
\end{aligned}$$





## Appendix H

# Interaction between an RWG and a Layered Space

In this appendix, we will evaluate<sup>1</sup> the inner product between the electric and magnetic modal fields for a layered space and an RWG function.

The electric and magnetic modal fields within the layered space are given by equations 2.174, 2.175, 2.181 and 2.182. The RWG function has been defined by equation 3.90 as [88]

$$\mathbf{f}_n(\boldsymbol{\rho}) = \begin{cases} \frac{l_n^+}{2A_n^+}(\boldsymbol{\rho} - \boldsymbol{\rho}_n^+) & \text{if } \boldsymbol{\rho} \in T_n^+, \\ \frac{l_n^-}{2A_n^-}(\boldsymbol{\rho}_n^- - \boldsymbol{\rho}) & \text{if } \boldsymbol{\rho} \in T_n^-, \\ \mathbf{0} & \text{otherwise.} \end{cases} \quad (\text{H.1})$$

See section 3.7.5 for a detailed explanation of the RWG function. See figure H.1 for a graphical representation of the domain, vectors and scalars used in the RWG function. If we use the expressions for the electric and magnetic modal fields within the layered space, i.e., equations 2.174, 2.175, 2.181 and 2.182, we evaluate the following four possible combinations of inner products

$$\langle \mathbf{e}'_t(\mathbf{k}_t) | \mathbf{f}_n \rangle = \frac{j}{2\pi} \hat{\mathbf{k}} \cdot \hat{\mathbf{f}}_n(\mathbf{k}_t), \quad \langle \mathbf{e}''_t(\mathbf{k}_t) | \mathbf{f}_n \rangle = \frac{j}{2\pi} \hat{\boldsymbol{\alpha}} \cdot \hat{\mathbf{f}}_n(\mathbf{k}_t), \quad (\text{H.2})$$

$$\langle \mathbf{h}'_t(\mathbf{k}_t) | \mathbf{f}_n \rangle = -\frac{j}{2\pi} \hat{\boldsymbol{\alpha}} \cdot \hat{\mathbf{f}}_n(\mathbf{k}_t), \quad \langle \mathbf{h}''_t(\mathbf{k}_t) | \mathbf{f}_n \rangle = \frac{j}{2\pi} \hat{\mathbf{k}} \cdot \hat{\mathbf{f}}_n(\mathbf{k}_t), \quad (\text{H.3})$$

where  $\hat{\boldsymbol{\alpha}} = \hat{\mathbf{k}} \times \hat{\mathbf{z}}$ , and in which the so-called spectrum of an RWG function is given by

$$\hat{\mathbf{f}}_n(\mathbf{k}_t) = \langle \exp(-j\mathbf{k}_t \cdot \boldsymbol{\rho}) | \mathbf{f}_n \rangle. \quad (\text{H.4})$$

---

<sup>1</sup>Computation of the projection matrix between an RWG function and a layered space mode.

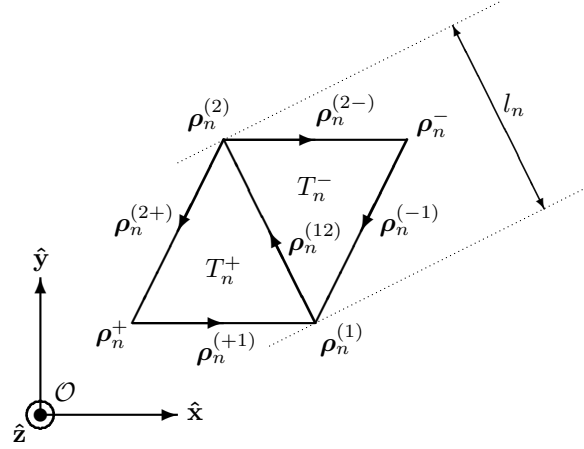


Figure H.1: Domain, vectors and scalars used in the RWG function.

Therefore, it suffices to evaluate  $\hat{\mathbf{f}}_n(\mathbf{k}_t)$ . If we substitute the expression for the RWG function, i.e., equation H.1, in equation H.4, we obtain

$$\hat{\mathbf{f}}_n(\mathbf{k}_t) = \int_{T_n^+} \frac{l_n}{2A_n^+} (\boldsymbol{\rho} - \boldsymbol{\rho}_n^+) \exp(-j\mathbf{k}_t \cdot \boldsymbol{\rho}) dA + \int_{T_n^-} \frac{l_n}{2A_n^-} (\boldsymbol{\rho}_n^- - \boldsymbol{\rho}) \exp(-j\mathbf{k}_t \cdot \boldsymbol{\rho}) dA, \quad (\text{H.5})$$

which can be rewritten as

$$\hat{\mathbf{f}}_n(\mathbf{k}_t) = \frac{l_n}{2A_n^+} \{ \mathbf{g}_n^+(\mathbf{k}_t) - \boldsymbol{\rho}_n^+ h_n^+(\mathbf{k}_t) \} + \frac{l_n}{2A_n^-} \{ \boldsymbol{\rho}_n^- h_n^-(\mathbf{k}_t) - \mathbf{g}_n^-(\mathbf{k}_t) \}, \quad (\text{H.6})$$

in which

$$\mathbf{g}_n^+(\mathbf{k}_t) = \int_{T_n^+} \boldsymbol{\rho} \exp(-j\mathbf{k}_t \cdot \boldsymbol{\rho}) dA, \quad \mathbf{g}_n^-(\mathbf{k}_t) = \int_{T_n^-} \boldsymbol{\rho} \exp(-j\mathbf{k}_t \cdot \boldsymbol{\rho}) dA, \quad (\text{H.7})$$

$$h_n^+(\mathbf{k}_t) = \int_{T_n^+} \exp(-j\mathbf{k}_t \cdot \boldsymbol{\rho}) dA, \quad h_n^-(\mathbf{k}_t) = \int_{T_n^-} \exp(-j\mathbf{k}_t \cdot \boldsymbol{\rho}) dA. \quad (\text{H.8})$$

Let  $\nabla_k$  be the transverse gradient operator with respect to the vector  $\mathbf{k}_t$ . By using the chain rule for partial differentiation with respect to the vector  $\mathbf{k}_t$ , we can rewrite the expression for  $\mathbf{g}_n^+(\mathbf{k}_t)$  as

$$\mathbf{g}_n^+(\mathbf{k}_t) = \int_{T_n^+} \boldsymbol{\rho} \exp(-j\mathbf{k}_t \cdot \boldsymbol{\rho}) dA = \int_{T_n^+} j\nabla_k \exp(-j\mathbf{k}_t \cdot \boldsymbol{\rho}) dA, \quad (\text{H.9})$$

which reduces to

$$\mathbf{g}_n^+(\mathbf{k}_t) = j\nabla_k \int_{T_n^+} \exp(-j\mathbf{k}_t \cdot \boldsymbol{\rho}) dA = j\nabla_k h_n^+(\mathbf{k}_t). \quad (\text{H.10})$$

For  $\mathbf{g}_n^-(\mathbf{k}_t)$ , we find a similar relation

$$\mathbf{g}_n^-(\mathbf{k}_t) = \mathbf{j} \nabla_k h_n^-(\mathbf{k}_t). \quad (\text{H.11})$$

We can now rewrite equation H.6 as

$$\hat{\mathbf{f}}_n(\mathbf{k}_t) = \frac{l_n}{2A_n^+} \{\mathbf{j} \nabla_k - \boldsymbol{\rho}_n^+\} h_n^+(\mathbf{k}_t) + \frac{l_n}{2A_n^-} \{\boldsymbol{\rho}_n^- - \mathbf{j} \nabla_k\} h_n^-(\mathbf{k}_t). \quad (\text{H.12})$$

At this point, we are left with the calculation of  $h_n^+(\mathbf{k}_t)$  and  $h_n^-(\mathbf{k}_t)$ . First, note that<sup>2</sup>

$$\begin{aligned} (\nabla_t \cdot \nabla_t + k_t^2) \exp(-\mathbf{j} \mathbf{k}_t \cdot \boldsymbol{\rho}) &= 0 \Leftrightarrow \\ \exp(-\mathbf{j} \mathbf{k}_t \cdot \boldsymbol{\rho}) &= -\frac{1}{k_t^2} \nabla_t \cdot \nabla_t \exp(-\mathbf{j} \mathbf{k}_t \cdot \boldsymbol{\rho}). \end{aligned} \quad (\text{H.13})$$

If we use this identity, we can rewrite  $h_n^+(\mathbf{k}_t)$  as

$$h_n^+(\mathbf{k}_t) = \int_{T_n^+} \exp(-\mathbf{j} \mathbf{k}_t \cdot \boldsymbol{\rho}) dA = -\frac{1}{k_t^2} \int_{T_n^+} \nabla_t \cdot \nabla_t \exp(-\mathbf{j} \mathbf{k}_t \cdot \boldsymbol{\rho}) dA. \quad (\text{H.14})$$

Applying Gauss' divergence theorem, and evaluating  $\nabla_t \exp(-\mathbf{j} \mathbf{k}_t \cdot \boldsymbol{\rho})$ , results in

$$\begin{aligned} h_n^+(\mathbf{k}_t) &= -\frac{1}{k_t^2} \oint_{\partial T_n^+} \nabla_t \exp(-\mathbf{j} \mathbf{k}_t \cdot \boldsymbol{\rho}) \cdot \hat{\boldsymbol{\nu}} d\ell \\ &= \frac{\mathbf{j}}{k_t^2} \oint_{\partial T_n^+} \exp(-\mathbf{j} \mathbf{k}_t \cdot \boldsymbol{\rho}) (\mathbf{k}_t \cdot \hat{\boldsymbol{\nu}}) d\ell. \end{aligned} \quad (\text{H.15})$$

We further define the following tangential  $\hat{\boldsymbol{\tau}}_n^{(AB)}$  and normal  $\hat{\boldsymbol{\nu}}_n^{(AB)}$  unit-length vectors along the contour of the triangle  $T_n^+$

$$\begin{aligned} \hat{\boldsymbol{\tau}}_n^{(12)} &= \boldsymbol{\rho}_n^{(12)} / \|\boldsymbol{\rho}_n^{(12)}\|, & \hat{\boldsymbol{\nu}}_n^{(12)} &= \hat{\boldsymbol{\tau}}_n^{(12)} \times \hat{\mathbf{z}}, \\ \hat{\boldsymbol{\tau}}_n^{(2+)} &= \boldsymbol{\rho}_n^{(2+)} / \|\boldsymbol{\rho}_n^{(2+)}\|, & \hat{\boldsymbol{\nu}}_n^{(2+)} &= \hat{\boldsymbol{\tau}}_n^{(2+)} \times \hat{\mathbf{z}}, \\ \hat{\boldsymbol{\tau}}_n^{(+1)} &= \boldsymbol{\rho}_n^{(+1)} / \|\boldsymbol{\rho}_n^{(+1)}\|, & \hat{\boldsymbol{\nu}}_n^{(+1)} &= \hat{\boldsymbol{\tau}}_n^{(+1)} \times \hat{\mathbf{z}}. \end{aligned} \quad (\text{H.16})$$

If we split the contour integrals in equation H.15 into separate corresponding straight-line integrals, we can rewrite  $h_n^+(\mathbf{k}_t)$  as

$$\begin{aligned} h_n^+(\mathbf{k}_t) &= \mathbf{j} \frac{\mathbf{k}_t \cdot \hat{\boldsymbol{\nu}}_n^{(12)}}{k_t^2} \int_{\boldsymbol{\rho}_n^{(1)}}^{\boldsymbol{\rho}_n^{(2)}} \exp(-\mathbf{j} \mathbf{k}_t \cdot \boldsymbol{\rho}) d\ell + \\ &\quad \mathbf{j} \frac{\mathbf{k}_t \cdot \hat{\boldsymbol{\nu}}_n^{(2+)}}{k_t^2} \int_{\boldsymbol{\rho}_n^{(2)}}^{\boldsymbol{\rho}_n^{(+)}} \exp(-\mathbf{j} \mathbf{k}_t \cdot \boldsymbol{\rho}) d\ell + \\ &\quad \mathbf{j} \frac{\mathbf{k}_t \cdot \hat{\boldsymbol{\nu}}_n^{(+1)}}{k_t^2} \int_{\boldsymbol{\rho}_n^{(+)}}^{\boldsymbol{\rho}_n^{(1)}} \exp(-\mathbf{j} \mathbf{k}_t \cdot \boldsymbol{\rho}) d\ell. \end{aligned} \quad (\text{H.17})$$

<sup>2</sup>A special word of thanks goes to prof.dr. A.G. Tjihuis for providing me with this clue.

We can cast each line integral in the following form

$$\int_{\rho_A}^{\rho_B} f d\ell = \int_0^\ell f(\mathbf{h}(\ell)) d\ell = \int_0^1 f(\mathbf{g}(t)) \|\mathbf{g}'(t)\| dt, \quad f = \exp(-j\mathbf{k}_t \cdot \boldsymbol{\rho}), \quad (\text{H.18})$$

where  $\mathbf{h}(\ell)$  represents the arc-length curve. Subsequently, we choose the following parametrization for  $\mathbf{g}(t)$

$$\mathbf{g}(t) = \boldsymbol{\rho}_A + \boldsymbol{\rho}_{AB}t, \quad \boldsymbol{\rho}_{AB} = \boldsymbol{\rho}_B - \boldsymbol{\rho}_A, \quad t \in [0, 1], \quad (\text{H.19})$$

and we write equation H.18 as

$$\begin{aligned} \int_{\rho_A}^{\rho_B} f d\ell &= \int_0^1 \exp(-j\mathbf{k}_t \cdot [\boldsymbol{\rho}_A + \boldsymbol{\rho}_{AB}t]) \|\boldsymbol{\rho}_{AB}\| dt \\ &= \|\boldsymbol{\rho}_{AB}\| \exp\left(-\frac{1}{2}j\mathbf{k}_t \cdot [\boldsymbol{\rho}_A + \boldsymbol{\rho}_B]\right) \text{sinc}\left(-\frac{1}{2}\mathbf{k}_t \cdot \boldsymbol{\rho}_{AB}\right). \end{aligned} \quad (\text{H.20})$$

With the aid of this result, we can rewrite  $h_n^+(\mathbf{k}_t)$  as

$$\begin{aligned} h_n^+(\mathbf{k}_t) &= j\|\boldsymbol{\rho}_n^{(12)}\| \xi(\mathbf{k}_t, \boldsymbol{\rho}_n^{(1)}, \boldsymbol{\rho}_n^{(2)}) + \\ &\quad j\|\boldsymbol{\rho}_n^{(2+)}\| \xi(\mathbf{k}_t, \boldsymbol{\rho}_n^{(2)}, \boldsymbol{\rho}_n^+) + \\ &\quad j\|\boldsymbol{\rho}_n^{(+1)}\| \xi(\mathbf{k}_t, \boldsymbol{\rho}_n^+, \boldsymbol{\rho}_n^{(1)}), \end{aligned} \quad (\text{H.21})$$

in which

$$\xi(\mathbf{k}_t, \boldsymbol{\rho}_A, \boldsymbol{\rho}_B) = \frac{\mathbf{k}_t \cdot \hat{\boldsymbol{\nu}}_{AB}}{k_t^2} \exp\left(-\frac{1}{2}j\mathbf{k}_t \cdot [\boldsymbol{\rho}_A + \boldsymbol{\rho}_B]\right) \text{sinc}\left(-\frac{1}{2}\mathbf{k}_t \cdot \boldsymbol{\rho}_{AB}\right). \quad (\text{H.22})$$

In a similar way, we define the following tangential  $\hat{\boldsymbol{\tau}}_n^{(AB)}$  and normal  $\hat{\boldsymbol{\nu}}_n^{(AB)}$  unit-length vectors along the contour of the triangle  $T_n^-$

$$\begin{aligned} \hat{\boldsymbol{\tau}}_n^{(12)} &= \boldsymbol{\rho}_n^{(12)} / \|\boldsymbol{\rho}_n^{(12)}\|, & \hat{\boldsymbol{\nu}}_n^{(12)} &= \hat{\boldsymbol{\tau}}_n^{(12)} \times \hat{\mathbf{z}}, \\ \hat{\boldsymbol{\tau}}_n^{(-1)} &= \boldsymbol{\rho}_n^{(-1)} / \|\boldsymbol{\rho}_n^{(-1)}\|, & \hat{\boldsymbol{\nu}}_n^{(-1)} &= \hat{\boldsymbol{\tau}}_n^{(-1)} \times \hat{\mathbf{z}}, \\ \hat{\boldsymbol{\tau}}_n^{(2-)} &= \boldsymbol{\rho}_n^{(2-)} / \|\boldsymbol{\rho}_n^{(2-)}\|, & \hat{\boldsymbol{\nu}}_n^{(2-)} &= \hat{\boldsymbol{\tau}}_n^{(2-)} \times \hat{\mathbf{z}}. \end{aligned} \quad (\text{H.23})$$

Now, we can write  $h_n^-(\mathbf{k}_t)$  as

$$\begin{aligned} h_n^-(\mathbf{k}_t) &= -j\|\boldsymbol{\rho}_n^{(12)}\| \xi(\mathbf{k}_t, \boldsymbol{\rho}_n^{(1)}, \boldsymbol{\rho}_n^{(2)}) + \\ &\quad -j\|\boldsymbol{\rho}_n^{(-1)}\| \xi(\mathbf{k}_t, \boldsymbol{\rho}_n^-, \boldsymbol{\rho}_n^{(1)}) + \\ &\quad -j\|\boldsymbol{\rho}_n^{(2-)}\| \xi(\mathbf{k}_t, \boldsymbol{\rho}_n^{(2)}, \boldsymbol{\rho}_n^-). \end{aligned} \quad (\text{H.24})$$

Further, we define

$$\zeta(\mathbf{k}_t, \boldsymbol{\rho}_A, \boldsymbol{\rho}_B) \equiv \nabla_k \xi(\mathbf{k}_t, \boldsymbol{\rho}_A, \boldsymbol{\rho}_B). \quad (\text{H.25})$$

By evaluating the gradient operator  $\nabla_{\mathbf{k}}$ , we can rewrite  $\zeta(\mathbf{k}_t, \boldsymbol{\rho}_A, \boldsymbol{\rho}_B)$  as

$$\begin{aligned} \zeta(\mathbf{k}_t, \boldsymbol{\rho}_A, \boldsymbol{\rho}_B) = & \frac{1}{k_t^2} \exp\left(-\frac{1}{2}j\mathbf{k}_t \cdot [\boldsymbol{\rho}_A + \boldsymbol{\rho}_B]\right) \left\{ \text{sinc}\left(-\frac{1}{2}\mathbf{k}_t \cdot \boldsymbol{\rho}_{AB}\right) \right. \\ & \left[ -\frac{2\mathbf{k}_t}{k_t^2}(\mathbf{k}_t \cdot \hat{\boldsymbol{\nu}}_{AB}) + \hat{\boldsymbol{\nu}}_{AB} - \frac{1}{2}j(\mathbf{k}_t \cdot \hat{\boldsymbol{\nu}}_{AB})(\boldsymbol{\rho}_A + \boldsymbol{\rho}_B) \right] - \\ & \left. \frac{1}{2}\boldsymbol{\rho}_{AB}(\mathbf{k}_t \cdot \hat{\boldsymbol{\nu}}_{AB})\text{sinc}'\left(-\frac{1}{2}\mathbf{k}_t \cdot \boldsymbol{\rho}_{AB}\right) \right\}. \end{aligned} \quad (\text{H.26})$$

If we use equation H.26, we can rewrite  $\mathbf{g}_n^+(\mathbf{k}_t)$  as

$$\begin{aligned} \mathbf{g}_n^+(\mathbf{k}_t) = & -\|\boldsymbol{\rho}_n^{(12)}\|\zeta(\mathbf{k}_t, \boldsymbol{\rho}_n^{(1)}, \boldsymbol{\rho}_n^{(2)}) + \\ & -\|\boldsymbol{\rho}_n^{(2+)}\|\zeta(\mathbf{k}_t, \boldsymbol{\rho}_n^{(2)}, \boldsymbol{\rho}_n^+) + \\ & -\|\boldsymbol{\rho}_n^{(+1)}\|\zeta(\mathbf{k}_t, \boldsymbol{\rho}_n^+, \boldsymbol{\rho}_n^{(1)}), \end{aligned} \quad (\text{H.27})$$

and  $\mathbf{g}_n^-(\mathbf{k}_t)$  as

$$\begin{aligned} \mathbf{g}_n^-(\mathbf{k}_t) = & \|\boldsymbol{\rho}_n^{(12)}\|\zeta(\mathbf{k}_t, \boldsymbol{\rho}_n^{(1)}, \boldsymbol{\rho}_n^{(2)}) + \\ & \|\boldsymbol{\rho}_n^{(-1)}\|\zeta(\mathbf{k}_t, \boldsymbol{\rho}_n^-, \boldsymbol{\rho}_n^1) + \\ & \|\boldsymbol{\rho}_n^{(2-)}\|\zeta(\mathbf{k}_t, \boldsymbol{\rho}_n^{(2)}, \boldsymbol{\rho}_n^-). \end{aligned} \quad (\text{H.28})$$

Finally, we can express the spectrum of an RWG function, as defined in equation H.4, as

$$\begin{aligned} \hat{\mathbf{f}}_n(\mathbf{k}_t) = & -\frac{l_n}{2A_n^+} \left\{ \|\boldsymbol{\rho}_n^{(12)}\|\zeta(\mathbf{k}_t, \boldsymbol{\rho}_n^{(1)}, \boldsymbol{\rho}_n^{(2)}) + \|\boldsymbol{\rho}_n^{(2+)}\|\zeta(\mathbf{k}_t, \boldsymbol{\rho}_n^{(2)}, \boldsymbol{\rho}_n^+) + \right. \\ & \|\boldsymbol{\rho}_n^{(+1)}\|\zeta(\mathbf{k}_t, \boldsymbol{\rho}_n^+, \boldsymbol{\rho}_n^{(1)}) + j\boldsymbol{\rho}_n^+ \|\boldsymbol{\rho}_n^{(12)}\|\xi(\mathbf{k}_t, \boldsymbol{\rho}_n^{(1)}, \boldsymbol{\rho}_n^{(2)}) + \\ & \left. j\boldsymbol{\rho}_n^+ \|\boldsymbol{\rho}_n^{(2+)}\|\xi(\mathbf{k}_t, \boldsymbol{\rho}_n^{(2)}, \boldsymbol{\rho}_n^+) + j\boldsymbol{\rho}_n^+ \|\boldsymbol{\rho}_n^{(+1)}\|\xi(\mathbf{k}_t, \boldsymbol{\rho}_n^+, \boldsymbol{\rho}_n^{(1)}) \right\} + \\ & -\frac{l_n}{2A_n^-} \left\{ \|\boldsymbol{\rho}_n^{(12)}\|\zeta(\mathbf{k}_t, \boldsymbol{\rho}_n^{(1)}, \boldsymbol{\rho}_n^{(2)}) + \|\boldsymbol{\rho}_n^{(-1)}\|\zeta(\mathbf{k}_t, \boldsymbol{\rho}_n^-, \boldsymbol{\rho}_n^1) + \right. \\ & \|\boldsymbol{\rho}_n^{(2-)}\|\zeta(\mathbf{k}_t, \boldsymbol{\rho}_n^{(2)}, \boldsymbol{\rho}_n^-) + j\boldsymbol{\rho}_n^- \|\boldsymbol{\rho}_n^{(12)}\|\xi(\mathbf{k}_t, \boldsymbol{\rho}_n^{(1)}, \boldsymbol{\rho}_n^{(2)}) + \\ & \left. j\boldsymbol{\rho}_n^- \|\boldsymbol{\rho}_n^{(-1)}\|\xi(\mathbf{k}_t, \boldsymbol{\rho}_n^-, \boldsymbol{\rho}_n^1) + j\boldsymbol{\rho}_n^- \|\boldsymbol{\rho}_n^{(2-)}\|\xi(\mathbf{k}_t, \boldsymbol{\rho}_n^{(2)}, \boldsymbol{\rho}_n^-) \right\}. \end{aligned} \quad (\text{H.29})$$



## Appendix I

# Interaction between a Thin Strip and a Layered Space

In this appendix, we evaluate<sup>1</sup> the inner product between the electric and magnetic modal fields for a layered space and a thin-strip function. The thin-strip function serves as an approximate modal function where the expected electromagnetic behavior (modal sine functions in the length direction and an edge singularity in the width direction) on the thin strip is modeled in an explicit way.

The electric and magnetic modal fields within the layered space are given by equations 2.174, 2.175, 2.181 and 2.182. The thin-strip function has been defined by equation 3.79 as

$$\mathbf{f}_n(\boldsymbol{\rho}) = \begin{cases} \hat{\mathbf{p}}_n \frac{1}{\sqrt{1-\left(\frac{2y'}{w_n}\right)^2}} \sin\left(\frac{\pi m_n}{l_n} \left[x' + \frac{l_n}{2}\right]\right) & \text{if } \boldsymbol{\rho} \in S_n, \\ \mathbf{0} & \text{otherwise.} \end{cases} \quad (\text{I.1})$$

See section 3.7.2 for a detailed explanation of the thin-strip function. See figure I.1 for a graphical representation of the domain, vectors and scalars used in the thin strip function. From the expressions for the electric and magnetic modal fields within the layered space, i.e. equations 2.174, 2.175, 2.181 and 2.182, we can distinguish the following four possible combinations of inner products

$$\langle \mathbf{e}'_t(\mathbf{k}_t) | \mathbf{f}_n \rangle = \frac{j}{2\pi} \hat{\mathbf{k}} \cdot \hat{\mathbf{f}}_n(\mathbf{k}_t), \quad \langle \mathbf{e}''_t(\mathbf{k}_t) | \mathbf{f}_n \rangle = \frac{j}{2\pi} \hat{\boldsymbol{\alpha}} \cdot \hat{\mathbf{f}}_n(\mathbf{k}_t), \quad (\text{I.2})$$

$$\langle \mathbf{h}'_t(\mathbf{k}_t) | \mathbf{f}_n \rangle = -\frac{j}{2\pi} \hat{\boldsymbol{\alpha}} \cdot \hat{\mathbf{f}}_n(\mathbf{k}_t), \quad \langle \mathbf{h}''_t(\mathbf{k}_t) | \mathbf{f}_n \rangle = \frac{j}{2\pi} \hat{\mathbf{k}} \cdot \hat{\mathbf{f}}_n(\mathbf{k}_t), \quad (\text{I.3})$$

in which the so-called spectrum of a thin strip function is given by

$$\hat{\mathbf{f}}_n(\mathbf{k}_t) = \langle \exp(-j\mathbf{k}_t \cdot \boldsymbol{\rho}) | \mathbf{f}_n \rangle. \quad (\text{I.4})$$

---

<sup>1</sup>Computation of the projection matrix between a thin strip function and a layered space mode.



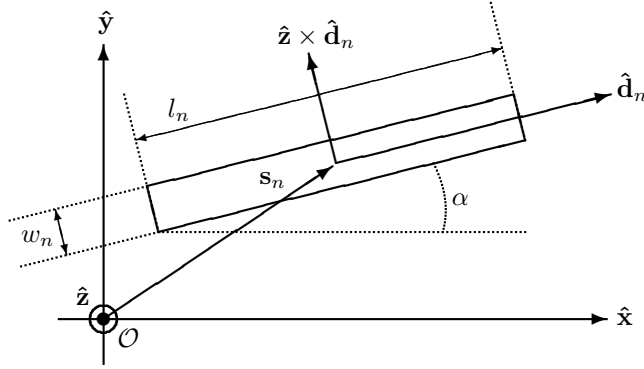


Figure I.1: Domain, vectors and scalars used in the thin strip function.

Therefore, it suffices to evaluate  $\hat{\mathbf{f}}_n(\mathbf{k}_t)$ . After substituting the expression for the thin strip function, equation I.1, in equation I.4, we arrive at

$$\hat{\mathbf{f}}_n(\mathbf{k}_t) = \hat{\mathbf{p}}_n \exp(j\mathbf{k}_t \cdot \mathbf{s}_n + \frac{1}{2}jl_n k'_x) \frac{1}{4} w_n l_n m_n \pi^{2j} j^{m_n+1} J_0\left(\frac{1}{2}w_n k'_y\right) \frac{\sin\left(\frac{1}{2}[k'_x l_n + \pi m_n]\right)}{\left[\left(\frac{1}{2}k'_x l_n\right)^2 - \left(\frac{1}{2}\pi m_n\right)^2\right]}, \quad (\text{I.5})$$

in which

$$k'_x = \mathbf{k}_t \cdot \hat{\mathbf{d}}_n, \quad k'_y = \mathbf{k}_t \cdot (\hat{\mathbf{z}} \times \hat{\mathbf{d}}_n), \quad (\text{I.6})$$

and in which  $J_0(z)$  denotes the zero-order Bessel function of the first kind [2, chapter 9].

## Appendix J

# Interaction between a Patch and a Layered Space

In this appendix, we evaluate<sup>1</sup> the inner product between the electric and magnetic modal fields for a layered space and a patch function. The patch function serves as an approximate modal function where the expected electromagnetic behavior on the patch is modeled in an explicit way [1].

The electric and magnetic modal fields within the layered space are given by equations 2.174, 2.175, 2.181 and 2.182. The patch function has been defined in equation 3.82 as

$$\mathbf{f}_n(\boldsymbol{\rho}) = \begin{cases} \hat{\mathbf{u}}_n C_{p_n}(x', l_n) D_{q_n}(y', w_n) & \text{if } \boldsymbol{\rho} \in S_n \text{ and } \mathbf{f}_n \text{ is } \hat{\mathbf{u}}_n\text{-directed,} \\ \hat{\mathbf{v}}_n D_{q_n}(x', l_n) C_{p_n}(y', w_n) & \text{if } \boldsymbol{\rho} \in S_n \text{ and } \mathbf{f}_n \text{ is } \hat{\mathbf{v}}_n\text{-directed,} \\ \mathbf{0} & \text{otherwise.} \end{cases} \quad (\text{J.1})$$

See section 3.7.3 for a detailed discussion of the patch function. See figure J.1 for a graphical representation of the domain, vectors and scalars used in the patch function. From the expressions for the electric and magnetic modal fields within the layered space, i.e., equations 2.174, 2.175, 2.181 and 2.182, we identify the following four possible combinations of inner products

$$\langle \mathbf{e}'_t(\mathbf{k}_t) | \mathbf{f}_n \rangle = \frac{j}{2\pi} \hat{\mathbf{k}} \cdot \hat{\mathbf{f}}_n(\mathbf{k}_t), \quad \langle \mathbf{e}''_t(\mathbf{k}_t) | \mathbf{f}_n \rangle = \frac{j}{2\pi} \hat{\boldsymbol{\alpha}} \cdot \hat{\mathbf{f}}_n(\mathbf{k}_t), \quad (\text{J.2})$$

$$\langle \mathbf{h}'_t(\mathbf{k}_t) | \mathbf{f}_n \rangle = -\frac{j}{2\pi} \hat{\boldsymbol{\alpha}} \cdot \hat{\mathbf{f}}_n(\mathbf{k}_t), \quad \langle \mathbf{h}''_t(\mathbf{k}_t) | \mathbf{f}_n \rangle = \frac{j}{2\pi} \hat{\mathbf{k}} \cdot \hat{\mathbf{f}}_n(\mathbf{k}_t), \quad (\text{J.3})$$

in which the so-called spectrum of a patch function is given by

$$\hat{\mathbf{f}}_n(\mathbf{k}_t) = \langle \exp(-j\mathbf{k}_t \cdot \boldsymbol{\rho}) | \mathbf{f}_n \rangle. \quad (\text{J.4})$$

---

<sup>1</sup>Computation of the projection matrix between a patch function and a layered space mode.

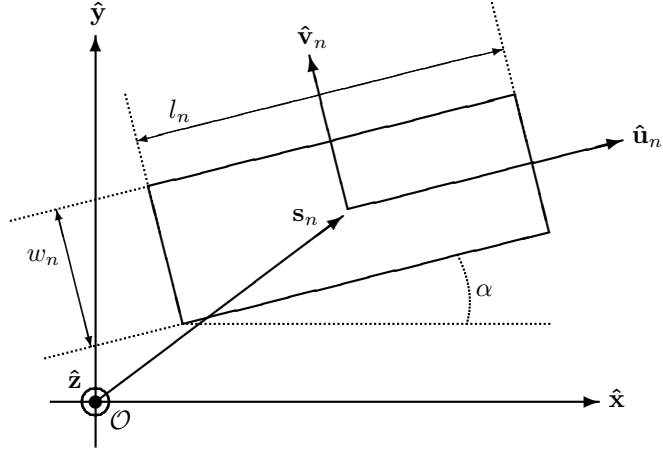


Figure J.1: Domain, vectors and scalars used in the patch function.

Therefore, it suffices to evaluate  $\hat{\mathbf{f}}_n(\mathbf{k}_t)$ . Upon substituting the expression for the patch function, i.e., equation J.1, in equation J.4, we arrive at

$$\hat{\mathbf{f}}_n(\mathbf{k}_t) = \phi_n \begin{cases} \hat{\mathbf{u}}_n \hat{C}_{p_n}(k'_x, l_n) \hat{D}_{q_n}(k'_y, w_n) & \text{if } \mathbf{f}_n \text{ is } \hat{\mathbf{u}}_n\text{-directed,} \\ \hat{\mathbf{v}}_n \hat{D}_{q_n}(k'_x, l_n) \hat{C}_{p_n}(k'_y, w_n) & \text{if } \mathbf{f}_n \text{ is } \hat{\mathbf{v}}_n\text{-directed,} \end{cases} \quad (\text{J.5})$$

in which

$$k'_x = \mathbf{k}_t \cdot \hat{\mathbf{u}}_n, \quad k'_y = \mathbf{k}_t \cdot \hat{\mathbf{v}}_n, \quad \phi_n = \exp\left(\frac{1}{2}j\mathbf{k}_t \cdot [l_n \hat{\mathbf{u}}_n + w_n \hat{\mathbf{v}}_n + 2\mathbf{s}_n]\right), \quad (\text{J.6})$$

and in which the Fourier transforms  $\hat{C}_m(k, w)$  of  $C_m(x, w)$  and  $\hat{D}_m(k, w)$  of  $D_m(x, w)$  are given by

$$\hat{C}_m(k, w) = \frac{1}{k} J_{m+1}\left(\frac{k w}{2}\right), \quad \hat{D}_m(k, w) = J_m\left(\frac{k w}{2}\right). \quad (\text{J.7})$$

$J_m(z)$  denotes the  $m$ -order Bessel function of the first kind [2, chapter 9]. Finally, note that

$$\lim_{k \rightarrow 0} \hat{C}_m(k, w) = \frac{w}{4}. \quad (\text{J.8})$$

## Appendix K

# Floquet Analysis of Periodic Structures

In this appendix we describe how the spectral integrals involved in the computation of the linear operator  $L$  are converted into summations, if the structure is periodic, and if the incident field is a plane wave. The analysis of the infinite periodic structure is essentially reduced to that of the central unit cell [112, chapter 7].

In section 3.5 we have defined a set of expansion functions that are contained within the central unit cell. The extension of these functions to the entire periodic structure, however, is not unique. We will propose two different choices for this extension, derive corresponding spectral representations, and examine the properties that are relevant in the computations.

First we consider an array of unit cells, regularly arranged in a so-called direct (or Bravais) lattice defined by the basis vectors  $\mathbf{d}_1$  and  $\mathbf{d}_2$ . Without loss of generality, we choose the  $x$ -axis to be in parallel with  $\mathbf{d}_1$ . A graphical representation of the direct lattice is given in figure K.1.

We assume that the periodic structure is excited by an incident plane wave  $\mathbf{E}_t^{\text{inc}}(\mathbf{r})$ , expressed as

$$\begin{aligned}\mathbf{E}_t^{\text{inc}}(\mathbf{r}) &= \mathbf{E}_{t;0}^{\text{inc}} \exp(-j\mathbf{k}^{\text{inc}} \cdot \mathbf{r}) \\ &= \mathbf{E}_{t;0}^{\text{inc}} \exp(-j\mathbf{k}_t^{\text{inc}} \cdot \boldsymbol{\rho}) \exp(-jk_z z) \\ &= \mathbf{E}_t^{\text{inc}}(\boldsymbol{\rho}) \exp(-jk_z z).\end{aligned}\tag{K.1}$$

Then we define a so-called translation operator  $T_{m,n}$  as

$$T_{m,n}\mathbf{f}(\boldsymbol{\rho}) \equiv \mathbf{f}(\boldsymbol{\rho} + m\mathbf{d}_1 + n\mathbf{d}_2), \quad m, n = 0, \pm 1, \pm 2, \dots\tag{K.2}$$

Subsequently, if an arbitrary vector field  $\mathbf{f}(\boldsymbol{\rho})$  is of the form  $\mathbf{g}(\boldsymbol{\rho}) \exp(-j\mathbf{k}_t^{\text{inc}} \cdot \boldsymbol{\rho})$  where  $T_{m,n}\mathbf{g}(\boldsymbol{\rho}) = \mathbf{g}(\boldsymbol{\rho})$ , then  $\mathbf{f}(\boldsymbol{\rho})$  satisfies

$$T_{m,n}\mathbf{f}(\boldsymbol{\rho}) \equiv \mathbf{f}(\boldsymbol{\rho} + m\mathbf{d}_1 + n\mathbf{d}_2) = \mathbf{f}(\boldsymbol{\rho}) \exp(-j\mathbf{k}_t^{\text{inc}} \cdot [m\mathbf{d}_1 + n\mathbf{d}_2]),\tag{K.3}$$

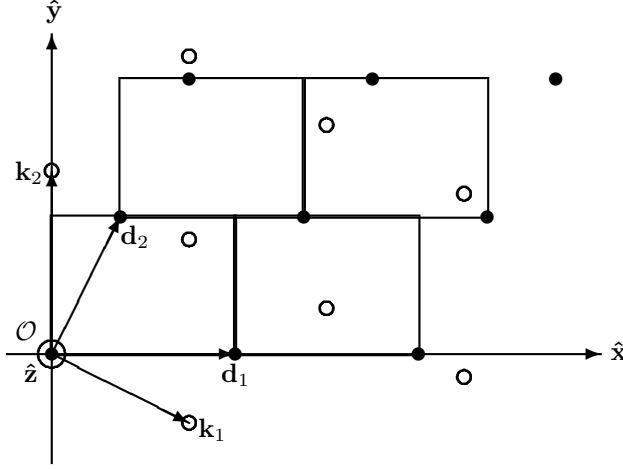


Figure K.1: Direct Bravais lattice (closed circles) and reciprocal Floquet lattice (open circles).

the so-called pseudo-periodicity relation [112, equation 7.4]. It is well known from the general theory of wave propagation in the presence of a periodic structure (a periodic  $\mathbf{g}(\boldsymbol{\rho})$ ), that the fields excited by a plane wave must have the same periodicity as the structure, apart from a phase shift associated to the incident field. This means that the field distributions must satisfy the aforementioned pseudo-periodicity relation. To see that this is true, we apply the translation operator to the incident plane wave. Doing this results in

$$T_{m,n}\mathbf{E}^{\text{inc}}(\boldsymbol{\rho}) = \mathbf{E}^{\text{inc}}(\boldsymbol{\rho}) \exp(-j\mathbf{k}_t^{\text{inc}} \cdot [m\mathbf{d}_1 + n\mathbf{d}_2]). \quad (\text{K.4})$$

Furthermore, since the structure is invariant under the translation expressed in  $T_{m,n}$ , any induced current distribution  $\mathbf{J}(\boldsymbol{\rho})$  must also satisfy the pseudo-periodicity relation, i.e.,

$$T_{m,n}\mathbf{J}(\boldsymbol{\rho}) = \mathbf{J}(\boldsymbol{\rho}) \exp(-j\mathbf{k}_t^{\text{inc}} \cdot [m\mathbf{d}_1 + n\mathbf{d}_2]). \quad (\text{K.5})$$

Now, if the arbitrary vector field  $\mathbf{f}(\boldsymbol{\rho})$  satisfies the pseudo-periodicity relation, the corresponding spectrum  $\hat{\mathbf{f}}(\mathbf{k}_t)$  is discrete. To demonstrate this, we apply a Fourier transformation on both sides of the pseudo-periodicity relation K.3. We apply the definition of the translation operator on the left side, and we apply the Fourier shift theorem on both sides of the equation. We thus obtain

$$\exp(-j\mathbf{k}_t \cdot [m\mathbf{d}_1 + n\mathbf{d}_2]) \hat{\mathbf{f}}(\mathbf{k}_t) = \exp(-j\mathbf{k}_t^{\text{inc}} \cdot [m\mathbf{d}_1 + n\mathbf{d}_2]) \hat{\mathbf{f}}(\mathbf{k}_t), \quad (\text{K.6})$$

which can be rewritten as

$$\begin{aligned} & \exp(-j\mathbf{k}_t^{\text{inc}} \cdot [m\mathbf{d}_1 + n\mathbf{d}_2]) \\ & [\exp(-j[\mathbf{k}_t - \mathbf{k}_t^{\text{inc}}] \cdot [m\mathbf{d}_1 + n\mathbf{d}_2]) - 1] \hat{\mathbf{f}}(\mathbf{k}_t) = \mathbf{0}. \end{aligned} \quad (\text{K.7})$$

A non-trivial solution for  $\hat{\mathbf{f}}(\mathbf{k}_t)$  exist if  $\exp(-j[\mathbf{k}_t - \mathbf{k}_t^{\text{inc}}] \cdot [m\mathbf{d}_1 + n\mathbf{d}_2]) = 1$ , and is satisfied if

$$\mathbf{k}_t - \mathbf{k}_t^{\text{inc}} = p\mathbf{k}_1 + q\mathbf{k}_2, \quad (\text{K.8})$$

for arbitrary integers  $p$  and  $q$ , and with

$$\mathbf{k}_i \cdot \mathbf{d}_j = 2\pi\delta_{i,j}. \quad (\text{K.9})$$

Equation K.8 defines a so-called reciprocal (Floquet) lattice which is spanned by the two basis vectors  $\mathbf{k}_1$  and  $\mathbf{k}_2$  defined by equation K.9 [112, section 7.2], [2, section 20.3]. A graphical representation of the reciprocal lattice is also given in figure K.1. On this lattice  $\hat{\mathbf{f}}(\mathbf{k}_t)$  is nonzero for discrete values for  $\mathbf{k}_t$ , i.e.,  $\mathbf{f}(\boldsymbol{\rho})$  has a discrete spectrum. From equation K.9, we find the basis vectors of the reciprocal lattice as

$$\mathbf{k}_1 = 2\pi \frac{\mathbf{d}_2 \times \hat{\mathbf{z}}}{A}, \quad \mathbf{k}_2 = 2\pi \frac{\hat{\mathbf{z}} \times \mathbf{d}_1}{A}, \quad (\text{K.10})$$

where

$$A = (\mathbf{d}_1 \times \mathbf{d}_2) \cdot \hat{\mathbf{z}}, \quad (\text{K.11})$$

represents the area of the unit cell. We define a so-called Dirac brush function [112, definition 7.12], which is a two-dimensional generalization of the Dirac comb function, as

$$\prod_{\mathbf{d}_1, \mathbf{d}_2} (\boldsymbol{\rho}) = \sum_{p, q} \delta(\boldsymbol{\rho} - p\mathbf{d}_1 - q\mathbf{d}_2). \quad (\text{K.12})$$

Its corresponding spectrum is discrete, and can be expressed in terms of the same Dirac brush function as

$$F \left\{ \prod_{\mathbf{d}_1, \mathbf{d}_2} (\boldsymbol{\rho}) \right\} = \frac{4\pi^2}{A} \prod_{\mathbf{k}_1, \mathbf{k}_2} (\mathbf{k}_t), \quad (\text{K.13})$$

According to the solution technique discussed in chapter 3.4, a set of expansion functions are defined to represent either the induced magnetic current distribution on the apertures, or the induced electric current distribution on subdomains within the unit cell. Since the induced current distribution is pseudo-periodic, a suitable set of expansion functions with this property must be constructed. To this end, let  $\mathbf{f}_k(\boldsymbol{\rho})$  be a set of expansion functions defined only on the central unit cell (and is zero outside this domain). Many different choices are possible to extend such a function to the periodic structure such that equation K.3 is satisfied.

The first choice (which is generally assumed in the literature [112, section 7.3]) for a periodic extension is the so-called staircase phase function  $\mathbf{f}_k^{\mathcal{S}}(\boldsymbol{\rho})$ , and is expressed as

$$\mathbf{f}_k^{\mathcal{S}}(\boldsymbol{\rho}) \equiv \sum_{p, q} \mathbf{f}_k(\boldsymbol{\rho} - p\mathbf{d}_1 - q\mathbf{d}_2) \exp(-j\mathbf{k}_t^{\text{inc}} \cdot [p\mathbf{d}_1 + q\mathbf{d}_2]), \quad (\text{K.14})$$

This periodic extension satisfies the pseudo-periodicity relation

$$\begin{aligned}
T_{m,n}\mathbf{f}_k^S(\boldsymbol{\rho}) &\equiv \mathbf{f}_k^S(\boldsymbol{\rho} + m\mathbf{d}_1 + n\mathbf{d}_2) \\
&= \sum_{p,q} \mathbf{f}_k(\boldsymbol{\rho} - (p-m)\mathbf{d}_1 - (q-n)\mathbf{d}_2) \exp(-j\mathbf{k}_t^{\text{inc}} \cdot [p\mathbf{d}_1 + q\mathbf{d}_2]) \\
&= \sum_{p',q'} \mathbf{f}_k(\boldsymbol{\rho} - p'\mathbf{d}_1 - q'\mathbf{d}_2) \exp(-j\mathbf{k}_t^{\text{inc}} \cdot [(p'+m)\mathbf{d}_1 + (q'+n)\mathbf{d}_2]) \\
&= \exp(-j\mathbf{k}_t^{\text{inc}} \cdot [m\mathbf{d}_1 + n\mathbf{d}_2])\mathbf{f}_k^S(\boldsymbol{\rho}),
\end{aligned} \tag{K.15}$$

and represents an eigenvalue problem where the eigenvalue of the transmission operator has a magnitude equal to one. The eigenvalue problem tells us that the behavior of all unit cells can be regarded as equal in magnitude, except for a stepwise phase difference between the unit cells. The second choice for a periodic extension is the so-called linear phase function  $\mathbf{f}_k^L(\boldsymbol{\rho})$ , and is expressed as [112, section 7.3]

$$\mathbf{f}_k^L(\boldsymbol{\rho}) \equiv \exp(-j\mathbf{k}_t^{\text{inc}} \cdot \boldsymbol{\rho}) \sum_{p,q} \mathbf{f}_k(\boldsymbol{\rho} - p\mathbf{d}_1 - q\mathbf{d}_2), \tag{K.16}$$

This periodic extension satisfies the pseudo-periodicity relation

$$\begin{aligned}
T_{m,n}\mathbf{f}_k^L(\boldsymbol{\rho}) &\equiv \mathbf{f}_k^L(\boldsymbol{\rho} + m\mathbf{d}_1 + n\mathbf{d}_2) \\
&= \exp(-j\mathbf{k}_t^{\text{inc}} \cdot [\boldsymbol{\rho} + m\mathbf{d}_1 + n\mathbf{d}_2]) \sum_{p,q} \mathbf{f}_k(\boldsymbol{\rho} - (p-m)\mathbf{d}_1 - (q-n)\mathbf{d}_2) \\
&= \exp(-j\mathbf{k}_t^{\text{inc}} \cdot [m\mathbf{d}_1 + n\mathbf{d}_2]) \exp(-j\mathbf{k}_t^{\text{inc}} \cdot \boldsymbol{\rho}) \sum_{p',q'} \mathbf{f}_k(\boldsymbol{\rho} - p'\mathbf{d}_1 - q'\mathbf{d}_2) \\
&= \exp(-j\mathbf{k}_t^{\text{inc}} \cdot [m\mathbf{d}_1 + n\mathbf{d}_2])\mathbf{f}_k^L(\boldsymbol{\rho}),
\end{aligned} \tag{K.17}$$

and represents an eigenvalue problem where the eigenvalue of the transmission operator has a magnitude equal to one. The eigenvalue problem tells us that the behavior of all unit cells can be regarded as equal in magnitude, except for a linear phase difference along the unit cells. Note that if we replace  $\mathbf{f}_k(\boldsymbol{\rho})$  with  $\mathbf{f}_k(\boldsymbol{\rho}) \exp(-j\mathbf{k}_t^{\text{inc}} \cdot \boldsymbol{\rho})$  in the periodic extension for  $\mathbf{f}_k^S(\boldsymbol{\rho})$  as

$$\begin{aligned}
\mathbf{f}_k^S(\boldsymbol{\rho}) &= \sum_{p,q} \mathbf{f}_k(\boldsymbol{\rho} - p\mathbf{d}_1 - q\mathbf{d}_2) \\
&\quad \exp(-j\mathbf{k}_t^{\text{inc}} \cdot [\boldsymbol{\rho} - p\mathbf{d}_1 - q\mathbf{d}_2]) \exp(-j\mathbf{k}_t^{\text{inc}} \cdot [p\mathbf{d}_1 + q\mathbf{d}_2]) \\
&= \sum_{p,q} \mathbf{f}_k(\boldsymbol{\rho} - p\mathbf{d}_1 - q\mathbf{d}_2) \exp(-j\mathbf{k}_t^{\text{inc}} \cdot \boldsymbol{\rho}) \\
&= \exp(-j\mathbf{k}_t^{\text{inc}} \cdot \boldsymbol{\rho}) \sum_{p,q} \mathbf{f}_k(\boldsymbol{\rho} - p\mathbf{d}_1 - q\mathbf{d}_2) = \mathbf{f}_k^L(\boldsymbol{\rho}),
\end{aligned} \tag{K.18}$$

we obtain  $\mathbf{f}_k^L(\boldsymbol{\rho})$ . To appreciate the advantages of  $\mathbf{f}_k^L(\boldsymbol{\rho})$  compared to  $\mathbf{f}_k^S(\boldsymbol{\rho})$ , we must concentrate on the spectral domain. If we use equation K.12, we can

rewrite  $\mathbf{f}_k^S(\boldsymbol{\rho})$  as

$$\mathbf{f}_k^S(\boldsymbol{\rho}) = \exp(-j\mathbf{k}_t^{\text{inc}} \cdot \boldsymbol{\rho}) \left[ \{ \mathbf{f}_k(\boldsymbol{\rho}) \exp(j\mathbf{k}_t^{\text{inc}} \cdot \boldsymbol{\rho}) \} * \prod_{\mathbf{d}_1, \mathbf{d}_2} (\boldsymbol{\rho}) \right]. \quad (\text{K.19})$$

where  $*$  denotes convolution over  $\boldsymbol{\rho}$ . Its corresponding spectrum is given by

$$\hat{\mathbf{f}}_k^S(\mathbf{k}_t) = \frac{4\pi^2}{A} \hat{\mathbf{f}}_k(\mathbf{k}_t) \prod_{\mathbf{k}_1, \mathbf{k}_2} (\mathbf{k}_t - \mathbf{k}_t^{\text{inc}}). \quad (\text{K.20})$$

Note that  $\hat{\mathbf{f}}_k^S(\mathbf{k}_t)$  is not rigidly connected to the reciprocal lattice, which means that  $\hat{\mathbf{f}}_k(\mathbf{k}_t)$  is sampled at different points ( $\mathbf{k}_t^{\text{inc}} + p\mathbf{k}_1 + q\mathbf{k}_2$ ) when  $\mathbf{k}_t^{\text{inc}}$  changes due to a change in frequency or angle of incidence. Finally, if we use equation K.12, we can rewrite  $\mathbf{f}_k^{\mathcal{L}}(\boldsymbol{\rho})$  as

$$\mathbf{f}_k^{\mathcal{L}}(\boldsymbol{\rho}) = \exp(-j\mathbf{k}_t^{\text{inc}} \cdot \boldsymbol{\rho}) \left[ \mathbf{f}_k(\boldsymbol{\rho}) * \prod_{\mathbf{d}_1, \mathbf{d}_2} (\boldsymbol{\rho}) \right]. \quad (\text{K.21})$$

Its corresponding spectrum is given by

$$\hat{\mathbf{f}}_k^{\mathcal{L}}(\mathbf{k}_t) = \frac{4\pi^2}{A} \hat{\mathbf{f}}_k(\mathbf{k}_t - \mathbf{k}_t^{\text{inc}}) \prod_{\mathbf{k}_1, \mathbf{k}_2} (\mathbf{k}_t - \mathbf{k}_t^{\text{inc}}). \quad (\text{K.22})$$

Note that  $\hat{\mathbf{f}}_k^{\mathcal{L}}(\mathbf{k}_t)$  is rigidly connected to the reciprocal lattice, which means that  $\hat{\mathbf{f}}_k(\mathbf{k}_t)$  is sampled in the same points ( $p\mathbf{k}_1 + q\mathbf{k}_2$ ) even when  $\mathbf{k}_t^{\text{inc}}$  changes due to a change in frequency or angle of incidence.





# Bibliography

- [1] C.K. Aanandan, P. Debernardi, R. Orta, R. Tascone, and D. Trincherio. Problem-Matched Basis Functions for Moment Method Analysis - An Application to Reflection Gratings. *IEEE Transactions on Antennas and Propagation*, 48(1):35–40, January 2000.
- [2] M. Abramowitz and I.A. Stegun. *Handbook of Mathematical Functions with Formulas, Graphs, and Mathematical Tables*. Dover Publications, Inc., New York, 1964.
- [3] S.T.M. Ackermans and J.H. van Lint. *Algebra en Analyse*. Acedemic Service Den Haag, 1976.
- [4] N.I. Akhiezer and I.M. Glazman. *Theory of Linear Operators in Hilbert Space*. Dover Publications, Inc., New York, 1993.
- [5] N. Amitay, V. Galindo, and C.P. Wu. *Theory and Analysis of Phased Array Antennas*. A Wiley-Interscience Publication, J. Wiley & Sons, Inc., 1972.
- [6] I. Anderson. On the Theory of Self-Resonant Grids. *The Bell System Technical Journal*, 54(10):1725–1731, December 1975.
- [7] C.A. Balanis. *Antenna Theory, Analysis and Design*. A Wiley-Interscience Publication, J. Wiley & Sons, Inc., 1982.
- [8] C.A. Balanis. *Advanced Engineering Electromagnetics*. A Wiley-Interscience Publication, J. Wiley & Sons, Inc., 1989.
- [9] D.J. Bekers. *Finite Antenna Arrays, An Eigencurrent Approach*. PhD thesis, Eindhoven University of Technology, 2004.
- [10] C.M. Bender and S.A. Orszag. *Advanced Mathematical Methods for Scientists and Engineers*. McGraw-Hill Book Company, 1978.
- [11] A.K. Bhattacharyya. Multimode Moment Method Formulation for Waveguide Discontinuities. *IEEE Transactions on Antennas and Propagation*, 42(8):1567–1571, 1994.

- [12] A.K. Bhattacharyya. A Numerical Model for Multilayered Microstrip Phased-Array Antennas. *IEEE Transactions on Antennas and Propagation*, 44(10):1386–1393, 1996.
- [13] A.K. Bhattacharyya. Analysis of Multilayer Infinite Periodic Array Structures with Different Periodicities and Axes Orientations. *IEEE Transactions on Antennas and Propagation*, 48(3):357–369, March 2000.
- [14] A.K. Bhattacharyya. On the Convergence of Method of Moments and Mode Matching Solutions for Infinite Array and Waveguide Problems. *IEEE Transactions on Antennas and Propagation*, 51(7):1599–1606, 2003.
- [15] H. Blok. Theory of Electromagnetic Waveguides: Part I. Collegediktaat et01-34, Laboratory of Electromagnetic Research, Faculty of Electrical Engineering, Delft University of Technology, Delft, The Netherlands, 1995.
- [16] H. Blok and P.M. van den Berg. Electromagnetic Waves, An Introductory Course. Collegediktaat et01-20, Laboratory of Electromagnetic Research, Faculty of Electrical Engineering, Delft University of Technology, Delft, The Netherlands, 1995.
- [17] R.R. Boix, M.J. Freire, and F. Medina. New Method for the Efficient Summation of Double Infinite Series Arising From the Spectral Domain Analysis of Frequency Selective Surfaces. *IEEE Transactions on Antennas and Propagation*, 52(4):1080–1094, April 2004.
- [18] J. Bornemann and F. Arndt. Modal S-Matrix Design of Metal Filled Waveguide Components and its Application to Transformers and Filters. *IEEE Transactions on Microwave Theory and Techniques*, 40(7):1528–1537, July 1992.
- [19] E. Brookner. *Practical Phased-Array Antenna Systems*. Artech House, Inc., 1991.
- [20] D. Budimir. Optimized E-Plane Bandpass Filters with Improved Stop-band Performance. *IEEE Transactions on Microwave Theory and Techniques*, 45(2):212–220, February 1997.
- [21] L.Q. Bui, D. Ball, and T. Itoh. Broad-Band Millimeter-Wave E-Plane Bandpass Filters. *IEEE Transactions on Microwave Theory and Techniques*, MTT-32(12):1655–1658, December 1984.
- [22] K.K. Chan and K. Chadwick. APAR Antenna Simulations IX. Technical report, Chan Technologies Inc., Department of National Defence, Ottawa, Ontario, Canada, October 1998. Presentation at Hollandse Signaalapparaten B.V., October 1998, Hengelo, Overijssel, The Netherlands.
- [23] K.K. Chan, K. Chadwick, and R. Martin. APAR Antenna Simulations VII. Technical report, Chan Technologies Inc., Radar & Space Division,

- Defence Research Establishment Ottawa, Department of National Defence, Ottawa, Ontario, Canada, June 1997. Presentation at Hollandse Signaalapparaten B.V., June 1997, Hengelo, Overijssel, The Netherlands.
- [24] K.K. Chan, K. Chadwick, and R.M. Turner. APAR Antenna Simulations IV. Technical report, Chan Technologies Inc., Radar & Space Division, Defence Research Establishment Ottawa, Department of National Defence, Ottawa, Ontario, Canada, July 1994. Presentation at Hollandse Signaalapparaten B.V., July 1994, Hengelo, Overijssel, The Netherlands.
- [25] K.K. Chan, K. Chadwick, and R.M. Turner. APAR Antenna Simulations V. Technical report, Chan Technologies Inc., Radar & Space Division, Defence Research Establishment Ottawa, Department of National Defence, Ottawa, Ontario, Canada, February 1995. Presentation at Hollandse Signaalapparaten B.V., February 1995, Hengelo, Overijssel, The Netherlands.
- [26] K.K. Chan, K. Chadwick, R.M. Turner, and F. Tremblay. APAR Antenna Simulations VI. Technical report, Chan Technologies Inc., Radar & Space Division, Defence Research Establishment Ottawa, Department of National Defence, Ottawa, Ontario, Canada, November 1995. Presentation at Hollandse Signaalapparaten B.V., November 1995, Hengelo, Overijssel, The Netherlands.
- [27] K.K. Chan and R.M. Turner. APAR Antenna Simulations I. Technical report, Chan Technologies Inc., Radar & Space Division, Defence Research Establishment Ottawa, Department of National Defence, Ottawa, Ontario, Canada, May 1993. Presentation at Hollandse Signaalapparaten B.V., May 1993, Hengelo, Overijssel, The Netherlands.
- [28] K.K. Chan and R.M. Turner. APAR Antenna Simulations II. Technical report, Chan Technologies Inc., Radar & Space Division, Defence Research Establishment Ottawa, Department of National Defence, Ottawa, Ontario, Canada, September 1993. Presentation at Hollandse Signaalapparaten B.V., September 1993, Hengelo, Overijssel, The Netherlands.
- [29] K.K. Chan and R.M. Turner. APAR Antenna Simulations III. Technical report, Chan Technologies Inc., Radar & Space Division, Defence Research Establishment Ottawa, Department of National Defence, Ottawa, Ontario, Canada, April 1994. Presentation at Hollandse Signaalapparaten B.V., April 1994, Hengelo, Overijssel, The Netherlands.
- [30] W.K. Chen. *The Circuits and Filters Handbook*. CRC Press, and IEEE Press, 1995.
- [31] R.E. Collin. *Foundations for Microwave Engineering*. McGraw-Hill Book Company, Inc., second edition, 1992.
- [32] S. Contu and R. Tascone. Scattering from Passive Arrays in Plane Stratified Regions. *Electromagnetics*, 5(4):285–306, 1985.

- [33] Ansoft Corporation. HFSS v9.0. Getting Started with HFSS. 2003.
- [34] B.P. de Hon and R. Orta. Electromagnetic Theory of Waveguides. Lecture notes 5MH20, Laboratory of Electromagnetic Research, Faculty of Electrical Engineering, Eindhoven University of Technology, Eindhoven, The Netherlands, February 2005.
- [35] A.T. de Hoop. Radiation and Scattering of Electromagnetic Waves. Collediktaat L12, Laboratory of Electromagnetic Research, Faculty of Electrical Engineering, Delft University of Technology, Delft, The Netherlands, 1991.
- [36] A.T. de Hoop. *Handbook of Radiation and Scattering of Waves: Acoustic Waves in Fluids, Elastic Waves in Solids, and Electromagnetic Waves*. Academic Press Limited, 1995.
- [37] A.T. de Hoop. Electromagnetic Wavefield Computation - A Structured Approach based on Reciprocity. Report Et/EM 1996-23, Laboratory of Electromagnetic Research, Faculty of Electrical Engineering, Delft University of Technology, Delft, The Netherlands, 1996.
- [38] R. d’Inverno. *Introducing Einstein’s Relativity*. Clarendon Press, Oxford, 1992.
- [39] B. Dunnebier. Large Microstrip Phased Array Antennas, Analysis and Numerical Implementation. Technical report, Information and Communication Technology, Stan Ackermans Institute, Eindhoven University of Technology, November 1999.
- [40] P. Ewald. *Ann. Phys., Lpz.*, 64:253, 1921.
- [41] M. Favreau, J.M. Goutoule, R. Orta, P. Savi, and R. Tascone. Design of a 45 Degree Incidence Millimeter Wave Diplexer. *Annales des Telecommunications*, 47:539–540, September 1992.
- [42] M. Favreau, J.M. Goutoule, R. Orta, P. Savi, and R. Tascone. A Free-Space Double-Grid Diplexer for a Millimeter-Wave Radiometer. *Microwave and Optical Technology Letters*, 6(2):121–124, February 1993.
- [43] N. Fourikis. *Phased Array-Based Systems and Applications*. A Wiley-Interscience Publication, J. Wiley & Sons, Inc., 1997.
- [44] A.K. Golshayan, P. van Genderen, and S. van der Schoot. Active Phased Array Radar. In *Proceedings of the International Conference and Exhibition on Radar Systems*. Brest, France, May 17-21 1999.
- [45] I.S. Gradshteyn and I.M. Ryzhik. *Table of Integrals, Series, and Products*. Academic Press, sixth edition, 2000.

- [46] P.W. Grounds and K.J. Webb. Numerical Analysis of Finite Frequency Selective Surfaces with Rectangular Patches of Various Aspect Ratios. *IEEE Transactions on Antennas and Propagation*, 39(5):569–575, May 1991.
- [47] M.A. Haider, S.P. Shipman, and S.Venakides. Boundary-Integral Calculations of Two-Dimensional Electromagnetic Scattering in Infinite Photonic Crystal Slabs: Channel Defects and Resonances. *Society for Industrial and Applied Mathematics*, 62(6):2129–2148, 2002.
- [48] R.C. Hall, R. Mittra, and K.M. Mitzner. Analysis of Multilayered Periodic Structures using Generalized Scattering Matrix Theory. *IEEE Transactions on Antennas and Propagation*, 36(4):511–517, April 1988.
- [49] H. Haskal. Matrix Description of Waveguide Discontinuities in the Presence of Evanescent Modes. *IEEE Transactions on Microwave Theory and Techniques*, pages 184–188, March 1964.
- [50] H.A. Haus and J.R. Melcher. *Electromagnetic Fields and Energy*. Prentice Hall, Englewood Cliffs, New Jersey 07632, 1989. Massachusetts Institute of Technology.
- [51] H. Hertz. *Untersuchungen über die Ausbreitung der Elektrischen Kraft*. Johann Ambrosius Barth, Leipzig, 1892.
- [52] A. Jeffrey. *Handbook of Mathematical Formulas and Integrals*. Academic Press, 1995.
- [53] R.P. Kanwal. *Generalized Functions*. Birkhäuser, Boston, 1998.
- [54] J.J.J. Kokkedee. *Klassieke Mechanica en Relativiteitstheorie*. Collediktaat, Laboratory of Theoretical Physics, Faculty of Applied Physics, Delft University of Technology, Delft, The Netherlands, 1992.
- [55] H. Kwakernaak and R. Sivan. *Modern Signals and Systems*. Prentice-Hall International, Inc., 1991.
- [56] J.Y. Kwon and H.J. Eom. Electromagnetic Transmission of an Oblique Waveguide Array. *IEEE Transactions on Antennas and Propagation*, 52(10):2596–2602, October 2004.
- [57] A.C. Ludwig. The Definition of Cross Polarization. *IEEE Transactions on Antennas and Propagation*, pages 116–119, January 1973.
- [58] S. Maci, M. Caiazzo, A. Cucini, and M. Casaletti. A pole-zero Matching Method for EBG Surfaces Composed of a Dipole FSS Printed on Grounded Dielectric Slabs. *IEEE Transactions on Antennas and Propagation*, 53(1):70–81, 2005.

- [59] E. Magill and H. Wheeler. Wide-Angle Impedance Matching of a Planar Array Antenna by a Dielectric Sheet. *IEEE Transactions on Antennas and Propagation*, 14(1):49–53, 1996.
- [60] R.J. Mailloux. *Phased Array Antenna Handbook*. Artech House, Inc., 1994.
- [61] J.E. Marsden and M.J. Hoffman. *Basic Complex Analysis*. W.H. Freeman and Company, New York.
- [62] J.C. Maxwell. *A Treatise on Electricity and Magnetism*. Clarendon Press, Oxford, 1873.
- [63] S. Monni. *Frequency Selective Surfaces Integrated with Phased Array Antennas, Analysis and Design using Multimode Equivalent Networks*. PhD thesis, Eindhoven University of Technology, 2005.
- [64] J.P. Montgomery. Scattering by an Infinite Periodic Array of Thin Conductors on a Dielectric Sheet. *IEEE Transactions on Antennas and Propagation*, AP-23(1):70–75, January 1975.
- [65] B.J. Morsink, G.H.C. van Werkhoven, and A.G. Tijhuis. A Coupled Feed-Radiator-Frequency Selective Surface Model for the Next Generation Active Phased Array Systems. In *Proceedings of the 25th ESTEC Antenna Workshop on Satellite Antenna Technology*. ESTEC, Noordwijk, The Netherlands, September 18-20 2002.
- [66] B.J. Morsink, G.H.C. van Werkhoven, A.G. Tijhuis, and S.W. Rienstra. Acceleration Techniques for Coupled FSS-Multilayer Antennas. In *Proceedings of the IEEE International Symposium on Phased Array Systems and Technology*, pages 470–475. Boston, Massachusetts, United States, October 14-17 2003.
- [67] B.J. Morsink, S.W. Rienstra, and A.G. Tijhuis. Modeling Frequency Selective Surfaces with Multiple Metallization and Continuously Layered Dielectric Substrates. In *Proceedings of the 24th ESTEC Antenna Workshop on Innovative Periodic Antennas: Photonic Bandgap, Fractal and Frequency Selective Structures*, pages 163–167. ESTEC, Noordwijk, The Netherlands, May 30-June 1 2001.
- [68] B.A. Munk. *Frequency Selective Surfaces: Theory and Design*. A Wiley-Interscience Publication, J. Wiley & Sons, Inc., 2000.
- [69] B.A. Munk and G.A. Burrell. Plane-Wave Expansion for Arrays of Arbitrarily Oriented Piecewise Linear Elements and Its Application in Determining the Impedance of a Single Linear Antenna in a Lossy Half-Space. *IEEE Transactions on Antennas and Propagation*, AP-27(3):331–343, May 1979.

- [70] F.L. Neerhof. *Elektrische Circuits: Model, Structuur en Dynamica, Deel 1*. Delftse Uitgevers Maatschappij, 1992.
- [71] A. Neto, S. Maci, G. Vecchi, and M. Sabbadini. A Truncated Floquet Wave Diffraction Method for the Full Wave Analysis of Large Phased Arrays - Part I: Basic Principles and 2-D Cases. *IEEE Transactions on Antennas and Propagation*, 48(3):594–600, March 2000.
- [72] A. Neto, S. Maci, G. Vecchi, and M. Sabbadini. A Truncated Floquet Wave Diffraction Method for the Full Wave Analysis of Large Phased Arrays - Part II: Generalization to 3-D Cases. *IEEE Transactions on Antennas and Propagation*, 48(3):601–611, March 2000.
- [73] R. Orta, P. Savi, and R. Tascone. Multiple Frequency-Selective Surfaces Consisting of Ring Patches. *Electromagnetics*, 15:417–426, 1995.
- [74] R. Orta, P. Savi, and R. Tascone. Numerical Green's Function Technique for the Analysis of Screens Perforated by Multiply Connected Apertures. *IEEE Transactions on Antennas and Propagation*, 44(6):765–776, June 1996.
- [75] R. Orta, R. Tascone, and R. Zich. A Unified Formulation for the Analysis of General Frequency Selective Surfaces. *Electromagnetics*, 5(4):307–329, 1985.
- [76] R. Orta, R. Tascone, and R. Zich. Efficient Choice of Basis Functions in Moment Method Analysis of Frequency-Selective Surfaces. *Electronics Letters*, 23(11):586–587, May 1987.
- [77] R. Orta, R. Tascone, and R. Zich. Multiple Dielectric Loaded Perforated Screens as Frequency-Selective Surfaces. *IEE Proceedings*, 135(2):75–82, April 1988.
- [78] R. Orta, R. Tascone, and R. Zich. Multiple-Grid Frequency-Selective Surfaces as Periodically Loaded Structures. *Electronics Letters*, 24(8):449–450, April 1988.
- [79] A. Papoulis. *Systems and Transforms with Applications in Optics*. Kreiger, Malabar, Fla., 1981.
- [80] M.J. Park and S. Nam. Efficient Calculation of the Green's Function for Multilayered Planar Periodic Structures. *IEEE Transactions on Antennas and Propagation*, 46(10):1582–1583, October 1998.
- [81] E.A. Parker and A.N.A. El Sheikh. Convolutd Array Elements and Reduced Size Unit Cells for Frequency-Selective Surfaces. *IEE Proceedings-H*, 138(1):19–22, February 1991.
- [82] E.A. Parker, S.M.A. Hamdy, and R.J. Langley. Modes of Resonance of the Jerusalem Cross in Frequency-Selective Surfaces. *IEE Proceedings*, 130(3):203–208, April 1983.



- [83] Y. Peleg, R. Pnini, and E. Zaarur. *Schaum's Outline of Theory and Problems of Quantum Mechanics*. McGraw-Hill Book Company, Inc., 1998.
- [84] E.L. Pelton and B.A. Munk. Scattering from Periodic Arrays of Crossed Dipoles. *IEEE Transactions on Antennas and Propagation*, AP-27(3):323–330, May 1979.
- [85] M. Porto. Ewald Summation of Electrostatic Interactions of Systems with Finite Extent in Two of Three Dimensions. *Journal Applied Physics and Mathematics*, 33:6211–6218, 2000.
- [86] D.M. Pozar. The Active Element Pattern. *IEEE Transactions on Antennas and Propagation*, 42(8):1176–1178, August 1994.
- [87] D.M. Pozar and D.H. Schaubert. Scan Blindness in Infinite Phased Arrays of Printed Dipoles. *IEEE Transactions on Antennas and Propagation*, 32(6), 1984.
- [88] S.M. Rao, D.R. Wilton, and A.W. Glisson. Electromagnetic Scattering by Surfaces of Arbitrary Shape. *IEEE Transactions on Antennas and Propagation*, 30(3):409–418, 1982.
- [89] S.W. Rienstra. A General Acceleration Method for the Analysis of Frequency Selective Surfaces. Technical report, Mathematics and Computer Science Department, Eindhoven University of Technology, Eindhoven, The Netherlands, January 2002. Report of Study Contract WDC262A.
- [90] T.E. Rozzi. Network Analysis of Strongly Coupled Transverse Apertures in Waveguide. *Circuit Theory and Applications*, 1:161–178, 1973.
- [91] Y. Saad. *Iterative Methods for Sparse Linear Systems*. PWS Publishing Company, 1996.
- [92] P. Savi, D. Trincherò, R. Tascone, and R. Orta. A New Approach to the Design of Dual-Mode Rectangular Waveguide Filters with Distributed Coupling. *IEEE Transactions on Antennas and Propagation*, 45(2):221–228, February 1997.
- [93] S. Singh, W. Richards, J. Zinecker, and R. Wilton. Accelerating the Convergence of Series Representing the Free Space Periodic Green's Function. *IEEE Transactions on Antennas and Propagation*, 38(12):1958–1962, 1990.
- [94] M.I. Skolnik. *Introduction to Radar Systems*. McGraw-Hill Book Company, second edition, 1981.
- [95] M.I. Skolnik. *Introduction to Radar Systems*. McGraw-Hill Book Company, third edition, 2001.

- [96] A.B. Smits and P. van Genderen. The APAR Multifunction Radar - System Overview. In *Proceedings of the IEEE International Symposium on Phased Array Systems and Technology*, pages 241–246. Boston, Massachusetts, United States, October 14-17 2003.
- [97] A.B. Smolders. *Microstrip Phased-Array Antennas: A Finite-Array Approach*. PhD thesis, Eindhoven University of Technology, 1994.
- [98] M. Spivak. *Calculus on Manifolds: A Modern Approach to Classical Theorems of Advanced Calculus*. The Advanced Book Program, Perseus Books, Cambridge, Massachusetts, 1965.
- [99] G. Strang. *Linear Algebra and its Applications*. Hacourt Brace Jovanovich, Publishers San Diego, 1988.
- [100] S.Venakides, M.A. Haider, and V. Papanicolaou. Boundary-Integral Calculations of Two-Dimensional Electromagnetic Scattering by Photonic Crystal Fabry-Perot Structures. *Society for Industrial and Applied Mathematics*, 60(5):1686–1706, 2000.
- [101] S.H. Tan. Comments on: On the Use of rho-Algorithm in Series Acceleration. *IEEE Transactions on Antennas and Propagation*, 46(11):1766, November 1998.
- [102] R. Tascone, P. Savi, D. Trincherio, and R. Orta. Scattering Matrix Approach for the Design of Microwave Filters. *IEEE Transactions on Antennas and Propagation*, 48(3):423–430, March 2000.
- [103] A.G. Tijhuis. Elektromagnetisme 2. Collegedictaat 5F080, Laboratory of Electromagnetic Research, Faculty of Electrical Engineering, Eindhoven University of Technology, Eindhoven, The Netherlands, August 1998.
- [104] A.G. Tijhuis. Plane-Wave Excitation of Two-Dimensionally Periodic Metallized Structures in Plane-Stratified Dielectric Media. Technical report, Electromagnetics Section, Division of Telecommunication Technology and Electromagnetics, Eindhoven University of Technology, Eindhoven, The Netherlands, January 2002. Report of Study Contract WDC262A.
- [105] A.G. Tijhuis and M.C. van Beurden. Elektromagnetische Golven en Straling. Collegedictaat 5GG40, Laboratory of Electromagnetic Research, Faculty of Electrical Engineering, Eindhoven University of Technology, Eindhoven, The Netherlands, February 2004.
- [106] C.H. Tsao and R. Mittra. Spectral-Domain Analysis of Frequency Selective Surfaces Comprised of Periodic Arrays of Cross Dipoles and Jerusalem Crosses. *IEEE Transactions on Antennas and Propagation*, AP-32(5):478–486, May 1984.

- 
- [107] R. Vahldieck. Quasi-Planar Filters for Millimeter-Wave Applications. *IEEE Transactions on Microwave Theory and Techniques*, 37(2):324–334, February 1989.
- [108] M.C. van Beurden. *Integro-Differential Equations for Electromagnetic Scattering, Analysis and Computation for Objects with Electric Contrast*. PhD thesis, Eindhoven University of Technology, 2003.
- [109] P.M. van den Berg. Iterative Computational Techniques in Scattering Based Upon the Integrated Square Error Criterion. *IEEE Transactions on Antennas and Propagation*, AP-32(10):1063–1071, October 1984.
- [110] S. van den Berg. *Modelling and Inversion of Pulsed Eddy Current Data*. PhD thesis, Delft University of Technology, 2003.
- [111] A.W.M. van den Enden and N.A.M. Verhoeckx. *Discrete-time Signal Processing, An Introduction*. Prentice Hall International (UK) Ltd, 1989. Philips Research Laboratories, Eindhoven, The Netherlands.
- [112] J.C. Vardaxoglou. *Frequency Selective Surfaces, Analysis and Design*. Research Studies Press Ltd, A Wiley-Interscience Publication, J. Wiley & Sons, Inc., 1997.
- [113] D.V. Widder. *The Laplace Transform*. Princeton University Press, 1946.
- [114] S. Wolfram. *The Mathematica Book*. Wolfram Research, Cambridge University Press, third edition, 1996.
- [115] A.P.M. Zwamborn. *Scattering by Objects with Electric Contrast*. PhD thesis, Delft University of Technology, 1991.

# Summary

Phased array antennas (PAAs) used in military naval radar systems contain a large number of simple and identical radiating elements regularly arranged in a planar grid. A recent and innovative example is the APAR multi-function search, track and missile guidance radar from Thales Nederland. APAR is an X-band radar and consists of four PAA faces where each PAA face has more than 3000 radiating elements. To have a successfully operating radar system in a stressful environment, these PAAs have to satisfy a large number of stringent requirements, such as a wide beam scanning range and a large frequency bandwidth with low losses. To achieve this, and further to reduce the costs of PAA prototype building, dedicated computational methods are used to simulate the electromagnetic (EM) behavior of PAAs. These methods support an efficient iterative PAA design process, where a number of specific design parameters is adjusted iteratively until the calculated EM response of the structure satisfies the requirements. Subsequently, a prototype is constructed and measurements are carried out. The comparison between the outcome of these measurements and the predictions determines whether the design can be finalized, or whether the design process should be continued.

On future PAAs the requirements on beam scanning ranges and frequency bandwidths will become more stringent. Furthermore, new requirements such as a low radar cross-section signature and a low EM interference (EMI) and a high EM compatibility (EMC) will be introduced. These requirements can only be met by selecting more complex radiating elements and by increasing the number of computational design iterations. Moreover, the design phase must include a sensitivity analysis, where the sensitivity of the EM behavior with respect to production variations is analyzed and minimized. The goal is to obtain a so-called production tolerant design. Most current design methods adjust the design parameters in a trial-and-error process. Future design methods will be more automated in this sense with the aid of synthesis techniques, which will allow a more structured design approach. These developments lead to a strongly increased number of computational design iterations. With the currently available numerical methods, this would lead to unacceptably long simulation times. The objective of this thesis was to develop a computational method that can be used in this process.

Since the number of radiating elements is large, we use the infinite-array

approach, which assumes an infinite number of identical radiating elements with a constant progressive phase shift between the elements. This approach reduces the computation of the EM behavior for the infinite structure essentially to that of a single radiating element. Typical radiating element structures, that can be analyzed with the computational method described in this thesis, consist of waveguide feeding elements, cavity backed patches, open-ended waveguides, and multi-layer frequency selective surfaces. To formalize the construction of such a typical unit-cell structure we use two types of building blocks: segments and junctions. Segments can be either pieces of waveguide or layered space (infinite dielectric slabs). Each junction separates two segments and can/must contain infinitely thin arbitrarily shaped metal. Within a single radiating element there are parts (basic structures) in which the junctions experience a significant EM coupling. Between the basic structures there is low EM coupling. To determine the total EM behavior efficiently we exploit this property, and separate the total calculation into one for each basic structure, and one for combining them.

The calculation of the EM behavior within a single basic structure requires the use of Maxwell's equations. Since we are dealing with a planarly stratified configuration, we derive a Green's function formulation for a planarly stratified medium. We distinguish here between two types of such media: the waveguide and the layered space. Then, we formulate the scattering problem and ensure the existence and uniqueness of a field solution within the basic structure by supplementing proper boundary conditions. From an electromagnetic engineering point of view these boundary conditions describe the domain where the Maxwell equations are to be solved. The final objective of the simulation is to compute the field radiated by a given source in a complicated structure. If the Green's function of this structure were known, the computation could be carried out without difficulty and there would be no need to apply the equivalence theorem. On the contrary, by closing some gaps or removing some metal parts, we obtain simpler regions where the Green's function is known, as a modal expansion. The equivalence theorem says that in order to have the same field in the original and the modified structure, it is necessary to introduce suitable current distributions. The actual value of these currents cannot be given explicitly, but can be determined by the solution of an integral equation. Integral, because the relationship between currents and fields is always of integral type, with a kernel which is the Green's function, which is known in each sub-domain. The equivalent scattering field problem is solved by using a so-called coupled field integral equation (CFIE) technique, where the (electric and magnetic) field integral equations for the separate corresponding junctions are combined. These unknown surface currents are discretized in terms of expansion functions, such as the rooftop and Rao-Wilton-Glisson (RWG) functions, and subsequently determined by the method of moments (MoM). This method approximates the integral equation by a matrix equation of type  $L\mathbf{u} = \mathbf{f}$  with linear operator  $L$ , unknown vector  $\mathbf{u}$ , and forcing vector  $\mathbf{f}$ . The matrix equation can be solved by means of simple inversion of  $L$ , or by making use of more sophisticated iterative schemes. Once we have solved the unknown surface currents with the method of moments, we calculate the total EM field at any given location within the basic

structure. To calculate the EM behavior of the total unit-cell structure, we must combine the individual EM behaviors of all basic structures. For this purpose we formulate a so-called generalized scattering matrix, which characterizes this behavior for all basic structures individually, by relating the outgoing waves to the incident waves. Then we formulate a procedure that cascades two generalized scattering matrices. The result is a new generalized scattering matrix that characterizes the EM behavior of the combination of the two basic structures.

Most of the computational effort in the procedure described above is spent in assembling the linear operator  $L$ . We present a novel acceleration technique that translates the evaluation of an asymptotically slowly converging series, which needs to be evaluated in assembling  $L$ , into a numerical integration over an exponentially fast converging series. This technique reduces the time needed to evaluate these series and consists of three steps. The first step is a Kummer transformation, where the asymptotically slowly converging part of the series is subtracted (resulting in a rapidly converging reduced series) and added (resulting in a slowly converging correction series). The second step is an Ewald transformation, where the asymptotically slowly converging correction series is converted into an integration over  $\tau$  of exponentially fast decaying functions. These functions contain an exponentially fast converging series for which the leading-order term is given by  $\exp(-k_t^2 \tau^{2\lambda})$ . The third step is to split the integration over  $\tau$  into one for small  $\tau$ , i.e., over the interval  $(0, \tau_1)$ , and one for large  $\tau$ , i.e., over the interval  $(\tau_1, \infty)$ . Then we apply a so-called Poisson transformation for the integration over small  $\tau$ , where the relatively slow convergence of the series within the exponentially fast decaying function, corresponding to the behavior of  $\exp(-k_t^2 \tau^{2\lambda})$  for small  $\tau$ , is converted into an exponentially fast converging series. The leading-order term for the integration over small  $\tau$  is given by  $\exp(-\rho^2/(4\tau^{2\lambda}))$ . The so-called transition point  $\tau_1$  is a compromise between the convergence behavior of the leading-order terms  $\exp(-k_t^2 \tau^{2\lambda})$  and  $\exp(-\rho^2/(4\tau^{2\lambda}))$ . The Poisson transformation step results in the evaluation of a so-called exponential regularization (ER) of (a combination of) the expansion and weighting functions. The overall success of this acceleration technique critically depends on the possibility of being able to quickly evaluate the ER. Since the ER is independent of angle of incidence, frequency and medium parameters we calculate it at the beginning of the computation and store it in an ER lookup table (ERLT). This ERLT generation creates a trade-off situation where we can decide whether or not we use the acceleration technique. Since it takes time to generate this ERLT, a critical amount of simulation steps (break-even point) exists where the computational method with the acceleration technique becomes faster than the unaccelerated version. Furthermore, we consider three specific choices for the expansion and weighting functions that lead to workable analytical solutions and numerical approximations for the ER. The first case is the rooftop function defined in an orthogonal grid, which creates a restriction in the modeling of the unknown surface currents. However most structures do not consist of arbitrarily shaped metal patches and apertures, and can therefore be captured in this orthogonal grid. An advantage of this grid is that we can express the ER in terms of complementary error functions. This method is the

fastest for a given test case, when compared with the other two methods. It has the lowest ERLT generation time and the time per step is almost eight times smaller compared to the time per step in the unaccelerated method. Break-even is already reached from the fifth step onwards. In some cases where the unit-cell structure cannot be captured in an orthogonal grid we use the second case, where the rooftop function is defined in an arbitrary grid. In this case, we express the ER as a convolution of two analytically known functions, both with "almost" compact support. This method has a higher ERLT generation time due to the numerical convolution. The time per step is almost eight times smaller compared to the time per step in the unaccelerated method. Break-even is reached at a higher number of steps. The third case involves the more general RWG function. With this triangular expansion function we can model the unknown currents in the most arbitrary way. In this case, we can express the ER as a convolution of two numerically approximated functions both with "almost" compact support. This method has a high ERLT generation time due to both the numerical convolution and the numerical integration within the regularization integral. An analytical alternative is given for the numerical integration. Break-even is reached at a much higher number of steps. The time per step is almost six times smaller compared to the time per step in the unaccelerated method. Using the acceleration technique leads to the conclusion that the computational method is fast.

We validate our computational method against available commercial software tools (such as the finite-element code ©HFSS), and (some of them) against waveguide simulator measurements. We do this for eight different practical and representative radiating structures, of which the first five structures represent different types of frequency selective surfaces, and where the last three structures are concerned with different types of radiators. Based on these validation results we argue that the computational method is besides fast also accurate.

# Samenvatting

Phased array antennas (PAAs) worden steeds vaker gebruikt in militaire marienradarsystemen. Zij bevatten een groot aantal simpele en identieke stralende elementen die in een regelmatig geordend plat vlak zijn geplaatst. Een recent en innovatief voorbeeld is de APAR multi-functie zoek-, volg- en raketbegeleidingsradar van Thales Nederland BV. APAR is een X-band radar die uit vier PAA platen bestaat. Ieder van deze platen bevatten meer dan 3000 stralende elementen. Om deze radars in een sterk belastende omgeving succesvol te laten functioneren, moeten de PAAs aan een groot aantal strenge specificaties voldoen. Voorbeelden hiervan zijn: een groot bundelstuurbereik en een grote operationele frequentiebandbreedte met lage verliezen. Om aan deze eisen te kunnen voldoen, en om bovendien de constructiekosten van PAA prototypes te reduceren, gebruikt men specifieke rekenmethoden die het elektromagnetische (EM) gedrag van PAAs voorspellen. Deze methoden staan een efficiënt iteratief ontwerpproces toe en ondersteunen dit. Dit proces wordt gekarakteriseerd door een iteratieve aanpassing van een aantal specifieke ontwerpparameters totdat het berekende EM gedrag aan de specificaties voldoet. Daarna wordt een PAA prototype gebouwd en wordt het bijbehorende EM gedrag gemeten. De vergelijking van de uitkomst van deze metingen en de voorspellingen bepalen of het ontwerp kan worden afgerond, of dat het ontwerpproces moet worden voortgezet.

Voor toekomstige PAAs zullen de bestaande eisen strenger worden. Bovendien komen er ook nieuwe eisen bij zoals een lage zichtbaarheid voor vijandelijke radars en een lage EM interferentie (EMI) en een hoge EM compatibiliteit (EMC). Hierdoor is men genoodzaakt ingewikkelder stralende elementen te gebruiken. Bovendien zullen meer ontwerpiteraties met deze rekenmethodes moeten worden doorlopen om aan de zwaardere eisen te voldoen. Verder moet de ontwerpfase ook een analyse bevatten van de gevoeligheid van het EM gedrag voor de productietoleranties. Het doel hierbij is een productietolerant ontwerp. De meeste huidige ontwerpprocessen passen de ontwerpparameters aan via trial-and-error. Toekomstige ontwerpprocessen zullen meer gestructureerde ontwerpmethodieken omvatten waarin dit proces geautomatiseerd is met behulp van synthese algoritmes. Deze nieuwe methodes geven naast de zwaardere specificaties ook aanleiding tot een sterk verhoogd aantal ontwerpiteraties met de rekenmethodes. Met de huidige beschikbare rekenmethodes zou dit tot



onaanvaardbare rekentijden leiden. Het doel van dit proefschrift is dan ook om een nieuwe snelle efficiënte rekenmethode te ontwikkelen om dit probleem op te lossen.

Omdat het aantal stralende elementen groot is maken we gebruik van de oneindige array benadering. Een eerste aanname bij deze methode is dat we te maken hebben met een PAA waarin een oneindig aantal identieke stralende elementen zijn geplaatst. Bovendien wordt aangenomen dat de elementen in deze methode worden aangestuurd met een constant progressief faseverschil tussen de elementen onderling. Een groot voordeel van deze methode is dat de uiteindelijke berekening van het EM gedrag van de oneindig grote PAA wordt gereduceerd tot het gedrag van een enkel stralend element. De typische stralende elementen die kunnen worden geanalyseerd met de rekenmethode beschreven in dit proefschrift, bestaan uit golfpijp voedingselementen, met metalen plaatjes afgesloten trilholttes, golfpijpen met open eindes en multilaags frequentie selectieve oppervlaktes (FSS). Om een enkel stralend element formeel te kunnen opbouwen maken we gebruik van twee bouwblokken: segmenten en juncties. Segmenten kunnen stukjes golfpijp of gelaagde media zijn. Elke junctie scheidt twee segmenten van elkaar. Bovendien kan een junctie oneindig dun willekeurig gevormd metaal bevatten. In een stralend element kunnen we gebieden (basisstructuren) onderscheiden waarbinnen de juncties een sterke EM koppeling ervaren. Tussen de basisstructuren onderling is er een zwakke EM koppeling. Om het volledige EM gedrag efficiënt te bepalen maken we gebruik van deze eigenschap, en delen we de totale berekening op in een berekening voor iedere basisstructuur en een procedure voor de koppeling van basisstructuren.

Aan de berekening van het EM gedrag binnen iedere basisstructuur liggen de Maxwell vergelijkingen ten grondslag. Omdat we in onze basisstructuren specifiek te maken hebben met planair willekeurig gelaagde structuren, leiden we hiervoor specifiek een formulering af in termen van modale Greense functies. We maken onderscheid tussen twee typen gelaagde media: de golfpijp en de vrije ruimte. Daarna formuleren we het veldverstrooiingsprobleem door de randvoorwaarden op te stellen die het bestaan van eenduidige EM velden garanderen. Dit veldverstrooiingsprobleem kunnen we in eerste instantie niet oplossen omdat we de Greense functie van deze configuratie met de metalen plaatjes en de gaten niet kennen. Door echter de metalen plaatjes in de juncties te verwijderen, of de gaten tussen de metalen plaatjes op te vullen met metaal, ontstaat een situatie waarin we de Greense functie in modale vorm kennen en reeds hadden afgeleid. Met behulp van het equivalentietheorema kunnen we deze nieuwe configuratie zodanig aanpassen – met behoud van kennis van de Greense functie – dat de oplossing van elektromagnetische velden identiek is aan die van de oorspronkelijke configuratie. Dit betekent dat er oppervlaktestromen geïntroduceerd moeten worden in de nieuwe configuratie. Deze oppervlaktestromen zijn nog onbekend en kunnen worden bepaald met een integraalvergelijking methode. Integraal, omdat we de velden als een convolutie in termen van de stromen hebben uitgedrukt. Het nu ontstane equivalente veldverstrooiingsprobleem lossen we op met behulp van een gekoppelde veldintegraalvergelijking, waarin de veldintegraalvergelijkingen voor de afzonderlijke juncties gecombineerd worden. De

oppervlaktestromen discretiseren we met behulp van ontwikkelfuncties. Voorbeelden die we behandelen zijn de rooftop en de Rao-Wilton-Glisson (RWG) ontwikkelfunctie. Daarna lossen we met behulp van de methode van de momenten de gediscretiseerde onbekende oppervlaktestromen op. Dit gehele proces reduceert de gekoppelde veldintegraalvergelijking tot een eenvoudige matrixvergelijking van het type  $L\mathbf{u} = \mathbf{f}$  met lineaire operator  $L$ , onbekende vector  $\mathbf{u}$ , en forceringsvector  $\mathbf{f}$ . Deze matrixvergelijking kan worden opgelost door gebruik te maken van eenvoudige inversie van  $L$  of van meer geavanceerde iteratieve oplossingschema's. Nadat we de oppervlaktestromen hebben berekend kunnen we het totale EM veld overall binnen de basisstructuur bepalen. Om het EM gedrag van de gehele stralende structuur te bepalen moeten we de individuele EM gedragingen van iedere afzonderlijke basisstructuur combineren. Dit doen we met behulp van de gegeneraliseerde verstrooiingsmatrix die dit gedrag voor iedere basis karakteriseert door de uitgaande EM golven te relateren aan de ingaande golven. Daarna formuleren we een procedure die twee van deze gegeneraliseerde verstrooiingsmatrices cascadeert. De uitkomst is een gegeneraliseerde verstrooiingsmatrix die het gedrag van de gecombineerde basisstructuren representeert.

In de totale berekening wordt het grootste deel van de tijd besteed aan het "vullen" van de lineaire operator  $L$ . We presenteren een nieuwe versnellingstechniek die een asymptotisch langzaam convergerende reeks bij de bepaling van  $L$  vertaalt in een numerieke integratie over een exponentieel snel convergerende reeks. Deze techniek reduceert de evaluatietijd van deze reeks en bestaat uit drie stappen. De eerste stap is een Kummer transformatie waarin het asymptotisch langzaam convergerende deel van de reeks wordt afgetrokken (hetgeen resulteert in een snel asymptotisch convergerende gereduceerde reeks) en wordt opgeteld (hetgeen resulteert in een langzaam asymptotisch convergerende correctiereeks). De tweede stap is een Ewald transformatie waarin de langzaam asymptotisch convergerende correctiereeks wordt vertaald in een integratie over  $\tau$  van exponentieel snel afvallende functies. Deze functies bevatten een exponentieel snel convergerende reeks waarvan de leidende term de vorm  $\exp(-k_t^2 \tau^{2\lambda})$  heeft. De derde stap is een opdeling van het integratieinterval over  $\tau$  in een deel voor kleine  $\tau$ , d.w.z.  $(0, \tau_1)$ , en een deel voor grote  $\tau$ , d.w.z.  $(\tau_1, \infty)$ . Daarna passen we een Poisson transformatie toe waarin de relatief langzame convergentie van de reeks in de exponentieel snel afvallende functies, veroorzaakt door het gedrag van  $\exp(-k_t^2 \tau^{2\lambda})$  voor kleine  $\tau$ , wordt omgezet in een exponentieel snel convergerende reeks. De leidende term voor het deel voor kleine  $\tau$  heeft de vorm  $\exp(-\rho^2/(4\tau^{2\lambda}))$ . De keuze voor het omslagpunt  $\tau_1$  van grote  $\tau$  naar kleine  $\tau$  is een compromis tussen de convergentiesnelheid voor de termen  $\exp(-k_t^2 \tau^{2\lambda})$  en  $\exp(-\rho^2/(4\tau^{2\lambda}))$ . Deze Poisson transformatie resulteert in een evaluatie van een zogenaamde exponentiële regularisatie van (een combinatie van) de expansie- en weegfuncties. Het uiteindelijke succes van de versnellingstechniek staat of valt met de mogelijkheid om deze exponentiële regularisatie snel te kunnen berekenen. Omdat de exponentiële regularisatie onafhankelijk is van de hoek van inval, de frequentie en van elke mediumparameter, kunnen we deze aan het begin van de totale berekening opslaan in een tabel. Dit leidt ertoe dat we kunnen afwegen of we gebruik gaan maken van deze versnellingstechniek. Omdat het

tijd kost om de tabel te genereren is de versnelde methode pas sneller dan de onversnelde vanaf een kritiek aantal simulatie stappen. Verder beschouwen we drie specifieke keuzes voor de ontwikkel- en weegfuncties. Deze drie keuzes leiden tot werkbare analytische oplossingen en numerieke benaderingen voor de exponentiële regularisatie. Als eerste beschouwen we de rooftop ontwikkel-functie (Cartesisch product van een driehoek- en een stapfunctie) gedefinieerd op een orthogonaal rooster. Deze keuze beperkt ons in het modelleren van de onbekende EM stroom in de structuur. De meeste structuren bevatten echter geen willekeurig wild gevormde metalen oppervlakten en de meesten hiervan zijn te vangen in dit orthogonale rooster. Een groot voordeel van dit rooster is dat we de exponentiële regularisatie kunnen schrijven in termen van complementaire error functies. Deze methode is voor een in dit proefschrift beschreven testvoorbeeld de snelste van de drie en heeft de minste tijd nodig om de exponentiële regularisatietabel te genereren. De tijd per simulatiestap is bijna acht keer korter in vergelijking met de onversnelde methode. Het kritieke moment wordt al bereikt bij de vijfde simulatie stap. In die speciale gevallen waarin de structuren in de eenheidscel niet te vangen zijn in een orthogonaal rooster kunnen we gebruik maken van de rooftop functie met een willekeurige oriëntatie. In dit geval kunnen we de exponentiële regularisatie schrijven als een convolutie van twee analytische functies die ieder een bijna begrensde bandbreedte hebben. Deze methode is voor hetzelfde testvoorbeeld langzamer dan de voorgaande. Dit komt doordat meer tijd nodig is voor de numerieke convolutie in de generatie van de exponentiële regularisatietabel. De tijd per simulatiestap is ook bij deze methode bijna acht keer korter dan de onversnelde methode. Het kritieke moment wordt pas bereikt bij een hoger aantal simulatiestappen. Als laatste beschouwen we de RWG functie. Met deze functie kunnen we de meest willekeurig gevormde metalen structuren in de eenheidscel beschrijven. In dit geval kunnen we de exponentiële regularisatie schrijven als een convolutie van twee numeriek benaderde functies die ieder bijna een begrensde bandbreedte hebben. Deze methode heeft voor hetzelfde testvoorbeeld de meeste tijd nodig om de exponentiële regularisatietabel te genereren. Dit komt naast de tijd die nodig is voor de numerieke convolutie ook door de extra tijd die nodig is voor het numeriek benaderen van de functies zelf. Een analytisch alternatief voor de numerieke benadering is beschikbaar. Het kritieke moment wordt pas bereikt na een groot aantal simulatiestappen (meer dan 600). Hier is de tijd per simulatiestap bijna zes keer korter dan de onversnelde methode. We kunnen concluderen dat het gebruik van deze versnellingsstechniek resulteert in een snelle rekenmethode.

Tot slot valideren we de rekenmethode door de gegenereerde resultaten te vergelijken met resultaten van commerciële softwarepakketten (zoals de eindige elementenmethode van ©HFSS) en met resultaten van golfpijpsimulatiormetingen. We doen dit aan de hand van acht verschillende vanuit de praktijk representatieve teststructuren, waarvan de eerste vijf verschillende typen frequentie selectieve oppervlaktes voorstellen, en de laatste drie verschillende typen stralers. Aan de hand van deze resultaten maken we aannemelijk dat de rekenmethode naast snel ook nauwkeurig is.

# Curriculum Vitae

Bart Johan Morsink was born in Alphen aan den Rijn, the Netherlands, on October 22, 1974. After he finished secondary school at the Christelijk Lyceum in Alphen aan den Rijn in 1993, he started as a student in Electrical Engineering at the Delft University of Technology. For his M.Sc. thesis he carried out research on the analysis and optimization of pulsed eddy current inspection techniques. These techniques are used within the oil industry to locate defects in pipelines due to corrosion without having to dismantle the whole pipeline. The result of this research was a software package that calculates electromagnetic fields and eddy currents in highly conductive planarly layered materials. The package was used to optimize a transmitter/receiver coil configuration which is part of the pulsed eddy current inspection technique. The research was done at the Shell Research and Technology Centre in Amsterdam and at the Laboratory of Electromagnetic Research under the supervision of prof.dr.ir. H. Blok. In 1997 he received the M.Sc. degree (cum laude).



Subsequently, he started in 1997 as an employee at Thales Netherlands (formerly known as Hollandse Signaalapparaten B.V.) in Hengelo, Overijssel, the Netherlands as a researcher/radar engineer at the antenna research and development department. Within Thales he has been involved for five years in the development and testing of APAR, the first naval X-band active phased array radar in operation within the Dutch and German navy. He has contributed by writing and using antenna simulation software for testing and validating the antenna concept in a compact antenna range (and on land and sea trials). Further within this project, he has validated and improved antenna calibration processes, beam-steering algorithms and special beam forming. The APAR project has given him in-depth knowledge on phased array antennas both in theory and practice.

The following two years up to the moment of this writing he has been involved in the development of a prototype Ka-band active phased reflective array antenna for guided ammunition support. Design and implementation of beam-steering

algorithms and antenna calibration processes, analysis of mechanical deformations and beam pointing accuracies have been studied in depth. Later on during this project he has verified the results of these studies by (re)writing and (re)using antenna simulation software (used for APAR) for testing and validating the antenna concept in a compact antenna range. The added value of this project compared to the APAR project is the developed in-depth knowledge on various design problems of reflective phased array antennas in particular.

In 2001 and in parallel with his work at Thales, he enrolled as a Ph.D. student at the Eindhoven University of Technology under the supervision of prof.dr. A.G. Tijhuis and dr.ir. G.H.C. van Werkhoven, where he carried out research on the fast analysis of planar phased array antennas and frequency selective surfaces to reduce design time. The work resulted in a fast computational method (with a numerical implementation called Luxaflex) described in this thesis which was presented at several international conferences [65, 66, 67].

# Acknowledgements

Many people have guided and helped me throughout this project over the past four years. The first person I would like to mention is my promotor Anton Tjihuis and I would like to thank him for all his suggestions and advice on the research, for providing me with elegant mathematical solutions and simplifications, and for the time he has taken to read my thesis which resulted in many suggestions for improvement. Next I would like to thank my copromotor and good colleague Gertjan van Werkhoven for the many numerous detailed in-depth discussions we have had for the last eight years on EM modeling problems, validation techniques and numerical/measurement results.

Then I would like to thank my second promotor Hans Blok and the remaining members of the reading committee Sjoerd Rienstra, Renato Orta, Peter Zwamborn and Piet van Genderen for their remarks and suggestions. In particular I would like to thank Renato Orta for his many suggestions for improvement of this thesis, and Sjoerd Rienstra for devising the first part of the acceleration technique described in this thesis.

Further I would like to thank my employer Thales Nederland B.V. in general for giving me the opportunity to do this Ph.D. Especially I would like to thank the management of the JRS-TU Antenna department for having the strong belief that this type of fundamental research (where some are allowed a certain degree of academic freedom) is the key to keeping alive a "high-tech" industry in the long term, and that cost issues in this matter play a less important role in the short term.

I would like to thank the members and several former members of the JRS-TU Antenna department at Thales Nederland B.V. for their interest and the many discussions we have had. In particular I would like to express my gratitude to my colleagues Simon van den Berg, Peter-Paul Borsboom and Stef van der Poel, who have contributed in many different ways, by providing me with their insights, simulation results from Luxaflex and results from other commercial software packages. They have helped a great deal in debugging and maturing Luxaflex. A special word of thanks goes to Bert Groenenboom for his in-depth mathematical explanations and discussions, and for correcting my proofs by contradiction.

Further I would like to thank my colleagues Hans Schipper, Corné Stoffels, Ton Polman, Jan Beuze, and Ronnie Spekhorst for sharing with me their knowledge on phased array antennas and measurement techniques. They have shown

me that the world is more than theory alone and starts with experiments to validate the theory. I am also grateful to John de Groot for providing me with the waveguide simulator measurements and to Dave Bekers for a number of discussions on the mathematical difficulties of the acceleration technique. Further, I would like to mention and thank Mark van Oudheusden, Arjan ter Huerne, Erik van der Wal, Jelmer Vos, Mark Vossen, Kiman Velt and Auke Ditzel for being truly nice colleagues for such a long time.

I would like to express my gratitude to my friends Andreas Feijen and David Ellerbeck for being my "paranimfen" during the defense of this thesis. Finally I would like to thank my friends Marnix van Bochove and Gjalt Reitsma for their support, and my friends in Twente: David Ellerbeck, Annemiek Schokker, Robert de Meijer, Cathelijne Burgman, Gilian Mischker, and Elles and Henk Luinge for the very nice time here in Twente and for the nice weekly dinners we have had together for a very long time now. Furthermore, I want to thank my mother for the support she gave me. Last but not least I would like to thank my brother Maarten, his girlfriend Emmeline, and my girlfriend Myrna for their love and support through thick and thin.